A PRIMER IN APPLIED RADIATION PHYSICS

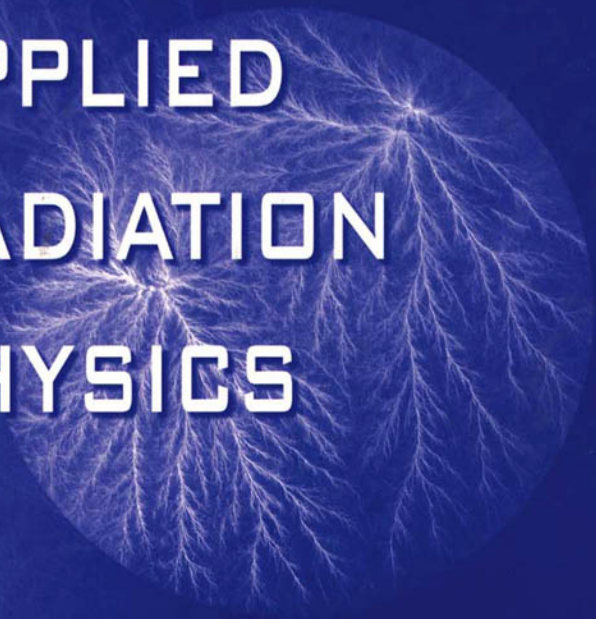

F A SMITH

World Scientific

A PRIMER IN

APPLIED RADIATION PHYSICS

A PRIMER IN APPLIED RADIATION PHYSICS

F A SMITH
Queen Mary & Westfield College, London

World Scientific
Singapore • New Jersey • London • Hong Kong

Published by

World Scientific Publishing Co. Pte. Ltd.

P O Box 128, Farrer Road, Singapore 912805

USA office: Suite 1B, 1060 Main Street, River Edge, NJ 07661

UK office: 57 Shelton Street, Covent Garden, London WC2H 9HE

British Library Cataloguing-in-Publication Data
A catalogue record for this book is available from the British Library.

A PRIMER IN APPLIED RADIATION PHYSICS

ISBN 981-02-3712-X
ISBN 981-02-3713-8 (pbk)

Printed in Singapore by Uto-Print

To Mary

(for her patience)

PREFACE

The aim of this volume is threefold. It is intended, firstly, as a revision aid for students on Masters level degree courses in Radiation Science. These will already have received lectures at various levels of detail on most of the topics covered here. Experience has shown, however, that in preparing for examinations, especially oral examinations, students benefit from an opportunity to put details in the context of the whole. This I have tried to do by drawing attention to important connections that exist between topics treated in different chapters. These generally involve an understanding of basic interaction processes.

Secondly, now that many universities and colleges offer courses in Radiation or Medical Physics to undergraduates, I have included a few examples of the basic concepts at a rather more elementary level in order to provide an introduction to the field. I will have achieved my aim of widening the appreciation of radiation science if this then leads to further study.

Thirdly, it is hoped that the book will provide a general introduction to Radiation Physics in general. My aim has been to make a comprehensive survey of what I believe to be the most significant current practices and techniques. In the interests of completeness I have included a treatment of neutron interactions and some of their applications, even though neutrons have not lived up to their expectations, either as a mode of radiotherapy or as the foundation of power generation.

The book is therefore not a textbook. Still less, is it a practical manual for hospital physicists, although it may act occasionally in both capacities. Its aim is to draw together the diversity of a subject that touches on aspects of biology and chemistry as well as on many branches of physics.

Although it is ionizing radiation that is of prime concern, the importance of magnetic resonance as an imaging modality is acknowledged briefly. Even though a similar case could be made for ultrasound imaging, there is a less obvious connection with radiation, and this topic is not covered. In any case, imaging as a whole has a vast array of literature, with many excellent reviews already extant. The imaging chapter is therefore no more than a personal survey of selected topics.

The material is based on my role as both lecturer and examiner on the University of London M.Sc. course in Radiation Physics, and also on my experience in teaching a third year B.Sc. course at Queen Mary and Westfield College.

I am most grateful to those of my colleagues who took the trouble to offer constructive comments and criticisms on some of my early drafts. Amongst these I particularly thank John Barton, Ian Blair, Alan Edwards, Gerry Lowe, Seeni Naidu, Beate Planskoy, Robert Speller and Jane Taylor. Additional advice and data for some of the figures and tables came from Julie Horrocks, John Lowe, Cyril Nimmon and Mark Roper. At the inception of the project the encouragement, enthusiasm and general bonhomie of the late Stan Klevenhagen gave me considerable insight into all aspects of hospital physics.

My more amateurish sketches were redrawn willingly by Steve Adams, to whom I am also extremely indebted for greatly assisting in the overall presentation.

ACKNOWLEDGEMENTS

Many of the diagrams in this book have been adapted from originals that have appeared in other books and journal articles. These have been identified in the captions and also in the references. I am most grateful to the publishers concerned, and their authors, for granting me permission to use their material.

Academic Press
American Institute of Physics
Cambridge University Press
CRC Press
Institute of Physics Publishing
The McGraw-Hill Companies
Medical Physics Publishing
Springer-Verlag GmbH
B.G.Teubner GmbH
Charles C.Thomas
John Wiley & Sons

CONTENTS

CHAPTER 5 : DETECTORS

CHAPTER 6 : MICRODOSIMETRY and RADIATION EFFECTS

CHAPTER 10 : IMAGING

CHAPTER 11 : RADIATION PROTECTION

CHAPTER 1

SOURCES OF RADIATION

1.1 Introduction

The radiation to which humans are exposed varies widely in :

- type and energy distribution,
- geographical distribution, and with
- occupation.

The main sources of radiation can be categorized as follows :

Category	Source/Machine	Radiation
Environmental	Cosmic Rays	neutrons, protons, electrons, photons
	Radioactivity	α- and β- particles, γ-rays, neutrons
Artificial	orthovoltage X-rays	kV X-rays
	linac/betatron	MV X-rays, electrons and radioactivity
	Van de Graaff and Cyclotron	protons, neutrons and radioactivity
	Synchrotron	electrons, protons, X-rays, uv photons
	Nuclear Reactor	neutrons, γ-rays, residual radioactivity

The minimum requirements for a full understanding of radiation action are :

- the energy spectrum of the incoming radiation,
- the energy-dependent cross-sections of the medium,
- the density and atomic number of the medium.

Table (1.1) Terrestrial sources of radiation averaged over the UK population [1]. The unit of exposure (μSv yr^{-1}) is defined in section 7.1. Large differences from these means are received by certain population groups (see chapter 11). Data for 1994 come from [1] in chapter 11.

Category	Main source	1986	1994
nuclear power	^{235}U fission products, ^{90}Sr,^{137}Cs	2	0.4
occupational exposure	X-rays, isotopes	8	7
weapons tests	^{235}U, ^{239}Pu fission products	10	5
everyday sources	coal, tobacco, air travel	10	0.4
medical tests	X-rays, radioisotope scans	250	370
cosmic rays	protons, electrons, neutrons	300	260
food	^{40}K, ^{137}Cs, ^{14}C,^{131}I	370	300
rocks and buildings	^{238}U, ^{235}U, ^{232}Th	400	350
atmosphere	^{222}Rn,^{137}Cs	800	1300
TOTAL		2150	2593

This chapter considers the energy spectra from some of the most important sources of radiation and, in the case of artificial sources, its dependence on the means of production. In the consideration of background radiation, Table (1.1) shows that there are contributions from both natural and man-made sources.

The natural environment accounts for ~ 80% of the radiation exposure of the UK population. Of this, α-particle emissions from atmospheric radon are by far the most important. Some building materials contain long-lived actinide elements in small quantities while traces of naturally occurring isotopes (^{40}K and ^{12}C) are present in all of us. More detailed figures are given in Chapter 11.

1.2 Cosmic Rays

Cosmic rays span a very wide range of energies (keV to GeV) and include charged particles as high in mass as the transition elements. From the radiation protection point of view, the most important are likely to be neutrons, electrons and protons (terrestrial cosmic rays). These are the consequence of interactions of primary cosmic rays with the earth's atmosphere. They span an approximate energy range from keV to MeV and are important at altitudes from sea level up to the height of commercial air travel.

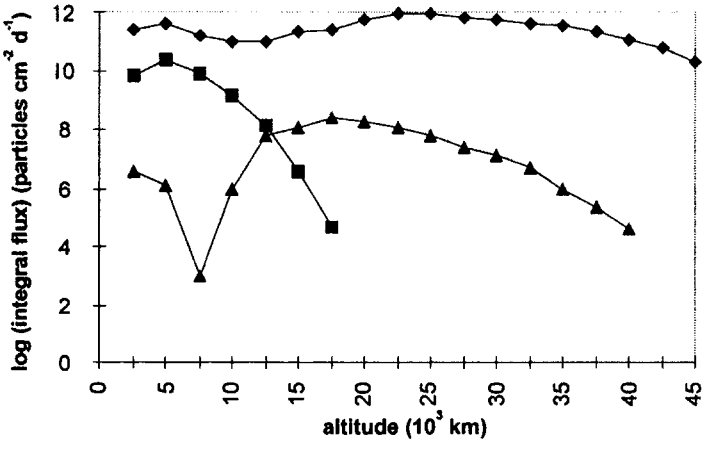

Fig. (1.1) Estimated log(integral flux) of electrons and protons versus altitude above mean sea level (MSL) in the equatorial plane. Units are particles cm^{-2} day^{-1}. Data taken from [2]. ◆ electrons > 0.5 MeV ■ protons > 10 MeV ▲ electrons > 4 MeV. Approximate fluxes at MSL are : neutrons 0.01 cm^{-2} s^{-1} MeV^{-1}, muons 0.009 cm^{-2} s^{-1} sr^{-1}, electrons 0.002 cm^{-2} s^{-1} sr^{-1}, protons 0.0002 cm^{-2} s^{-1} sr^{-1} [3].

At higher altitudes the very high fluxes of energetic charged particles, Fig. (1.1), may well affect the instrumentation required for satellite and space exploration. These cosmic rays are both galactic and solar in origin, the latter showing a variation due to the occurrence of solar flares.

Galactic and solar cosmic rays are affected by the earth's magnetic field. This gives rise to the radiation belts with the features known as the *polar horns* and the *South Atlantic anomaly*.

1.3 Radioactive Sources

Radioactive decay is the process by which a nucleus in an unstable state is able to

achieve greater stability by emitting a particle or photon.

The probability per second that the emission takes place is the decay constant. If there are N_0 nuclei present originally (at time $t = 0$), then at a later time t, there will be :

$$N_t = N_0 \exp(-\lambda t)$$

The decay constant, λ, is independent of t.

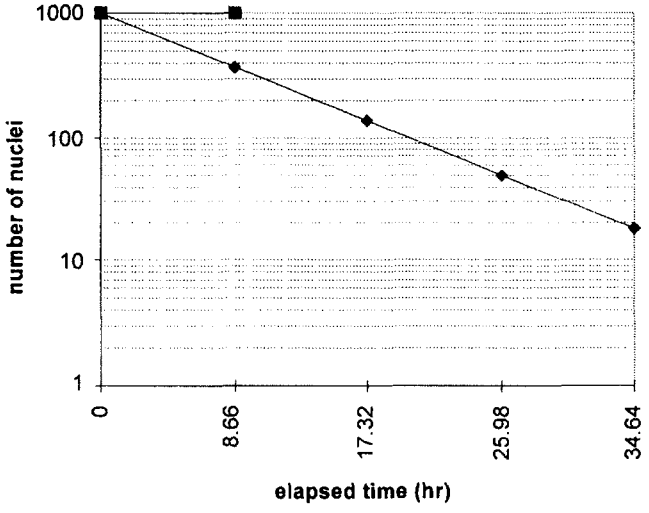

Fig.(1.2) Decay of ^{99m}Tc. $T_{1/2}$ = 6hr, τ = 8.66hr. N_0 = 1000 nuclei. As elapsed time goes from 0, τ, 2τ, 3τ.... the number of nuclei that have not decayed decreases from 1000, 1000/e, 1000/e^2, 1000/e^3... The area under the graph = N_0 since as time proceeds towards infinity, all nuclei will decay. This area is also the same as the rectangle defined by the original activity ($N_0\lambda$) times the mean lifetime (τ).

The mean lifetime against decay is $\tau = 1/\lambda$. This is the average time for the number of radioactive nuclei to decrease by *1/e* (1/2.71828 = 0.36788). An alternative measure of this probability is the average time for the number of radioactive nuclei to halve. In this case, $N_t = N_0/2$, so $T_{1/2} = \ln 2/\lambda = 0.693/\lambda$.

The activity of a radioactive substance, A, is defined as the number of disintegrations per second, i.e. $A = N\lambda$. Therefore :

$$A_t = A_0 \exp(-\lambda t) \qquad (1.1)$$

and the unit of activity, the Becquerel (Bq) = 1 disintegration per second. The old

unit is the Curie (Ci) which is the activity of 1g of radium = 3.7×10^{10} Bq. A convenient benchmark worth remembering is 100 μCi = 3.7 MBq.

At any one time, the number of radioactive atoms present is the product of the activity and the mean lifetime, i.e. $(N\lambda)\tau = N$.

1.3.1 Beta decay

The three forms of beta decay are β^- emission, β^+ emission and electron capture and they are called isobaric decay because the mass number of the nucleus does not change. The charge of the nucleus, Z, changes by ±1.

$$n \rightarrow p + e^- + \bar{\nu}_e$$
$$p \rightarrow n + e^+ + \nu_e$$
$$p + e^- \rightarrow n + \nu_e$$

In β^- emission, the massive residual nucleus receives only a small fraction of the available kinetic energy. This means that energy is essentially conserved between the electron and the accompanying antineutrino. However, because of the presence of the residual nucleus, momentum need not be conserved between the two emitted particles – the electron and the antineutrino.

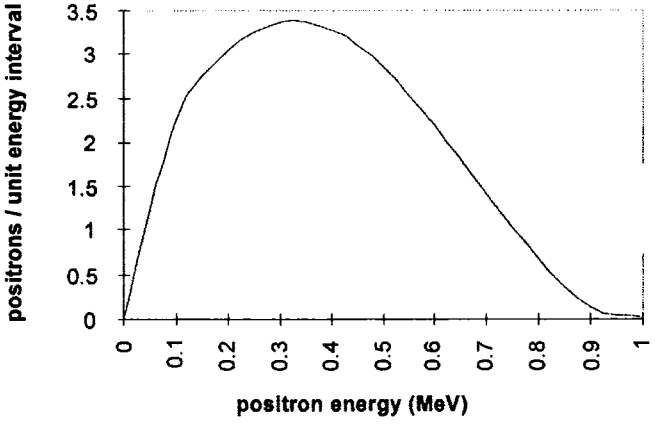

Fig.(1.3) Approximate energy spectrum of positrons from ^{11}C assuming F(Z,W) and $|P|^2$ are both unity. $E_{\beta,max}$ = 0.97 MeV.

The energy spectrum for an allowed decay can be re-expressed from the expression for the momentum distribution, [4], as :

$$N(W)\,dW = \frac{|P|^2}{\tau_0} F(Z,W)\left(W^2-1\right)^{1/2}\left(W_0-W\right)^2 W\,dW \qquad (1.2)$$

This gives the number of β particles emitted with an energy between W and $W+dW$ where W is the total electron energy normalized to the rest mass energy, $(W= (E_\beta/m_0c^2)+1)$. W_0 is the total energy of the transition, $W_0 = (E_{\beta,max}/m_0c^2)+ 1$. The other three terms in this expression are :

- the square of the transition matrix element $|P|^2$. This represents the overlap of the nucleon wave functions of the initial state before the decay, and the final state after the decay has taken place. For allowed transitions this is of the order of unity.
- the Coulomb correction factor, $F(Z,W)$. This accounts for the force exerted on the emitted electron or positron when it is still within the vicinity of the nucleus. The deceleration of an electron produces more low energy β^- particles, and the acceleration of a positron fewer low energy β^+ particles than would otherwise be expected when their energies are measured at infinity. For the (unrealistic) case of Z=0, the function $F(Z,W)=1$.
- the β-decay constant, $\tau_0 = h^7/(64\pi^4 m_0^5 c^4 g^2)$ with a value of ≈ 7000 s. The precise value depends on the value of the Fermi constant, $g \approx 10^{-48}$ m^3 J.

The shape of Fig.(1.3) will alter as both the Coulomb correction factor and the square of the interaction matrix element depart from unity. In particular :

- when a realistic $F(Z,W)$ is used for the ^{11}C spectrum, it will show fewer positrons emitted at low energies.
- for an allowed β^- emitter, the number of low energy particles will be enhanced. This means that the electron energy spectrum will not fall to zero at low energies.
- a change of shape also occurs when the decay becomes less allowed [4].

The decay constant is given by the integration of Eq.(1.2) over all energies :

$$\lambda = \frac{0.693}{T_{1/2}} = \int_1^{W_0} N(W)\,dW \qquad (1.3)$$

1.3.2 Gamma decay

When a nucleus de-excites by the emission of γ-radiation, the energy spectrum will be discrete since it is governed by transitions between quantized nuclear energy levels.

The selection rules which govern these transitions are determined by the spins and parities of the levels involved. For levels having energies and spins E_0, I_0 and E_1, I_1 the energy of the emission is :

$$h\nu = E_1 - E_0 \tag{1.4}$$

while the change in angular momentum is :

$$\Delta I = I_1 - I_0 \leq \ell \leq I_1 + I_0 \tag{1.5}$$

where ℓ is the non-zero angular momentum carried away by the emitted photon.

The multipolarity of the radiation is 2^{ℓ} such that $\ell = 0,1,2...$ corresponds to monopole, dipole, quadrupole.... radiation respectively. However, transitions are prohibited between states having $I_1 = I_0 = 0$. This is because the transverse nature of electro-magnetic radiation prohibits the emission of an $\ell = 0$ monopole.

A distinction is made between electric and magnetic radiation on the basis of the parity change, $\Delta\pi$. Electric radiation corresponds to a change of $(-1)^{\ell}$ and magnetic radiation to $-(-1)^{\ell}$. Thus, for a transition between levels in which there is no change in parity, ℓ can only be 0 or even for electric radiation and odd for magnetic radiation.

An approximate relation between the energy of electric radiation and the probability of its emission is given by [5] :

$$\lambda_{el} = \frac{1}{\tau_{el}} = S\,\frac{2\pi\nu}{137}\left(\frac{R}{\lambda}\right)^{2\ell} \tag{1.6}$$

for a nucleus of mass number A and radius $R=R_0 A^{1/3}$ ($R_0 = 1.20 \pm 0.03$ fm is the nuclear unit radius). S is a statistical factor [4] given by :

$$S = \frac{2(\ell+1)}{\ell\left[1\times 3\times 5\ldots(2\ell+1)\right]^2}\left(\frac{3}{\ell+3}\right)^2 \tag{1.7}$$

Since the probability of a transition is proportional to S, it decreases rapidly as ℓ becomes larger than unity.

For the same multipolarity, the probability of a magnetic transition is smaller by a factor of about 10.

$$\frac{\tau_m}{\tau_{el}} \approx 4.4 \times A^{2/3} \tag{1.8}$$

In Fig.(1.4) the difference in spin of the 171keV transition is unity, with no parity

change. The most likely emission is therefore M1 with a small admixture of E2. Even though an ℓ =2 transition is less likely than ℓ = 1 by a factor of 210, Eq.(1.7), an electric transition of the same angular momentum is more likely by a factor of 102, Eq.(1.8).

A difference in the relative probabilities of 102/210 is not sufficiently small to make the decay pure M1 in character. Since these arguments work the other way when ℓ =2 with no parity change, the 245 keV line is pure E2.

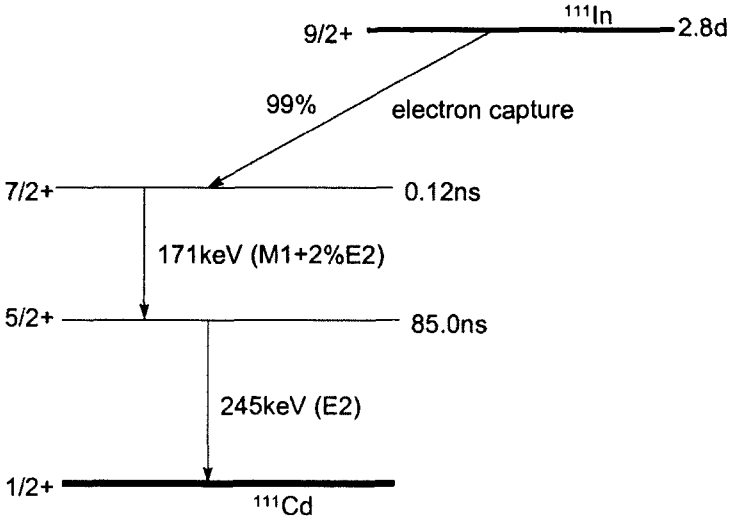

Fig.(1.4) Partial decay scheme of ^{111}In.

1.3.3 Alpha decay

The emissions from α-decay are also discrete in energy. Being an assembly of 2 protons and 2 neutrons, the energetics of α-particle emission can be understood initially using the semi-empirical mass formula [4]. This gives the total mass of a nucleus in terms of the number of protons and neutrons. Neglecting any electronic binding energy :

$$M(Z,A) = Zm_p + (A-Z)m_n - k_v A + k_s A^{2/3} + k_c Z^2 / A^{1/3} + k_a (A-2Z)^2 / A \pm \delta \qquad (1.9)$$

where k_v, k_s, k_c, k_a and δ are called the volume, surface, Coulomb, asymmetry and pairing constants. The binding energy of the nucleus *M(Z,A)* is the sum of the last

five terms in Eq.(1.9).

Energy released when a parent nucleus, mass number A and charge number Z, decays to a daughter of mass A - 4 and charge Z - 2, is :

$$Q = M(Z,A) - M(Z-2,A-4) - M(^4He) \tag{1.10}$$

where $M(Z,A)$ is the mass of the parent nucleus.

Substitution of Eq.(1.9) into Eq.(1.10), and using 28.3 MeV for the binding energy of the ^{4}He nucleus, gives the α-decay energy. This can be written :

$$E_\alpha = 28.3 - 4k_v + \frac{8}{3}\frac{1}{A^{1/3}}k_s + 4k_c\frac{Z}{A^{1/3}}\left(1-\frac{Z}{3A}\right) - 4k_a\left(1-\frac{2Z}{A}\right)^2 \tag{1.11}$$

Eq.(1.11) applies to ground-state to ground-state transitions between parent and daughter nuclei. In this transition Z and A refer to the mean values of the two nuclei. A transition which involves an excited state of either of the nuclei will add to, or subtract from, E_α.

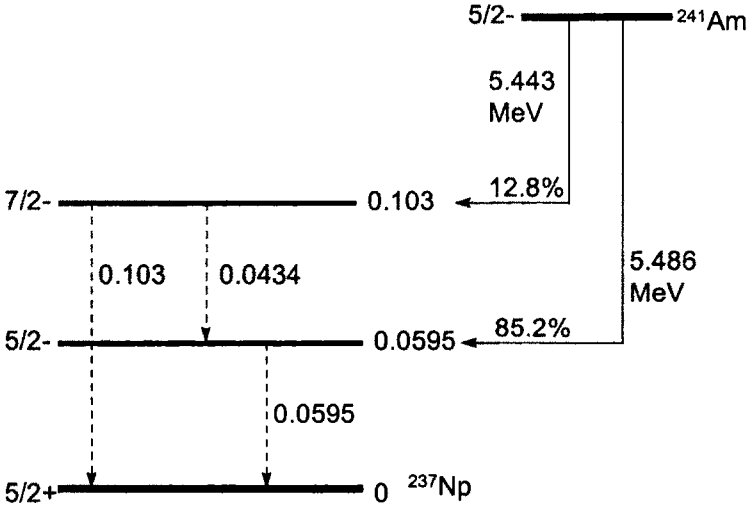

Fig.(1.5) Partial decay scheme of ^{241}Am → ^{237}Np. The two principal α-particle energies are 5.486 MeV (85.2%) and 5.443 MeV (12.8%), both to excited states of the ^{237}Np daughter nucleus. The subsequent decay of the 0.0595 MeV state is by γ-emission to the ^{237}Np ground state. The α-energies not shown in the figure lie in the range 5.545 MeV to 4.800 MeV. ^{241}Am has a half-life of 433 yr.

1.3.4 Neutron (fission) decay

Certain of the actinide nuclei are capable of undergoing spontaneous (as opposed to induced) fission. They are also all α -particle emitters. As Table 1.2 shows, however, the probability of α-emission is always greater than the probability of spontaneous fission, although in ^{252}Cf the probabilities are much closer. Since there is in addition a greater neutron yield, ^{252}Cf is the isotope of choice for the production of a fission neutron spectrum.

All neutron-emitting sources are encapsulated within a high-quality welded stainless steel container that has a thickness greater than the range of the most energetic a-particle. For high-activity sources the energy deposited into the walls of the container will result in a perceptible rise in temperature.

Table (1.2) Some spontaneous fission neutron sources

Nuclide	α-emission half-life	n-emission half-life	neutron per fission	neutron $mg^{-1}\ s^{-1}$
^{242}Cm	162.8 d	6.1×10^{6} yr	2.3	1.7×10^{4}
^{244}Cm	18.1 yr	1.35×10^{7} yr	2.6	9×10^{3}
^{252}Cf	2.64 yr	82.5 yr	3.5	2.7×10^{9}

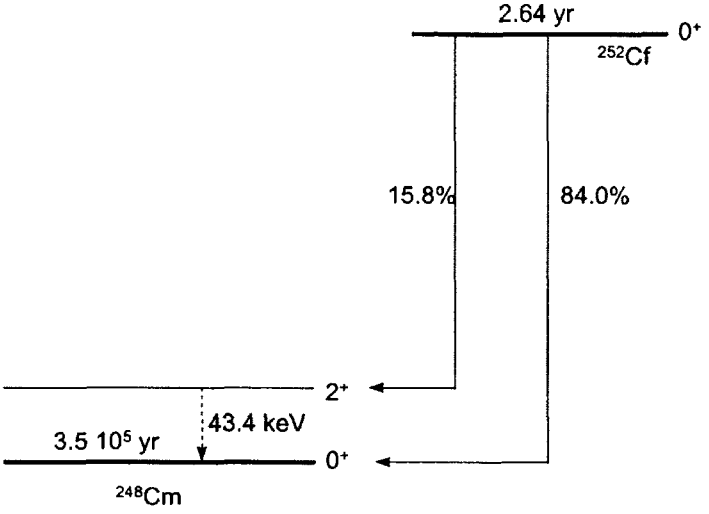

Fig.(1.6) Principal decay scheme of ^{252}Cf. The α-particle energies are 6.118 MeV (84%) and 6.076 MeV (15.8%).

An empirical expression [6] which gives the fraction $S(E)dE$ of fission neutrons with energy in the range between E and $E+dE$ is :

$$S(E) = 0.771\sqrt{E}\,\exp(-0.776 \times E) \tag{1.12}$$

This is normalized to unity such that :

$$\int_0^\infty S(E)dE = 1$$

and plotted in Fig.(1.7). The mean energy of the distribution, Eq.(1.13), has a value of 1.93 MeV.

$$\overline{E} = \frac{\int_0^\infty E\,S(E)\,dE}{\int_0^\infty S(E)\,dE} \tag{1.13}$$

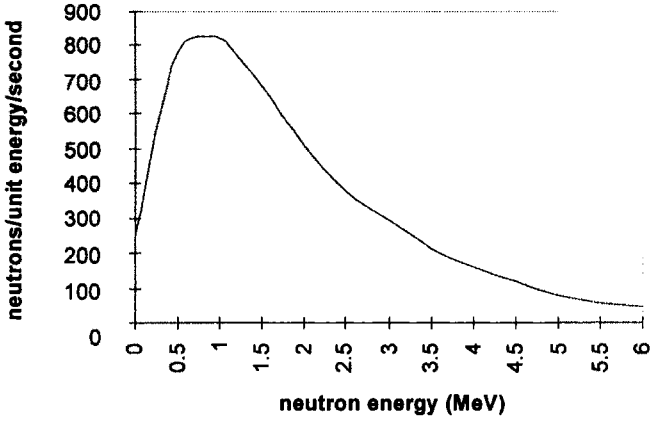

Fig.(1.7) Energy spectrum of fission neutrons.

1.4 Accelerators

1.4.1 Cockcroft-Walton generator

The Cockcroft–Walton voltage multiplier rests on the principle of the sequential sharing of charge between two columns of capacitors. In Fig.(1.8), a voltage V applied across capacitor C_1 is shared with capacitor K_1 when the switch mechanism is down. When the switch is moved up, the initial charge on K_1 (VK_1) is shared with C_2 to produce a voltage $VK_1/(K_1+C_2)$ on the left-hand column. When the switch moves down again, K_1 is recharged to voltage V and the charge on C_2 is shared with K_2. This step-wise transfer of charge between the left-hand and right-hand columns finally results in steady voltages of 2V, 3V... between the capacitors on the left-hand column.

In practice, the initial voltage is supplied from the secondary windings of a transformer (at frequency $\omega = 2\pi f$), and the capacitor columns are connected via rectifiers. The oscillatory nature of the input voltage performs the same function as the mechanical switch, since charge can be shared between capacitors when the driving voltage on the right-hand column is in the negative half cycle.

When the base of the left-hand column is grounded, as in Fig.(1.8), the base of the right-hand column swings between +V and -V (*i.e.* V $\sin\omega t$). Voltages between the capacitors on the right-hand column are then V + V $\sin\omega t$, 3V + V $\sin\omega t$, 5V + V $\sin\omega t$ and so on.

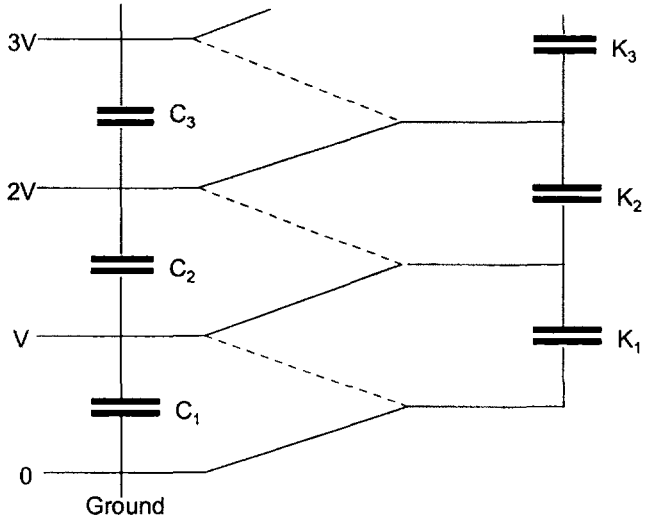

Fig.(1.8) The principle of a Cockcroft–Walton Voltage Multiplier. A bank of capacitors is charged in parallel and discharged in series.

For a total number N of equal-value capacitors C in both columns, the steady output voltage generated at the top of the left hand column is approximately :

$$V_{out} = N\,V_{in} - \frac{2\pi I N^3}{12\omega C} \qquad (1.14)$$

where I is the particle current drawn from the ion source at the top of the left-hand column [7]. This current tends to reduce V_{out}.

The optimum number of multiplying stages in such a generator is obtained by differentiating Eq.(1.14) with respect to N. In addition, there will be a ripple ΔV on the output voltage.

$$N_{optimum} = \sqrt{\frac{2\omega C V_{in}}{\pi I}}$$

$$\Delta V = \frac{I\pi}{8\omega C} N(N+2)$$

From Eq.(1.14) it is seen that large terminal potentials are produced with large values of C and ω and a small I. These conditions also result in a small ripple, ΔV, once the optimum number of stages has been determined.

1.4.2 Van de Graaff generator

The electrostatic charging of a metallic sphere takes place by means of two sets of corona points (a "comb" made of small diameter wires). One of these is at ground potential and the other is inside the high voltage terminal. To achieve a positive terminal potential the corona points at ground potential have one end connected to the positive terminal of a dc power supply. The other end has sharp points which lightly touch a flexible insulating belt, the purpose of which is to carry the charges up the potential gradient to the high voltage terminal. Inside the terminal the corona points are also in light contact with the belt and are connected to the spherical terminal through a large resistor R.

If the charging current carried upwards by the belt into the terminal (capacitance C with respect to ground) is dq/dt C s^{-1}, then the rate of increase of terminal potential is :

$$\frac{dV}{dt} = \frac{1}{C}\frac{dq}{dt}$$

The capacitance of a sphere of radius r is $C = 4\pi\varepsilon_0 r$. In SI units, C is in Farads, r in

metres and ε_0, the permittivity of free space, is 1.11×10^{-10} Fm^{-1}.

For practical reasons, the terminal must be enclosed within an outer sphere, radius R. In this case, the capacitance to ground becomes, [7] :

$$C = 1.11 \times 10^{-10} \frac{R\,r}{R-r}$$

For R = 1 m, r = 0.5 m and a charging current of 0.5 mA, dV/dt is 4.5 MV s^{-1}.

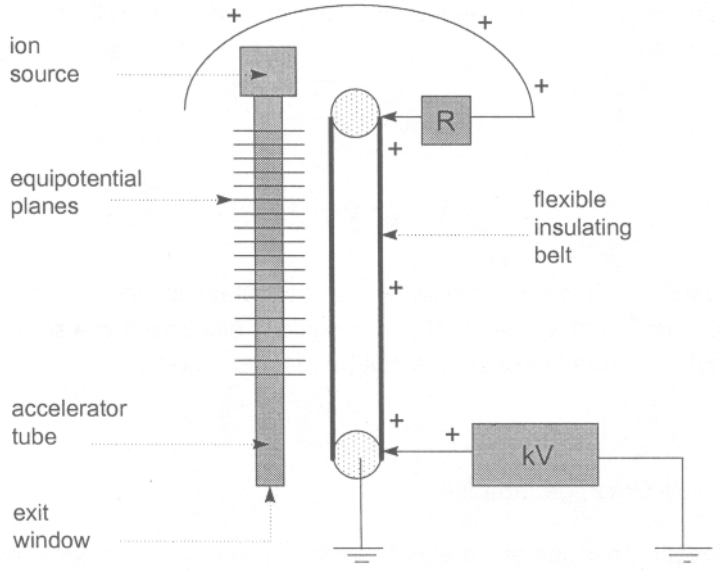

Fig.(1.9) The main features of a Van de Graaff generator. Corona points connected to the positive terminal of a dc power supply attract negative charge from a flexible insulating belt, rendering it positive. Because the belt is insulating, the charges remain in place and are carried upwards towards a similar set of corona points in the centre of a hollow metallic terminal sphere. These excess charges are neutralized by electrons drawn from the sphere which then becomes positively charged. The reverse process takes place as the belt moves downwards towards ground potential.

This acceleration method can be used with either positive or negative terminal potentials. For electron acceleration, the terminal voltage is generally lower than for positive ions, but the available beam current is generally higher.

Electrical breakdown

The electric field on the surface of the inner sphere, V/r, will be in the order of MV m^{-1}. If this exceeds the breakdown strength of the medium surrounding the

sphere, electrical discharge and loss of terminal voltage will result. Even dry air at atmospheric pressure has a breakdown strength in the MV m^{-1} region.

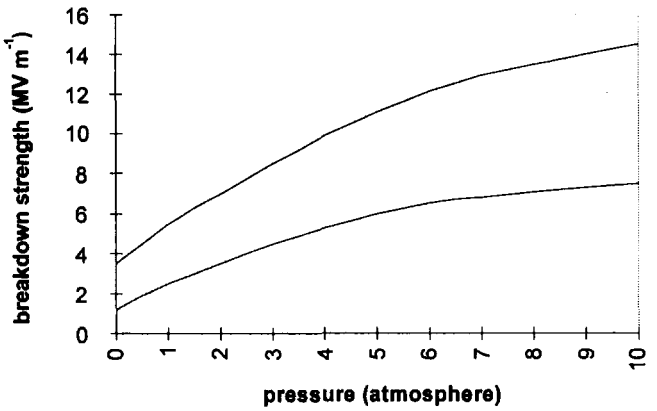

Fig.(1.10) Pressure dependence of breakdown strength (MV m^{-1}) in gases: dry air (bottom), sulphur hexafluoride, SF_6 (top), [7].

Although gases such as freon, CCl_2F_6, and sulphur hexafluoride, SF_6, have much greater dielectric strengths, their use is restricted because of their corrosive nature. As a result there is a tendency to produce breakdown products which impair the surface cleanliness of spark gaps on equi-potential rings, resistor chains, and other structural members. In time, this contamination leads to loss of insulation, thereby negating the advantages of the high breakdown strength of the gas itself. The most widely-used high pressure gas combination is ~ 80% N_2 and ~ 20% CO_2.

Electron loading

The accelerator tube consists of a series of conducting rings (generally aluminium) that are separated by high quality quartz insulators. High value resistors (~1 – 2 MΩ) across successive rings maintain a uniform potential drop from the terminal voltage to ground. Since there is no opportunity for beam focusing during the acceleration stage, the accelerated particles can strike the sides of the accelerator tube and release secondary electrons.

When the terminal potential is positive, these electrons are accelerated towards the terminal where they can generate *bremsstrahlung* X-rays. The two consequences are :

- The electron current that flows up the potential gradient adds to the positive current down the gradient. The load on the terminal potential is thereby increased.
- Secondary electrons produced near ground potential are accelerated to the maximum extent, and produce X-rays in the terminal structure very efficiently.

The effect constitutes a radiation protection problem near the terminal end of all positive ion Van de Graaff generators.

Tandem acceleration

In a conventional single-stage accelerator, the ion source is located within the high voltage terminal. Particles can be accelerated to double the terminal potential (although with much less efficiency) by using certain techniques of adding electrons to, and then stripping electrons from, an ion.

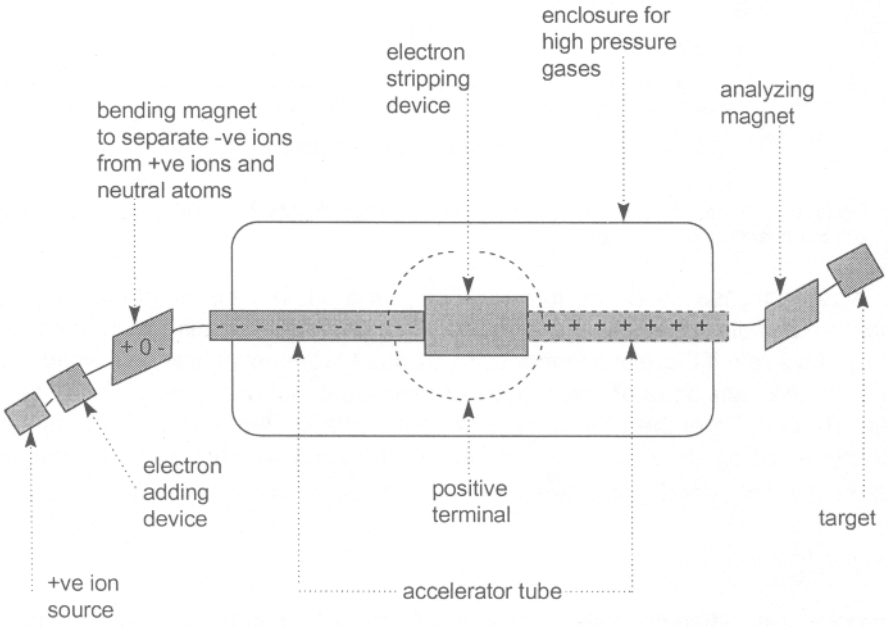

Fig.(1.11) A schematic diagram of the tandem Van de Graaff principle, [7].

When low energy protons pass through low pressure hydrogen gas, the emerging particles consist mainly of protons, with small quantities of neutral hydrogen atoms and even smaller quantities of H^- ions. These can be separated magnetically and the H^- accelerated towards the high positive terminal potential. When they reach this high energy, and are passed through a similar low pressure gas (or carbon foil), the probability of electron stripping becomes much higher than electron addition. The ions therefore emerge as protons once again, to be accelerated down to ground potential.

The efficiency of electron addition depends upon ion velocity and gas pressure, but is generally not greater than ~1%. The efficiency of electron stripping is much higher. This use of a single terminal potential to double the energy of the particles

has been achieved at the cost of reducing the particle current by a factor of 10^{-2} - 10^{-3}.

An ion source which could deliver a current of 1mA from a 6 MV terminal would be reduced to ~10 μA at ~12 MV in the tandem mode.

Induction rather than electrostatic charging

Continual abrasion of the belt surface by the corona points produces surface irregularities which gradually render the belt no longer capable of transferring charge. Such limitations can be overcome by the use of an induction mechanism.

This replaces the electrostatic belt by a series of stainless steel and aluminium conductors separated by glass-loaded nylon insulators. In this "laddertron" arrangement beam currents of ~ 0.5 mA can be produced from terminal voltages approaching 30 MV.

1.4.3 Cyclotron

A conventional cyclotron uses resonance radio-frequency (rf) acceleration of heavy charged particles in a uniform dc magnetic field. This is achieved by placing an ion source at the centre of two "D"-shaped semicircular, hollow electrodes. The rf field is applied across the electrodes such that each "D" goes alternately positive and negative at the rf frequency, f_0. The cyclotron can only be used to accelerate heavy ions (p, d, He, H^- ....).

The motion of a particle of mass m and charge ze having velocity v, moving in a magnetic induction *B* with radius r, is governed by the Lorentz and centripetal forces.

$$B\ ze\ v = m\frac{v^2}{r} \tag{1.15}$$

The total energy *E* of the particle having kinetic energy *T*, is :

$$E = T + W_0 = T + m_0c^2 = mc^2 = \frac{m_0c^2}{\sqrt{\left(1-\beta^2\right)}} \tag{1.16}$$

where W_0 is the rest energy of the particle and $\beta = v/c$. Using Eqs.(1.15) and (1.16), the orbital frequency of the ion can be written :

$$f_i = \frac{v}{2\pi r} = \frac{ze\ B}{2\pi m} = \frac{ze\ B\ c^2}{2\pi\left(W_0 + T\right)} \tag{1.17}$$

The resonance acceleration can be maintained only for a constant frequency, f_0. Since the kinetic energy of the particle increases with each crossing of the gap, the condition $f_i = f_0$ is only possible if $T << W_0$, *i.e.* at low energies.

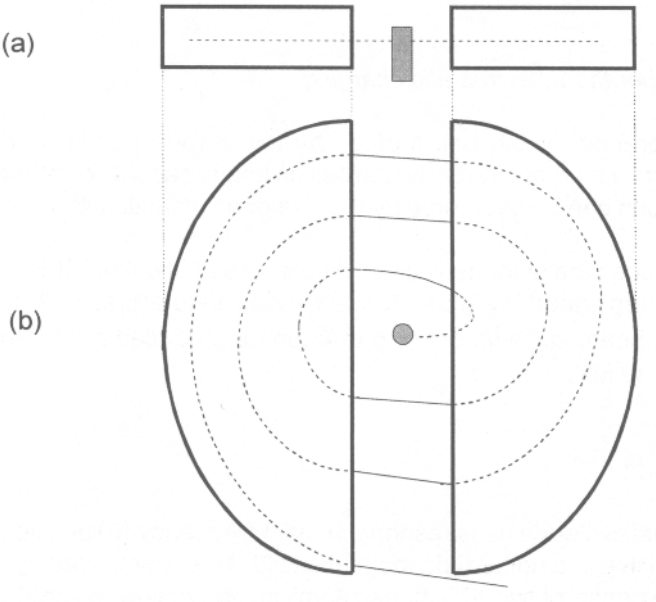

Fig.(1.12) Schematic diagram of the "D" structure of a cyclotron. (a) cross section (b) plan view. The ion source is at the centre and the dc magnetic field lines are perpendicular to the plane of the diagram, [7].

A positive ion which emerges from the source in Fig.(1.12) is accelerated when the right-hand D is in the negative half cycle. There is no accelerating field within the hollow D so the particle experiences only the magnetic field. The particle follows a semicircular path until it reaches the edge of the D. If the time to traverse this path is the same as the time necessary for the left-hand D to become negative, the acceleration process will continue. For continuous acceleration the phase of the rf field must be slightly ahead of the phase at which the particle crosses the gap. This is the resonance condition.

Weak-focusing

The requirement is that the lines of magnetic induction are always concave inwards towards the centre of revolution of the ions. This is achieved by the introduction of shim material, Fig.(1.13), in the central regions of the field together with the shaping of the pole pieces at the extremities of the field.

To set up the condition of weak-focusing, the magnetic induction B_0 at a final orbit radius of r_0 is first specified. At any other radius, r, the magnetic induction must then be given by :

$$B = B_0\left(\frac{r_0}{r}\right)^n$$

where $0<n<1$ for particles travelling near the final orbit radius. The consequence of this restoring force is that there are oscillations of the ion in both radial and axial di

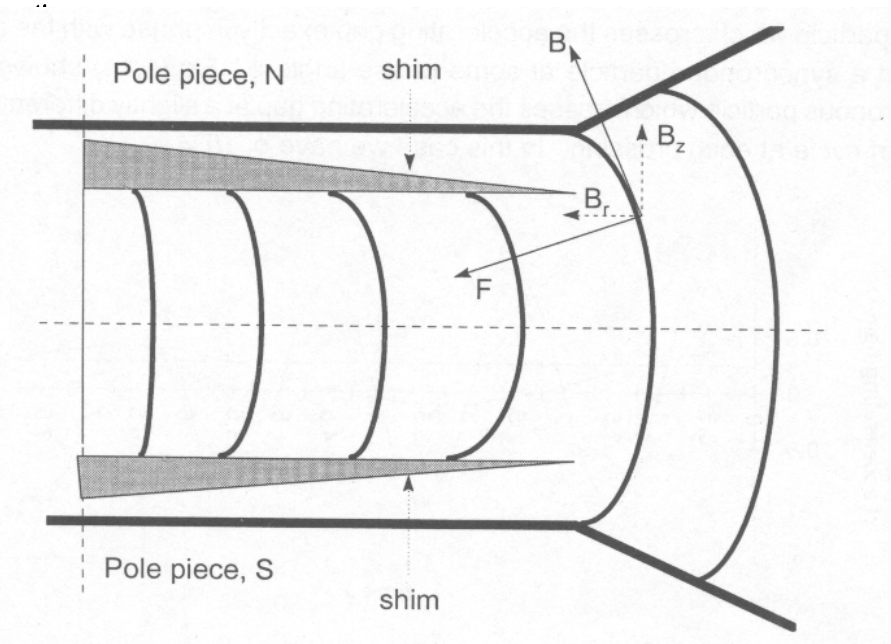

Fig.(1.13) Lines of magnetic induction in a weak-focusing field. A particle which is not travelling on the central plane will experience a force F which always tends to restore it into the central plane. This has an axial component F_z towards the central plane and a radial component F_r towards the centre of revolution, [7].

These oscillations have frequencies, [7] :

$$\text{Axial: } f_z = n^{1/2} f_i$$

$$\text{Radial: } f_r = (1-n)^{1/2} f_i$$

and are always smaller than the ion frequency, hence the name 'weak-focusing'. The overriding requirement is that the magnetic induction decreases as the radius increases.

Phase stability

The above requirement for weak-focusing is not consistent with the resonance

condition in Eq.(1.17). As T becomes significant with respect to W_0 the ion frequency f_i decreases. In order to maintain the resonance condition in a constant magnetic field, either :

- the rf frequency f_0 must also decrease or,
- if f_0 remains constant, B must increase as r increases. Certainly it cannot decrease, as in weak-focusing.

A particle which crosses the accelerating gap exactly in phase with the rf field is termed a synchronous particle at some phase angle ϕ_s. Fig.(1.14) shows a non-synchronous particle which crosses the accelerating gap at a slightly different phases of the rf cycle at each crossing. In this case we have $\phi_{ns}(t) \neq \phi_s$.

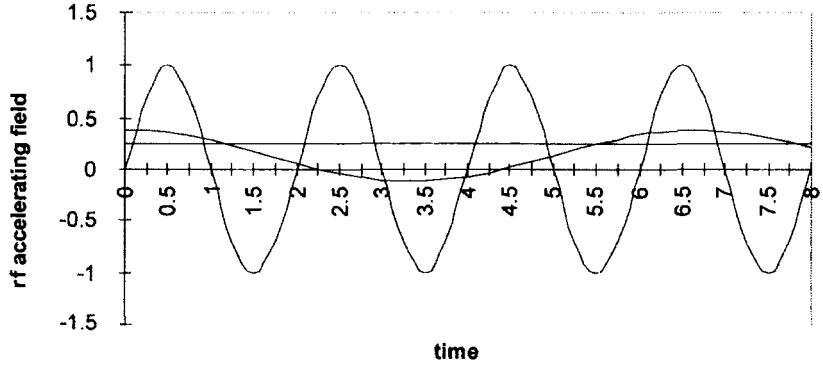

Fig.(1.14) A representation of a sinusoidal constant-frequency rf accelerating field. The equilibrium condition for a synchronous particle is that it always crosses the gap at the same phase (e.g. when the rf field is +0.25 arbitrary units). If a non-synchronous particle crosses the gap when the field is 0.28 and the phase equivalent to 0.8, when it next crosses the gap (when the phase is 3.05) it experiences a decelerating field (-0.1).

From Eq.(1.15) and the relation $pc=(T(T+2W_0))^{1/2}$, the radius of motion of a relativistic particle is given by :

$$r = \frac{\left[T(T + 2W_0)\right]^{1/2}}{B\ ze\ c} \tag{1.18}$$

Thus if a non-synchronous particle crosses the gap at a slightly earlier phase than ϕ_s, it receives more energy than it would if it crossed the gap at ϕ_s. From Eq.(1.18) the radius is therefore larger and the time taken before it makes its next crossing is longer than would otherwise be the case. The accelerating field at the next crossing is thus reduced, so the radius, and therefore the orbital transit time, is increased. A non-synchronous particle therefore oscillates in both phase and energy about the values for a synchronous particle.

This problem was overcome in the synchrocyclotron by modulating the rf frequency and only accelerating the particles on the decreasing frequency part of the modulation cycle. The alternative is to modify the magnetic field in order that the resonance condition in Eq.(1.17) is maintained. This method is used in the isochronous or azimuthally-focused cyclotron.

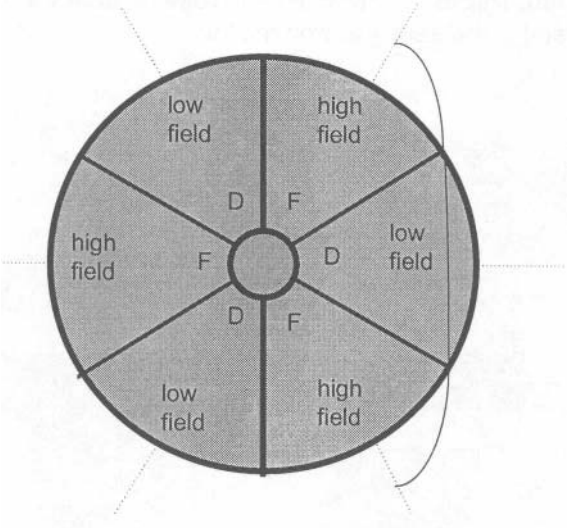

Fig.(1.15) The principle of focusing and de-focusing in a sector (or azimuthally) -focused cyclotron showing three high (focusing-F) and three low (defocusing-D) magnet sectors. A schematic trajectory of a non-equilibrium particle traversing a single focusing-de-focusing-focusing element is shown.

Isochronous cyclotron

An isochronous cyclotron is one in which the particle has an orbital period independent of energy. To use the principle of Alternating Gradient Focussing in the cyclotron, where the particle orbit increases continuously as the energy increases, the magnetic pole pieces are sectored Figure (1.15). Adjacent sectors produce a field round the orbit which is alternately high and low. This creates the necessary focusing and de-focusing conditions. The particle orbit is then no longer circular but has oscillations imposed upon it with a frequency determined by the number of sectors.

The result is a fixed frequency cyclotron in which a particle in a final non-equilibrium orbit is alternately focused and de-focused about the equilibrium orbit. The radial oscillation frequency in Fig.(1.15) is $f_r = 3f_i$. Typical proton energies of ~ 500 MeV can be reached with such a system.

1.4.4 Electron linear accelerator (electron linac)

The principle of the cyclotron can be considered as a resonance acceleration across a gap between two electrodes connected to a high frequency rf supply. This is followed by the drift of the particle in a magnetic field during which no additional energy is imparted. This "drift" principle is also used in heavy-ion linear accelerators and was also used in the early electron machines.

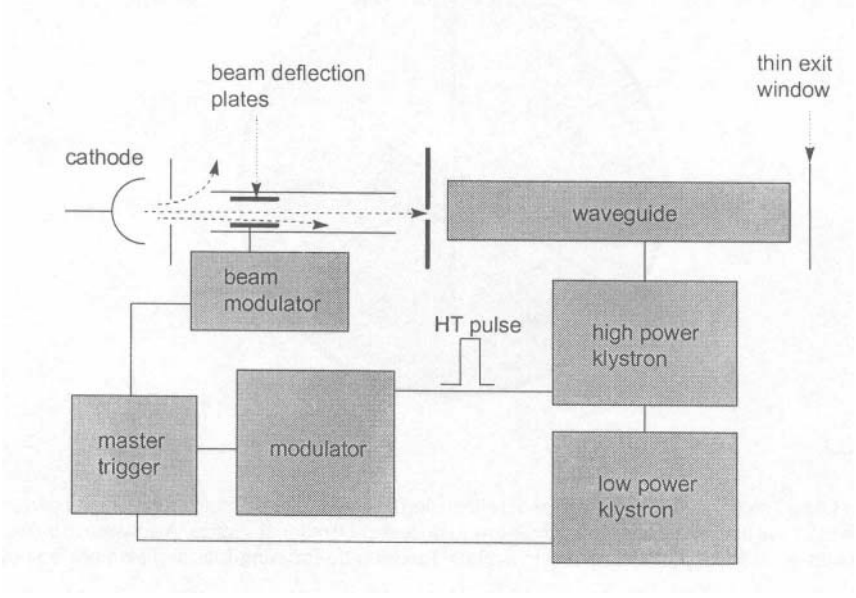

Fig.(1.16) Simplified block diagram of a modern high energy electron linac.

Modern electron linacs, however, use the resonance acceleration of a bunch of electrons whose velocity is in phase with a travelling wave. A simplified schematic diagram of a modern linac is shown in Fig.(1.16).

The principal components are :

- a gun to produce electrons between 50 - 100 keV,
- a stable radio-frequency master oscillator to provide the trigger signal,
- devices for producing radio-frequency power to the wave-guide structures,
- a corrugated wave-guide to provide a series of resonant cavities in which acceleration is achieved,
- magnetic coils – not shown in Fig.(1.16) – to focus the electrons during the acceleration process,
- cooling for the wave-guide structures and the final exit window.

in which there is an axial electric field component. The cavity must be excited in such a way that the magnetic field lines are transverse to, and the electric field lines along, the axis of the cavity, Fig.(1.17). In this Transverse-Magnetic mode there are three main components, [7] :

- axial electric: $E_z = E_0 \sin\left(\omega t - \omega \int \frac{dz}{v}\right)$
- radial electric: $E_r = E_0 \frac{\omega r}{2v} \cos\left(\omega t - \omega \int \frac{dz}{v}\right)$
- azimuthal magnetic: $B_\theta = E_0 \frac{r}{2c^2} \cos\left(\omega t - \omega \int \frac{dz}{v}\right)$

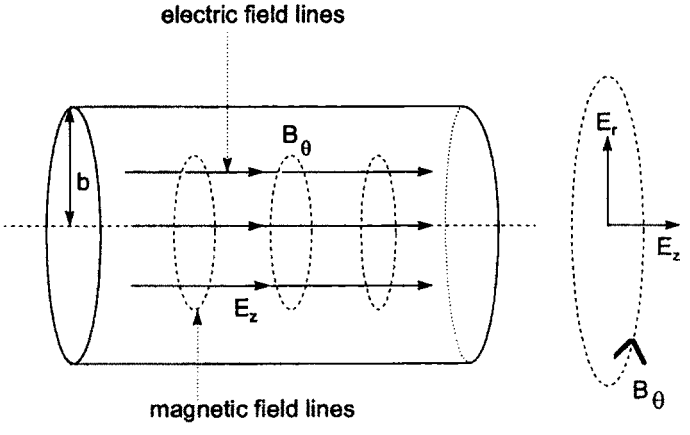

Fig.(1.17) Electric and magnetic field lines in the TM_{01} mode, [7].

The reference field E_0 varies with radial distance r from the central axis of the cavity and to a first approximation can be written :

$$E_0 \propto \left[1 + \left(\frac{\pi r}{\lambda}\right)^2 \left(\frac{1}{\beta^2} - 1\right)\right] \qquad (1.19)$$

where v is the particle velocity, ω the angular frequency ($\lambda = 2\pi c/\omega$) and $\beta = v/c$. z is the distance along the axis of the cavity.

the distance along the axis of the cavity.

A particular resonance mode, the TM_{01}, is excited when the cavity radius b has the value $b = 2.405c/\omega$ [7]. The radial electric field E_r then becomes zero.

Since most electron linacs operate in the S-band at a frequency of 2.998 GHz the wavelength is 10 cm. Optimum dimensions of the cavity are a diameter ~8 cm which is loaded with discs spaced every quarter wavelength (2.5 cm), each one having a central hole of diameter 2.5 cm. The central hole couples the microwave power from one cavity section to the next and also allows the electrons to be accelerated down the axial electric field of the wave-guide.

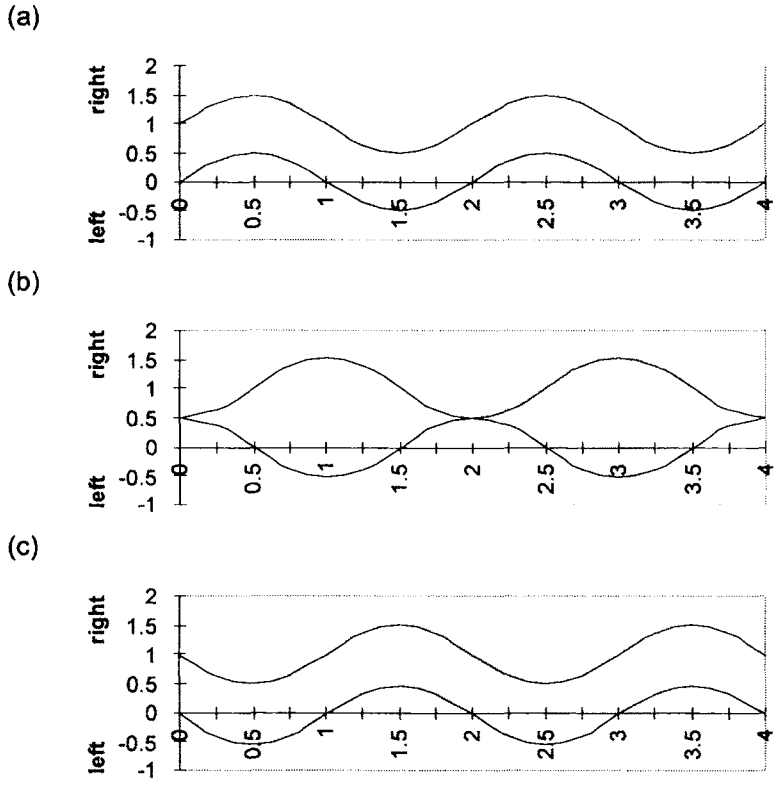

Fig.(1.18) Standing wave structures set up in a cavity in which discs are placed at 0.25, 0.75, 1.25, 1.75, 2.25, 2.75, 3.25, 3.75. (a) waves combine to show a maximum field in cavities centred at 0.5 and 2.5 (b) waves cancel throughout. The top wave has moved one quarter cycle to the right and the bottom wave one quarter cycle to the left (waves shown separated by 1 unit in amplitude for convenience). In (c) another one quarter cycle shift has taken place, top to the right and bottom to the left so that the waves combine to show a maximum in the cavities centred at 1.5 and 3.5.

Travelling wave structure

At any point in the wave-guide, the net axial electric field oscillates in direction. At any time, the maximum accelerating field is present one wavelength apart in separation. This maximum field travels down the wave-guide at the phase velocity. Only the electron bunch in one of the four cavities is therefore accelerated, electrons in the other three seeing either a decelerating field or no field at all.

Standing wave structure

The total length of the wave-guide must now be arranged to achieve reflected waves which combine to increase the field strength and enable more than one electron bunch to be accelerated per wavelength.

Fig.(1.18) shows that for the cavity centred at position 0.5, the total field goes from +1 to 0 to -1 in one half cycle. Thus a particle which receives maximum acceleration at position 0.5, drifts through the cavity centred at 1.0 and then receives maximum acceleration again in the cavity at 1.5.

Modern electron linacs have complex cavity designs which allow electrons to be accelerated to different energies [8].

Magnetrons and Klystrons

Radio-frequency power can be supplied to the wave-guides by two types of source:

- a magnetron – generally used for electron energies up to ~15 MeV,
- a klystron – used for energies greater than ~15 MeV.

These devices have to be kept tuned to the resonant frequency in order to optimize the rf power match with the wave-guide cavities [9]. The principle of the magnetron is shown in Fig.(1.19). A central cathode is surrounded by a number of cylindrical cavities, usually six, machined out of a block of solid copper which forms the anode.

A strong magnetic field, B, is applied perpendicular to the cross-sectional plane of the cavities. When a pulsed dc voltage is applied between anode and cathode, the electrons leaving the cathode simultaneously see two fields. An electric field attracts them to the anode and a magnetic field causes them to travel in circular paths in the perpendicular plane. These complex trajectories sweep the electrons past the gaps which link the cavities to the cathode chamber. The electron charge interacts with the pulsed dc field across the gap. This interaction radiates rf energy into the resonator cavity under suitable conditions of electron flux density and anode potential. An output aerial transfers this rf radiation from one of the cavities to the

accelerating wave-guide.

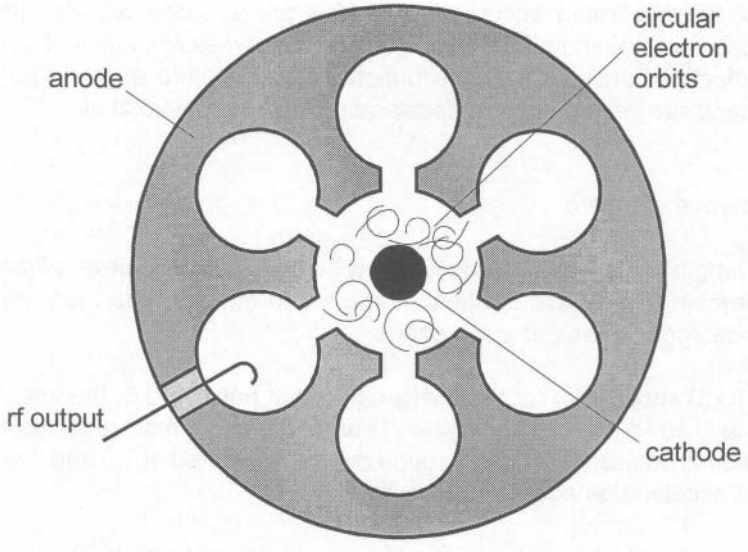

Fig.(1.19) A schematic cross-section through a magnetron.

A typical S-band magnetron for machines up to 10 - 15 MeV can deliver ~2 MW of peak power (~2 kW mean) in microsecond pulses at repetition frequencies of several hundred Hertz.

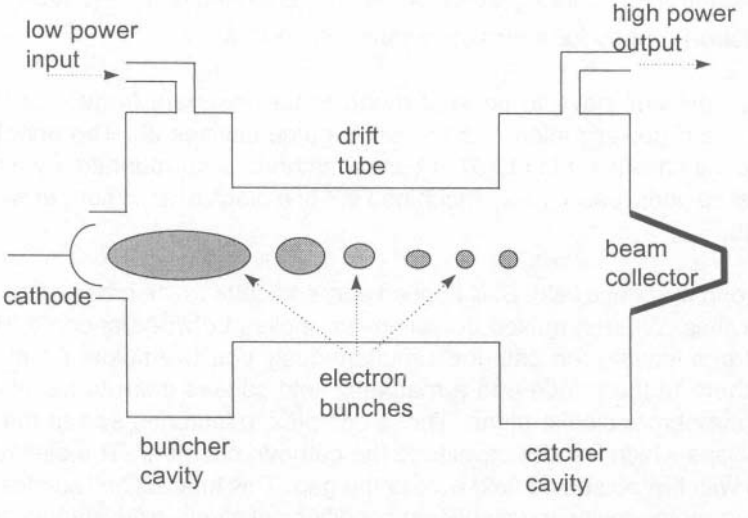

Fig.(1.20) A schematic diagram of a high power klystron. For reasons of clarity the static magnetic fields which focus the electrons down the drift tube are not shown, [9].

Whereas a magnetron is itself a high-powered oscillator, a klystron functions as an rf amplifier. This has to be driven by an rf master oscillator and a low power driver source. With the advantage of much higher power (up to > 15 MW) comes the disadvantage of greater weight and size together with the added complexity of two extra components.

The klystron valve consists of two electron cavities separated by a drift space and a beam collector. Electrons produced at the cathode are velocity-modulated in the buncher cavity by the input radio-frequency power. As these move down the field-free region of the drift tube, the faster particles overtake the slower ones in such a way that regions of high and low electron density begin to form. The deceleration of these electron bunches in the catcher cavity causes them to radiate the, by now, greatly amplified radio-frequency signal.

The need for an extra low power klystron presents no real problem in a static research machine. An isocentric clinical machine, however, requires a rotating gantry in order to direct the beam to the patient from many different angles. For machines operated at > 20 MeV, a flexible rf coupling joint between the klystron and the waveguide structure is necessary. Such a joint is prone to failure.

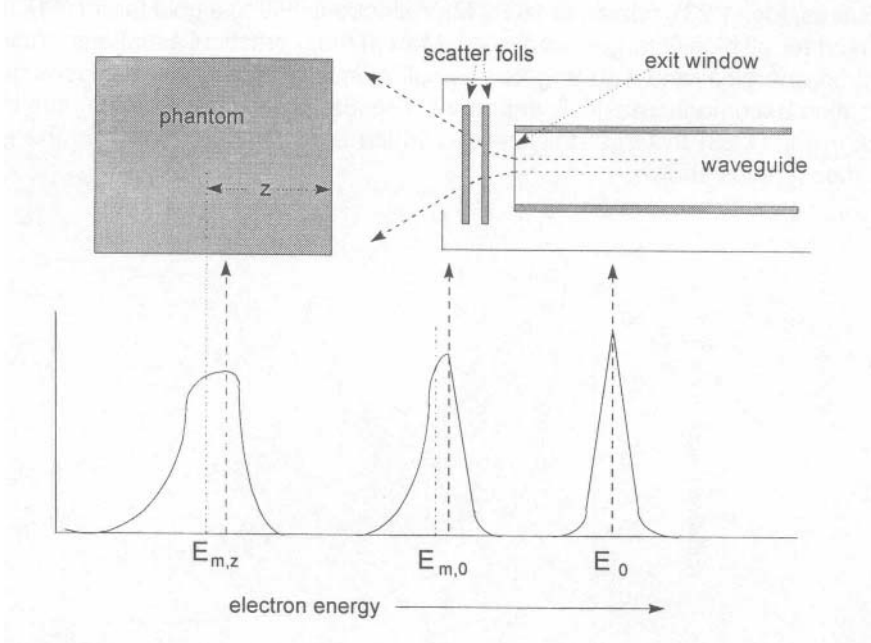

Fig.(1.21) Representation of electron energy spectrum at different points as the beam emerges from the linac. The intrinsic width at the exit window has the mean energy coinciding with the modal energy at E_0. After emerging through the exit window and scatter foils the spectrum becomes asymmetric with the mean energy $E_{m,0}$ lower than the mode. This would be the spectrum at the surface of a phantom or patient (see chapter 9). At a depth z in the phantom, the spectrum is broadened further with the mean energy $E_{m,z}$ even lower than the modal energy than it was at the surface, [10].

Energy Spectra

The spectrum of electrons that emerges from a linac is modified by the combined effects of the exit window and any scattering foils required to disperse the beam. An intrinsic width of ~10% is expected for a standing wave accelerator and ~5% for a travelling wave machine. The more material such a spectrum has to penetrate, the lower the mean energy and the broader the distribution.

X-ray production with electron linear accelerators

Production of *bremsstrahlung* when energetic electrons impinge on a target is determined by the energy of the electrons, the atomic number of the target and the radiation length of the target, Fig.(1.22) (see also Chapter 2). The latter is defined as the distance along the beam direction in which the energy of a typical electron is reduced to 1/e of its original value.

Most of the photons are emitted in the forward direction, *i.e.* along the original direction of the electron. Although the curve of relative photon intensity versus target thickness, Fig.(1.23), relates to 16.93 MeV electrons hitting a gold target [11], it can be used for all high-Z targets above ~ 5 MeV in most practical situations. At lower electron energies, and with targets of small atomic number, energy losses due to ionization become increasingly important. This has the effect of moving the broad peak in Fig.(1.23) to target thicknesses which are rather smaller than the ~ 0.3 radiation lengths shown.

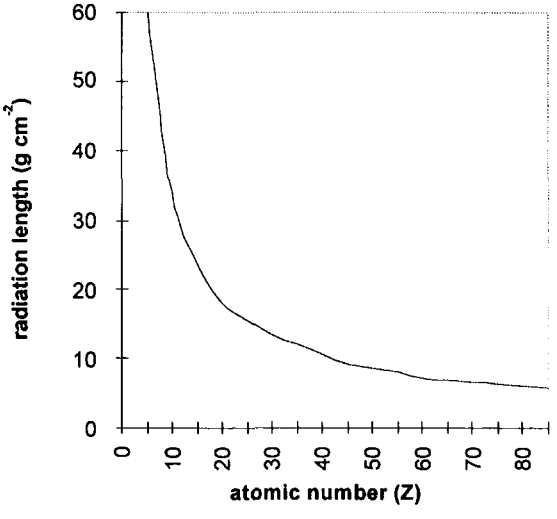

Fig.(1.22) Electron radiation lengths (g cm^{-2}) versus atomic number of target, [11].

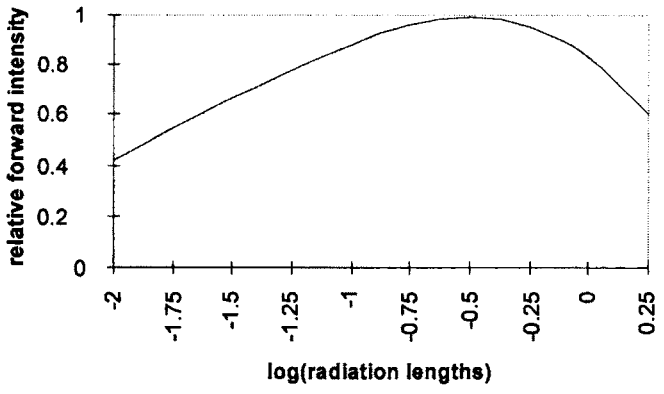

Fig.(1.23) Relative forward photon intensity versus log (target thickness) in radiation lengths. Data are for 16.93 MeV electrons hitting a gold target, [11].

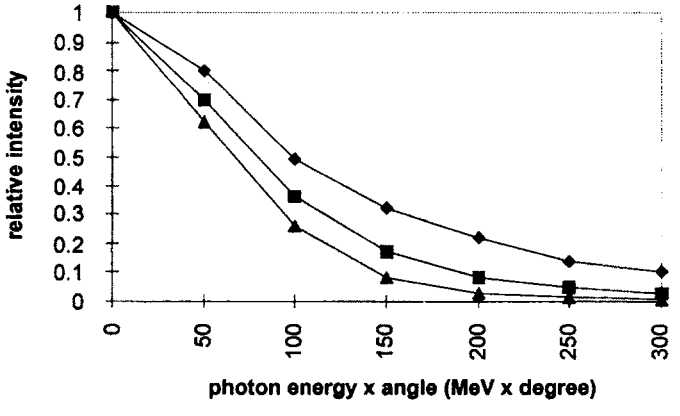

Fig.(1.24) Angular distribution for different target thickness in radiation lengths (g cm^{-2}).
◆ t = 0.125 : ■ t = 0.04 : ▲ t = 0.0, [11], [12].

The angular distribution of photon intensity is conveniently expressed in terms of the product of the photon energy and the angle at which it is emitted. Fig.(1.24) shows that the thinner the target, the more forward-directed is the emission [11]. It is seen from Fig.(1.23) that the thickest target (t = 0.125 radiation lengths) is close to the optimum thickness for maximum forward intensity. This corresponds to ~ 950 mg cm^{-2} (0.5 mm) of gold.

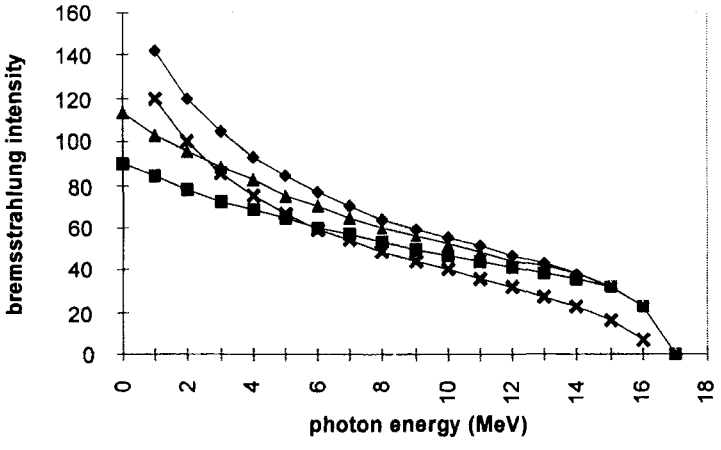

Fig.(1.25) *Bremsstrahlung* intensity distribution, in units of $E_0/4\phi$, from 16.93 MeV mono-energetic electrons. $\phi = Z^2 r_0^2/137$, r_e = the classical electron radius = e^2/mc^2. After [12].
◆ unscreened nucleus : ■ gold : ▲ beryllium : ✖ *bremsstrahlung* from electron-electron collisions.

The energy spectrum of photons is relatively independent of angle for thin targets only. Theoretical calculations of thin target spectra, which agree with experimental determinations at 16.93 MeV [11], are shown in Fig.(1.25).

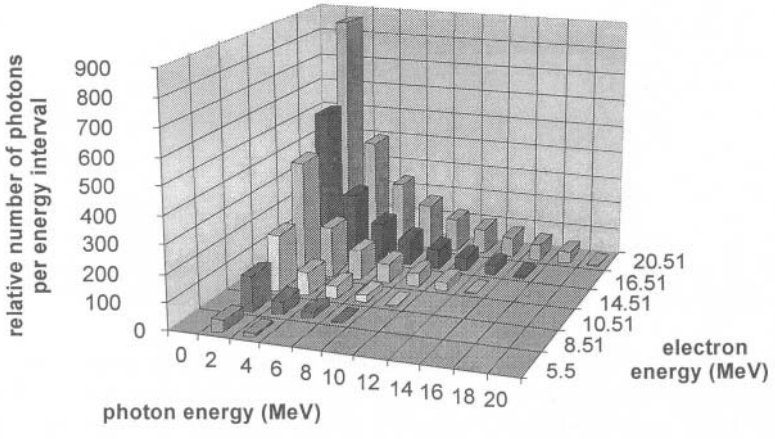

Fig.(1.26) Histogram of relative number of photons per unit energy interval at different (total) electron energies, [12].

Considerable multiple scatter of the incident electron takes place in thick targets, due to the increased importance of interactions :

- at non-relativistic energies,
- from partially screened nuclei,
- with atomic electrons.

A somewhat different shaped spectrum is the result, Fig.(1.26), having a higher preponderance of low energy photons. For the purposes of shielding calculations, an effective photon energy is often used. This is ~ 7 MeV for 20 MeV electrons and ~ 3 MeV for 6 MeV electrons.

1.5 Other Accelerator-based Sources

Other large scale charged-particle accelerators include :

- the Betatron. This uses a magnetic induction principle for the acceleration of electrons in a constant radius – typically no more than ~1 metre. It is limited to energies of ~300 MeV because of synchrotron radiation losses. Before the more widespread use of electron linear accelerators, betatrons were used for radiotherapy at a small number of centres.
- the Microtron. An electron achieves relativistic velocities at much lower energies than a proton. The cyclotron principle can therefore not be used because the electron velocity is approximately constant throughout the acceleration process. The electron source, together with the rf accelerating gap, must be located at the periphery of the final orbit rather than at its centre.
- the Proton Linear Accelerator. The most famous example of this machine is the Stanford Linear Accelerator (SLAC) which accelerates protons to GeV energies. Because of the more gradual approach to relativistic velocities compared with an electron linac, this machine has to use the drift-tube method of acceleration.
- the Electron synchrotron. Originally used for particle physics, this machine has experienced a renaissance as an efficient source of photons over a wide energy range.

1.5.1 The electron synchrotron

Synchronous acceleration of an electron becomes possible when its velocity approaches that of light. When, in addition, the electron is constrained to move in a circular path, the imposition of a central accelerating force causes energy – synchrotron radiation – to be emitted.

In the early 1970's electron synchrotrons with energies less than 10 GeV almost simultaneously became rather less useful to particle physics and more useful to condensed matter physicists, chemists and biologists. The first reason for this

situation was the particle physicists' need for energies approaching the TeV region. Secondly, the non-particle scientists began to exploit with great success the intense radiation emitted tangential to the circular orbit of an energetic electron. This resulted in the burgeoning use of synchrotron radiation as a major research tool with many applications in applied as well as pure science and engineering.

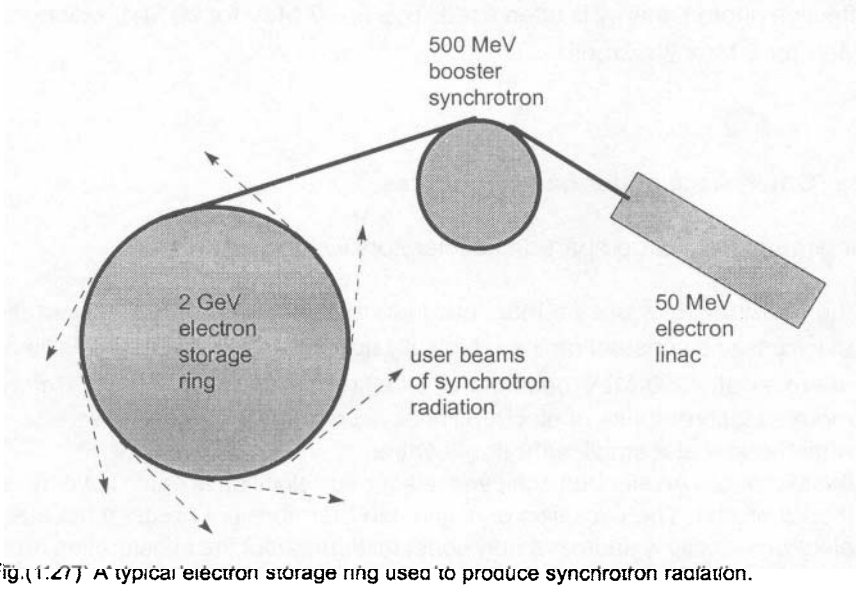

Fig.(1.27) A typical electron storage ring used to produce synchrotron radiation.

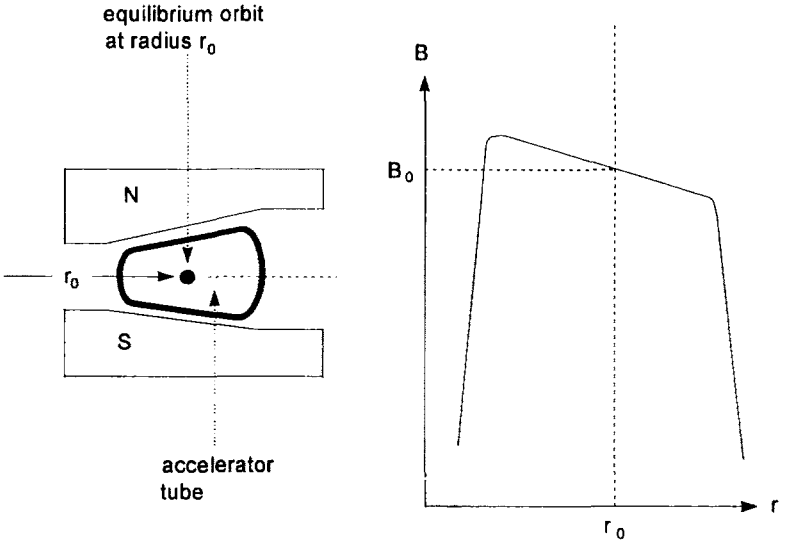

Fig.(1.28) A sketch of the radial decrease in field at the equilibrium orbit brought about by the shaping of the magnet poles, [7].

Fig.(1.27) shows the general sequence of acceleration stages required to achieve a filled storage ring of 2 GeV electrons. The synchrotron principle uses a series of magnetic fields interspersed at intervals by rf accelerating gaps to maintain the energy of the synchronous electrons.

The section across a typical synchrotron magnet, Fig.(1.28), shows the linear decrease in field with increasing radius in order to maintain weak focusing.

1.6 Synchrotron Radiation

The earliest circular-orbit electron accelerators were energy-limited because of the emission of synchrotron radiation. Higher energies could be achieved only through the insertion of a number of rf accelerating gaps round the electron orbit. These additional accelerating gaps, together with the magnet structure in Fig.(1.27), resulted in the electron synchrotron. The machine quickly became adapted to the sole purpose of generating this radiation which spans a continuous range from the infra-red (eV) to hard X-rays (10^5 eV).

Like any other source of electromagnetic radiation, synchrotron radiation can be characterized by its :

- energy (or wavelength),
- spectral brightness (expressed in photons s^{-1} mm^{-2} mr^{-2} (0.1% bandwidth)$^{-1}$),
- polarization (defined by the plane of oscillation of the electric vector),
- coherence (the phase relation between photons),
- emittance (extent of angular divergence and finite size of the source).

Complete details of the foundation of synchrotron radiation sources can be found in the proceedings of recent international conferences and summer schools [13],[14],[15],[16] and [17].

The energy distribution of photons emitted in synchrotron radiation is determined by the energy of the electron and its orbit radius. It is described in the first instance by the characteristic photon energy, ε_c. This is defined as the central energy which divides the emitted power distribution into two halves. When the electron energy is normalized to its rest energy, we have γ = electron energy/m_0c^2, where m_0 is the electron rest mass and :

$$\varepsilon_c = \hbar\omega_c = \frac{\hbar 3c\gamma^3}{2\rho} \qquad (1.20)$$

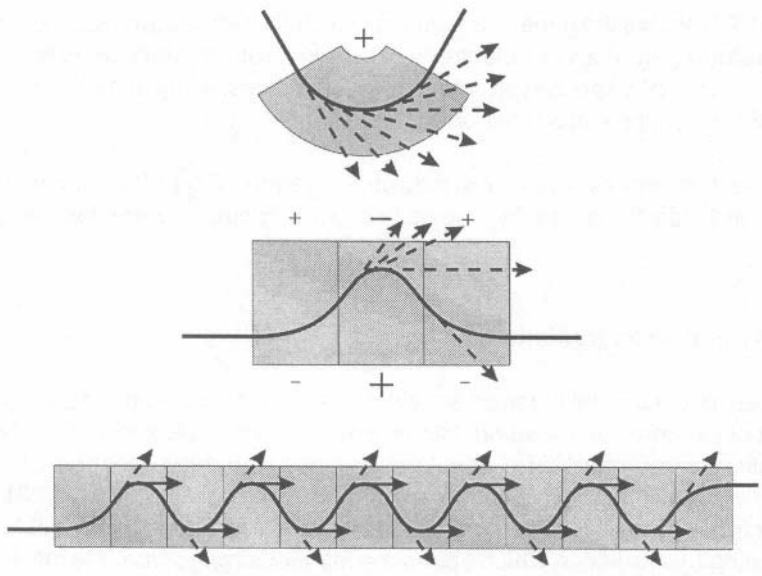

Fig.(1.29) Types of magnet structures used for imposing sinusoidal variations onto the otherwise circular electron orbit.

The instantaneous radius of the electron path, ρ, is equal to the equilibrium synchrotron radius, r_0, except when sinusoidal magnetic structures, Fig.(1.29), are inserted into the storage ring. Expressing ε_c in keV we have :

$$\varepsilon_c = \hbar\omega_c = h\nu_c = 2.218\frac{E^3}{r_0} = 0.665E^2B \qquad (1.21)$$

In Eq.(1.21), E is the electron beam energy in GeV, B is the magnetic field in Tesla and r_0 is the orbit radius in metres. A 2 GeV beam energy and a 20 m radius therefore has a characteristic photon energy of 887 eV with a wide distribution of photon energies about this value.

Conservation of momentum requires that the radiation is emitted in a narrow cone-shaped beam tangential to the orbit. The nominal angular width of this cone is $\sim 1/\gamma$. Furthermore, the polarization is linear, with an electric vector which is horizontal when observed in the plane of the bending magnets.

The energy, coherence and polarization of the radiation can be tailored to various uses by altering :

- the type of magnet structure. These are either circular (bending) or sinusoidal (wiggler or undulator), Fig.(1.29),
- the energy (or wavelength) mono-chromators. These use a combination of mirrors and gratings, Fig.(1.30), which can be adjusted independently or in

combination to select the appropriate energy range,
- the direction in which the radiation is viewed.

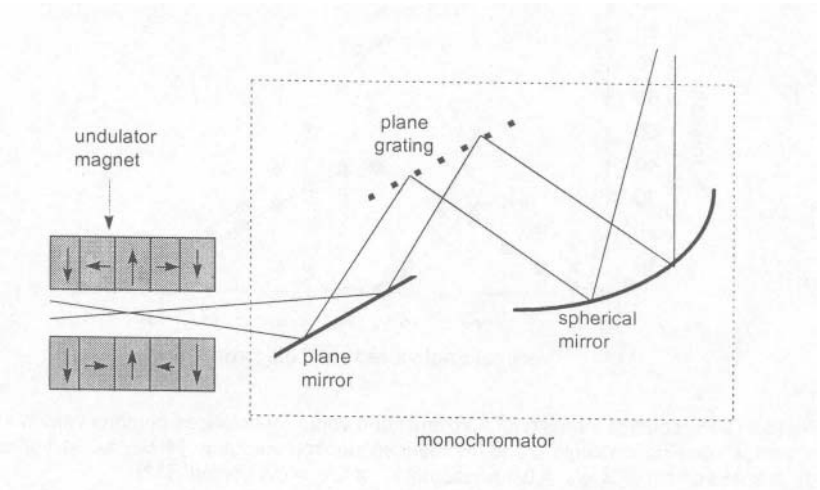

Fig.(1.30) A typical arrangement of optical elements in a monochromator used in conjunction with an undulator magnet. Only 1-pole of the undulator is shown, although the number N can be several hundred, Table (1.3).

1.6.1 Polarization

A general expression for the double differential angular distribution of photon flux, f_s, within, and perpendicular to, the electron orbit plane [14] is :

$$\frac{d^2 f_s}{d\theta d\psi} = \frac{3\alpha}{4\pi^2}\gamma^2 \frac{\Delta\omega}{\omega}\frac{I}{e}\left(\frac{\omega}{\omega_c}\right)^2 \left(1+\gamma^2\psi^2\right)^2 \left[K_{2/3}^2(x) + \frac{\gamma^2\psi^2}{1+\gamma^2\psi^2} K_{1/3}^2(x)\right] \qquad (1.22)$$

In Eq.(1.22), $x = \omega(1+\gamma^2\psi^2)^{3/2}/2\omega_c$, $\alpha \cong 1/137$ is the fine structure constant, I is the beam current, and θ and ψ are the angles of observation in the horizontal and vertical planes respectively. The $K_{2/3}(x)$ and $K_{1/3}(x)$ terms are Bessel functions of the second kind and refer to the horizontal and vertically polarized intensity components. These are illustrated graphically in Fig.(1.31).

Consider a beam energy of 2 GeV and a photon energy of $\varepsilon/\varepsilon_c = 0.01$. An abscissa value of 4 in Fig.(1.31) gives an observation angle of $\psi = 4\times 0.511/2000 = 1.02 \times 10^{-3}$ mrad. out of the horizontal plane. The normalized vertical and horizontal intensities in this case are 37% and 65% respectively. The major : minor axes of the polarization ellipse are therefore given by the square root of the ratio of intensities 1.33 : 1.

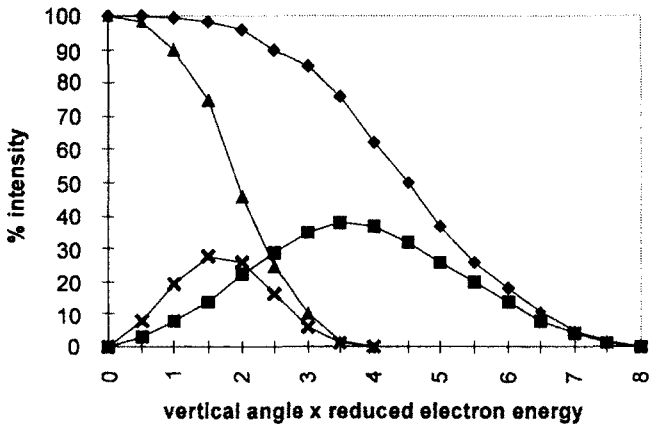

Fig.(1.31) Percentage intensity of horizontal and vertically polarized photons versus the product of vertical observation angle ψ and the reduced electron energy γ. ◆ $\varepsilon/\varepsilon_c$ = 0.01 horizontal : ■ $\varepsilon/\varepsilon_c$ = 0.01 vertical : ▲ $\varepsilon/\varepsilon_c$ = 0.1 horizontal : ✖ $\varepsilon/\varepsilon_c$ = 0.1 vertical, [17].

1.6.2 Coherence

The use of periodic magnetic structures requires the definition of a deflection parameter K. This is expressed as :

$$K = \frac{eB_0\lambda_u}{2\pi m_0 c} = 0.934\lambda_u B_0 \qquad (1.23)$$

where the magnetic field, perpendicular to the electron orbit, varies sinusoidally along the *z* axis with a maximum value of B_0 and a period of λ_u. Thus :

$$B = B_0 \sin\left(2\pi \frac{z}{\lambda_u}\right)$$

where B_0 is in Tesla, and λ_u is in cm. The maximum angular deflection of the orbit is given by $\delta = K/\gamma$.

The deflection parameter *K* provides the distinction between the two types of periodic magnet structures [17] :

- Wiggler structures have $K > 1$, when radiation from the different parts of the trajectory add incoherently. If there are *N* magnet periods, the total photon flux produced is $2N$ times the expression for a bending magnet, Eq.(1.22). The

polarization will always be linearly polarized.

- Undulator structures have $K \leq 1$. In this case the deflection angles are within the cone angle $1/\gamma$. The radiation from each period then adds coherently to give a strong fundamental with its weaker harmonics.

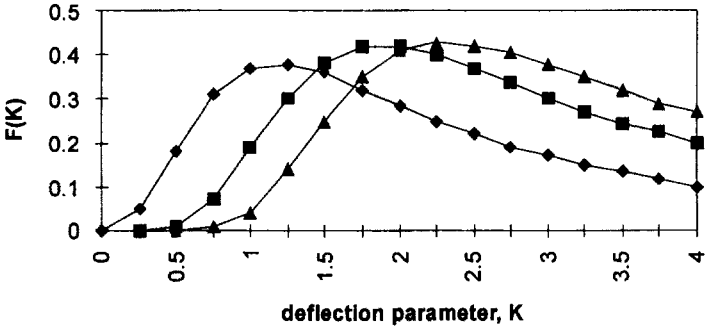

Fig.(1.32) The function $F_n(K)$, Eq.(1.27), for n = 1 (◆): n = 3 (■): n = 5 (▲), [17].

The wavelength of the fundamental radiation measured on the axis of an undulator (when $\theta = \psi = 0$) is :

$$\lambda_1 = \frac{\left(1 + K^2 / 2\right)}{2\gamma^2}\lambda_u = \frac{13.056\lambda_u}{E^2}\left(1 + \frac{K^2}{2}\right) \tag{1.24}$$

where E is the electron energy in GeV and λ_u is the undulator period in cm. The corresponding energy in keV is :

$$\varepsilon_1 = 0.950\frac{E^2\lambda_u}{\left(1 + K^2 / 2\right)} \tag{1.25}$$

and the fractional bandwidth for order n is :

$$\frac{\Delta\varepsilon}{\varepsilon} \cong \frac{1}{nN} \tag{1.26}$$

On the axis, the differential angular distribution of photon flux is non-zero only for odd orders (n = 1,3,5..). In the orbit plane ($\psi = 0$) we have :

$$\frac{d^2 f_s}{d\theta d\psi} = \alpha N^2 \gamma^2 \frac{\Delta\omega}{\omega}\frac{I}{e}F_n(K) \tag{1.27}$$

The function $F_n(K)$ is given for orders n = 1,3 and 5 in Fig.(1.27).

When Eq.(1.27) is expressed in practical units it becomes :

$$\frac{d^2 f_s}{d\theta d\psi} = 1.74 \times 10^{14} N^2 I F^2 F_n(K) \qquad (1.28)$$

1.6.3 Emittance

Eqs.(1.22) and (1.28) overestimate the photon flux because of the finite source size and the finite angular divergence. Emittance is specified in both horizontal (x) and vertical (y) planes by the product of the root mean square (rms) beam size $\sigma_x \sigma_y$ and the beam divergence $\sigma_{x'} \sigma_{y'}$. For the two planes therefore :

$$\varepsilon_x = \sigma_x \sigma_{x'}, \quad \varepsilon_y = \sigma_y \sigma_{y'}$$

However, emittance is only one of a number of factors needed to convert photon flux to brightness β. The latter is defined as photon flux per unit phase-space volume. It requires a consideration of the transverse and longitudinal coherence in defining the effective source area [15]. Thus :

$$\beta = \frac{d^2 f_s}{d\theta d\psi} \Big/ (\text{effective source area})$$

Table (1.3) Calculated parameters of synchrotron beams at 6 GeV electron energy and 100 mA storage ring current [13]. Note the small value of K for the undulator brought about by the large number of small period oscillations. Energy values in column 8 refer to the characteristic photon energy for the bend and wiggler magnets and the fundamental energy for the undulator.

Source	σ_x (mm)	σ_y (mm)	N	λ_u (cm)	K	B_0 (T)	ε_c or ε_1 (keV)	β
bend	0.34	0.14	-	-	-	1.0	23.94	2.3×10^{14}
wiggler	0.34	0.14	4	34	57.1	1.8	43.10	1.8×10^{15}
undulator	0.34	0.14	344	1.6	0.200	0.13	20.9	2.5×10^{17}

1.7 Neutron Sources

Although neutrons can be produced spontaneously by the radioactive decay of certain heavy nuclei (section 1.3.4), their principal means of production uses either a nuclear reactor or an accelerator-based reaction process.

1.7.1 Reactors

Reactors can be used for :

- isotope production (see chapter 8),
- industrial radiography,
- boron neutron capture therapy (BNCT) (see chapter 9),
- providing neutron beams for research.

The main components and processes inside the reactor, Fig.(1.33), are :

- the induced fission of fissile material (fuel : ^{235}U, ^{239}Pu for thermal fission and ^{238}U for fast fission). In a fast reactor, the fission takes place at high (> MeV) energies. In a thermal reactor, the spectrum of neutrons released in the fission process, Fig.(1.7), must be degraded to thermal energies in order to initiate further fission. The energy degradation is achieved by the moderator.
- the moderator. This is composed of light nuclei (H_2O, D_2O, C) with which the energetic neutrons collide and lose energy. These collisions are elastic in the centre-of-mass co-ordinate system. The neutron loses energy in the laboratory system because of the recoil of the struck nucleus.
- the coolant system. Kinetic energy imparted to all the fission products – neutrons, fission fragments and their decay products – is recovered by a coolant system. This energy can then be converted into usable heat.

As a source of radiation the nuclear reactor is primarily a source of neutrons. The induced-fission spectrum of neutrons emitted from the fuel rods is the same as the spectrum from a spontaneous-fission radioactive source, Fig.(1.7), Eq.(1.12).

In a thermal reactor, the moderator degrades the energy spectrum. It comprises:

- a Maxwell-Boltzmann distribution in equilibrium with the core temperature. This describes the neutrons already thermalized and,
- a slowing down (1/E) component which results from the continual moderation of neutrons from the fission spectrum, Fig.(1.34).

A crucial factor in the operation of a nuclear reactor is the production of fission fragments – the two heavy elements into which the original fuel nucleus has been split. In binary fission, these fragments have a yield distribution shown in Fig.(1.35).

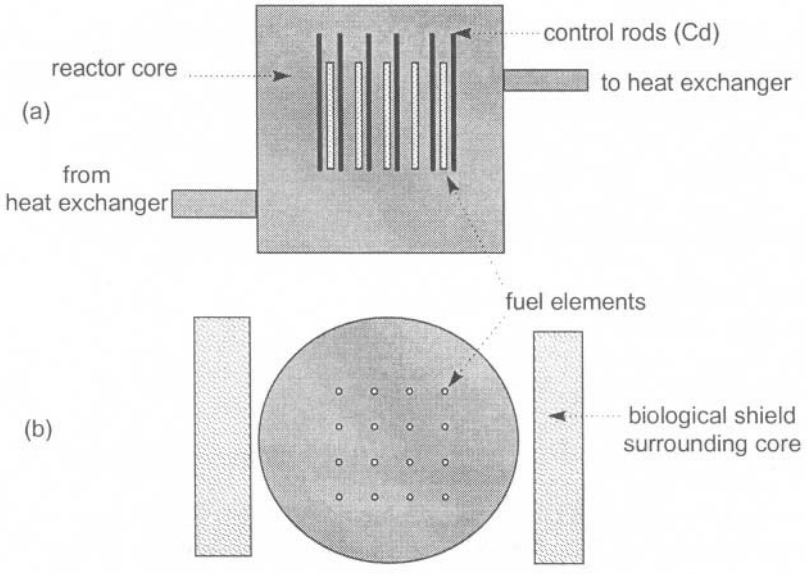

Fig.(1.33) A schematic diagram of a reactor core. Moveable control rods, which have a high thermal neutron absorption cross section, are interspersed within a lattice of fuel rods. The positioning of these rods allows the neutron flux to be held at a constant value, called the criticality condition. Rods fully withdrawn will allow the neutron flux to rise exponentially. In this event the reactor becomes super-critical. When fully inserted, the flux falls exponentially to give the sub-critical condition.

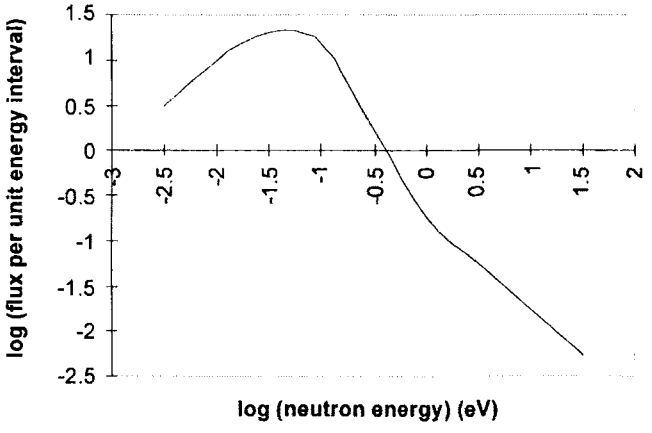

Fig.(1.34) A typical neutron spectrum in a thermal reactor is given by the summation of a Maxwell-Boltzmann distribution for neutron energies up to ~ 5 kT and a 1/E slowing-down distribution above ~ 5 kT.

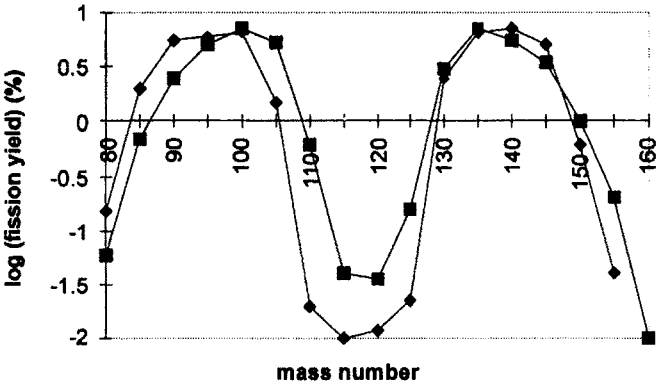

Fig.(1.35) The fission-fragment yield versus mass from the fission of ^{235}U (◆) and ^{239}Pu (■). In binary fission, there are two fragments produced per fission. The integrated areas of the two curves therefore each add up to 200%.

The radioactive decay of these fission-fragments results in :

- prompt γ-rays,
- delayed neutrons (mainly from the decay of isotopes of bromine and iodine),
- decay γ-rays.

There is a wide variety of fission fragments whose decay gives rise to delayed neutrons. These are generally grouped together on the basis of their decay half-life, Table (1.4). Typical examples of fission-fragment decays in groups 2 and 3 are :

$$^{87}Br \xrightarrow{\beta 5.56s} {}^{87}Kr \xrightarrow{n} {}^{86}Kr$$

$$^{137}I \xrightarrow{\beta 22s} {}^{137}Xe \xrightarrow{n} {}^{136}Xe$$

Table (1.4) The 6 major groups of delayed neutrons following the fission of ^{235}U. The groups are classified according to their β-decay half-lives. It is these neutrons which permit the control of criticality in the reactor.

Group	Half-life (s)	Decay constant λ_i (s^{-1})	Mean energy (keV)	Yield (n/fission)	Fraction β_i
1	55.72	0.0124	250	0.00052	0.000215
2	22.72	0.0305	560	0.00346	0.001424
3	6.22	0.111	405	0.00310	0.001274
4	2.30	0.301	450	0.00624	0.002568
5	0.610	1.14	-	0.00182	0.000748
6	0.230	3.01	-	0.00066	0.000273
Total				0.0158	0.0065

In addition to the release of delayed neutrons, the fission-fragments are also responsible for the emission of two categories of γ-ray – prompt and decay. Fig.(1.36) gives the mean number of γ-rays emitted per fission from each of the categories. Note that 0.4% are in the energy range 5 - 7 MeV.

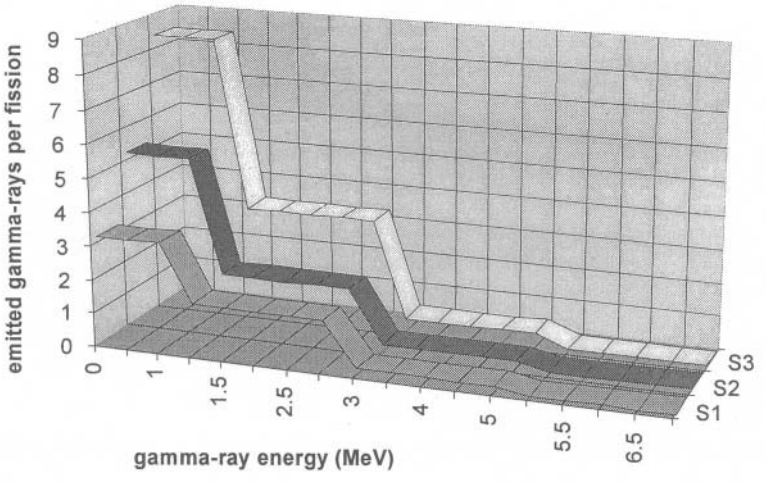

Fig.(1.36) The numbers of γ-rays emitted per fission. The smallest contribution (series 1) comes from the "slow" decay of fission products. Most (series 2) come from the prompt de-excitation of compound nuclei. Series 3 gives the summation of prompt and decay γ-rays. Note the non-linear energy scale, which is used for clarity. In total, these components are responsible for the intense γ flux inside a reactor, [11], [12].

1.7.2 Neutrons from charged-particle reactions

Many of the charged-particle-induced reactions used for activation (Chapter 8) have a neutron as the exiting particle. Some of these were used intensively in the past for neutron cross-section determinations and for the production of neutron beams for radiotherapy. Because neither of these activities are currently widespread, most radio-isotopes that could be (intentionally) produced by neutron activation are now approached via different – charged particle – routes. Although neutron beams *per se* are no longer popular, it is essential that charged-particle reactions are considered because of their importance in radiation protection.

Most importance attaches to neutron production by heavy charged particles – mainly protons, deuterons, α-particles. Electrons are important only in so far as they can produce *bremsstrahlung* photons in dense and high atomic-number materials. These can then produce neutrons via photo-neutron reactions.

A basic requirement in a charged-particle-induced reaction is to produce a

compound nucleus with an amount of excitation energy which exceeds the binding energy of the "last neutron" (see sections 8.1 and 4.2.2). This neutron is then very likely to be ejected from the compound nucleus. The Q-value of a reaction is defined as :

$$Q = \left[\left(m_p + m_t\right) - \left(m_n + m_r\right)\right]c^2 / 2$$

where the masses of the projectile, target, exiting and residual nuclei are m_p, m_t, m_n, and m_r respectively.

Some examples of the most common charged-particle-induced reactions, with their associated Q-values, are :

- (p,n): ^{7}Li (p,n) ^{7}Be : Q = - 1.646 MeV
  ^{3}H (p,n) ^{3}He : Q = - 0.764 MeV
- (d,n): ^{9}Be(d,n)^{10}B : Q = + 4.362 MeV
  ^{3}H (d,n)^{4}He : Q = + 17.588 MeV
  ^{2}H (d,n)^{3}He : Q = + 3.265 MeV

For a given reaction, it is necessary to define the relation between the Q-value and the following :

- the energies of the incoming particle, E_p, and the outgoing neutron, E_n,
- the energy given to the residual nucleus, E_r,
- the angles of emission of the neutron and the recoil nucleus with respect to the direction of the incoming particle, θ and φ respectively.

Conservation of energy and momentum for (a) non-relativistic energies and (b) for the case where no excitation energy is given to the residual nucleus, then gives:

$$\begin{aligned} E_p + Q &= E_n + E_r \\ \sqrt{2m_pE_p} &= \sqrt{2m_nE_n}\cos\theta + \sqrt{2m_rE_r}\cos\varphi \\ 0 &= \sqrt{2m_nE_n}\sin\theta - \sqrt{2m_rE_r}\sin\varphi \end{aligned} \qquad (1.29)$$

Eqs.(1.29) can be combined to give the Q-equation, [18] :

$$Q = E_n\left(1 + \frac{m_n}{m_r}\right) - E_p\left(1 - \frac{m_p}{m_r}\right) - \frac{2\sqrt{m_pE_pm_nE_n}}{m_r}\cos\theta \qquad (1.30)$$

Since Eq.(1.30) is quadratic in $\sqrt{E_n}$ it can be solved to give the useful relation :

$$E_n = E_p \frac{m_p m_n}{(m_n + m_r)^2} \left\{ \begin{array}{l} 2\cos^2\theta + \dfrac{m_r(m_r + m_n)}{m_p m_n}\left[\dfrac{Q}{E_p} + \left(1 - \dfrac{m_p}{m_r}\right)\right] \\ \pm 2\cos\theta \sqrt{\cos^2\theta + \dfrac{m_r(m_r + m_n)}{m_p m_n}\left[\dfrac{Q}{E_p} + \left(1 - \dfrac{m_p}{m_r}\right)\right]} \end{array} \right\} \quad (1.31)$$

Eq.(1.31) is a general relation for any angle of neutron emission, θ, and for $Q > 0$ (exothermic) or $Q < 0$ (endothermic) reactions. Only the positive sign is used for exothermic reactions (otherwise it could give $E_n > E_p$ at $\theta = 0$ when the negative sign is used, which is energetically not possible). In this case there is a unique relation between E_n, E_p and θ.

Neutron energies from endothermic reactions are governed by a threshold incident particle energy given by :

$$E_{p,threshold} = |Q| \frac{m_p + m_t}{m_t} \quad (1.32)$$

When $E_p < E_{p,threshold}$ there is no reaction. When $E_p = E_{p,threshold}$ the reaction products are just formed with zero energy in the CM system, but they move forward with the velocity of the centre of mass in the laboratory system. As $E_p > E_{p,threshold}$, two neutron energies are produced, one for the negative and one for the positive sign in Eq.(1.31). These are emitted within a cone of semi-angle :

$$\cos\theta = \left| \sqrt{\frac{m_r(m_n + m_r)}{m_p m_n}\left[\frac{|Q|}{E_p} - \left(1 - \frac{m_p}{m_r}\right)\right]} \right| \quad (1.33)$$

Eventually, E_p will become so large that the lower neutron energy becomes zero, at which point only the positive sign is used in Eq.(1.31) to give a mono-energetic neutron [18].

Eq.(1.31) shows that for a given reaction, and for given values of E_p and θ, a mono-energetic neutron is produced. This applies to the ideal case of an infinitely thin target in which there is no energy degradation of the incident charged particle. In practice, of course, the incident particle will lose energy and may also scatter. The resulting neutron spectrum is therefore determined by :

- the energy spread of charged particles from the accelerator which impinge on the target. This will generally be small (~ 5%),
- the energy-dependent cross-section, $\sigma_{d,n}(E_p)$(see also section 8.4),
- the thickness of the target, d, compared with the range of the incident charged particle in the target material, R. If R < d then neutron production can take place at all energies between the incident energy E_p and zero for $Q > 0$, and between E_p and $E_{p,threshold}$ for $Q < 0$.

Charged particle reaction cross-sections are shown in Fig.(1.37) for deuterons on tritium (Q = 17.588 MeV) and deuterium (Q = 3.265 MeV). Note that the maximum neutron yield is achieved for $E_d \sim 100$ keV.

The significance of the (d,n) reactions in tritium and deuterium is two-fold. Firstly, in their former use as energetic neutron beams for radiotherapy (up to 14.7 MeV), and secondly, as the continuing basis of thermonuclear power generation, both solar and terrestrial.

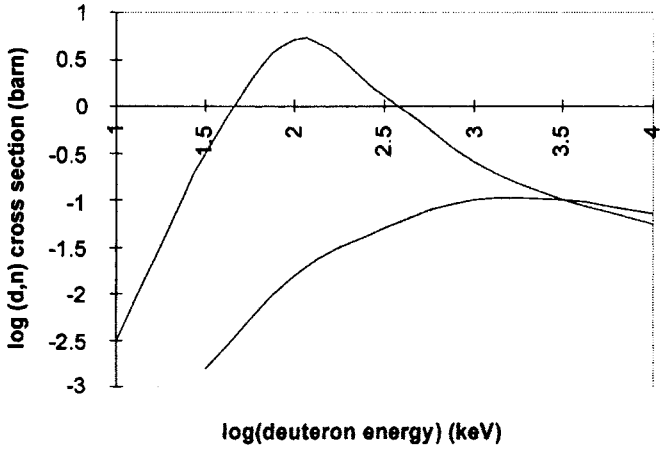

Fig.(1.37) Deuteron-induced cross-sections in tritium and deuterium versus incident deuteron energy. $\sigma_{d,n}(E_p)$, in tritium (upper curve) and deuterium (lower curve).

1.7.3 Neutrons from photon-induced reactions

The main characteristics of a neutron source based on photo-neutron reactions are:

- they are always endo-thermic ($Q < 0$) because of the mass-less incident particle,
- photo-neutron cross-sections are much smaller than those using charged particles. The yield (neutrons/incident photon) is therefore less,
- the incident photons are never completely stopped in the target. This means

that there is always a residual photon background.

Photoneutron sources can use either γ-rays from a radioactive source (section 1.3.2) or energetic *bremsstrahlung* X-rays from an electron accelerator (section 1.4.4).

The excitation energy of the compound nucleus of the target must exceed the binding energy of the least-bound neutron before neutron emission can take place. Radioactive (γ,n) sources are therefore restricted to targets which have the smallest binding energy. These are deuterium (Q = - 2.225 MeV) and beryllium (Be^9, Q = - 1.665 MeV).

Bremsstrahlung-based sources will generally use high-Z targets which must be capable of withstanding the high power density of the incoming electron beam.

For these reasons, tungsten and gold are preferred. However, an increased yield can be obtained through the use of a secondary, fissile, target. In this case the photons produced in the primary (tungsten) target produce photo-fission reactions in the secondary (usually uranium) target.

Conservation of energy and momentum in the reaction gives

$$\begin{aligned} h\nu - |Q| &= E_n + E_r \\ \frac{h\nu}{c} &= m_n v_n - m_r v_r \end{aligned} \qquad (1.34)$$

in the special case where the neutron is emitted at 0° to the direction of the incident photon, Eq.(1.29).

The equivalent expression for photo-neutron reactions to Eq.(1.31) for charged particle reactions is, [18] :

$$E_n = \frac{A-1}{A}[h\nu - |Q|] \pm h\nu\sqrt{\frac{2(A-1)\times[h\nu - |Q|]}{931\times A^3}} \qquad (1.35)$$

where A is the atomic number of the target material. Since the factor 931 is the approximate energy equivalent in MeV of one atomic mass unit, the energies of E_n, $h\nu$ and Q must also be expressed in MeV.

Eq.(1.35) shows that the fractional energy spread of neutrons emitted along the line of an incident mono-energetic photon is given by :

$$\frac{\Delta E_n}{E_n} = \frac{2h\nu\sqrt{\dfrac{2(A-1)\times\left[h\nu-|Q|\right]}{931\times A^3}}}{\dfrac{(A-1)}{A}\left[h\nu-|Q|\right]} \tag{1.36}$$

A 2 MeV incident photon on a ^{9}Be target will thus give a neutron energy of 0.3 MeV at an emission angle of 0°. The fractional energy spread is 0.0112/0.3 ≈ 4%. In practice, of course, a much larger energy spread is observed because of the variation of Eq.(1.34) at different angles, and the spread in incident photon energies, Figs.(1.25) and (1.26).

References

[1] United Kingdom Atomic Energy Authority Information Services Branch *Radiation and You*, (1986 London)

[2] A.G.Holmes-Seidle, A.K.Ward, R.Bull, N.Blower and L.Adams, *Proc.ESA Space Environment Analysis Workshop*, ESTEC Report No.**WPP-23** (1978)

[3] S.Hayakawa, *Cosmic Ray Physics*, (Wiley Interscience, New York 1969)

[4] R.D.Evans, *The Atomic Nucleus*, (McGraw-Hill, New York 1972)

[5] V.F.Weisskopf, *Phys.Rev.* **83** (1951) 1073L

[6] D.J.Bennet and J.R.Thomson, *The Elements of Nuclear Power*, 3rd Edition, (Longman UK 1989)

[7] M.S.Livingston and J.P.Blewett, *Particle Accelerators*, (McGraw Hill, New York 1962)

[8] C.J.Karzmark, *Med.Phys.* **11**(2) (1984) 105

[9] S.C.Klevenhagen, *Physics and Dosimetry of Therapy Electron Beams*, (Medical Physics Publishing, Madison, Wisconsin 1993)

[10] C.J.Karzmark and R.J.Morton, *A Primer on Theory and Operation of Linear Accelerators in Radiation Therapy*, (Medical Physics Publishing, Madison, Wisconsin 1989)

[11] L.H.Lanzl and A.O.Hanson, *Phys. Rev.* **83**(5) (1951) 959

[12] H.W.Koch and R.E.Carter, *Phys. Rev.* **77** (1950) 165

[13] D.T.Attwood and K.-J.Kim, *Nucl.Instr.Meth.Phys.Res.* **A246** (1986) 86

[14] K.-J.Kim, ibid. p.67

[15] K.-J.Kim, ibid. p.71

[16] H.Maezawa, Y.Suzuki, H.Kitamura and T.Sasaki, ibid p.82

[17] X-ray Data Booklet **PUB-490** Rev Lawrence Berkeley Laboratory (1986)

[18] K.H.Beckurts and K.Wirtz, *Neutron Physics* (Springer-Verlag, Berlin 1964)

CHAPTER 2

INTERACTIONS of CHARGED PARTICLES

2.1 Introduction

When ionizing radiation falls on a material, it is necessary to be able to answer three questions for a full understanding of the consequences. These are :

- how far into the material does the radiation penetrate?
- how much energy is deposited within the material?
- what secondary radiation or particles are emitted as a result?

The probability that an interaction takes place is described by its cross-section σ. This is a parameter which depends on both the type of interaction and the energy of the radiation. It describes the effective area which the entity (electron, nucleus, atom, molecule..) presents to the radiation in units of barn (1 barn = 10^{-28} m^2). Accordingly, each radiation will have a number of energy-dependent partial cross-sections. These can be segregated according to whether they are absorption, inelastic scattering, elastic scattering or radiative in character. In most circumstances the partial cross-sections *i* add algebraically to give the total, so that :

$$\sigma_{total} = \sum_i \sigma_i$$

In others – *e.g.* in neutron scattering – it is sometimes the amplitudes and not the intensities of the scattered waves which must be added. This means that the phases of the component waves have to be considered, leading to a more complex description of the total cross-section (see Chapter 4).

An important characteristic of charged particles which distinguishes them from photons and neutrons is that their penetration into a material cannot be described by an exponential function. Although there is a finite probability that a photon, however low in energy, can penetrate to an infinite depth, this is not the case for a charged particle. There is always an ultimate depth beyond which a charged particle will not reach. This leads to the concept of an energy-dependent Stopping Power of a medium towards a charged particle. It is defined as the average energy loss per unit path length traversed. Associated with this is the concept of Range, about which great care must be taken in order to distinguish between the various definitions.

The penetration of a charged particle into a medium is governed by stochastic (*i.e.* random) interactions which cause energy loss and changes of direction. When

a particle has lost all its energy it can diffuse throughout the medium for a short while as a charged entity until it acquires a neutralizing charge. The complete description of a large number of particles which traverse a medium therefore requires all the relevant partial cross-sections. These must be differential in both energy and angle, in order to define the probabilities at each collision that a given type of interaction will result. For example, if the cross-sections for absorption, elastic scatter and inelastic scatter at a certain energy are σ_a, σ_s and σ_{inel}, the probability that the collision will be an inelastic one is $\sigma_{inel}/(\sigma_a+\sigma_s+\sigma_{inel})$.

Estimates of the mean free path between collisions, and the probability of energy loss in each one, can be made in a Monte-Carlo type of calculation. Here, a random number generator and a large data-base of cross-sections is used to compile a statistically meaningful number of particle histories. The technique provides a powerful means of predicting the effects of radiation on different materials in different conditions. However, care must be taken to incorporate the correct probability distributions into the calculations. These and other relevant considerations can be found in more specialized texts [1].

2.2 Definitions of Range

Two approximations to the complete stochastic nature of charged particle interactions are provided by :

- the Continuous Slowing Down Approximation (csda),
- the Straight Ahead Approximation.

In the former, all energy-loss fluctuations are neglected and the particles are assumed to lose their energy continuously along their tracks at a rate given by the stopping power. Since the stopping power is assumed to be a smooth function of energy, the csda range, r_0, can be defined as the integral with respect to energy of the reciprocal of the stopping power.

$$r_0 = \int_0^{T_0} \frac{1}{dE/dx}\, dE \qquad (2.1)$$

The limits in Eq.(2.1) show that the particle is assumed to come to rest after slowing down from energy T_0. It should be noted that the csda range refers only to interactions which result in energy loss. It does not include any possibility of multiple scatter without energy loss, or thermal diffusion either before, or after, neutralization. For this reason, r_0 is always smaller – sometimes significantly so – than the mean value of the path lengths actually travelled. Sometimes it is necessary to specify the csda range to exclude, for example, all sub-ionization events. In this case the lower limit of integration in Eq.(2.1) becomes the energy of the lowest ionization potential of the medium and not zero.

In the Straight Ahead Approximation, all changes in direction of the particle as the result of multiple elastic scatter are neglected so that the track is assumed to be rectilinear. This is a good approximation in the case of heavy particles such as protons and α-particles.

Any departure from linearity is discussed in terms of a Detour Factor. This relates the csda range with the mean penetration depth (sometimes called the mean projected range) along the original direction of the particle, z_{av}, and is always <1. Thus, the Detour Factor, d is given by :

$$d = \frac{z_{av}}{r_0} \tag{2.2}$$

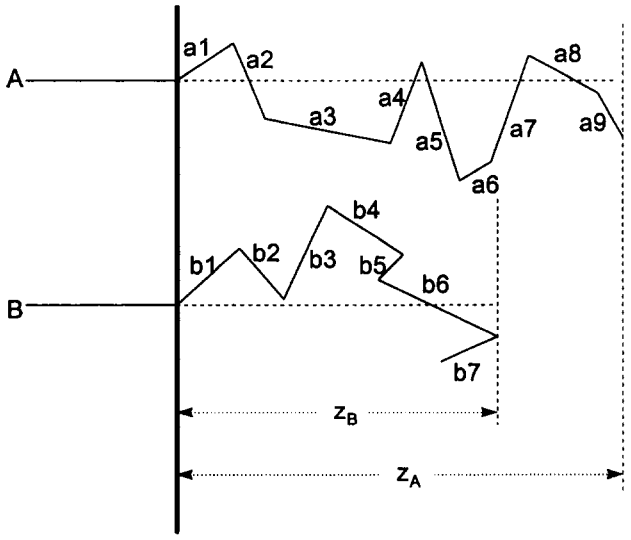

Fig.(2.1) Schematic of two charged particle tracks at the same incident energy. In the csda approximation the range, r_0, would correspond to the mean path length of a large number of such tracks, i.e. the mean of a1+..+a9, b1+..+b7, etc. so long as the individual interaction sites were energy loss events and there was no multiple scatter. With an increasing amount of multiple scatter, the average path length becomes larger than r_0.
The Detour Factor specified for track B is z_B /(b1+b2+b3+b4+b5+b6+b7).

An experimental determination of the Detour Factor can be made only by a visual inspection of a particle track in a cloud or bubble chamber. An early observation of 19 keV electron tracks in oxygen at atmospheric pressure found a ratio of 0.5 for the mean penetration depth to mean path length [2]. More usually, however, it is obtained from a Monte-Carlo calculation. These show that the Detour Factor depends on the nature of the particle and its energy as well as on the atomic number of the medium, Figs.(2.2) and (2.3).

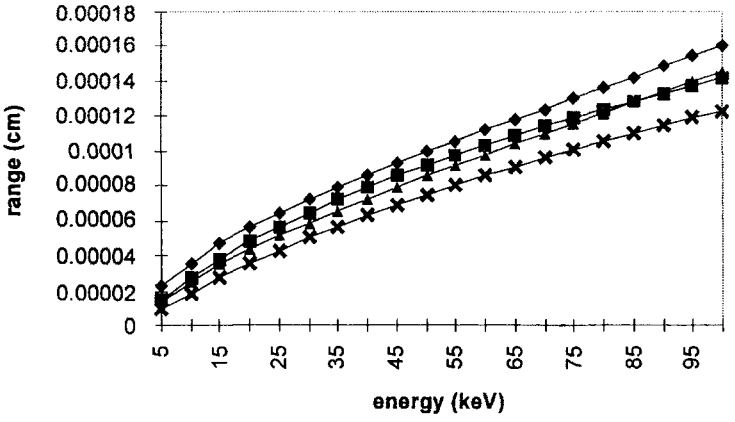

Fig.(2.2) The csda range r_0 and mean penetration depth z_{av} in liquid water as a function of particle energy. Data taken from [3].
proton : csda range ◆ : mean penetration depth ▲ :
alpha particle : csda range ■ : mean penetration range ✖ .
Detour Factors in the two cases above vary between 0.61 at 5 keV to 0.86 at 100 keV for alpha particles and 0.63 at 5 keV to 0.91 at 100 keV for protons.

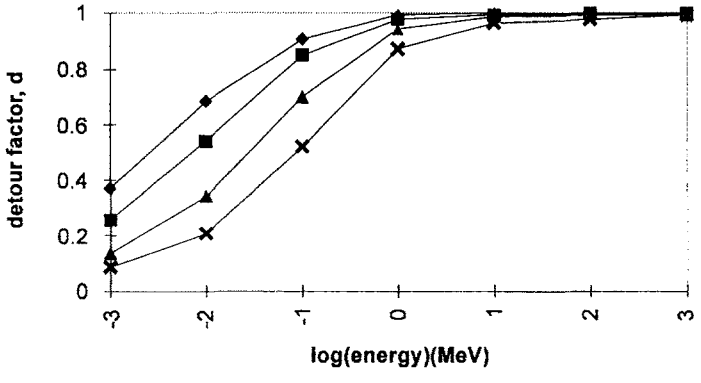

Fig.(2.3) Detour factor, *d*, versus proton energy (MeV) in various materials. ◆ carbon : ■ aluminium : ▲ copper : ✖ tungsten, [3].

From an experimental point of view, the determination of a quantity which reflects the penetrating power of an energetic charged particle can be carried out in two ways :

- by measuring the fraction of particles that are transmitted through increasing thicknesses of the medium,
- by measuring the depth-dependence of the response of a detector actually in the medium.

The parameters yielded by these two methods have slightly different meanings.

2.2.1 *The transmission method*

The decrease of the transmitted fraction of particles N_x/N_0 as x increases depends on the geometry in an experiment of this type. This is because the transmitted beam experiences a larger divergence as the thickness x of the absorber increases. The transmitted fraction is therefore a combination of particles stopping completely through energy loss, and particles which have been scattered out of the beam. The latter is determined by the position of the detector.

Precautions have to be taken either to reduce the scatter fraction as much as possible or to correct for it. In addition, there is the possibility that the detector may have an energy-dependent efficiency which becomes very small at low energies. This could seriously underestimate the number of particles transmitted through a very thick absorber.

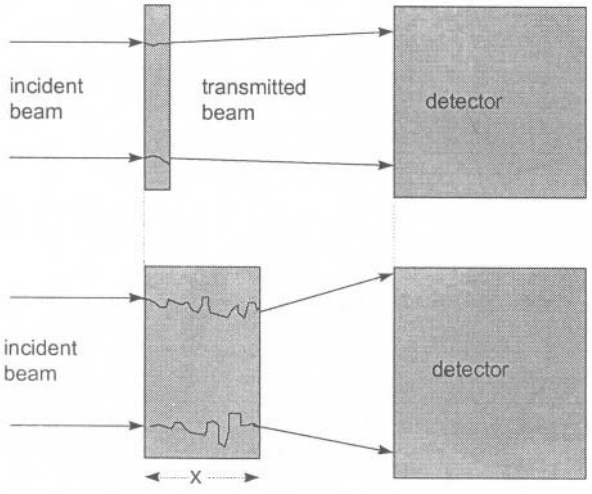

Fig.(2.4) The determination of the penetration, and hence the mean range, of a charged particle in a medium can be obtained by counting the number of particles N_x transmitted through a thickness x of the medium.

If such a transmission experiment were correctly performed, the number of particles N_x transmitted through thickness x, normalized to the number of incident particles N_0, is given by :

$$\frac{N_x}{N_0} = 1 - \int_{-\infty}^{x} \frac{1}{\alpha\sqrt{\pi}} \exp\left(-\frac{(x-R)^2}{\alpha^2}\right) dx \qquad (2.3)$$

In Eq.(2.3) the integration of the normal distribution in the second term proceeds up to thickness x, [4]. It is expressed in terms of two parameters, the range straggling parameter α and the mean range parameter R. The magnitude of R is defined as the thickness x for which $N_x/N_0 = ½$ and is determined by the energy of the particle. The width of the distribution of ranges, *i.e.* the range straggling, determines the magnitude of α. A light particle, which is subjected to large fluctuations in direction during its passage through the material, will have a large straggling parameter with the converse for a heavy particle.

In addition to range straggling, there is also the phenomenon of energy straggling. This describes the variations in the energy of a particle after it has travelled through a given thickness of material.

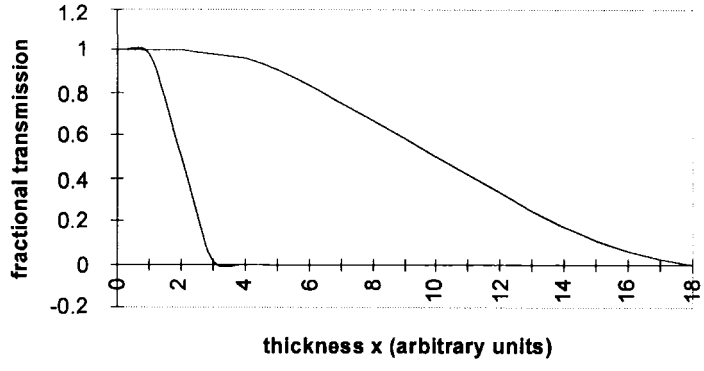

Fig.(2.5) A schematic representation of the percentage transmission of a charged particle through thickness x of absorbing material. The left-hand curve represents small values of R and α , e.g. a low energy alpha-particle, and the right-hand curve large values of R and α, e.g. a high energy electron. The mean ranges are 2.0 and 10.0 thickness units respectively.

2.2.2 *The depth-dependence method*

This method is used routinely in radiotherapy physics for two purposes. Firstly, to determine the mean range of the radiation and secondly, to achieve some measure of its quality (*i.e.* the spectral distribution). This is done largely through the measurement of the Tissue Phantom Ratio (TPR) which will receive more detailed attention in Chapter 9.

A beam of electrons is incident on the top surface of a tank of water in which a small-volume detector can move along the central beam axis, Fig.(2.6). The detector measures the energy deposited in its sensitive volume. For this reason the depth-dependence of the signal is called a Depth:Dose Distribution.

Fig.(2.7) differs from Fig.(2.5) in two important respects. Firstly, the absorbed dose when z is small is less than the maximum, D_m, because of the effect of Build-Up (see Chapter 7). Secondly, for large z, the dose does not become zero. This is due to the presence of *bremsstrahlung* radiation produced in the beam-defining collimators. The intersection of the line through the inflection point of the sigmoid portion of the curve (at R_{50}), and the straight line defining the *bremsstrahlung* tail defines the Practical Range, R_p. R_{50} corresponds to the mean range in Fig.(2.5). R_{ex} is the Extrapolated Range given by the extrapolation of the sigmoid portion onto the z-axis.

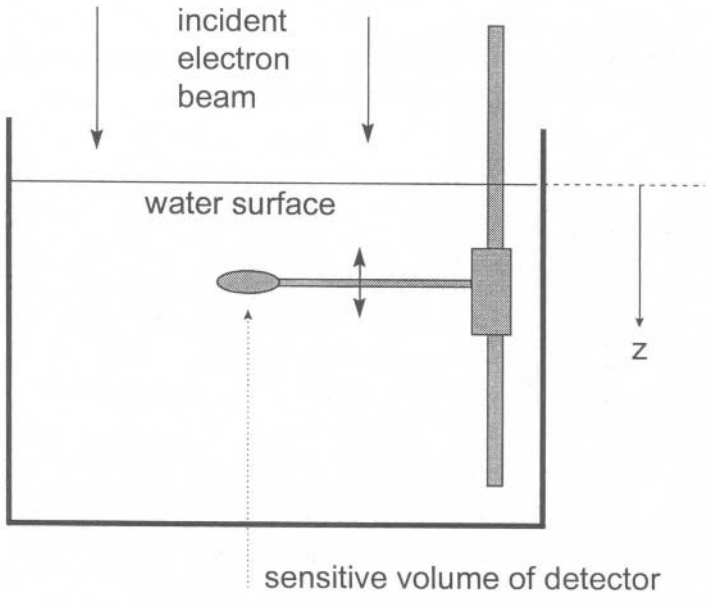

Fig.(2.6) Determination of the penetration of an electron beam in a tank of water. A (waterproofed) detector measures the ionization recorded in the sensitive volume as a function of depth, z, in the water.

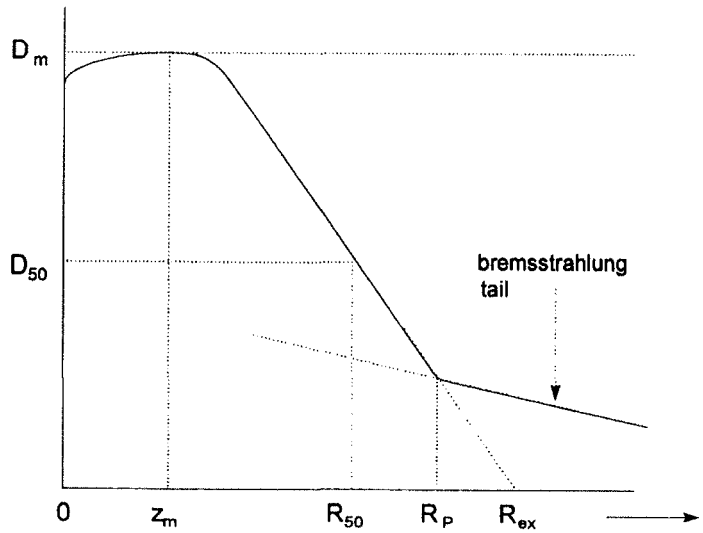

Fig.(2.7) The Depth Dose response of the detector in Fig.(2.6) as a function of depth z, in the irradiation of water by a beam of high energy electrons.

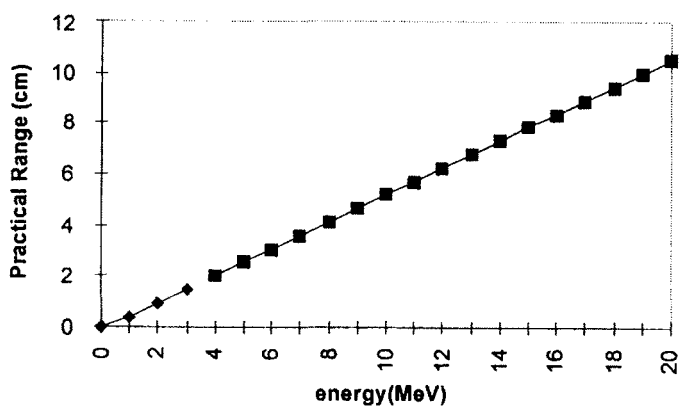

Fig.(2.8) The practical range of electrons in water.
◆ Using Eq.(2.4), for E=2 MeV, R_p = 0.95 cm. ■ Using Eq.(2.5), for E = 10 MeV, R_p = 5.2 cm.

The following is a summary of the various parameters which relate to the penetration of a charged particle into a medium [5] :

r_0 – the csda range. This is approximately equal to the total path length, but can never be greater than it.

z_{av} – the mean projected range (or mean penetration depth).

mean path length. This is the summation of the individual distances travelled by the particle between energy loss events. It is slightly larger than r_0 because of the effects of multiple scatter and thermal diffusion.

d – the detour factor (z_{av}/r_0). This gives a measure of the non-linearity of the track of the particle ($d < 1$).

R – the mean range. In Fig.(2.1) this is z_{av}. In Fig.(2.7) it is R_{50}. In the experimental determination which uses the method of Fig.(2.6), there is also the Mean Practical Range R_p and the Mean Extrapolated Range R_{ex}. When there is no background or *bremsstrahlung* tail to the curve in Fig.(2.7), then $R_p = R_{ex}$.

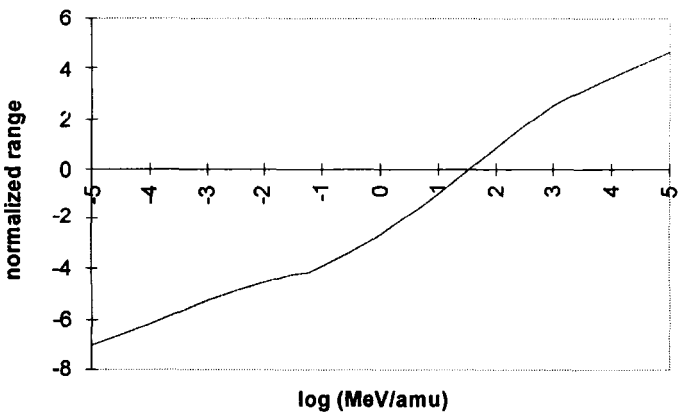

Fig.(2.9) Normalised range of heavy charged particles $(z^2/m_i)R\rho$ versus particle energy in log(MeV/amu). R = range of particle, m_i = mass of particle, z = charge on particle, ρ = density of medium, [7].

A number of empirical expressions have been proposed to relate the mean practical range, R_p, in water with the incident electron energy. As a general rule of thumb, the mean practical range in cm is half the incident energy in MeV. For example :

In the energy range $0.01 \leq E \leq 3$ MeV, for $n = 1.265 - 0.0954 \ln E$

$$R_p = 0.412E^n \qquad (2.4)$$

In the energy range $2.5 \leq E \leq 20$ MeV,

$$R_p = 0.530E - 0.106 \tag{2.5}$$

A useful source of range data for heavy charged particles is provided by the calculations of Barkas and Berger [6] for protons in water. Fig.(2.9) expresses the normalized range against energy/atomic mass unit.

2.3 Types of Charged Particle Interaction

Charged Particle Interactions fall into three broad groups :

(1) interactions with the individual electrons of atoms or molecules in the material. These interactions are by far the most important, and lead to excitation and/or ionization of the atoms or molecules.

- A collision is inelastic if the electron receives energy sufficient either to excite it into a higher bound state of the atomic system, or to eject it into an unbound state.
- If the amount of energy transferred is less than the smallest energy difference of the atomic or molecular levels (*i.e.* a sub-excitation collision) then the collision is regarded as an elastic scatter process in which energy and momentum are conserved. Clearly, the struck electron cannot be regarded as being isolated in these cases.

(2) interactions with nuclei. When the incoming particle is heavy (its mass is large compared to that of the electron), these include :

- nuclear reactions – in which the particle is first absorbed into the nucleus with the formation and subsequent decay of a compound nucleus (treated further in Chapter 8),
- nuclear (Potential) or Coulomb (Rutherford) scattering which lead to the phenomenon of Multiple Scattering. When the incident charged particle is an electron however, the inelastic scattering from the strong Coulomb field surrounding the nucleus gives rise to *Bremsstrahlung* radiation. This accounts for a significant contribution to the energy loss of electrons at high energies.

(3) interactions with the whole Coulomb field surrounding an atom. Here, the interaction is between the incident particle and the coupled system of nucleus plus orbiting electrons. This type of interaction occurs only for low energy incident particles, either :

- those below the excitation potential of the target atoms (molecules) or
- very heavy particles with low velocities. This type of collision is often, but inappropriately, called a nuclear collision.

Within each of these three groups, the outcome of a collision is determined by a further three parameters :

- the velocity of the collision, v,
- the distance of closest approach of the participants, r_{min}, and
- the range of the potential which governs the interactions between the incident particle and the target.

Table (2.1) Qualitative categorization of different types of collision.

Type of collision	soft ⇒ "isothermal"	hard ⇒ "adiabatic"
duration of collision	long	short
distance of closest approach	large	small
ion velocity/ orbital electron velocity	small	large
energy transferred	low	high

Table (2.1) shows how these three parameters lead to a distinction between soft or hard collisions. A collision is soft or hard when the distance of closest approach is either large or small compared with a characteristic range of the interaction potential. Similarly, fast or slow collisions are those characterized by projectile velocities which are high or low compared with the orbital velocity of the electrons in the target atom. If the collision time is short compared with a characteristic lifetime of the target system, we have an adiabatic collision with large energy transfer. As the collision time increases, there is a decrease in the amount of energy that can be transferred to the system.

The type of collision is determined by the random nature of the trajectory of the incoming particle with respect to the target. In addition, the range of the interaction potential between target and projectile influences the hardness or softness of the interaction. The following section now briefly considers the development of the theory of charged particle interactions.

2.4 Energy Transfer in an Elastic Collision - Classical Theory

The most likely outcome of the transport of a fast charged particle through a medium is the transfer of energy, via Coulomb interactions, to the electrons of the medium. In the non-relativistic condition, the kinetic energy of the incident charged particle,

T, is much smaller than its rest mass, Mc^2.

We therefore consider the collision between an incident particle of mass M, charge ze and velocity v with an electron of mass m_0, charge $-e$. The target electron is initially stationary in the Laboratory (L) System of coordinates. As a result of the collision, energy E is transferred from M to m_0, the latter being ejected at an angle ϑ with respect to the initial direction of mass M, [4].

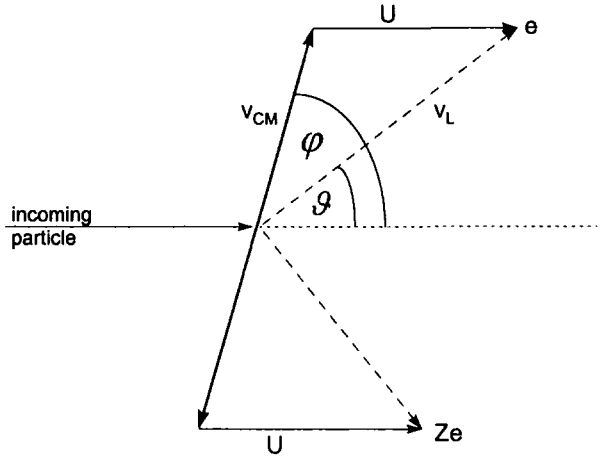

Fig.(2.10) Energy transfer between a mass M and an electron initially at rest in the Laboratory frame of reference. After the collision, the velocities of the struck electron in the L and Centre of Mass (CM) systems are v_L and v_{CM}. These make angles of ϑ and φ respectively with the initial particle direction. U is the velocity of the Centre of Mass.

In the L system, the total momentum is Mv and the Centre of Mass moves to the right in Fig.(2.10) with velocity $U=Mv/(M+m_0)$. In the CM system, the incident particle has a velocity before the collision of :

$$v - \frac{Mv}{M+m_0} = \frac{vm_0}{M+m_0}$$

Since the linear momenta are equal and opposite before and after the collision, the velocities of the two particles are in the inverse ratio of their masses. The electron velocity after the collision is therefore :

$$v_{CM} = \frac{Mv}{M + m_0}$$

giving an isoceles triangular relation between v_L, v_{CM} and U. The velocity of the electron in the L system is then given by :

$$v_L = 2\frac{Mv}{M + m_0}\cos\vartheta$$

where ϑ is the ejection angle of the electron with respect to the incoming particle trajectory. The energy of the recoil electron is :

$$E = \frac{1}{2}m_0\left(\frac{2Mv}{M + m_0}\right)^2 \cos^2\vartheta$$

If the ejection angle of the electron is φ in the CM system then, because the triangle is isoceles, we have $\varphi = 2\vartheta$. So :

$$E = 2m_0\frac{M^2v^2}{(M + m_0)^2}\frac{(1 + \cos\varphi)}{2}$$

For maximum energy transfer, $\cos\varphi \rightarrow 1$. When, in addition, the incoming particle is heavy so that $M >> m_0$, we have the condition that the maximum energy that a heavy particle can transfer to a stationary electron is :

$$E_{max} = 2m_0v^2 \qquad (2.6)$$

When the incident particle is an electron, we have $E_{max} = m_0v^2/2$. Note that m_0 is the mass of the (struck) electron, and v is the velocity of the incoming particle of mass M. When the incident particle becomes relativistic, we use $\tau = T / Mc^2$ to express the ratio of the kinetic energy of the particle to its rest energy. Eq.(2.6) is then more correctly expressed as :

$$E_{max} = \frac{2\tau(\tau + 2)m_0c^2}{\left[1 + 2(\tau + 1)(m_0/M) + (m_0/M)^2\right]} \qquad (2.7)$$

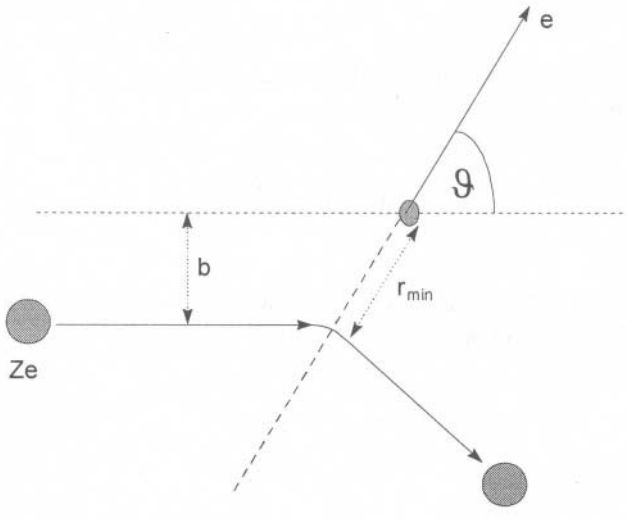

Fig.(2.11) The meaning of the impact parameter, *b*, and the collision diameter, r_{min}. ϑ is the scattering angle of the struck electron in the L system.

It is now necessary to consider the two distances which define a classical collision. The first is the impact parameter *b* which gives the separation of the two trajectories. The second is the collision diameter r_{min} which gives the minimum separation distance between the colliding particles, Fig.(2.11).

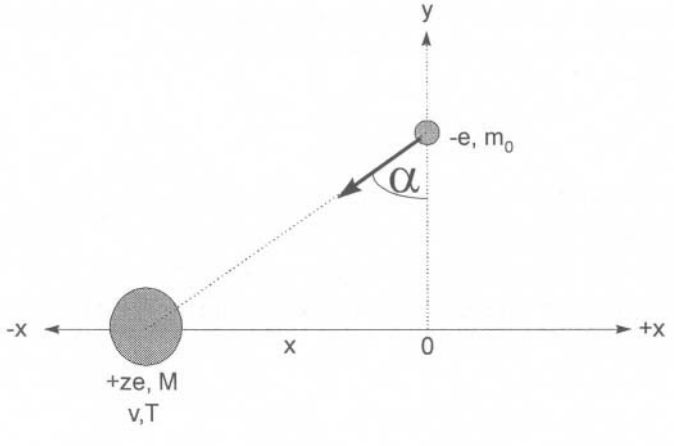

Fig.(2.12) The charged particle interaction between mass *M* and a free electron. The distance, *x*, goes from - to + infinity during the collision. The impact parameter, *b*, is the perpendicular distance between the trajectory and the target electron.

Two assumptions are made – firstly, that $M >> m_o$, so that the trajectory can be considered to be straight and secondly, that the electron is stationary before the collision. Fig.(2.12) represents the collision in terms of the kinetic energy of the projectile T and its impact parameter b.

The collision diameter, r_{min}, is related to b through the deflection angle in the L frame by :

$$b = \frac{r_{min}}{2} \tan \vartheta$$

When the electron is ejected at 45° in the L frame, the collision diameter is twice the impact parameter.

The attractive Coulomb force between the two particles is :

$$F = \frac{ze.e}{4\pi\varepsilon_0 (b / \cos\alpha)^2}$$

Since the x-component of F cancels over the duration of the collision, the remaining y-component is :

$$F_y = \frac{ze^2 \cos^3 \alpha}{b^2}$$

after omitting the permittivity term. The momentum transferred to the electron is :

$$q = \int F_y dt ,$$

where the duration of the collision, t, may be approximated as $b \tan \alpha / v$. Therefore $dt = (b/v) \sec^2 \alpha \, d\alpha$ and the momentum transfer becomes :

$$q = \frac{ze^2}{bv} \int_{-\pi/2}^{\pi/2} \cos\alpha . d\alpha = \frac{2ze^2}{bv}$$

The energy transfer for a given value of b is then :

$$E = \frac{q^2}{2m_0} = \frac{2z^2e^4}{m_0 b^2 v^2} \qquad (2.8)$$

Note the reciprocal relationship between the energy transferred and the square of the impact parameter. Although b goes to zero in a head-on collision, we cannot have $E \rightarrow \infty$, since Eqs.(2.6) and (2.7) give the maximum (finite) energy transfer possible in such a case. Therefore, there is a non-zero value of the smallest impact parameter given by, [4] :

$$b_{min} = \sqrt{\left(\frac{2z^2e^4}{m_0E_{max}v^2}\right)} = \frac{ze^2}{m_0v^2} \qquad (2.9)$$

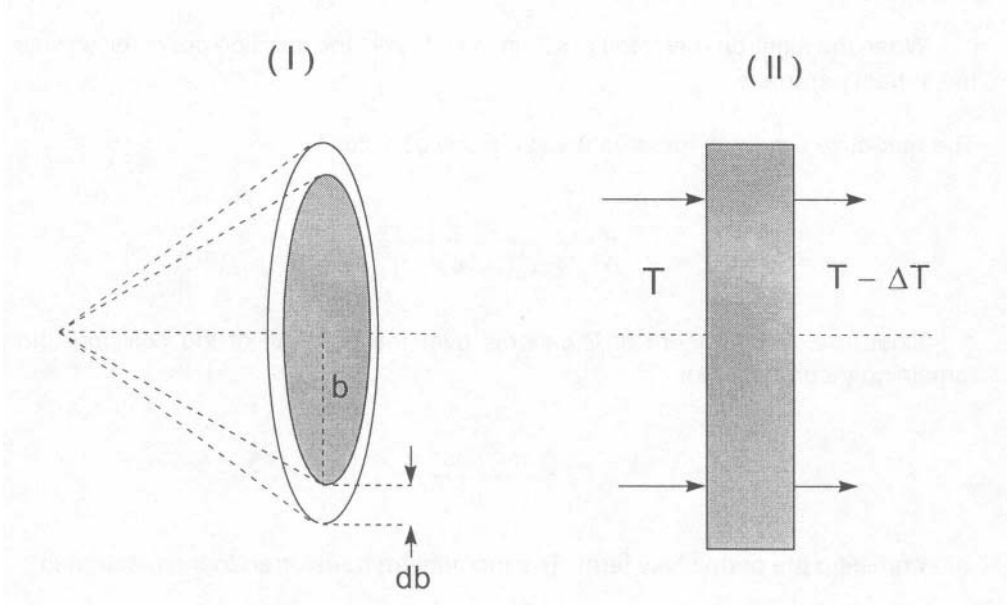

Fig.(2.13) (I) The definition of differential cross-section, $d\sigma$, for an impact parameter lying between b and b+db, is simply the area of the annulus of radius b and thickness db.
(II) We consider the energy loss ΔT in material of thickness Δx, atomic number Z, containing N atoms cm^{-3}.

When the struck electron is free, there is no lower limit to the energy transferred (and hence no upper limit to the impact parameter, b). For bound electrons, however, the initial velocity of the electron will not be zero but determined by its orbital period, $T_0 = 1/\omega$, where ω is the orbital angular velocity. If we specify a characteristic time of the collision, $\tau_c = b/v$, such that $\tau_c < T_0$ then we have an adiabatic collision which results in energy transfer. If, on the other hand, $\tau_c > T_0$, the collision is deemed to be "soft", causing a deformation and relaxation of the electron orbit without any transfer of energy. The maximum impact parameter is given by the condition $\tau_c = T_0$ which yields $b_{max} = v/\omega$ and :

$$E_{min} = \frac{2z^2e^4\omega^2}{m_0v^4} \tag{2.10}$$

Eqs.(2.6) and (2.10) now give the maximum and minimum limits within which energy transfer from incident (heavy) ion to (light) electron can take place.

The total energy loss ΔT ($<<T$) is made up of a large number of individual collisions in which the amount of energy transferred, E, depends on the value of b. If dn is the number of collisions in which the energy transferred is between E and $E+\Delta E$, and the incident particle flux sees υ electrons per unit area, then :

$$\Delta T = \int E\, dn = \upsilon \int_{E_{min}}^{E_{max}} E\, d\sigma$$

For a material of thickness Δx, atomic number Z and atomic density N (atoms cm^{-3}), we have $\upsilon = N\,Z\,\Delta x$. Further, from Fig.(2.13), the interaction cross-section is by definition, $d\sigma = 2\pi b\, db$. By differentiating Eq.(2.8), we get the differential cross-section in units of cm^2/electron as :

$$d\sigma = 2\pi b\, db = \frac{2\pi z^2e^4}{m_0v^2}\frac{dE}{E^2} \tag{2.11}$$

This is an important result. The probability of an energy loss event taking place is inversely proportional both to the square of the velocity of the incoming particle and to the square of the amount of energy transferred in that collision.

The Stopping Power of the material towards the progress of the particle is then:

$$\frac{\Delta T}{\Delta x} = \frac{NZ2\pi z^2e^4}{m_0v^2}\int_{E_{min}}^{E_{max}}\frac{dE}{E} = \frac{4\pi NZz^2e^4}{m_0v^2}\ln\left[\frac{m_0v^3}{ze^2\omega}\right] \tag{2.12}$$

The classical description in Eq.(2.12) is unable to go beyond the case of a heavy particle interacting with a single electron orbiting an isolated atom. It does not consider :

- any details of those collisions which result in excited atoms or molecules,
- the differences between atoms in the isolated (gaseous) and condensed states,
- collisions approaching relativistic velocities,

- collisions at very low velocities where the incident particle sees the complex scattering potential due to the whole atomic electron cloud,
- interactions with the nucleus.

2.5 Stopping Power of a Charged Particle - the Bethe Formula

A quantum mechanical approach starts by using the Born approximation. This requires that the energy transferred is small compared with the energy of the projectile, when only the first order terms in the interaction energy are needed. In this case, the Bethe expression for energy loss of a heavy charged particle at non-relativistic velocities (the so-called electronic or collisional loss) is based on the following, [5] :

- it requires that $\frac{z\,Z}{\beta} << 1$. For the Born approximation to be valid, the velocity of the incoming ion or electron, v, must be much greater than the orbital velocity of the struck electron, u. If u is the Bohr-orbit velocity of a K-shell electron in the medium of atomic number Z, then :

$$\frac{u}{v} = \left(\frac{Z}{137\beta}\right) << 1$$

- it sums the contributions from hard and soft collisions,
- it introduces the mean excitation energy, I. This is a weighted average of all possible energy transfers from the incoming particle to an electron of the medium. It includes excitations as well as ionizations,
- it introduces the cut-off energy, E_c, to distinguish between hard and soft collisions.

The Bethe expression for the electronic contribution to the mass stopping power of a particle with velocity $\beta = v/c$ in a medium of density ρ is :

$$\frac{1}{\rho}\left(\frac{dT}{dx}\right)_{electronic} = \frac{4\,\pi\,r_e^{\,2} m_0 c^2}{\beta^2}\,\frac{1}{u}\,\frac{Z}{A}\,z^2\left[ln\left(\frac{2m_0c^2\beta^2\gamma^2}{I}\right) - \beta^2\right] \qquad (2.13)$$

In Eq.(2.13), $u = 1.6606 \times 10^{-24}$ g is the atomic mass unit, $r_e = e^2/m_0c^2 = 2.818 \times 10^{-13}$ cm is the classical electron radius and $\gamma^2 = 1/(1-\beta^2)$. The expression is valid only for projectile velocities which are large compared to the velocities of atomic electrons.

2.5.1 *Mean excitation energy,* I

The stopping power is only logarithmically dependent on the mean excitation energy and is therefore rather insensitive to changes in I. Nevertheless, the determination

of I from measured stopping power data in different materials is the most direct method. More accurate methods involve the use of optical oscillator strengths (derived from photo-absorption cross-sections) or dielectric response functions, but fewer data are available.

The oscillator strength f_i is used to denote the participation of the i'th electron in the energy loss process. For a given atom, we have :

$$\ln \mathrm{I} = \sum_i f_i \ln E_i \tag{2.14}$$

where E_i represents the energy transferred to the i'th electron. This can be an electronic excitation of the atom or molecule or an excitation into the continuum, *i.e.* an ionization.

A comprehensive tabulation of I values is given [3]. For high atomic number materials, $\mathrm{I} \approx 10\ Z$ (eV). Other empirical expressions have been given by Barkas and Berger [6] :

$$\mathrm{I}(Z) = 12Z + 7 \text{ eV} \qquad \text{for } Z \leq 13$$

$$\mathrm{I}(Z) = 9.76Z + 58.8Z^{-0.19} \text{ eV} \qquad \text{for } Z \geq 13$$

For mixtures and compounds containing N_w atoms cm^{-3} of atom w having atomic number Z_w, use can be made of the Bragg Additivity Rule :

$$\ln \mathrm{I} = \frac{\sum_w \mathrm{N_w} Z_w \ln \mathrm{I_w}}{\sum_w N_w Z_w} \tag{2.15}$$

2.5.2 *The cut-off energy, E_c, and restricted stopping power*

The use of a cut-off energy makes it possible to restrict the energy deposited in a medium to events which are localized. The extent of the localization is determined by the size of the cut-off energy. Energy depositions which result in the production of very energetic secondary electrons can therefore be excluded and treated as separate events. Eq.(2.13) can be rearranged to include the limiting cut-off energy as follows :

$$\frac{1}{\rho}\left(\frac{dT}{dx}\right) = \frac{4\,\pi\, r_e^2 m_0 c^2}{\beta^2}\frac{1}{u}\frac{Z}{A}z^2\left[ln\left(\frac{2m_0c^2\beta^2\gamma^2}{I}\right) - \beta^2\right]$$

$$= \frac{2\,\pi\, r_e^2 m_0 c^2}{\beta^2}\frac{1}{u}\frac{Z}{A}z^2\left[2\,ln\left(\frac{2m_0c^2\beta^2\gamma^2}{I}\right) - 2\beta^2\right]$$

$$\left[ln\left(\frac{\left(2m_0c^2\beta^2\gamma^2\right)^2}{I^2}\right) - 2\beta^2\right]$$

$$\left[ln\left(2m_0c^2\beta^2\gamma^2\right)^2 - 2\,ln\,I - 2\beta^2\right]$$

$$\left[ln\left(2m_0c^2\beta^2\gamma^2E_c\right) - 2\,ln\,I - 2\beta^2\right]$$

where E_c gives the limiting energy cut-off. The maximum energy that can be transferred to an unbound electron is given in Eq.(2.6) for a heavy incident particle. For a smaller energy transfer limit, determined only by the velocity of the incoming ion, we have :

$$E_c = 2m_0c^2\beta^2\gamma^2$$

The square bracket term is now divided by 2 to give :

$$\frac{1}{\rho}\left(\frac{dT}{dx}\right)_{E_c} = \frac{4\,\pi\, r_e^2 m_0 c^2}{\beta^2}\frac{1}{u}\frac{Z}{A}z^2\left[\frac{1}{2}ln\left(\frac{2m_0c^2\beta^2E_c}{\left(1-\beta^2\right)}\right) - ln\,I - \beta^2\right] \qquad (2.16)$$

Eq.(2.16) now gives the stopping power restricted to energy transfers smaller than E_c. Two conditions can then be specified :

- When E_c is larger than the largest binding energy of the atomic electrons in the medium. In this case E_c is much larger than the K-shell binding energy of the highest atomic number constituent. Energy losses by the incoming particle which are smaller than E_c must therefore result from collision impact parameters which are large compared to the atomic dimensions.
- When an energy transfer is larger than E_c. In this case the energy transfer must lie in the range E_c to E_{max}, Eq.(2.6). It must be the result of a collision at such a small impact parameter that the target electron can be considered to be free and at rest.

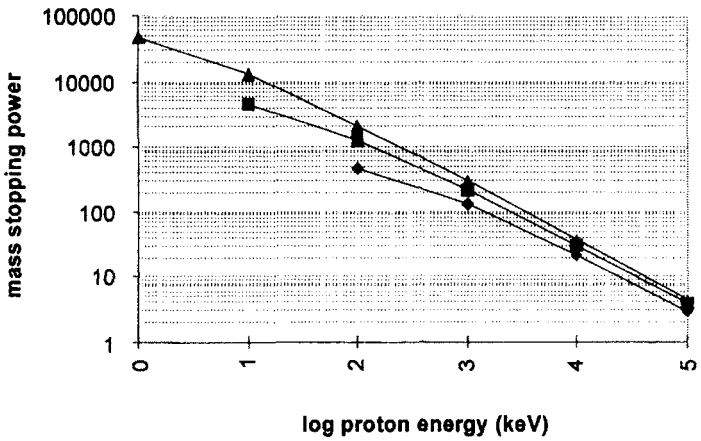

Fig.(2.14) The Mass Stopping Power (MeV cm^2 g^{-1}) of a proton in carbon using Eq.(2.16) and a Mean Excitation Energy, I , of 78 eV. The Cut-Off energies E_c are 100 eV (◆), 1000 eV (■) and 10000 eV (▲).

The factors before the square brackets in Eq.(2.16) give the gross features of the energy loss, having the value :

$$\frac{4\pi\, r_e^2 m_0 c^2}{u}\left(\frac{z^2 Z}{\beta^2 A}\right) = 0.307\left(\frac{z^2 Z}{\beta^2 A}\right) MeV\ cm^2\ g^{-1} \qquad (2.17)$$

Using Eq.(2.17) and $T_{proton} = \beta^2 \times 4.697 \times 10^5$ keV, the effect on the total mass stopping power of different cut-off energies E_c can be illustrated in Fig.(2.14) for a non-relativistic proton traversing carbon.

Note that no data points appear in Fig.(2.14) for the lowest incident energies and the lowest cut-off limits. This is because the energy transferred is so small that the sum of the two logarithmic terms in Eq.(2.16) becomes negative.

The quantity in the square brackets of Eq.(2.16) is frequently replaced by the dimension-less Stopping Number, *L*, to account for the fine details of the stopping process.

$$L(\beta) = L_0(\beta) + zL_1(\beta) + z^2 L_2(\beta) \qquad (2.18)$$

The principal term in Eq.(2.18) describes the effectiveness of the incident particle in ionizing a target atom or molecule. It contains the square brackets of Eq.(2.16) together with two correction terms. These are :

- the shell term C/Z. This accounts for the effects at low incident particle energies when the incoming velocities become smaller than the velocities of K, L,.. – shell electrons of the target atom. When the ion velocity is smaller than that of a K–shell electron, the latter no longer contributes to the stopping process and the stopping power is reduced by the negative term $-(C/Z)_K$. Similar terms account for the effects in L–shell, and even less tightly bound, electrons. The shell term increases as the Z of the material increases and as the velocity of the incident particle decreases [3].
- the density term $\delta/2$. At high incident velocities the fast moving charge polarizes the atoms of the medium in such a way as to reduce the electromagnetic field acting on the particle. Consequently a decrease is again seen in the stopping power.

The principal term in the stopping number is then :

$$L_0(\beta) = \frac{1}{2} ln\left(\frac{2m_0c^2\beta^2E_c}{1-\beta^2}\right) - \beta^2 - ln\, I - \frac{C}{Z} - \frac{\delta}{2}$$

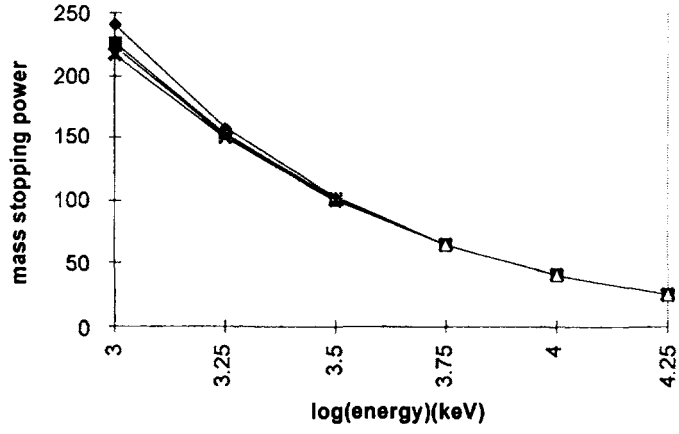

Fig.(2.15) The effects of Shell and Barkas correction terms on the mass stopping power of protons in carbon (MeV cm^{-2} g^{-1}). The cut-off energy E_c is given by Eq.(2.6) (i.e. the maximum value): ◆ Eq.(2.16); ■ Eq.(2.16) with K-shell correction term added; ▲ Eq.(2.16) with K-and L-shell terms added; ✖ Eq.(2.16) with K- and L-shell and Barkas terms added.
The Bloch $z^2L_2(\beta)$ and the density $\delta/2$ terms are insignificant at these incident energies. Data have been interpolated from [3].
These correction terms clearly become more important in reducing the mass stopping power, as given in Eq.(2.16), when the incident proton energy becomes smaller than 1 MeV.

The second term in Eq.(2.18), $zL_1(\beta)$, is known as the Barkas term. It contains the charge on the incident ion, z, raised to the first power. The term therefore changes

sign on going from particle to anti-particle. It has the effect of reducing the stopping power of an electron, for example, compared with that of a positron at the same energy. Further reference may be made to ICRU-49 [3] and ICRU-37 [5].

The third term, $z^2L_2(\beta)$, is the Bloch term. It accounts for the departures from the first-order Born approximation. It is inversely proportional to β^2, and has the effect of reducing the stopping power for low energy particles [3], [5].

Note that at low incident velocities, the electronic contribution to the mass stopping power of a charged particle is reduced when :

- there is a reduction in the cut-off energy E_c below that given by Eq.(2.6), see Fig.(2.14),
- the effects of the Shell and Barkas correction terms become important, see Fig.(2.15).

2.6 Theoretical Description for Light Charged Particles

An incoming electron has the same mass as the struck electron in an electronic energy loss process and is indistinguishable from it. The stopping power is therefore considered to apply to the faster of the two particles that emerge from the collision.

Eq.(2.11) gives the differential cross-section for the transfer of energy between E and $E + dE$ to a free electron. When the incoming particle is itself an electron we have $z = -1$. The differential cross-section for the incident electron to lose energy E to the struck electron, and emerge from the collision with energy $T - E$, is :

$$\frac{d\sigma}{dE} = \frac{2\pi e^4}{m_0 v^2}\frac{1}{E^2}$$

Because the incident and target electrons are indistinguishable, there is also the possibility that $T - E$ is transferred to the struck electron and the incident electron emerges with energy E. The total cross-section is the sum of these two possibilities:

$$\frac{d\sigma}{dE} = \frac{2\pi e^4}{m_0 v^2}\left[\frac{1}{E^2} + \frac{1}{(T-E)^2}\right]$$

$$= \frac{2\pi e^4}{m_0 v^2}\frac{1}{E^2}\left(\frac{T}{T-E}\right)^2\left[1 - 2\left(\frac{E}{T}\right) + 2\left(\frac{E}{T}\right)^2\right] \qquad (2.19)$$

In this case, the maximum energy transfer is now $T/2$ and the subsequent formulae for the stopping power therefore apply to energy transfers $E \leq T/2$. From Eq.(2.6) this gives $E \leq E_{max}/2$.

Just as in the case of heavy charged particles, a distinction is made between hard and soft collisions in the transition from a classical to a quantum mechanical description.

- a hard collision is one in which the energy transfer extends from the maximum ($T/2$) down to an arbitrary value E_H . This is large compared with the binding energy of the struck electron,
- in a soft collision, the energy transferred extends downwards from E_H to the minimum needed to produce either an excitation or an ionization of an atom or molecule of the medium.

The mass stopping power can therefore be given by :

$$\frac{1}{\rho}\left(\frac{dT}{dx}\right)_{electronic} = \frac{1}{\rho}\left(\frac{dT}{dx}\right)_{E<E_H} + \frac{1}{\rho}\left(\frac{dT}{dx}\right)_{E>E_H} \tag{2.20}$$

For incident electrons, hard collisions will be infrequent because they result in the loss of almost half of the incident energy.

When Eq.(2.19) is corrected for relativistic, spin and exchange effects, the total cross-section for energy loss becomes the Møller cross-section. This applies to the collision of indistinguishable particles. When combined with Eq.(2.20) it gives :

$$\frac{1}{\rho}\frac{dT}{dx} = \frac{2\pi r_e^2 m_0 c^2}{\beta^2}\left(\frac{Z}{uA}\right)\left[2\,ln\left(\frac{T}{I}\right) + ln\left(\frac{2+\tau}{2}\right) + F^{\pm}(\tau) - \delta\right] \tag{2.21}$$

In the comparison with Eq.(2.17), note the appearance of 2 instead of 4 in the pre-logarithmic term, and the fact that $z^2 = 1$ for an electron or positron. The function $F^{\pm}(\tau)$ is defined for an electron and a positron as :

$$F^{-}(\tau) = \left(1-\beta^2\right)\left[1 + \frac{\tau^2}{8} - (2\tau+1)\,ln\,2\right]$$

$$F^{+}(\tau) = 2\,ln\,2 - \left(\frac{\beta^2}{12}\right)\left[23 + \frac{14}{\tau+2} + \frac{10}{(\tau+2)^2} + \frac{4}{(\tau+2)^3}\right]$$

For non-relativistic electrons we have $\beta \rightarrow 0$ and $I << T << m_0c^2$. Eq.(2.21) then reduces to :

$$\frac{1}{\rho}\left(\frac{dT}{dx}\right)_{electronic} = \frac{4\pi e^4}{m_0 v^2}\left(\frac{Z}{uA}\right) ln\left(\frac{m_0 v^2}{I\sqrt{2}}\right) = \frac{2\pi e^4}{T}\left(\frac{Z}{uA}\right) ln\left(\frac{T\sqrt{2}}{I}\right) \qquad (2.22)$$

Fig.(2.16) shows that this is an acceptable approximation down to ~2 keV.

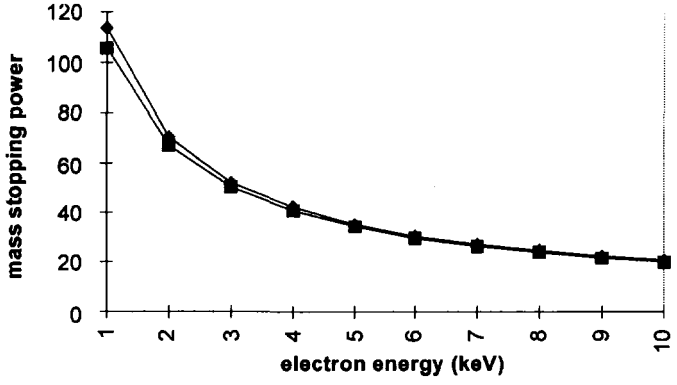

Fig.(2.16) Mass Stopping Power (MeV $cm^2 g^{-1}$) of electrons in carbon (graphite). ■ Eq.(2.21): ◆ Eq.(2.22).

Even over the energy range shown in Fig.(2.16), and certainly below 1 keV, the fractional energy loss in a single collision becomes increasingly large. Under these conditions, the use of the Continuous Slowing Down Approximation is inappropriate.

Table (2.2) Average fractional energy loss of an electron with a water molecule in the vapour phase, [5], [7].

Energy (keV)	fractional energy loss (%)
10	0.5
1	3.6
0.5	6.4
0.1	22

2.7 Interactions of Low Energy Electrons

Below ~2 keV, the Bethe-Bloch theory becomes inadequate for electrons, because the incident velocity becomes comparable to, and eventually smaller than, the Bohr orbital velocity.

At low energies it becomes more appropriate to consider energy loss in terms of the dielectric response of the medium. In this case the situation resembles that in electrostatics, when the effect of an external field is reduced if it induces a polarization of the medium. The extent to which this screening of the external field takes place is determined by the dielectric constant.

This principle is now generalised [8] to include :

- external fields which vary in both space and time – as in the case of a charged particle approaching an atom,
- a longitudinal electric field, $\Delta(r,t)$, which produces a charge density $\rho(r,t)$ in the medium at location r and time t,
- the assumption that the applied field is sufficiently weak that $\rho(r,t) \propto \Delta(r,t)$.

Equations which relate the internal field $\mathrm{E}(r,t)$, the displacement field $\Delta(r,t)$ and the charge density $\rho(r,t)$ are Fourier-transformed in space and time. The resulting fields can then be expressed in terms of $\varepsilon(q,\omega)$, the wave vector and frequency-dependent dielectric constant. Thus :

$$\mathrm{E}(q,\omega) = \frac{\Delta(q,\omega)}{\varepsilon(q,\omega)}$$

On a microscopic scale, the wave vector q and frequency ω denote the momentum transfer $(\hbar q)$ and energy loss $(\hbar\omega)$ arising from the passage of the charged particle. On the macroscopic scale, it is the rigidity of the electronic structure that determines the dielectric response. A comparison can therefore be drawn with the involvement of core and valence electrons in the energy loss of an electron as it travels through an insulating medium.

From the early consideration of interactions in a Fermi-Dirac electron gas [9], expressions have been found [10],[11] for :

- the inverse mean free path of an electron with initial energy E,

$$\mu(E) = \int_0^{0.583E} d(\hbar\omega)\frac{d\mu}{d(\hbar\omega)} \qquad (2.23)$$

  In Eq.(2.23) the upper limit of integration accounts approximately for the influence of exchange between the incident electron and the electrons in the medium,
- the differential inverse mean free path with respect to energy loss:

$$\tau(E,\hbar\omega) = \frac{d\mu}{d(\hbar\omega)} = \frac{1}{\pi r_B E}\int_{q-}^{q+}\frac{dq}{q}\,Im\left[\frac{-1}{\varepsilon(q,\omega)}\right] \qquad (2.24)$$

where the limits of integration of the momentum are given by

$\hbar q_{\pm} = \sqrt{2m_0}\left[\sqrt{E} \pm \sqrt{E-\hbar\omega}\right]$ for an energy loss between $\hbar\omega$ and $\hbar\omega + d(\hbar\omega)$.

$r_B = \hbar^2/m_0e^2$ is the Bohr radius,

- the stopping power $S(E) = \int_0^{0.583E} d(\hbar\omega)\;\hbar\omega\;\frac{d\mu}{d(\hbar\omega)}$ (2.25)

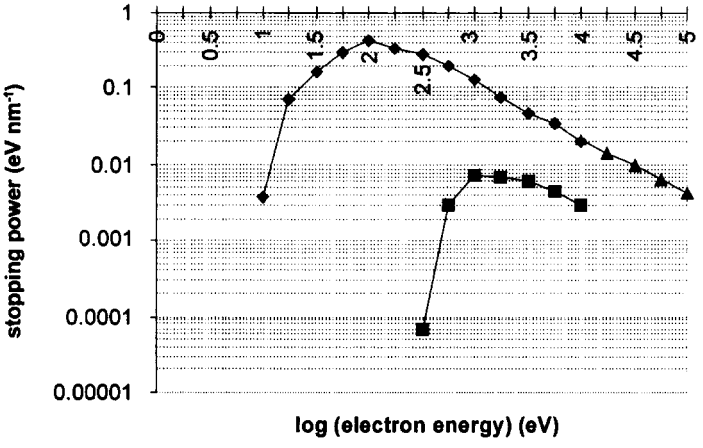

Fig.(2.17) Contributions to the stopping power (eV nm^{-1}) of polystyrene for electrons using Eqs. (2.26) and (2.27) with data from [10].
◆ valence electrons : ■ K-shell electrons : ▲ Bethe-Bloch theory.

It is the imaginary part of the optical dielectric function which leads to the determination of the energy-loss function $Im[-1/\varepsilon(q,\omega)]$. This requires the characterisation of the i'th electronic state in terms of the number n_i of electrons occupying this state. In addition, the state has a binding energy E_i^B and an orbit radius $\alpha_i r_B$ which is a factor α_i larger than the Bohr radius. Two categories of electrons of the medium are considered :

- valence electrons and
- core electrons.

The differential inverse mean free path, Eq.(2.24), can be re-expressed to include

ionisation and excitation events as:

$$\tau_i^{exc}(E,\hbar\omega) = \tau_i(E,\hbar\omega) + \tau_i\left(E, E_i^B + E - \hbar\omega\right) - \left[1 - \sqrt{\frac{E_i^B}{E}}\right]\sqrt{\tau_i(E,\hbar\omega) \times \tau_i\left(E, E_i^B + E - \hbar\omega\right)} \tag{2.26}$$

The contribution to the stopping power from the excitation of the *i'* th electron is then :

$$S_i(E) = \int_{E_i^B}^{(E+E_i^B)/2} d(\hbar\omega)\ \hbar\omega\ \tau_i^{exc}(E,\hbar\omega) \tag{2.27}$$

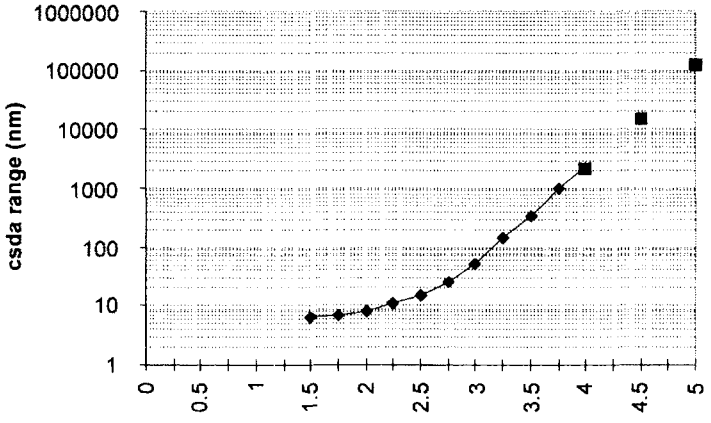

Fig.(2.18) The csda range (nm) of electrons in polystyrene from energy *E* down to 10 eV. ◆ calculation using Eq.(2.27) and the csda definition Eq.(2.1): ■ Bethe-Bloch theory.

2.8 Momentum Loss of Heavy Charged Particles

This contribution to the stopping power comes from the recoil of an atom of the medium following the Coulomb elastic scatter of the incident projectile. Although it is commonly referred to as nuclear collision loss, the process is not actually nuclear, but merely the scatter of an incoming charge *ze* by a target charge *Ze*. The potential between the two, when they are separated by distance r is :

$$V(r) = \frac{zZe^2}{r} F_s(r / r_s) \tag{2.28}$$

Here $F_s(r/r_s)$ is the parameter which takes account of the screening of the target charge by the atomic electrons.

The screening length r_s can be expressed in a number of ways. Numerical calculations of the screening function for many different combinations of projectile and target have been used to yield universal expressions for α-particles and heavier ions. For example, using the Bohr radius $r_B = \hbar^2/m_0e^2$, we have :

$$r_s = 0.88534 r_B \left(z^{.23} + Z^{0.23}\right)^{-1}$$
$$F_s(r / r_s) = 0.2\exp(-3.2r / r_s) + 0.5\exp(-0.9r / r_s) + 0.3\exp(-0.4r / r_s) + 0.3\exp(-0.2r / r_s)$$

An important aspect of the passage of positive ions through matter is the variation of charge state with energy. At each collision, a positive particle has a certain probability of picking up an electron and thereby reducing its positive charge state by one. At a subsequent collision there is a finite probability that the particle can lose this electron back to an atom of the medium. The ratio of these two probabilities, electron gain to electron loss, increases as the energy of the particle decreases. As a consequence, a positive ion ultimately becomes a neutral atom at the end of its range.

The steps necessary in the formulation of the nuclear collision stopping power from the scattering potential in Eq.(2.28) are now :

- the determination of the angle of scatter in the centre-of-mass system of co-ordinates using $$\theta = \pi - 2\int_{r_{min}}^{\infty} \frac{1}{r^2} \frac{1}{\left[1 - V(r)\frac{M + M_t}{T\,M_t} - \frac{b^2}{r^2}\right]^{1/2}} b\,dr$$ where r_{min}, M and b have the same meaning as in section 2.4. M_t is the mass of the target atom. (Note that in this expression θ is the angle of scatter of the incident positive ion, whereas ϑ in section 2.4 is the angle of scatter of an electron in an ionization event),
- the determination of the elastic scattering cross-section. This is obtained from the numerical differentiation of the above relation between θ and b using

$$\frac{d\sigma_{el}}{d\Omega} \sin\theta = -b\frac{db}{d\theta}$$

The mass nuclear stopping power is then given by :

$$\frac{1}{\rho}\left(\frac{dT}{dx}\right)_{nuclear} = -2\pi N \int_0^\infty b \frac{db}{d\theta} E(\theta,T) db$$

where $E(\theta,T) = E_m sin^2(\theta/2)$ is the energy transferred to the recoiling atom and E_M is the maximum amount that can be transferred in a single collision. This is given in section 2.4.

For the present situation we have $E_M = E_{max} = 4T\frac{M_t M}{(M+M_t)^2}$.

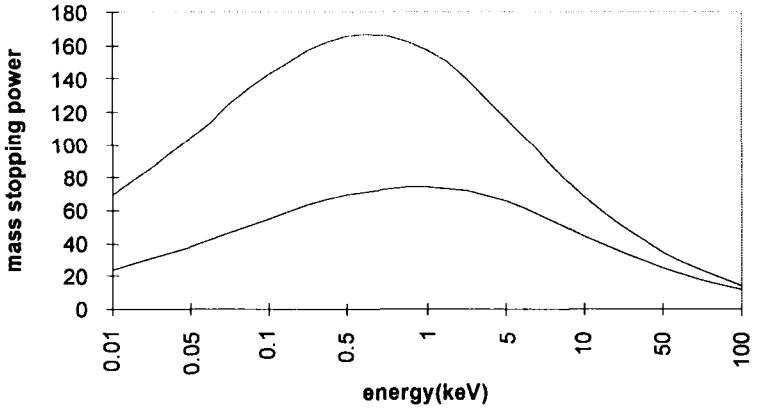

Fig.(2.19) The Mass Nuclear Stopping Power (MeV cm^2 g^{-1}) due to energy loss of α-particles in carbon (upper curve) and aluminium (lower curve), [3].

2.9 Coulomb Scattering of Heavy Charged Particles

Section 2.4 considered the elastic scatter of one charged particle by another. Interest centred on the amount of energy, E, transferred to the struck electron when it was ejected at an angle ϑ with respect to the direction of the incident particle. This angle was called φ in the CM system, Fig.(2.10).

When it is the scatter of the incident particle that is under consideration, the vector diagram Fig.(2.10) is modified. Now we allocate the scatter angles Θ in the Laboratory system and Φ in the CM system to the incident particle. The relations between scatter angles in the two systems depend on the ratio of the incident, M, and struck, M_t, particle masses, [4]. These are :

1. $M >> M_t$ $\quad \tan\Theta = \frac{M_t}{M}\sin\Phi$

2. $M << M_t$ $\quad \Phi = \Theta + \frac{M}{M_t}\sin\Theta$

3. $M = M_t$ $\quad \cot an\Theta = \cot an\Phi + \cos ec\Phi = \cot an\frac{\Phi}{2}$

Case 1 corresponds to the situation considered in section 2.4 when a heavy charged particle sees very little change in its trajectory as the result of an elastic collision with an electron.

Case 2 corresponds to the original Rutherford scattering experiment in which α-particles (charge ze) were scattered by gold atoms (charge Ze). The differential cross-section per unit solid angle $d\Omega$ for the scatter of mass M into angle Φ in the CM system is :

$$d\sigma = \frac{r_{min}^{\ 2}}{16}\frac{1}{\sin^4(\Phi/2)}d\Omega$$

Here, $r_{min} = 2Zze^2/M_0v^2$ is the collision diameter, $M_0 = MM_t/(M+M_t)$ is the reduced mass, and v is the velocity of the mass M. When the incoming particle is an electron, the classical cross-section per unit solid angle for Rutherford scatter in the Laboratory system by a nuclear charge Z is :

$$d\sigma = \frac{Z^2r_e^{\ 2}}{4}\frac{\left(1-\beta^2\right)}{\beta^4}\frac{1}{\sin^4(\Theta/2)} \text{ cm}^2\text{/nucleus}$$

Case 3 is appropriate for electron–electron scattering. Because these particles are indistinguishable, for a non-relativistic collision we have :

$$\varphi = 2\theta$$

$$\theta = \frac{1}{2}(\pi - \Phi)$$

The total differential scatter cross-section of either of the electrons into unit solid angle at a Laboratory angle greater than Θ is given by :

$$d\sigma = \left(\frac{e^2}{m_0v^2}\right)^2\left(\frac{1}{\sin^4\Theta} + \frac{1}{\cos^4\Theta}\right)4\cos\Theta$$

The quantum mechanical expression for electron-electron scattering was derived by Mott. Evans [4] gives an approximate relation which is adequate for electron energies greater than 1 keV :

$$d\sigma = \left(\frac{e^2}{mv^2}\right)^2 \left(\frac{1}{\sin^4\Theta} + \frac{1}{\cos^4\Theta} - \frac{1}{\sin^2\Theta\cos^2\Theta}\right) 4\cos\Theta$$

The foregoing refers to single scatter where the probability of a scattering event is very small. When the path length in the medium is large, so that the particle undergoes a large number of scatter collisions, we have the conditions of Multiple Scatter. In this case, statistical methods can be used to find the mean angle of deflection. The expressions for single scatter can still be used, within the approximation that the charge of the scattering nucleus is now $Z(Z+1)$ instead of Z^2.

2.10 Inelastic Scattering of Light Particles—Radiation Loss

Whenever a charged particle suffers an acceleration – either a deflection of its path or a change in velocity – it radiates electromagnetic energy (*bremsstrahlung*). The wave amplitude of this radiation is proportional to the acceleration times the charge. For a particle mass M and charge ze being accelerated by a charge Ze, the acceleration is proportional to zZe^2/M. The intensity of the emitted radiation is therefore proportional to $(ze \times zZe^2/M)^2$. Consequently, an electron is approximately six orders of magnitude more efficient at producing *bremsstrahlung* radiation than a proton of the same velocity.

Two questions therefore need to be addressed :

(1) What is the intensity of the radiated energy, and
(2) What is the rate of energy loss of the charged particle per unit thickness of material traversed?

The answers to the above come largely from quantum mechanical calculations. These consider the plane wave of an electron which enters a nuclear Coulomb field. The electron is scattered and in the process emits a photon with a small probability.

Expressions for the cross-section depend on the energy region being considered, and on the degree to which the extra-nuclear electrons of an atom tend to screen out the nuclear charge. Different analytical expressions therefore apply to relativistic, non-relativistic, screened and non-screened situations. Since, in addition, there is also the (smaller) possibility of radiation from electron-electron collisions, a full treatment of radiative loss becomes long and involved.

As a result, most theories deal with the Thin Target case. In this a mono-energetic

electron passes through a target so thin that the probability of interaction through any other kind of interaction is negligible. Thus the possibility of ionization, elastic scatter or more than one inelastic scatter, is neglected.

Principle points to note are the following :

- In the classical view, an incoming electron can radiate any fraction of its energy from zero to its total kinetic energy T_0 in each collision.
- The quantum mechanical model states that there is a small probability of photon emission at each collision at which a relatively large amount of energy is radiated.
- On average, however, the amounts of energy radiated are approximately the same in both models, even though the spectral distributions are different.
- The momentum of the incoming electron is shared after the collision between the outgoing photon, the recoiling nucleus and the scattered electron. Except at extreme relativistic energies, the momentum of the photon *(hν/c)* is small compared with the electron momentum so it can be emitted in any direction.

The differential cross-section given by quantum mechanics for the emission of *bremsstrahlung* in the energy range $h\nu$ to $h\nu + d(h\nu)$ is [4] :

$$d\sigma_{rad} = \alpha r_e^2 B Z^2 \frac{T + m_0c^2}{T} \frac{d(h\nu)}{h\nu} \qquad (2.29)$$

Here the electron has initial kinetic energy T and interacts with a nucleus of charge number Z. B is a dimension-less function of Z and T which was evaluated by Heitler [12] and $\alpha = 1/137$ is the Fine Structure Constant. The units of $d\sigma_{rad}$ are cm^2/ nucleus.

The intensity of radiation is given by the product of the cross-section and the amount of energy radiated. Re-arrangement of Eq.(2.29) can therefore be used to define B as the intensity of radiation emitted between $h\nu$ and $h\nu + d(h\nu)$:

$$B = \frac{1}{\alpha r_e^2 Z^2} \frac{T}{\left(T + m_0c^2\right)} h\nu \frac{d\sigma_{rad}}{d(h\nu)}$$

The total energy loss of an electron as it traverses unit distance in a medium, dT/dx, is equal to the energy radiated, $h\nu$, times the probability of this emission. Since this process takes place at all energies as the electron slows down from its initial kinetic energy T, we have :

$$\frac{dT}{dx} = N\int_0^T h\nu \, d\sigma_{rad} = N\alpha r_e^2 Z^2 \left(T + m_0c^2\right)\int_0^1 B \, d\left(\frac{h\nu}{T}\right) \qquad (2.30)$$

in units J cm^{-1} if there are N nuclei cm^{-3}. In Eq.(2.30), the integration limits have changed from 0 to T for the electron, to 0 to 1 for the fractional emission $h\nu/T$, [4], [12].

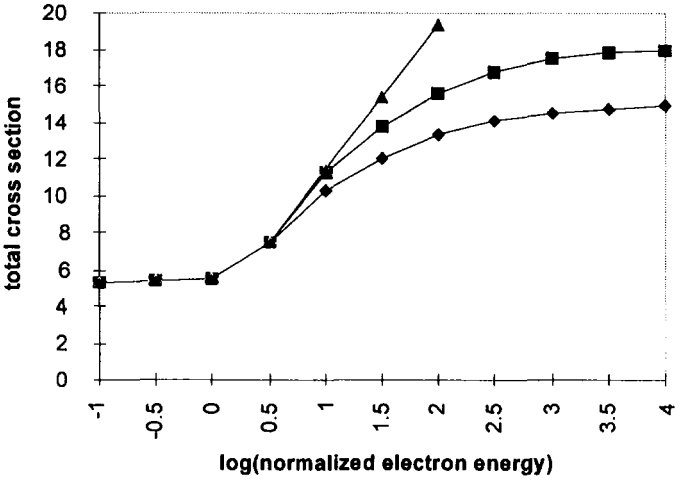

Fig.(2.20) The total *bremsstrahlung* cross-section $\overline{B}$ $(= \sigma_{rad}/\alpha r_e^2 Z^2)$ in units of $\alpha r_e^2 Z^2$ plotted against log (T/m_0c^2). ◆ lead : ■ water : ▲ no screening, [4], [12].

The total cross-section (cm^2/nucleus) is then given by :

$$\sigma_{rad} = \frac{dT}{T + m_0c^2}\frac{1}{N\,dx} = \alpha r_e^2 Z^2 \int_0^1 B \, d\left(\frac{h\nu}{T}\right) = \alpha r_e^2 Z^2 \overline{B} \qquad (2.31)$$

where the constant $\overline{B}$ is the result of integrating B over $h\nu/T$.

The radiative mass stopping power can be obtained from Eq.(2.30) for a target material of atomic number Z, atomic weight A, density ρ and Avogadro constant N_A. This is :

$$\frac{1}{\rho}\left(\frac{dT}{dx}\right)_{rad} = \frac{N_A \alpha r_e^2}{A} Z^2 \left(T + m_0c^2\right)\overline{B} \qquad (2.32)$$

In Fig.(2.20) note that :

- up to an electron energy of 5MeV, log(normalised energy) ≈ 1, the value of $\bar{B}$ is independent of Z to ~10%. Even at the highest energies the difference between water and lead is less than 20%.
- the correction for the screening of the nuclear Coulomb field by the atomic electrons is greatest for large Z and large energy. It is negligible for all materials at electron energies less than 1 MeV.

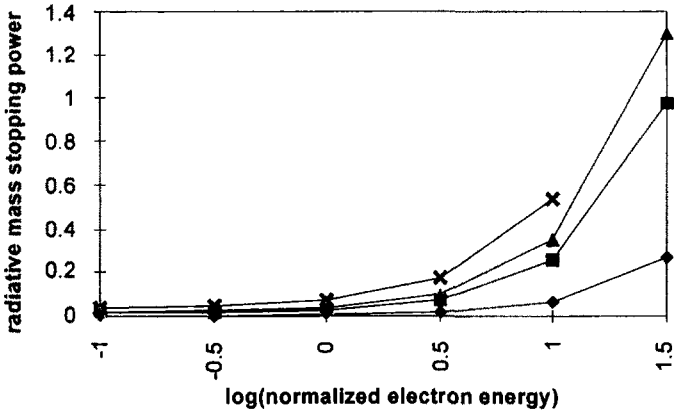

Fig.(2.21) Tabulated values [5] of Radiative Mass Stopping Power (MeV cm^2 g^{-1}) against log(T/m_0c^2). ◆ carbon (Z=6) : ■ copper (Z=29) : ▲ molybdenum (Z=42) : ✖ tungsten (Z=74).

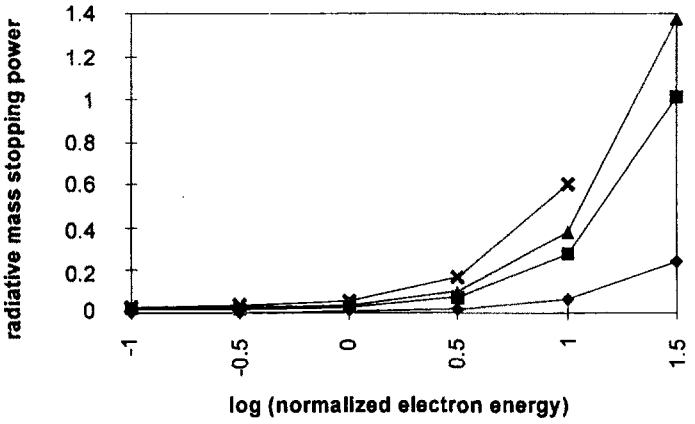

Fig.(2.22) Radiative Mass Stopping Power (MeV cm^2 g^{-1}) against log(T/m_0c^2) using Eq.(2.32) and interpolated values of $\bar{B}$ from Fig.(2.20). (kinetic energy in MeV, N_A/A in nuclei g^{-1}, r_e^2= 7.94 × 10^{-26} cm^2, $\alpha \approx 1/137$). Symbols as in Fig.(2.21).

Comparisons between the tabulated Radiative Stopping Powers from [5] and the calculated values using Eq.(2.32) can be made in Figs.(2.21) and (2.22). They differ by as much as 20% for certain combinations of T and Z, especially at the two highest electron energies, 5 and 16.2 MeV and the two highest atomic numbers, 42 and 74. There are two reasons which are largely responsible for the differences.

2.10.1 Corrections for the inadequacy of the Born approximation

The Born approximation formed the basis of Eqs.(2.31) and (2.32). However, the approximation is invalid for collisions in which the incoming electron suffers a large change in energy (*e.g.* when $T \sim h\nu$). This can occur either because its initial energy is small or because it is deflected by a large Coulomb potential.

The complete description of electron-nucleus *bremsstrahlung* considers three energy regions :

- $T > 50$ MeV, where a Coulomb term $f(Z)$ corrects for the assumption that the electron energy before and after the collision is large compared to the electron rest mass.
- $T < 2$ MeV, where the calculation of the matrix elements cannot be carried out using plane waves for the electron wave functions, but must use exact partial wave function expansions. This procedure requires a numerical solution of the Dirac equation and a numerical evaluation of the *bremsstrahlung* matrix elements.
- 2 MeV $< T <$ 50 MeV, where the cross-section has only a small dependence on both Z and T. In this case, an interpolation procedure between the two extreme energy regions can be used to complete the description.

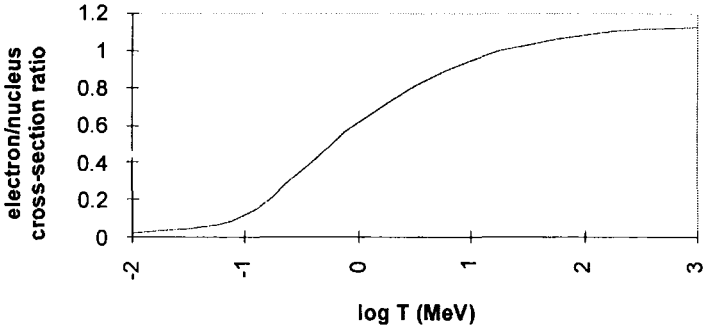

Fig.(2.23) Ratio of electron-electron to electron-nucleus *bremsstrahlung* cross-sections. The curve is the mean of those given in ICRU 37 [5] for carbon and gold. At any energy the cross-section ratio will be correct to ≤ 5% for any value of Z. Note that above ~10 MeV the ratio becomes greater than unity.

2.10.2 *Additional contribution of electron-electron bremsstrahlung*

At high energies electron-electron *bremsstrahlung* begins to become important.

- In this case the recoiling electron can take up a large fraction of the energy and momentum of the incoming electron.
- A total radiative cross-section can be obtained to sufficient accuracy by replacing Z^2 in the Eq.(2.29) by $Z(Z+(\phi_{rad,e}/\phi_{rad,n}))$. The ratio $(\phi_{rad,e}/\phi_{rad,n})$ is a smooth sigmoid function of T and is only weakly dependent on Z. The function plotted in Fig.(2.23) comes from [5].
- The total radiative stopping power is then proportional to $Z^2\phi_{rad,n} + Z\phi_{rad,e}$.

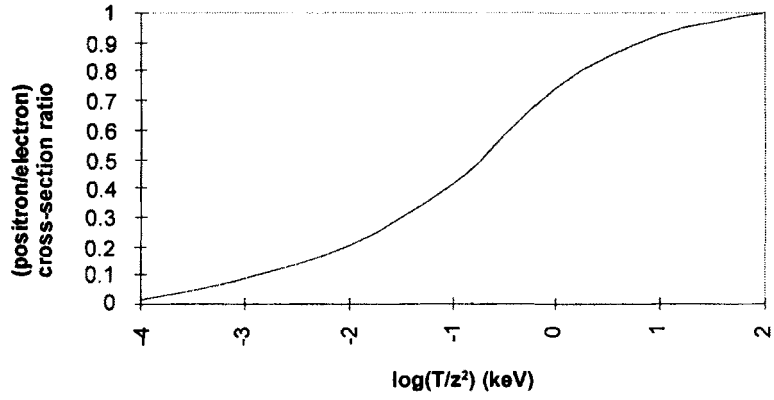

Fig.(2.24) The ratio of positron-nucleus to electron-nucleus *bremsstrahlung* cross-sections, versus the log of the ratio of positron or electron kinetic energy T to the Z^2 of the medium, [5].

Energetic positrons can also produce *bremsstrahlung*. In this case, the incoming positron is repelled by the nuclear charge and attracted by the atomic electrons. Cross-section differences between positrons and electrons are small at high energies (T > 100 keV), but at lower energies, positrons produce considerably less *bremsstrahlung* than electrons at the same energy, Fig.(2.24).

All the corrections discussed above have been applied in the ICRU tabulations [3],[5].

It is now appropriate to compare the major contributions to the total mass stopping powers of water for electrons, protons and α-particles, Fig.(2.25). Important features in this comparison are the following :

- the small rise in total stopping power as incident energy decreases for α-particles

at keV energies. This is due to the contribution of nuclear collision losses which become comparable to electronic losses at low energies (section 2.8).

- the rapid rise in electron stopping power for $E > 10$ MeV due to radiation losses (section 2.10).
- electron data for $E < 10$ keV becomes unreliable due to the loss of meaning in the concept of stopping power. At low energies, an electron can lose a considerable fraction of its energy in a single collision (Table 2.2). In this case the assumptions underlying the Continuous Slowing Down Approximation no longer hold. It then becomes necessary to use a dielectric response function, $\varepsilon(k,\omega)$, to express the energy loss to the medium in terms of momentum loss $\hbar k$ and energy loss $\hbar\omega$ (Section 2.7).

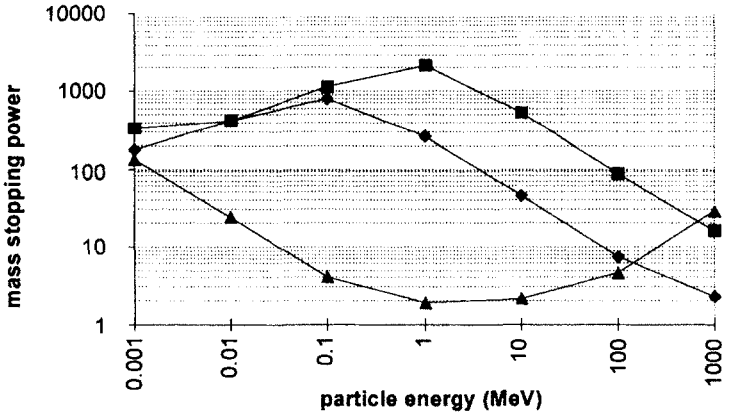

Fig.(2.25) Total Stopping Powers in MeV $cm^2 g^{-1}$ of electrons (▲), protons (◆) and alpha particles (■) in liquid water at selected energies [3],[5]. These curves include electronic, nuclear and radiative losses. In unit density material 10 MeV $cm^2 g^{-1}$ = 1 keV μm^{-1}.

2.11 Consequences of Charged Particle Interactions

2.11.1 Other secondary radiation

In addition to the continuous distribution of *bremsstrahlung* radiation due to the inelastic scattering of charged particles, there is also the possibility of radiation emitted at discrete energies.

Characteristic radiation arises as one of the consequences of an inner-shell ionization event. It may be due to :

- an inelastic collision involving a heavy charged particle,

- a photoelectric absorption interaction,
- an internal-conversion decay process.

The de-excitation of the atomic system following an inner shell process can result in either the emission of characteristic radiation or the ejection of Auger electrons. In the former case, the photons are emitted at discrete energies given by the difference between the binding energies of the bound electrons involved in the de-excitation. They are therefore characteristic of the atom (see section 3.2.8).

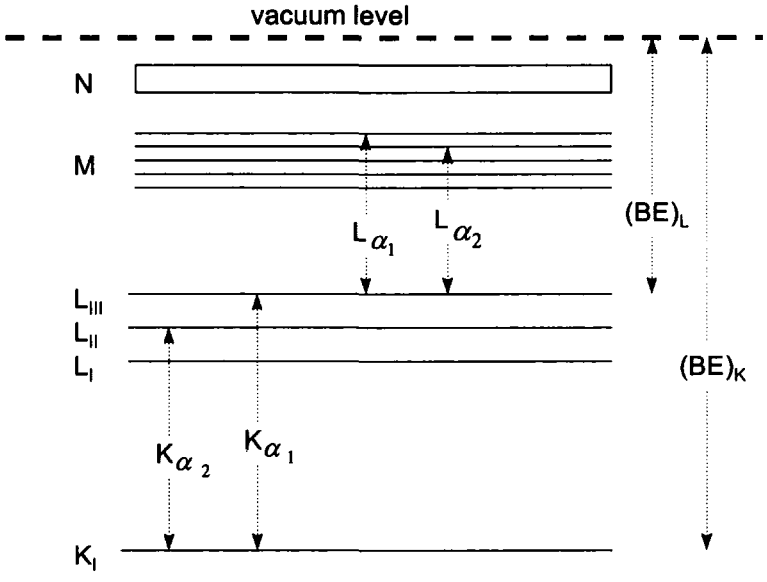

Fig.(2.26) A schematic diagram of electron sub-shell energy levels and the principal X-ray emission lines. The binding energies of only the K and L_{III} shells are indicated.

2.11.2 Ionization yields

(a) *Definitions*

When radiation dosimetry is based on the collection of charge following ionization events, there is a crucial link between the measured ionization current – or total charge – and the energy deposited. This link is provided by the W-value (Chapter 7.4) in gas detectors and the w-value in semiconductor devices. Comprehensive summaries are given in [5],[13].

When a particle of kinetic energy T loses all its energy in a gas, there is a certain probability $P(T,j)$ that it will produce j ionization events. This distribution has a mean number of ionizations $n(T)$ – the first moment, and a variance $\sigma^2(T)$ – the second

moment, as follows :

$$n(T) = \sum_{j=0}^{\infty} jP(T,j) \tag{2.33}$$

$$\sigma^2(T) = \sum_{j=0}^{\infty} [j - n(T)]^2 P(T,j) \tag{2.34}$$

The W-value is then defined as the mean energy expended by the particle per ion pair if all the energy is lost in the gas. *i.e.* $W(T) = T/n(T)$ – the zeroth moment divided by the first, [14], 17].

The Fano Factor is $F(T) = \sigma^2(T)/n(T)$ – the second moment divided by the first. This represents the capability of the ionization chamber in detecting the j'th ionization event. In other words, the energy resolution. The ionization yield is $T/W(T) = n(T)$.

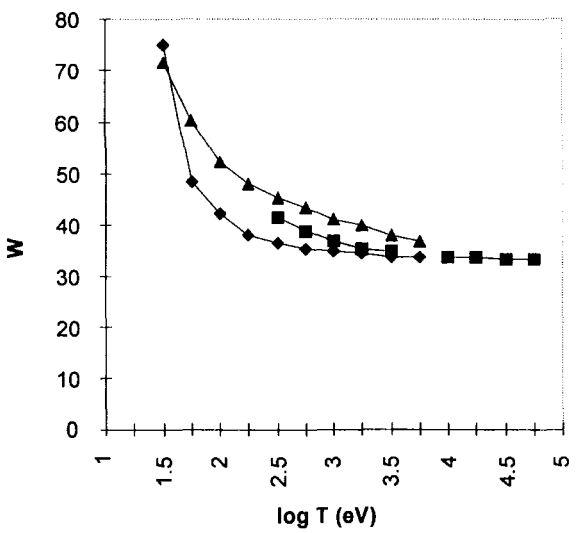

Fig.(2.27) The W-value for electrons in dry air at Standard Temperature and Pressure as a function of electron energy T (eV). ◆ [14] : ■ [15] : ▲ [16].

(b) *Relation between W-value at high energies (W_h) and Ionization Potential*

Fig.(2.27) shows that the W-value for electrons in air approaches a constant value of ~34 eV at energies ~10 keV and above. At lower energies, the W-value increases sharply because of the greater likelihood of excitation and multiple scatter events. The association between the W-value of a gas and its ionization potential I_p – the minimum energy required to produce ionization – has been discussed by Grosswendt [17].

For a given amount of energy deposition in gases with different ionization

potentials, it would be expected that W_h would be proportional to I_p. This is indeed the case. However, the monatomic noble gases have a significantly smaller proportionality constant (W_h/I_p = 1.74 ± 0.1) compared with the poly-atomic gases (2.38 ± 0.21). This points to the importance of molecular electronic configurations in the medium in defining the precise details of energy deposition.

(c) *Energy dependence of W at low energies*

The usefulness of the W-value in relating ionization yield to energy deposited in a gas is well illustrated by the linear dependence of $n_h(T)=T/W_h(T)$ on T for electron energies above 1 keV, Fig.(2.28).

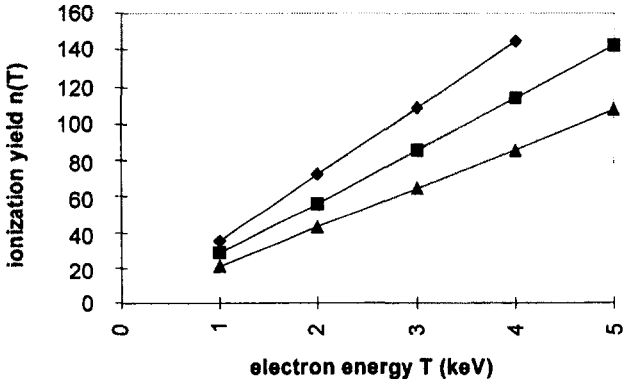

Fig.(2.28) High energy ionization yield $n_h(T)$ versus electron energy. ◆ CH_4 : ■ N_2 : ▲ He. Data taken from [18], [19], [20].

Detailed consideration of the types of collision which give rise to energy deposition in a gas must distinguish between excitation and ionization events. However, it must be recognised that a primary ionization can lead to secondary ionization events if the energy given to the primary electron is above the ionization potential of the medium.

If the probability of excitation to a state having energy k_v is called $p_v(T)$, then $p_i(T)$ is the probability of ionization with ionization potential I_p. Calling U the mean kinetic energy of all sub-ionization electrons – those electrons which can only deposit energy via excitation processes – then the ionization yield can be re-expressed as:

$$n_h(T) = \frac{(T-U)}{W_h} \tag{2.35}$$

$$W_h = \sum_{v=1}^{n} k_v \frac{p_v(T)}{p_i(T)} + I_p + U \tag{2.36}$$

From Eq.(2.36), the energy-independence of W_h can be explained by the energy-independence of the ratio of the probabilities of excitation and ionization. Although it is expressed in terms of W_h, this equation can also be used for energies down to 20 eV, using values of U between 8 eV and 15 eV for the gases in Fig.(2.28). Differences no greater than 10% are obtained when comparison is made with experimental data.

Similar considerations are used to adapt the expression [21] for the Fano Factor:

$$F = \frac{\left[\sum_{v=1}^{n} k_v^2 \frac{p_v(T)}{p_i(T)}\right]}{W_h^2} + \left[1 - \frac{(I_p + U)}{W_h}\right]^2 \tag{2.37}$$

The Fano Factor is thus inversely proportional to the square of the high energy W-value.

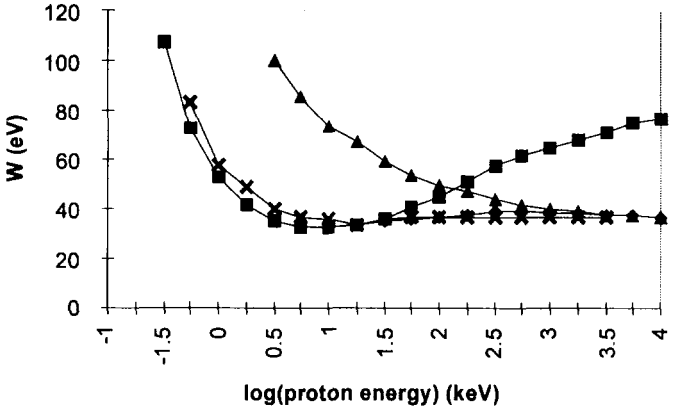

Fig.(2.29) W-value for protons in nitrogen. ✖ mean of experimental data taken from [23] : ◆ model including ionizations from primary protons, secondary electrons and charge exchange effects : ■ model neglecting ionization from secondary electrons : ▲ model neglecting charge exchange.

(d) *W-values for protons*

An important additional effect in the low energy interactions of heavy charged particles is that of charge-exchange. In this process a particle can pick up an electron during a low energy collision which may be stripped away by a neutral molecule in a subsequent collision. An incident proton, for example, therefore has a reduced probability of interacting as a particle with charge +1 as its energy decreases.

In addition to charge-exchange, it is also necessary to consider ionizations caused by the secondary electrons as well as those due to the primary particle. Grosswendt [22] has considered these contributions in the modelling of the W-value and the Fano Factor for protons in tissue-equivalent gas and air up to 500 MeV.

Fig.(2.29) shows that the combined effects of charge-exchange and secondary electron ionizations contribute to the experimentally-observed minimum in W at 30 eV proton energy.

Table (2.3) Experimental values of W for protons and electrons in air. Note that the W-value for protons at low energies (<300 eV) becomes very much larger than that for electrons. This has important implications for neutron dosimetry using ionization chambers.

Particle energy (keV)	0.03	0.1	0.3	1	3	10	30	100
protons in nitrogen	-	-	110	56	40	36	36	37
electrons in air	70	43	38	36	35	34	33	-

(e) *W-values in gas mixtures - the Jesse Effect*

A binary gas mixture will generally have a combined W-value which depends on the values of the pure components, W_i and W_j, and their partial pressures P_i and P_j. The combined value would be expected to lie somewhere between the individual values with the relation taking the form :

$$W_{ij} = \left(W_i - W_j\right) K_{ij} + W_j \qquad (2.38)$$

In Eq.(2.38) the parameter K_{ij} is a constant for each pair of gases [24]. It should depend upon the partial pressure, the W-value and the stopping power towards the radiation of each of the individual gases. Using suggestions by several workers [25],[26], K_{ij} may be expressed as :

$$K_{ij} = \frac{P_i W_j S_i}{P_i W_j S_i + P_j W_i S_j}$$

where S_i and S_j are the stopping powers in the two components. From the linear relation in Eq.(2.38), this has resulted in the tabulation of the measured ratios $W_i S_j / W_j S_i$ for a number of combinations of molecular gases [24],[26].

There is a number of cases, however, for which the linear relation in Eq.(2.38) between W_{ij} and K_{ij} does not exist. For certain gases, small quantities of an impurity can result in significant changes in total ionization when compared against that in the pure gas. This effect has become known as the *Jesse Effect* and is illustrated in Fig.(2.30) for argon and neon impurities in helium. The current explanation is made in terms of the magnitude of the ionization potentials of the two components relative to the energies of any meta-stable states which may be formed [27].

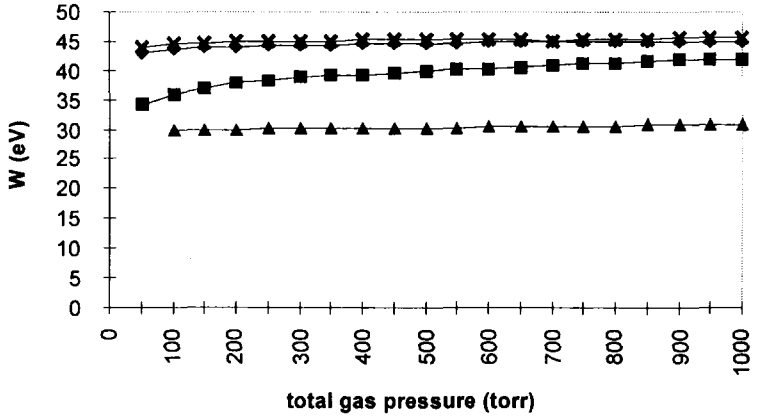

Fig.(2.30) The Jesse Effect in pure helium showing the W-value as a function of total gas pressure. ◆ pure helium: ■ He + 0.00249% Ar: ▲ He + 0.0985% Ar: ✖ He + 0.00497% Ne, [24]. Note the reduction in W value for added Ar and the small increase for added Ne.

References

[1] T.M.Jenkins, W.R.Nelson and A.Rindi (eds.), *Monte Carlo Transport of Electrons and Photons*: (Plenum Press, New York 1988).

[2] E.J.Williams, *Proc.Roy.Soc.* **A130** (1931) 310.

[3] *International Commission on Radiation Units and Measurement* Report **49** (Maryland USA 1993).

[4] R.D.Evans, *The Atomic Nucleus* (McGraw Hill, New York 1972).

[5] *International Commission on Radiation Units and Measurements* Report **37** (Maryland, USA,1984).
[6] W.H.Barkas and M.J.Berger, *Studies in Penetration of Charged Particles in Matter* NRC Report **1133**, (Nat.Acad.Sci. USA 1964).
[7] H.G.Paretzke and M.J.Berger, *Sixth Symposium on Microdosimetry* Report **EUR 6064** eds. J.Booz and H.G.Ebert (Harwood, London 1978) p.749.
[8] D.Pines and P.Nozieres, *The Theory of Quantum Liquids*, Vol.1 (W.A.Benjamin, New York 1966).
[9] R.H.Ritchie, *Phys.Rev.* **114**(3) (1959) 644.
[10] J.C.Ashley, C.J.Tung and R.H.Ritchie, *IEEE Trans. Nucl.Sci.* **NS25**(6) (1978) 1566.
[11] J.C.Ashley, *IEEE Trans.Nucl.Sci* **NS27**(6) (1980) 1454.
[12] W.Heitler, *The Quantum Theory of Radiation* (Clarendon Press, Oxford 1954).
[13] D.Srdoc, M.Inokuti and I.Krajcar-Bronic, *International Atomic Energy Agency* Report **TECDOC-799**, (1995) 547.
[14] E.Waibel and B.Grosswendt, *Radiat.Res.* **76** (1978) 241.
[15] W.Gerbes, *Ann.Phys.* **23** (1935) 648.
[16] A.Cole, *Radiat.Res.* **38** (1969) 7.
[17] B.Grosswendt, *Proc. International Congress on Radiation Research* (1995).
[18] E.Waibel and B.Grosswendt, *Nucl.Instr.Meth.* **211** (1983) 487.
[19] E.Waibel and B.Grosswendt: *Proceedings 8th Symposium on Microdosimetry* (1982).
[20] B.Grosswendt, *J.Phys.B* **17** (1984) 1391.
[21] M.Kimura, M.Inokuti and M.A.Dillon, *Adv.Chem.Phys.* **84** (1993) 193.
[22] B.Grosswendt and W.Y.Baek, *Radiat.Prot.Dosim.* **61** (1995) 267.
[23] B.Grosswendt, G.Willems and W.Y.Baek, *Radiat.Prot.Dosim.* **70**(1-4) (1997) 37.
[24] *International Commission on Radiation Units and Measurement* Report **31** (Washington DC, USA 1979).
[25] W.Haeberli, P.Huber and E.Baldinger, *Helv.Phys.Acta.* **26** (1953) 145.
[26] T.D.Strickler, *J.Phys.Chem.* **67** (1963) 825.
[27] G.S.Hurst and C.E.Klots, *Advances in Radiation Chemistry,* Vol.5. eds.M.Burton and J.L.Magee, (J.Wiley, New York, 1976).

CHAPTER 3

INTERACTIONS of PHOTONS

3.1 Introduction

A photon interacts by one of four major processes. The probability of each is determined by a cross-section which depends on the photon energy and on the density and atomic number of the medium.

- Rayleigh (coherent) scatter – the photon interacts with the total electron cloud of an atom.
- Compton (incoherent) scatter – the photon interacts with an individual electron whose binding energy is low compared to that of the incident photon.
- Photoelectric absorption – the photon interacts with an inner atomic electron.
- Pair production – the photon converts into an electron-positron pair when it enters the strong Coulomb field surrounding an atomic nucleus.

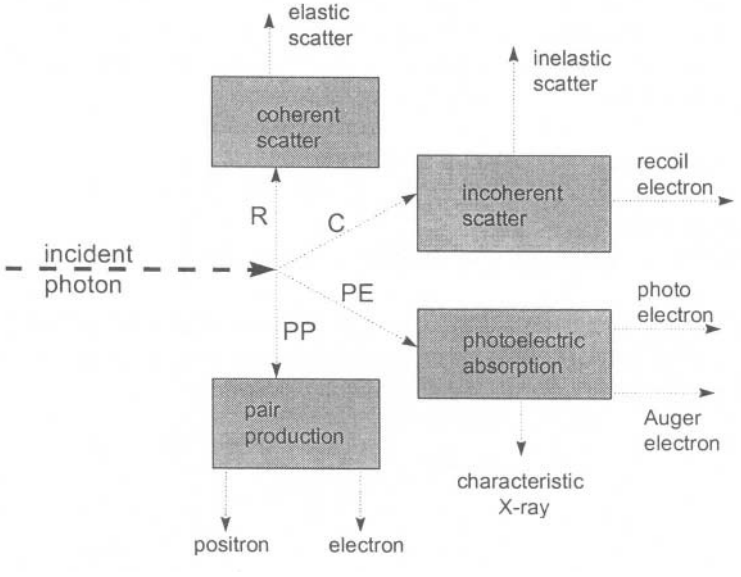

Fig.(3.1) Primary photon interaction processes with their secondary emissions.

In addition to the consideration of each individual interaction, it is important to bear in mind the following :

- The attenuation of a beam of photons includes scatter as well as absorption processes. Thus Attenuation = Scatter + Absorption.
- Apart from coherent scatter, all the interaction processes result in the production of electrons. These provide the means by which the major fraction of the photon's energy is imparted to the medium. Consequently, photons are known as indirectly ionizing radiation.
- Secondary photons that emerge from the primary processes – from Rayleigh or Compton scattering of the primary beam or as a characteristic X-ray from a photoelectric absorption – can still undergo any of the four interactions if they are energetically possible.

3.2 Attenuation coefficients (linear, mass, atomic and electronic)

The exponential decrease in the initial number of photons/unit area, Φ_o, which have traversed thickness x of a medium,

$$\Phi = \Phi_0 \, exp(-\mu x) \tag{3.1}$$

is expressed in terms of a linear attenuation coefficient, μ. The quantity Φ_0 is called the photon fluence and is considered further in Chapter 7. All of the four processes are included in μ if they are energetically possible.

Fig.(3.2) illustrates the distinction between Good (or narrow) geometry, in which the detection of scattered photons is minimized (position A), and Bad (or wide) geometry, when the effects of scatter are prominent, as in position B. The two cases depend upon :

- the distance between detector and material,
- the size of the detector compared with the width of the beam,
- the energy of the photons,
- the density and mean atomic number of the material.

By definition, the dimension of μ must be reciprocal in length (*e.g.* cm^{-1}). Its dependence on density is conveniently removed to provide an expression for the mass attenuation coefficients of the individual processes.

$$\frac{\mu}{\rho} = \frac{\sigma_{coh}}{\rho} + \frac{\sigma_{incoh}}{\rho} + \frac{\tau}{\rho} + \frac{\kappa}{\rho} \tag{3.2}$$

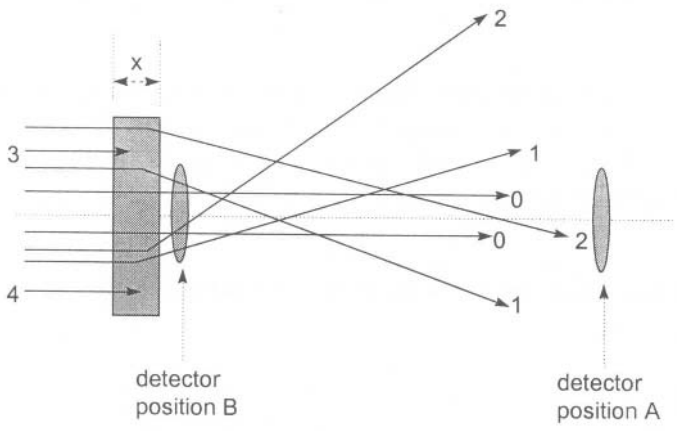

Fig.(3.2) Representation of possible interaction processes in thickness x of material. Photons labelled "0" have not interacted. Photons labelled "1" might have undergone coherent scatter and both missed the detector at A. Photons labelled "2" might have Compton scattered but only one has been recorded by the detector at A. Photons "3" and "4" have both been absorbed in the material.
If the detector is now moved to position B, it will again record both "0" 's, and one each of the Rayleigh "1" and Compton "2" scattered photons, both of which had previously missed the detector.

The mass attenuation coefficient (μ/ρ) therefore has units $cm^2\ g^{-1}$ ($m^2\ kg^{-1}$) when the density is in $g\ cm^{-3}$ ($kg\ m^{-3}$). This gives the total attenuation in terms of the individual cross-sections specified per gram (kg) of material.

Greater meaning is achieved by expressing the cross-sections *per electron* (for Compton) or *per atom* (for Rayleigh and Photoelectric) since these are the primary targets for the incident photon in each particular case. This is easily done using the Avogadro constant (N_A) and the atomic mass (A) of the material to determine the number of electron and atoms per gram (kg). We therefore have :

$$N_A/A = atoms\ g^{-1} \ : \ 1000N_A/A = atom\ kg^{-1}.$$

$$ZN_A/A = electrons\ g^{-1} \ : \ 1000ZN_A/A = electron\ kg^{-1}.$$

This leads to the relations :

$$\frac{\tau}{\rho}\left(cm^2\ g^{-1}\right) = \frac{\tau}{\rho}\ \frac{A}{N_A}\left(cm^2\ atom^{-1}\right)$$

$$\frac{\sigma_{incoh}}{\rho}\left(cm^2\ g^{-1}\right) = \frac{\sigma_{incoh}}{\rho}\ \frac{A}{ZN_A}\left(cm^2\ electron^{-1}\right)$$

The number of electrons per gram is constant to within ~10% for all materials (apart from hydrogen which has no neutron in its nucleus). This means that the probability of a Compton interaction depends largely on the density of the material and hardly at all on its atomic number.

3.3 Classical (Thomson) scatter from a single electron

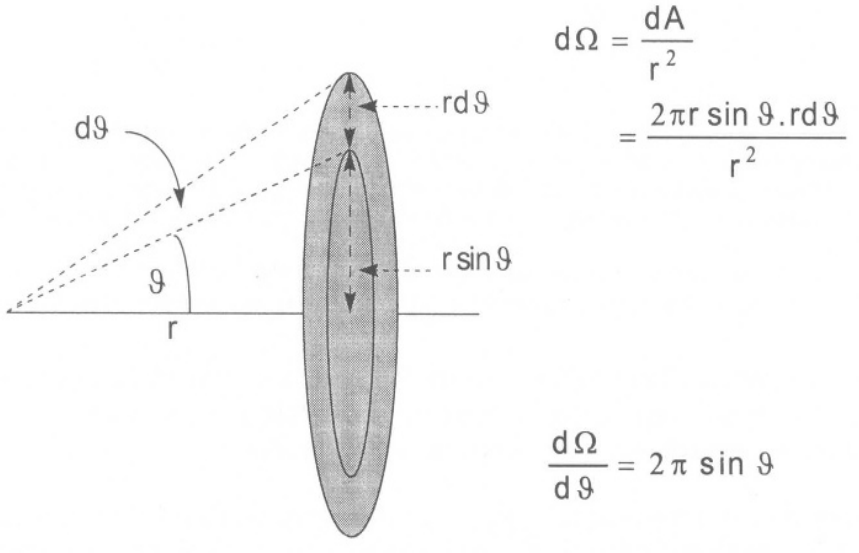

Fig.(3.3) Relation between ϑ and $d\Omega$ in the scattering of a photon by an electron.

In the classical picture, the incoming electromagnetic wave sets up an electric field at the site of an electron, which is accelerated and which therefore radiates. The probability that the energy contained within the incident wave is scattered into a solid angle $d\Omega$ at an angle of ϑ with respect to the incident direction is called the differential scatter cross-section :

$$\frac{d\sigma_0}{d\Omega} = \frac{r_0^{\,2}}{2}\left(1 + \cos^2\vartheta\right) \qquad (3.3)$$

where $r_0 = e^2/m_0c^2 = 2.8179 \times 10^{-15}$ m is the classical electron radius. Integration over all angles gives the total cross section σ_0. From Fig.(3.3), we get :

$$\frac{d\sigma_0}{d\vartheta} = \frac{d\sigma_0}{d\Omega}\,\frac{d\Omega}{d\vartheta} = \frac{r_0^2}{2}\left(1+\cos^2\vartheta\right)2\pi\sin\vartheta \qquad (3.4)$$

The integration of Eq.(3.4) over all angles gives the total Thomson scatter cross-section. This is the area under the ■ symbols in Fig.(3.4) . The result is :

$$\sigma_0 = \frac{8}{3}\pi r_0^2 = 66.53\times10^{-30}\,m^2 / electron \qquad (3.5)$$

At low incident photon energies this is independent of energy. As the energy increases the electron recoil reduces the probability of photon scatter below that given in Eqs.(3.4) and (3.5).

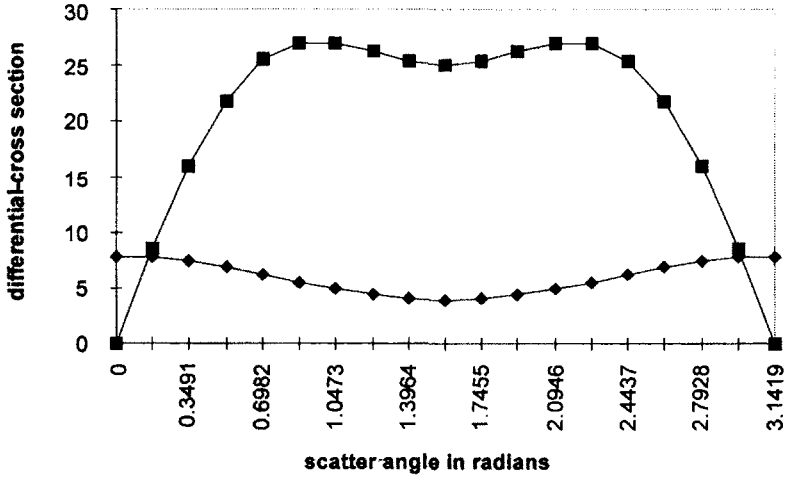

Fig.(3.4) Angular dependence of the differential (classical) scatter coefficient per electron per unit solid angle (◆) from Eq.(3.3) using the differential scatter cross-section per electron : (■) from Eq. (3.4). Ordinate axis ($\times 10^{-30}\,m^2\,electron^{-1}$).

3.4 Coherent (Rayleigh) scatter

This interaction is due to photon scatter from atomic electrons whose binding energy is considerably greater than the incoming photon energy. The waves interfere constructively to produce a coherent scattered wave. No energy is transferred to the medium (scattered wavelength = incident wavelength) as the Z electrons in the atom take up the recoil momentum without absorbing any energy. Rayleigh scatter becomes more important as the photon energy decreases and the atomic number of the medium increases.

In this case, the Thomson cross-section is multiplied by a form factor, *F(x,Z)*, where *Z* is the atomic number of the atom, $x = sin(\vartheta/2)/\lambda$, and λ is the wavelength of the photon. *F(x,Z)* represents the spatial electron distribution in the atom from which the photon can be scattered without any momentum transfer.

$$\frac{d\sigma_{coh}}{d\vartheta} = \frac{r_0^2}{2}\left(1+\cos^2\vartheta\right)\left[F(x,Z)\right]^2 2\pi \sin\vartheta \qquad (3.6)$$

At large angles of scatter, *F(x,Z)* tends to zero, but the smaller the angle, the more nearly it approximates to *Z*. This is an atomic cross-section since we are dealing with coherent scatter from all the atomic electrons.

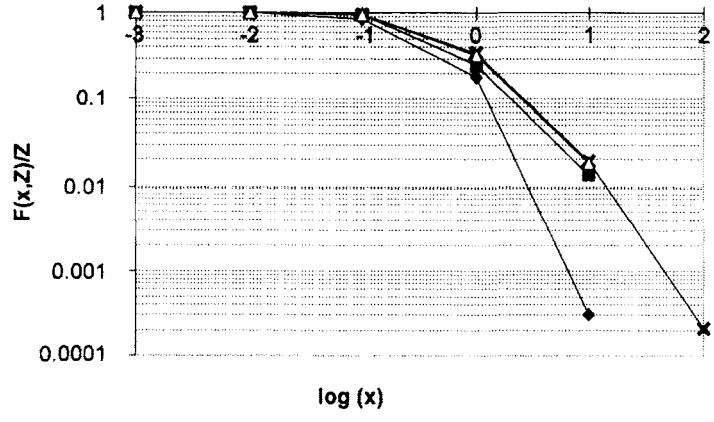

Fig.(3.5) The atomic form factor *F(x,Z)* normalized to Z, versus log(sin(ϑ/2)/λ) for different elements: ● C: ■ Cu: ▲ Sn: ✖ W. Note that the value of the form factor *F(x,Z)* tends to the value of the atomic number *Z* as $x \rightarrow 0$, [1].

The energy dependence of Rayleigh scatter resides in the form factor *F(x,Z)* through the wavelength. This is expressed in Compton units using the electron rest energy :

$$E_0 = m_0 c^2 = \frac{9.1095\times10^{-31}\left(2.0079\times10^{8}\right)^2}{1.6022\times10^{-19}} = 511003.4eV$$

For photon energy *E* (eV) the wavelength is then :

$$\lambda = \frac{1}{k} = \frac{E_0}{E} \tag{3.7}$$

It is not easy to express $F(x,Z)$ analytically, but its value has been calculated on the basis of several models [1].

Fig.(3.5) shows that $F(x,Z)$ is essentially independent of Z for $x < 0.1$. As x increases beyond this – for large λ and hence small E – the form factor decreases rapidly.

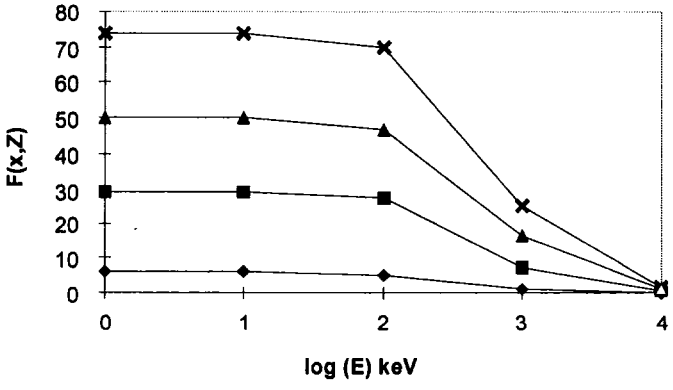

Fig.(3.6) The atomic form factor at a scatter angle $\vartheta = 61.4°$. At this angle, $\sin\vartheta/2=0.511$. From Eq.(3.7), we have x = photon energy E in units of keV. ◆ C: ■ Cu: ▲ Sn: ✖ W, [1].

3.5 Incoherent (Compton) scatter

For this interaction the classical theory, which adequately describes low energy photon scatter, has to be replaced by relativistic considerations. This is because the photon energy approaches the rest mass of an electron m_0c^2 = 511 keV. The characteristic features of Compton scatter are :

- The momentum of the incident photon is conserved between the outgoing photon and the struck electron.
- Incoherent scattering takes place from individual electrons which, in the majority of cases, appear unbound. When the photon energy becomes comparable with the electron binding energy, it is more probable that photoelectric absorption takes place. However, corrections can be made for Compton scatter from bound electrons using the incoherent scatter function $S(x,Z)$.
- As in all other cases, it is important to distinguish between the probability of an

interaction taking place and the amount of energy transferred in that process. For a free electron, the former is described by the Klein-Nishina formula, and the latter by the energy and momentum conservation equations.

We consider an incoming photon of energy $E = h\nu_0$ being scattered by an electron, [2]. If the electron is not free, its binding energy must be $<< h\nu_0$.

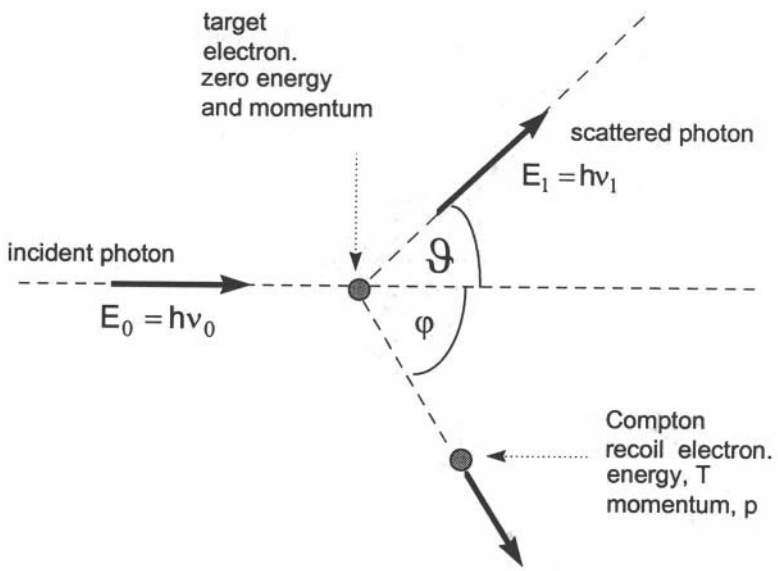

Fig.(3.7) A schematic diagram of a Compton collision. The incident photon energy is normalized to the electron rest mass using $\alpha = h\nu_0/m_0c^2$.

Energy and momentum are conserved between the electron and photon in Fig.(3.7). Together with the relativistic relation between energy and momentum of the electron we obtain the following equations :

$$h\nu_0 = h\nu_1 + T \tag{3.8}$$

$$\frac{h\nu_0}{c} = \frac{h\nu_1}{c}\cos\vartheta + p\cos\varphi \tag{3.9}$$

$$0 = \frac{h\nu_1}{c}\sin\vartheta - p\sin\varphi \tag{3.10}$$

$$pc = \sqrt{T\left(T + 2m_0c^2\right)} \tag{3.11}$$

Algebraic manipulation of the above, with $\alpha = h\nu_0/m_0c^2$, gives the following relationships :

(a) Compton wavelength shift : $$\Delta\lambda = \lambda_1 - \lambda_0 = \frac{c}{\nu_1} - \frac{c}{\nu_0} = \frac{h}{m_0 c}(1 - \cos\vartheta) \quad (3.12)$$

The ratio h/m_0c in Eq.(3.12) is the wavelength of a photon whose energy is just equal to the electron rest mass. It is known as the Compton wavelength, λ_c. Notice that the wavelength shift depends only on scattering angle and not on the incident photon energy.

(b) Energy of scattered photon : $$h\nu_1 = \frac{m_0c^2}{1 - \cos\vartheta + (1/\alpha)} = \frac{h\nu_0}{1 + \alpha(1 - \cos\vartheta)} \quad (3.13)$$

(c) Energy of the recoil electron : $$T = h\nu_0 \frac{\alpha(1 - \cos\vartheta)}{1 + \alpha(1 - \cos\vartheta)} \quad (3.14)$$

(d) When the collision is head-on and the photon is scattered through 180°, ($\cos\vartheta = -1$), we have the minimum scattered photon energy and the maximum electron recoil energy :

$$T_{max} = h\nu_0 \frac{2\alpha}{1 + 2\alpha}$$
$$h\nu_{1,min} = h\nu_0 \frac{1}{1 + 2\alpha} \quad (3.15)$$

(e) When the collision is grazing (large impact parameter in the notation of section 2.4), then the electron has a minimum energy $T \rightarrow 0$ and the photon retains its original energy $h\nu_0$. This takes place when $\vartheta \rightarrow 0$, so from Eqs.(3.8) and (3.9), $p \rightarrow 0$ and $\varphi \rightarrow 90°$.

3.5.1 The Klein-Nishina cross-section for Compton scatter

Having established the kinetics of the collision, we can now consider the probability that the photon is scattered at an angle ϑ with respect to the original direction. This probability is composed of two parts :

- the probability that a collision takes place, *i.e.* that a photon is removed from the incident beam, $d(_e\sigma)$. The subscript e refers to the fact that we are dealing with scattering from an individual electron.
- the probability that energy is scattered into angle ϑ by the photon, $h\nu_1/h\nu_0$.

The differential cross-section for scatter into angle ϑ is then given by :

$$\frac{d({}_e\sigma_s)}{d\Omega} = \frac{h\nu_1}{h\nu_0}\,\frac{d({}_e\sigma)}{d\Omega} \tag{3.16}$$

The collision probability can be expressed in terms of the angle, η, between the plane containing the scattered photon and the plane containing the electric vector of the incident photon, Fig.(3.8).

$$\frac{d({}_e\sigma)}{d\Omega} = \frac{r_0^2}{2}\left(\frac{\nu_1}{\nu_0}\right)^2\left(\frac{\nu_0}{\nu_1} + \frac{\nu_1}{\nu_0} - 2\sin^2\vartheta\cos^2\eta\right) \tag{3.17}$$

This probability is always largest when $\eta \rightarrow 90°$. It shows that both the photon and the electron tend to emerge at right angles to the electric vector of the incident photon.

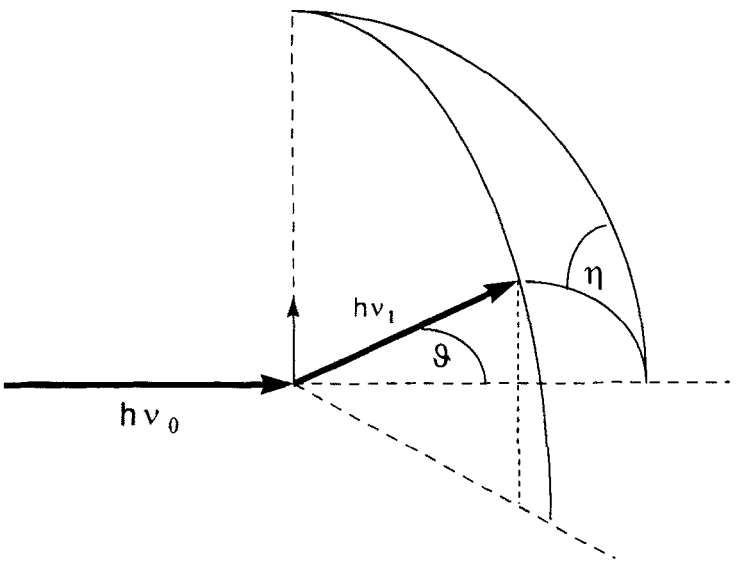

Fig.(3.8) Compton scatter angles for an incident photon polarized with the electric vector in the plane of the paper [2]. With permission from the McGraw Hill Companies.

The differential scattering cross-section for unpolarized radiation can be obtained by summing equal contributions from radiation polarized at right-angles. When the polarization vector is parallel and perpendicular to the plane of the paper in Fig.(3.6), for example, we have $\eta = 0$ and 90°. Combining Eqs.(3.16) and (3.17) then gives :

$$\frac{d({}_e\sigma_s)}{d\Omega} = \frac{{r_0}^2}{2}\left(\frac{h\nu_1}{h\nu_0}\right)^3\left(\frac{\nu_0}{\nu_1} + \frac{\nu_1}{\nu_0} - \sin^2\vartheta\right)$$

This can be rewritten in terms of the Thomson scatter cross-section as :

$$\frac{d({}_e\sigma_s)}{d\Omega} = \frac{{r_0}^2}{2}\left(1+\cos^2\vartheta\right)\left(\frac{1}{1+\alpha(1-\cos\vartheta)}\right)^3\left(1+\frac{\alpha^2(1-\cos\vartheta)^2}{\left(1+\cos^2\vartheta\right)\left[1+\alpha(1-\cos\vartheta)\right]}\right) \tag{3.18}$$

Using Eq.(3.3) and a Form Factor, F_{KN}, this is simplified to :

$$\frac{d({}_e\sigma_s)}{d\Omega} = \left(\frac{d\sigma}{d\Omega}\right)_{KN} = \frac{d\sigma_0}{d\Omega}\,F_{KN} \tag{3.19}$$

- For low incident energies, $\alpha \rightarrow 0$, the form factor tends to unity, and the Klein-Nishina cross-section reduces to the classical expression.
- When the scattering angle, $\vartheta \rightarrow 0$, and the electron recoil energy $T \rightarrow 0$, again $F_{KN} \rightarrow 1$ and the classical expression is valid.

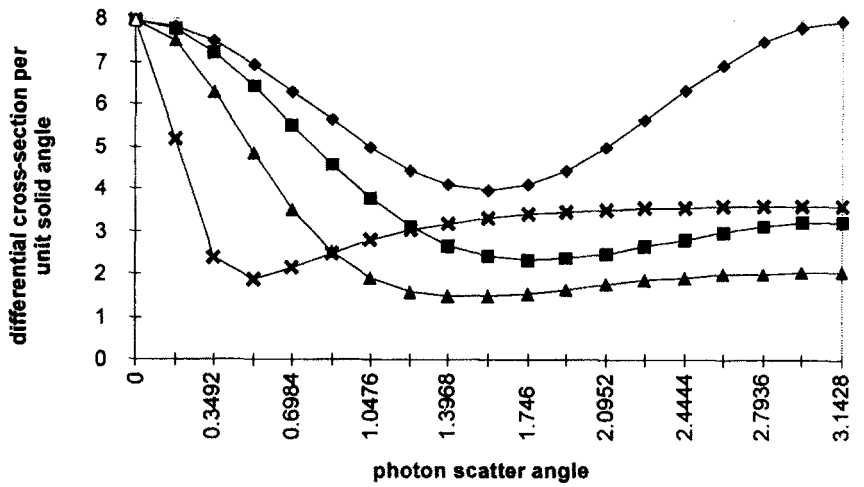

Fig.(3.9) Differential scatter cross-section per unit solid angle (× 10^{-30} m²/electron/steradian) for unpolarized radiation using Eq.(3.19). ◆ α =0 : ■ α = 0.2 : ▲ α = 1 : ✖ α = 10

3.5.2 Compton scatter from atomic electrons - the effect of electron binding

The process of photon scatter from an electron or group of electrons involves a momentum change. For a single "unbound" electron – assumed in the Klein-Nishina treatment – the momentum transferred to the electron is related to the recoil energy via Eq.(3.11). If the struck electron has a binding energy which is not negligible compared to the incident photon energy, this momentum is distributed amongst all the electrons in the atom. In a situation where the electrons return to their original states after the interaction, no energy is transferred to the atom and Rayleigh scatter results.

When an electron absorbs some of this momentum, it can be excited into a higher atomic state or emitted from the atom altogether. In either case, the emitted photon has less energy and the scattering is incoherent. This is most likely to occur when the incident photon energy is small and the atomic number is large.

If $q_0=h\nu_0/c$ and $q_1=h\nu_1/c$ are the momenta of the incident and scattered photons, Fig.(3.7), the momentum transferred in the collision, Δq, is :

$$(\Delta q)^2 = q_0^2 + q_1^2 - 2q_0q_1 \cos\vartheta \tag{3.20}$$

From Eq.(3.13), there is very little change in photon energy when the incident energy is low. In this case, we have $\alpha = h\nu_0/m_0c^2 \rightarrow 0$, $h\nu_1 \approx h\nu_0$ and $q_0 \approx q_1$. Eq.(3.20) then reduces to :

$$\Delta q \approx \frac{h\nu}{c}\sqrt{2(1-\cos\vartheta)} = \frac{2h\nu}{c}\sin(\vartheta/2)$$

The momentum change is therefore just $2h$ times the parameter x used in the atomic form factor $F(x,Z)$.

Not all of the atomic electrons are able to receive the transferred momentum, q, to the same extent. To account for this, an incoherent scatter function, $S(q,Z)$, is defined as:

$$S(q,Z) = Z - \sum_{i=1}^{Z} \left| f_0^i(q) \right|^2 \tag{3.21}$$

In Eq.(3.21), $f_0^i(q)$ expresses the probability that the $i'th$ electron is not excited or detached from the atom, even though it has received recoil momentum q. Thus, if all the electrons are able to participate, the incoherent scatter function is equal to the total number in the atom *i.e.* the atomic number Z.

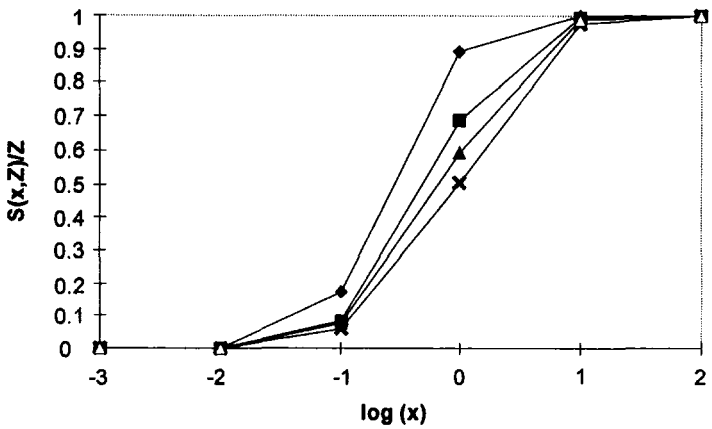

Fig.(3.10) The normalized incoherent scatter function $S(x,Z)/Z$ versus log (x): ◆ C: ■ Cu: ▲ Sn: ✖ W [1]

It can be seen in Fig.(3.10), that as $x \rightarrow 0$, then $S(x,Z) \rightarrow 0$. At low photon energies, therefore, there are no electrons capable of receiving any momentum. These are the conditions for coherent scatter. At very high photon energies, $S(x,Z) \rightarrow 1$ and all the electrons can receive momentum. The condition for maximum energy transfer and momentum change of the photon is a scatter angle of 180°. In this case, $sin(\vartheta/2)=1$.

Table (3.1) gives the incident photon energies above which all the atomic electrons are capable of receiving momentum. At energies less than these minimum values the incoherent scatter function, and hence the cross-section, decreases.

Table (3.1) Values of the minimum photon energy required for the incoherent scatter function to remain at unity.

	Z	K-shell binding energy (keV)	value of x when S(x,Z) =1	minimum photon energy (MeV)
C	6	0.284	7	3.577
Cu	29	8.979	50	25.55
Sn	50	29.20	50	25.55
W	74	69.525	80	40.88

The incoherent cross-section in Eq.(3.19) is then corrected for the effects of bound electrons by :

$$\frac{d\left({}_e\sigma_s\right)}{d\Omega} = \frac{d\sigma_0}{d\Omega}\, F_{KN}\, S(x,Z) \tag{3.22}$$

3.5.3 *Electron recoil energy in Compton collisions*

The energy distribution of recoil electrons is important for two reasons :

- it plays an important role in the energy response of radiation detectors,
- it is important in radiation dosimetry.

The distribution can be obtained from the Klein-Nishina cross-section, Eq.(3.19), together with $d\Omega/d\vartheta$ from Fig.(3.3) and the reciprocal of $dT/d\vartheta$ from Eq.(3.14) :

$$\frac{d\left({}_e\sigma_s\right)}{dT} = \frac{d\left({}_e\sigma_s\right)}{d\Omega}\,\frac{d\Omega}{d\vartheta}\,\frac{d\vartheta}{dT}$$

$$\frac{d\left({}_e\sigma_s\right)}{dT} = \frac{3}{8}\sigma_0\,\frac{1}{\alpha h\nu_0}\left\{1+\cos^2\vartheta + \frac{\alpha^2(1-\cos\vartheta)^2}{1+\alpha(1-\cos\vartheta)}\right\}$$

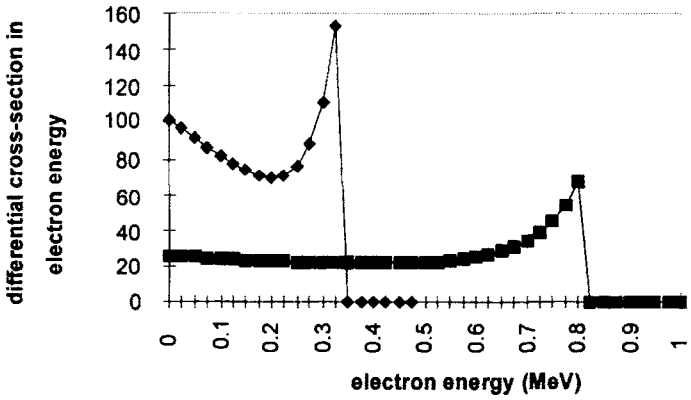

Fig.(3.11) Compton cross-section differential in electron energy Eq.(3.23) for incident photon energies 0.5 MeV (◆) and 1.0 MeV (■). The ordinate axis is in units of m^2 electron^{-1} MeV^{-1} × 10^{-30}. The maximum electron energies in the two cases are 0.331 MeV and 0.796 MeV respectively, Eq.(3.15). The above curves do not show an infinitely sharp edge (the Compton edge) at these energies because of the finite energy increments taken along the abscissa axis.

The dependence on the scattered photon angle ϑ is eliminated using Eq.(3.14)

to yield the final expression :

$$\frac{d({}_e\sigma_s)}{dT} = \frac{3}{8}\frac{\sigma_0}{\alpha h\nu_0}\left\{2 - \frac{2T}{\alpha(h\nu_0 - T)} + \frac{T^2}{\alpha^2(h\nu_0 - T)^2} + \frac{T^2}{h\nu_0(h\nu_0 - T)}\right\} \qquad (3.23)$$

3.5.4 Electron momentum distributions from Compton profiles

Atomic electrons, by virtue of their binding energies, cannot be assumed to be free and stationary. A more complete description should include the initial momentum of the struck electron as well as the polarization vectors of the photon before and after the collision.

A comprehensive review by Cooper [3] refers to an impulsive collision between an incident photon and the free, but moving, electrons. In a collision of this type, the interaction is so rapid that the potential seen by the target electron is the same immediately before, and immediately after, the collision. Conservation of energy can then be stated without the need for any potential energy term, since it cancels from both sides of the equation. This is known as the Impulse Approximation.

Rearrangement of Eq.(3.12) gives the scattered photon energy in terms of the angular frequencies ω_0 and ω_1 :

$$\omega_1 = \frac{\omega_0}{\left[1 + \frac{\omega_0}{m_0c^2}(1 - \cos\vartheta)\right]} \qquad (3.24)$$

When the scattering vector $\overline{K} = \overline{k}_0 - \overline{k}_1$ is chosen to lie along the z - co-ordinate axis, as in Fig.(3.12), the change in photon energy during the collision is equal to the sum of two terms. The first describes the normal Compton shift expressed in Eqs.(3.13) and (3.24). The second gives the energy associated with the momentum change of the electron along the *z*-axis. We then have :

$$\omega_0 - \omega_1 = \frac{\hbar^2\left|\overline{K}\right|^2}{2m_0} + \hbar\frac{\overline{K}\cdot\overline{p}_z}{m_0} \qquad (3.25)$$

The energy shift of the photon thereby gives information on the distribution of electron momenta. If the target electrons are described by a probability density distribution, *n(p)*, the projection of this distribution along the z-axis gives the Compton

profile, $J(p_z)$, along the scattering vector as :

$$J(p_z) = \int_{p_x}\int_{p_y} n(p_x, p_y, p_z)\,dp_x dp_y \tag{3.26}$$

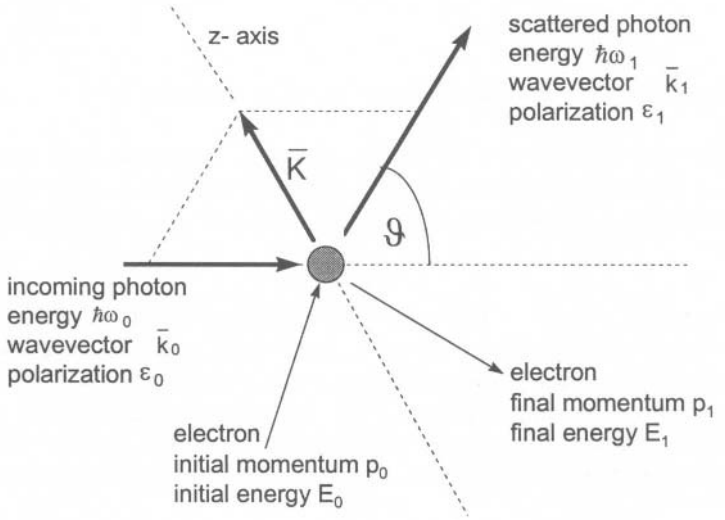

Fig.(3.12) The modification of Fig.(3.7) to include the initial and final momenta and energies of the electron, and the polarization vectors of the initial and scatter photon.

At low photon energies ($\hbar\omega_0 << m_0c^2$) the photon energy shift can be related to the momentum of the target electrons by the expression :

$$\omega_0 - \omega_1 = \frac{2\omega_0}{m_0 c} \sin\left(\frac{\vartheta}{2}\right) p_z \tag{3.27}$$

The usefulness of Compton profiling can be illustrated by the application of Eq.(3.27) to a typical situation. Consider a photon scattered through an angle of 180° as the result of an interaction with an electron having a component velocity of 2×10^6 m s^{-1} along the scattering vector K. This is the approximate value for an electron at the Fermi surface of aluminium. We have :

$$\sin(\vartheta/2) = 1,\ p_z/m_0c = 0.67\times 10^{-2},\ (\omega_0 - \omega_1)/\omega_0 \approx 1.3\%$$

An energy resolution of this magnitude is well within the capability of high purity Ge detectors (Chapter 5). Fig.(3.13) shows the separation of Doppler-shifted photon

energies due to scatter from tightly-bound core electrons and the less tightly-bound conduction electrons in aluminium. The core electron contribution extends to larger energy shifts and signifies photon scatter from higher velocity electrons.

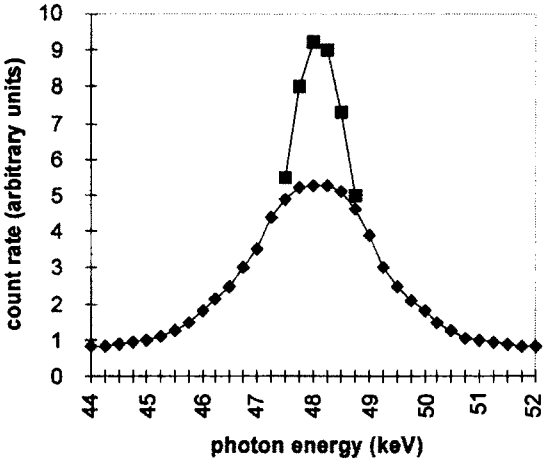

Fig.(3.13) An illustration of a Compton profile using 59.54 keV photons from ^{241}Am incident on aluminium and scattered at an angle of 171°. Contributions to the total profile come from the 10 core electrons (◆) and the 3 conduction electrons (■) in aluminium, [3].

It is conventional to use atomic units (au) in the determination of electron momenta. These set $e = \hbar = m_0 = 1$ and $c = 137$. The conduction electron component in Fig.(3.13) has a width which extends to ~ 0.8 keV either side of the centroid at ~ 48.2 keV. A maximum conduction electron momentum of $p_z = 0.926$ au is therefore obtained by substituting the following into Eq.(3.27) :

$$\omega_0 - \omega_1 = 0.8 \text{ keV}, \quad \sin(171/2) = 0.997, \quad \omega_0 = 59.54 \text{ keV}, \quad c = 137, \quad m_0 = 1.$$

In the Impulse Approximation, the cross-section is still expressed in terms of the Thomson scatter cross-section, Eq.(3.3), but is now modified to include the Compton profile integral from Eq.(3.26) :

$$\frac{d^2\sigma}{d\Omega d\omega} = \frac{d\sigma_0}{d\Omega}\frac{\omega_1}{\omega_0}\frac{m_0}{|K|}J(p_z) \tag{3.28}$$

Data taken over many scatter angles is then used to determine the Compton profile using Eq.(3.29) to convert between the energy and momentum scales.

$$\frac{p_z}{m_0 c} = (\omega_0 - \omega_1) \pm \frac{\omega_0 \omega_1}{m_0 c^2}(1 - \cos\vartheta)\left(\omega_0^2 + \omega_1^2 - 2\omega_0\omega_1 \cos\vartheta\right)^{-1/2} \tag{3.29}$$

Although a photon detector with a high energy resolution is a prime requirement in Compton profile measurements, other experimental conditions must also apply.

- There is generally an upper limit on the atomic number, Z, of the target. This arises for two reasons. (1) The $\sim Z^{3.5}$ dependence of the electronic photoelectric absorption cross-section makes the relative probability of Compton scatter rather unfavourable except at the highest energies. In this case, however, the absolute scatter cross-section also tends to be small. (2) The validity of the Impulse Approximation requires that the recoil energy given to the electron is much larger than the electron binding energy. For low energy photons, the samples are confined to low values of Z.
- The incident photon flux must be mono-energetic. X-ray sources using the $K_{\alpha 1}$ line are therefore disadvantaged by contamination from $K_{\alpha 2}$ and K_β lines as well as from *bremsstrahlung.*
- In the analysis of the scattered photon spectrum, due regard must be paid to : (1) energy calibration of the detector, (2) background subtraction, (3) detector efficiency, (4) absorption of incident photons in the sample, and (5) the deconvolution of the detector resolution function.

Synchrotron radiation sources possess attributes which make them ideal vehicles for Compton profile measurements. Such sources are available over a wide and selectable energy range with high brightness, good stability and excellent energy resolution. An important additional feature is their polarizability. This leads to the study of spin-dependent momentum distributions (see Section 1.6).

3.6 Photoelectric Absorption

In this process the photon gives up all its energy in overcoming the binding energy of a bound electron. Any remainder is imparted to the electron as kinetic energy. The photoelectrons so produced from the K, L,...-shells then have kinetic energies:

$$\begin{aligned} E_K &= h\nu_0 - BE_K \\ E_L &= h\nu_0 - BE_L \end{aligned} \tag{3.30}$$

A free electron cannot absorb a photon (and thereby become a photoelectron) because there is no third body to conserve momentum. The tightness of the electron's binding energy increases the ability of the third body (the atom) to absorb the recoil momentum. For this reason, the photoelectric absorption cross-section should be

specified in units of m^2 $atom^{-1}$. An absorption edge occurs whenever the photon energy reaches an electron binding energy, the discontinuities being greatest for the most tightly bound (K-shell) electrons.

Theoretical computations of the photoelectric cross-section have generally assumed the following :

- the Born approximation. This is based on plane waves for the electron wave function and neglects the attraction of the nuclear charge on the electron as it leaves the atom. Furthermore, this approximation is not valid for incident photon energies comparable to the ionization potential of the atom.
- the initial state is that of a single electron in the central field of the nucleus whose charge is screened by the other electrons.

On this basis Heitler [4] determined the atomic cross-section for K-shell electrons in an atom of atomic number Z as :

$$ {}_a\tau_K = \frac{8}{3}\pi r_0^2 Z^5 \alpha^4 2^{5/2}\left(\frac{m_0c^2}{h\nu_0}\right)^{7/2} \qquad (3.31) $$

In this equation $r_0 = e^2/m_0c^2$, $\alpha = 2\pi e^2/hc = 1/137$ is the fine structure constant, m_0c^2 is the rest mass of the electron and $h\nu_0$ is the incident photon energy.

Later refinements to Eq.(3.31) have sought to extend the treatment :

- to higher electron shells,
- to consider the angular distribution of the emitted electron and its polarization with respect to that of the photon,
- to use partial wave expansions for the outgoing electron wave function.

Comprehensive tables which draw together the results from both experimental and theoretical work appear in [5]. Fig.(3.14) shows some of these data, and indicates that the energy dependence changes from approximately E^{-3} (up to ~150keV) to E^{-1} (above ~5 MeV) as the photon energy increases. For Z-values smaller than those shown in Fig.(3.14), the low energy dependence tends to $E^{-7/2}$ rather than E^{-3}.

A rather similar uncertainty is recognized in the dependence on Z. Computation of ${}_a\tau.Z^{-5}$ over a wide range [5] shows that the Z–dependence is greater for low values. At low Z the dependence of the atomic cross-section goes approximately as $Z^{4.8}$ but this decreases to ~ $Z^{4.0}$ for higher Z-values.

Since there are Z electrons in each atom, the Z-dependence of the electronic

cross-section is $Z^{3.8}$ for low Z-values and Z^3 for higher Z-values. With the exception of hydrogen, the number of electrons per gram for most elements is approximately constant. This means that the cross-section per gram has the same Z-dependence as the cross-section per electron, namely, $Z^{3.8}$ at low Z and Z^3 at high Z.

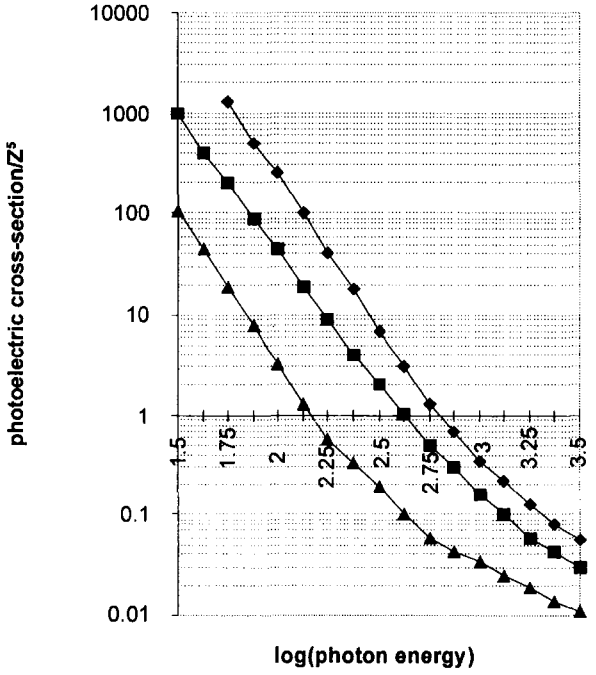

Fig.(3.14) The atomic photoelectric cross-section ${}_a\tau/Z^5$ against log $h\nu_0$. ◆ Z=82: ■ Z=13: ▲ three section line showing theoretical dependence on $h\nu^{-3}$ (low energies), $h\nu^{-2}$ (medium energies) and $h\nu^{-1}$ (high energies), [5].

3.6.1 Characteristic X-rays and Auger electrons

A vacancy in a K- (or L-, M-..) shell following photoelectric absorption results in a de-excitation of the atomic system, either by characteristic X-ray or Auger- electron emission. The relative probability of these de-excitation processes is given by the fluorescence yield. For a K-shell vacancy, this is :

$$\omega_K = \frac{P_{KX}}{P_{KX} + P_{KA}}$$

where P_{KX} is the probability of K X-ray emission and P_{KA} is the probability of K Auger

emission.

Fluorescence yield is strongly dependent on Z, being small for light atoms and large for heavy atoms. Different semi-empirical relations for the Z-dependence have been proposed. The two most widely quoted are :

$$\omega_K = \frac{Z^4}{a + bZ^4}$$

$$\omega_K = \left(-A + BZ - CZ^3\right)^4 \qquad (3.32)$$

where a, b, A, B, and C are constants. Photoelectric absorption in light atoms is therefore dominated by Auger electron emission, Fig.(3.15).

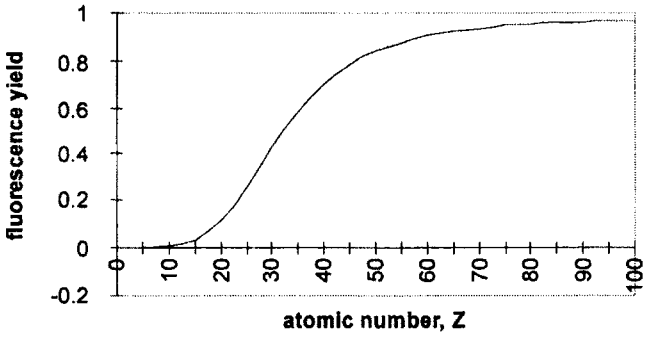

Fig.(3.15) Fluorescence yield versus atomic number using Eq.(3.32) and constants A=0.064, B=0.034, C=0.00000103.

Auger emission is classified by the atomic energy levels involved. Thus, a vacancy initially created in the K-shell can be filled by an electron from one of the L shells (say L_1). The energy released in this de-excitation process is transferred to another electron in a shell having a smaller binding energy (say L_3). This transition would be designated ($K\,L_1\,L_3$).

A precise treatment of the emitted electron energies in the Auger effect [6] must consider :

- screening and Coulomb interactions between electrons,
- exchange and spin-orbit interactions.

For practical purposes, however, adequate determinations of Auger electron energies can be obtained from tabulations of sub-shell binding energies [7].

The energy of a (K L_1 L_3) Auger electron is obtained from Table (3.2) as :

$$2149 - 189 - 135 = 1825 \text{ eV}.$$

In heavy atoms, a special case arises when the transitions take place amongst sub-shells of the same level. These are called Coster-Kronig transitions. Thus, when a primary vacancy in the L level (say L_1) is filled by an electron from the L_3 sub-shell, the energy difference may be sufficient to expel an electron from a higher shell (say, M_4 or M_5).

For tungsten, Table (3.2) shows that the Coster-Kronig electron energies in each of these cases are :

$$(L_1\ L_3\ M_4) = 12099 - 10205 - 1872 = 22 \text{ eV}.$$
$$(L_1\ L_3\ M_5) = 12099 - 10205 - 1810 = 84 \text{ eV}.$$

Table (3.2) Sub-shell electron binding energies (eV) in phosphorous and tungsten, [7].

	K	L1	L2	L3	M1	M2	M3	M4	M5
P (Z=15)	2149	189	136	135	16	10	-	-	-
W (Z=74)	69525	12099	11542	10205	2820	2575	2281	1872	1810

3.7 Pair Production

In contrast to the main energy dependence of Rayleigh, Compton and photoelectric interaction processes, the probability of pair production increases with increasing photon energy. It takes place in the field of a charged particle – mostly in the strong Coulomb field of the nucleus, although it can also take place at high energies in the field of an electron.

Pair production has a threshold photon energy equal to the combined rest mass of two electrons. Thus :

$$h\nu = (T^+ + m_0c^2) + (T^- + m_0c^2)$$

As in the case of photoelectric absorption, the interaction is treated initially on the basis of the Born approximation [8]. Here the assumption is that :

- $Ze^2/h\nu \ll 1$. Such a treatment is therefore not valid for large Z or small photon (and hence positron or electron) energies.
- When the interaction takes place close to the nucleus, pair production takes

place in the Coulomb field of the nucleus. At larger distances, this field is screened by the orbiting electrons by an amount which depends on distance from the nucleus. The part played by these electrons is assumed only to affect the screening of the nuclear charge and not to affect the dynamics of the collision.

- The emitted electrons are represented by plane waves.

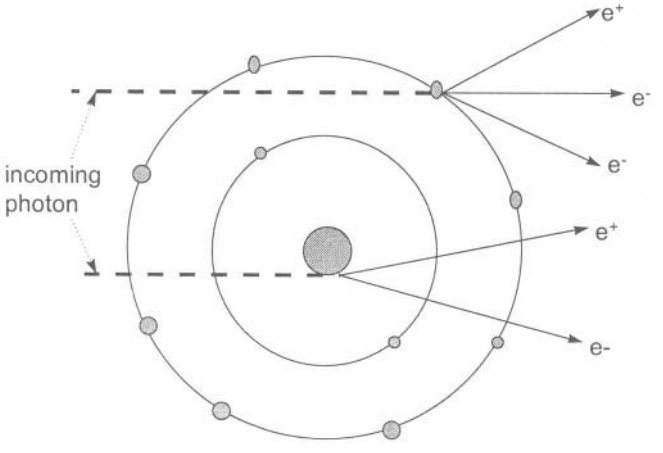

Fig.(3.16) Representation of pair production close to the nucleus (threshold energy 1.02 MeV) and triplet production far from the nucleus (threshold energy 2.04 MeV), [9]. With permission from Charles C. Thomas Ltd., Springfield, Illinois.

Momentum and energy are conserved in the collision by the involvement of the heavy nucleus and the light electrons.

- In a collision close to the nucleus, the nuclear recoil means that momentum is not conserved between the photon and the positron/electron pair.
- At larger distances from the atomic centre, however, the need to conserve momentum can impart energy to an electron sufficient to overcome its binding energy within the atom. Three particles are therefore produced – the positron/electron pair together with the original electron – albeit with a much lower probability. This is known as triplet production.
- The use of the Born approximation does not take into account the Coulomb interaction between the nucleus and the emitted particles. In this case the energies of the positron and electron are equal. When Coulomb interactions are considered, especially at photon energies just greater than the threshold, the energies become unequal. Because of its repulsion by the nucleus, the positron receives a slightly higher kinetic energy on average than the electron which is attracted to the nucleus. This asymmetry is reduced at higher photon energies. The cross-section calculated using the Born Approximation (high energies, small

Z and no screening) is :

$$ {}_a\kappa = \frac{1}{137} r_0^2 Z^2 \left(\frac{28}{9} ln\left(\frac{2h\nu}{m_0 c^2} \right) - \frac{218}{27} \right) \qquad (3.33) $$

where $r_0 = e^2/m_0c^2$ = classical electron radius = 2.818×10^{-15}m. The constant factor $r_0^2/137$ is equal to 5.80×10^{-32} m^2 nucleus^{-1}.

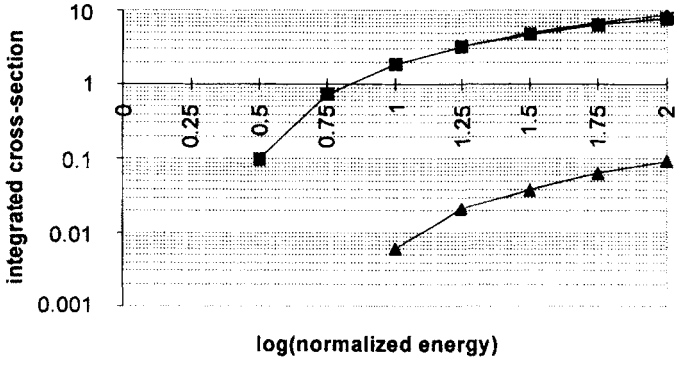

Fig.(3.17) Pair and Triplet production cross-sections in units of $r_0^2Z^2/137$ cm^2/nucleus versus $\log(h\nu_0/m_0^2c^2)$. ◆ pair - no screening: ■ pair - lead : ▲ triplet - lead [8].
Note that the effect of screening becomes important only at the highest energies. This is because at high energies an appreciable fraction of pair-production interactions take place at large distances from the nucleus. In such cases the effective charge of the nucleus is reduced, especially in an atom as large as lead.

A result for triplet production due to [10] gives :

$$ {}_a\kappa_{triplet} = \frac{1}{137} r_0^2 Z \frac{\pi\sqrt{3}}{972} \left(\frac{h\nu - 4m_0c^2}{m_0c^2} \right)^2 \qquad (3.34) $$

Note that Eqs.(3.33) and (3.34) give the cross-sections in m^2/nucleus and show a Z^2 (pair) and Z (triplet) dependence respectively.

Later attempts to remove the assumptions underlying the Born Approximation treatment have resulted in a number of semi-empirical relations for the pair production cross-section. Together with later developments to the theory of triplet production, these are presented in [5].

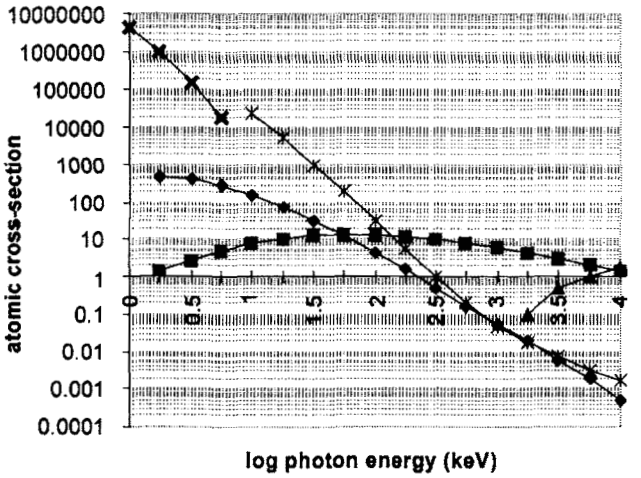

Fig.(3.18) Atomic cross-sections ($\times 10^{-28}$ m^2 atom^{-1}) in copper. ◆ coherent scatter : ■ incoherent scatter : ▲ pair production : ✖ photoelectric absorption. The K-edge is at 8.98 keV. The L1-edge is at 1.096 keV (not shown). Cross-sections can be converted to mass attenuation coefficients by multiplying by 9.478×10^{24} atom kg^{-1}, [9].

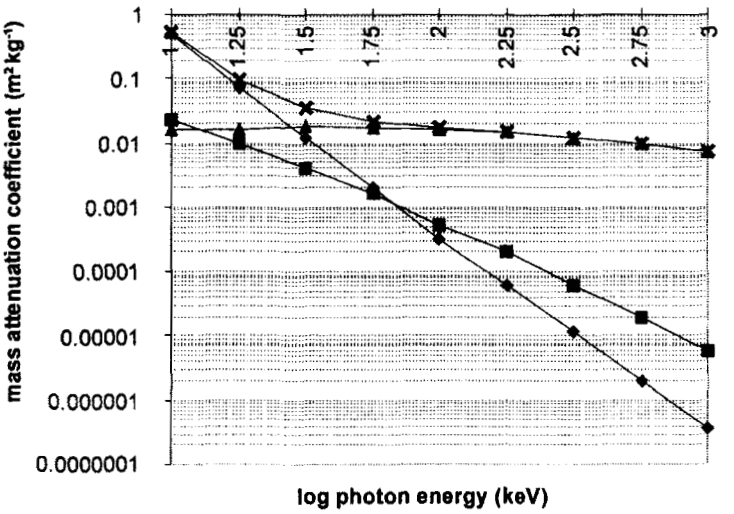

Fig.(3.19) Mass Attenuation Coefficient (m^2 kg^{-1}) in water versus photon energy (log scale). ◆ τ/ρ photoelectric absorption: ■ σ_{coh}/ρ Rayleigh scatter: ▲ σ_{incoh}/ρ Compton scatter: ✖ μ/ρ total attenuation. [11].

Total atomic cross sections are compared for copper over four decades in energy in Fig.(3.18), and as mass attenuation coefficient for water over two decades in energy in Fig.(3.19).

Noteworthy features are :

- at 2 MeV coherent scatter and photoelectric absorption have approximately the same probability in copper, but they are still almost two orders of magnitude smaller than Compton scatter at this energy.
- Compton scatter is the most important interaction in copper over the range $0.3 \leq h\nu_0 \leq 7$ MeV.
- Compton scatter is by far the most likely interaction in water at all energies except those below ~ 30 keV when photo-electric absorption becomes dominant.

References

[1] J.H.Hubbell et.al., *J.Phys.Chem. Ref. Data*, **4**(3) (1975) 471.
[2] R.D.Evans, *The Atomic Nucleus*, (McGraw-Hill, New York 1972).
[3] M.J.Cooper, *Rep.Prog.Phys.* **48** (1985) 415.
[4] W.Heitler, *The Quantum Theory of Radiation*, (Clarendon Press, Oxford 1954).
[5] C.M.Davisson in *Alpha-,Beta- and Gamma-Spectroscopy, Vol.1*, ed. K.Seigbahn, (North-Holland Publishing Company, Amsterdam 1968).
[6] E.H.S.Burhop, *The Auger Effect and other Radiation-less Transitions*, (Cambridge University Press, London 1952).
[7] C.M.Lederer and V.S.Shirley, (eds), *Table of Isotopes,* 7th Edition, (Wiley Interscience, USA 1978).
[8] H.A.Bethe and W.Heitler, *Proc.Roy.Soc.* **A146** (1934) 83
[9] H.E.Johns and J.R.Cunningham, *The Physics of Radiology*, 4th Edition, (Charles C. Thomas, Springfield, Illinois 1983).
[10] V.Votruba, *Phys.Rev.* **73** (1948) 1468.
[11] ICRU Report 46, (International Commission on Radiation Units and Measurements, USA,1992).

CHAPTER 4

INTERACTIONS of NEUTRONS

4.1 General Considerations

The neutron has a net charge of zero and a rest-mass slightly greater than that of the proton. β^- decay is therefore possible according to :

$$n \rightarrow p + e^- + \overline{\nu}_e$$

The maximum electron energy is 781.32 keV and half-life in free space is 11.7 ± 0.3 minutes.

In condensed materials neutron interaction cross-sections show a dependence on energy and on the nuclear properties of the medium. Being massive and uncharged, the neutron sees no Coulomb potentials but only the complex nuclear potential produced by all the nucleons in the target nucleus.

There are three possible consequences of a neutron interaction :

- The incoming neutron can be scattered by the nuclear potential (Direct or Potential Scattering) (section 4.2.1),
- The neutron can enter the nucleus to form a compound nucleus (section 4.2.2),
- At very high energies, a spallation reaction (the break-up of the nucleus) can occur (section 9.3.3).

Neutron interactions are classified in broad terms in Table 4.1 by their energy and by the mass of the target nucleus.

Table (4.1) Energy classification of neutrons and mass classification of targets.

Energy classification	slow (cold)	0 - 0.005 eV
	thermal	0.005 - 0.5 eV
	epithermal	0.5 - 1000 eV
	intermediate	1 - 100 keV
	Fast	0.1 - 10 MeV
Target Nuclei	light	$A < 25$
	medium	$25 < A < 80$
	heavy	$A > 80$

4.1.1 Classification in terms of energy

The general relations between energy and momentum for a relativistic particle are :

$$E_{tot} = T + E_0 \qquad \text{and} \qquad E_{tot}^2 = p^2c^2 + E_0^2$$

where E_0 is the particle rest energy, T its kinetic energy and p its linear momentum. These can be combined to express the de Broglie wavelength as :

$$\lambda\!\!\!^{-} = \frac{\hbar}{p} = \frac{\hbar c}{\sqrt{T(T + 2E_0)}} \tag{4.1}$$

In the extreme non-relativistic limit, $E_0 >> T$ and $\lambda\!\!\!^{-} = \hbar/mv$, where v is the neutron velocity and m the neutron mass. Since the equivalent rest-energy of the neutron is 939.565 MeV, all energies below 10 MeV can be treated safely using non-relativistic dynamics.

The mean energy of a neutron in thermal equilibrium with a medium at temperature T is obtained from the Maxwellian distribution $(3kT / 2)$. The most probable energy is $kT/2$ and the most probable velocity is :

$$v = \sqrt{\frac{2kT}{m}}$$

where k is the Boltzman constant = 1.381×10^{-23} J K^{-1}.

At T = 295 °K, v is 2206 m s^{-1}, the de Broglie wavelength is $\lambda = 2\pi\lambda\!\!\!^{-} = 0.179$ nm and the energy at this velocity is 0.0254 eV. Thermal neutrons, therefore, have wavelengths comparable to lattice dimensions in crystalline materials, and velocities which are sufficiently low for time-of-flight (TOF) studies. Colder neutrons have wavelengths suitable for probing the structure and dynamics of large molecular systems such as those in biological materials.

4.2 Neutron Interactions

4.2.1 Direct (potential) scattering

The neutron is scattered by the real part of the (generally complex) potential due to all the nucleons in the nucleus. When there is no angular momentum transfer between the neutron and the nucleus, the scattering is considered to be s-wave, when the quantum number change, ℓ, is zero. In this case the scattering amplitude f_0 is

isotropic and is related to the total elastic scattering cross-section [1] by :

$$\sigma = 4\pi|f_0|^2 = \frac{4\pi}{k_1^2} sin^2\,\delta_0 \qquad (4.2)$$

In this expression the wave-vector of the incoming neutron wave, k_1, is given by :

$$k_1 = \frac{2\pi}{\lambda} = \frac{M_R v_L}{\hbar}$$

where M_R is the reduced mass of the collision, $mM/m+M$, between the neutron mass m and the target mass M, and v_L is the neutron velocity in the laboratory system of co-ordinates.

A phase change, δ_0, is introduced into Eq.(4.2) for the general case of elastic scattering. Since low energy neutrons are scattered with a phase change which is close to either 0° or 180°, the scattering amplitude, a, is introduced. The cross-section then becomes, $\sigma = 4\pi a^2$.

4.2.2 Compound nucleus formation

This is a resonance reaction and can be represented in Fig.(4.1) when the left hand scale represents total energy. A compound nucleus is formed when the total input energy, $(mc^2 + Mc^2 + T)$, is equal to the sum of the compound nucleus rest-mass and the excitation energy of one of the resonance states, say $(M_{CN}c^2 + E_{k=4})$.

The lifetimes of excited states in a compound nucleus are generally very short, ($\sim 10^{-16}$s). De-excitation takes place through one, or more, of the following channels. The probability of each one is determined by its own cross-section, $\sigma(n,X)$, in which X denotes the emerging particle or radiation.

- A neutron can be emitted with the same energy as the incident neutron. This is a *compound elastic* collision and it leaves the original target nucleus in the same state as it was before the collision. It is denoted by (n,n).
- A neutron of smaller energy emerges from a *compound inelastic* collision. In this case, the energy difference between the energy of the incident and the outgoing neutron is emitted as one or more γ-rays. This is denoted as an $(n,n'\gamma)$ reaction.
- When all the excitation energy of the compound nucleus is emitted as one or more γ -rays, the collision is termed *radiative capture*, (n,γ). The residual nucleus is the compound nucleus in its ground state and it is frequently unstable against β^- decay. An activation reaction has therefore taken place (Chapter 8). The original neutron is absorbed and ceases to exist after the collision.

- When the kinetic energy of the incident neutron, T, is sufficiently high, more than one neutron or a charged particle can be emitted. The possibilities are the reactions described as *(n,p), (n,d), (n,α), (n,np), (n,2n), (n,3n),.....*
- Heavy target nuclei can undergo fission reactions, *(n,f).*

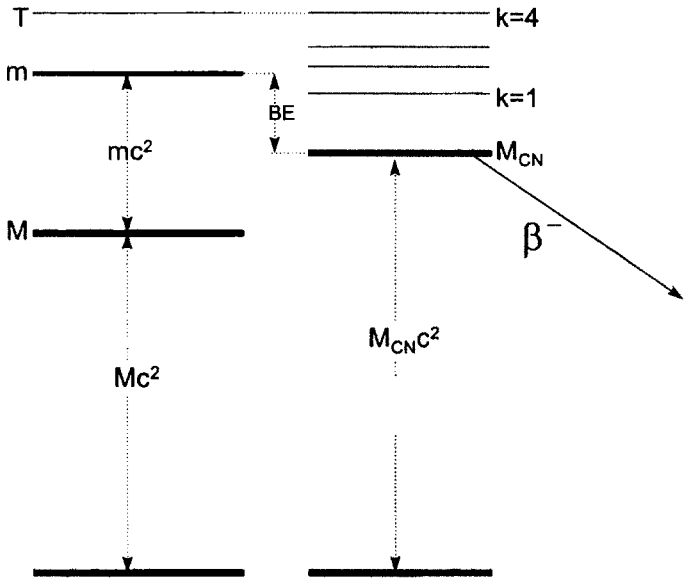

Fig.(4.1) Formation of a compound nucleus by the reaction $m + M \rightarrow M_{CN}$ where m is the neutron mass, having kinetic energy T, and M is the target mass. The binding energy of the neutron in the product compound nucleus M_{CN} is denoted by BE. Excited (resonance) states of the compound nucleus are represented by k = 1...4.

When the target nucleus is ^{115}In the following reactions are possible :

$$ {}^{1}_{0}n + {}^{115}_{49}In \rightarrow {}^{116}_{49}In^{*} \rightarrow {}^{115}_{49}In + {}^{1}_{0}n \qquad (4.3) $$

$$ \rightarrow {}^{115}_{49}In + {}^{1}_{0}n' + \gamma \qquad (4.4) $$

$$ \rightarrow {}^{116}_{49}In + \gamma \qquad (4.5) $$

$$ \rightarrow {}^{115}_{48}Cd + {}^{1}_{1}p \qquad (4.6) $$

The cross-section for compound formation is largest (σ_{th} = 160 ± 2 barn) for a (n,γ) reaction when the incident excitation energy is in the thermal region (Table 4.1). In this case Eq.(4.6) cannot occur because the binding energy of a proton in the compound nucleus is greater than that of a neutron. Subsequent decay of ^{116}In

in Eq.(4.5) takes place by β^- emission to ^{116}Sn. Two categories of γ -emission result from this reaction – the prompt photons from the de-excitation of the compound nucleus ^{116}In* and the decay photons from the de-excitation of the ^{116}Sn nucleus, Fig.(4.2).

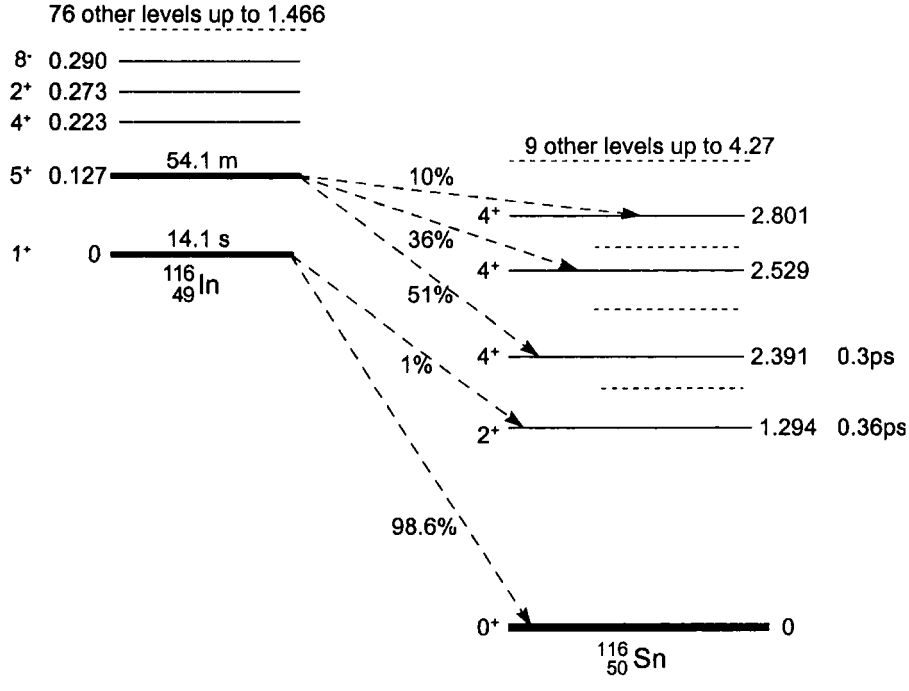

Fig.(4.2) Decay scheme of ^{116}In. Lifetimes and spin-parities of the nuclear states are given where known, as are the β^- branching ratios. Energies are in MeV.

4.2.3 *Partial decay lifetimes of compound nucleus states*

Each of the excited states of the compound nucleus, k = 1...4 in Fig.(4.1), have characteristic lifetimes $(\tau_1 \ldots \tau_4)$ whose reciprocal gives the total probability of decay from that state. For the excited state having k = 4, the equation :

$$\frac{1}{\tau_4} = \frac{\hbar}{\Gamma}$$

gives this probability in terms of the total width Γ. This is expressed in terms of the partial widths of elastic scatter (also called the neutron width), inelastic scatter width, radiative width, charged particle width... :

$$\Gamma = \Gamma_{n,n} + \Gamma_{n,n'\gamma} + \Gamma_{n,\gamma} + \Gamma_{n,p} \ldots\ldots$$

The relative probability of *radiative capture* is therefore $\Gamma_{n,\gamma}/\Gamma$.

For light nuclei, $\Gamma_{n,n} >> \Gamma_{n,\gamma}$, and neutron resonance scattering is much more probable than *radiative capture*. For heavy nuclei, $\Gamma_{n,\gamma} >> \Gamma_{n,n}$ and *radiative capture* becomes more probable.

Although *radiative capture* widths show very little energy dependence, neutron widths increase with the energy of the resonance approximately as $\sqrt{E}$. Thus :

$$\Gamma_{n,n} = \Gamma_{n,0}\sqrt{E} \tag{4.7}$$

where $\Gamma_{n,0}$ is specified for a particular nucleus.

4.2.4 The formula for the Breit-Wigner cross-section

For resonances which are widely separated in energy, the general Breit-Wigner cross-section formula can be used. This applies to the formation of a compound nucleus in a reaction, a + A $\rightarrow$ C* $\rightarrow$ B + b. It has a Lorenztian form :

$$\sigma_{CN} = \pi\lambda\!\!\!^{-2}(2\ell + 1)\,\frac{\Gamma_a\Gamma}{(E - E_R)^2 + \left(\frac{\Gamma}{2}\right)^2} \tag{4.8}$$

In Eq.(4.8), $\lambda\!\!\!^{-}$ is the rationalized de Broglie wavelength of the incident neutron, ℓ is the orbital angular momentum quantum number associated with the collision (i.e. the amount transferred from the incident neutron to the compound nucleus), while Γ_a and Γ represent the partial and total widths. The decay into entity b is then expressed as :

$$\sigma_{ab} = \sigma_{CN}\,\frac{\Gamma_b}{\Gamma}$$

The energy-dependent cross-sections for *compound elastic* scattering and *radiative capture* are then given by:

$$\sigma_{n,n} = \pi\lambda\!\!\!^{-2}\,\frac{\Gamma_{n,n}{}^2}{(E - E_R)^2 + \left(\frac{\Gamma}{2}\right)^2} \tag{4.9}$$

$$\sigma_{n,\gamma} = \pi\lambda\!\!\!^{-2} \frac{\Gamma_{n,n}\Gamma_{n,\gamma}}{(E - E_R)^2 + \left(\frac{\Gamma}{2}\right)^2} \qquad (4.10)$$

for s-wave (ℓ=0) collisions.

- When $E = E_R$, the cross-section is a maximum, $\sigma_{n,\gamma}(E_R) = 4\pi\lambda\!\!\!^{-2}\Gamma_{n,n}\Gamma_{n,\gamma}/\Gamma^2$.
- When $E = E_R \pm \Gamma/2$, the cross-section is half of the maximum, indicating that Γ is the full-width at half maximum (FWHM) of the resonance peak.
- When $E \rightarrow 0$ and $\Gamma << E_R$, the Breit-Wigner expression for the (n,γ) cross-section can be used to show the low energy dependence of *radiative capture* in the vicinity of a single resonance.

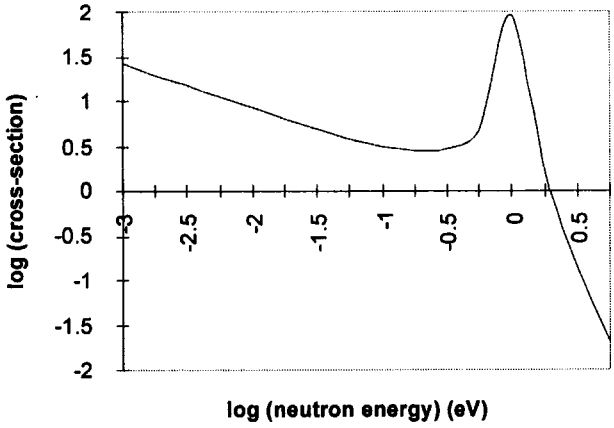

Fig.(4.3) The *radiative capture* cross-section, in arbitrary units, as given by the Breit-Wigner formula for energies below a single resonance at E_R= 1.0 eV having width Γ = 0.07 eV. The $1/v$ dependence at low energies is evident.

Eq.(4.10) for *radiative capture* in the vicinity of a low energy resonance gives $\sigma_{n,\gamma}(E) \rightarrow \pi\lambda\!\!\!^{-2}\Gamma_{n,n}\Gamma_{n,\gamma}/E_R^2$. The energy dependence as $E \rightarrow 0$ is dominated by an increase in the de Broglie wavelength.

Using Eq.(4.7) and $\lambda\!\!\!^{-2} = \hbar^2/2mE$ and $\lambda\!\!\!^{-2}_R = \hbar^2/2mE_R$ we get :

$$\sigma_{n,\gamma}(E) = \pi\lambda\!\!\!^{-2}_R \frac{\Gamma_{n,0}\Gamma_{n,\gamma}}{E_R} \frac{1}{\sqrt{E}} \propto \frac{1}{v} \qquad (4.11)$$

The important low energy *1/v* dependence in this cross-section is seen by plotting Eq.(4.11) in Fig.(4.3) for the case when E_R = 1.0 eV and Γ = 0.07 eV.

4.3 Neutron Fields in Non-Multiplying Media

Energetic neutrons entering a condensed medium can interact via the two principle processes of direct scatter and compound nucleus formation. Like any other radiation, neutron interactions are conveniently segregated into elastic scatter, inelastic scatter and absorption events. In terms of the relevant cross- sections we have :

- elastic scatter, $\sigma_{s,el}$: contributions come from direct scatter, σ_{pot}, in Eq.(4.2), and from scatter following compound nucleus formation, $\sigma_{n,n}$, in Eq.(4.3),
- inelastic scatter, $\sigma_{s,inel}$: the scattered neutron emerges with less energy, $\sigma_{n,n'\gamma}$, in Eq.(4.4),
- absorption $\sigma_{n,\gamma}$: *radiative capture* now gives an activated target of the same element, Eq.(4.5),
- absorption $\sigma_{n,p}$: an absorption event gives an activation route to a different element, Eq.(4.6).

The total cross-section is then given by :

$$\sigma_t = \sigma_{s,el} + \sigma_{s,inel} + \sigma_{ab.}$$
$$\sigma_t = \left(\sigma_{pot} + \sigma_{n,n}\right) + \left(\sigma_{n,n'\gamma}\right) + \left(\sigma_{n,\gamma} + \sigma_{n,p} + \ldots\right)$$

Two processes are responsible for the energy loss of a neutron as it penetrates a medium :

- an inelastic scatter event such as the one described in Eq.(4.4),
- momentum loss due to the recoil of a nucleus from which the neutron scatters elastically in the centre of mass system of co-ordinates. Even though this is an elastic scatter event there is energy loss in the laboratory system.

4.3.1 Definition of flux and current density

The total flux of neutrons, Φ – defined as the number of neutrons of all energies crossing unit area per second – changes with distance dx according to :

$$d\Phi = -\Phi\sigma_t N dx$$

where N is the number density of interaction centres (i.e. nuclei cm^{-3}). This reduces to the exponential expression :

$$\Phi_x = \Phi_0 \exp(-\Sigma_t x)$$

where Σ_t is the total macroscopic cross-section (see also section 8.3.4).

When neutrons are introduced into a material, their number depends on :

- their position in the medium, r,
- their energy, E,
- the direction of travel, ω.

A complete description of a neutron field therefore involves the vector flux $F(r,E,\omega)$. This restricts the number of neutrons only to those at position r, having energy E which travel in direction ω. The number contained within the sphere in Fig.(4.4), is $n(r,E,\omega)$ with units cm^{-3} eV^{-1} st^{-1}. The number crossing the disc per second in direction ω with velocity v (corresponding to energy E), is the vector flux $F(r,E,\omega) = vn(r,E,\omega)$ and it has units cm^{-2} s^{-1} eV^{-1} st^{-1}.

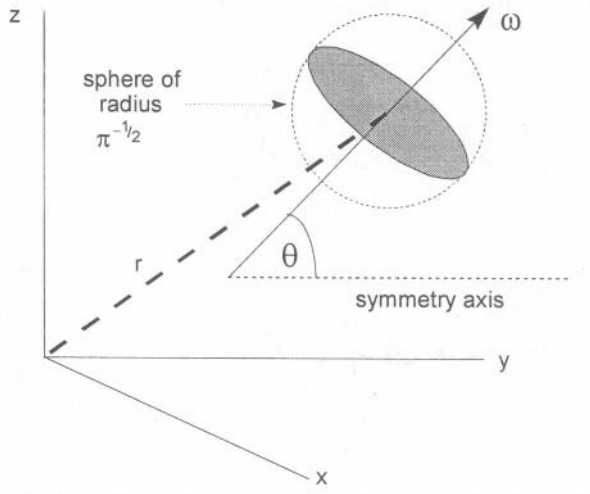

Fig.(4.4) The definition of total flux is the number of neutrons travelling in all directions which intersect a sphere of radius $\pi^{-1/2}$, centred at position r, [2]. With permission from Springer-Verlag, Berlin.

Under the assumption that $F(r,E,\omega)$ is isotropic, the total flux can be obtained by integrating over all angles :

$$\Phi(r) = \int_{4\pi} F(r,\omega)\, d\omega \qquad (4.12)$$

When there is asymmetry with only a single axis of symmetry, as in Fig.(4.4), the flux is defined as the number of neutrons crossing unit area perpendicular to the symmetry axis per second. This is termed the neutron current density, *J(r)*.

$$J(r) = \int_{4\pi} F(r,\omega)\ \cos\theta\ d\theta$$

The vector flux is then given by :

$$F(r,\omega) = \frac{1}{4\pi}\Phi(r) + \frac{3}{4\pi}J(r)\ \cos\theta$$

4.3.2 *Collision dynamics*

Energy loss by elastic scatter is an important aspect of most neutron fields. It is, for example, a particular requirement in the proper functioning of thermal nuclear reactors. Treatment of the collision dynamics of a neutron, mass *m*, impinging on a heavy nucleus, mass *M*, is similar to the classical derivation given in section 2.4 for a heavy charged particle, mass *M*, that collides with an electron of mass m_0.

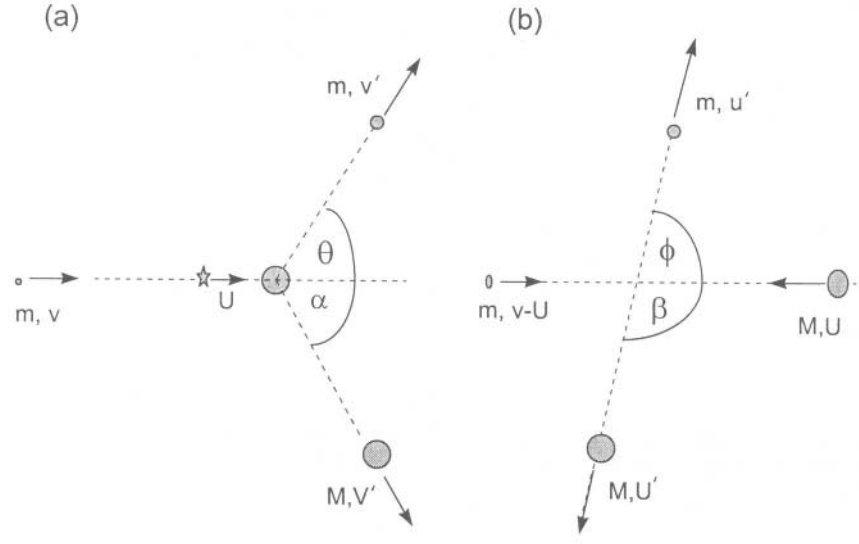

Fig.(4.5) The collision of a neutron, mass *m*, with a target nucleus, mass *M*, in laboratory (a) and centre of mass (b) co-ordinate systems. The initial neutron velocity is *v* in the L system and *u'* in the CM system. The centre of mass of the two particles moves towards the stationary target mass in the L system with a velocity *U*.

In the laboratory (L) system the target nucleus, mass *M*, is at rest. The velocity of

In the laboratory (L) system the target nucleus, mass *M*, is at rest. The velocity of the centre of mass is given by the conservation of momentum :

$$mv = (m+M)U \tag{4.13}$$

The centre of mass is stationary in the CM system, so the neutron velocity before the collision is :

$$v - U = v - \left(\frac{m}{M+m}\right)v = v\left(\frac{M}{M+m}\right) \tag{4.14}$$

For an elastic collision, the CM velocities of the neutron before and after the collision are the same. So $u' = v - U$.

Using Eqs.(4.13) and (4.14) the triangle of neutron velocities in Fig.(4.6) gives the neutron velocity in the L system :

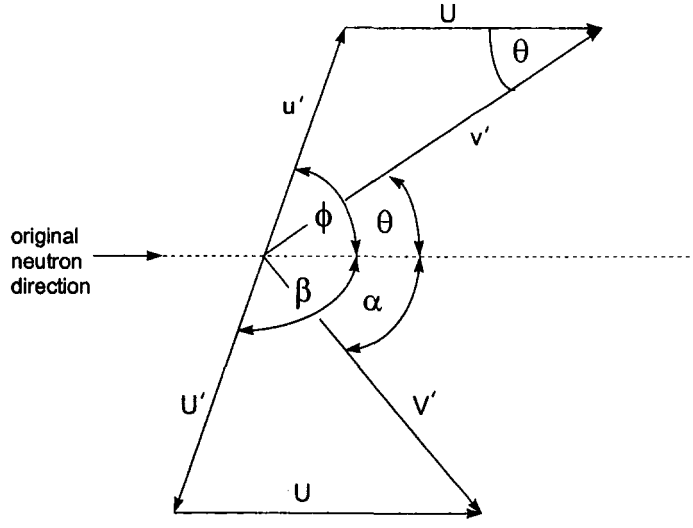

Fig.(4.6) The vector diagram which relates neutron velocities v', u' and the struck nucleus velocities V', U' in the L and CM systems.

$$\begin{aligned} v'^2 &= u'^2 + U^2 - 2u'U\cos(180-\phi) \\ &= u'^2 + U^2 + 2u'U\cos\phi \\ &= v^2\left(\frac{M}{M+m}\right)^2 + v^2\left(\frac{m}{M+m}\right)^2 + 2v^2\left(\frac{M}{M+m}\right)\left(\frac{m}{M+m}\right)\cos\phi \end{aligned} \tag{4.15}$$

The non-relativistic energies in the L system are :

$$E_0 = \frac{1}{2}mv^2 \quad \text{and} \quad E = \frac{1}{2}mv'^2$$

Taking the neutron mass m = 1 and the target mass $M = A$, we get :

$$\frac{E}{E_0} = \left(\frac{A}{A+1}\right)^2 + \left(\frac{1}{A+1}\right)^2 + \frac{2A}{(A+1)^2}\cos\phi$$

$$= \frac{A^2 + 2A\cos\phi + 1}{(A+1)^2} \tag{4.16}$$

Eq.(4.16) gives a minimum neutron energy after the collision when $\cos\phi = -1$, i.e. in a head-on collision, when $\phi = \theta = 180°$. In this case :

$$\frac{E_{min}}{E_0} = \left(\frac{A-1}{A+1}\right)^2 = \alpha \tag{4.17}$$

In a single elastic collision, therefore, the neutron energy cannot fall below αE_0. Re-arrangement of Eqs.(4.13), (4.14) and (4.15) gives the angle of scatter in the L system as, [2] :

$$\cos\theta = \frac{A\cos\phi + 1}{\sqrt{A^2 + 2A\cos\phi + 1}} \tag{4.18}$$

4.3.3 Distributions in energy and angle of scatter

Neutron scattering is usually considered to be isotropic in the CM system at energies below ~1 MeV. In a single collision, therefore, the probability is unity that the neutron is scattered through an angle between 0 and π (a change in $\cos\phi$ from +1 to -1). Thus we write $d(\cos\phi)_{max} = 2$. Scatter through any other angle, $d(\cos\phi)$, is constant and independent of angle.

$$p = 1\,\frac{d(\cos\phi)}{d(\cos\phi)_{max}} = \frac{d(\cos\phi)}{2}$$

The unique relation between the energy loss and the CM angle of scatter in a single event, Eq.(4.16), can be used to relate this scatter angle to energy loss. By

differentiation, we get :

$$\frac{d}{dE}(\cos\phi) = \frac{(A+1)^2}{2AE_0}$$

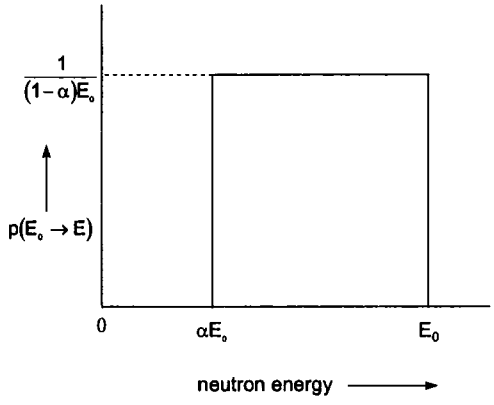

Fig.(4.7) The probability versus scattered neutron energy for a single collision.

Using Eq.(4.17) the required probability for a single scatter event from E_0 to E is therefore :

$$p(E_0 \to E) = \frac{1}{2}\,\frac{(A+1)^2}{2AE_0} = \frac{1}{(1-\alpha)E_0} \tag{4.19}$$

4.3.4 Mean scatter angle and energy loss in a single collision

Fig.(4.7) shows that the probability of scatter is independent of angle and depends only on A and E_0. The probable angle of scatter in the L system is found using, [2]:

$$\langle\cos\theta\rangle = \int_{-1}^{+1} \cos\theta\; p$$

$$= \frac{1}{2}\int_{-1}^{+1} \frac{A\cos\phi + 1}{\sqrt{A^2 + 2A\cos\phi + 1}}\; d(\cos\phi)$$

$$= \frac{2}{3A} \tag{4.20}$$

For isotropic scattering in the CM system, the average value of the cosine of the scattering angle in the L system is simply related to the mass of the struck nucleus. The smaller the nuclear mass from which the neutron scatters, the smaller will be the mean scatter angle. For massive nuclei, θ tends to 90° and the scatter becomes

isotropic in the L system.

The mean neutron energy following a single isotropic scatter event in the CM system can be expressed as :

$$\langle E \rangle = \int_{\alpha E_0}^{E_0} E\, p(E_0 \rightarrow E)\, dE$$

$$= \int_{\alpha E_0}^{E_0} E \frac{1}{(1-\alpha)\, E_0}\, dE$$

$$= \frac{E_0}{2}(1+\alpha) \qquad (4.21)$$

The mean energy loss per collision, $E_0 - \langle E \rangle$, is more conveniently expressed as a logarithmic ratio. This is the average logarithmic energy decrement :

$$\xi = \left\langle ln\left(\frac{E_0}{E}\right)\right\rangle \qquad (4.22)$$

Now Eq.(4.22) can be redefined, using the result of Eq.(4.19) to give an expression which is independent of energy :

$$\xi = \left\langle ln\left(\frac{E_0}{E}\right)\right\rangle = \int_{\alpha E_0}^{E_0} ln\left(\frac{E_0}{E}\right)\, p(E_0 \rightarrow E)\, dE$$

$$\xi = 1 + \frac{\alpha}{(1-\alpha)} ln\, \alpha \qquad (4.23)$$

4.3.5 Extension to multiple collisions

Since the average logarithmic energy decrement, ξ, for a single collision is independent of energy, the mean number of collisions necessary to reduce the neutron energy to a particular value is readily estimated. From Eq.(4.22) :

$$\xi = ln\, E_0 - \langle ln\, E \rangle$$

$$\approx ln\, E_0 - ln \langle E \rangle$$

In a single collision :

$$\langle E \rangle = E_0 \, exp(-\xi)$$

After n collisions the mean energy is given by :

$$\langle E_n \rangle = E_0 \, exp(-n\xi)$$

Alternatively, we can define the final energy precisely and express the mean numbers of collision necessary to reach, say E' :

$$\langle n \rangle = \frac{ln(E_0 / E')}{\xi} \tag{4.24}$$

It must be remembered that $\langle n \rangle$ is only an estimate. Approximations made in its derivation are, [2] :

- Isotropic scatter in the CM system is assumed to take place at all energies. Furthermore, when E' is at thermal energy the expression does not account for possible energy-gain collisions as the neutron approaches thermal velocities,
- Collisions are assumed to be purely elastic,
- It is assumed that $\langle ln\, E' \rangle = ln\langle E' \rangle$.

The actual number of collisions needed to reach E' is distributed about $\langle n \rangle$ with a distribution which is approximately Gaussian for large values of n [3].

$$p(E')dE' = k \times exp\left[\frac{-6(u - n\xi)^2}{4n\xi^2}\right]dE' \tag{4.25}$$

Eq.(4.25) gives the probability of finding a neutron with energy between E' and E' +dE' having made n collisions. k is a constant and u is called the "lethargy" to energy E' ($u = ln(E_0 / E')$). Lethargy is zero at the start of the slowing-down process and in Age Theory (section 4.5) is assumed to increase continuously as moderation proceeds.

Table (4.2) Neutron collision parameters for selected nuclei. Note that the mean number of collisions required to reduce the neutron energy from 10 MeV down to thermal is only 10% greater than that needed for 1 MeV to thermal. Moderation efficiency is therefore greatest at high energies, [3].

	H	D	C	O	U
A	1	2	12	16	238
α	0	0.111	0.716	0.779	0.983
$\langle\cos\theta\rangle$	0.667	0.333	0.056	0.042	0.003
ξ	1	0.726	0.158	0.120	0.009
n(10 MeV→1/40 eV)	20	27	125	165	2201
n(1 MeV→1/40 eV)	18	24	111	146	1945

4.3.6 *The Slowing-Down Energy Spectrum*

Earlier consideration of vector flux, together with the distributions in energy and angle of the scattered neutron, now permits the expression of a neutron balance equation. As the name implies, the (time) rate of change of the number of neutrons specified by $F(r,E,\omega)$ in a certain volume of medium has to be set equal to zero.

$$\frac{\partial}{\partial t} n(r,E,\omega) = \frac{1}{v} \frac{\partial}{\partial t} F(r,E,\omega) = 0$$

In general, a neutron can :

- lose energy until its mean energy reaches equilibrium with the medium. If the medium is at temperature T, this thermal energy is $3kT/2$ [2],
- be absorbed, either by a resonance absorption at high and epithermal energies or by $1/v$ absorption in the thermal region,
- escape the medium all together.

The slowing down spectrum is first expressed for an infinite volume. In this case the flux, $\Phi(E)$, is independent of r and is a function only of E.

We first consider the slowing down of neutrons emitted into a medium from a monoenergetic source of strength S neutrons s^{-1} at energy E_S. The energy at which the flux is to be specified, E, is within the range $3kT/2 < E < E_S$. Neutrons which contribute to $\Phi(E)$ will therefore have made widely differing numbers of collisions before reaching energy E. In this case, it is convenient to define the Slowing Down Density $q(E)$, or $q(u)$, as the number of neutrons slowed down past energy E, or lethargy u, per cm^{-3} s^{-1}.

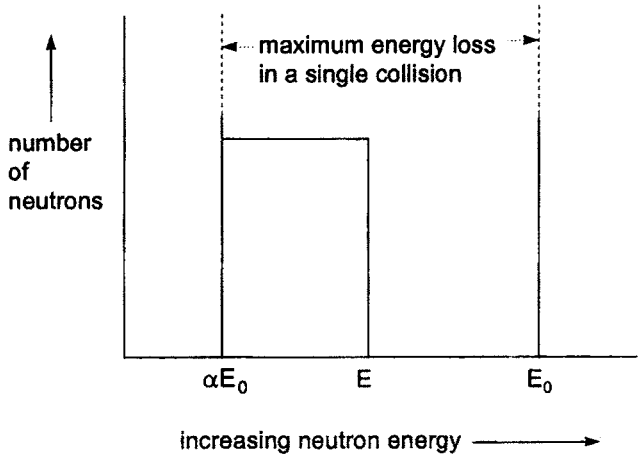

Fig.(4.8) A representation of the Slowing Down Density $q(E)$. This is the number of neutrons slowed down in a single collision per unit volume per unit time from any energy $E<E_{initial}<E_0$ to any energy $\alpha E_0 < E_{final} < E$.

Using the definition in Eq.(4.19), the total number of neutrons slowing down past energy E in a single collision is, [2] :

$$\Phi(E_0)\,\Sigma_s(E_0)\int_{\alpha E_0}^{E} p(E_0 \rightarrow E_{final})\,dE_{final}$$

where $\Sigma_s(E_0)$ is the macroscopic scatter cross-section at energy E_0 (section 4.3.1). Integrating over all available energies E_0, we get the final result for the slowing down density at E :

$$q(E) = \int_{E}^{E/\alpha} \Phi(E_0)\,\Sigma_S(E_0) \int_{\alpha E_0}^{E} p(E_0 \rightarrow E_{final})\,dE_{final}\,dE_0$$

Substituting for p, Eq.(4.19), and performing the inner integration gives :

$$q(E) = \int_{E}^{E/\alpha} \Phi(E_0)\,\Sigma_s(E_0)\,\frac{(E-\alpha E_0)}{(1-\alpha)\,E_0}\,dE_0 \qquad (4.26)$$

For the special case of hydrogen, Eq.(4.17) gives $\alpha = 0$, so Eq.(4.26) reduces to :

$$q(E) = E \int_{E}^{\infty} \Phi(E_0)\ \Sigma_S(E_0)\ \frac{dE_0}{E_0} \tag{4.27}$$

The neutron balance equation at energy E can be expressed for maximum energy loss in a single collision as :

$$\left[\Sigma_a(E) + \Sigma_S(E)\right] \Phi(E) = \int_{E}^{E/\alpha} \Sigma_S(E_0)\ \Phi(E_0)\ \frac{1}{(1-\alpha)\ E_0}\ dE_0 + S(E) \tag{4.28}$$

Terms on the left-hand side of Eq.(4.28) account for the loss of neutrons by absorption, $\Sigma_a\Phi(E)$, and scatter, $\Sigma_S\Phi(E)$, at energy E. The right-hand side accounts for the gain of neutrons. The first term integrates the product of flux, scatter cross-section and probability of scatter from all available higher energies E_0 down past E. The second term accounts for any source neutrons emitted at energy E.

Eqs.(4.27) and (4.28) can be combined to give an expression for the flux in hydrogen :

$$\Phi(E) = \frac{q(E)}{\left[\Sigma_a(E) + \Sigma_S(E)\right] E} + \frac{S(E)}{\left[\Sigma_a(E) + \Sigma_S(E)\right]} \tag{4.29}$$

A monoenergetic source which produces neutrons only at energy E_s must have $S(E) = 0$. In hydrogen $\Sigma_a << \Sigma_S$, so all neutrons produced at the source energy E_S will eventually scatter down to energy E without any absorption giving $q(E) = S(E_S)$. Eq.(4.29) then reduces to :

$$\Phi(E) = \frac{S(E_S)}{\Sigma_S(E)\ E}$$

4.3.7 *Slowing down in hydrogen in the presence of absorption*

We now consider a material in which neutron moderation is achieved by hydrogen ($\alpha = 0$), and in which there is a second material which does not contribute to moderation but which does introduce absorption. In this case, the slowing down density $q(E)$ is modified by the inclusion of a probability $p(E)$, called the Resonance Escape Probability. This is the probability that a neutron will escape absorption during its moderation from E_0 to E. We now have :

$$q(E) = S(E_S)\ p(E) \tag{4.30}$$

The rate of change of slowing down density $q(E)$ at energy E is determined by the ratio of absorption to the total cross-section, [2].

$$\frac{dq(E)}{dE} = \frac{\Sigma_a(E)}{\Sigma_a(E)+\Sigma_S(E)} \frac{q(E)}{E} \tag{4.31}$$

Eq.(4.31) can be expressed in terms of an energy, E', between the energy of interest, E, and the source energy, E_S, and rearranged to give :

$$\frac{dq(E')}{q(E')} = \frac{\Sigma_a(E')}{\Sigma_a(E')+\Sigma_S(E')} \frac{dE'}{E'}$$

Integrating between E and E_S gives :

$$\left[\ln q(E)\right]_{E_S}^{E} = \int_{E_S}^{E} \frac{\Sigma_a(E')}{\Sigma_a(E')+\Sigma_S(E')} \frac{dE'}{E'}$$

$$q(E) = q(E_S)\ exp\left\{\int_{E_S}^{E} \frac{\Sigma_a(E')}{\Sigma_a(E')+\Sigma_S(E')} \frac{dE'}{E'}\right\} \tag{4.32}$$

In the absence of absorption, the number of neutrons slowed down past energy E ($cm^{-3}\ s^{-1}$) is equal to the output of the source, i.e. $q(E) = S(E_S)$. When absorption is present, for any energy $E < E_S$, only the scattered fraction of all interactions contributes to the slowing down density, so we have :

$$q(E_S) = \frac{\Sigma_S(E_S)}{\Sigma_S(E_S)+\Sigma_a(E_S)}\ S(E_S) \tag{4.33}$$

Combining Eqs.(4.30), (4.32) and (4.33) we get the expression for the resonance escape probability :

$$p(E) = \frac{\Sigma_S(E_S)}{\Sigma_S(E_S)+\Sigma_a(E_S)}\ exp\left\{-\int_{E}^{E_S} \frac{\Sigma_a(E')}{\Sigma_a(E')+\Sigma_S(E')} \frac{dE'}{E'}\right\} \tag{4.34}$$

Eq.(4.34) can now be substituted into Eqs.(4.30) and (4.29) to give the energy dependent flux when $S(E) = 0$.

$$\Phi(E) = \frac{1}{[\Sigma_a(E)+\Sigma_S(E)]E} S(E_S) \frac{\Sigma_S(E_0)}{[\Sigma_S(E_0)+\Sigma_a(E_0)]} exp\left\{ - \int_E^{E_S} \frac{\Sigma_a(E')}{\Sigma_a(E')+\Sigma_S(E')} \frac{dE'}{E'} \right\} \tag{4.35}$$

By taking the logarithm of Eq.(4.35), a linear relation can be obtained between *ln* $\Phi(E)$ and *ln* $\{\Sigma_s(E)\, E\}$ with a gradient of -1, [1].

$$ln\,\Phi(E) = ln(constant) - ln\left\{\left(\Sigma_a(E)+\Sigma_S(E)\right) E\right\} - \int_E^{E_S} \frac{\Sigma_a(E')}{\Sigma_a(E')+\Sigma_S(E')} \frac{dE'}{E'} \tag{4.36}$$

The effect on the flux of a single resonance absorption is shown schematically in Fig.(4.9).

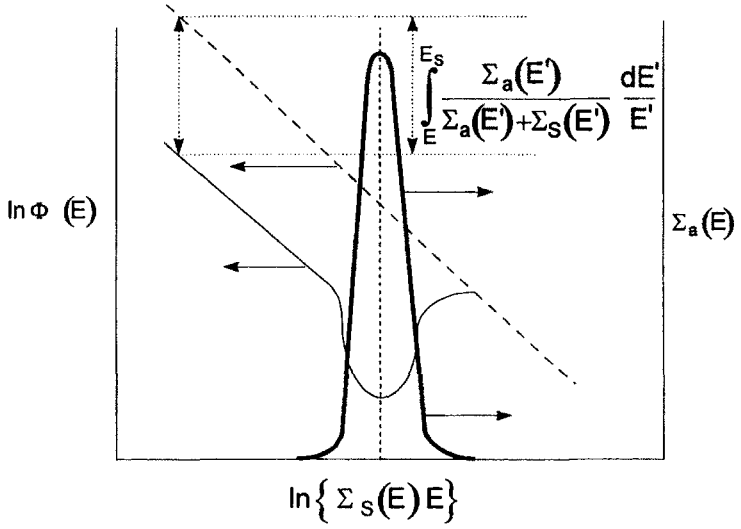

Fig.(4.9) The effect of a single resonance absorption (right hand scale) on the natural logarithm of the flux at energy E (left hand scale). At energies either side of the resonance the relation between *lnΦ(E)* and *ln*$\{\Sigma_s(E)\, E\}$ is linear with a gradient of -1. The dotted line is the case for zero absorption. The solid line shows the depression in the flux due to the final, integral, term in Eq.(4.36) at energies below the resonance maximum, [3].

4.3.8 Slowing down in media heavier than hydrogen

When moderation is achieved by scatter from nuclei with mass greater than unity, and hence with $\alpha \neq 0$, there is an increased probability of resonant absorption because the neutron makes many more collisions. The following assumptions are

made :

- A large number of collisions have already been made. In this case the energy of interest, E, is much less than the source energy, E_S, so the mean energy loss per collision is very small,
- The medium in which moderation proceeds is infinite in extent,
- The source does not emit neutrons at the energy of interest.

Eq.(4.29) is modified by the inclusion of the mean logarithmic energy decrement, ξ, to :

$$\Phi(E) = \frac{q(E)}{\xi\left[\Sigma_a(E) + \Sigma_S(E)\right] E} \tag{4.37}$$

Eq.(4.37) is known as the *Wigner Approximation*. Its solution cannot use the simplification in Eq.(4.30), since we are no longer dealing with $\alpha = 0$. Instead, $p(E)$ must be re-expressed in terms of ξ. The ensuing treatment is lengthy and complex and rests on a number of important assumptions. These are necessary because :

- There are fluctuations in the neutron flux, – *Placzek Wiggles* – during the early stages of the moderation process when the number of collisions is small,
- It is necessary to consider the widths as well as the separation of the absorption resonances.

Further details, together with an extensive bibliography, are given in [2].

4.4 Neutron Diffusion

Up to this point the discussion of moderation has ignored any dependence on spatial position. It has assumed that energy loss can take place through isotropic scatter in the CM system without any change in the position vector. This is the Moderation without Diffusion approximation.

4.4.1 Neutron balance equation for thermal energies

We now treat the other extreme, *viz.* the diffusion of a neutron without any change in its energy. This can only occur when the neutron is in thermal equilibrium with the medium. Since the thermal condition of the medium is characterized by a Maxwell distribution of velocities, successive collisions can now result in small amounts of energy gain as well as energy loss about the mean thermal energy. This is the Diffusion without Moderation approximation.

The neutron energy distribution is now neither in true equilibrium nor is it Maxwellian, since it is determined by :

- The finite extent of the medium in which the neutrons are diffusing. This leads to leakage from the volume under consideration,
- The loss of flux through absorption.

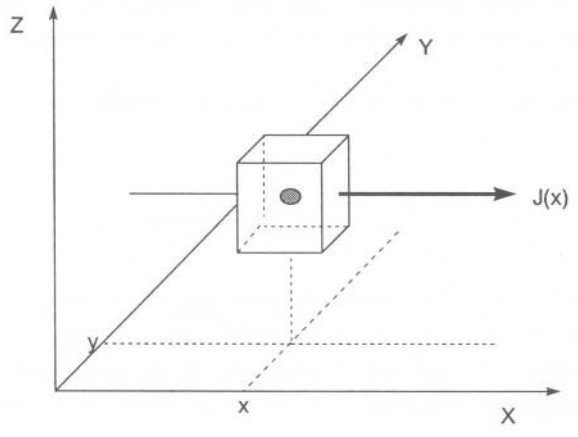

Fig.(4.10) A unit cube, centred at position x,y,z, through which passes a current density J(x).

The neutron balance equation for the cubic volume in Fig.(4.10) expressed in one-dimension along the X-axis is [2] :

$$\frac{d}{dx}J(x) + \Sigma_a \Phi(x) = S(x) \tag{4.38}$$

where $J(x)$ is the neutron current at position x. The first term in Eq.(4.38) represents the divergence of this current and gives the leakage out of the unit cube. To this is added the number of neutrons absorbed. The sum gives the total neutrons which are lost from the volume. This number must be balanced by the source neutrons $S(x)$.

When the vector flux in a direction ω is resolved onto a symmetry axis along which $J(x)$ is specified, the current density can be expressed in terms of a flux gradient :

$$\frac{d}{dx}\Phi(x) + 3J(x)\left[\Sigma_a + \Sigma_{S0} - \Sigma_{S1}\right] = 0 \tag{4.39}$$

The scattering cross-section Σ_{S_1} accounts for any anisotropic scatter in the laboratory co-ordinate system. Recall that although scatter is assumed to be isotropic in the CM system there is a most probable scatter angle in the L system, given by

Eq.(4.20), which depends on the mass of the scattering nucleus. In this case, we have $\Sigma_{s0} = \Sigma_s$(isotropic) with :

$$\Sigma_{s1} = \Sigma_{s0} \langle cos\theta \rangle \text{ and } \Sigma_{tr} = \Sigma_{s0}(1 - \langle cos\theta \rangle)$$

This shows that light nuclei will preferentially scatter in the forward direction. The scatter cross-sections in Eq.(4.39) can now be replaced by the transport cross-section, Σ_{tr}, and a diffusion coefficient, $D = 1/(3[\Sigma_a + \Sigma_{tr}])$. Note that the increasing anisotropy in scatter for light nuclei means that the mean free path length is larger than in the case of heavy nuclei.

$$\langle \cos\theta \rangle_{\text{large A}} < \langle \cos\theta \rangle_{\text{small A}}$$
$$(\Sigma_{tr})_{\text{large A}} > (\Sigma_{tr})_{\text{small A}}$$
$$(\lambda_{tr})_{\text{large A}} < (\lambda_{tr})_{\text{small A}}$$

The Elementary Diffusion Equation is now obtained by re-expressing Eq.(4.39) and substituting the result in Eq.(4.38). Thus :

$$J(x) = -\frac{1}{3[\Sigma_a + \Sigma_{tr}]} \frac{d}{dx}\Phi(x) = -D \frac{d}{dx}\Phi(x)$$

$$D\frac{d^2\Phi(x)}{dx^2} - \Sigma_a\Phi(x) + S(x) = 0 \qquad (4.40)$$

The validity of Eq.(4.40) is restricted to the following :

- A single axis of symmetry along which it is natural to specify $J(x)$. This means that the neutron flux is symmetric only about this axis and not in any other direction,
- A point, or a plane, source of neutrons and a medium which is infinite in extent,
- A situation in which the probability of absorption is much less than that of scatter, $\Sigma_a << \Sigma_s$,
- Positions, x, which are not closer than about two total mean free path lengths ($\lambda_t = 1/(\Sigma_a + \Sigma_s)$) from either the source or the edge of the medium. Otherwise, in the first case the neutrons may not have achieved a uniform energy distribution, and in the second the effect of leakage out of the medium is likely to cause a sharp drop in flux. For similar reasons, the large flux gradients in the vicinity of a strong absorber must also be avoided.

4.4.2 *Solution of elementary diffusion equation*

The physical meaning of an important parameter, used in many branches of radiation science, comes out of the solution of Eq.(4.40) for the special case of a point source in an infinite medium. This is the Diffusion Length, L, which is defined as $\sqrt{(D/\Sigma_a)}$.

Re-writing Eq.(4.40) for one- and then three-dimensions, we get [2] :

$$\frac{d^2}{dx^2}\Phi(x) - \frac{1}{L^2}\Phi(x) + \frac{S(x)}{D} = 0$$

$$\nabla^2\Phi(r) - \frac{1}{L^2}\Phi(r) + \frac{S(r)}{D} = 0 \qquad (4.41)$$

The solution of Eq.(4.41) is accomplished by :

- Requiring that the neutron source is located only at r = 0,
- Using the mathematical relation $\nabla^2\Phi \equiv \nabla.\nabla\Phi \equiv \nabla.r\frac{d\Phi}{dr} = \frac{d^2\Phi}{dr^2} + \frac{2}{r}\frac{d\Phi}{dr}$

At any position $r \neq 0$, there are no source neutrons contributing to the flux, so Eq.(4.41) now reduces to :

$$\frac{d^2\Phi(r)}{dr^2} + \frac{2}{r}\frac{d\Phi(r)}{dr} - \frac{\Phi(r)}{L^2} = 0$$

This has a general solution :

$$\Phi(r) = \frac{A}{r}exp\left(-\frac{r}{L}\right) + \frac{B}{r}exp\left(\frac{r}{L}\right) \qquad (4.42)$$

where A and B are constants. The boundary conditions in this case demand that $B = 0$ since otherwise $\Phi(r)$ would increase as r increases. This is physically impossible for our considered situation of a point source and a homogeneous medium in which $\Sigma_a << \Sigma_s$.

For an infinite medium, all source neutrons must eventually be absorbed. So the number of absorption events in unit time is given by :

$$S = \int \Sigma_a \Phi(r) dV = \Sigma_a \int_0^\infty \Phi(r)\, 4\pi r^2 dr = \Sigma_a \int_0^\infty \frac{A}{r} exp\left(\frac{-r}{L}\right) 4\pi r^2 \; dr$$

Integration by parts gives $S = 4\pi\, \Sigma_a A\, L^2$ and an expression for the flux :

$$\Phi(r) = \frac{S}{4\pi\Sigma_a L^2}\frac{1}{r} exp\left(\frac{-r}{L}\right) = \frac{S}{4\pi D}\frac{1}{r} exp\left(\frac{-r}{L}\right) \qquad (4.43)$$

Eq.(4.43) can now be used to find the number of neutrons absorbed at a distance r from the source. In a spherical shell of radius r and thickness dr this number is $\Phi(r)\Sigma_a 4\pi r^2 dr$ with units of s^{-1}. The probability of absorption at position *r*, *P(r)*, is just this number divided by the number of source neutrons emitted per second.

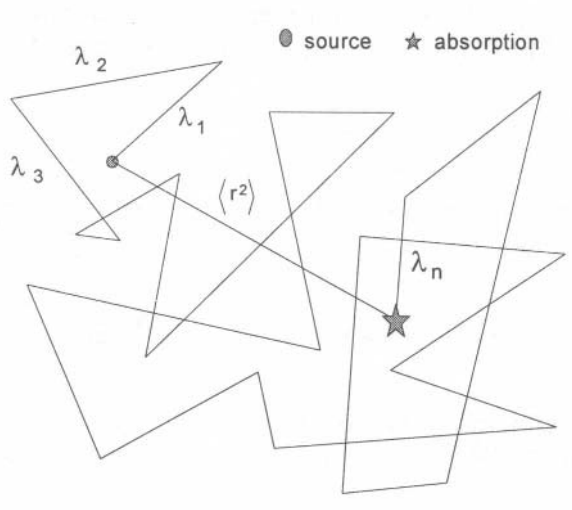

Fig.(4.11) A schematic diagram to show the difference between the root mean square distance for absorption, $\langle r^2 \rangle$, and the mean free path length for absorption, λ_a, [2].

The mean square distance at which absorption occurs is therefore :

$$\langle r^2 \rangle = \int_0^\infty r^2 \; P(r) = \int_0^\infty r^2 \; \frac{\Phi(r)\Sigma_a 4\pi r^2 dr}{S} = \frac{1}{L^2}\int_0^\infty r^3 \, exp\left(\frac{-r}{L}\right) dr = 6L^2 \qquad (4.44)$$

Eq.(4.44) represents the mean radial distance from the source at which absorption occurs. This must be distinguished from the distance actually travelled between emission from the source and eventual absorption. The latter is the mean

free path for absorption :

$$\lambda_a = \frac{1}{\Sigma_a} = \lambda_1 + \lambda_2 + \lambda_3 + \ldots\ldots\ldots \lambda_n$$

4.5 Moderation and Diffusion

Two principal methods of approximation are used in the solution of the neutron balance equation when both energy and spatial position are considered. It is necessary to account for all neutrons which leave or enter a specified unit volume as the result of a change in either *r* or *E*.

- Age theory. Here a new variable is introduced – the neutron Age – which increases continuously as moderation proceeds.
- Multigroup theory. In the simplest version – one-group theory – the elementary diffusion formalism is used with an appropriate modification of the diffusion length.

4.5.1 Age theory.

Using the definition of Slowing Down Density *q(E),* (section 4.3.6), the difference in the number density of neutrons slowed down per unit volume to energies *E* and *E* + *dE* (or lethargy *u* and *u* + *du*) is :

$$q(E+dE) - q(E) \approx \frac{\partial q}{\partial E}\, dE = \frac{\partial q}{\partial u}\, du$$

When no diffusion was considered (as in section 4.3), this change in the number of neutrons could be balanced only by their absorption in order to achieve neutron balance.

The possibility of diffusion makes it possible to equate this slowing down gain of neutrons with the diffusion loss of neutrons. Together with the assumption that the probability of leakage out of the unit volume is much greater than the probability of absorption, *i.e.* that $\Sigma_a \rightarrow 0$, it becomes possible to write :

$$div J + \frac{\partial q}{\partial E} = 0 \quad \text{or} \quad div J + \frac{\partial q}{\partial u} = 0$$

After re-expressing Eq.(4.40) for flux at energy *E* and position *r* in three-dimensions instead of position *x* in only one-dimension, we have for the steady state :

$$D.\nabla^2\Phi(r,E) = \frac{\partial}{\partial E} q(r,E) \tag{4.45}$$

The left-hand side of Eq.(4.45) is first expanded in terms of the slowing down density by making use of the Wigner approximation in Eq.(4.37), under the assumptions that :

- Absorption is negligible, $\Sigma_a \rightarrow 0$,
- Average energy loss per collision is small, thereby restricting consideration to heavy media and to conditions pertaining after a large number of collisions have taken place,
- The scattering cross-section is independent of energy.

When expressed in terms of lethargy, $u = ln(E_0/E)$, we get :

$$\Phi(r,u) = \frac{q(r,u)}{\xi\Sigma_S}$$

with a denominator which is independent of energy (lethargy). The slowing down term on the right-hand side of Eq.(4.45) is then modified by the inclusion of the age parameter :

$$\tau = \int_E^{E_0} \frac{1}{3\xi\Sigma_S{}^2(E')\left[1-\langle\cos\theta\rangle\right]} \frac{dE'}{E'} = \int_0^u \frac{1}{3\xi\Sigma_S{}^2(u')\left[1-\cos\langle\theta\rangle\right]}\, du'$$

This increases as moderation proceeds and has units of cm^2. When the scattering cross-section is not a function of energy, the age can be written :

$$\tau = \frac{1}{3\xi\Sigma_S{}^2\left[1-\langle\cos\theta\rangle\right]} ln\left(\frac{E_0}{E}\right) = \frac{u}{3\xi\Sigma_S{}^2\left[1-\langle\cos\theta\rangle\right]} \tag{4.46}$$

The Age Equation can now be compiled from the foregoing and :

$$\frac{\partial q}{\partial u} = \frac{\partial q}{\partial \tau}\frac{\partial \tau}{\partial u} = \frac{\partial q}{\partial \tau}\frac{1}{3\xi\Sigma_S{}^2\left[1-\langle\cos\theta\rangle\right]}$$

$$\frac{D}{\xi\Sigma_S}\nabla^2 q(r,u) = \frac{\partial}{\partial \tau} q(r,u)\frac{1}{3\xi\Sigma_S{}^2\left[1-\langle\cos\theta\rangle\right]}$$

$$\nabla^2 q(r,\tau) = \frac{\partial}{\partial \tau} q(r,\tau) \tag{4.47}$$

At the start of the moderation, $E = E_0$ and $\tau = 0$. As moderation proceeds, E decreases and u increases, Fig.(4.12).

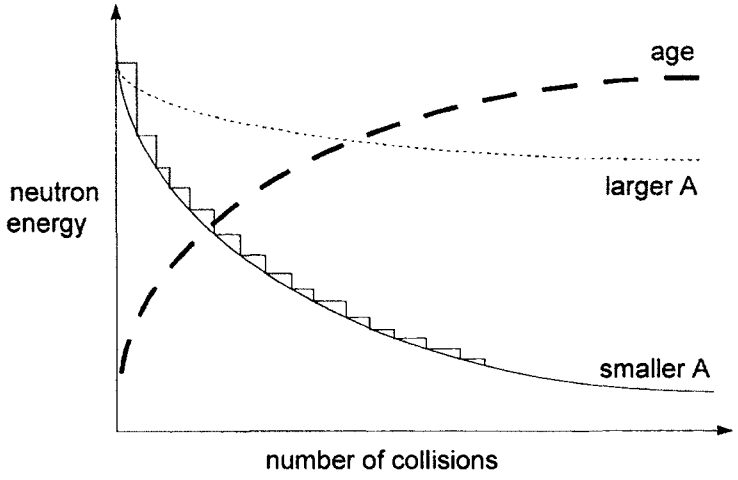

Fig.(4.12) The approximation of a discontinuous neutron energy as moderation proceeds by a continuous function for two different masses of the scattering nuclei of the medium. A better approximation to continuous energy change is seen for the larger mass A. This leads to a more reliable age parameter (solid dotted line).

4.5.2 *Solution of the age equation for a point source and an infinite medium*

Using a similar approach to the solution of the Elementary Diffusion equation, Eq.(4.47) can be solved for a point source at $r = 0$ in an infinite medium. The expression for the Age in Eq.(4.46) shows that it depends on the final neutron energy, through the lethargy u, and on the material of the medium through the involvement of ξ and Σ_s.

Table (4.3) The moderating properties of light and heavy water [3]. The Age τ is the age to the indium resonance at 0.45 eV. Microscopic Scattering σ_s and Absorption σ_a cross-sections are quoted in barn molecule^{-1} at a thermal energy of 0.025 eV. Columns 6 and 7 give the Moderating Power and the Moderating Ratio respectively. Values given for D_2O depend on purity.

	L (cm)	τ (cm^2)	σ_s (barn mol^{-1})	σ_a (barn mol^{-1})	$\xi \Sigma_s$ (cm^{-1})	$\xi \Sigma_s / \Sigma_a$
H_2O	2.7	27	103	0.66	1.53	72
D_2O	~110	111	13.6	~0.001	0.17	~12000

$$q(r,\tau) = \frac{S}{(4\pi\tau)^{3/2}} exp\left(\frac{-r^2}{4\tau}\right) \qquad (4.48)$$

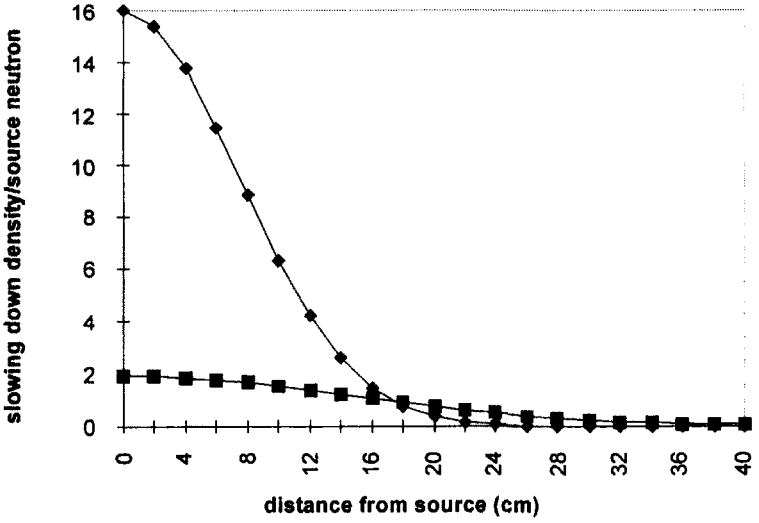

Fig.(4.13) The slowing down density per source neutron, $q(r,\tau)/S$ versus distance r (cm) using Eq.(4.48) with $S = 10^5$ neutron s^{-1} and τ = age to the Indium resonance at $E = 0.45$ eV.
◆ H_2O with $\tau = 27$ cm². ■ D_2O with $\tau = 111$ cm².

Differences in the slowing down density/neutron in Fig.(4.13) between light and heavy water illustrate the difference between Moderating Power and Moderating Ratio. Although D_2O has a smaller moderating power, $\xi\Sigma_s$, the smaller absorption cross-section yields a vastly superior moderating ratio.

4.5.3 One-group theory

The simplest approximation in group theory is to make no distinction between neutron energies and to replace the thermal diffusion length, *L*, with a migration length *M*. The life-history of the neutron is now considered in two distinct parts :

- from birth as a fast neutron to its moderation as a thermal neutron,
- its diffusion as a thermal neutron until absorption.

Using Eqs.(4.40) and (4.44) from diffusion theory, we can write :

$$L^2 = \frac{D}{\Sigma_a} = \frac{\langle r^2 \rangle}{6} = \frac{1}{3\,\Sigma_a(\Sigma_a + \Sigma_{tr})} \tag{4.49}$$

When $\Sigma_a << \Sigma_{tr}$ Eq.(4.49) reduces to $\langle r^2 \rangle = 2\,\lambda_a\,\lambda_{tr} = 6L^2$, where the mean free paths, λ_a and λ_{tr}, apply to thermal energies.

In one-group theory, it is not possible to associate the mean free paths with any energy, thermal or otherwise. Instead, a slowing down length L_S is used to describe the slowing down from the fast to the thermal regime during which the neutron makes a mean number of collisions $\langle n_S \rangle$. Similarly, the thermal part of the neutron history is described by the diffusion length L and a mean number of collisions $\langle n_{th} \rangle$. The total number of collisions between emission as a fast neutron and absorption as a thermal neutron is $N = \langle n_S \rangle + \langle n_{th} \rangle$.

Assuming a sufficiently large number of neutrons, together with a scattering mean free path which is independent of energy, the total number of collisions can be expressed as the ratio :

$$N = \frac{\lambda_a(E_{th})}{\lambda_S(E_{th})} = \frac{\Sigma_S(E_{th})}{\Sigma_a(E_{th})} \tag{4.50}$$

This is done because in the one-group model, all neutrons are considered alike and can be described by the Elementary Diffusion Eq.(4.41). On this basis, the total mean free path between emission as a fast neutron and absorption as a thermal neutron is :

$$\langle r_T^{\,2} \rangle = 2\,\lambda_a(E_{th})\,\lambda_{th}(E_{th}) \tag{4.51}$$

From Eq.(4.50), we can write $\lambda_a(E_{th}) = N\lambda_s(E_{th}) = [\langle n_s \rangle + \langle n_{th} \rangle]\lambda_s(E_{th})$, so Eq.(4.51) can be written :

$$\langle r_T^{\,2} \rangle = 2\,\left[\langle n_S \rangle + \langle n_{th} \rangle\right]\,\lambda_S(E_{th})\,\lambda_{tr}(E_{th})$$

The mean distances travelled for slowing down and for diffusion are now written in the same way as in the case of thermal diffusion :

$$\langle r_S^{\,2} \rangle = 2\,\langle n_S \rangle\,\lambda_S\,\lambda_{tr} = 6\,L_S^{\,2}$$

$$\left\langle r_{th}^{\,2} \right\rangle = 2 \left\langle n_{th} \right\rangle \lambda_S \ \lambda_{tr} = 6 \ L^2$$

with the total mean square distance as :

$$\left\langle r_T^{\,2} \right\rangle = 6\left(L_S^{\,2} + L^2\right) = 6 \ M^2$$

There is no correlation between the vectors which represent the Slowing Down and Diffusion lengths, so the angle ϕ in the CM system between the two can take any angle between 0 and 2π. In the resultant vector :

$$r_0^{\,2} = r_1^{\,2} + r_2^{\,2} - 2 \ r_1 \ r_2 \ \cos\phi$$

the final term averages out to zero, so again we have :

$$M = \sqrt{L_S^{\,2} + L^2}$$

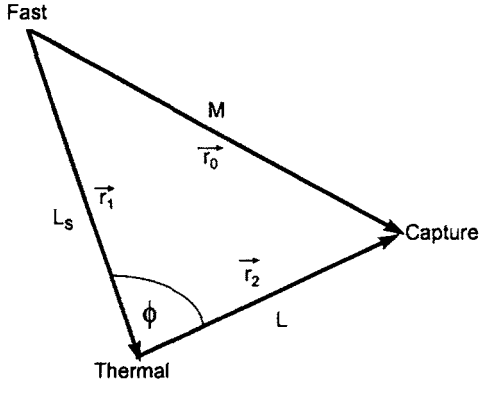

Fig.(4.14) A vector diagram representing Slowing Down length L_S, Diffusion length L and Migration length M, [3].

The flux at position r in an infinite medium can now be given in one-group theory by modifying Eq.(4.43) as :

$$\Phi_{1G}(r) = \frac{S}{4\pi D} \ \frac{1}{r} \ exp\left(\frac{-r}{M}\right) \qquad (4.52)$$

Fig.(4.15) illustrates the migration of neutrons over a greater distance in D_2O

because of the larger diffusion length which results from the smaller absorption cross-section.

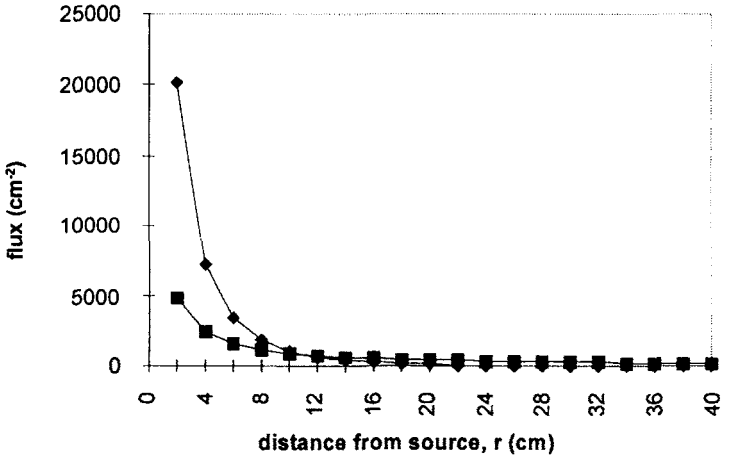

Fig.(4.15) The neutron flux, given by Eq.(4.52), versus distance from a point source of strength $S=10^5$ n cm^{-2} .

◆ H_2O using : diffusion coefficient D = 0.14 cm : diffusion length, L = 2.7 cm : age to indium resonance at 0.45 eV, τ = 27 cm^2 : migration length, M = 5.86 cm.

■ D_2O using : diffusion coefficient, D = 0.82 cm : diffusion length, L = 110 cm : age to indium resonance at 0.45 eV, τ = 111 cm : migration length, M = 110.5 cm. [3]

References

[1] R.D.Evans, *The Atomic Nucleus* (McGraw-Hill, New York, 1972), p.882.

[2] K.H.Beckurts and K.Wirtz, *Neutron Physics* (Springer-Verlag, Berlin, 1964).

[3] D.Jackman, *Physics of Nuclear Reactors*, (English Universities Press, London, 1966).

CHAPTER 5

DETECTORS

5.1 Introduction

Radiation detectors fall into two broad categories :

- Real-time – when the detector responds instantaneously, and
- Time-integrating – when information about the radiation is accumulated and read-out at a later time. This category includes nuclear emulsions, thermoluminescence detectors and track etch detectors.

A detector is characterized by :

- the size, the material and the state of aggregation of the sensitive volume in relation to its stopping power to the radiation, and
- the thickness and material of the window (if any) through which the radiation must pass before entering the sensitive volume. It is most important that the combination of window and sensitive volume is treated together. Radiation which has interacted in the window may produce secondary electrons which can then enter the sensitive volume to produce a response.

The important experimental characteristics are :

- the efficiency of the detector towards a given radiation,
- its energy resolution,
- its time resolution (for a real-time detector).

5.2 Gas Detectors

The three forms of gas detector (ionization, proportional and Geiger-Mueller) are distinguished mainly by the ratio :

$$\frac{\text{electric field strength between anode and cathode}}{\text{pressure of gas in the chamber.}}$$

Fig.(5.1) is a typical curve showing the number of ion pairs collected/unit volume as the polarization voltage is increased. The precise shape of the curve is determined by the geometry of the field (cylindrical or parallel) and by the nature of the gas. The values quoted along the axes are likely to be appropriate to an anode/cathode separation in the range 1 – 5 mm and a gas pressure in the range 0.1 – 0.5 torr. (1 torr = 1mm Hg).

Distinct voltage regions can be seen in Fig.(5.1) for both a densely-ionizing

particle (such as an α-particle) and for sparsely-ionizing radiation (such as electrons or photons). These regions are :

- From 0 to ~ 30 V. The applied field is not strong enough to overcome geminate recombination (recombination of the initial electron-ion pair).
- The plateau region from ~ 30 V to ~ 250 V. This signifies the collection of all the ion pairs. Specific ionizations in this region (10^1 and 10^4 ion pairs/unit volume) result from the collection of all the primary electrons produced in the gas volume. This is the ionization chamber region.
- From ~ 200 V to ~ 400 V. Here, the production and collection of ion pairs increases rapidly with applied voltage. So long as the curves remain approximately parallel, the charge collected is proportional to the amount of charge produced in the initial event. This defines the proportional region.
- Further increases in voltage up to ~ 750 V produce even larger amounts of ionization, but with less discrimination between the size (i.e. the ion pairs/unit volume) of the initial event. This is the region of limited proportionality.
- Above ~800 V there is another plateau, at ~10^{10} ion pairs/unit volume, which is independent of the amount of initial ionization. This is the Geiger-Mueller region.

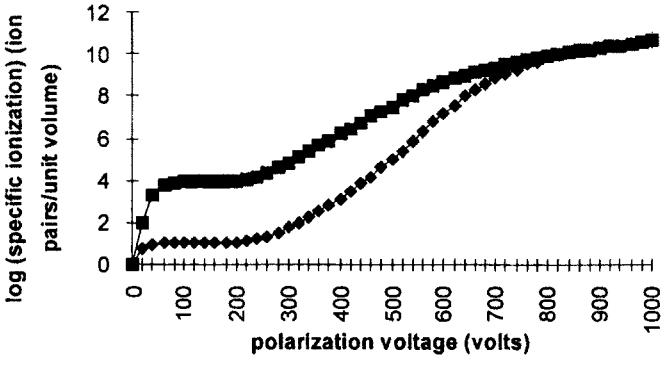

Fig.(5.1) Specific ionization versus applied voltage between anode and cathode.
■ densely-ionizing : ◆ sparsely-ionizing.

Following an ionization event, the positive (ions) and negative (electron) species can :

- move under the influence of the applied field towards the appropriately charged electrode,
- recombine with carriers of opposite sign,
- undergo electron attachment or charge exchange reactions with any impurities present.

An efficient detector must minimize the last two processes. An absolute dosimeter must ensure that they are zero.

5.2.1 *Drift of charged species in electric fields*

The main influence on ions and electrons in a gas detector is the drift along the imposed electric field lines (also magnetic field lines in certain cases). Effects of thermal diffusion, however, will tend to reduce the influence of the applied field.

While both charge carriers undergo collisions with un-ionized atoms or molecules as they move towards their respective electrodes, thermal diffusion increases their mean free paths (the mean distance travelled between collisions). A simple model for the case of a gas consisting of one type of atom or molecule [1] gives :

$$\lambda_e = 5.66\lambda_{ion}$$

where λ_e and λ_{ion} are the electron and ion mean free paths respectively.

The drift velocity of a positive ion is proportional to the reduced electric field and can be readily defined as :

$$v_d^+ = k_{ion}\,\frac{E}{p} \qquad (5.1)$$

where k_{ion} is the mobility of the ion (m^2 atm s^{-1} V^{-1}), E is the electric field and p is the gas pressure relative to standard pressure, *i.e.* the gas pressure in atmospheres. The linear form of Eq.(5.1) is only reliable for E/p values up to $\sim 5 \times 10^6$ V m^{-1} atm^{-1}. In stronger fields the drift velocity depends on the n'th power of the reduced field, where n lies in the approximate range $0.5 \leq n \leq 1$.

The electron drift velocity, however, does not show the same dependence on reduced field. This is due to :

- a much larger electron mean free path (and therefore the larger kinetic energy increase between collisions),
- a large mass difference between an electron and a gas molecule (and therefore a smaller probability of energy loss),
- different elastic and inelastic collision cross-sections and different excitation energies of different gases.

As a result of these effects, electrons behave differently from ions. There is a minimum in the electron collision cross-section – the Ramsauer minimum – which prevents the definition of a single constant of proportionality between the drift velocity and the applied field (*i.e.* the mobility). This minimum occurs when the de Broglie wavelength of a drifting electron becomes comparable to the mean diameter of the electron orbitals of the scattering molecule. In noble gases, the energy at which this happens is ~ 1 eV and it results in a large decrease in the scattering cross-section.

The electron mean free path is thereby increased and the electron temperature decreased.

The electron drift velocity can now be expressed as [1] :

$$v_d^- = \frac{qE}{m_0}\left[\frac{2}{3}\left\langle\frac{\lambda_e(v)}{v}\right\rangle + \frac{1}{3}\left\langle\frac{d\lambda_e(v)}{dv}\right\rangle\right] \qquad (5.2)$$

where q/m_0 is the charge/mass ratio of the electron and v is the electron velocity. This is shown in Fig.(5.2) for a number of widely-used detector gases.

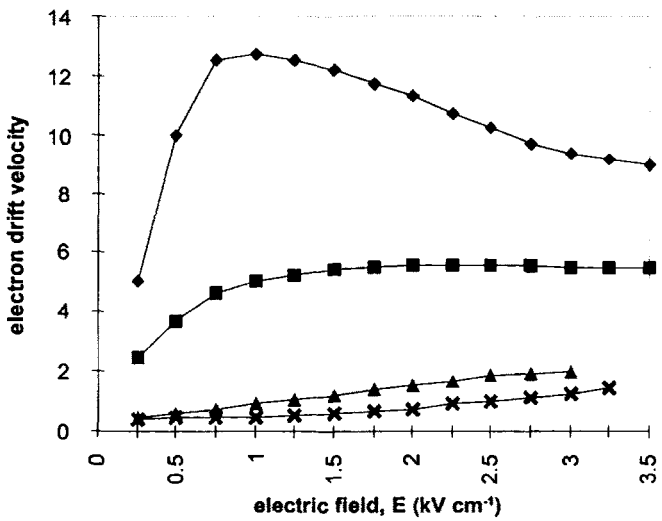

Fig.(5.2) Electron drift velocity (cm μs^{-1}) vs electric field in some pure detector gases at standard temperature and pressure: ◆ CH_4 : ■ C_2H_4 : ▲ N_2 : ✖ Ar. Data taken from [1].

There is a large difference in drift velocity between the poly-atomic gases (e.g. CH_4) and monatomic Ar at a given field strength. This can be ascribed to the tendency for energy to flow into internal molecular states. Although the electron mean free path in a poly-atomic molecule is smaller than in a noble gas, the ratio $\lambda_e(v)/v$ increases because of the even sharper decrease in electron velocity.

5.2.2 *Recombination of charge carriers of opposite sign*

From a practical stand-point, recombination in ionization chamber dosimetry is considered in terms of initial recombination and general (sometimes called volume) recombination (see also section 7.9.4). More detailed consideration divides initial recombination into :

- Geminate – where the electron recombines with the ion from the same neutral molecule. This tends to be most important in high pressure detectors, and
- Columnar – where ions along the same radiation track are recombined. This is of greatest importance in the detection of densely ionizing particles.

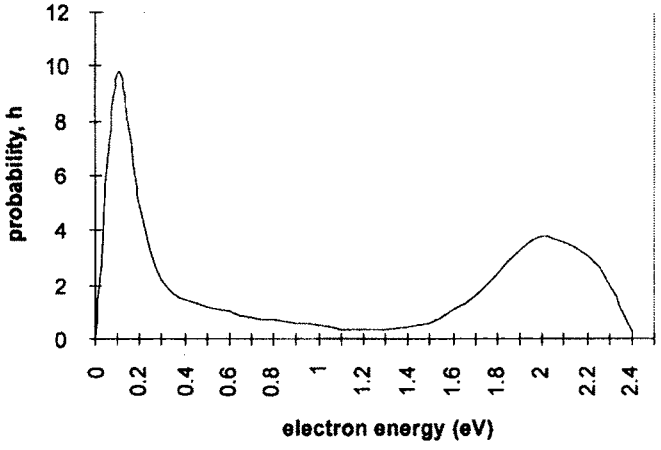

Fig.(5.3) Probability (h × 10^4) of electron capture by oxygen molecules vs electron energy (eV) [2].

The definition of a coefficient of recombination, α, applies only to general (volume) recombination when there is a uniform spatial distribution of charged species.

$$\frac{dn_{ion}}{dt} = \frac{dn_e}{dt} = -\alpha\, n_{ion} n_e \tag{5.3}$$

This coefficient gives the rate of loss of charge carriers per unit volume in terms of the number of each species present at any time. Practical aspects are given in Eq. (7.13). Although in the first approximation, α is independent of gas density and pressure, a re-formulation of Eq.(5.3) is needed when :

- there are significant impurities present in the gas,
- the specific ionization is so high that there are space charge effects, and
- the gas pressure is so high that three-body collisions might result.

Volume recombination is important mainly in ionization chambers operated in the integrating (dc) mode.

5.2.3 *Electron attachment*

The presence of electronegative impurities in the main gas may result in a reduction in the number of electrons collected at the electrodes. Trace quantities of O_2, H_2O vapour and halogens such as Cl_2, Br_2, can scavenge electrons to form negative ions. These are clearly not desirable from the point of view of rapid and efficient collection of charge [2].

The fraction of electrons lost through attachment is given by the average number of collisions with a scavenger molecule × the probability per collision. In Fig.(5.3), h lies in the range $10^{-3} - 10^{-4}$. An electron "temperature" η can be defined [2] as :

$$\eta = \frac{\text{electron mean kinetic energy}}{\text{thermal energy of gas molecules}}$$

The thermal energy corresponding to the most probable gas molecule velocity at 295 K is kT = 0.025 eV. Fig.(5.3) shows that the probability of attachment is a minimum when the electron energy is between 0.6 eV and 1.4 eV. In an air chamber, containing 20% oxygen, this effect is therefore minimized when the electron temperature is in the range 24 – 56 (0.6/0.025 to 1.4/0.025). The optimum reduced field strength in such a case is one which produces a mean electron temperature in this range.

The inert nature of noble gases should prevent any negative ion production when they are used as the main component of a gas detector. They may nevertheless contain trace quantities of electronegative impurities. Their effects can be mitigated by the addition of small quantities of CO_2, CH_4 or N_2, which can shift the optimum reduced field strength into the region where h is a minimum. In the Geiger-Mueller region, however, the effects of electron attachment and charge exchange are deliberately exploited by the use of a quench gas additive (see section 5.2.8).

5.2.4 *Optimum conditions*

The above considerations point to some desirable characteristics of a gas detector. These are :

- a high electron drift velocity for rapid charge collection,
- the smallest possible recombination probability, and
- the highest main-gas purity to prevent negative ion formation.

Practical reasons dictate that air is the most appropriate filling gas in chambers used for dosimetry. Apart from being readily available, air has an effective atomic number (7.78) which is very close to those for water (7.51) and muscle tissue (7.64). Its use is widespread despite its oxygen content, which is an electron scavenger,

(see section 2.11.2). For other gas detector uses, it is the noble gases that are mostly employed.

Fig.(5.2) shows that pure argon has a very low electron drift velocity even in large electric fields. The addition of methane however :

- greatly increases the drift velocity. Commercial gases of this type are known as Px, where x is the percentage of methane, - thus P10, P30 *etc.* In addition,
- it ensures that there is a minimum in the electron capture probability (argon itself being inert).

5.2.5 Ionization chambers

Ionization chambers either have cylindrical or parallel plate geometry, each of which can be operated in one of two modes :

Current (integrating) mode

The applied field should be high enough such that all the ion pairs are collected at the electrodes. If there are no recombination or electron attachment effects, the ionization current is given by :

$$I = N\, e = C\, \frac{dV}{dt} \tag{5.4}$$

In Eq.(5.4) N is the number of ion pairs produced per second, e is the electronic charge, C is the total capacity of the electrodes and electrometer and dV/dt is the rate of voltage increase between the electrodes. In this mode :

- It is vital that the integrity of the insulation between the electrodes is maintained. When a polarizing voltage up to ~ 300 V is applied between the electrodes, it is the dark current that limits the minimum ionization current that can be detected. The dark current should therefore be as small as possible.
- The electrometer itself must be sufficiently stable and sensitive to record currents less than pico-amperes.
- In parallel-plate geometry a guard-ring is used to ensure that charge collection takes place in a uniform field and in a well-defined gas volume (see section 7.6).
- In cylindrical chambers the central electrode is generally operated at a negative potential (see section 7.9.3). Since the diffusion constant of free electrons is considerably greater than that of positive ions, it is more efficient to collect the electrons at the outer electrode where the radial field is smaller.

Current mode ionization chambers are routinely used for measurements of radiation intensity and absorbed dose. For γ- and X-ray photon fields in radiotherapy and radiation protection, the chambers usually contain air in cylindrical geometry.

Pulse mode

At the instant of its creation (time t = 0), the ion pair induces equal charges on the electrodes, $q^+(0)$ and $q^-(0)$. The drift of these charges towards their respective electrodes increases the induced charge at different rates due to the different mobility of the electron and the positive ion. A slow movement of the positive ion towards the negative electrode produces an induced charge which is effectively constant. The time, *t,* that it takes the electron to travel to the positive electrode, however, is much shorter. Thus, $q^-(t)$ quickly attains its final value of -e while $q^+(t)$ is constant at q^+.

The charge induced on the collecting electrode (capacity *C*), and the corresponding voltage can then be expressed as :

$$q(t) = q^+(t) + q^-(t) = q^+ - e \quad \text{and} \quad V(t) = \frac{q(t)}{C} = \frac{q^+ - e}{C} \tag{5.5}$$

In the parallel-plate configuration, the constant electric field between electrodes separated by distance d is $E=V_p/d$ when there is a grounded anode and a negative polarizing voltage [2].

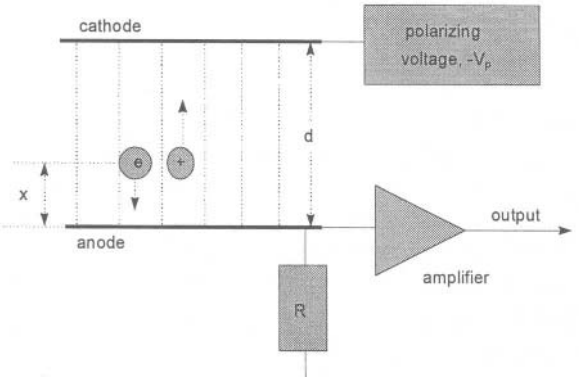

Fig.(5.4) A schematic diagram of an ion pair created distance x from the anode in a parallel plate ionization chamber. Electrodes are separated by distance d, [1]. With permission from *Detektoren fur Teilchenstrahlung* by K.Kleinknecht, 3e/1992 B.G.Teubner, Stuttgart.

The total voltage generated at the collecting electrode (anode) is the summation of the opposite charges drifting in opposite directions. These contributions are determined by their drift velocities. Thus, for an initial event at distance x from the collecting electrode, Fig.(5.4), the contributions are :

$$dV^- = -\frac{Ne}{Cd}\, v_d^-\, dt^- = -\frac{Ne}{C}\,\frac{x}{d}$$
$$dV^+ = -\frac{Ne}{Cd}\, v_d^+\, dt^+ = -\frac{Ne}{C}\,\frac{d-x}{d} \qquad (5.6)$$

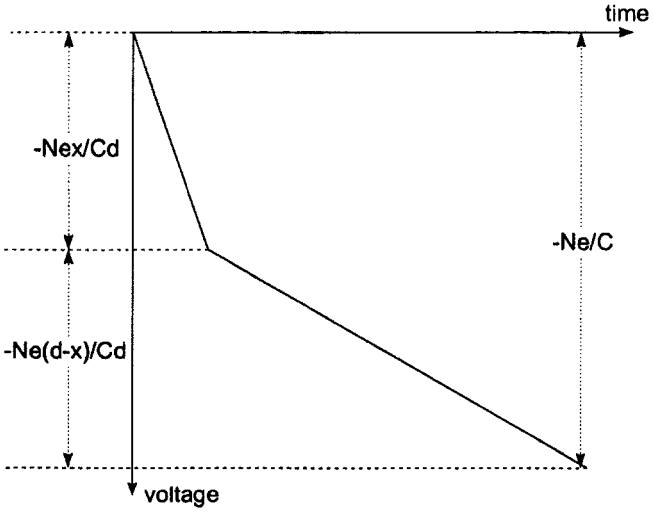

Fig.(5.5) The summation of fast (electron) and slow (positive ion) components in a parallel-plate ionization chamber, [1]. With permission from *Detektoren fur Teilchenstrahlung* by K.Kleinknecht, 3e/1992 B.G.Teubner, Stuttgart.

The voltage pulse is independent of the position of the initial ionization event in the chamber, except when the time constant of the detector, RC, becomes smaller than the time, dt^+, required for the positive ion to drift to the cathode.

5.2.6 Special applications of ionization chambers

(a) Electron detection

Air chambers with parallel-plate geometry operated in current mode are frequently used to measure absorbed dose from directly-ionizing radiation. The incident charged particles enter the gas volume through a window which must be as thin as possible.

Typical parameters [3] for such a chamber lie within the ranges :

- gas volume: 0.05 – 1.0 cm^3,
- electrode spacing: 2.0 – 2.4 mm,
- entrance window material: graphite, polyethylene, aluminized polyester, etc.,

- window thickness: 0.5 – 500 mg cm^{-2},
- collector diameter: 5 – 25 mm,
- guard ring width: 0.5 – 5 mm.

A particular design makes use of a moveable collecting electrode to provide a variable gas volume. Called an Extrapolation, or Gradient, chamber, this allows the determination of the incremented charge, ΔI, per incremented volume, ΔV, i.e. the gradient $\Delta I/\Delta V$.

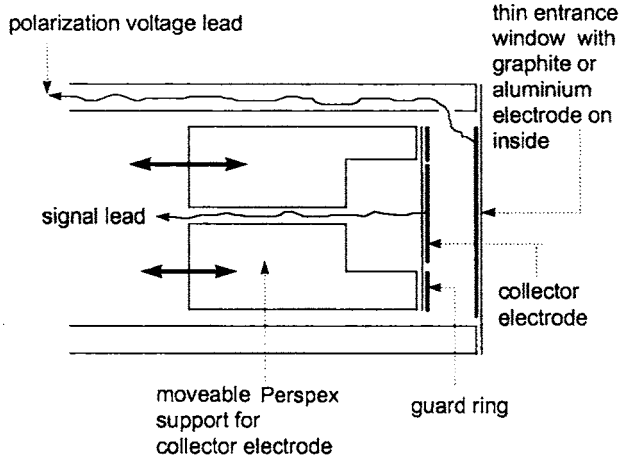

Fig.(5.6) The principle of the extrapolation chamber.

(b) Neutron detection

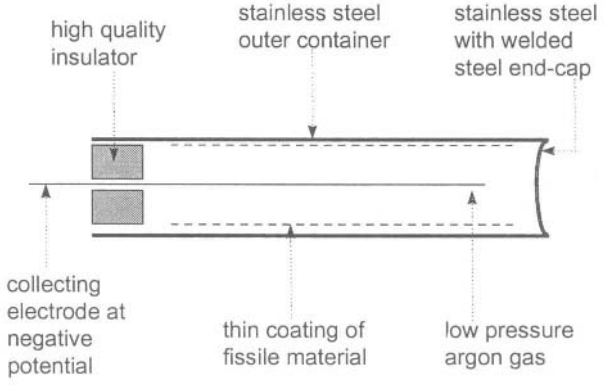

Fig.(5.7) A schematic diagram of a fission ionization chamber.

A fission chamber for neutron detection uses fission fragments from a neutron-induced reaction to produce ionization in the gas. The production of these fragments takes place in a thin layer of fissile material (~ 1mg cm^{-2}) which lines the inside wall of a cylindrical chamber. This contains a high pressure noble gas, generally argon Fig.(5.7).

The layer of fissile material must be thin enough to admit into the gas the strongly-ionizing heavy fission fragments. Because the layer is so thin, the efficiency is generally rather low. However, Fig.(5.8) shows that the thermal cross-section is very high for ^{235}U and ^{239}Pu, so the use of even slightly enriched uranium in the lining partly overcomes this difficulty. By making use of fully depleted uranium (which contains only ^{238}U), the fission chamber can be made sensitive only to fast (> 2 MeV) neutrons, albeit with very low efficiency.

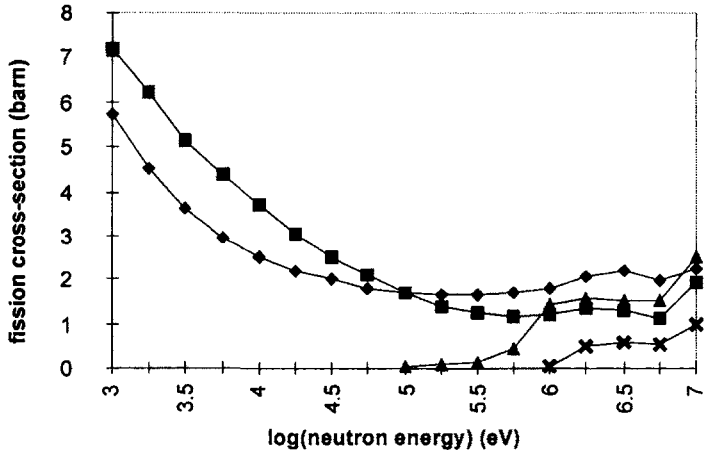

Fig.(5.8) The fission cross-section for a number of fissile materials : ■ ^{235}U : ◆ ^{239}Pu : ▲ ^{240}Pu : ✖ ^{238}U.

All actinides are unstable against α - decay. Although less densely-ionizing than the tracks of fission fragments, these emissions create a background which must be biased-out with a low energy threshold discriminator. A positive advantage in the use of a fission chamber for detecting neutron fields, however, is its insensitivity to γ photons. This is particularly useful in monitoring neutron flux in the intense γ fields such as those inside nuclear reactors.

5.2.7 Proportional chambers

The process in which an electron, initially produced in a primary ionization event, is given sufficient energy to cause further secondary ionization is called gas amplification. Many such electron generations can be produced if the reduced electric field *(E/p)* is strong enough, leading eventually to a Townsend discharge. This effect

is characterized by a gas amplification factor, A, determined by :

- the reduced electric field. Greater amplification is obtained for large mean free paths (low gas pressures) and high electric field strengths.
- the type of gas. Large ionization cross-sections give correspondingly large amplification factors.
- chamber geometry. Cylindrical chambers have a field which decreases rapidly with distance from the central anode wire, whereas parallel plate chambers produce a uniform field.
- the high fields necessary for amplification are most easily obtained in cylindrical geometry, using a thin diameter (20 μm - 100 μm) anode wire.

If n_0 is the initial number, the number of additional ionizations in a distance dx is:

$$dn = n_0 \ \xi \ dx$$

where ξ is the multiplication factor per unit distance (the Townsend coefficient).

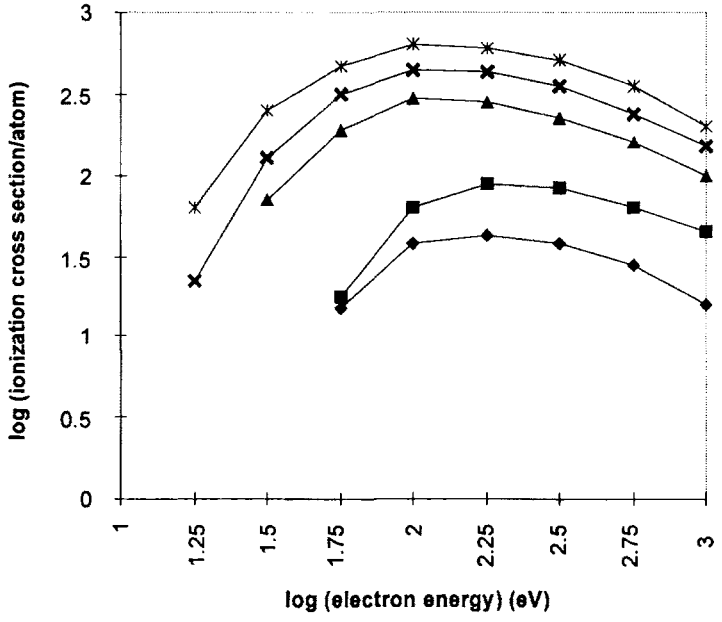

Fig.(5.9) log (ionization cross-section atom^{-1}) (× 10^{-18} cm^2) versus electron energy for noble gases. ✳ Ze : ✖ Kr : ▲ Ar : ■ Ne : ◆ He , [1].

This is related to the electron mean free path λ_e, the ionization cross-section σ_i, and the number of electrons n by :

$$\lambda_e = \frac{1}{\xi} = \frac{1}{n\ \sigma_i} \tag{5.7}$$

The parameter ξ is constant for parallel plate geometry, Fig.(5.4), but depends on the radial position of the ionization event in cylindrical geometry. Since $A = n/n_0$ the amplification factors are :

$$\text{parallel plate : } A = exp(\xi\ x) \tag{5.8}$$

$$\text{cylindrical (radius r) : } A = exp \int_0^r \xi(x)\ dx \tag{5.9}$$

Note the similarity in shape between the ionization cross-sections in the noble gases, Fig.(5.9), and the stopping power of electrons in polystyrene, Fig.(2.17). In all these cases there is a broad maximum at electron energies in the range 100 - 300 eV.

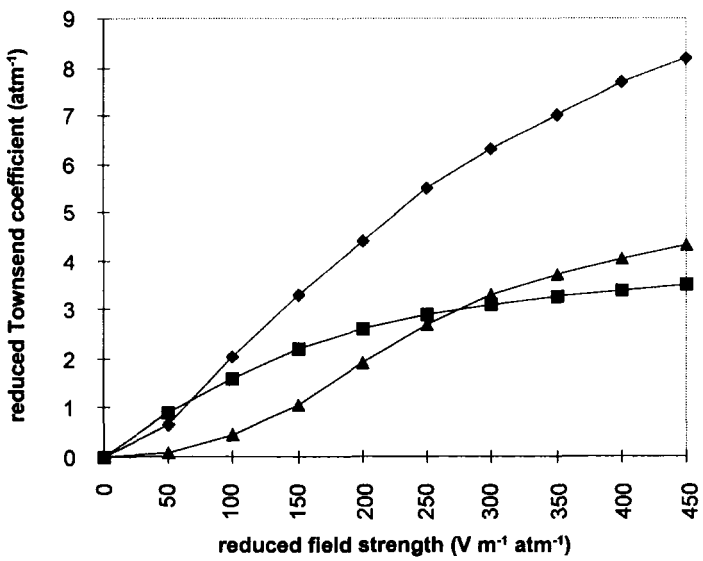

Fig.(5.10) Reduced Townsend coefficient, ξ/p (atm^{-1}), plotted against reduced field strength E/p (V m^{-1} atm^{-1}). ◆ Ar : ■ Ne : ▲ N_2, [2].

The Townsend coefficient for a given gas does not show a simple dependence on reduced field strength, Fig.(5.10). This is due to the onset at high field strengths of a number of additional processes which accompany the ionization of the gas molecule by an accelerated primary electron. These include :

- the further ionization initiated by uv photons emitted from the residual ions. These can arise either from the de-excitation of the ion itself, or from a recombination event (see Chapter 6, section 6.5.1). They can then produce further electrons via the photoelectric effect.
- the uv photons can also release electrons from the metallic surface of the cathode.
- the impact by residual positive ions of polyatomic molecules on the cathode surface can also release electrons.

True proportionality exists only while the gas amplification factor A is independent of the amount of initial ionization. It is limited to an approximate range $50 \leq A \leq 10^5$. At higher values, the electric field begins to become distorted by the build-up of space charge created by the positive ions. These drift slowly towards the cathode in a time much longer than that needed to collect the electrons. Together with photoelectron production, this leads to a loss of proportionality.

The electron build-up in successive generations is given by :

$$n_0 A\left[1 + A\nu + A^2\nu^2 + A^3\nu^3 + \ldots\ldots\right] \approx \frac{n_0 A}{1 - A\nu} \qquad (5.10)$$

where ν is the average number of photoelectrons produced by each electron in the avalanche, and n_0 is the number of primary electrons. When $A\nu > 1$, Eq.(5.10) diverges, signifying a continuous discharge. The two consequences are :

- the discharge no longer depends on the amount of initial ionization, and
- the discharge must be quenched before a subsequent ionizing event can be detected.

When A is kept below $\sim 10^5$, the proportional counter mode can be used for :

(a) neutron detection by recoil protons in a hydrogenous filling gas, (b) neutron detection using nuclear reactions in a BF_3 gas, (c) γ-ray detection using a multiwire proportional mode and (d) detection of low energy photons where the initial ionization is small, e.g. soft X-rays.

(a) The recoil proton method of neutron detection

A proton recoil counter contains an hydrogenous gas, generally CH_4 or H_2, up to 2 atmospheres pressure. A collision between an energetic neutron, energy E_n, will impart energy E_p to a stationary proton which will recoil at an angle ϑ (in the laboratory reference frame).

$$E_p = E_n \cos^2 \vartheta$$

Since scattering is isotropic in the centre-of-mass frame, all proton energies between 0 and E_n are equally probable. Thus, if E_p and ϑ are simultaneously measured, the spectrum of the incoming neutron flux can be determined in principle.

Because the range of the recoil protons tends to be large (~ 25 mm in H_2 at 1 atm for 0.5 MeV neutrons), collisions with the tube walls give rise to electron and photon emission and the destruction of proportionality. The recoil proton principle is more successfully exploited in solid or liquid scintillation detectors.

If the neutron spectrum is known, the proton-recoil counter can measure fast neutron fluxes with an efficiency of ~1% in the range 0.03–3 MeV. Below 30 keV the proton ionization merges into the noise while above 3 MeV the wall effects become too large. A further disadvantage is that the γ sensitivity can be almost as high as the neutron sensitivity.

(b) Neutron-induced nuclear reactions

Heavy charged particles can be generated from neutron–induced nuclear reactions in $^{10}BF_3$ gas. The isotopic abundance of ^{10}B in natural boron is 19.8%. A neutron absorption reaction has a cross-section of 3840 barn (1 barn = 10^{-28} m^2) at a neutron energy of 0.025 eV, with two possible pathways :

$$\begin{aligned} &{}^{10}_{5}B + {}^{1}_{0}n = {}^{7}_{3}Li + {}^{4}_{2}He + 2.79MeV(6\%) \\ &{}^{10}_{5}B + {}^{1}_{0}n = {}^{7}_{3}Li^{*} + {}^{4}_{2}He + 2.31MeV(94\%) \\ &{}^{7}_{3}Li^{*} = {}^{7}_{3}Li + \gamma + 0.478MeV \end{aligned} \qquad (5.11)$$

The Q-values of these reactions are obtained from the general mass-energy conservation formula [4], when energies are expressed in the laboratory system. When the ejection angle of the He ion with respect to the original neutron direction is called ϑ, we get :

$$Q = 2.79 = E_{He}\left(1 + \frac{M_{He}}{M_{Li}}\right) - E_n\left(1 - \frac{M_n}{M_{Li}}\right) - \frac{2\sqrt{M_n E_n M_{He} E_{He}}}{M_{Li}} \cos\vartheta \qquad (5.12)$$

The products distribute their energies in inverse proportion to their masses [4]. For a thermal neutron, $E_n \rightarrow 0$, the energies of the products in Eq.(5.11) and their relative intensities are easily obtained using Eq.(5.12). These are E_{He} = 1.78 MeV (6%) and 1.47 MeV (94%), E_{Li} = 1.01 MeV (6%), E_{Li}^{*} = 0.84 MeV (94%).

The pulse height spectrum observed from such a chamber depends on the size

of the gas volume compared to the range of the product ions in the gas. For a very large chamber, when the ions deposit their energy mostly in the gas and not in the tube walls, two peaks are observed. The larger (94%) corresponds to a deposition energy of 2.31 MeV which is released when the excited state of ^{7}Li is formed. The smaller (6%) comes from the population of the ground state ^{7}Li.

(c) Multi Wire Proportional Chamber (MWPC)

This is used as the basis of a position-sensitive photon detector, Fig.(5.11). The central anode comprises a grid of fine wires of ~10 μm diameter, separated by ~2 mm, and held at a voltage of 4–5 kV. These are sandwiched between orthogonal cathode wires of larger diameter (~100 μm), the cathode planes being separated from the anode plane by 5–6 mm. Amplification factors of 10^5 are typical.

Ionization events occur anywhere within the gas volume. This is generally filled with xenon, mixed with smaller quantities of methane, isobutane, or carbon dioxide. The primary electrons drift towards the strong electric field surrounding the anode wires producing secondary ionizations as they do so. The resulting avalanche cloud of electrons moves towards the anode inducing a corresponding pulse at the cathode due to the slow-moving ions. Because of the low mobility of the positive ions, the cathode pulses retain information on the position of the original ionization event.

The time of arrival of the induced pulses on the wires in the two orthogonal cathode planes is compared with the prompt anode pulse to give a two-dimensional representation of the initial ionization.

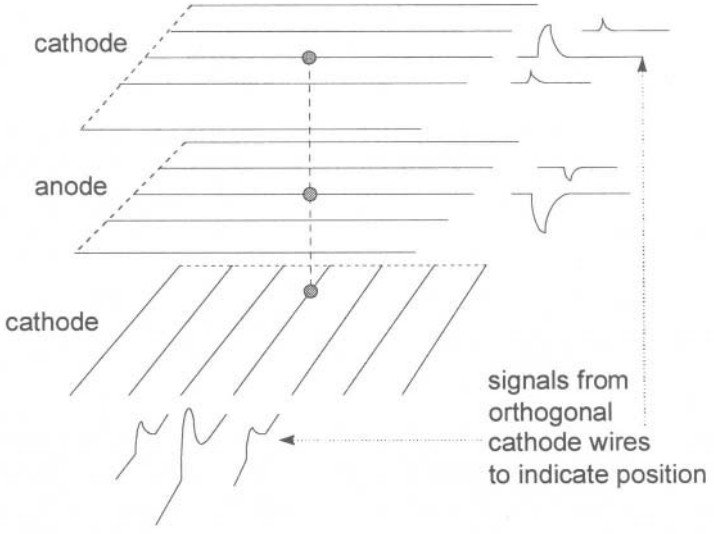

Fig.(5.11) Schematic diagram of Multiwire Proportional Chamber, [1]. With permission from *Detektoren fur Teilchenstrahlung* by K.Kleinknecht, 3e/1992 B.G.Teubner, Stuttgart.

(d) Ultra-soft X-rays

A sufficiently thin entrance window and a sufficiently thin anode wire, enable a proportional counter to be used to detect ultra-soft X-rays. Fig.(5.12) shows a counter designed for a flow of argon-methane gas (P10 or P50 - see section 5.2.4) at or near atmospheric pressure. Gas flow is used in order to maintain stable gas amplification at low pressures and as a means of preventing voltage breakdown under conditions of high humidity. The soft x-rays enter the gas volume through a thin polypropylene or VYNS window (25 $\mu g\ cm^{-2}$) supported on a metallic grid (VYNS contains ~ 90% vinyl chloride and 10% vinyl acetate). An anode voltage of 1.5 kV is applied to a central stainless steel anode wire 50 μm in diameter [5]. X-ray energies down to the carbon K-lines at 277 eV are readily resolved with a gas multiplication factor of $\sim 10^3$.

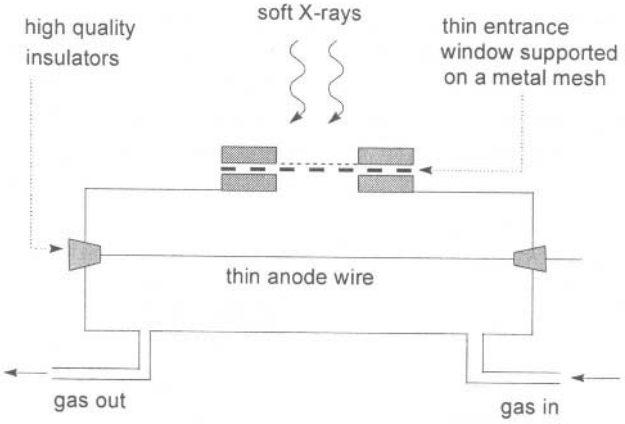

Fig.(5.12) Soft X-ray proportional chamber (supplied by J.E.Manson Co.Inc., Concord, Mass.).

5.2.8 Geiger-Mueller chambers

In the GM region, the factors which lead to the loss of proportionality at high reduced field strengths become so dominant that the gas amplification factor approaches $\sim 10^{10}$. In this event, the discharge becomes almost self-sustaining and must be quenched if a subsequent particle or photon is to be detected.

Quenching can be achieved either :

- by the addition of a quench gas (generally an organic molecule) to the main counter gas which is usually a noble gas, or
- by electronic means.

A quench gas must have two essential properties :

- it must absorb efficiently those uv photons which contribute to the loss of proportionality (section 5.2.7). These are emitted in the de-excitation of the residual main gas ion following ionization, or in any possible recombination or dissociation processes of the main gas.
- it must have an ionization potential smaller than that of the main gas. This ensures that in a collision between an ionized main gas molecule and an un-ionized quench gas molecule, charge is likely to be transferred from the former to the latter.

In addition, the cathode material must have a high work function. This will suppress any possible electron emission, which might follow the arrival at the cathode of either a uv photon or a positive ion of the main gas molecule. Thus :

$$wf_{cathode} > IP_{quench} \quad and \quad IP_{main} > IP_{quench}$$

In the electronic method of quenching, the output time constant $R_A C$ must be longer than the time needed for the positive ions to drift towards the cathode, Fig. (5.13). The full high voltage is thereby prevented from being reapplied to the anode until the whole discharge is completed. This time can be as long as 200 – 300 μs. Alternatively, the high voltage may be temporarily reduced by appropriate circuit design.

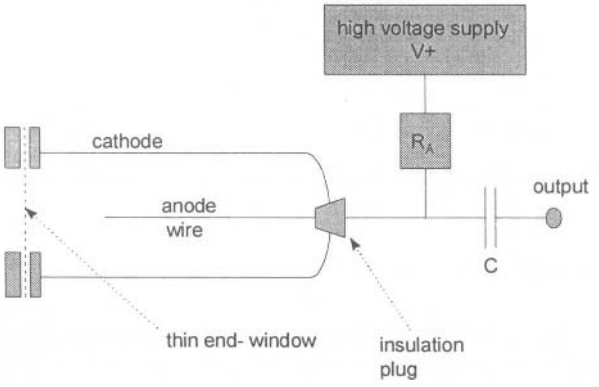

Fig.(5.13) Output circuitry of a Geiger-Mueller counter.

5.3 Scintillation Detectors

Weakly interacting radiation gives poor detection efficiency in gas detectors, largely because of the low density of material in the sensitive volume. A condensed medium, such as a scintillator, offers an improvement of at least three orders of magnitude in this respect. The term luminescence is used as a general description of this process.

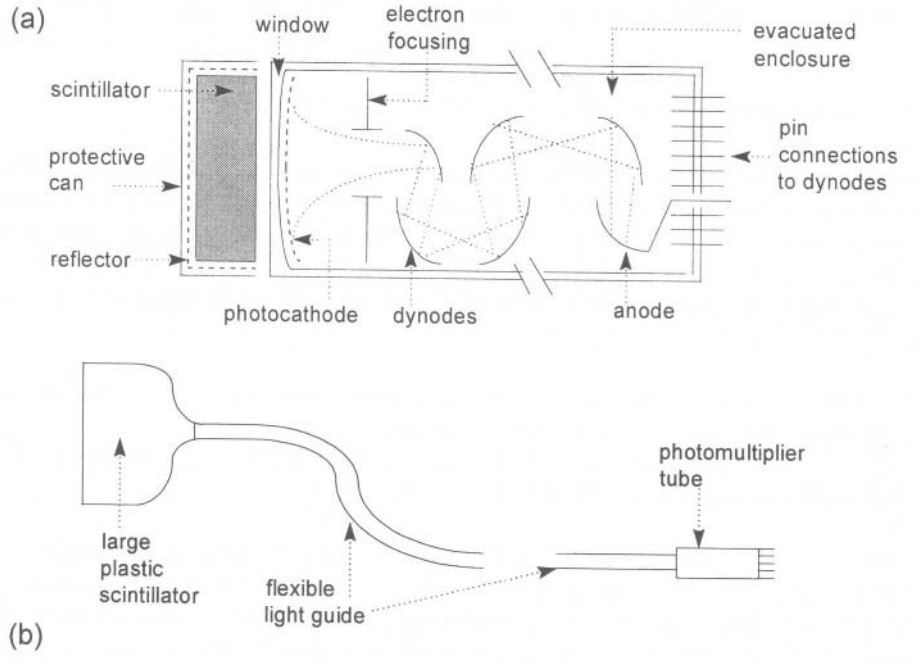

Fig.(5.14) Schematic diagrams of scintillator systems. (a) direct coupling to a PMT (b) a light-pipe for use in high magnetic or radiation fields.

A scintillation detector consists of :

- the scintillator material (organic or inorganic). This produces optical photons whenever an ionization event has occurred (sections 5.3.1 and 5.3.2). The scintillator is enclosed in a light-tight protective can and coupled to either a light guide or the entrance window of a photomultiplier. This coupling is made with a thin layer of fluid (often silicone oil or grease) which transmits the photons with minimum absorption.
- the reflector. The emission of scintillation light is isotropic. Since 4π collection is not generally available, an efficient detector relies on the recovery of photons which would otherwise miss the photomultiplier.
- a light guide. This is sometimes required when the scintillator itself is not immediately coupled to the photomultiplier tube. Situations in which a light guide is used include: (1) when measurements need to be made in a magnetic field: (2) when the size of the scintillator is larger than the size of the photomultiplier (although this causes a large loss of light).
- the photomultiplier tube (PMT). This consists of an evacuated housing (generally glass or quartz) into which the photons are admitted through a window backed by a photocathode material. The window material must have very low absorption, and the photocathode material a very high absorption, towards the incident scintillation light. Electron emission from the cathode is focused onto a series of

dynodes held at an increasingly high positive potential with respect to the cathode.

5.3.1 *Light production mechanism in inorganic scintillators*

Inorganic scintillators are crystalline materials and they therefore possess long-range order. Deposition of energy results in the excitation of an electron from the valence to the conduction band. The first stage of the process is always the elevation of an electron from the valence band. This produces either an electron-hole pair if the deposited energy is greater than the band gap energy, E_g, or an exciton if it is less than E_g (see also Section 6.10 and [6]). Thus if :

- $E > E_g$: a mobile electron and its less mobile hole is produced. These can diffuse independently of each other throughout the crystal.
- $E < E_g$: the coupled electron-hole system can transport excitation energy (the exciton), but not charge, through the crystal.

An inorganic scintillator relies on the presence of localized trapping centres in the crystal which produce energy states within the band gap. It is the population of these states, followed by their de-excitation by photon emission, that results in the production of light which is used for radiation detection. There are two essential requirements on the emitted photon energy :

- it must be different from the band-gap energy in order to prevent self-absorption within the crystal, and
- it must be in the visible or near ultra-violet part of the spectrum for convenient conversion and amplification by a photomultiplier or photodiode.

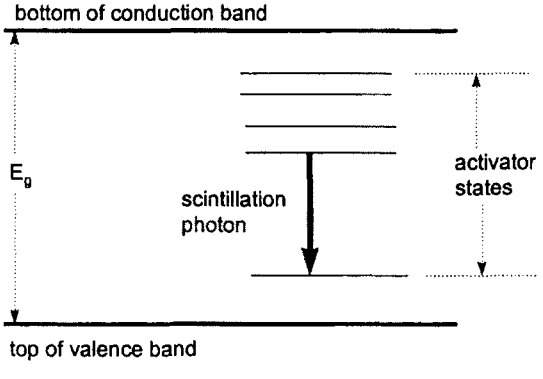

Fig.(5.15) Schematic diagram of activator states within the band gap of an inorganic scintillator. Deactivation of any of the higher excited states to the first excited state will take place rapidly ($<10^{-10}$s). Deactivation of the first excited state to the ground state takes place with a lifetime $\sim 10^{-7}$s. It is this lifetime which determines the response (decay) time of the scintillator.

Trapping centres may be produced in a variety of ways. The mechanism of scintillation depends slightly on the type and concentration of these centres. However, there is still no full understanding of how impurity concentration or crystal temperature, for example, determines efficiency, luminescence decay time or pulse-shape.

Inorganic scintillation materials generally fall into two broad groups :

- crystals that are without additives. This category includes crystals which may contain strains or dislocations, or which may have trace quantities of impurity atoms. Caesium fluoride, CsF, and barium fluoride, BaF_2, are two such examples. They have the fastest decay times of the most widely used inorganic phosphors. There is still no evidence to confirm that a perfect crystal, without strain or trace impurities, will not scintillate.
- an otherwise perfect crystal in which there are added impurities (called activators), e.g. sodium iodide which has been doped with thallium, NaI(Tl). The activator is usually a large atom (Tl with Z=69) compared with the host material, Na (11) and I (53). An exception is CsI(Na).

Table (5.1) Characteristics of some widely-used inorganic scintillators, [6]. Note that: (1) BGO has the highest density, (2) BaF_2 has the shortest decay time and therefore the best timing resolution, (3) CsI(Tl) has the highest photon yield, (4) to a large extent, NaI(Tl) combines all of these advantages. The disadvantage with NaI(Tl) is that it is hygroscopic and it therefore needs canning (i.e. hermetic sealing) to prevent moisture absorption.

	Na(Tl)	CsI(Tl)	$Bi_4Ge_3O_{12}$ (BGO)	BaF_2
Density ($g\ cm^{-3}$)	3.67	4.51	7.13	4.89
Principal decay time (μs)	0.23	1.0	0.35	0.62 (slow) 0.0006 (fast)
Maximum emission (nm)	415	540	505	310 (slow) 220 (fast)
Yield (photons/MeV)	3.8×10^4	5.2×10^4	8.2×10^3	10^4

A qualitative description of the inorganic scintillation process can be made with reference to Fig.(5.15) as follows :

- When the deposited energy is greater than E_g, an electron can be transferred from the valence to the conduction band. The electron can diffuse through the conduction band with relatively high mobility, but the positively charged hole diffuses through the valence band with a much lower mobility. In the event that geminate recombination takes place, it is highly likely that the resulting photon

will have an energy close to E_g and be absorbed within the crystal.

- The presence of the activator (or other type of defect) modifies the band structure in that region of the crystal. This creates localized energy states, within the band gap which the electron can occupy. Thus, the initially-created hole state can diffuse through the crystal and become trapped at the activator site. This site will remain ionized, *i.e.* it has a positive charge, until it traps the electron which has been migrating through the crystal with high mobility.
- Upon trapping, the electron is likely to occupy first an excited activator state from where it rapidly de-excites to the ground state. As it does so, it emits a photon whose energy is smaller than the host lattice band gap E_g. This photon forms the scintillation light which emerges from the crystal. The time between the initial energy deposition and the emission of the photon, is determined by the migration time of the hole, and the lifetime of the activator states. Both of these are considerably longer than the migration time of the electron.
- The de-excitation of the activator states is governed by quantum mechanical selection rules. Depending on these rules, different host-activator systems give rise to prompt (fluorescence) photon emission or delayed (phosphorescence) emission. Certain combinations have selection rules which prohibit photon emission entirely. In these cases the energy can be dissipated through phonon emission when energy flows into the host lattice as low grade heat. This is referred to as a quenching process.

Some alkali halide systems are able to trap electrons in metastable inter-band states. This is the basis of the (integrating) thermoluminescence dosimeter (see section 7.13).

5.3.2 Light production mechanism in organic scintillators

The performance of an organic scintillator is virtually independent of its state of aggregation. It can be in a crystalline, liquid, polymer or amorphous state so long as it is transparent to the emitted photons. The only requirement is that the light emission spectrum of the material does not overlap with its absorption spectrum.

By comparison with its inorganic counterpart, an organic scintillator is distinguished by :

- a lower density,
- a lower atomic number, and hence a lower efficiency for photons interacting primarily by the photoelectric effect ($\propto Z^{3.5}$),
- a better time resolution,
- a worse energy resolution.

The scintillation process in organic materials involves transitions between electronic, vibrational and rotational states. A precise description requires accurate knowledge of the wavefunctions of the initial and final states involved. Although these are not easily determined for polyatomic molecules, the underlying principles

of a scintillator can be illustrated using the picture of a diatomic system.

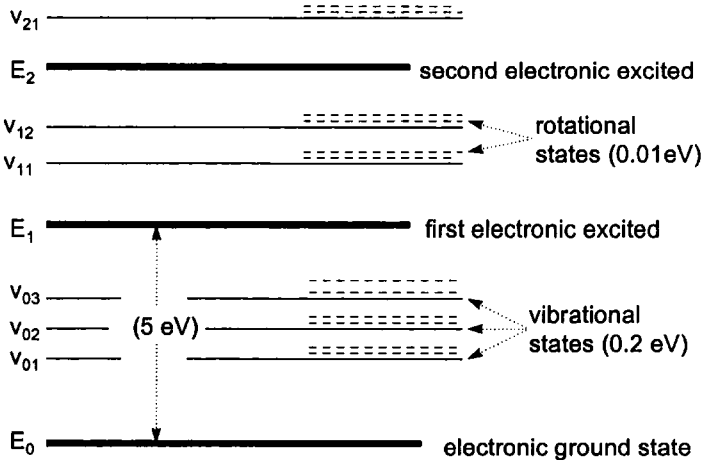

Fig.(5.16) A schematic diagram of the molecular energy levels of an organic system. Electronic (E_0,E_1,E_2..) vibrational (v_{00}, v_{01}, v_{02} ..) and rotational states are separated by approximately 5, 0.2 and 0.01 eV respectively (values decrease with energy). In this simple scheme the ground vibrational states, v_{00}, v_{10}, etc. are assumed to lie at the same energies as their electronic levels, E_0 , E_1, etc.

Apart from the crystalline materials – anthracene and stilbene are the most common – there is no long range order in organic scintillator materials. Deposition of energy results in the excitation of a molecular system, represented in Fig. (5.16), from the ground to one of several excited electronic states.

De-excitation is determined by one or more of the following possibilities :

- if there is enough deposited energy to ionize a molecule, the electron is unlikely to be sufficiently mobile to escape the residual molecular ion. Geminate recombination is then most likely to follow.
- when the energy deposited is sufficient to populate a higher electronic state, there is rapid decay (~10^{-12}s) of the system to the first excited electronic state. This occurs through radiation-less transitions as excitation energy flows into vibrational and rotational states. Thermal equilibrium is eventually reached with neighbouring molecules.
- the decay of the first excited electronic state can take place to the various vibrational states of the ground electronic state (*i.e.* v_{10} to .... v_{02}, v_{01} or v_{00}) with the emission of fluorescence light.

The Franck-Condon principle states simply that the time required to make a transition is very short compared to the vibrational periods of the molecule. This means that the inter-nuclear separation remains constant during the transition. In Fig.(5.17) the vertical line represents the transition between v_{00} and v_{12}. This is the

most probable outcome since the wavefunction overlap is larger than in the case of $v_{00} \rightarrow v_{10}$ or $v_{00} \rightarrow v_{11}$. Transitions to higher electronic states, which are also possible, quickly relax to the ground vibrational level v_{10} of electronic state E_1. In doing this, the excitation energy is dissipated non-radiatively.

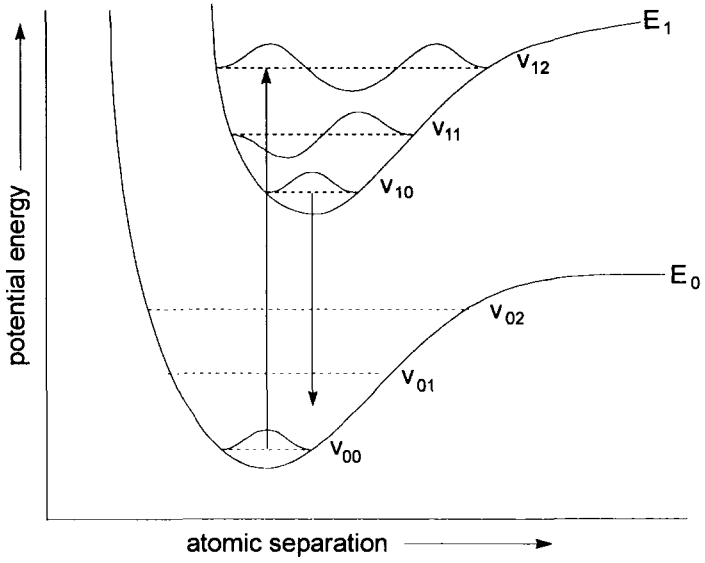

Fig.(5.17) Application of the Franck-Condon principle to the organic scintillation process, [7]. With permission from John Wiley and Sons, Inc.

The final de-excitation from state v_{10} to the ground state means that the photon emission has a lower energy than the energy initially absorbed.

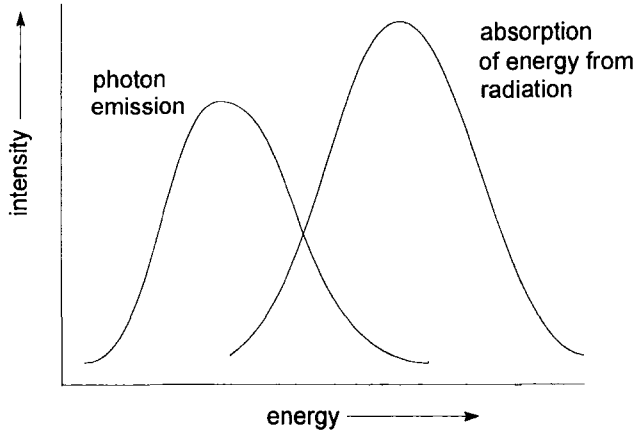

Fig.(5.18) Schematic spectra of energy absorbed and radiated from an organic scintillator.

Figs.(5.16) and (5.17) show that many electronic and vibrational levels are involved in the organic scintillation process. These lead to the typical spectra of absorbed and emitted energy in Fig.(5.18). Non-radiative (quenching) processes compete with fluorescence in the de-excitation of the scintillator molecules, and account for the smaller integrated area of the photon emission (fluorescence) spectrum.

An important feature of Fig.(5.18) is the area of overlap between the two spectra. Photons emitted in this region are likely to be absorbed in their passage out of the scintillator. As a consequence, the light output depends on the size and shape of the scintillator material. A thin scintillator has a greater overall efficiency than one in which the optical path length is large. This problem can be partly overcome by the introduction of a second (solute) molecule chosen because :

- its absorption spectrum matches the emission spectrum of the primary (solvent) molecule, and
- its emission spectrum is shifted to even lower energies.

Additionally, there is requirement to match the emission spectrum to the absorption spectrum of the photocathode. Sometimes a second solute molecule is added for this purpose. This is called a wavelength shifter.

Table (5.2) Characteristics of some organic scintillators (data taken from [6]). In a comparison with comparable data for inorganic scintillators in Table (5.1), note :
(1) the much shorter decay constants compared with inorganic scintillators,
(2) that the efficiency of organic scintillators is always compared to that for anthracene,
(3) that the densities are not very different from unity,
(4) that discrimination between different types of radiation can be made in some cases by pulse shape discrimination (stilbene, NE 213) and in others by loading the scintillator with the appropriate elements (Gd for neutrons and Sn for photons).

Type	scintillator	density ($g\ cm^{-3}$)	light output (%)	main decay constant (ns)	maximum emission (nm)	main application
crystal	anthracene	1.25	100	30	447	γ,α,β, fast n
crystal	stilbene	1.16	50	4.5	410	γ, fast n
plastic	pilot U	1.032	67	1.36	391	γ, fast n
plastic	NE 115		35	225	385	
plastic	NE 102	1.032	65	2.4	423	γ,α,β, fast n
liquid	NE 213	0.874	78	3.7	425	fast n
liquid	NE 224	0.877	80	2.6	425	γ, fast n
liquid	NE 226	1.61	20	3.3	430	γ only
Gd loaded liquid	NE 313	0.88	62	4.0	425	n only
Sn loaded liquid	NE 316	0.93	35	4.0	425	γ, X-rays

Certain scintillator molecules have triplet (s = 1) as well as singlet (s = 0) levels which are the result of electronic configurations having π-bonding orbitals and generally longer lifetimes. Excitation energy can flow from singlet to triplet states and produce a much slower (delayed) fluorescence.

5.3.3 *Efficiency of scintillation detectors*

Factors which affect the overall efficiency, and both the time– and energy– resolution of a scintillation detector are :

- the intrinsic efficiency of the scintillation process in the conversion of energy absorbed from the radiation into optical photons,
- the efficiency of the transportation process of the above photons to the photocathode,
- the efficiency of multiplying the number of electrons released from the photocathode into a measurable charge pulse at the anode.

(a) Intrinsic efficiency (organic)

The high efficiency of crystalline anthracene makes it the frequently used standard against which all other organic scintillators are compared. For the same reasons, inorganic scintillators are usually compared against the performance of sodium iodide crystals.

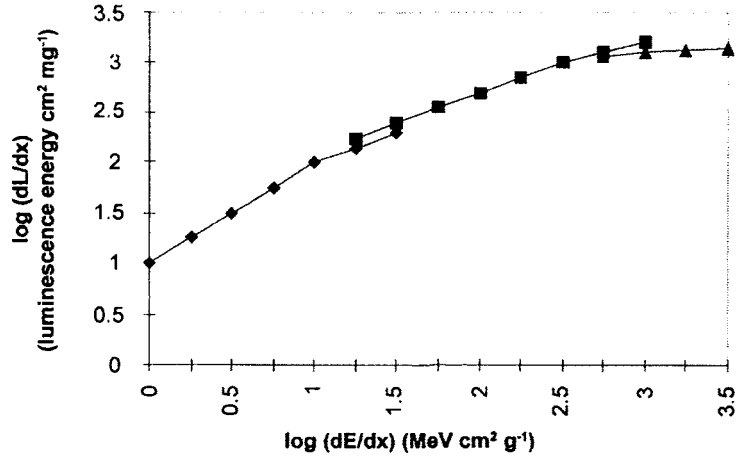

Fig.(5.19) Specific Luminescence energy versus particle stopping power for an anthracene scintillator crystal. ◆ electrons (600 – 5 keV) : ■ protons (20 – 1 MeV) : ▲ α-particles (20 – 1 MeV). The response to photons is determined by the response to electrons. Data from [2].

From a practical point of view, the light output of the scintillator must depend primarily

on the efficiency of energy deposition by the incoming radiation. To a first approximation therefore,

$$\text{light output} = \text{constant} \times \frac{dE}{dx}$$

where the proportionality constant depends on the scintillation mechanism. This is therefore different for organic and inorganic materials.

As Fig.(5.19) shows, this dependence is not linear except at low stopping powers, and shows a tendency to saturate at high stopping powers. This non-linearity is due to the various quenching mechanisms (a de-excitation process which does not result in the emission of photons). These reduce the efficiency of light emission and can take place either in close proximity to, or some distance away from, the original site of energy deposition.

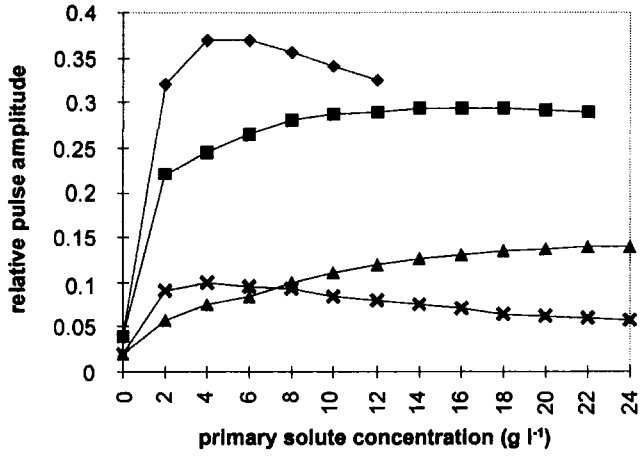

Fig.(5.20) Relative pulse amplitude in a plastic scintillator comprising a polystyrene solvent and different primary solutes at the given concentrations (g litre^{-1}). ◆ 1,1,4,4-tetraphenyl-1-3-butadiene (TPB) : ■ p-terphenyl : ▲ anthracene : ✖ stilbene, [2].

A number of semiempirical formulae have been used to relate the specific photon production rate (*dL/dx*) to the charged particle stopping power (dE/dx) [2], [8]. Light output is expressed as the amount of luminescence energy emitted per unit length of a particle track, *dL/dx*. The most widely used formula is :

$$\frac{dL}{dx} = \frac{A(dE/dx)}{1 + B(dE/dx)} \qquad (5.13)$$

where *A* and *B* are fitted parameters.

There is now widespread use of organic scintillators in plastic form. These comprise a solvent with a primary solute together with a secondary solute as wavelength shifter. The actual molecules and their concentrations used in the plastic can be varied in order to alter the characteristics shown in Table (5.2). Relative efficiencies of light output – as measured by pulse amplitude for a given radiation flux – also vary as a consequence of different solute concentrations, Fig.(5.20).

(b) Intrinsic efficiency (inorganic)

A semiempirical relation between specific light output and stopping power, similar to Eq.(5.13), is also appropriate for inorganic materials. In this case, however, the detection process is initiated by the excitation of a valence electron into the conduction band. Production of usable light from this de-excitation depends on the presence of thallium (or other) activator centres.

The influence of thallium ion concentration on the response of NaI(Tl) scintillators to energetic particles at high stopping powers is shown in Fig.(5.21) [9]. For deuterons and α-particles there is an optimum thallium mole fraction of ~ 0.0015. Note the ordinate scaling factors on pulse amplitude in Fig.(5.21). When the α-particle data are expressed in terms of stopping power in Fig.(5.22), the specific luminescence is seen to be almost independent of stopping power but strongly dependent on thallium concentration.

As the stopping power falls below ~ 0.1 MeV cm^2 mg^{-1}, however, the specific luminescence becomes strongly dependent on stopping power and hardly at all on thallium ion concentration, Fig.(5.22).

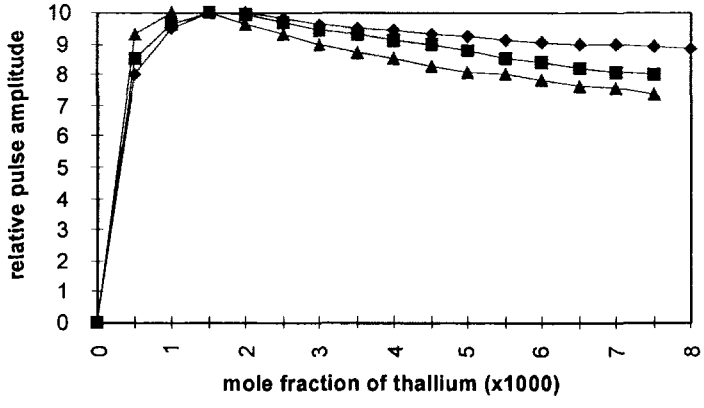

Fig.(5.21) Relative pulse amplitude from α-particle and deuteron detection in a NaI(Tl) crystal scintillation detector versus thallium concentration (mole fraction × 1000), [9].
◆ polonium α-particles (5.3 MeV) (× 3.33) : ■ 23 MeV α-particles (× 0.573) :
▲ 11.5 MeV deuterons (× 0.861).

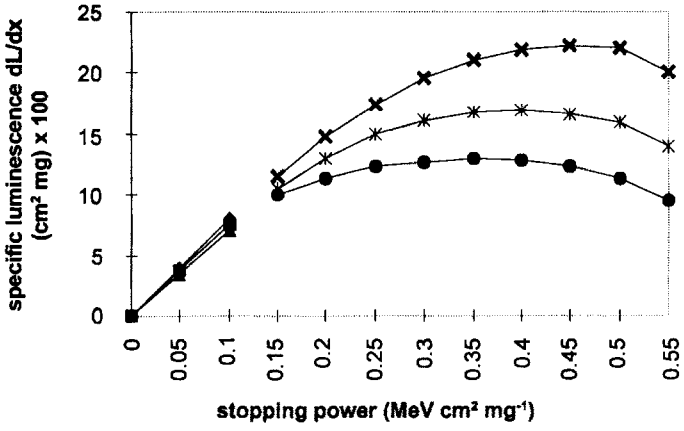

Fig.(5.22) Specific luminescence, dL/dx, (energy $cm^2\ mg^{-1}$)(×100) versus particle stopping power, dE/dx (MeV $cm^2\ mg^{-1}$) in NaI(Tl) at different thallium mole fractions. Data taken from [9].
◆ 0.0077 mole fraction, proton energies 10 to 1 MeV
■ 0.0013 mole fraction, proton energies 10 to 1 MeV, (ordinate × 0.6)
▲ 0.00018 mole fraction, proton energies 10 to 1 MeV (ordinate × 1.5)
✖ 0.0077 mole fraction, α-particle energies, 22 to 1 MeV
✱ 0.0013 mole fraction, α-particle energies, 22 to 1 MeV (ordinate × 0.6)
● 0.00018 mole fraction, α-particle energies, 22 to 1 MeV (ordinate × 1.5)

Recent efforts to remove the native trace actinide impurities in sodium iodide [10], have shown that comparable detection efficiencies are obtained using NaI(Tl) crystals with thallium mole fractions that vary between 0.0001 and 0.00001. These have detected α-particle spectra from ^{238}U and ^{232}Th, whose energies span the approximate range 5 - 7 MeV, with stopping powers in NaI in the range 0.36 - 0.31 MeV $cm^2\ mg^{-1}$.

Fig.(5.22) suggests, however, that differences of 50 - 100% in specific luminescence should be observed. It is clear that there is still a need to carry out controlled studies of the parameters which determine the absolute efficiencies of inorganic crystal scintillators.

(c) Additional factors affecting scintillation detector efficiency

An early value for the absolute efficiency (*i.e.* the conversion of absorbed energy into usable photons) of a NaI(Tl) crystal was 14.1± 0.7% [11], with later values in the order of 12% [12]. Similar values for the absolute efficiency of crystalline anthracene vary between 1 and 10% [13].

In addition to the importance of thallium concentration in NaI(Tl), and solute concentration in organic scintillators, there are other practical factors which affect

the efficiency of scintillation detectors. The most important of these are :

- The isotropic emission of scintillation photons. Detection of these photons is ideally made over 4π. However, they are usually extracted through only one face of the crystal using a diffuse reflecting material on all other surfaces (*e.g.* MgO paint). This introduces a further reduction in efficiency.
- The window material between scintillator and photocathode, and the material of the photocathode itself. This window must be transparent to the scintillation photons to enable the maximum photon flux to reach the photocathode. From the photocathode electrons are drawn towards the first dynode of the photomultiplier tube by an applied voltage. Each photocathode material has a wavelength-dependent conversion efficiency. The spectral efficiency of the photocathode, which should be matched to the spectrum of photons emerging from the crystal, is quantified using :

$$\text{quantum efficiency (QE)} = \frac{\text{number of emitted photoelectrons}}{\text{number of incident photons}}$$

Quantum efficiency at wavelength λ is related to radiant sensitivity, R, by :

$$QE(\%) = \frac{124}{\lambda(nm)} \times R(mA/W)$$

Most photocathodes are of the alkali-antimonide type and consist of various atomic combinations, such as Sb-K-Cs, Sb-Na_2-K-Cs, etc., which determine the range of spectral sensitivity.
From the wavelengths of maximum emission of the scintillators in Tables (5.1) and (5.2), the most appropriate photocathode materials can be selected. These have highest sensitivity – in the uv for Pilot U and BaF_2 – in the blue for NaI(Tl) and anthracene and – in the red for CsI(Tl) and BGO.

- Electron multiplication along the dynode chain. The gain factor of each stage of the photomultiplier is frequently called δ. In such a case, δ electrons are produced by the first dynode for each electron which is incident from the photocathode. For further multiplication at n dynodes, the overall electron gain should therefore be δ^n. However, δ is not a linear function of inter-dynode voltage because space charge effects suppress the gain at the later dynodes. The mean gain of a system of n dynode stages, Fig.(5.14), is therefore more appropriately given by:

$$\overline{G_n} = f\ A\ V^n\ exp\left(-n\frac{V}{V_{max}}\right) \qquad (5.14)$$

- In Eq.(5.14), f is the efficiency of collecting onto one dynode all the electrons emitted from the previous dynode and A is the efficiency of secondary electron emission from the dynode surface. V is the applied voltage difference between

stages and V_{max} is the value of V at which secondary electron emission is a maximum. This formula implies that the voltage per stage is constant. In practice, focusing and pulse shaping requirements make the inter-dynode voltages near the photocathode and the anode different from those in the rest of the chain.

- Other systematic factors affecting the efficiency in solid scintillators are the homogeneity of the activator or solute within the primary material, together with its size, shape, purity and surface condition.

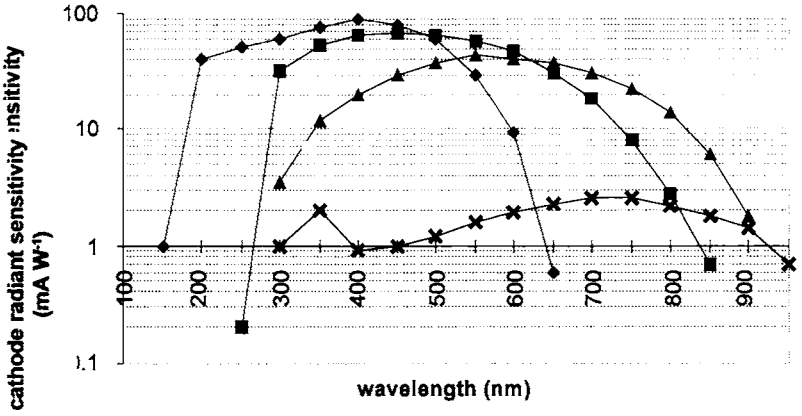

Fig.(5.23) Spectral sensitivity for opaque photocathode materials: ◆ uv : ■ blue : ▲ red : ✖ infra-red.

Attempts are sometimes made to relate the energy deposited in the scintillator to the final charge produced at the end of the electron multiplication stage. This is quite inappropriate, since the factors which contribute to the loss of efficiency in this conversion process relate only to a particular system. As a consequence, they are rarely quantified.

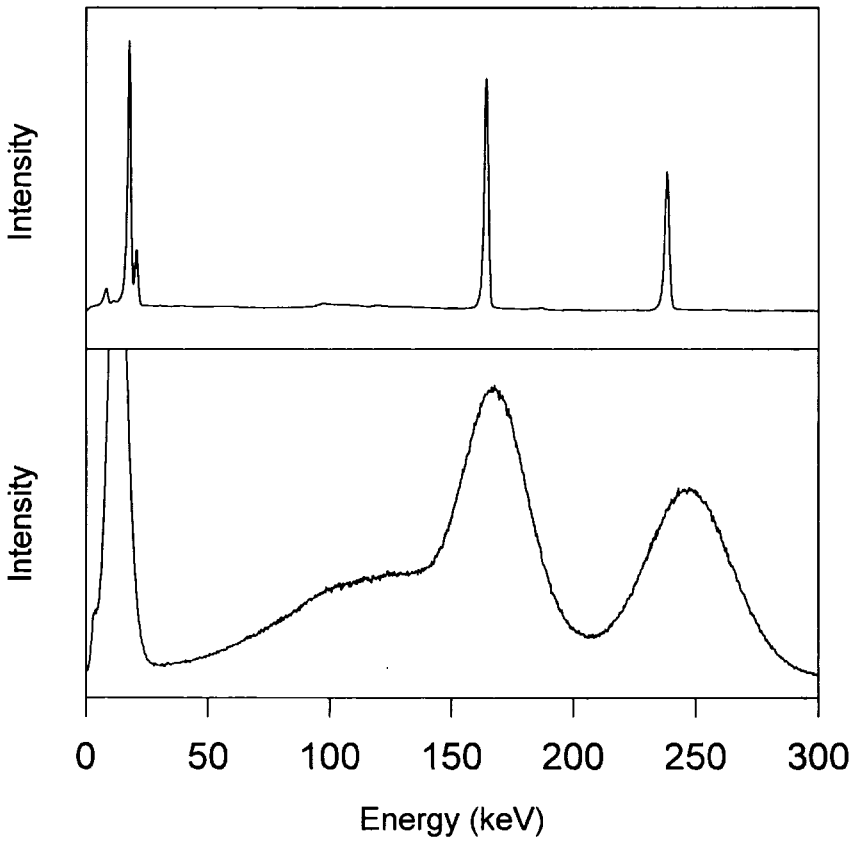

Fig. (5.24) Response of Ge (top) and BaF_2 (bottom) detectors to photon emissions from ^{111}In. Note the resolved $K\alpha_1$ and $K\beta_1$ X-ray peaks in cadmium at 23.17 keV and 26.1 keV respectively by the Ge detector (see the decay scheme in Fig.(1.4)). The shoulder in the BaF_2 spectrum near 100 keV is likely to be due to poor crystal quality and inadequate optical coupling to the photomultiplier tube.

5.3.4 Energy resolution of scintillation detectors

Combined statistical and systematic variations in the processes involved in a scintillation detector lead inevitably to a consideration of energy resolution. The variation in the pulse output when an energy $\overline{E}$ is deposited in the scintillator can be expressed [14] as :

$$\Gamma^2\left(\overline{E}\right) = \Gamma_c^{\,2}\left(\overline{E}\right) + \frac{5.56 \times \overline{G}}{\overline{n}\overline{p}\left(\overline{G}-1\right)} \qquad (5.15)$$

In Eq.(5.15), $\Gamma\left(\overline{E}\right)$ is the Full Width Half Maximum of the response of the detector

when energy $\overline{E}$ is deposited, and $\Gamma_c(\overline{E})$ is the contribution to the observed peak due to the intrinsic resolution of the scintillator alone. The mean number of photons per scintillation event is $\overline{n}$, while $\overline{p}$ is the mean probability that a photon which hits the photocathode produces an electron which arrives at the first dynode. The mean gain per dynode stage is $\overline{G}$.

Table (5.3) Best estimates of intrinsic and overall energy resolution with approximate energy dependence for "standard" scintillation detectors.

Crystal	approximate energy dependence	$\frac{\Gamma_c(\overline{E})}{\overline{E}}$	$\frac{\Gamma(\overline{E})}{\overline{E}}$	reference
NaI(Tl)	$E^{-1/2}$ at 662 keV	4% at 662 keV	6 - 10 %	[15]
anthracene	E^{-1} at ∞ energy	9% at ∞ energy	15 - 25%	[16]

Purely statistical contributions lead to a simple relationship between the width of a photopeak and the energy deposited in the scintillator. In most practical situations, statistical broadening dominates over other contributions [6]. On this assumption, we can define the energy resolution R as :

$$R \propto \frac{\Gamma(\overline{E})}{\overline{E}} = \text{constant} \times \frac{\sqrt{\overline{E}}}{\overline{E}} = \text{constant} \times \frac{1}{\sqrt{\overline{E}}} \qquad (5.16)$$

5.4 Semiconductor Detectors

These are the solid state analogue of the ionization detector. An ionization event in the sensitive volume is followed by charge separation achieved by the application of a voltage bias.

A semiconductor device has a number of important advantages over the gas-based detector :

- the sensitive material has a far greater density and therefore the interaction efficiency rises in proportion.
- the deposited energy required to produce an ion pair (W-value in a gas) is a factor of 10 lower. (W in air for fast electrons = 33.8 eV/ion pair: w in crystalline silicon = 3.55 eV/electron-hole pair).
- the speed of charge collection is greater due to the higher mobility of both charge carriers. Drift velocities of an ion and an electron in air at one atmosphere

are 1.4 and 1.9 $cm^2\ V^{-1}\ s^{-1}$ respectively. Mobilities of holes and electrons in crystalline silicon are 450 and 1450 $cm^2\ V^{-1}\ s^{-1}$ respectively.

- their energy resolution is very high. For photons in the range 1.5 to 10 MeV manufacturers might expect a resolution (FWHM) between 0.08 and 0.1%. Various factors that arise in the production process worsen this to the range 0.1 - 3% depending on the geometry, purity, etc.
- advances in silicon and germanium technology enable a semiconductor to be miniaturized and adapted to meet many different needs.

Disadvantages include :

- poor time resolution for photon detection compared with scintillator detectors,
- a loss of sensitivity after prolonged irradiation. This effect is most pronounced in n-type materials.

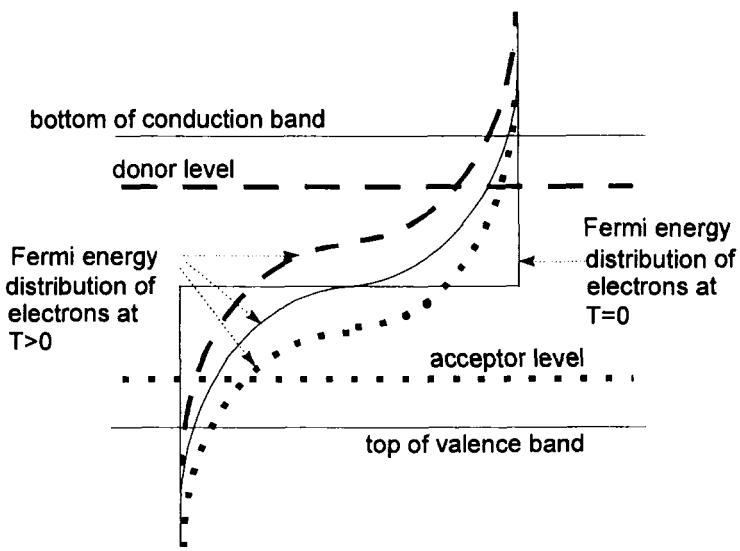

Fig.(5.25) Fermi energy distribution of electrons in a semiconductor. The three curves correspond to intrinsic (solid line), n-type (dash line) and p-type (dotted line), [2].

In an intrinsic (pure) material at absolute zero, there is an infinitely sharp jump between 1 and 0 exactly at the half-way point of the energy band gap. This indicates that at T = 0 there is maximum probability of finding the electron in the valence band and zero probability of finding one in the conduction band. As the temperature increases, thermal excitation gives rise to a non-zero probability that the electron resides in the conduction band. This is balanced by a corresponding reduction in the probability of finding it in the valence band.

An extrinsic (doped) semiconductor has an excess of charge carriers. These

are electrons (n-type) when the valence of the dopant is greater than the valence of the host (*e.g.* P in Si), and holes (p-type) when it is smaller (*e.g.* B in Si).

In n-type material the impurity atom, having one more electron than is required for lattice binding of the host atoms, provides an excess electron. Although still localized on the impurity, this has a reduced binding energy and a larger orbit radius, Fig.(5.26). This electron occupies a donor state.

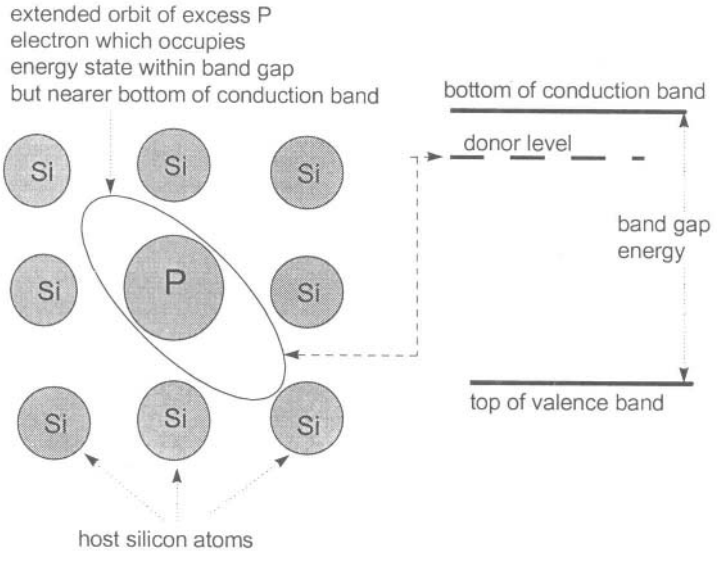

Fig. (5.26) Representation of the orbit and reduced binding energy of an excess electron in an n-type semiconductor, [12]. With permission from John Wiley and Sons, Inc.

Because even the purest silicon contains small amounts of boron, native silicon is always p-type. The situation is then the reverse of that shown in Fig. (5.26). A boron impurity has one fewer valence electron (3) than the surrounding silicon atoms (4), thereby creating an unsaturated covalent bond between the B and Si atoms. This "hole" is termed an acceptor state. An electron falling into this state has a slightly smaller binding energy than would be the case if the boron atom were replaced by a host silicon atom. The energy level is therefore not at the top of the valence band but slightly above it *i.e.* just into the band gap.

5.4.1 The p - n junction

All semiconductor detectors rely on charge compensation to produce a region which is initially devoid of free charge carriers. This charge-compensated region, called the depletion layer, must :

- have a high resistivity in order to maintain the electric field needed to collect charges produced following the interaction of radiation,

- have a known thickness in order to be able to assess the nature of the incident radiation,
- be bounded by sufficiently thin electrode materials that the energy spectrum of the incident radiation is not de-graded as it enters the depletion layer.

Given that totally intrinsic material is practically impossible to achieve, charge compensation can be attained in the vicinity of the junction between n-type and p-type material (see Fig.(5.25) and section 7.14). Commercial detectors are based almost entirely on silicon or germanium host materials, with boron, phosphorus, lithium and arsenic as the most widely-used dopants.

The large difference in the melting temperatures of silicon (1410°C) and germanium (959°C) is one of the principle reasons at present why silicon cannot be purified to the same degree as germanium. A consequence is that available silicon depletion depths are smaller (less than 2 mm) and suitable only for charged particle detection or, in certain cases, soft X-rays. An exception is the use of lithium. When slowly diffused into high purity silicon, lithium can occupy interstitial sites. These can provide donor compensation in p-type silicon over a thickness up to 10 mm.

Compensation in silicon can be made in three ways [6] :

- Using a Diffused Junction method – a starting layer of p-type (silicon) is exposed at high temperature to a vapour containing phosphorus. The diffusing P ions over-compensate the boron nearest the surface and produce n-type material. The p-n junction is thereby created at some depth into the silicon. In addition, there is a significant layer of n-type material to be traversed by the radiation before it is detected in the depletion layer.
- Using a Surface Barrier method – a region in which there is a large concentration of electrons in an otherwise n-type material can also function as a p-n junction. This is the situation in the Surface Barrier detector. Here, the surface of n-type material is etched and followed by the evaporation of a thin gold layer. These surface electron states act as acceptor levels to create the p-type layer. Use can also be made of p-type silicon as the starting material when the etching is followed by the deposition of aluminium. The advantage of the Surface-Barrier method is that there is a very small thickness of uncompensated material for the radiation to traverse before it reaches the depletion zone. A possible disadvantage is that the device may be sensitive to ambient light if the window materials are not sufficiently thick.
- By Ion Implantation – native p-type silicon can be irradiated with 10 keV phosphorus or boron ions to produce n-type or p-type silicon. Variation of the beam current and energy is used to control the concentration and penetration depth of the depletion.

Surface Barrier detectors tend to be less rugged than either Diffused-Junction or Ion-Implanted detectors. Furthermore, the lower annealing temperatures required

after the ion-implantation procedures, coupled with the better control of the doping, now make ion-implantation the most widely-used method of compensation in silicon.

5.4.2 *Germanium detectors*

The higher atomic number of germanium (Z=32) and the higher attainable purity make possible the widespread use of high purity germanium (HPGe) photon detectors. Production steps for HPGe are :

- polycrystalline germanium is first zone-refined, after which the impurity levels will have fallen by a factor of about 100,
- a single crystal is grown from the melt by the *Czochralski* method,
- the crystal is cut, machined and lapped to the required dimensions. A co-axial detector is cylindrical with a blind axial hole for the central electrode contact.
- contacts are made using lithium ion diffusion for the n-type contact (~700 μm thick) and boron implantation for the p-type contact (~0.3 μm). These are illustrated for the two configurations in Fig.(5.27).

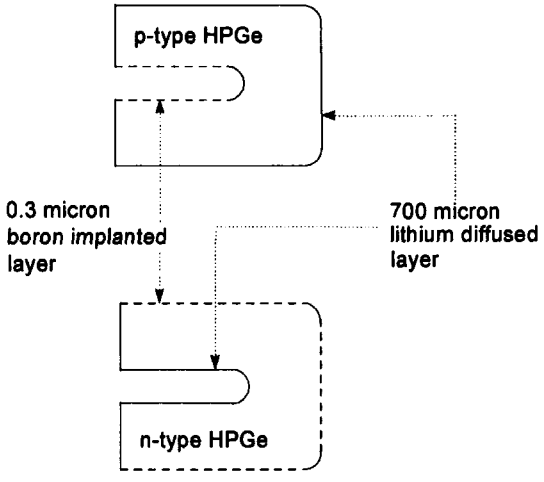

Fig. (5.27) Basic configurations of HPGe detectors, [17].

The crystals shown in Fig.(5.27) are mounted onto the end of a copper cooling rod which dips into a liquid nitrogen reservoir. A field-effect-transistor (FET) is also mounted on this rod as close as possible to the crystal. The cooled FET plays an important role in reducing signal noise. It is also prone to failure if the high bias voltage that is required (~ 2.5 – 3.5 kV) is applied suddenly. A good illustration of the physical configuration of the elements in a HPGe detector is given by Knoll [6].

The efficiency of a HPGe detector is usually compared against a "standard" 76 cm thick, 76 cm diameter NaI(Tl) scintillator. Other parameters of practical interest

are the energy resolution at 122 keV and 1330 keV, and the Peak:Compton ratio. Energy resolution is specified as the Full Width at Half maximum divided by the mean energy as in Eq.(5.16). The Peak:Compton ratio is specified as the ratio of the highest count in the photopeak to a count in the Compton continuum associated with that peak. Table (5.4) shows some typical performance parameters for co-axial HPGe detectors.

Table (5.4) Typical specification of co-axial HPGe detectors. Data taken from [17].

Efficiency (%)	% resolution at (122 keV)	% resolution at (1330 keV)	Peak:Compton
150	1.07	0.17	90:1
100	0.98	0.16	83:1
10	0.68	0.13	41:1

5.4.3 Nuclear spectroscopy using a Ge photon detector

The response of any detector, whether designed for photons or particles, is mainly determined by the following :

- the size of the sensitive volume compared with the characteristic attenuation length of the radiation,
- the thickness of any window material through which the incident radiation has to travel before reaching the sensitive volume,
- the proximity of any material which can scatter back into the sensitive volume radiation which might otherwise have escaped.

For photons the response is entirely due to energy deposition by secondary electrons. It is the range, angle of scatter and energy distribution of these electrons that distinguishes one detector arrangement from another. The larger the crystal the greater the probability that an incoming photon is completely absorbed. This gives rise to a full-absorption peak (also called a photopeak) which characterizes the energy of the photon. A detector with a smaller sensitive volume has a larger probability that part of the photon energy is not deposited within the detector. In this case a pulse of lower amplitude is produced.

An example is provided by the likely response to 1.5 MeV photons of a 50 mm thick, 50 mm diameter Ge crystal surrounded by an annulus of lead. Assuming a relative efficiency somewhat less than 100%, Table (5.4) suggests that a Peak/ Compton ratio of ~50 : 1 might be expected. Data from Table (5.5) is then required to consider :

- the photons interacting directly with Ge,
- the photons initially interacting in the Pb shielding and then being scattered into the Ge,

- the photons being transmitted through the Ge and then being back-scattered from the copper cooling rod and other backing material.

Total cross-section data in Table (5.5) can be used to show that 72% of a flux of 1.5 MeV photons incident normally on the face of the crystal interact within it. The remainder do not interact and are transmitted into the material behind the crystal. Eq.(3.15) shows that these photons can be scattered back into the Ge with an energy of ~ 0.22 MeV (using $\alpha = h\nu_0/m_0c^2 = 1.5/0.511 = 2.935$).

Table (5.5) Cross-sections (barn atom^{-1}) and total mass attenuation coefficient for 1.5 MeV photons [18]. σ(coh) = Rayleigh coherent scatter; σ(inc) = Compton incoherent scatter; σ(PE) = photoelectric absorption; σ(PP) = pair production absorption; σ(tot) = total.
$\mu = \sigma(\text{tot})\, N_A / A$, where N_A is the Avogadro constant.

	ρ (g cm^{-3})	Z	A	σ(coh)	σ(inc)	σ(PE)	σ(PP)	σ(tot)	μ (cm^2 g^{-1})
Ge	5.46	32	72.63	0.0323	5.490	0.0397	0.0531	5.615	0.04656
Pb	11.35	82	207.22	0.4636	14.02	2.863	0.6144	17.96	0.05220
Cu	8.93	29	63.54	0.0246	4.976	0.0251	0.0424	5.068	0.04803

The relative probabilities in Table (5.5) indicate that ~98% ($\sigma_{inc}/\sigma_{tot}$) of the initial interactions in each of the three materials involve Compton incoherent scatter. In the Ge crystal therefore the interactions are: 0.6% Rayleigh scatter, 0.71% photoelectric absorption, 97.8% Compton scatter and 0.95% pair production. Many of the subsequent interactions of the initially Compton-scattered photons, however, can also result in full absorption of the 1.5 MeV incoming energy.

Photon interactions which contribute to the energy-dependent response of a detector in this simple example can therefore be summarized as follows :

(a) Photo-electric absorption

In addition to the photo-electron, photo-electric absorption produces one or more characteristic X-rays or Auger electrons. When the interaction takes place within the crystal and both of these secondary radiations are absorbed locally, the total deposited energy contributes to the photopeak. Although the range of the Auger electrons is generally small enough for this always to be the case, a characteristic X-ray may have sufficient energy to escape the crystal. In this case, a small peak will appear just below the main photopeak. The energy difference will be equal to the X-ray energy. Equally, a characteristic X-ray generated in nearby shielding material may enter the crystal from outside. In the case of a lead shield in the above example, it is likely that a peak due to the most prominent characteristic lead X-ray (K_{α_1} at 74.97 keV) would be detected.

(b) Compton scatter

A single Compton scatter event at 1.5 MeV produces a photon with an energy between zero and 1.282 MeV. If the crystal is sufficiently large, a single 1.5 MeV photon can suffer many collisions (multiple scatter) via the Compton process. If this photon does not leave the crystal volume (i.e. it is ultimately absorbed), the event registers as a total absorption and contributes to the photopeak at 1.5 MeV. However, if the photon is able to leave the crystal after several Compton scatter events, the energy deposited in the crystal will be less than 1.5 MeV. It will contribute to the energy region between the photopeak and the Compton edge for single scatter. Photons which interact in the Ge crystal after scatter from any surrounding material will show a broad energy distribution. The mean energy is lower for back-scattered photons than for those that have suffered only a small change of direction.

(c) Pair production

A pair production interaction in the crystal gives rise to two photons with energy 0.511 MeV. If both photons are absorbed then, again, there is a contribution to the photopeak. If one is able to escape the crystal, the energy deposited will be 1.5 MeV minus 0.511 MeV. If both escape, a peak will appear at 1.5 - 1.022 = 0.478 MeV. If pair production takes place in the lead shield and one annihilation photon interacts in the crystal, a peak is observed at 0.511 MeV.

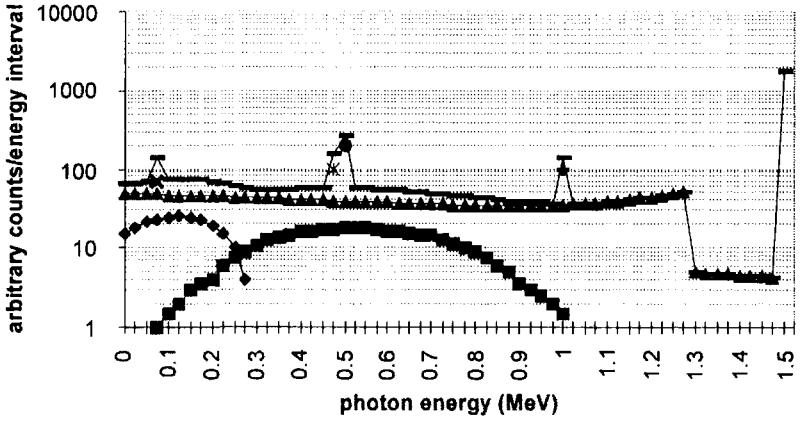

Fig.(5.28) A schematic diagram of the contributions to the total response of a Ge detector to 1.5 MeV photons.

- ▲ Compton scatter in the crystal showing the edge at 1.28 MeV and the small multiple-scatter background between the edge and the full energy absorption peak at 1.5 MeV.
- ◆ backscatter from detector material behind the crystal
- ■ in-scatter into the crystal from the lead shield
- ✖ characteristic lead Kα X-ray peak at 75 keV
- ✳ annihilation double escape peak at 0.478 MeV
- ● annihilation photon from lead shield at 0.511 MeV
- ✚ annihilation single escape peak at 0.99 MeV
- ▬ total

Fig.(5.28) illustrates the way the various interactions contribute to the overall energy spectrum produced in a high resolution HPGe detector.

5.4.4 Microstrip and Charge Coupled Devices

These two types of detector have been developed as a result of advances in three important areas of semiconductor technology :

- metal-oxide-silicon (MOS) structures. These use a basic substrate of silicon, on one surface of which is formed a thin layer of oxide. This is achieved by heating up a silicon wafer, typically 300 – 650 μm thick, to ~1100°C. The formation of the oxide layer terminates the otherwise chemically active covalent bonds which exist on the surface of pristine silicon. Known as passivation, this process protects the silicon surface with a thin layer which is also a good quality electrical insulator. The metal electrodes are added later in the process.
- photolithography. This is the technique used to open up the oxide layer and expose the bare silicon surface. First, the whole oxide surface is coated with a layer of resist material and then covered by a mask which defines the pattern to be cut in the oxide. Ultra-violet light is then shone through the mask to degrade the resist which can then be selectively removed by chemical means. An oxide etch is then carried out. This removes the unprotected oxide but does not affect the oxide beneath the resist which was protected by the pattern of the mask. Finally, the remaining resist is removed from the surface of the patterned oxide.
- ion implantation techniques. The selected ions are implanted over the whole wafer. For an originally n-type silicon substrate, p-type ions, e.g. boron, are used. These are implanted into interstitial positions, to a depth determined by the initial ion energy, into both the bare silicon and the remaining oxide layer. To repair radiation damage caused by the implantation, and to move the ions into lattice positions, the wafer is annealed to ~1000°C. Dopant ions are thereby distributed to a depth of ~ 0.1 μm.

The most widely-used form of charge coupled device (CCD) in radiation science consists of a silicon wafer which contains a two-dimensional matrix of pixels. These pixels consist of potential wells in which accumulated charge may be stored temporarily. Photoelectrons generated in the silicon by photon interactions, for example, can therefore be integrated and stored over a short period of time. Subsequent transfer of these charges into an output register enables the image of the spatial photon flux distribution to be recreated.

A typical CCD to be used for imaging is fabricated as follows :

- An array of narrow electrodes is insulated from a silicon substrate by a thin layer of silicon dioxide, Fig.(5.29a). The electrodes are usually made of heavily-doped polycrystalline silicon (polysilicon).
- Beneath the layer of insulation is created a depletion zone which is generally

produced by ion implantation into a layer of epitaxial silicon.

- The depletion zones are formed in narrow "buried" channels which are orthogonal to the electrodes and which are separated from each other by channel stops, Fig.(5.29b).
- Potential wells are created at the intersections of the electrodes and buried channels by the application of a positive voltage on the electrodes.
- Charges trapped in the potential wells can be moved along the buried channels by the sequential change of voltage on successive electrodes, Fig.(5.30).
- A sequence of drive pulses, Fig.(5.31), moves the charges to the end of the buried channels from where they are transferred into a store section. The timed arrival of these charges at the end of the channel denotes their original position.

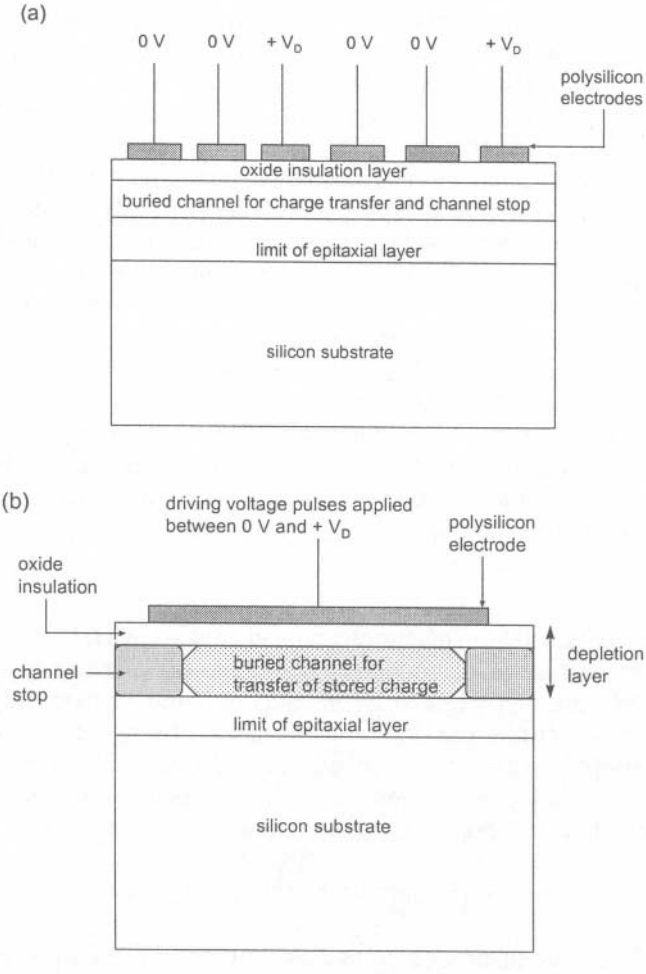

Fig.(5.29) Schematic views of a CCD device. (a) a cross-sectional view at right angles to the buried channels, (b) a magnified view along one of the buried channels. Typical thicknesses are: oxide 0.1 μm : depletion layer 7 μm : epitaxial layer 20 μm : silicon substrate 625 μm. With permission from EEV, Chelmsford, Essex.

A silicon-strip detector has a basic design which is similar to that of the CCD. The main difference is that the charge is not integrated, stored and read out at a later time. In the micro-strip detector, a bias voltage is applied between the electrodes and an ohmic contact at the base of the silicon substrate. This generates an electric field within the depletion region leading to a small current pulse which, when amplified, signifies the detection of an ionization event.

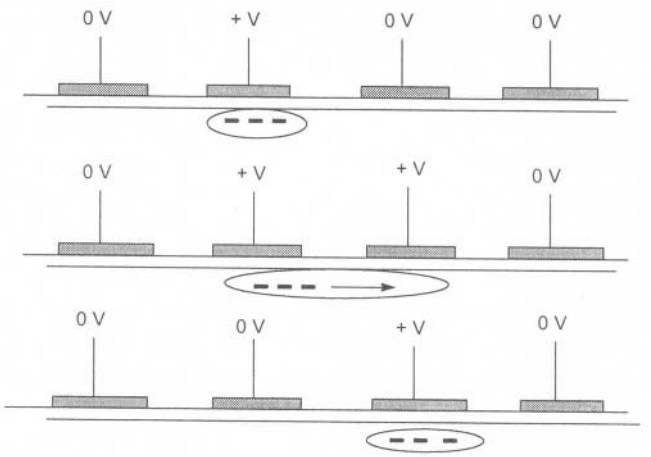

Fig.(5.30) Voltage pulse sequences for charge transfer along the buried channels. With permission from EEV, Chelmsford, Essex.

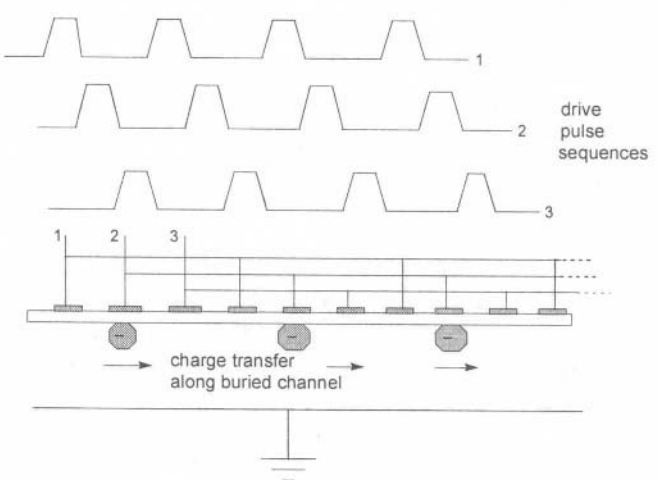

Fig.(5.31) Drive pulse sequences for transfer of charge along the buried channels. With permission from EEV, Chelmsford, Essex.

5.5 Channel Electron Multipliers

Single Channel Electron Multipliers (SCEM), together with Channel Electron Multiplier Arrays (CEMA), are widely used methods for counting low energy charged particles. Although they use a similar electron-multiplication process as in the dynode chain of a photomultiplier tube, they differ in not having a window material to provide a self-contained vacuum. It is therefore essential to operate both SCEM and CEMA detectors only in a vacuum which is better than ~13 mN m^{-2} (10^{-4} torr).

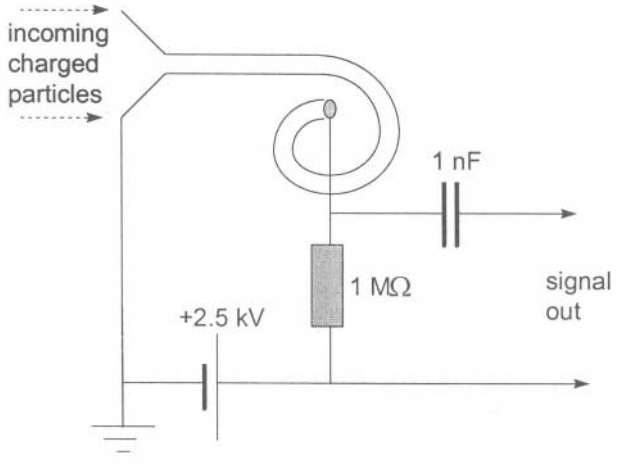

Fig. (5.32) A typical circuit for a grounded-cone Single Channel Electron Multiplier, [19].

A typical SCEM arrangement, Fig.(5.32), consists of a narrow glass tube, approximately 2 mm in diameter. The inside wall of the tube has a high resistance (~10^8 MΩ) in order to maintain a large potential drop between the input cone and the tail. Secondary electrons, produced by the impact on the entrance cone of incoming charged particles or photons, are then accelerated down the tube producing an avalanche of further ionizations as they strike the tube walls.

Space charge limitation occurs when the electron cloud near the tail of the channel reaches ~10^9 electrons. Once a charge cloud of this magnitude has built up it prevents further secondary electrons from acquiring sufficient energy to contribute to the output. The tube therefore reaches its saturation condition in a way similar to that in the Geiger-Muller detector.

The SCEM is most often used with pulse counting circuits and charge-sensitive preamplifiers, as in Fig. (5.32), in order to detect individual particles. When the closed-end tail is replaced by an open-end which terminates in a separate electrode, the SCEM may be used in an analogue mode as a current amplifier. Operational

characteristics include :

- Ionic feedback. This effect occurs when the electron cloud near the output tail is sufficiently dense to ionize residual gas molecules remaining in the tube. Positive ions so produced drift towards the input (more negative) end. If these ions are allowed to gain too much energy before hitting the tube walls, additional secondary electrons can be produced giving rise to spurious pulses at the collector. This effect is identical to the electron-loading problem in the Van de Graaff accelerator (see section 1.4.2) and is the reason why the SCEM tube is curved.
- The increase in gain with applied voltage. The gain of the tube increases rapidly up to ~2 kV. At higher voltages there is a broad quasi-linear plateau region in count-rate for applied voltages in the range 2 – 3 kV. This is the region for optimum operation.
- The decrease of gain with count-rate. When the tube is operated at count- rates below the onset of saturation, there is an approximate proportionality between input and output. In Fig.(5.33) this is the case up to ~10^5 counts s^{-1}. At higher count-rates the gain decreases.
- Detection efficiencies for both electrons and positive ions are energy dependent, Fig.(5.34).

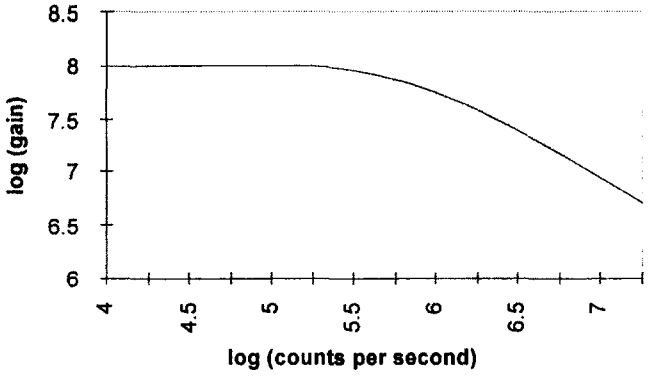

Fig.(5.33). Reduction of gain with increase in count-rate for a typical SCEM, [19].

Multichannel arrays (CEMA) consist of thin plates of special glass (~0.5 mm) through which pass thin channels of diameter 10 - 25 μm set at an angle of 6 - 13° to the plate surface. A typical open-area ratio (hole diameter/septum thickness) is 60%.

Thin nickel-chromium electrodes cover the septa on each side of the plate, Fig.(5.35), and permit the application of a potential in the order of ~1 kV to generate secondary electrons, as in the SCEM. Although the linear channels in each plate

are prone to the problem of ionic feedback, the device of placing two plates in cascade with channels lying in opposite directions makes it possible to achieve high gain without excessive ionic feedback and the consequent loss in linearity.

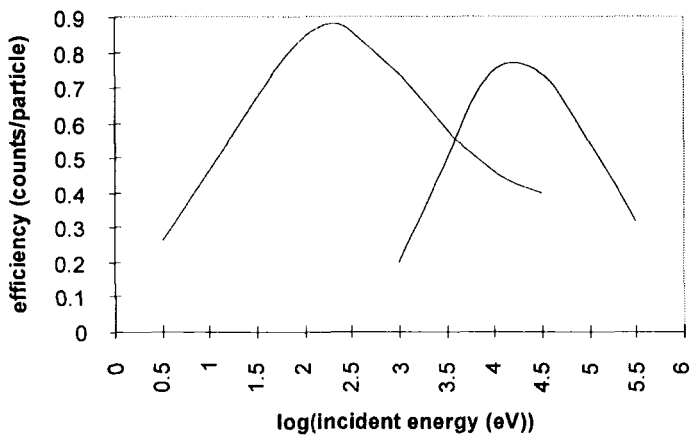

Fig.(5.34) Typical detection efficiencies for incident electrons (left hand curve), and protons and other positive ions (right hand curve). Data taken from [19]. For efficiency data for positive and negative oxygen ions, see also [20].

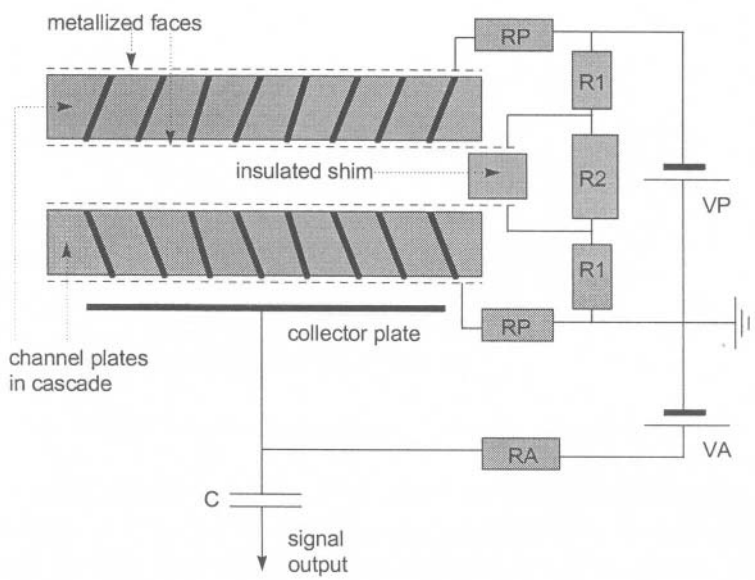

Fig. (5.35) Two multichannel plates in cascade. Typical component values of RP, R1 and R2 are ~ 1MΩ, RA is generally in the range 0.1 - 1 MΩ and C usually in the range 0.1 - 10 nF.

One considerable advantage of the CEMA is that the uniform length/diameter ratio of the channels over the whole area of the plate gives a constant gain per

channel. The system is then suitable as an image intensifier for electron or photon fluxes impinging on the front surface. In this case the collector plate in Fig.(5.35) is replaced by a multianode device or a charge coupled detector (CCD). In operation, great care has to be taken to guard against excessive stress on the plates when placing them in their mountings and when making the high voltage contacts to the metallized layers.

References

[1] K.Kleinknecht, *Detectors for Particle Radiation* (C U P, Cambridge 1986).

[2] E.Fenyves and O.Haiman, *The Physical Principles of Nuclear Radiation Measurements*, (Academic Press, New York, 1969).

[3] S.C.Klevenhagen, *Physics and Dosimetry of Therapy Electron Beams* (Medical Physics Publishing, Madison, Wisconsin 1993).

[4] R.D.Evans, *The Atomic Nucleus*, (McGraw-Hill, New York, 1972), p. 411.

[5] E.A.Jones, F.A.Smith, D.T.Goodhead and J.Oriel, *Phys.Med.Biol.* **33**(12) (1988) 1385.

[6] G.F.Knoll, *Radiation Detection and Measurement* (2nd Edition) (J.Wiley, New York, 1989).

[7] W.G.Richardson and P.R.Scott, *Structure and Spectra of Molecules* (J.Wiley and Sons, Chichester, 1985).

[8] J.B.Birks, *The Theory and Practice of Scintillation Counting* (OUP Oxford 1964).

[9] F.S.Eby and W.K.Jentschke, *Phys.Rev.* **96** (1954) 911.

[10] J.Barton, I.M.Blair and J.A.Edgington, Proc.Int.Workshop on Dark Matter, Sheffield (1996).

[11] W.J.van Sciver and L.Bogart, *Bull. Am.Phys.Soc*, **2** (1957) 142.

[12] J.E.Turner, *Atoms, Radiation and Radiation Protection, (*2nd Edition J.Wiley, New York 1995).

[13] R.C.Sangster and J.W.Irvine, *J.Chem.Phys.* **24**(4) (1956) 670.

[14] J.R.Prescott and P.S.Takhar, *IRE Trans.Nucl Sci.* **NS-9**(3) (1962) 36.

[15] G.G.Kelley, P.R.Bell, R.C.Davies and N.H.Lazar, *IRE Trans.Nucl. Sci.* **NS-3**(4) (1956) 57.

[16] J.I.Hopkins, *Phys.Rev.* **77** (1950) 406.

[17] EG&G Ortec, *Catalogue 95* (1994).

[18] J.H.Hubbell, H.A.Gimm and I Overbo, *J.Phys.Chem.Ref.Data* (1980).

[19] Philips Photonics Electron Multipliers Handbook (1990).

[20] C.A.Keller and B.H.Cooper, *Rev.Sci.Instr.* **67**(8) (1996) 2760.

CHAPTER 6

MICRODOSIMETRY and RADIATION EFFECTS

6.1 Introduction

Each type of radiation produces a different spatial pattern of deposited energy along its track. This initial energy distribution then evolves due to the secondary particles produced and takes place temporally, on the sub-picosecond to microsecond time scale, as well as spatially on the nanometre to millimetre distance scale.

Microdosimetry [1] is concerned with the way these effects can be quantified over the track of an individual particle, rather than averaging them over a significant mass as in the study of (macro) dosimetry.

In order to describe radiation effects over smaller and smaller distances, we need to introduce some stochastic variables and their distributions in order to account for the random nature of the interaction processes.

The most important of these are :

- specific energy z
- lineal energy y
- proximity function

These variables lead to other important concepts such as Linear Energy Transfer (LET) and the radial track distribution.

6.2 Basic Definitions of the Variables

6.2.1 Energy deposited ε

At each small volume where energy is deposited (transfer point) we can write

$$\varepsilon_i = T_{in} - T_{out} + Q_{\Delta m} \tag{6.1}$$

where T_{in} and T_{out} refer to the kinetic energy of the incoming particle and the sum of the energies of all the outgoing particles respectively, and $Q\Delta_m$ accounts for any change in rest mass (> 0 for a decrease and < 0 for an increase in rest mass).

Around each transfer point we consider the weighted mean energy imparted in a spherical volume of radius *x* within which there are *k* secondary transfer points.

A track *j* can therefore be pictured in Fig.(6.1) :

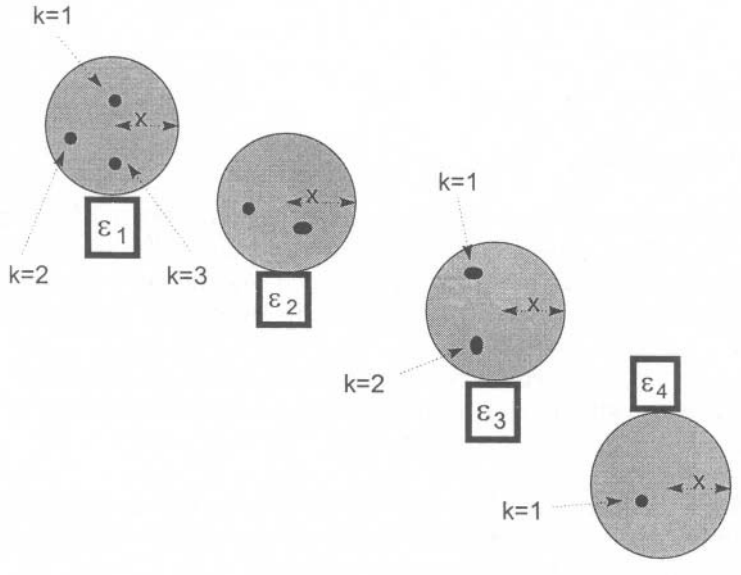

Fig.(6.1) The concept of a proximity function in a typical radiation track.

The proximity of all the energy transfer points can be expressed as a stochastic quantity :

$$\overline{T_j(x)} = \frac{\sum_i \sum_k \varepsilon_i \varepsilon_k}{\sum_i \varepsilon_i} \tag{6.2}$$

where the ε_i run over all energy transfer points in the *j'* th track and the ε_k run over all transfer points (from secondary electrons) within distance *x* from each primary transfer point, [1].

If there is a total number of *n* tracks in the selected volume, the mean value of the quantity in Eq.(6.2) is the integral proximity function in the limit as n tends to infinity .

$$T(x) = \frac{1}{n} \sum_{j=1}^{n} \overline{T_j(x)} \tag{6.3}$$

The total energy imparted to the selected volume is $\varepsilon = \sum_i \varepsilon_i$

6.2.2 *Specific energy imparted, z = ε /m*

When the selected volume has a mass m, the quantity *z* has units of J kg^{-1} and is equivalent to dose. It has a distribution function, *F(z)*, which gives the probability that the specific energy is equal to or less than *z*. Alternatively, it gives the number of energy deposition events required to achieve a certain *z*. As *z* increases, the number of such events reaches an asymptote determined by :

- the range of secondary electrons,
- the number of such electrons needed in a certain mass to make the specific energy uniform.

The derivative of *F(z)* with respect to *z* gives the probability density *f(z)* which is the probability of occurrence of an event of given size *z*. Thus :

$$f(z) = \frac{d}{dz} F(z) \tag{6.4}$$

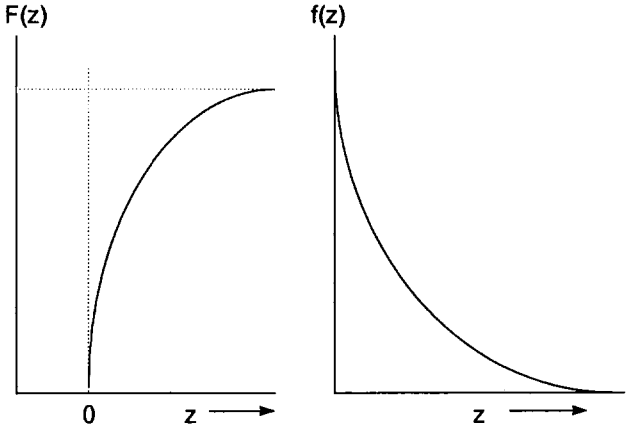

Fig.(6.2) The distribution function *F(z)* and the probability density *f(z)*, [1].

The probability density reaches a high value as $z \rightarrow 0$, indicating a large probability of zero energy deposition.

The mean specific energy $\bar{z}$ is the expectation value defined by the integrated

product of a given value of z and the probability density of that value. This is called the Frequency-Mean specific energy :

$$\overline{z_F} = \int_0^\infty z\, f(z)\, dz \tag{6.5}$$

It is possible to define a Dose-Mean specific energy in the same way, by using the relation between the frequency distribution and the dose distribution.

$$d(z) = \frac{z}{\overline{z_F}}\, f(z) \tag{6.6}$$

The Dose Mean is then given by :

$$\overline{z_D} = \int_0^\infty z\, d(z)\, dz = \frac{1}{\overline{z_F}} \int_0^\infty z^2\, f(z)\, dz \tag{6.7}$$

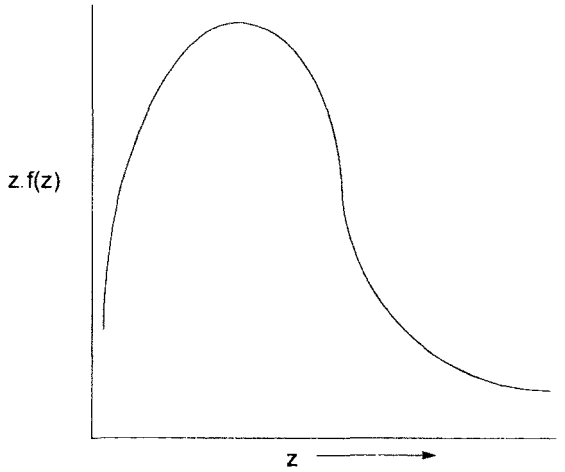

Fig.(6.3) The frequency distribution versus event size, z, [1].

6.2.3 *Lineal energy,* $y = \varepsilon / \bar{\ell}$

This gives the quantity of energy imparted in a single event to a volume having a mean chord length $\bar{\ell}$. The units are J m^{-1}, or more usually, keV μm^{-1}. The mean chord length is the average length of randomly oriented chords through the volume. For a convex volume V, surface area A, we have $\bar{\ell} = 4V / A$.

The lineal energy is also a stochastic quantity, and can therefore be described using the same distribution functions as in the case of specific energy. The comparable expressions for lineal energy can now be given in the same way as for specific energy, Eqs.(6.4), (6.5), (6.6) and (6.7).

We therefore have :

- the distribution function $F(y)$: the probability that the lineal energy is equal to or less than y,
- the frequency probability density $f(y)$: the probability of occurrence of an event size y,
- the frequency-mean lineal energy : $\overline{y_F} = \int_0^\infty y\, f(y)\, dy$
- dose probability density $d(y) = \frac{y}{y_F}\, f(y)$
- dose-mean lineal energy $\overline{y_D} = \int_0^\infty y\, d(y)\, dy = \frac{1}{y_F} \int_0^\infty y^2\, f(y)\, dy$

The distributions for lineal energy have similar forms as those shown in Figs.(6.2) and (6.3) for specific energy. The most important distribution is that of $y\, d(y)$ against y, because it gives the fraction of absorbed energy deposited at a given value of lineal energy. It can therefore be determined experimentally.

6.3 Experimental Determination of Microdosimetric Spectra

Gas proportional counters are the principal means by which event-size distributions are determined. A spherical, micron-sized volume of tissue, density 1 g cm^{-3}, is simulated by a larger volume of low density, tissue-equivalent, gas. For an acceptable simulation :

- the energy loss in, and the atomic composition of, the two volumes must be identical,
- the stopping power of the radiation must be energy independent.

We then require :

$$\Delta E_t = \left(\frac{S}{\rho}\right)_t \rho_t d_t = \Delta E_g = \left(\frac{S}{\rho}\right)_g \rho_g d_g \qquad (6.8)$$

In Eq.(6.8) the subscripts t and g refer to tissue and gas respectively, S/ρ to the mass stopping power of the radiation and ρ and d to the density and diameter of the spherical volumes. The densities and diameters are chosen such that $\rho_t d_t = \rho_g d_g$.

A 2.54 cm diameter volume of air at STP ($\rho_g = 0.001293$ g cm^{-3}) will then simulate 32.8 μm of unit density tissue. Lower gas pressure will simulate smaller tissue volumes.

6.4 Practical Considerations

As in any form of accurate dosimetry, the condition of electronic equilibrium must be established. This requires that the energy spectrum of secondary electrons does not change over the volume of material under consideration. It is discussed further in the next chapter. Particular precautions in microdosimetry include the following :

A walled counter must have a wall that is :

- commensurate with the counter gas,
- thick enough to ensure that secondary charged particles cross the sensitive gas volume (*i.e.* they neither start nor stop in the sensitive volume),
- thin enough not to unduly attenuate the primary radiation,
- without any gaseous impurities.

Particular types of wall effects receive detailed consideration in [1]. In the use of a wall-less counter, the following further precautions must be taken :

- the sensitive volume must be sufficiently well-defined,
- there must be no (electrode) material of different density or composition between the sensitive volume and the remainder of the medium,
- in the conversion of measured charge to energy absorbed within the simulated volume, the assumption of a constant W-value may not be adequate, particularly at low energies,
- in the energy calibration of a gas proportional counter, the secondary electrons from the mono-energetic X - or γ - rays must be much less than the diameter of the gas volume. In the simulation of very small tissue volumes, only very low energy characteristic X-rays can be used,
- although the available dynamic range of a proportional chamber can extend up to five orders of magnitude by increasing either the gas gain or the electronic gain of the system, extreme care has to be taken at the boundaries between one gain setting and the next. Microdosimetric spectra frequently have sharp discontinuities.

6.5 Primary Radiation Effects

The initial consequences of radiation action are ionization and excitation of the constituent atoms of the medium.

$$A \rightarrow A^+ + e^-$$
$$A \rightarrow A^*$$

Subsequent reactions of the products of these reactions are relatively easily followed in the gas phase, but are much more difficult to quantify in the condensed phase.

6.5.1 Reactions of ions (A^+)

The principal reactions which involve the positive ions are (a) neutralization, (b) reactions with neutral molecules and (c) charge-transfer reactions.

(a) *Neutralization*

- Positive ions can be neutralized by any negative species, the most likely being the one produced in the initial ionizing event. This is called the geminate electron.
- When the ionization takes place at such high energies that the electron moves beyond the electrostatic influence of the positive ion, other reactions become more likely.
- If the neutralization is achieved via an electron, the atom receives energy equal to, or greater than, its ionization potential and can therefore reach a highly excited state :

  $$A^+ + e^- \rightarrow A^{**}$$

  Particularly in condensed media, some or all of this energy can be dissipated via photon emission, $A^{**} \rightarrow A^* + h\nu$. If the positive ion is also a radical, R, (an atomic species which contains an unpaired electron), neutralization gives rise to a highly reactive hot radical $R^{\bullet +} + e^- \rightarrow R^{\bullet **}$.
- Neutralization by another ion will generally give two neutral species where one or both may be excited :

  $$A^+ + B^- \rightarrow A^* + B$$
  $$A^+ + B^- \rightarrow A^* + B^*$$

(b) Ion-Molecule reactions

These can occur very rapidly, the most usual being the transfer of an H atom from a molecule to an ion to create a different ion and a free radical :

$$RH^+ + RH \rightarrow RH_2^+ + R^\bullet$$

(c) Charge transfer reactions

These can also be very fast reactions and take place when an ion transfers its charge to a neutral molecule :

$$A^+ + B \rightarrow A + B^+$$

The ionization potential of A must be greater than that of B and the reaction is most likely to proceed when this difference is small. This is the reaction that is used in the quenching of a Geiger Mueller detector (section 5.2.8).

6.5.2 Reactions of electrons

Reactions that involve the electron are (a) simple capture, (b) dissociative capture, (c) the particular case of sub-excitation electrons and (d) solvation.

(a) Simple capture

In addition to the process of neutralization, an electron can become attached to a neutral molecule to form a negative ion.

$$A + e^- \rightarrow A^-*$$

- This is most likely to occur when the molecule has a large electron affinity (*e.g.* molecular oxygen, halogens *etc.*).
- The amount of energy equal to the electron affinity of A plus the kinetic energy of the electron, must be accommodated by A^-*. This can only take place when this energy is equal to the energy difference between two atomic levels of A^-. In other words, it is a resonance process.
- The excited negative ion can be de-excited by photon emission :

$$A^-* \rightarrow A^- + h\nu$$

(b) Dissociative capture

This is a process which competes with neutralization, ($A^+ + e^- \rightarrow A**$), especially at early times following the initial ionization from densely ionizing radiation. It is most likely to take place before the diffusion of the species becomes possible.

It occurs when the electron affinity of a molecule, due to either an electronegative group or atom within it, is greater than the bond strength of that group or atom in the remainder of the molecule.

$$A + e^- \rightarrow B^- + C^\cdot$$

$C^\cdot$ will usually be a free radical and B^- a free radical ion which has a high electron affinity such as a halogen (B = Cl, Br, I, CN...).

(c) Sub-excitation electrons

These are low energy electrons with energies smaller than the lowest excitation energy of the medium. They generally :

- have longer lifetimes than faster electrons, and
- become important in mixtures in which one component, (*e.g.* an impurity), has a significantly lower excitation energy than the remainder of the mixture. In this event, the impurity can become excited to a much greater degree than would otherwise be expected on the basis of its concentration alone.

(d) Solvation of electrons

The process of solvation is one in which a charged entity polarizes the solvent around it. A sheath of polarized solvent molecules is thereby created around the entity, as in Fig.(6.4). It can take place with high probability in situations where an electron (or positron) manages to :

- escape recombination,
- when its reaction rate with other species is sufficiently low, and
- when it is in a medium with a large dielectric constant.

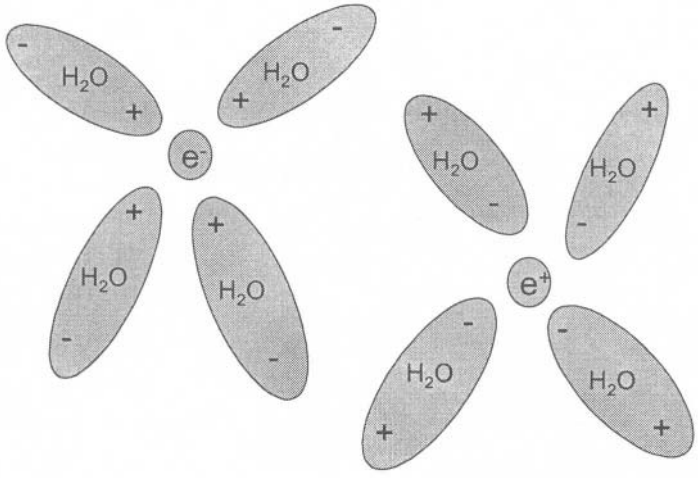

Fig.(6.4) Solvation of an electron and a positron by polarizable molecules such as water.

6.5.3 Rate constants governing the time evolution of radiation products

In principle, any of the above reactions may take place within, or in the vicinity of, a radiation track in which the primary species A^+ , e^- and/or A^* are first generated.

The probability per unit time that a reaction $e^- + R \rightarrow R^-$ will proceed, can be expressed as :

$$-\frac{d}{dt}F(t) = k_R\ [R]\ F(t) \tag{6.9}$$

where $F(t)$ is the probability (s^{-1}) that an electron thermalized at time $t = 0$ has still not reacted at time t. The reaction rate constant, k_R ($l\ M^{-1}\ s^{-1}$) is appropriate for scavenging species R which is present in concentration $[R]$ ($M\ l^{-1}$). The number of electrons which have a life span of t, and which then react between t and $t+dt$ is $F(t)\ k_R\ dt$. When integrated to infinity, this gives the original number of electrons scavenged by species R, and is the area under the curve in Fig.(6.5) :

$$Area = \int_0^\infty F(t)\ k_R\ dt = \int_0^\infty k_R\ F(0)\ exp(-k_R\ t)\ dt = F(0)$$

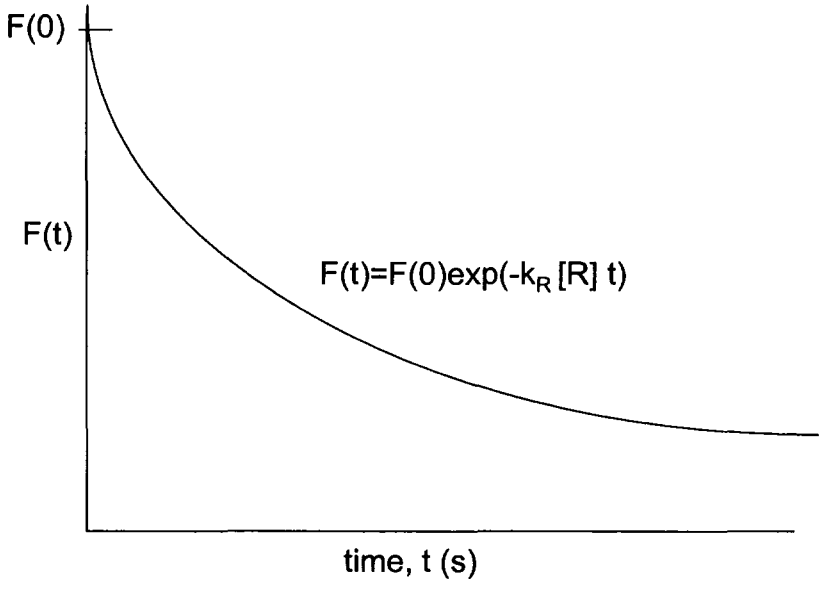

Fig.(6.5) The exponential solution of Eq.(6.9), $F(t)$, gives the number of electrons which have a lifetime longer than t.

6.5.4 *Practical determination of rate constants*

The exponential relation between reaction probability and time, Eq.(6.9), is used in the Pulse Radiolysis technique to determine either the concentration of reaction products, say $[R^{\cdot}]$, or the reaction rate constant, k_R, knowing one or other beforehand.

The technique rests on the ability to distinguish species by their optical absorption spectra, using picosecond light pulses gated from a pulsed beam of electrons [1].

6.6 Track Structure

6.6.1 *Temporal considerations*

Energy deposition along the track of the primary particle initiates the foregoing series of subsequent reactions. If the primary event results in ionization, it is the energy of the secondary electron which largely determines the second stage. When the secondary electron possesses sufficient energy to move away from the attractive potential of the residual positive ion, a localized region called a spur is said to have been created.

- With typical ionization potentials in the range 15 - 50 eV, and additional kinetic energy provided by the incoming radiation, a spur can be loosely thought of as a region in which 15 - 100 eV has been deposited. Thus, if the medium has a mean ionization potential of 20 eV, and 80 eV of kinetic energy is supplied in addition, the range of the 80 eV electron defines the approximate size of the spur. In water, this is ~20 nm.
- As the amount of deposited energy becomes greater, the number of electrons, as well as their energy (and hence range), also becomes larger. Several individual spurs may be formed in close proximity to create a region of space in which upwards of 500 eV is deposited. Such a sequence of events occupies a larger region of space and is called a blob.
- Even more energy leads to the formation of a sequence of spurs or blobs along an identifiable track. This corresponds to an energy deposition in the range 500 - 5000 eV.

If a spur is created by the deposition of 20 eV, then the shortest time within which this can occur can be estimated from the Heisenberg Uncertainty Principle. Setting ΔE = 20 eV we have [2] :

$$\Delta t \approx \hbar/\Delta E \geq 6.6 \times 10^{-16} \text{ eV s} / 20 \text{ eV} = 0.33 \times 10^{-16} \text{ s}.$$

This is, therefore, the earliest time that can be specified in the act of energy deposition from incoming radiation.

In a similar fashion, the specification of distance comes from $\Delta x = \hbar / \Delta p$, where Δp is the change in linear momentum associated with the radiation. This is related to the change in energy for a relativistic particle by $\Delta p = \Delta E/c$, where c is the velocity of light. Again, for ΔE = 20 eV, we have :

$$\Delta x \approx \hbar c / \Delta E = 6.6 \times 10^{-16}\ \text{eV s} \times 3 \times 10^{8}\ \text{m s}^{-1} / 20\ \text{eV} = 10^{-8}\ \text{m} = 10\ \text{nm}$$

This puts a lower limit on a definition of the position. The subsequent evolution of energy deposition, following an initial event in water, can then be broadly described in the following terms :

- on the 10^{-16} s time scale, the primary events are :

$$H_2O \rightarrow H_2O^+ + e^-$$
$$H_2O \rightarrow H_2O^*$$

  Here, the positive ion can also be excited, and the excited molecule can also be superexcited if sufficient energy is available. On a slightly longer time scale, ($\sim 10^{-15}$ s), it is possible for the H_2O^+ ion to move by charge transfer in a resonance process such as : $H_2O^+ + H_2O \rightarrow H_2O + H_2O^+$.
- on the 10^{-14} s time scale, which is approximately the period of molecular vibrational oscillations, energy can begin to move into vibrational and rotational modes. In this situation, it is possible for excited and superexcited species (H_2O^* and H_2O^{**}) to dissociate. Of greater significance, however, is:

$$H_2O^+ + H_2O \Rightarrow H_3O^+ + OH^\cdot$$

- on the 10^{-13} s time scale, energy can flow into translational modes to make temperature a meaningful quantity.

Thus, if the radiation takes place at a temperature of 300 K, we have :

$$\Delta t \approx \hbar / kT = 1.05 \times 10^{-34}\ \text{J s} / 1.38 \times 10^{-23}\ \text{J K}^{-1} \times 300\ \text{K} = 0.33 \times 10^{-13}\ \text{s}.$$

Within this period, the thermalization, trapping and hydration of all energetic species will take place, whether they are electrons, ions or radicals. Any that are not trapped, *i.e.* localized, may begin to diffuse away from the site of their production. Radicals or ions, which are heavy, can only move a small amount ($\sim$0.05 nm), but a dry, non-hydrated, electron could move many nanometres [2].

6.6.2 Spatial considerations

In section 2.4, the classical criteria by which energy transfer between an incoming

energetic particle was deemed to be possible, rested on the hardness or softness of the collision. The ratio of the transit time of the particle, $2b/v$, to the excited state lifetime of the target, $\hbar/E$, was <<1 for an adiabatic collision and efficient energy transfer, and >>1 for a soft collision. Here, b and v are the impact parameter and particle velocity respectively, while E is an excitation state of the target atom/molecule.

The same idea is used to specify an impact parameter which causes the excitation of a target in a glancing collision, as a result of the transit time being equal to the reaction time. Thus :

$$\frac{2b}{v} = \frac{\hbar}{E}$$

gives a characteristic distance, $b = r_c$, which defines a track core radius containing energy from all glancing collisions. However, the head-on collisions whose secondary electrons from ionization interactions have ranges less than r_c will alsocontribute to the core. Generally, a deposition limit of 100 eV is used to define a track core.

Head-on collisions which result in a larger deposited energy, and whose secondary electrons have ranges larger than r_c contribute to the penumbra. By definition, secondary electrons having energy greater than 100 eV penetrate into the penumbra.

6.6.3 Equipartition principle of stopping power

This principle states that the total stopping power of an energetic particle in a medium has approximately equal contributions from :

- a large number of glancing collisions having a low energy loss per event, and
- a small number of head-on collisions that have high energy loss per event.

Note that the track core has contributions from both glancing as well as head-on collisions, but the penumbra contains only secondary electrons from head-on collisions. Thus, we have :

$$-(dE/dx)_{total} = -(dE/dx)_{glancing} - (dE/dx)_{head\text{-}on}$$

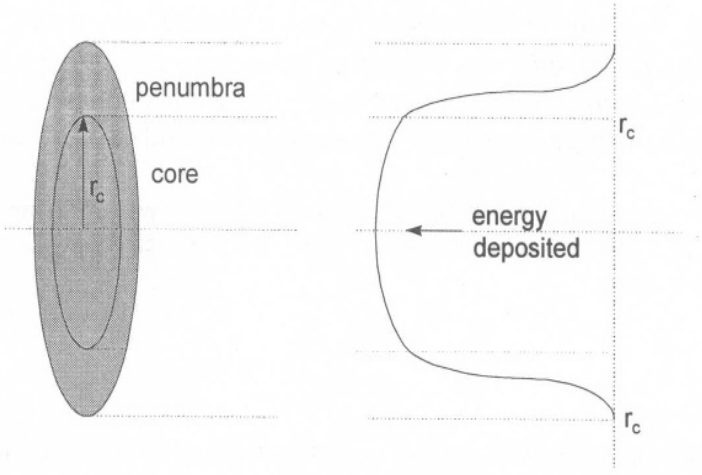

Fig.(6.6) The concept of core and penumbra regions of a charged particle track. The radius of the core is approximately $r_c = \hbar v / 2E$, where v is the velocity of the particle and E is the lowest excitation energy of the molecules of the medium.

6.7 Radiation Effects in Condensed Systems

To be of practical use, the foregoing material must now be applied to specific condensed materials. Although the objective is clear, the pathway is complicated by the stochastic nature of radiation action and the temporal as well as spatial effects which can result. For this reason there is often only a partial understanding of the link between :

- the microdosimetry in the foregoing sections,
- the macro-dosimetry in Chapter 7 and
- the final outcome (in the protection of humans, for example) in Chapter 11.

It is the continuing challenge in radiation physics, chemistry and biology to improve these levels of understanding.

Many materials respond, in some way or other, to ionizing radiation. When the characteristics of the radiation – type, energy and particularly intensity – are not excessive, such materials can be used as detectors. As intensity increases, however, permanent damage will eventually result. Under intense irradiation the response of the following systems can be :

- biological : deterministic effects *e.g.* skin erythema (reddening), eye cataract formation, acute medical conditions, etc. (see chapter 11),
- crystalline solids : the production of defects, dislocations, etc. which impair and, eventually prevent, their use as radiation detectors,
- polymers : loss of both di-electric and mechanical strength having a profound

influence on the insulating properties,
- glasses : changes in spectral absorption bands which give rise to a reduction in transmission.

The following sections consider briefly the most important radiation effects in materials which have some biological and technological relevance.

6.8 Radiolysis of Water

The radiolysis of any condensed medium is determined by the migration and subsequent reactions of the products from the initial interaction events. In water, the reactions up to about 10^{-16}s are those given in section 6.6.1. If the time scales of the subsequent reactions are represented by the time during which the reaction is half completed, the half-life $T_{1/2}$, then the initial reactions are [2] :

$$\begin{aligned} H_2O &\rightarrow H_2O^+ + e^- && T_{1/2} \approx 10^{-16}\text{s} \\ H_2O^+ + H_2O &\rightarrow H_3O^+ + OH^\bullet && T_{1/2} \approx 10^{-14}\text{s} \\ e^- + H_2O &\rightarrow e^-_{aq} && T_{1/2} \approx 10^{-10}\text{s} \\ e^- + H_2O &\rightarrow H^\bullet + OH^- && T_{1/2} \approx \text{long} \end{aligned} \qquad (6.10)$$

After about 10^{-10} s, the products of the above reactions interact further, within the low LET spurs and high LET tracks in which they are formed. The quoted reaction rate constants have generally been determined experimentally.

$$\begin{aligned} e^-_{aq} + H_3O^+ &\rightarrow H^\bullet + H_2O && k = 2.3 \times 10^{10}\ \text{l M}^{-1}\text{ s}^{-1} \\ e^-_{aq} + OH^\bullet &\rightarrow OH^- + H_2O && k = 3 \times 10^{10}\ \text{l M}^{-1}\text{ s}^{-1} \\ e^-_{aq} + e^-_{aq} &\rightarrow H_2 + 2OH^- && k = 6 \times 10^{9}\ \text{l M}^{-1}\text{ s}^{-1} \\ OH^\bullet + OH^\bullet &\rightarrow H_2O_2 && k = 4 \times 10^{9}\ \text{l M}^{-1}\text{ s}^{-1} \end{aligned} \qquad (6.11)$$

As time evolves the products of these reactions diffuse from their spur or track. Note that the stable molecular products, H_2O_2 and H_2 are formed from radical-radical interactions.

- If diffusion is too easy, as in the case when radicals are formed in isolated spurs, then the molecular product yield would be expected to be small.
- In a track, where the spurs are much closer together, the high radical concentration gives much higher molecular yields.

6.9 The Fricke Dosimeter

It is customary to quantify the radiation-induced changes in the concentration of ions or radicals in a material by making use of the G-value. This is the number of a given species produced for every 100 eV of energy deposited.

The Fricke dosimeter system uses a 1 mM l^{-1} air-saturated solution of ferrous ammonium sulphate in 0.4 mM l^{-1} dilute sulphuric acid. Radiation-induced conversion of ferrous to ferric ions enables its use as a secondary dosimetry standard in the range 20 - 200 Gy (Chapter 7). Optical absorption of the solution is measured at a wavelength of 304 nm at which the ferric ion absorbs strongly and the ferrous ion not at all. It is therefore necessary to know the G-value for the conversion of ferrous to ferric ions, to be able to relate the measured number of ferric ions produced to the energy deposited.

Because the concentrations are small, the system can be considered to be effectively water, producing molecular products as in Eqs.(6.10) and (6.11). A slightly acidic solution is used because the dissociation of the products H_2O_2 and $OH^{\bullet}$ have their equilibrium states to the right of the equations :

$$H_2O_2 \leftrightarrow H^+ + O_2H^- \tag{6.12}$$

$$OH^{\bullet} \leftrightarrow H^+ + O^- \tag{6.13}$$

In other words, it is more probable than not to find the molecule (or ion) in its undissociated state. In chemical parlance, the pK of the reaction is high (>11) so an acidic solution ($pH < 7$) will have most of the molecules existing as molecules (or radicals) and not as charged ions.

Any ferrous (Fe^{++}) ions in solution could therefore be oxidized by the undissociated species according to the equations :

$$Fe^{2+} + OH^{\bullet} \rightarrow Fe^{3+} + OH^- \tag{6.14}$$

$$Fe^{2+} + H_2O_2 \rightarrow Fe^{3+} + OH^{\bullet} + OH^- \tag{6.15}$$

The $OH^{\bullet}$ radical in Eq.(6.15) can then oxidize a further Fe^{2+} ion according to the first reaction.

Even though it is more probable that the equilibrium state lies to the left in Eqs.(6.12) and (6.13), there will still be some H^+ ions present. These can react with the radical $H^{\bullet}$ from Eq.(6.11), to give a molecular ion which can oxidize a ferrous ion according to :

$$H^{\bullet} + H^{+} \rightarrow H_2^{+}$$
$$H_2^{+} + Fe^{2+} \rightarrow H_2 + Fe^{3+} \qquad (6.16)$$

Thus, in the absence of any free oxygen, it is possible to say that each molecule of H_2O_2 will produce two Fe^{3+} ions, and each primary $OH^{\bullet}$ radical will produce one Fe^{3+} ion. Furthermore, the consequence of Eqs.(6.16) will ensure that an additional Fe^{3+} ion is produced for each $H^{\bullet}$ radical. Because of the speed of the reactions in Eqs.(6.11), it is not possible to separate the aqueous electron from the $H^{\bullet}$ radical, and so the G-value relation is therefore written with their combined concentrations as :

$$\left(G_{Fe^{3+}}\right)_{vacuum} = 2G_{H_2O_2} + G_{OH} + \left(G_H + G_{e_{aq}^-}\right) \qquad (6.17)$$

However, when there is oxygen present, the $H^{\bullet}$ radical produced in Eq.(6.10) can react with any molecular oxygen that may be present to form another highly reactive radical :

$$H^{\bullet} + O_2 \rightarrow HO_2^{\bullet} \qquad k = 1 \times 10^{10} \text{ l M}^{-1}\text{s}^{-1}$$

which then oxidizes another Fe^{2+} ion according to :

$$HO_2^{\bullet} + Fe^{2+} \rightarrow Fe^{3+} + HO_2^{-}$$

This product ion reacts further with H_3O^{+} to give more H_2O_2 :

$$HO_2^{-} + H_3O^{+} \rightarrow H_2O_2 + H_2O \qquad k = 3 \times 10^{10} \text{ l M}^{-1}\text{s}^{-1}$$

which in turn produces more ferric ions by Eq.(6.15). This then produces a ferric ion for every three $H^{\bullet}$ radicals (or aqueous electron) rather than the one in Eq.(6.17). Thus we have :

$$\left(G_{Fe^{3+}}\right)_{oxygen} = 2G_{H_2O_2} + G_{OH} + 3\left(G_H + G_{e_{aq}^-}\right) \qquad (6.18)$$

6.10 Ionic crystals

Alkali halide crystals have a particular role in radiation science because of their use in scintillation and thermoluminescence detectors. They also have a particular interest

because of their propensity to form colour centres, the formation mechanisms of which also underlie their response to prolonged irradiation. Both are caused by defects in an otherwise perfect lattice [3].

A perfect and un-irradiated crystal has optical absorption bands which appear at wavelengths determined by the lattice spacing and the lattice stiffness constants.

- An alkali halide crystal, for example, with an energy band gap, E_g, of 8 eV, has an inter-band transition at a wavelength of 150 nm (= hc/E_g, where h = Planck constant, c = velocity of light).
- Vibrational frequencies, typically $0.6\times10^{14}\ s^{-1}$, correspond to energy quanta of 0.25 eV and will therefore absorb in the vicinity of 5000 nm.
- When the crystal is perfect, absorption of photons can take place only at these energies.

The presence of defects, whether natural or radiation-induced, introduces permissible energy levels within the band gap. Two energy states are used to describe such a defected system :

- an exciton. This is a bound state of an electron and hole, which can move throughout a crystal as a free exciton transporting energy but not charge. Such a state can become trapped (*i.e.* localized) to create a self-trapped exciton.
- a polaron. This is a mobile lattice distortion which is created when the positive and negative ions of the crystal which surround a positively charged hole are repelled or attracted. The movement of this distortion throughout the crystal is called a polaron. This effect is analogous to the polarization of a solvent molecule which results from a thermalized electron.

The binding energy (in eV) of an exciton in the state n can be expressed in the same terms as those of the hydrogen atom, [3] :

$$BE_n = \frac{-2\pi^2\mu e^4}{\varepsilon^2 h^2 n^2} = -13.6\frac{m_0}{\mu\varepsilon^2 n^2} \qquad (6.19)$$

In Eq.(6.19), e is the electronic charge, ε is the dielectric constant of the crystal, h is the Planck constant, n is the quantum number and μ is the reduced mass of the electron hole pair. The reduced mass of the pair, μ, is expressed in terms of the mass of the free electron, m_0, and the effective masses of the electron, m_e, and hole, m_h, as :

$$\frac{m_0}{\mu} = \frac{m_0}{m_e} + \frac{m_0}{m_h}$$

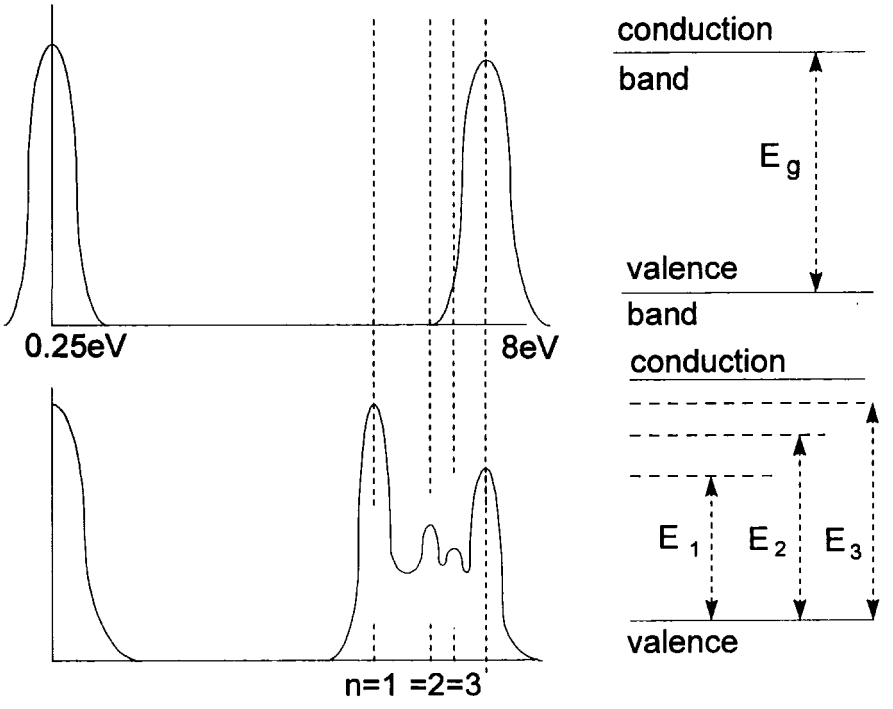

Fig.(6.7) A schematic diagram of the optical absorption of a perfect alkali halide crystal, showing only the interband transitions at 8 eV and vibrational bands at 0.25 eV (top). Defects produce intraband exciton levels which introduce absorption at intermediate energies (bottom), [3]. With permission from CRC Press, Boca Raton, Fla., USA.

Energy levels of each exciton state within the band gap are then given by :

$$E_n = E_g - BE_n.$$

These are shown for n = 1,2,3 in Fig.(6.7), and can be populated by uv photon absorption or by energy deposition from ionizing radiation. In either case an electron is moved from the valence band to one of the exciton levels.

The occupancy of such a level is termed a free exciton, Fig.(6.8 a). Energy has been absorbed in the neighbourhood of an iodine atom which is not sufficient to eject an electron into the conduction band. The electron is therefore bound by the Coulomb force to the positive hole created at the site of the negative ion. This electron hole pair is the free exciton and can move throughout the crystal, transporting energy but not charge.

A Self-Trapped Exciton (STE), Fig.(6.8 b), can be formed either from a free exciton which becomes trapped at an impurity ion or as the result of a lattice distortion. The diagram shows a distortion which produces a potential which traps the hole

itself. The hole in a halogen ion becomes trapped within picoseconds and is immediately shared with neighbouring halogen ions. This process takes place faster than the trapping of an electron in the formation of a free exciton. In the STE the inter-ion distance can be shortened by up to 40% of the normal separation.

If a defect is produced, either by an impurity atom or by a displacement brought about by radiation damage, the exciton can become trapped. This can occur :

- when it dissipates its energy through phonons, or
- when it causes a local lattice distortion which lowers the free energy of the hole to create a self-trapped hole. An electron can then also become trapped to form the self-trapped exciton.

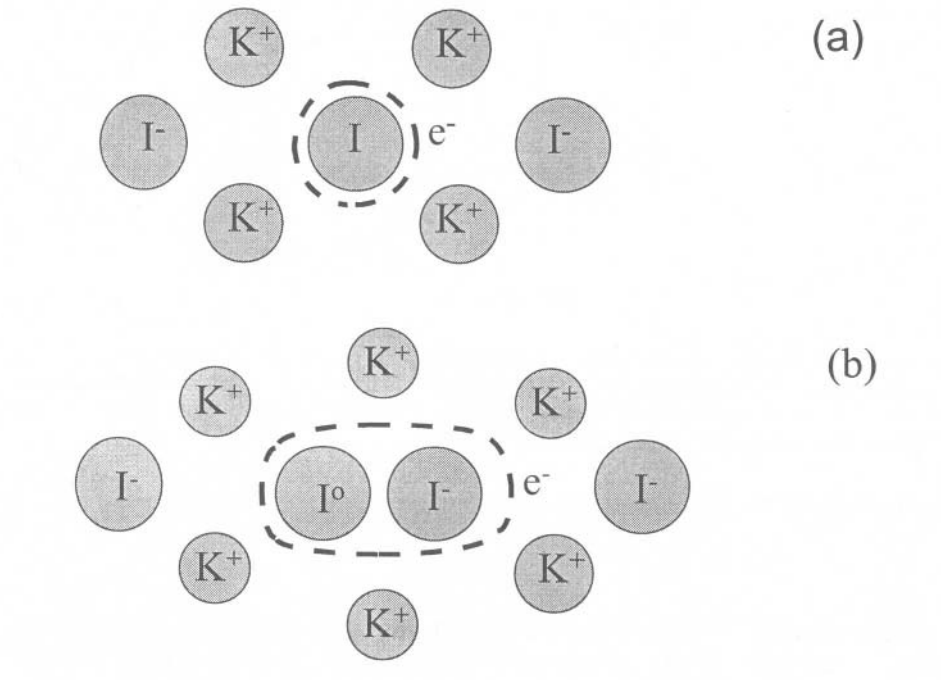

Fig.(6.8) (a) A Free Exciton, (b) A Self-Trapped Exciton, [3]. With permission from CRC Press, Boca Raton, Fla., USA.

The lattice site at which an exciton becomes trapped, whether it is the positive or the negative ion, distinguishes the nature of the exciton. If the electron is trapped at a negative ion vacancy, the exciton is termed an F-centre. If the trapping takes place at a positive ion vacancy a neutral atom results and a V-centre is formed.

A number of studies have been carried out into the effects of intense photon

irradiation on the detection efficiency of CsI(Tl) and Bismuth Germanate (BGO) scintillator crystals. Optical transmission energy spectra of these crystals are altered due to :

- the intrinsic production of colour centres. This depends on the nature of both the host material and the incident radiation,
- the extrinsic effects of impurities in the crystal. These are considered to be largely responsible for afterglow and other time-dependent changes in emission spectra.

Radiation-induced changes have been observed in the optical transmission energy spectra of CsI(Tl) up to 10^3 Gy [4] and in BGO up to 50 Gy [5]. An important consequence of efficiency loss after prolonged irradiation is the change that occurs in pulse height, sometimes over a considerable period of time. Partial recovery of detection efficiency appears to be due to a certain amount of annealing and points, amongst other things, to the importance of the initial crystal growth and its subsequent thermal treatment. These time-dependent effects have implications for the energy calibration of scintillators placed in inaccessible locations and used in high radiation environments over long periods of time [6].

In addition to the band structure modifications referred to above, intense irradiation affects many of the bulk physical properties of ionic crystals, such as conductivity, density and hardness. Potassium iodide crystals, for example, have been shown to have the following response to different types of radiation [7] :

- an air kerma of 1.55×10^3 C kg^{-1} from ^{60}Co γ-rays gives rise to a reduction factor of ~10 in ionic conductivity. Conductivity can be returned almost to its pre-irradiation value by annealing the crystal to 240 °C.
- exposure to a flux of 3×10^{18} fast neutrons $cm^{-1}s^{-1}$ increases the conductivity by ~100.
- intense high LET radiation (protons and low energy electrons) produces a marked increase in surface hardness.
- prolonged exposure to intense fluxes of X-rays eventually causes a decrease in density of all alkali halide crystals. This is apparent through increases in both lattice defects and lattice parameters.

6.11 Radiation Effects in Polymers

The production of long-chain polymers from smaller sub-units – the monomer to polymer conversion – can generally be achieved through chemical, thermal or radiation means, although with widely differing efficiencies. Once formed, however,

polymers can respond to ionizing radiation of sufficient intensity in two principal ways - crosslinking and degradation [8], [9], [10], [11].

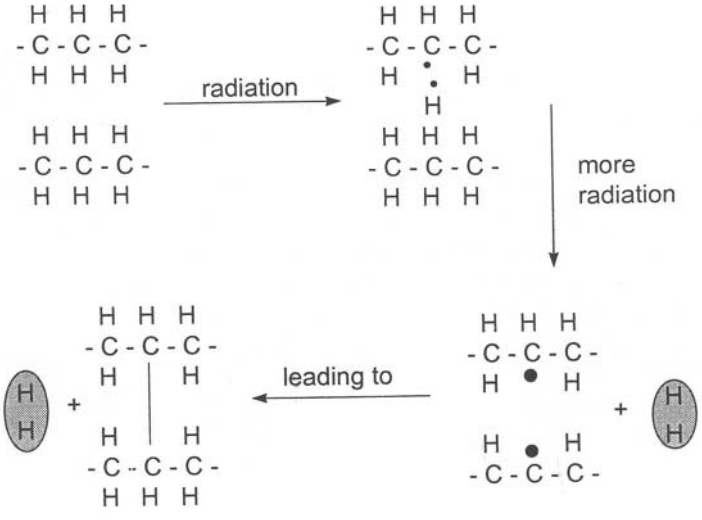

Fig.(6.9) A schematic representation of how a crosslink bond is made between two adjacent polymer molecules. The release of radiolytic hydrogen gas is a often a feature of polymer irradiation, [7].

An example of radiation-induced crosslinking is afforded by polythene, Fig.(6.9). Two neighbouring strands of (- CH_2 - CH_2 - CH_2 -)$_n$ can be linked together to form a single, higher molecular weight molecule. The crosslink is thought to progress in stages as radiation produces radicals on adjacent chains, with the release of radiolytic hydrogen.

Prolonged irradiation eventually produces one very large molecule which can only be broken down again by the scission of chemical bonds through the application of heat. A polymer which has been crosslinked is characterized by :

- a higher viscosity,
- a lower solubility in solvents,
- a higher melting temperature.

In a rather similar way to the reactions in liquid water, the presence of molecular oxygen has a considerable effect on the radiation response of a polymer such as polythene. This appears to be the case whether the oxygenation takes place during or after the irradiation.

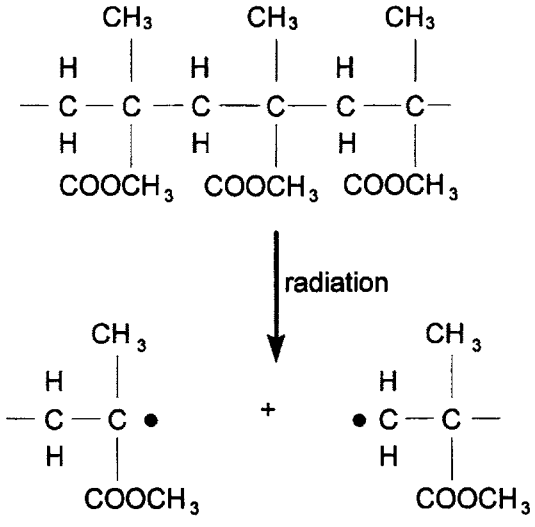

Fig.(6.10) The degradation of poly-methyl-methacrylate by radiation. One of the *C-C* bonds is broken to produce a radical on each of the two fragments, [7].

In contrast, some polymers undergo degradation on exposure to high doses of radiation. This process results in a decrease of the molecular weight when the polymer chains are broken without any rejoining of the ends. A prime example is provided by poly-methyl-methacrylate (known variously as PMMA, Perspex or Lucite).

Subsequent reactions of the two radicals may lead to further breaking of the polymer chain. Whether or not this happens, the radicals are likely to achieve more stable structures of the form $-CH=C$ and CH_3-C-. One consequence of degradation is that the polymer loses its mechanical strength. In the presence of excess oxygen, prolonged irradiation of PMMA will eventually reduce the polymer to a powder.

A graphic example of cumulative radiation damage in PMMA is given in Fig.(6.11). This shows a 1cm thick PMMA flange on an evacuated target chamber in which was held a venetian-blind arrangement of tungsten foils. These were irradiated by X-rays from a 15 MeV electron linac. The PMMA flange had not been exposed to the direct photon flux from the *bremsstrahlung* target, and was therefore subjected only to scattered photons and re-emitted electrons and positrons from pair production interactions within the tungsten foils. For several years after the end of all experimentation, there was no visible sign of any radiation damage in the flange. Over a longer period (~15 years), however, thin branches appeared which gradually became thicker and longer until the whole of the flange became suffused with the "radiation trees" damage shown in Fig.(6.11). This effect illustrates the cumulative collapse of the polymer structure after an initial seeding of damage has occurred.

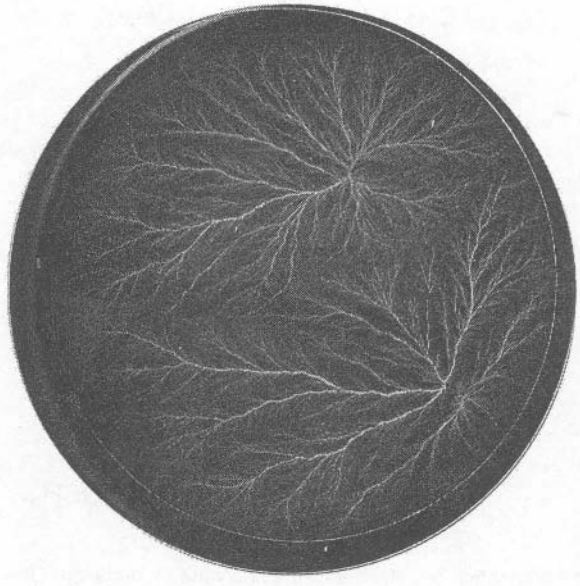

Fig.(6.11) "Radiation Trees" produced in a 1cm thick disc of PMMA ~15 years after having been exposed to high energy X-rays, electrons and positrons. For several years after the irradiation there was no visible sign of any degradation.

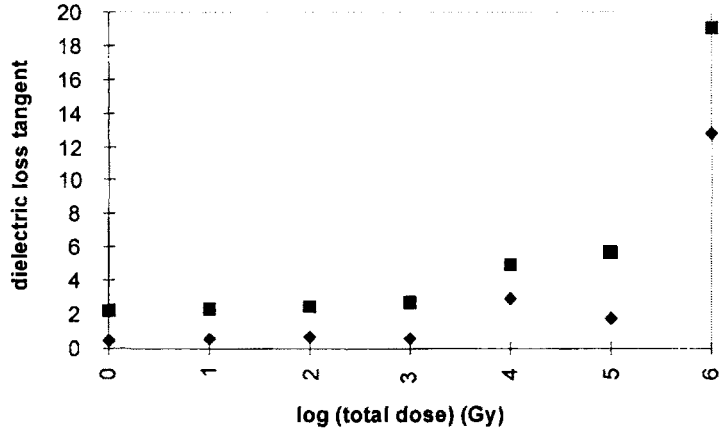

Fig.(6.12) Dielectric loss tangent, tan δ ($\times 10^{-4}$), of polypropylene film irradiated by 1 MeV electrons. Measured at frequencies 50 Hz (◆) , and 10 kHz (■) [12].

In addition to radiation-induced changes in mechanical strength some insulators, polymers amongst them, undergo an increase in conductivity. This tendency has profound effects on the manufacture, design and usage of detectors as primary or secondary radiation standards. Sub-pico-Coulombs of charge cannot be measured reliably in an ionization chamber repeatedly used in high radiation fluxes, if the insulation between electrodes gradually deteriorates. Mainly for this reason, a primary radiation standard instrument is only exposed to radiation when used for relatively infrequent batch calibration of secondary standard instruments.

The importance of polymeric materials in providing high dielectric strength components in satellite and spacecraft instrumentation has lead to studies of their radiation hardness. A typical study of capacitor-grade polypropylene [12] exposed to 1 MeV electrons showed :

- a 5 - 6% increase in dielectric constant at 10^5 Gy,
- a 5 - 10% decrease in breakdown strength at 10^6 Gy,
- a substantial increase in dielectric loss tangents Fig.(6.12) between 10^3 and 10^6 Gy.

In addition to the changes in mechanical properties of this widely used insulating material, the study demonstrated an electrical deterioration under prolonged exposure. This is likely to be due to slow oxidation following the formation of free radicals and ionization by-products.

6.12 Radiation Effects in Glasses

The effects of intense radiation on an amorphous network of - *O* - *Si* - *O* - *Si* - atoms are complex. They are critically determined by :

- the nature and level of doping - by Al, alkali halides, Pb, Zn, Ba etc.
- the thermal and mechanical treatment. This depends on whether the material was pyrolytic fused silica, synthetic crystalline silica, and whether or not it was drawn into fibres.

Many of the above glasses produce colouration which is visible to the naked eye when exposed to doses as low as 10 Gy [13], [14],[15].

Fig.(6.13) indicates that fused silica shows little or no detrimental response to radiation (up to 10^5 Gy) in the infra-red and visible regions. Beyond 3.5 eV, however, there is a loss of ~ 1 dB km^{-1} Gy^{-1} [14] which approximately doubles on irradiation. The doped glass show losses which are larger by almost a factor of 10, even in the infra-red and visible regions.

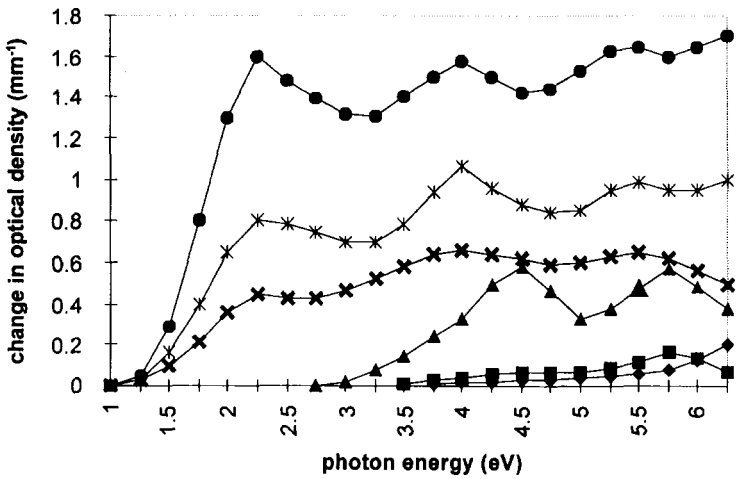

Fig.(6.13) Radiation-induced loss (change in optical density mm^{-1}) in fused silica doped with aluminium and alkali metals when irradiated to a dose of 10^5 Gy. The visible spectral region extends between ~1.75 and ~3 eV, [14].
● unexposed : ■ undoped : ▲ Al(H) : ✖ Al(K) : ✳ Al(Na) : ● Al(Li) .

6.13 Intense Irradiation of Graphite

Pre-cursors of the radiation effects so far discussed have been primarily chemical in origin. Recall that energy deposition has, in these cases, lead to electronic excitation – ionization, radical formation, *etc.* – and its eventual de-excitation, sometimes over considerable periods of time.

High neutron fluxes in nuclear reactors are an important cause of physical effects. Nowhere are these more apparent than in the ability of graphite to store energy in radiation-induced crystal defects after prolonged and intense exposure to neutrons. All materials in a nuclear reactor receive large cumulative radiation doses during the course of a fuel cycle (the time between consecutive refuelling operations - generally 3 to 4 weeks). In a graphite-moderated reactor, however, there is an important safety issue concerning the rise in temperature of the large mass of graphite which results from this radiation damage. An uncontrolled release of this stored energy is known as a *Wigner* energy release.

Under normal circumstances the temperature of a mass of material having specific heat capacity, C_g, (see section 7.10.1) will rise by ΔT if energy ΔH from an external source is totally absorbed. If a portion ΔE is stored as a certain concentration of defects, rather than resulting in an immediate increase in lattice vibrations (*i.e.* temperature), it can be restored at a rate $\Delta E/\Delta T$. When this temperature coefficient

is much smaller than C_g (they both have the same dimensions, J kg^{-1} K^{-1}), any release of stored energy is not sufficient to cause an appreciable rise in temperature. There is therefore no severe perturbation in the normal thermal properties of the material. As $\Delta E/\Delta T$ becomes comparable to C_g, however, a self-sustaining energy release can occur which may be high enough to lead to a conflagration.

At a time t the rate of annealing of the defects and the total quantity of stored energy are related by the following expressions [16] :

$$\frac{dE(t)}{dt} = -F(E)\exp(-Q/kT)$$
$$C_g(T)\frac{dT}{dt} = -\frac{dE}{dt} + h(T,t) \qquad (6.20)$$

In Eq.(6.20) $F(E)$ describes the defected state of the graphite and Q is the activation energy for annealing. $C_g(T)$ is the temperature-dependent specific heat capacity and $h(T,t)$ is the amount of heat transferred either from or to the surroundings. Table (6.1) confirms the effect of increasing the irradiation temperature on vacancy and other defect concentrations in graphite, even at high neutron flux levels.

Table (6.1) Production of defects and vacancies in pyrolytic graphite at various neutron fluxes and irradiation temperatures, [16].

Irradiation temperature (°C)	Neutron flux (10^{20} n cm^{-2})	Defect concentration (%)	Vacancy concentration (%)
150	1	1	1.5
300	4	0.03	1.2
450	5	0.01	0.5

Fig.(6.14) shows the temperature-dependent specific heat of pyrolytic graphite, together with the temperature coefficient dE/dT when under intense irradiation. The reactor power levels are given in units of MW day per (adjacent) tonne of uranium fuel at a specified temperature [16]. Note that :

- when irradiation takes place at 150 °C, the stored energy accumulates rapidly and remains a significant fraction of the specific heat even at 600 °C.
- an increase in the irradiation temperature from 150°C to 220°C at 5000 MW day $tonne^{-1}$ reduces the stored energy by a factor of 5 - 6.

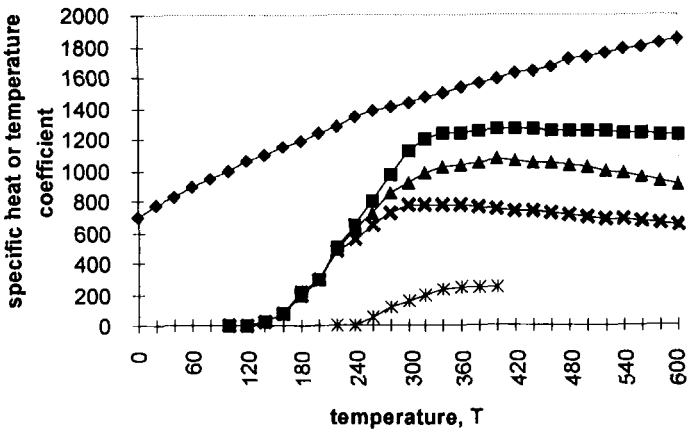

Fig.(6.14) Specific heat (J $kg^{-1}K^{-1}$) of un-irradiated pyrolytic graphite (◆). Temperature coefficient *dE/dT* for the release of stored energy *E* at temperature *T* (J $kg^{-1}K^{-1}$) for various irradiation conditions. ■ 10000 Mega-Watt days/tonne U fuel at 150°C : ▲ 5000 Mega-Watt days/tonne U fuel at 150°C: ✖ 2000 Mega-Watt days/tonne U fuel at 150°C : ✳ 5000 Mega-Watt days/tonne U fuel at 220°C, [16].

The safety implications of the stored-energy effect in graphite are therefore not important so long as the temperature is not allowed to rise in an uncontrolled fashion after the reactor has been shut down. During operation the high temperatures ensure that there is sufficient self-annealing of the defects.

6.14 Radiation Effects in Silicon

Silicon-based detectors play vital roles in two areas where the effects of radiation damage are certainly important, and possibly crucial, in fulfilling design expectations. These are :

- silicon microstrip detectors in the new particle physics experiments at CERN and elsewhere. These must record the time and spatial position of energy deposition events against a background of intense, high stopping power radiation. The gradual deterioration in efficiency and resolution of such detector systems over time is likely [17], [18].
- space-borne communications and imaging systems are subject to large fluxes of energetic electrons together with a somewhat smaller incidence of high stopping power radiation (section 1.1). These result in events such as latch-up, single-event upset and displacement damage [15], [19], Fig.(6.15).

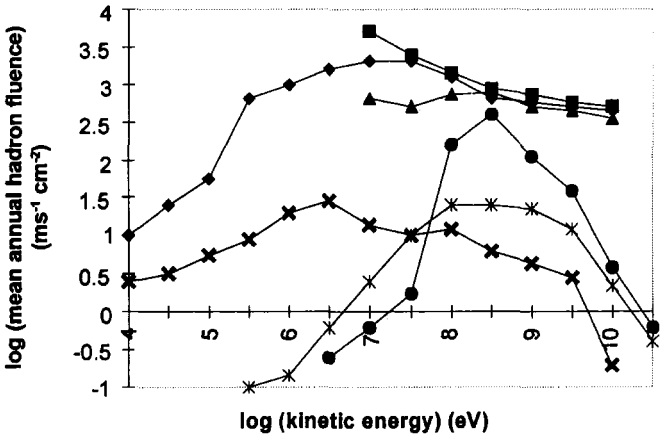

Fig.(6.15) Expected mean annual energy fluences of neutrons, pions and other hadrons at an inner tracker of the Large Hadron Collider (LHC) versus kinetic energy *E* (eV). The ordinate units, *E.dN/dE.dt.dA*, give the number of particles *N* having energy between *E* and *E+dE* crossing unit area per ms. ✖ neutrons : ● pions : ✳ other hadrons :
Also shown are the damage curves in silicon for neutrons, protons and pions relative to 1 MeV neutrons (ordinate scale divided by 10^3 - i.e. the log scale runs from -4 to +1).
◆ neutrons : ■ protons : ▲ pions, [20].

References

[1] International Commission on Radiation Units, **Report 36** (ICRU, Maryland, USA 1983).

[2] J.L.Magee and A.Chatterjee, in *Radiation Chemistry - principles and applications,* ed. Farhataziz and M.A.J.Rogers (VCH Publishers, New York, 1987).

[3] M.Hirai, in *Pulse Radiolysis,* ed.Y,Tabata (CRC Press, Boca Baton 1991).

[4] M.Kobayashi and K.Sakuragi, *Nucl.Instr.Meth.Phys.Res.* **A254** (1987) 275.

[5] G.J.Bobbink, A.Engler, R.W.Kraemer, J.Nash and R.B.Sutton, *Nucl.Instr.Meth.Phys.Res*, **227** (1984) 470.

[6] Ch.Bieler, D.Burkart, J.Marks, M.Riebesell, H.Spitzer and K.Wittenburg, *Nucl.Instr.Meth.Phys.Res.* **A234** (1985) 435.

[7] J.W.T.Spinks and R.J.Woods, *An Introduction to Radiation Chemistry,* (J.Wiley, New York, 1964), p.402.

[8] A.Charlesby, *Atomic Radiation and Polymers*, (Pergamon Press, Oxford 1960).

[9] D.W.Clegg and A.A.Collyer, *Irradiation effects on Polymers*, (Elsevier Applied Science, London 1991).
[10] H.Wilski, *Radiat.Phys.Chem.* **28** (1987) 1.
[11] H.J.Wintle, *Radiology*, **33** (1960) 706.
[12] A.N.Hammoud, J.R.Laghari and B.Krishnakumar, *IEEE Trans.Nucl.Sci.* **NS34(6)** (1987) 1822.
[13] E.Lell, *Physics and Chemistry of Glasses*, **3** (1962) 84.
[14] E.Lell, N.J.Kreidl and J.R.Hensler, *Progress in Ceramic Science*, **4** (1966) p.1.
[15] A.Holmes-Siedle and L.Adams, *Handbook of Radiation Effects*, (Oxford University Press, Oxford, 1993).
[16] J.Gittus, *Irradiation Effects in Crystalline Solids*, (Applied Science Publishers, London,1978).
[17] RD2 Status Report CERN/DRDC/93-18 (1993).
[18] RD20 Status Report CERN/DRDC/94-39 (1994).
[19] A.M.Chugg, *IEE Eng.Sci.Education J.* (June 1994) 123.
[20] M.Huhtinen and P.A.Aarnio, *Nucl.Instr.Meth.Phys.Res.* **A335** (1993) 580.

CHAPTER 7

DOSIMETRY

7.1 Definitions

In the discussion of external beam parameters for radiation dosimetry, it is customary not to use physical quantities such as intensity, current and power, but to refer instead to fluence.

(a) Particle fluence : The total number of particles, n, crossing unit area, da.

$$\Phi = \frac{n}{da}$$

(b) Energy fluence : The summation over all the particles, n, of the number of particles, N_m, times their energy, $h\nu_m$, crossing unit area.

$$\Phi_E = \frac{\sum_{m=1}^{n} N_m \; h\nu_m}{da}$$

(c) Particle fluence rate : The total number of particles crossing unit area per second.

(d) Energy fluence rate : The summation of particle number times particle energy, per unit area per second.

(e) Exposure :

- This is related to the old unit of the Roentgen, which was defined originally as 1 e.s.u (electrostatic unit) of charge liberated in 1 cm^3 of dry air at STP (Standard Temperature of 20°C and Pressure of 760 mm Hg). It implied the use of an ionization chamber irradiated by an external beam of X-rays.
- Using S.I. units, exposure is now defined as the amount of charge liberated in 1 kg of dry air at STP. So Exposure is $X = dQ/dm$ with units of C kg^{-1}.
- The conversion to the Roentgen (R) is :

$$1 \text{ R} = 2.58 \times 10^{-4} \text{ C kg}^{-1}.$$

(f) Kerma :

- This is the Kinetic Energy Released in the Material (or per unit Mass). As in all considerations of radiation effects, it is necessary to specify completely the volume (or mass) in which energy is transferred from the incoming radiation to the medium. This is because of the large variety of secondary radiations that can follow the primary interaction. These may have ranges which are either much smaller or much larger than the specified volume.
- Eq.(6.1) describes the stochastic release of energy in a given (small) volume. As the size of the volume increases, we get a mean value of energy released (transferred). This is the non-stochastic kerma value, $K = dE_{tr}/dm$ in units of J kg^{-1}. E_{tr} is the average amount of energy transferred from the incoming radiation to the electrons of the medium.
- Kerma has two components. Collision Kerma : K_{coll}. All the energy that is transferred to the medium is given to secondary particles, generally electrons, which deposit all their energy locally. That is, they subsequently undergo only ionization and excitation collisions. Radiation kerma : K_{rad}. Here, the secondary electrons have such high energies that their subsequent interactions all result in the production of penetrating *bremsstrahlung* radiation which transports the energy away from the site of primary interaction. Thus $K = K_{coll} + K_{rad}$. If the fraction of energy lost to *bremsstrahlung* radiation is g, then $K_{rad} = g\,K$ and so :

$$K_{coll} = K(1 - g) \tag{7.1}$$

(g) Absorbed Dose :

- This is the amount of energy actually absorbed in the specified mass. Thus $D = dE_{ab}/dm$ in units of J kg^{-1}. The S.I. unit of absorbed dose is the Gray (Gy). 1Gy = 1 J kg^{-1}. The old unit of absorbed dose is the rad, which is defined as 100 erg g^{-1}. The relation between old and new units is : 1rad = 0.01 Gy = 1cGy.
- As the specified volume becomes infinitely large, the absorbed dose D must approach K, since all energy transferred will eventually be absorbed in a large medium, even if K_{rad} is large.
- At low energies, when the secondary particles have low energies (so that $K_{rad} \rightarrow 0$), and ranges no larger than the specified volume, then $K = D$.
- At high energies, the secondary particles can have ranges larger than the distance over which the primary beam has a significant drop in intensity. In this case $K \neq D$.

(h) Equivalent Dose :

- This signifies the different effects that different radiation types have on biological material. Each radiation type is assigned a Weighting Factor,

ω, based on decades of study of radiobiological experiments, radiation accidents and atomic bomb incidents (see chapter 11). It is related to the physical absorbed dose by the relation:

Equivalent Dose (Sievert) = Absorbed Dose (Gray) × Weighting Factor

7.2 Charged Particle Equilibrium

Charged Particle Equilibrium (CPE) is said to exist in a given volume of material if the number of charged particles of a given type and energy leaving the volume is equal to the number entering it over the same period of time. This definition implies that the energy spectrum is always constant throughout the volume.

For CPE to exist in a given volume, therefore :

- There must be no attenuation of the radiation field over the whole volume. This condition applies principally to indirectly ionizing radiation (X- and γ-rays). Charged particles, in particular those that are heavy, will always suffer significant reduction of energy as well as fluence as they travel through a medium.
- The specified volume must not be so small that it contains significant statistical fluctuations in fluence.
- The medium must have a homogeneous density and atomic composition throughout the volume.
- There must be no electric or magnetic fields to cause a change in energy fluence across the volume.

There are two clear instances where Charged Particle Equilibrium is not expected to be achieved – (a) at an interface being irradiated with low energy photons and (b) in the build-up region of a material being irradiated with any high energy radiation.

7.2.1 An interface irradiated by low energy photons

Fig.(7.1) illustrates the secondary electron tracks at an interface between materials having a change in density, ρ, or atomic number, Z, or both. When there is a difference only in Z, low energy photon interactions are dominated by the photoelectric interaction. For a difference only in ρ, it is the Compton interaction that is the most important. In either case, there is a preponderance of secondary electrons at one side of the interface. For a change in Z we have :

- Near the interface the electrons which appear in region A originate in both materials. In region B they only come from the high Z-material so long as B is at a distance from the interface which is greater than the secondary electron range.
- For the same incident photon fluence, the large difference in photoelectron

production rate from the photoelectric interaction ($\propto Z^{3.5}$) ensures that CPE will exist in B but not in A.

- This situation obtains whatever the momentum given to the secondary electrons. Even at very low energies, where the angular distribution of the photoelectrons is nearly isotropic, it is the difference in Z which is important.

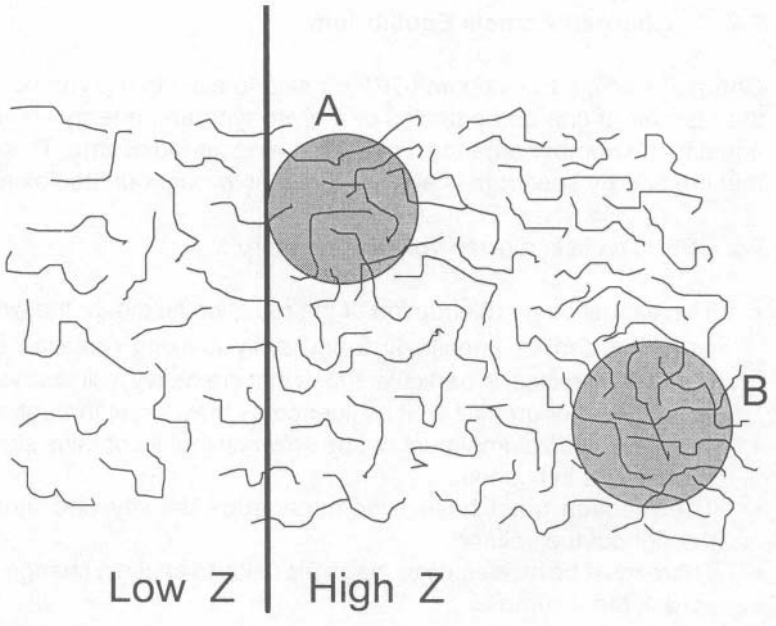

Fig.(7.1) Secondary electrons resulting from photoelectric interactions at an interface between low and high atomic number materials.

7.2.2 *The build-up region for high energy radiation*

In the build-up region near the surface of a medium irradiated at high energies, secondary electrons tend to be emitted anisotropically in the forward direction, Fig.(7.2). It is assumed in Fig.(7.2) that there is no attenuation of the radiation with distance. For an incoming high energy photon beam we assume :

- Four electron tracks start in each depth increment. Since there is no change in photon energy with depth, the track lengths are constant with a mean range of three depth increments. For no reduction in intensity with depth, the collision kerma must also be constant in each of the depth increments.
- For the purposes of illustration in Fig.(7.2), it is assumed that the electrons deposit energy uniformly along their track length. *i.e.* dE/dx is constant.
- The number of tracks crossing each of the 10 incremented layers are 4,8,12,15,15,15,15,15,15,15. The spectrum of electrons cannot be the same in the first 4 layers since both the number of tracks, as well as the portion of each

track, is different. CPE therefore exists only at depths beyond the 4th layer.

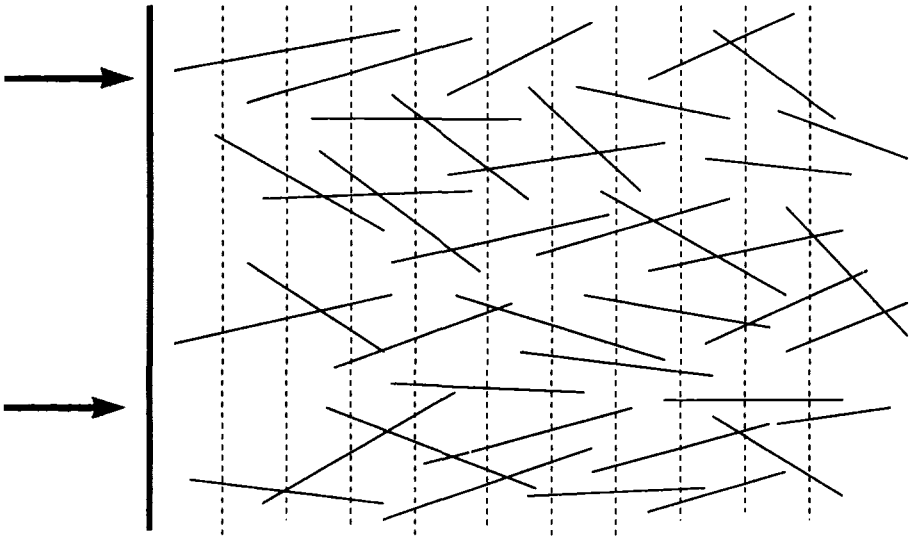

Fig.(7.2) An illustration of the lack of CPE in the region near the surface of a material being irradiated with high energy photons. The phenomenon of build-up is observed in all high energy radiation and is due to the production of forward-directed secondary charged particles. For incident neutrons, the initial charged particles are protons which then generate electrons.

In a realistic situation there is always some attenuation of the incident fluence with depth because of scatter and absorption. Fig.(7.3) considers a similar case to Fig.(7.2) but now includes attenuation. Again, we assume that no energy is lost to radiation, $K_{rad} = 0$ and $K = K_{coll}$, and that the kerma is approximately proportional to the length of the electron track (i.e. 3 depth increments). Fig.(7.3) shows that the first two depth increments each have 5 electrons starting within them, the next two increments have 4 electrons starting, and so on.

- The attenuation of the incident beam causes the collision kerma to be larger than the absorbed dose at depths greater than the 3rd layer.
- The point at which the collision kerma and absorbed dose curves become parallel – the 4th layer and beyond in Fig.(7.3) – is where Transient Charged Particle Equilibrium exists.
- When K_{rad} becomes significant it is constant with depth for incident photons. However, it decreases with depth for incident charged particles as they lose energy and become less efficient at producing *bremsstrahlung*. The total kerma can therefore become greater than the absorbed dose at all depths.

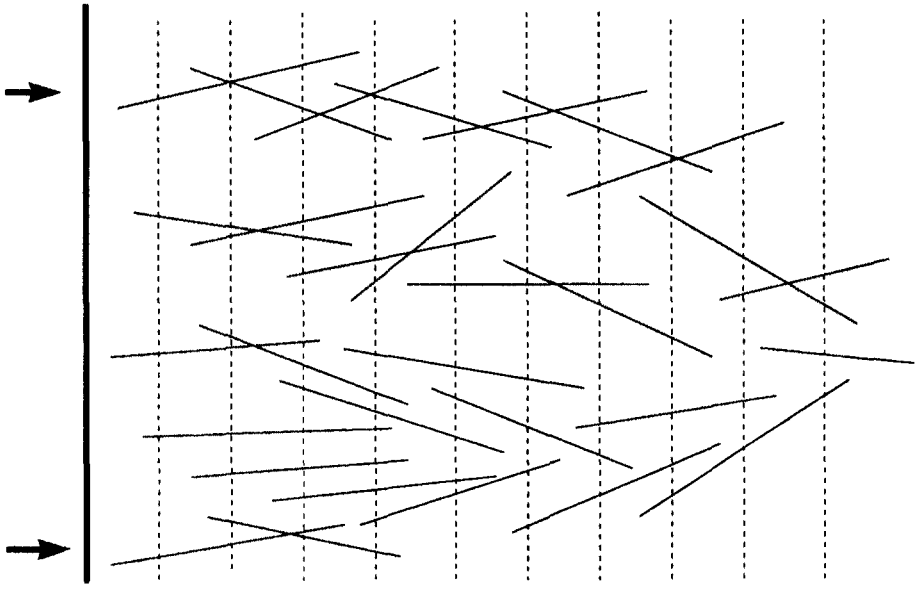

Fig.(7.3) An illustration of Transient CPE which obtains when the incident high energy radiation is attenuated. Under the simplifying conditions used, the collision kerma in each of the depth increments will be proportional to the number of tracks times the energy equivalent (3) of each, i.e. 15, 15, 12, 12, 9, 9, 6, 6, 3, 3. The absorbed dose, however, is proportional to 5, 10, 14, 18, 17, 13, 11, 10, 8, 6. These figures can be checked by counting the number of track segments in each layer.

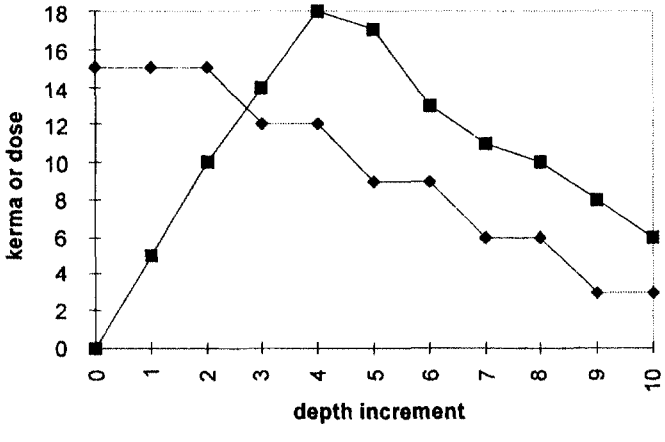

Fig.(7.4) Absorbed dose (■) and kerma (◆) as a function of depth in arbitrary units, Fig.(7.3). The poor statistics are due to the small number of tracks considered and the crude assumptions made regarding the relationship between track length and energy deposited (each track 3 units long containing 3 units of energy). Consideration of a larger number of particles, together with the correct descriptions of angular scatter and electron stopping powers, will yield smooth curves.

Fig.(7.4) illustrates the dependence of both kerma and absorbed dose on depth in this simple example.

7.3 Photon Interaction Coefficients

In order to introduce the probability of interaction into the definitions given in section 7.1, we can express kerma as :

$$K = \Phi\left(\frac{particles}{area}\right) \times \frac{\mu}{\rho}\left(\frac{m^2}{kg}\right) \times \overline{E_{tr}}(J) \tag{7.2}$$

where $\overline{E_{tr}}$ is the mean energy transferred from the incident radiation to the electrons, and μ/ρ is the total mass attenuation coefficient. If E is the energy of the incoming photon and μ_{tr}/ρ is the mass energy transfer coefficient :

$$\frac{E_{tr}}{E} = \frac{(\mu_{tr}/\rho)}{(\mu/\rho)}$$

Eq.(7.2) can also be expressed as :

$$K = \Phi \times \frac{\mu_{tr}}{\rho} \times E \tag{7.3}$$

In a similar manner, energy absorbed can be specified as :

$$\frac{E_{en}}{E} = \frac{(\mu_{en}/\rho)}{\mu/\rho}$$

where μ_{en}/ρ is the mass energy absorbed coefficient. The absorbed dose is then given by :

$$D = \Phi \times \frac{\mu_{en}}{\rho} \times E \tag{7.4}$$

However, all three quantities in Eqs.(7.2), (7.3) and (7.4) depend on the energy of the incoming radiation, as well as on the energy of the secondary electrons produced in the interaction. It is therefore necessary to consider how energy given to each of the individual electrons can be summed to describe the overall energy deposition.

We assume an initial interaction gives energy E_i to an electron with an associated range R_i. The local deposition of energy therefore can be described [1] by a mean stopping power for this one electron as :

$$\bar{S}(E_i) = \frac{E_i(1-g)}{R_i} \tag{7.5}$$

It is important to correctly assign the range here. Clearly, the csda range is inappropriate since we require energy deposited in a given length of the medium. A mean or a projected range would be more suitable. The actual stopping power will, of course, vary over the path of the electron. Eq.(7.5) therefore represents the average of the stopping power over the individual electron track.

When the initial interactions give rise to a spectrum of secondary electron energies, we require a further averaging process to give the mean stopping power :

$$\bar{\bar{S}}(E_i) = \frac{\int_0^{E_i} \frac{d\Phi(E)}{dE}\, \bar{S}(E)\, dE}{\int_0^{E_i} \frac{d\Phi(E)}{dE}\, dE} \tag{7.6}$$

where $d\Phi(E)/dE$ describes the energy-dependent secondary electron fluence. This spectrum could arise from any monoenergetic incident radiation. If, for example, it was produced by a monoenergetic photon, the secondary electron fluence could be described by :

$$\frac{d\Phi(E)}{dE} = \frac{dN(E_i)}{dE_i}$$

where $dN(E_i)/dE_i$ represents the distribution of electron energies resulting from a single photon energy.

Clearly, if there is more than one photon energy present, there has to an additional average taken over this photon energy distribution. The mean stopping power is then a triple average :

$$\bar{\bar{S}}(h\nu) = \frac{\int_0^{h\nu_{max}} \frac{d\Phi(h\nu)}{d(h\nu)} \bar{\bar{S}}(h\nu)\, d(h\nu)}{\int_0^{h\nu_{max}} \frac{d\Phi(h\nu)}{d(h\nu)}\, d(h\nu)} \tag{7.7}$$

This integration extends over all possible photon energies up to the maximum, $h\nu_{max}$. $d\Phi(h\nu)/d(h\nu)$ represents the energy-dependent photon fluence [1].

It is important to remember that the use of the term "stopping power" in the context of photon beams refers to the stopping power of the secondary electrons that result from the photon interactions, and not to the photons themselves.

A similar averaging process to that used in the definition of mean stopping power, can also be used to specify the mean kerma resulting from an incident photon spectrum. In such a case we have :

$$K = \int_0^{h\nu_{max}} \frac{d\Phi(h\nu)}{d(h\nu)} \frac{\mu(h\nu)}{\rho} E_{tr}(h\nu)\, d(h\nu) \tag{7.8}$$

The comparable expression to Eq.(7.2) which defines absorbed dose is now :

$$D = \Phi \times \frac{\mu}{\rho} \times \overline{E_{en}} \tag{7.9}$$

where $\overline{E_{en}}$ is the mean energy deposited in mass dm.

Note that μ/ρ in Eqs.(7.8) and (7.9) refers to the total mass stopping power of the photon. Multiplying by the photon flux and by E_{tr} or E_{en} gives the kerma and dose quantities respectively.

7.4 Relations between Exposure, Kerma and Absorbed Dose

From the definition of exposure in section 7.1 it is necessary to relate the liberation of charge (of one sign) from a mass of material, with the energy needed to effect that liberation. When ionization chambers are used to determine absorbed dose, the parameter required is the W-value. This is defined as the mean energy expended in the production of one ion pair.

The W-value has been determined experimentally only for a small number of gases. It has been shown to be constant at incident energies greater than ~10 keV, but it rises rapidly at low energies as excitation and scattering processes become more probable (see section 2.11.2).

For dry air at STP, the W-value has been determined to be 33.92 eV electron^{-1}. It is commonly expressed as :

$$\frac{W}{e} = \frac{33.92eV / electron \times 1.602 \times 10^{-19} J / eV}{1.602 \times 10^{-19} C / electron} = 33.92 J C^{-1}$$

- Under conditions of electronic equilibrium, the absorbed dose in a mass of air which receives exposure X (C kg^{-1}) is, $D_{air} = X\ W/e$ (J kg^{-1}).
- Alternatively, since ionization can only be the result of collision kerma we can write for exposure in air, $X = K_{coll} / 33.92$ (C kg^{-1}).

7.5 Calculation of Specific Air Kerma

An important and widely used method of gas detector calibration is to determine its response in air to an accurately known flux of γ-rays.

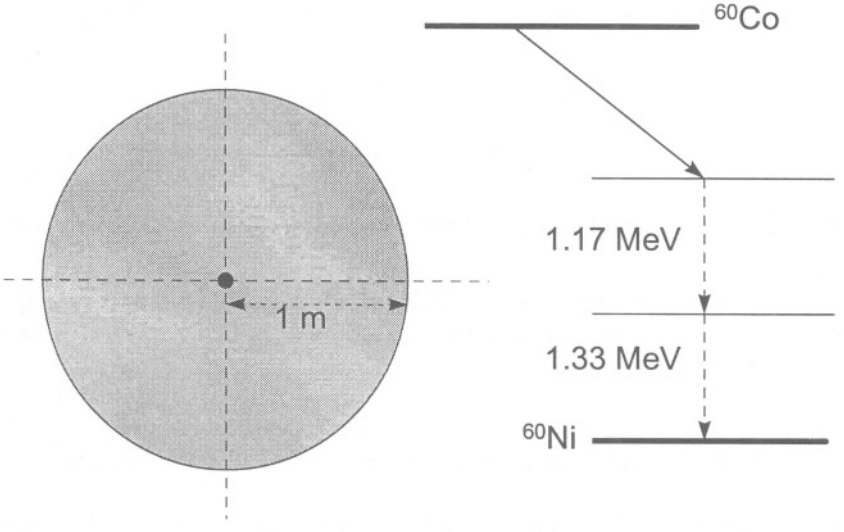

Fig.(7.5) In the calibration of a gas detector for radiation dosimetry or protection purposes, a measurement is made of its response to a point source of precisely-known activity A placed 1 m away. This measurement is then compared with the Specific Air Kerma which can be calculated easily for any known γ-ray source.

In order to calculate Specific Air Kerma it is necessary to know precise values of the following :

- the source activity, A
- the decay branching-ratio, f
- the total amount of γ-energy emitted per disintegration, E

For a point source and point detector placed d metres away, the energy fluence emitted through unit area on the surface of a sphere of radius d is :

$$\Phi_E = \frac{A\,E\,f}{4\pi d^2}$$

If the mass energy transfer coefficient of the medium between the source and detector is (μ_{tr}/ρ) then, from Eq.(7.2) the kerma rate – specifically, the collision kerma rate – is given by :

$$\frac{dK_{coll}}{dt} = \frac{A\,E\,f\,(\mu_{tr}/\rho)1.6\times10^{-13}}{4\pi d^2} \qquad (7.10)$$

where the numerical factor converts from MeV to Joule.

In the case of ^{60}Co, >99% of all decays proceed by β^- emission to the 2.5 MeV state of ^{60}Ni. This then de-excites by emitting two cascading γ-rays of energies 1.17 MeV and 1.33 MeV. The total γ energy emitted per decay is therefore E = 2.5 MeV and f > 0.99, Fig.(7.5).

Strictly speaking, the mass transfer coefficient should be found for the two energies separately. Eq.(7.10) should be evaluated for each in turn and the total kerma obtained from the sum of the two contributions. In the case of ^{60}Co, however, the two energies are sufficiently close that we can approximate by saying that instead of γ energies of 1.17 and 1.33 MeV, we have two emissions at 1.25 MeV. It is then only necessary to find the mass transfer coefficient at this mean energy. Thus :

$$(\mu_{tr}/\rho) = 2.7\times10^{-3}\ \mathrm{m^2\ kg^{-1}}$$

When d = 1 m, and A = 1 Bq, we have the Specific Air Kerma rate at 1 m :

$$\frac{dK_{coll}}{dt} = \frac{1\times2\times1.25\times0.99\times2.7\times10^{-3}\times1.602\times10^{-13}}{4\pi\times1^2} = 8.52\ 10^{-17}\ \mathrm{J\ s^{-1}\ Bq^{-1}}$$

The kerma rate at any other distance can be determined using the inverse square law.

7.6 Measurement of Exposure

Accurate measurements of exposure need to be made using a Free-air chamber. This is not a practical instrument because of its size, and measurements are usually carried out only in a Standards Laboratory. The principle rests on the collection of charge generated in a well-defined volume of air without any interference by, or contributions from, electrons from other sources.

- The volume from which electron collection is made is defined by the precise areas of (a) the incoming beam and (b) the field region from which charges are collected.
- The charge collection volume must be at distances greater than the largest possible range of secondary electrons generated in materials surrounding the specified volume.
- Charged particle equilibrium must be maintained throughout the specified volume. There must therefore be no net change in the number of electrons entering or leaving the volume.
- The technique is suitable only for photons up to ~300 keV. The csda range of electrons having maximum energy in air at this energy is ~73 cm. The central volume should therefore be at least half this distance from the nearest material (whether electrodes or collimator).

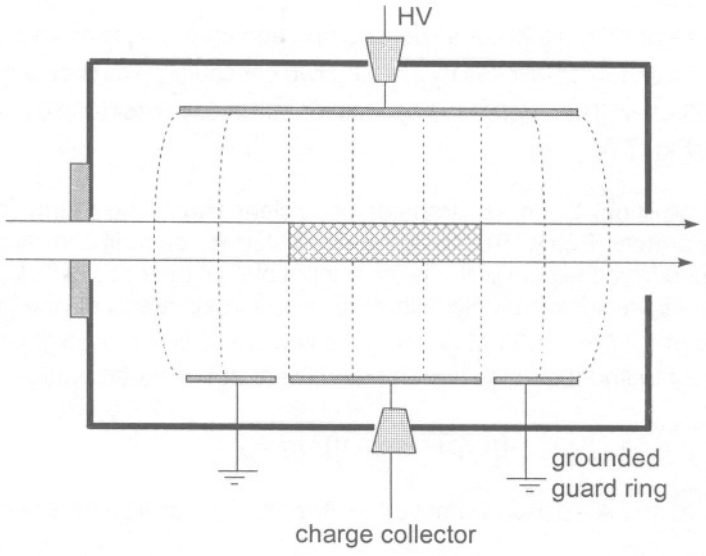

Fig.(7.6) A Free-Air chamber. The central hatched area is at a distance greater than the projected range of the most energetic secondary electron from any of the surrounding material. This applies particularly to the input collimator. In between the collector electrode and the HV electrode the field lines are parallel, thus defining the collection volume, [1]. With permission from Charles C.Thomas, Springfield, Ill. USA.

Secondary electrons which are generated on the up-stream side of the volume will not be swept into the collecting electrode. They may, however, drift into the volume and so be collected. It is therefore important that this number is compensated exactly by those electrons which are lost from the volume.

If the area of the beam in the central region is A, the length of the collector plate is L, the density of air is ρ, then if charge q is collected, the exposure at the centre of the hatched volume is $q/(A \times L \times \rho)$. Johns and Cunningham [1] show that the exposure at the more useful point at the centre of the entrance collimator having an area A_c, is $q/(A_c \times L \times \rho)$.

7.7 The Air-Wall Ionization Chamber

The need to maintain charged particle equilibrium in the sensitive volume in which exposure is measured, together with a requirement for a practical instrument, comes together in the air-wall chamber. The design rests upon the following principle.

Charged Particle Equilibrium will certainly exist within a small air volume located at the centre of a much larger volume which is uniformly irradiated by a beam of photons, Fig.(7.7).

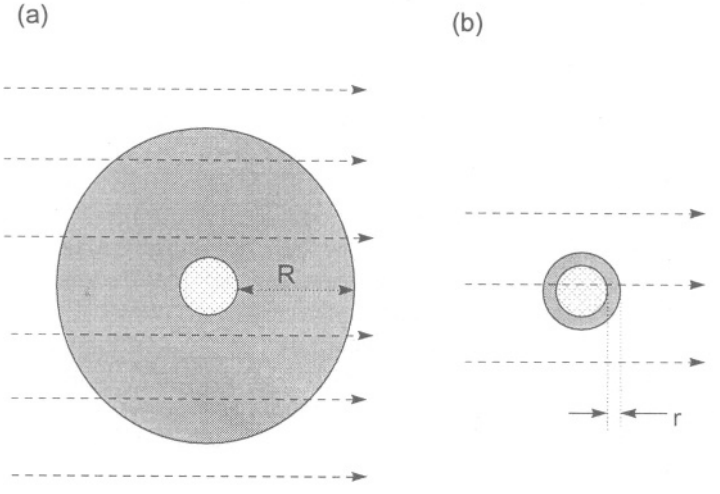

Fig.(7.7) (a) a large volume of air contains at its centre a small hatched volume, which is surrounded by a shell of thickness R. (b) When R is condensed into a solid shell of thickness r, charged particle equilibrium will still exist throughout the hatched volume. The requirement is that all the secondary electrons which cross the hatched volume, originate in the shell r and that none are generated within the volume.

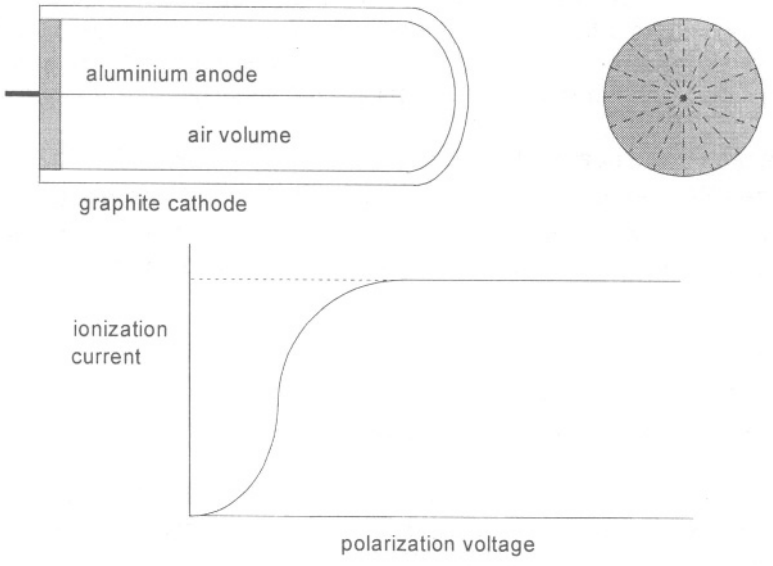

Fig.(7.8) A "thimble" ionization chamber. If the cathode material is non-conducting (e.g. an air-equivalent epoxy), its inner wall can be made suitable for use as an electrode by the application of a thin layer of colloidal graphite. The insulator between anode and cathode must be of the highest quality in order to keep the leakage current down to the order of picoamperes or less. The radial field lines mean that the field strength is highest nearest the anode. At a sufficiently high polarization voltage between anode and cathode, the ionization current saturates when all secondary electrons are collected. At lower polarization voltages recombination takes place.

Practical considerations for such a chamber are as follows:

- An ionization chamber for low energy photons, and which has an outer wall and an inner electrode having Z_{eff} approaching that of air (7.78), will approximate to an air-equivalent chamber. Such a practical chamber would therefore be one which had, for example, an outer cathode of graphite (Z=6) and an inner anode of aluminium (Z=13).
- If the wall material is made from a tissue-equivalent plastic, then a thin layer of conducting material must be placed on the inside surface.
- The wall thickness must not be so thick that it attenuates the incoming photon flux so much that the measured dose is lower than it otherwise would be.
- The wall thickness must be thick enough to ensure that all the secondary electrons which cross the air cavity arise only in the wall material and not in the air cavity itself.
- In practice the wall thickness of such a chamber is in the range 400 - 700 μm for photons in the energy range 150 - 300 keV. If the chamber is to be used for higher energies, then an air-equivalent build-up cap is placed around the graphite cathode in order to maintain CPE.
- An ionization chamber therefore measures the dose in the wall material by collecting the charge released into the air volume.

For an air cavity volume of V, air density ρ and measured ionization current i, the exposure rate is $i/(V \times \rho)$. The dose in the wall is then $(i \times W)/(V \times \rho)$.

7.8 Cavity Theories

The air-wall chamber is restricted to the measurement of exposure in a small volume of air, within an assumed larger volume of "solid" air. Low energy photons, which interact primarily by photoelectric and Compton processes, are assumed to maintain the condition of Charged Particle Equilibrium. The absorbed dose in "air" can then be obtained through the use of the W-value and the relations given in section 7.3.

Cavity theories, of which the most important is the Bragg-Gray theory, deal with the conditions and coefficients that are required in order to find the absorbed dose in a medium other than air. In particular, they enable the CPE condition to be relaxed so that dose can be determined in regions where the dose is changing rapidly. Two of these, discussed in section 7.2, relate to the build-up region of high energy beams and the neighbourhood of interfaces irradiated by low energy photons.

7.8.1 Bragg-Gray cavity theory

The starting assumptions in the Bragg-Gray theory are as follows :

- It applies to all radiations (directly and indirectly ionizing) and considers an interface between a gas and a wall material. A fluence of charged particles is assumed to cross this interface.
- If the fluence does not change, the energy absorbed either side of the boundary is in the ratio of the stopping powers of the charged particles in the two media. This definition includes both primary and secondary charged particles. Thus, the dose D is :

$$D_w = D_g \frac{(S/\rho)_w}{(S/\rho)_g}$$

  where the subscripts w and g refer to the wall and gas respectively, and S/ρ is the mass stopping power.
- The dose in the wall of an ionization chamber which measures exposure X is then :

$$D_w = X \frac{W}{e} \frac{(S/\rho)_w}{(S/\rho)_g} \qquad (7.11)$$

- This is similar to Eqs.(7.4) and (7.9), except that explicit correction is now made for the stopping power of the different materials, rather than relying on the

assumption that CPE always holds.

- The theory requires that the gas volume is small compared with the range of secondary charged particles that cross it. This implies that charged particles neither start nor stop in the gas volume.
- It further assumes that the energy losses along the tracks crossing the gas cavity are small, and that the fraction of energy lost by a primary charged particle is negligible compared to that from the secondary particles.
- Finally, Eq.(7.11) requires that the energy spectrum is known in order to be able to compute the stopping powers.

The stopping power ratio in Eq.(7.11) may be obtained using data given in [1] for the monoenergetic photon energies given in Table (7.1). The mean stopping power is obtained following the double integration, as in Eq.(7.6), using data for a graphite wall and an air volume of gas.

Table (7.1) Stopping power ratios for carbon to air. The anomalous ratio at 100 keV is due to the fact that the stopping power in air does not scale with the concentration of nitrogen and oxygen at this energy. Stopping power values in air, nitrogen and oxygen (MeV cm^2 g^{-1}) are 15.6, 17.0 and 15.0 compared with the values at 10 keV (31.8, 32.2 and 31.0) and 1000 keV (2.47, 2.48 and 2.43).

Energy (keV)	2	10	100	1000	2000	20000
$(S/\rho)_c / (S/\rho)_a$	1.034	1.025	1.186	1.008	0.945	0.915

7.8.2 Corrections to the Bragg-Gray cavity theory

The main corrections to the Bragg-Gray theory now account for the possibility that the size of the cavity may be comparable to, or even greater than, the range of the secondary electrons. In this case low energy electrons can now stop within the cavity, leading to a change of energy fluence over the cavity volume. Developments of the Bragg-Gray theory by Spencer-Attix [2] and Burlin [3] deal with changes in the electron spectrum across the cavity.

7.9 Practical Aspects of Ionization Chamber Dosimetry

7.9.1 Determination of absorbed dose in a medium

When the Bragg-Gray theory is valid the dose to a medium *m*, which replaces the ionization chamber under identical irradiation conditions, is expressed as :

$$D_m = X \frac{W}{e} \frac{(S/\rho)_w}{(S/\rho)_g} \frac{(S/\rho)_m}{(S/\rho)_w} \tag{7.12}$$

The subscripts *g,w,m* in Eq.(7.12) refer to the ionization chamber gas, wall material, and the medium respectively. Other quantities are defined in section 7.8.1. In practice, of course, the use of an air chamber reduces Eq.(7.12) to :

$$D_m = X \frac{W}{e} \frac{(S/\rho)_m}{(S/\rho)_{air}}$$

7.9.2 Temperature and pressure corrections

Density, and hence the mass of gas in a chamber cavity, is temperature and pressure dependent. The measurement of charge or current, Q_m, at temperature T (°C) and atmospheric pressure P (mm Hg) should therefore be related to standard conditions (STP) by :

$$Q_{STP} = Q_m \left[\frac{760}{P} \frac{273+T}{273+20} \right]$$

Multiplying the chamber reading by the quantity in square brackets thereby corrects the reading to a reference temperature of 20°C (22°C is used in the USA).

7.9.3 Polarity effects

A reversal of the polarizing voltage will generally result in a different amount of charge collected from an ionization chamber. The effect is due to :

- the attraction or repulsion of primary electrons by the collecting electrode. This will add to, or subtract from, the secondary charge produced by ionization in the chamber wall.
- the different mobilities of positive and negative ions. A different space charge distribution for different collecting electrode polarities will distort the local electric field.

The primary energy spectrum and the size and thickness of the collecting electrode are the main factors responsible. The effect is generally smaller at high (electron) energies and can be further reduced by using a collecting electrode which is thin in comparison with the thickness of the chamber sensitive volume.

The polarity correction is given by :

$$f_{pol} = \frac{|Q^+| + |Q^-|}{2Q}$$

where the superscripts + and - indicate the reading Q taken with a positive and negative collecting voltage respectively. Q in the denominator is the reading taken with polarity normally used in measurements (generally negative).

An empirical study on the energy dependence [4] finds a polynomial relation between the correction factor for a negative bias and the mean electron energy at a depth z in a phantom. For a number of widely used chambers this is :

$$f^{-} = a_0 + a_1 E_{m,z} + a_2 E_{m,z}^2 + a_3 E_{m,z}^3$$

where $E_{m,z}$ is the mean electron energies at depth z, and the coefficients a_0, a_1, a_2 and a_3 are of order unity, 10^{-3}, 10^{-4} and 10^{-6} respectively. Chamber Polarity effects are discussed in more detail in [5] and references therein.

7.9.4 Ion recombination

Fig.(7.8) shows the much reduced ionization current when the polarizing voltage is insufficient to draw all the electrons towards the collecting electrode. This is due to ion recombination and is a particular problem in pulsed beams where the peak generation rate of charge is orders of magnitude higher than the mean.

For a given chamber design, the polarizing voltage, the counter gas pressure and the incident dose rate are the factors which determine the importance of recombination.

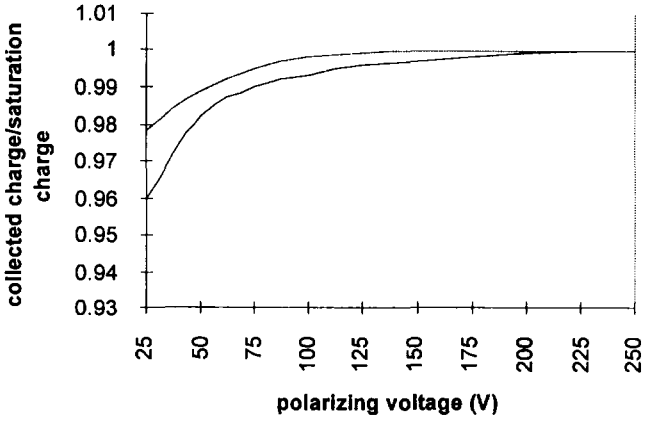

Fig.(7.9) The reduction in efficiency of a parallel plate ionization chamber at low polarizing voltage due to recombination. Top curve, 4 MeV electrons : Bottom curve, 18 MeV electrons. Data adapted from [5].

A distinction is made between initial and general recombination.

- In initial recombination the electrons and positive ions produced in the same event recombine along the original track. This is independent of dose-rate and is generally small, except where the density of electrons and ions becomes so great that the polarizing field is insufficient to separate them.
- In general recombination the diffusion of the primary charged species has taken place and the initial track structure has been lost. Recombination therefore involves neighbouring tracks, whose proximity clearly depends on dose. Since rapid collection of the ions is essential, dose-rate then becomes the important parameter.

When general recombination is present, the reduced collection efficiency of an ionization chamber is :

$$\frac{\text{measured charge}}{\text{saturation charge}}$$

This can be expressed as $F=[ln(1+u)]/u$ where u is dimension-less and is defined as :

$$u = \frac{\alpha}{e}\left(\frac{1}{k_e + k_{ion}}\right) r\, d\, \frac{d}{V} \qquad (7.13)$$

- the recombination coefficient, α, is the constant of proportionality which relates the chance of recombination per unit volume of gas per unit time to the product of the two ion concentrations, Eq.(5.3). It has a value in air of $\sim 1.6\ m^3\ s^{-1}$,
- e is the electronic charge,
- k_e and k_{ion} are the mobilities of the electron and positive ion respectively. Both their values in air are $\sim 1.8 \times 10^{-4}\ m^2\ s^{-1}\ V^{-1}$,
- r is the initial charge density liberated in a certain pulse of radiation,
- d is the electrode separation and V the collecting (polarization) voltage.

Note that a high collection efficiency (denoting minimum recombination) is achieved when u in Eq.(7.13) is small. This occurs when the mobilities of the charges are high, the electrode spacing is small, and when the polarizing field is high. The required correction to an ionization chamber to account for recombination is the reciprocal of the collection efficiency, *i.e. 1/F*.

Further details on recombination effects are provided in [5] and references therein.

7.10 Calorimetry

Calorimetry provides the best available route to an absolute determination of absorbed dose. It determines the energy deposited by the incoming radiation as heat in a unit mass of material, through the measurement of temperature rise. When correctly applied, the method can be used as a primary standard. However, corrections may need to be made for :

- heat loss though conduction, convection and radiation from the core,
- radiation loss through *bremsstrahlung* interactions in the core,
- any heat defect resulting from chemical reactions, which may be exo- or endothermic. These prevent all the absorbed energy from being converted into heat. In order to reduce these effects to a minimum, most standard calorimeters have a graphite core. This then introduces uncertainties in the conversion from measured dose in graphite to dose in another material, such as water, which is irradiated under identical conditions.
- poor thermal conductivity within the core which may result in an underestimated temperature rise.

As in the case of ionization chambers, the range of both primary and secondary charged particles is crucial in the interpretation of the amount of energy deposited.

- If all the energy of a beam is absorbed in the core of the calorimeter, the temperature rise indicates the total energy fluence in the beam. This is often the case with electrons, when the particle range may be significantly less than the core thickness.
- Only in the case where there are facilities available for differentiating the heat loss by a given thickness (and hence mass) of a material, can an interpretation of absorbed dose in that differentiated mass be made.

7.10.1 Calorimetry for low energy electrons using a graphite core

Electron beams are the least difficult to calibrate using calorimetry because of the efficient deposition of beam energy. A temperature rise of many degrees is often measured. Low energy electrons present a particular difficulty, however, because of their short range and the uncertainty this causes in specifying the mass undergoing the temperature rise. If "absolute" dose is required, a convenient strategy is to use the energy fluence measurement in the core to monitor the change in energy fluence resulting from energy absorption in incremented layers of thin dye films above the core, Fig.(7.10).

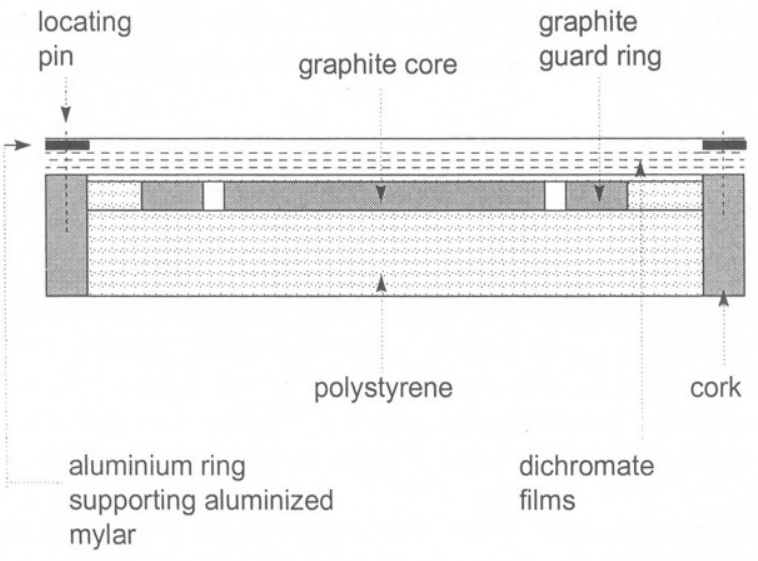

ow energy
electrons (250 - 500 keV). The thickness of the 2 mm core is much greater than the projected range of electrons. Expanded polystyrene surrounds both the core and the guard-ring. Immediately above the 1mm thick polystyrene on the radiation side of the core, is placed a number of dye films.

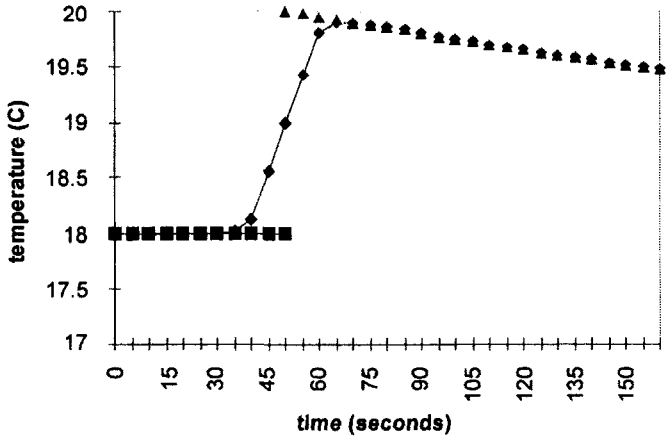

Fig.(7.11) A typical temperature-time response of a calorimeter. Irradiation begins at 35 seconds and ends at 65 seconds. Extrapolation of the temperatures before and after irradiation to the midpoint of the irradiation period (50 seconds) corrects for heat loss during the temperature rise, to give $\Delta T = 2.0\ ^{\circ}K$.

The absorbed dose to graphite (Gy) is then given as :

$$D = C_g \times \Delta T$$

When temperature ΔT is measured in °K, the specific heat capacity C_g is (644.9 + 2.94 × T) J kg^{-1} K^{-1}, whereT is the graphite core temperature in degrees Celsius.

7.10.2 Other calorimeter methods

For a calibration of electron beams at higher energies, the graphite core can be positioned at a certain depth along the axis of the depth dose distribution (generally at the maximum dose - see Chapter 9), and surrounded by graphite. This ensures a uniform field from both the thermal and radiation points of view. The measurement of temperature rise in the well-defined mass of the core now yields the dose (and not merely energy fluence which was the case at the lower energies).

At photon energies above 1 MeV, the calorimeter design is similar to Fig.(7.10) except that the graphite core is now insulated from, and backed by, a much larger volume of graphite. Temperature rise in the core (~1.5 mK Gy^{-1}) is now much smaller than it is in the case of an electron beam.

7.11 Standardization

The necessary procedures for the standardization of radiation dosimeters are set out in the appropriate Code of Practice. The most recent Codes of Practice in the UK are based on the recommendations of two Working Parties set up by the Institution of Physics and Engineering in Medicine and Biology (IPEMB - now the IPEM). These are for :

- Electron dosimetry of radiotherapy beams between 2 and 50 MeV based on air kerma calibration [6], and
- Absorbed dose for X-rays below 300 keV generating potential [7].

These supersede a number of earlier codes which date back to 1971 (electrons) and 1983 (X-rays). The purpose of each code is to recommend :

- the type of instrument to be used,
- the conditions under which the comparison is to be made (e.g. the depth in the phantom),
- the theoretical basis upon which the standarization is made.

Detailed reference should be made to these Codes for the full description of calibration and standardization procedures.

All institutions which require calibration of their routine dosimetry should be in possession of a transfer instrument. This is to be used as a secondary standard for

calibration against a primary standard at the National Laboratory. Routine dosimeters are then calibrated at regular intervals against this secondary standard under identical conditions. Different recommendations for the transfer instrument are made for different energy ranges.

In the case of photons these are specified by their measured Half-Value-Layers in a full-scatter water phantom. The "energy" of a photon beam is an unreliable parameter because of the slight differences in energy spectra which result from different filtration, collimation, etc. in user beams. The determination of dose is to be made at a designated depth using a specified Source Surface Distance (SSD) and field area.

Electron beams have a strong energy dependence with depth. This places strict requirements on the design of the chamber and the point in the phantom at which measurement is made.

7.11.1 Low and medium energy X-rays

The recommended secondary standard chambers in this energy range are :

- 0.5 - 4 mm Cu (160 - 300 kV) NE2561 or NE2622 cylindrical chambers,
- 1 - 8 mm Al (50 - 160 kV) NE2561 or NE2611 cylindrical chambers,
- 0.035 - 1.0 mm Al (8 - 50 kV) parallel plate chamber.

Specification of beam energy

The precise specification of photon energy is fundamental to the setting-up of reproducible calibration procedures. Although the most convenient method is the use of Half-Value-Layer (HVL) because of its simplicity, similar values of HVL can be obtained for two beams having quite different spectra. These could be produced by light filtration at a higher generating potential or by heavy filtration at a lower generating potential. A more reliable measure would therefore be provided by the determination of a complete axial depth dose curve.

The inadequacy of low energy photon beam specification using only the HVL method, was illustrated by a comparison of HVL against generating potential recently made in a large number of UK radiotherapy centres. These showed variations in the range 2 – 7.5 mm Al at the same generating potential of 100 kV [7].

A change of incident spectra with depth can occur because of scatter and absorption. At low energies, where the photoelectric effect is dominant, the spectra hardens slightly with depth because of the preferential removal of low energy photons. At higher energies, where the Compton process is dominant the scatter leads to a small reduction in mean energy.

Theoretical basis

The new code of practice for the above photon energy range is based on the measurement of air kerma – kinetic energy released per unit mass – rather than exposure – charge liberated per unit mass. From section 7.4 :

$$X = \frac{K_{coll}}{W/e} = \frac{K(1-g)}{W/e}$$

Therefore, the total air kerma is : $K_{air} = X \frac{W}{e} \frac{1}{(1-g)}$

If it is assumed that :

(1) at these low photon energies, $g = 0$, and
(2) charged particle equilibrium exists at the point of measurement in the phantom,

the dose in water is equal to the collision kerma in water ($D_w = K_{coll,w}$). Eq.(7.11) can then be rewritten :

$$D_{water} = K_{air} \frac{(S/\rho)_{water}}{(S/\rho)_{air}} = K_{air} \frac{\overline{(\mu_{en}/\rho)}_{water}}{\overline{(\mu_{en}/\rho)}_{air}} \qquad (7.14)$$

An air kerma calibration factor, N_K, for the chamber free in air is provided by the standards laboratory for each user's transfer instrument. This gives the air kerma at the point corresponding to the centre of the chamber in the absence of the chamber. Thus :

$$K_{air} = M \times N_K \qquad (7.15)$$

where M is the chamber reading in the user's beam. In order to obtain the air kerma at a depth in the water phantom, further corrections are now required which are specific to each of the above energy ranges.

0.5 - 4 mm Cu (160 - 300 kV)

The depth in water at which calibration is made is 2 cm. The aim is to calculate the dose at the chamber centre in water. Measurements are, however, made in air. Therefore, the following corrections have to be made :

- The fluence perturbation factor k_Q corrects for the disturbance of the medium (water) by a hole (air). This is likely to cause a change in the energy and angular distribution of photons incident on the surface of the hole (i.e. the chamber).
- A perturbation factor p_{dis} corrects for the replacement of the hole by the host phantom material. This combines the necessary reduction in chamber reading because of the increased attenuation due to the extra material, with the necessary increase due to the extra scatter.
- The stem correction k_{stem} is the ratio that $k_Q p_{dis}$ would have if it were possible to measure the air kerma with a stemless chamber. It is used to account for the slight field area dependence of the total correction factor.
- The change from air kerma to water kerma at the reference depth needs the water to air mass stopping power ratio evaluated for the photon energy spectrum at the reference depth (2 cm).

The absorbed dose at 2 cm depth in a water phantom finally becomes :

$$D_{water,z=2} = M \times N_K \times k_Q \times p_{dis} \times k_{stem} \frac{\left(\overline{\mu_{en} / \rho}\right)_{water}}{\left(\overline{\mu_{en} / \rho}\right)_{air}} \qquad (7.16)$$

The three explicit correction factors are often combined to give $k_{ch} = k_Q\, p_{dis}\, k_{stem}$.

1.0 - 8 mm Al (50 - 160 kV)

Dose determination is now performed at the surface of a water phantom. At this lower energy, the dose determination is first carried out by finding the air kerma of the user chamber in air. The latter has to have an air kerma calibration factor N_K traceable to the primary standard.

- Correction is first made to the chamber reading M for temperature, pressure and recombination, to give the air kerma free in air, as $K_{air,air} = M \times N_K$
- Conversion to water kerma free in air is then made using the mean water/air mass energy absorption coefficient for the particular HVL. This is averaged over the photon energy spectrum in air.

$$K_{w,air} = K_{air,air} \frac{\left(\overline{\mu_{en} / \rho}\right)_{water}}{\left(\overline{\mu_{en} / \rho}\right)_{air}} \qquad (7.17)$$

- Water kerma free in air is then converted to water kerma at the surface of a water phantom by multiplying by the backscatter factor. The latter is defined as

the ratio of the water kerma at the surface to the water kerma in air *i.e.*

$$B_w = \frac{K_{w,z=0}}{K_{w,air}} \tag{7.18}$$

- The water kerma at the surface is then equal to the absorbed dose just below the surface of the water at the point where charged particle equilibrium is first established

$$D_{w,z=0} = M \times N_K \times B_w \frac{\left(\overline{\mu_{en} / \rho}\right)_{water}}{\left(\overline{\mu_{en} / \rho}\right)_{air}} \tag{7.19}$$

0.035 - 1.0 mm Al (8 - 50 kV)

A parallel plate chamber is now used at the surface of the water phantom. An appropriate expression is Eq.(7.16) where the parameters are given for $z = 0$.

7.11.2 High energy photons (^{60}Co γ-rays and X-rays in the range 4 - 19 MeV)

The UK procedure in the higher X-ray energy region is to use the NPL primary standard of absorbed dose derived from a graphite calorimeter.

Specification of beam energy

Difficulties associated in the reliable determination of the photon energy spectrum in a typical X-ray beam, make it necessary to use an independent measurement of beam quality based upon the Tissue-Phantom Ratio. For this purpose, the TPR is measured at depths of 10 cm and 20 cm in a water phantom using a 10 cm × 10 cm field at a constant source-chamber distance.

Theoretical basis

Due to the total length of time required to take a calorimeter reading (at least 20 minutes), the procedure normally makes use of three working standard chambers at the national laboratory. All three are compared against the calorimeter, and a mean taken of at least 10 readings of each. A transfer instrument from a hospital can then be calibrated in absorbed dose to water against the three working standard chambers.

The calibration is made using the *dose ratio* method. In this, the calibration factor N_m for a chamber exposed in a phantom m to a dose D_m, is $N_m = D_m/Q_m$, where Q_m is the charge collected. For two different media, graphite and water, the ratio of

the calibration factors is :

$$\frac{N_w}{N_c} = \frac{D_w / Q_w}{D_c / Q_c} = \frac{D_w}{D_c}\,\frac{Q_c}{Q_w} \tag{7.20}$$

This is determined by the measured ratio of ionization currents and the calculated ratio of absorbed dose at the same points in the two media.

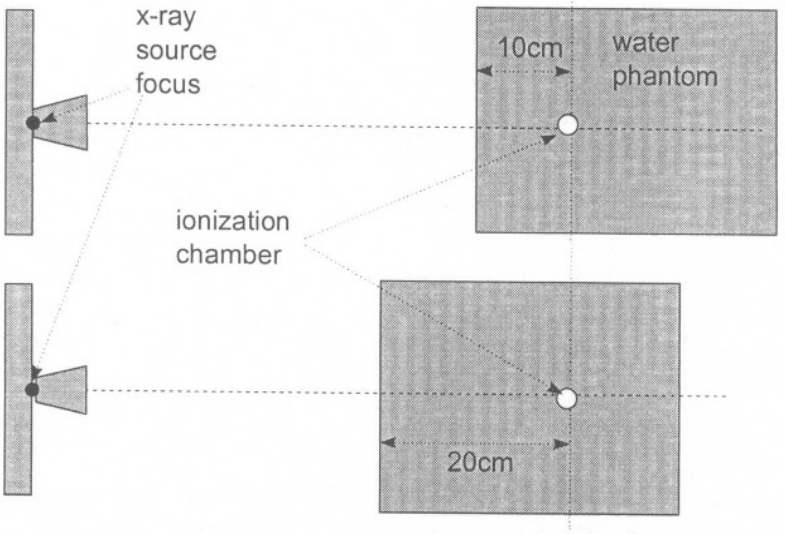

Fig.(7.12) Determination of high energy photon beam spectrum using Tissue : Phantom ratio at 10 cm and 20 cm at constant source : chamber distance, [1]. With permission from Charles C.Thomas Ltd., Springfield, Ill., USA.

7.11.3 Electrons

Fig.(2.7) shows the main parameters that define the penetration of an electron beam into a phantom material. These are :

- z_m, the depth at which absorbed dose reaches a maximum, D_{max},
- R_{50}, the depth at which the dose is 50% of the maximum, $D_{max}/2$,
- R_p, the practical range.

Specification of the point of measurement

The strong depth dependence of the electron energy spectrum demands that the nature of the chamber and the specification of the point of measurement are well defined. In the latest Code of Practice [6] the designated chambers are :

- the NE2571 cylindrical graphite-walled Farmer chamber,
- the parallel-plate NACP electron beam chamber,

- the parallel-plate PTW/Markus chamber,
- the parallel-plate Roos chamber, type 34001,

The cylindrical chamber is only recommended for use when the mean energy at the point of measurement is >5 MeV. The lowest energy at the surface must therefore be >10 MeV.

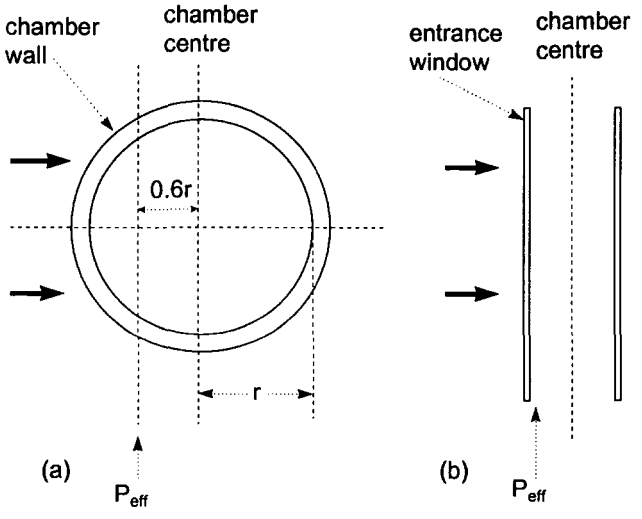

Fig.(7.13) Effective point of measurement, P_{eff}, for (a) cylindrical and (b) parallel-plate chambers. For all electron measurements, P_{eff}, must be placed at the depth of interest, [5].

The calibration of a user's electron chamber must be traceable back to the national primary standard. To do this, a secondary local standard (the transfer instrument) is first of all calibrated against the national secondary standard in terms of air kerma, using a beam of either 2 MV X-rays or ^{60}Co γ-rays. The user's working instrument can then be calibrated against the local standard.

Thus the user's local standard will receive a calibration factor :

- $N_{D,air,2571}$ for the cylindrical 2571 chamber when it is irradiated simultaneously with the national secondary standard at a depth of 5 cm in a PMMA (poly-methyl-methacrylate) phantom. The area of the phantom must be at least 20 cm × 20 cm and 12 cm thick, using a radiation field area of 10 cm × 10 cm and a source-surface distance (SSD) of 80 cm.
- $N_{D,air,pp}$ for a parallel plate chamber compared against a secondary standard 2571 chamber previously calibrated in an electron beam with a mean energy 17 - 22 MeV. Using appropriate water-proofing, each of the chambers should be irradiated in a water phantom in turn. The effective point of measurement, P_{eff}, of both chambers should be at the same depth in the phantom.

Each of the calibration factors must incorporate certain correction terms. Thus :

$$N_{D,air,2571} = \frac{M_{sec}}{M_{2571}} N_{K,sec} (1-g) k_{sec} \left(\frac{P^{\lambda}_{sec}}{P^{\lambda}_{cyl}} \right)_{PMMA} \quad (7.21)$$

The terms in Eq.(7.21) are :

- M_{sec} and M_{2571} are the instrument readings of the national secondary standard and the user's 2571 chamber respectively,
- $N_{K,sec}$ is the in air, air-kerma calibration factor of the secondary standard,
- g is the fraction of kerma lost to radiation,
- k_{sec} is a composite correction factor to account for the non-air equivalence of the chamber wall and build-up cap, attenuation and scattering in the wall and the non-air equivalence of the central electrode.
- (P_{sec}/P_{cyl}) corrects for the non-PMMA equivalence of the chamber wall, the non-air equivalence of the central electrode and the displacement effect due to the air cavity.

For the parallel plate chamber when the point of measurement is at depth z and the mean energy is $E_{m,z}$ we have :

$$N_{D,air,pp} = N_{D,air,2571} \frac{M_{2571}}{M_{pp}} \frac{p^{e}_{cav,2571}(E_{m,z})}{p^{e}_{pp}(E_{m,z})} \quad (7.22)$$

- $p^{e}_{cav,2571}$ is the in-scatter perturbation factor for the 2571 chamber at the mean energy appropriate to depth z. This denotes the difference in the electron fluence between the number entering and leaving the sensitive volume.
- p^{e}_{pp} is an overall perturbation factor for a parallel chamber. It is included because of slight differences in the best available comparisons between the recommended parallel plate chambers and other forms of dosimetry (e.g.Fricke). It is usually assigned a value of unity at high electron energies. For the Markus chamber in particular its value falls by 2% at low energies.

Specification of beam energy

Knowledge of the beam energy at the point of measurement is important because it is required for two purposes :

- the determination of correction terms for the calibration factors in Eqs.(7.21) and (7.22), and
- the final conversion of chamber reading to absorbed dose using the ratio of the energy dependent stopping powers, $S^{e}_{w/air}$.

Experimental range parameters provide the most convenient means of giving energy information about an electron beam (see chapter 9). For these purposes, measurement of R_{50} and R_p are made on the central axis of a phantom, at a minimum SSD of 100 cm, using a field size large enough to give scatter equilibrium on the central axis.

The relation between the mean energy of the beam at the surface of a phantom, $z = 0$, and the depth at which dose falls to 50% of its maximum value is usually assumed to be given by :

$$E_{m,0} = C \times R_{50} \tag{7.23}$$

In the comparison between beams of different energies, Eq.(7.23) is only valid if the beams are non-divergent, *i.e.* if it is the Source-Chamber-Distance (SCD) that is kept constant in the comparison (and not the more usual SSD).

In the context of precise dosimetry, however, the distinction is made between absorbed dose at a point in a medium and the ionization produced in a detector whose point of measurement, P_{eff}, lies at that point. There is thus a slight difference between $R_{50,D}$ and $R_{50,I}$.

For the measurement of *dose* in water, using $R_{50,D}$, the constant C is 2.33 MeV cm^{-1}. For the measurement of *ionization* in water, using $R_{50,I}$, the constant beomes 2.38 MeV cm^{-1}.

When beams are compared at constant SSD, the following polynomial relations are used to give the mean beam energy in MeV as follows [8] :

$$E_{m,0} = 0.818 + 1.935 \times R_{50,I} + 0.040 \times (R_{50,I})^2$$

$$E_{m,0} = 0.656 + 2.059 \times R_{50,D} + 0.022 \times \left(R_{50,D}\right)^2$$

Absorbed Dose at a reference point, z

The measurement of absorbed dose should be made with one of the designated chambers under the following conditions :

- Measurements are to be made in a water phantom having lateral dimensions large enough to ensure scatter equilibrium at the central axis.
- The thickness of the phantom in cm should be not less than 2+ 0.5 × E(MeV).
- The field size should be at least 10 cm × 10 cm.
- The effective point of measurement of the chamber should be on the central axis at the reference point of the beam. This should be either at the depth of the dose maximum, or at $z = 0.5 \times R_{50,D}$, whichever is the greater.

The absorbed dose to water when the chamber is replaced by water is then

$$D_w(z) = M \times N_{D,air,ch} \times S_{w/air}(E_{m,0}, z) \times p_{ch}(E_{m,z}) \qquad (7.24)$$

In Eq.(7.24) :

- M is the chamber reading corrected for temperature, pressure, polarity and recombination effects.
- $N_{D,air,ch}$ is the calibration factor for the chamber in use.
- $S_{w/air}(E_{m,0}, z)$ is the stopping power ratio between water and air for an electron beam having a mean energy $E_{m,0}$ at the surface of the phantom which is evaluated at the reference depth z in water.
- $p_{ch}(E_{m,z})$ is the perturbation factor to account for the displacement of the water by the chamber in order to make the measurement.

7.12 Chemical Dosimeters

The most widely used chemical dosimeter is the Fricke system (section 6.9) in which ferrous ions, Fe^{2+}, are converted to ferric ions, Fe^{3+}. It employs an air-saturated solution of 0.001 M ferrous ammonium sulphate and 0.4 M sulphuric acid sealed inside a soda glass ampoule of approximate volume 2 ml. Before irradiation, the ferrous solution is colourless and does not absorb photons at 304 nm. As the concentration of ferric ion builds up, there is a measurable increase in absorbance at this wavelength. For cell path lengths, x, of 10 mm, doses in the range 20 - 200 Gy are readily determined. The relationship between the reduction in transmitted light, I_x/I_0, and the concentration of Fe^{3+} ions $[S]$, is given by the Beer-Lambert law :

$$log_{10}\left(\frac{I_0}{I_x}\right) = \varepsilon_{304}\,[S]\,x$$

where ε_{304} is the extinction coefficient at 304 nm in units of $M^{-1}\,m^{-1}$. Important practical points to consider when using chemical dosimetry are the following :

- Chemicals of the highest available purity (Analar grade at least) should be used, and solutions should be made up with demineralized and triply-distilled water.
- The solution should be either fully air-saturated or fully de-oxygenated, in order that Eqs.(6.18) or (6.17) respectively are fully applicable.
- It should be remembered that there is a significant difference in the G-value for different radiations.
- Similarly, there is a small energy dependence of the G-value for a given radiation.
- Since the precision of the method depends on the measurement of optical density at 304 nm, an absorbed dose of 5 - 10 Gy is needed in order to achieve a sufficient colour change.

7.13 Thermo-Luminescence (TL) Dosimetry

Thermo-luminescence is a thermally stimulated emission of light following the storage of radiation-induced excitation in a crystalline lattice. This is achieved in some materials, such as alkali halides, having crystal imperfections which produce electron states in the otherwise forbidden energy gap, (see also section 6.10). These defect states are present in the natural form of some materials and they can also be produced by the deliberate doping of certain crystals.

Since the TL technique is so sensitive to the properties of these inter-band states, the unwanted introduction of strains and other contamination into the lattice can impair and sometimes even destroy the TL effects.

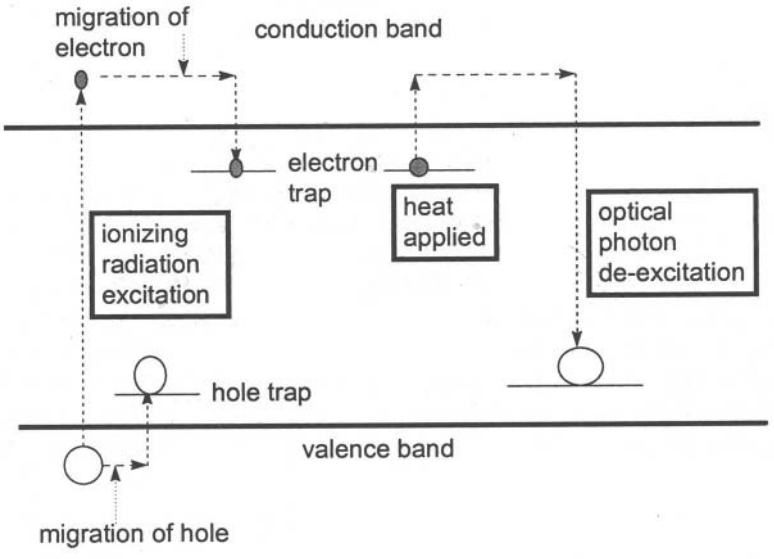

Fig.(7.14) A model of the TL process, [9]. With permission of CRC Press, Baco Raton, Fla., USA.

The sequence of events in Fig.(7.14) is as follows :

- The excitation of an electron from the valence band into the conduction band, as a result of the absorption of energy from ionizing radiation, is followed by the migration of the electron in the conduction band and the hole (with a much lower mobility) in the valence band.
- Trapping of both can take place in a lattice which contains defects.
- The application of heat drives the electron back into the conduction band, where it can again migrate freely until it encounters a hole state.
- Recombination then takes place with the emission of an optical photon.

Not shown in Fig.(7.14) is the possibility that, both before and after the application

of heat, the de-excitation can also take place via a radiation-less transition. In this case, energy is likely to be dissipated by phonon creation.

In the application of heat, the emission of optical photons is detected by a sensitive photomultiplier. This produces a pulse-height spectrum, called a glow-curve, Fig.(7.15), which is characteristic of the TL material and also reflects the following :

- the concentration and nature of the electron traps,
- the intensity of the radiation,
- the type of radiation,
- any pre-irradiation and annealing history,
- the glow-curve heating rate.

As temperature increases, electrons can be excited into the conduction band from electron states (traps) which lie deeper and deeper below the bottom of the conduction band. The glow curves tend to consist of one main component preceded at lower temperatures by one or more smaller peaks. The lower temperature peaks correspond to shallow electron traps which tend to have a weak correlation with exposure. Read-out does not therefore begin until these shallow traps have been emptied.

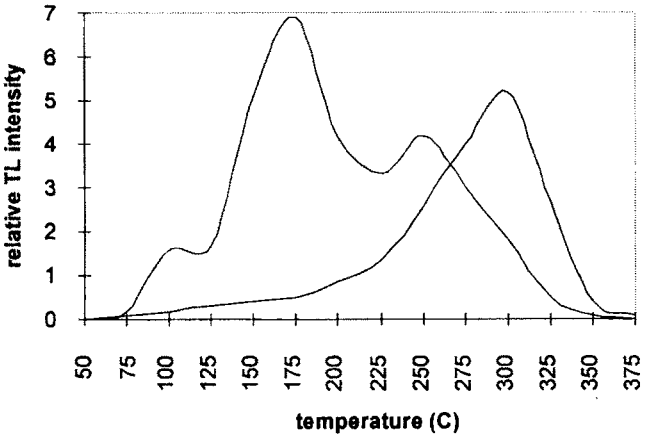

Fig.(7.15) Representation of a glow curve from LiF (TLD100), showing the total intensity of the emitted photons versus temperature. The left-hand curve corresponds to an exposure of 3.7×10^5 R : the right-hand curve to an exposure of 2.1×10^7 R [10].

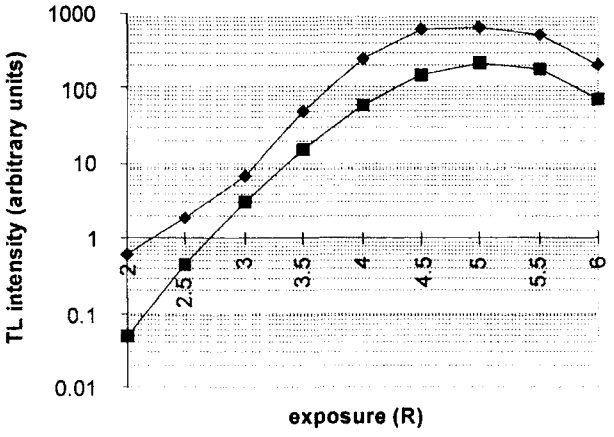

Fig.(7.16) The intensity of the major component in Fig.(7.15) for different exposures of Co^{60} radiation. ◆ no pre-exposure : ■ pre-exposure of 8.5×10^5 R [10].

Table (7.2) The main advantages and disadvantages of TL dosimetry

Advantages	Disadvantages
1.Their physical sizes are small – sometimes as little as 20 mg. Spatial resolution is therefore high.	1. They are not normally regarded as being tissue-equivalent. Exceptions can be made, e.g. $Li_2B_4O_7$:Mn.
2. They can be used over a large range – from ~10^{-5} Gy to ~10^4 Gy.	2. Calibration against a secondary standard is essential.
3. The storage time of dose information is long – readout can occur many months after exposure.	3. They are sensitive to mechanical strain, surface grease and scratches, other contamination.
4. With careful batch selection, precision of ~3% can be achieved.	4. Supra-linearity occurs at high doses.
5. They are easily re-annealed for further use.	5. Nominally identical batches can give significantly different responses.
6. They are insensitive to moisture, light, and most laboratory fumes.	6. Interface effects between the TLD and the medium can be severe.

7.14 Solid-State Dosimeters

These devices make use of a p-n junction based on silicon as the host material. The sensitive volume is the narrow depletion layer which is formed at the junction and which is widened to 10 - 1000 μm by the application of reverse bias (see also section 5.4).

A p-n junction diode is formed at the interface between p-type and n-type silicon. This is achieved by implanting n-type silicon, e.g. silicon containing phosphorus atoms, with a thin layer of p-type atoms such as boron. The implanted boron atoms create a narrow p-type region, up to a sharply defined depth, so long as their concentration exceeds that of the host n-type impurities.

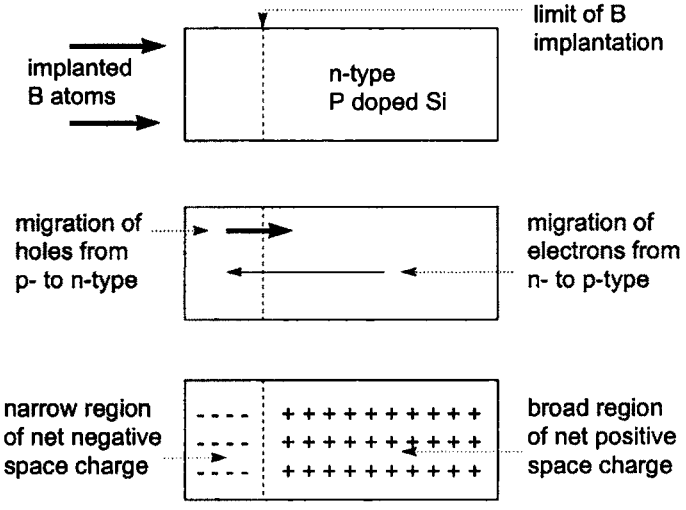

Fig.(7.17) Schematic diagram representing the implantation of p-type material into an n-type host. Highly mobile electrons will then migrate from n- to p-type and less mobile holes will migrate from p- to n-type. The migration will continue until the build-up of positive space charge in the n-type, and negative space charge in the p-type becomes large enough to prevent further movement.

The space charge so generated, Fig.(7.17), signifies the depletion regions either side of the interface which are devoid of free carriers, [11]. Once this region has been increased in width by the application of reverse bias, it forms the sensitive volume for the detection of radiation-induced charge.

Silicon detectors possess the following advantages :

- They have a thin detecting layer (~300 μm).
- The w-value is small (w ~ 3.6 eV). This confers greater intrinsic efficiency than

ionization chambers (W ≈ 33 eV).

- A small area gives good spatial resolution for the determination of isodose plots in radiotherapy and for imaging.

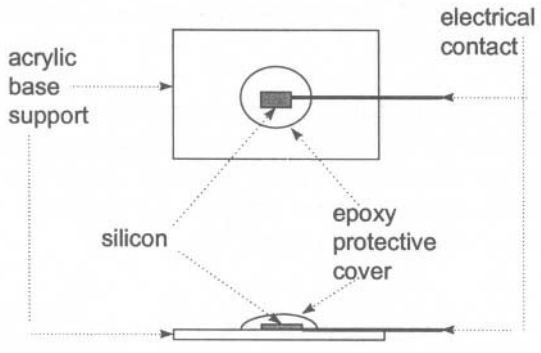

Fig.(7.18) A silicon detector of the type used for dosimetry. Dimensions are generally in the range 300 - 400 μm thick and 3 - 6 mm² in area.

These are balanced by the following disadvantages :

- There is a large difference in both Z and density between silicon and water and/ or tissue, Figs.(7.19) and (7.20). This complicates the charged particle equilibrium when placed in a water phantom. As Fig.(7.18) shows, there is also an acrylic base and an epoxy protective layer to add to the uncertainties.
- The definition of the exact centre of the detector, *i.e.* the effective point of measurement, may not be known to better than 0.5 mm.

Although the small size of a silicon detector makes it a very appropriate device for measuring electron beam isodose plots, care must be exercised over the interpretation of the charge measurements. In the build-up region, the radiative contribution to total stopping power in silicon is high, ~38% at 30MeV. Furthermore, the stopping power ratio of silicon/water shows a significant decrease of ~12% on going from 30 MeV to 10 MeV, Fig.(7.20). In addition, the response to the broad spectrum of *bremsstrahlung* radiation in the tail of the depth dose distribution, will also show an incorrect value. This is due to the deviation of the silicon and water data at high and low photon energies, Fig.(7.19). An overestimate of the *bremsstrahlung* component will be the result.

7.15 Film Dosimetry

A discussion of the practicalities of film dosimetry with electron beams has been given by Klevenhagen [5]. Initial deposition of energy in the silver bromide/gelatin

matrix of the emulsion converts the AgBr grains to elemental silver. This latent image is then amplified by the reducing action of the developer solution to create a measurable reduction of optical transparency, *i.e.* an increase in the optical density.

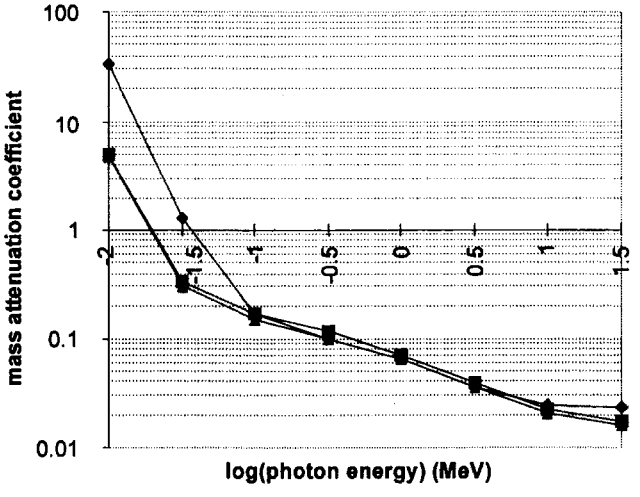

Fig.(7.19) Total mass attenuation coefficient ($cm^2\ g^{-1}$) versus log (photon energy) in MeV. ◆ silicon (ρ = 2.33 g cm^{-3}) : ■ water (ρ = 1 g cm^{-3}) : ▲ air (ρ = 0.00121 g cm^{-3}) [12].

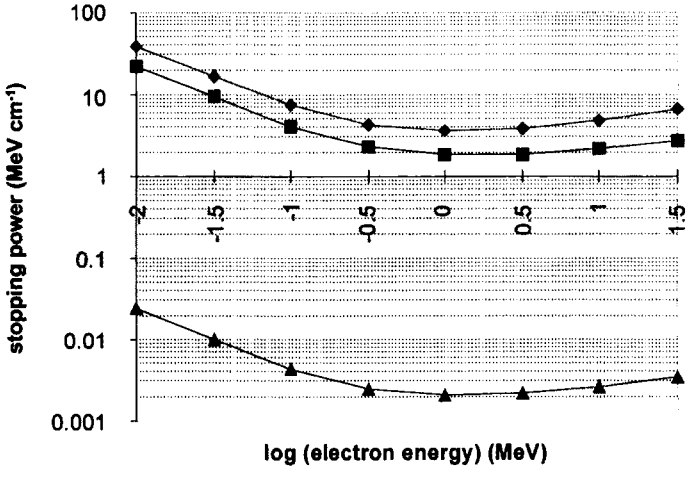

Fig.(7.20) Stopping Power (Note: NOT mass stopping power) versus log (electron energy) (MeV). ◆ silicon ■ water ▲ air. Note the increase in stopping power due to radiative loss above ~3 MeV. This gives rise to an increase in the silicon/water stopping power ratio at high energies, [13].

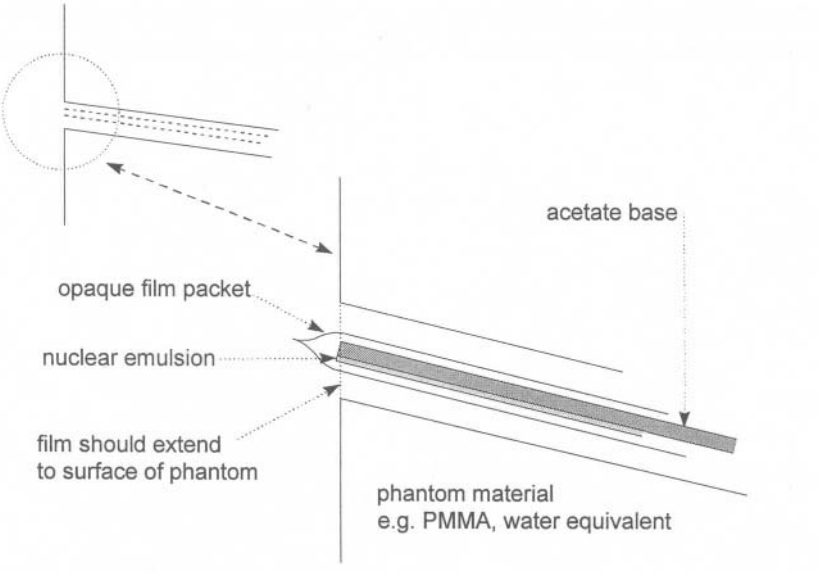

Fig.(7.21) One possible arrangement of a nuclear emulsion in a solid phantom (e.g.perspex or tissue-equivalent plastic). The film packet is placed at a shallow angle with respect to the incoming beam.

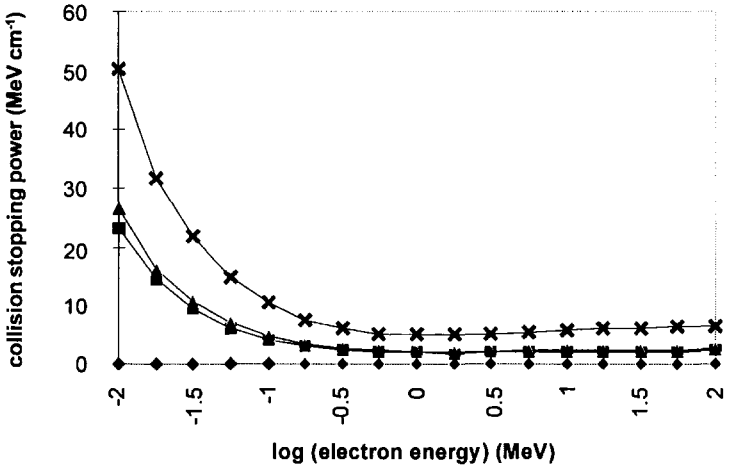

Fig.(7.22) The collision stopping power (MeV cm^{-1}) of electrons in air ◆ : water ■ : polymethylmethacrylate (PMMA, lucite or perspex) ▲ : nuclear emulsion ✖, [13].

So long as the fraction of converted AgBr grains is small, the optical density is proportional to absorbed dose in the emulsion. As with any other form of dosimetry,

however, account has to be taken of the energy dependence of the interactions together with the possible effects of secondary electron scatter. The latter can arise both within the dosimeter material itself and also between the dosimeter and the surrounding medium.

Precautions to be taken include:

- a minimum amount of air must exist between the emulsion and the phantom material. The sides of the phantom adjacent to the film packet must therefore be machined flat and the packet compressed between the two sides.
- the upstream edge of the film must be in line with the phantom surface.

References

[1] H.E.Johns and J.R.Cunningham, *The Physics of Radiology, 4'th edition* (Thomas, Springfield USA, 1983).
[2] L.V.Spencer and F.H.Attix, *Radiat.Res.* **3** (1955) 239.
[3] T.E.Burlin, in *Radiation Dosimetry Vol.1* eds.F.H.Attix and W.C.Roesch, (Academic Press, New York, 1968) p.331.
[4] J.Havercroft and S.C.Klevenhagen, *Phys.Med.Biol.* 38 (1993) 25.
[5] S.C.Klevenhagen, *Physics and Dosimetry of Therapy Electron Beams,* (Medical Physics Publishing, Madison, Wisconsin 1993).
[6] The IPEMB Code of Practice for Electron Dosimetry for Radiotherapy Beams of Initial Energy from 2 to 50 MeV based on Air Kerma, *Phys.Med.Biol.* **41** (1996) 2557.
[7] The IPEMB Code of Practice for the Determination of Absorbed Dose for x-rays below 300 kV generating potential (0.035mm Al - 4mm Cu HVL 10-300kV generating potential), *Phys.Med.Biol.* **41** (1996) 2605.
[8] *The use of Plane Parallel Ionization Chambers in High Energy Electron and Photon Beams. An International Code of Practice for Dosimetry,* (Report 381 IAEA Vienna, 1996).
[9] Y.S.Horowitz, ed. Thermoluminescence and Thermoluminescence Dosimetry, Vol. 1 (CRC Press, Boca Raton, Florida, 1984) p4.
[10] V.K.Jain, S.P.Kathuria and A.K.Ganguly, *J.Phys.C* **8** (1975) 2191.
[11] G.Hall in *Medical Radiation Detectors*, ed. N.F.Kember, (Institute of Physics Publishing, Bristol 1994)
[12] J.H.Hubbell, *Nat.Stand.Ref.Data.Ser.* (NBS Report 29 1969).
[13] ICRU report 37, *Stopping Powers for Electrons and Positrons*, (International Dommission on Radiation and Measurements, 1984, Bethesda, MD., USA).

CHAPTER 8

ACTIVATION

8.1 Introduction

The production of radioactive materials can involve different types of radiation and different energies. We exclude from consideration here those instances where the incoming radiation is designed to modify the target material in ways other than by activation. For example, no account is taken of the production of cellular effects in radio-biology or the induction of chemical or solid state effects due to ion implantation.

Some important examples of activation are :

- The manufacture of radioisotopes for use in nuclear medicine and other industrial tracer studies. Neutrons, protons or deuterons are used to activate a particular target material which is then chemically treated to separate out the isotope of interest. This is then inserted into a specific pharmaceutical for administration to a patient or adapted for use in an industrial process.
- The unwanted activity produced by energetic particle beams, in both medical and particle physics accelerators, because of the requirements of beam collimation. Background radiation is produced as a result. This can arise :
  (a) with high primary beams of electrons. These initially produce X-rays which then initiate the activation in the collimator,
  (b) from protons or heavier ions which can produce activity directly, and
  (c) via the production of secondary particles such as neutrons.
- The use of certain beams to determine the concentration of trace elements in materials such as forensic samples. This use is generally restricted to neutrons and is the basis of an important technique known as Neutron Activation Analysis (NAA).
- The use of high purity materials to determine the characteristics of certain particle beams. Here, the activation produced in ultra-pure thin foils can be used to determine the absolute flux and energy spectrum of the radiation field which produced the activity. Again, this is largely a neutron technique and, being the reverse of the NAA method, can be used as a neutron detector.

Heavy particles (neutrons, protons, α-particles, *etc.*) are the most important sources of radiation in the context of activation, although electrons and photons must also be considered under certain conditions. To understand fully the activation created by a given radiation, data must be available on the following :

- the energy spectrum of the radiation,
- the density and exact elemental composition of the material being irradiated,

- the interaction cross-sections and the product half-lives,
- the length of time during which the material is exposed to the radiation.

8.2 Basic Principles

We assume that an incident particle interacts with a target nucleus ${}^{A}_{Z}X$ of mass number A and charge number Z. The reaction may lead to a number of different residual nuclei and emitted particles whose values of A and Z are determined by the principles of mass/charge conservation. In general, the reaction is designated by :

target nucleus + incident particle $\rightarrow$ [CN] $\rightarrow$ emitted particle + residual nucleus

This signifies the production of a short-lived compound nucleus [CN] which subsequently decays into the residual nucleus and an emitted particle. The reaction has a Q-value which is given by the total energy-equivalent mass difference before and after the reaction. For masses M_T and M_R of the target and residual nuclei, and m_i and m_e of the incident and emitted particles respectively, the Q-value is given by

$$Q = \left[\left(M_T + m_i\right) - \left(M_R + m_e\right)\right]c^2 \tag{8.1}$$

When the Q-value is positive it determines the energy released in the reaction. When it is negative it gives the energy required before the reaction can proceed. These are called exothermic and endothermic reactions respectively. In the latter case, however, the energy required by the incident particle is greater than the Q-value because of the recoil of the target nucleus in the Laboratory (L) system.

The minimum kinetic energy of the incident particle in the Laboratory system required to initiate an endothermic (Q<0) reaction is :

$$E_{threshold} = -Q\left(\frac{M_T + m_i}{M_T}\right) \tag{8.2}$$

The decay of the Compound Nucleus may proceed via a number of different pathways, each of which has its own energy dependent cross-section.

The mass/energy relationships between different nuclei are illustrated by the Trilinear Chart [1] and the Segrè Chart [2]. Either of these, or their equivalent, provide essential information regarding the various routes that can be taken between a target and a product nucleus. The charts display the positions of all the known nuclei in terms of their mass number A, charge number Z, and neutron number $N = A-Z$. In

addition, they give the masses of each stable isotope from which the Q-value may be calculated using Eq.(8.1). By giving also the lifetimes of all the unstable nuclei, the time dependence can be determined for each of the possible activation reactions.

Numerical illustrations of activation reactions using neutrons and charged particles will be given after a consideration of some relevant cross-section data.

Table (8.1) Displacements caused by nuclear reactions. Isotopes of the same element are represented by a horizontal row (constant Z and increasing upwards). Isotones are represented by a vertical column (constant N and increasing to the right). Isobars are represented by a line running NW to SE (constant A increasing towards the NE). From the Segrè Chart scheme [2].

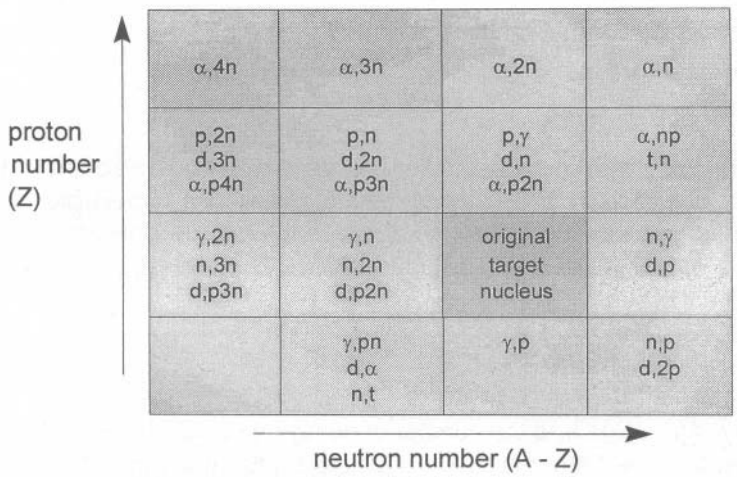

8.3 Basic Formulae

In general, we consider a volume of material in which there are N nuclei cm^{-3} of isotope i which interact with microscopic cross-section σ. The cross-sections are most conveniently expressed in barn nucleus^{-1}, where 1 barn = 10^{-24} cm^2. The macroscopic cross-section, in barn cm^{-1}, is $\Sigma = N\sigma$.

The inverse of the macroscopic cross-section has units of distance and gives the Mean Free Path length, $\Gamma = 1/\Sigma$, between interactions. (Note that Γ here is distinguished from the Γ in section 4.2.3. The latter refers to the energy width of a resonance reaction). All scattering, Σ_s, and all absorption, Σ_a, processes must be considered in following the penetration of the radiation into the material.

In the production of a particular nucleus, however, it may be the case that not all absorption interactions in the target give rise to the activation of interest. We must

therefore write :

$$\Sigma_a = \Sigma_{act} + \Sigma_{non\ act}$$

to include the non-productive absorption reactions. Only a fraction :

$$\Sigma_{act}/(\Sigma_{act} + \Sigma_{non\ act} + \Sigma_s)$$

of all the interactions are therefore of interest.

The number of activated nuclei formed per second per cm^2 is called the activation, *C*. This is obtained when a material of thickness *d* is placed in a radiation field of Φ particles per second per cm^2 [3]. Thus:

$$C = \Phi\ \Sigma_{act}\ d \tag{8.3}$$

corresponds to the maximum (saturation) activity which would be observed at infinite time. The total activation, *B(t)*, is the number of radioactive nuclei which are present at time *t*. It is given by the difference between the production rate and the decay rate. These clearly depend on the decay constant λ, and so *B(t)* is time-dependent.

$$B(t) = C\left[1 - exp(-\lambda t)\right] / \lambda \tag{8.4}$$

The activity, $A(t) = B(t)\ \lambda$, is the number of decaying nuclei at time *t*. If the material is irradiated for time t_1 the activity at any time t_2 after the end of the irradiation is given by :

$$A(t_1, t_2) = C\left[1 - exp(-\lambda t_1)\right] exp(-\lambda t_2) \tag{8.5}$$

Eq.(8.5) describes the ideal situation :

- where the radiation field is uniform over the whole of the material being irradiated, and
- when the radiation does not suffer any change in intensity (causing a change in flux, Φ) or energy (causing a change in cross-section, σ) as it traverses the material.

There are many instances where these ideal conditions do not apply. These occur:

- when there is a sharp fall-off in intensity at the edge of a beam,
- when the absorption cross-section Σ_a is so high that the radiation intensity is higher on one side of the material than the other, and

- when a charged particle loses energy over a short distance such that the activation cross-section Σ_{act} itself varies over the track of the particle.

In these cases Eq.(8.5) needs to be modified. Rather different corrections are required for activation by neutrons and by charged particles.

8.4 Irradiation by Neutrons

Neutrons are generally segregated into three energy groups – thermal, epithermal and fast. The distinctions are necessary because of the particular importance of activation in the following systems :

- Structural, collimator and shielding materials. These are prone to activation in the large fields of fast and epithermal neutrons found in reactor and particle accelerator installations.
- Human tissue. The hydrogenous nature of human tissue means that more importance attaches to thermal and epithermal reactions.
- Radioisotopes used for labelling pharmaceuticals. These use a small number of reactions which are induced mostly by thermal neutrons.
- Nuclei which are used in several convenient and precise methods of neutron detection are activated by both thermal and fast reactions. This technique is usually known as Neutron Activation Analysis (NAA).
- Radiographic purposes. These can employ activation induced by either thermal or fast neutrons.

8.4.1 Activation of structural materials

Fast neutron- and gamma-induced reactions occur in the structural components of nuclear reactors and particle accelerators. This can lead to radiation protection problems for certain categories of workers. A particular example is provided by both the activation in, as well as the production of neutrons from, collimators and shielding surrounding high energy medical electron accelerators. These effects follow the production of intense fluxes of *bremsstrahlung* X-rays which lead to neutrons via photo-neutron reactions, (section 9.2.13).

8.4.2 Activation of human tissue

The activation consequences of neutron irradiation of humans arise during neutron therapy and neutron whole-body activation procedures. They would also have arisen during the Nagasaki and Hiroshima bomb explosions. The former are not of widespread importance nowadays, but the latter do have significance from the radiation protection point of view. For this reason it is worth recalling the possible

reactions that can occur during irradiation by fast neutrons, Table (8.2), and thermal neutrons, Table (8.3). In a number of cases, the residual nucleus is formed in an excited state which subsequently decays by the emission of gamma photons.

Table (8.2) The principal fast-neutron reactions in tissue elements. The most important are the (n,γ) reaction on hydrogen, and the (n,α) reaction on oxygen.

Reaction	γ - Energy released	Q-value
$^{1}H(n,\gamma)^{2}H$	2.2 MeV	2.2 MeV
$^{12}C(n,\alpha)^{9}Be$		- 6.0 MeV
$^{12}C(n,n')3\alpha$		- 9.0 MeV
$^{14}N(n,p)^{14}C$	620 keV	+ 0.62 MeV
$^{14}N(n,2n)^{13}C$		- 11.3 MeV
$^{16}O(n,\alpha)^{13}C$	480 keV	- 3.7 MeV

Table (8.3) The principal thermal-neutron reactions in tissue elements. The most important are the (n,γ) reaction on hydrogen and the (n,γ) reaction on chlorine. The average cross-section assumed for the two reactions in nitrogen is 1.88 barn and for potassium it is 2.05 barn.

Reaction	σ(barn)	Target (g ml^{-1})	A	Σ(cm^{-1})
$^{1}H(n,\gamma)^{2}H$	0.33	0.1	1	2.12
$^{14}N(n,p)^{14}C$	1.82	0.02	14	0.22
$^{14}N(n,\gamma)^{15}N$	0.07		14	
$^{35}Cl(n,\gamma)^{36}Cl$	43	0.0016	35.5	0.9
$^{37}Cl(n,\gamma)^{38}Ca$	0.4		35.5	
$^{40}Ca(n,\gamma)^{41}Ca$	0.42	0.015	40	0.0096
$^{39}K(n,\gamma)^{40}K$	2.1	0.002	39	0.0067
$^{41}K(n,\gamma)^{42}K$	1.46		39	

8.4.3 Radioisotope production

One method of commercial radioisotope production is by the neutron irradiation of the target material in a nuclear reactor. This gives product nuclei which lie to the right of the target nucleus in Table (8.1). The neutron rich isotopes produced can then decay via β^- and γ emission. A disadvantage of the neutron-induced production method is that the product nucleus is an isotope of the same target element. Chemical separation is therefore difficult unless a *Szilard-Chalmers* reaction occurs. This is one in which the nuclear recoil that follows neutron capture is sufficient to rupture the chemical bonds holding the atom in place. In this case the atom which contains

the product nucleus can find itself in a different chemical state.

A good example is provided by the production of ^{99m}Tc. This is an isotope which is widely used in nuclear medicine because of its very favourable decay scheme.

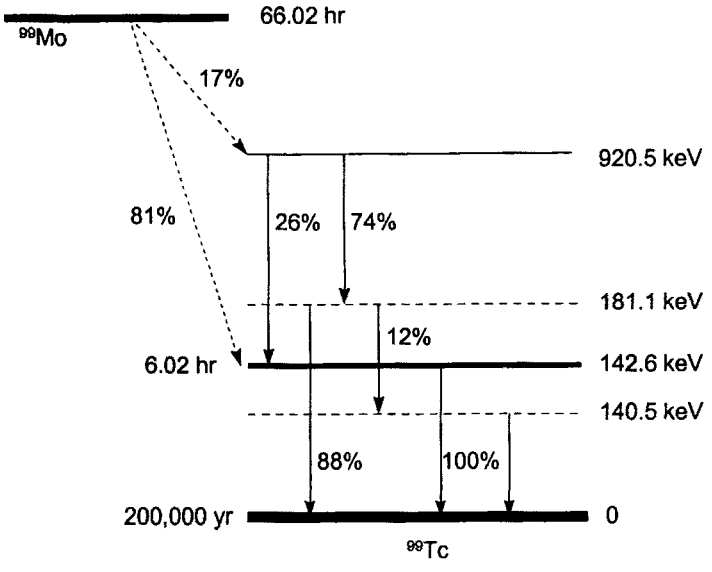

Fig.(8.1) The principal transitions in the decay scheme of ^{99}Mo. Following the β^- emissions from ^{99}Mo, the ground state of Tc is only accessible via the 142.6 keV isomeric state. This is denoted by ^{99m}Tc.

Production of ^{99m}Tc follows the neutron irradiation of ^{99}Mo via the reaction :

$$^{98}\text{Mo}(n,\gamma)^{99}\text{Mo} \rightarrow {}^{99m}\text{Tc} \rightarrow {}^{99}\text{Tc}$$

Natural molybdenum has seven stable isotopes, only three of which can be activated by an (n,γ) reaction, Table (8.4).

Table (8.4) shows that the thermal neutron irradiation of natural molybdenum produces three product nuclei. In spite of the relatively high abundance of A = 92 in the target, the ^{93}Mo product can be disregarded because of its insignificant cross-section. After an elapsed period of ~ 146 minutes following the end of irradiation, (*ie* 10 times the half-life), sufficient decay of ^{101}Mo has taken place that this product is also of no real consequence.

Table (8.4) The activation of natural Molybdenum by (n,γ) reactions

A	%	Thermal Activation cross-section (barn)	Product,	Half-life
92	15.86	< 0.006	^{93}Mo,	6.8 hr
94	9.12			
95	15.7			
96	16.5			
97	9.45			
98	12.75	0.50 ± 0.06	^{99}Mo,	66.02 hr
100	9.62	0.20 ± 0.05	^{101}Mo,	14.6 min

Subsequent decay of ^{99}Mo then proceeds via β^- and γ emission, according to Fig.(8.1), to give a prominent 142.6 keV gamma ray to the ground state of ^{99}Tc with a half-life of 6.02 hr. The chemical difference between molybdenum and technetium ensures that the latter can be separated easily from the former using elution techniques.

8.4.4 Neutron activation analysis (NAA)

Two aspects of NAA are important :

- When the intention is to determine the elemental content of a sample, having precise knowledge of the incident neutron flux Φ and the relevant interaction cross-sections, and
- When the need is to determine the flux Φ by the irradiation of a single element foil of precisely known geometry and composition.

The total flux at a certain position r in a medium, $\Phi(r)$, is generally taken to be an average over all direction angles, ω. It is now necessary to specify a vector flux $F(r,E,\omega)$. This is the number of neutrons at position r with energy E travelling in direction ω crossing unit area per second and it describes the neutron field precisely. When the vector flux is integrated over 4π we get :

$$\Phi(r,E) = \int F(r,E,\omega)\, d\omega$$

This defines the integrated, or total, flux as the number of neutrons which cross the surface of a sphere having an equatorial plane of area 1 cm^2. This is what is normally referred to as "flux". Notice that it is defined at a specific energy E.

For an irradiated material with a well-defined geometry, such as a thin foil, it is

customary to measure the foil thickness in terms of g cm^{-2} and the cross-section in units of cm^{-2} g (just as in the photon case). In this case the thickness of the foil, *d*, is replaced by the surface mass loading, $\delta = \rho\, d$, and the cross-section by the mass absorption coefficient, $\mu_a = \Sigma\, \rho^{-1}$.

8.4.5 *Effects of self-absorption in NAA*

In precise work, the simple relation between the measured activity and the incident particle flux and cross-section, Eq.(8.5), has to be corrected for neutron self-absorption within the foil. This correction has been treated in detail in [3] and accounts for the decrease in the number of neutrons penetrating the foil because of a significant amount of absorption.

The following assumptions are made :

- The neutron flux is constant over the area of the foil. This means that any dependence on *r* can be neglected.
- There is no change of neutron energy as it penetrates the foil. This is the case if only thermal neutrons are considered.
- There is no scattering within the foil, so that $\mu_{total} = \mu_a$. No neutrons enter the foil through its edges.

With these assumptions it is possible to express the probability per cm^2 per second that neutrons are absorbed at depths between *x* and *x* + *dx* from the upper surface, Fig.(8.2) as :

$$P(x)dx = \left[\int_0^{\pi/2}\int_0^{2\pi} F(\omega)\exp\left(\frac{-\mu_a(\delta - x)}{\cos\theta}\right)\sin\theta\, d\theta\, d\phi\right]\mu_a dx + \\ + \left[\int_{\pi/2}^{\pi}\int_0^{2\pi} F(\omega)\exp\left(\frac{-\mu_a x}{\cos\theta}\right)\sin\theta\, d\theta\, d\phi\right]\mu_a dx \qquad (8.6)$$

In Eq.(8.6) the first term describes the contributions from neutrons entering the foil from below and the second term from above, [3].

The activation is then :

$$C = \frac{\mu_{act}}{\mu_a}\int P(x)\, dx \qquad (8.7)$$

where *x* runs from 0 to δ. Although the integration of Eq.(8.7) involves Legendre polynomials, it can be simplified by the use of a dimension-less function $\varphi_0(\mu_a\delta)$.

This gives the absorption probability in an isotropic field of neutrons.

$$\varphi_0(\mu_a\delta) = \frac{2\mu_a\delta}{1+2\mu_a\delta} \tag{8.8}$$

The final expression gives the uniform activation cross-section across the area of the foil, the centre of which is positioned at *r*, as :

$$C = \frac{\mu_{act}}{\mu_a}\ \frac{\Phi(r)}{2}\ \varphi_0(\mu_a\delta) \tag{8.9}$$

where $\Phi(r)$ is the isotropic flux.

As the foil thickness decreases, $\delta \rightarrow 0$ and Eq.(8.8) gives $\varphi_0(\mu_a\delta) \rightarrow 2\mu_a\delta$. Eq.(8.9) then reduces to Eq.(8.3). Conversely, when the foil becomes thick we have $\mu_a\delta >> 1$, giving :

$$C = \frac{\mu_{act}}{\mu_a}\ \frac{\Phi(r)}{2} \tag{8.10}$$

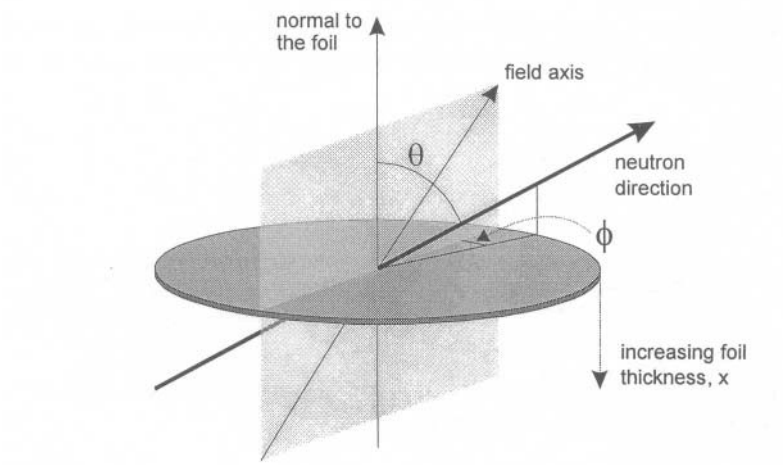

Fig.(8.2) The activation of a foil by a flux of neutrons F(r,E,ω), [3]. With permission from Springer Verlag, Berlin.

8.4.6 *Effects of energy-dependent cross-sections in NAA*

In their consideration of the Maxwell-Boltzmann distribution of neutron velocities, Beckurts and Wirtz [3] give kT as the energy of a neutron having the most probable velocity. Thus at 295 °K we have kT = 0.0254 eV. The mean energy, however, is $3kT/2$ = 0.0381 eV, and the most probable energy, $kT/2$ = 0.0127 eV (see also section 4.4.1 and 4.3.6).

Consideration of NAA up to this point has assumed that the neutrons are in thermal equilibrium with a medium at temperature, T = 295 °K. The cross-sections should therefore be specified at the mean energy, $3kT/2$. Usually, however, a thermal neutron is considered to be one with a velocity of 2200 m s^{-1}. This corresponds to an energy of 0.0253 eV at 293.6 °K.

If the field of neutrons causing the activation contains epithermal or fast neutrons, it becomes necessary to alter the activation cross-sections. In particular we need to consider the $1/v$ dependence of the cross-section at low energies, together with any possible resonant absorption processes. The Breit-Wigner expression, Eq.(8.11), gives the energy variation of the (n,γ) cross-section in the neighbourhood of a single isolated resonance, whose centroid is at energy E_R.

$$\sigma_{n,\gamma}(E) = \frac{\pi\hbar^2}{m^2v^2}\,\frac{\Gamma_n\Gamma_\gamma}{(E-E_R)^2+(\Gamma/2)^2} \tag{8.11}$$

The total energy width is $\Gamma = \Gamma_n + \Gamma_\gamma$ and $\Gamma/\hbar$ is the probability per second that the compound nucleus decays. It can occur in this case either by emitting the neutron in an elastic resonance scatter event or in a de-excitation event which involves gamma emission.

When $E_R >> \Gamma$ and as $E \rightarrow 0$, Eq.(8.11) reduces to :

$$\sigma_{n,\gamma}(E) = \frac{\pi\hbar^2}{m^2{v_R}^2}\,\frac{\Gamma_{n,0}\Gamma_\gamma}{{E_R}^2}\,\frac{1}{\sqrt{E}} \tag{8.12}$$

where m is the neutron mass, v_R and E_R are the neutron velocity and energy at the centroid of the resonance, and Γ_{n0} comes from a distribution of neutron widths which are characteristic of a particular nucleus such that $\Gamma = \Gamma_{n0}\sqrt{E}$.

Since $\sigma = (\mu\ \delta)/(d\ n)$, the absorption coefficient at an epithermal energy E is related to that at thermal energy kT by:

$$\mu_a(E) = \mu_a(kT)\sqrt{\frac{kT}{E}} \tag{8.13}$$

In the neighbourhood of resonance *i* the absorption coefficient has the form of a Lorenztian function which must be added to the 1/*v* dependence. This gives the relation :

$$\mu_a(E) = \mu_a(kT)\sqrt{\frac{kT}{E}} + \sum_i \frac{\mu_{a0}}{1+\left[2(E-E_R)/\Gamma\right]^2} \tag{8.14}$$

Here, the second term represents the summation over the *i* resonances, for each of which, μ_{a0} is the absorption coefficient at the resonant energy E_R, and Γ is the full width at half maximum of the resonance peak. Eq.(8.14) is a good approximation when $\Gamma << E_R$.

In order to determine the activation in a general case, Eqs.(8.7) and (8.9) or (8.10) require the integration over the energy-dependent cross-section in Eq.(8.14). Care must be taken to distinguish between those components of Eq.(8.14) which contribute to activation and those which do not. As Eq.(8.7) illustrates, there is only a certain fraction of all absorption events which are important in determining the activation. Complete details of epi-thermal and resonance activation are given in [3].

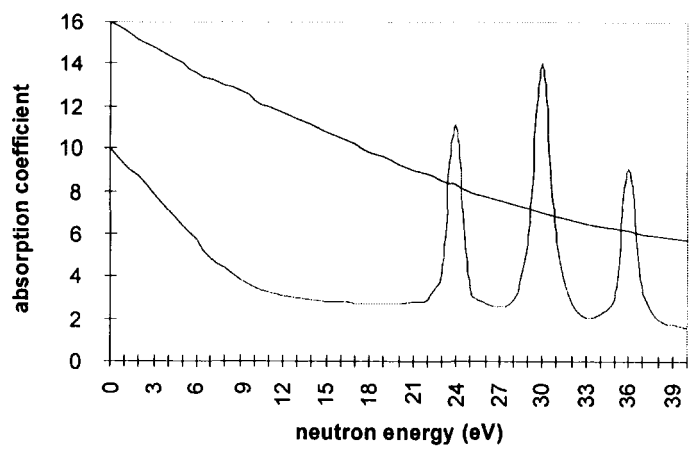

Fig.(8.3) A typical energy dependent flux in an epi-thermal/fast neutron field (upper curve) and a typical energy dependent absorption coefficient, described by Eq.(8.14) (lower curve), for an intermediate Z atom such as indium. The graph shows the 1/*v* dependence of the absorption coefficient at epi-thermal energies and the presence of resonance absorption peaks at higher energies. Actual resonance absorption peaks in indium are more numerous and more closely spaced than the ones shown.

8.5 Irradiation by Charged Particles

Activation by charged particles can also be quantified using Eq.(8.5). Now however, the isotropic neutron flux Φ (over 4π) is replaced by a unidirectional particle beam current J. Because there is a significant energy loss over the track lengths of charged particles, the energy dependence of the activation cross- section now assumes far greater importance than it did for neutrons. It now becomes necessary to consider the material thickness in relation to the particle range, and this leads to the distinction between a thin and a thick target, Fig.(8.4).

Heavy charged particles (p,d,α...) have a well-defined projected range along their original direction. If the thickness, d, is greater than this projected range, R, then the effective thickness of the sample is R, and the particle interacts along its track at all energies between the incident energy E_0 and zero. When $d < R$ the particle loses energy ΔE in the sample by an amount determined by d and the stopping power, and it emerges from the downstream side of the target with energy $E_0 - \Delta E$. In this case the activation cross-section will be that appropriate to energies between E_0 and $E_0 - \Delta E$.

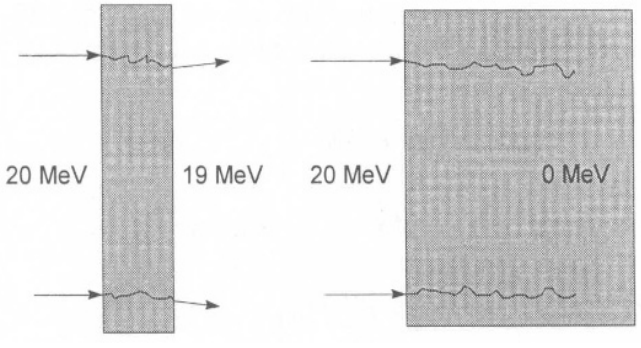

Fig.(8.4) A thin target is one in which all the target nuclei see the same incident particle flux at the same energy. As the interaction probability increases the target becomes thicker. A thick target could therefore be physically thin but be considered thick from a radiation physics point of view because its interaction cross-section is large. In this case, nuclei on the downstream side of the target see either a smaller particle flux or a lower energy than those upstream, i.e. a reduction in $F(r,E,\omega)$. A thin target corresponds to the condition $N_0\sigma_e d << 1$.

Consider a target composed of a large area foil of thickness d containing N_0 nuclei per unit volume. This is bombarded by a charged particle beam current J (units C cm^{-2} s^{-1}). Using the same terminology as in Eq.(8.3) for the microscopic activation cross-section, the probability per target nucleus, A, of producing a radioactive product, B, per unit area of beam is :

$$\lambda_A = J\ \sigma_{act}\ d \qquad (8.15)$$

Although this probability is very small, the initial number N_0 of target nuclei A is very

large, so that the product, $N_0\lambda_A$, is finite. The number of radioactive product nuclei produced is then equal to the reduction in the number of A nuclei, less the number that decay with decay constant, λ_B. Thus we have :

$$\left(\frac{dB}{dt}\right) = A\lambda_A - B\lambda_B$$

As the bombardment proceeds, the number of A nuclei decreases according to $A = N_0 exp(-\lambda_A t)$ to give :

$$\left(\frac{dB}{dt}\right) = N_0\lambda_A\, exp(-\lambda_A t) - B exp(-\lambda_B t) \qquad (8.16)$$

A general trial solution of this differential equation gives the number of B nuclei as a function of time as:

$$B = N_0\left[k_A\, exp(-\lambda_A t) + k_B\, exp(-\lambda_B t)\right] \qquad (8.17)$$

The coefficients k_A and k_B are evaluated by substituting Eq.(8.17) into Eq.(8.16). When the terms are collected, the condition to be fulfilled is :

$$exp(-\lambda_A t)\left[-k_A\lambda_A - \lambda_A + k_A\lambda_B\right] = 0$$

To be true for all values of t, therefore, it is necessary that :

$$k_A = \lambda_A / \left[\lambda_B - \lambda_A\right]$$

By definition, the number of B nuclei present at $t = 0$ is zero. Therefore from Eq.(8.17), we have $k_A = -k_B$. We can now write the final expression for the number of product nuclei as :

$$B = N_0\left(\frac{\lambda_A}{\lambda_B - \lambda_A}\right)\left[exp(-\lambda_A t) - exp(-\lambda_B t)\right]$$

Under the initial condition that $\lambda_A << \lambda_B$, the activity of the product nuclei, $B\lambda_B$, becomes :

$$B\lambda_B = N_0\lambda_A\left[1 - exp(-\lambda_B t)\right] \qquad (8.18)$$

In this context the Yield, Y, is defined as the product activity per total incident particle

charge. It may be given for three conditions :

1. The time of bombardment, t_1, is significantly less than the mean lifetime of B ($t_1 << 1/\lambda_B$). In this case Eqs.(8.15) and (8.18) give a time-independent yield which is linearly proportional to the total bombardment charge (*i.e.* to the bombardment time, if the particle current is constant).

$$Y = \left(\frac{B\,\lambda_B}{J\,t_1}\right) = N_0\;\sigma_{act}\;d\;\lambda_B$$

   The yield is expressed in units of MBq μA^{-1} hr^{-1} and can be found tabulated in a number of publications for a large number of reactions [4].

2. When the bombardment time is much larger than the mean lifetime ($t_1 >> 1/\lambda_B$) the saturation activity is reached, and the yield becomes independent of bombardment time. Only the current is important.

$$Y = \left(\frac{B\,\lambda_B}{J}\right) = N_0\;\sigma_{act}\;d$$

3. At intermediate times ($t_1 \approx 1/\lambda_B$) the yield depends on both current and time according to Eq.(8.18). Thus, for a bombardment time, t_1, the activity at a time t_2 after the end of bombardment (EOB) is :

$$B\lambda_B = N_0\;J\;\sigma_{act}\;d\left[1 - exp(-\lambda_B t_1)\right]exp(-\lambda_B t_2) \qquad (8.19)$$

8.6 A Practical Example - The Proton Irradiation of Natural Copper

Whenever possible, a target to be used with incident charged particles will generally comprise a stack of thin foils. Only those foils with the highest activity (those at the front of the stack which have been activated at the highest incident energy) need undergo the chemical extraction of the activated nuclei. This procedure maximises the specific activity (Bq ml^{-1}) of the aqueous solution obtained when the target is dissolved in acid. There is, of course, the option of chemically extracting the isotope from all the foils, if there are no constraints on specific activity.

In order to produce a given isotope, say ^{62}Zn, from natural copper, the possible products from the proton irradiation of all the stable copper isotopes must be considered using the Segrè (or similar) chart shown in Table (8.5). The factors that

determine the importance of each of the possibilities are :

- the abundance of the target isotope,
- the cross-section of the reaction,
- the half-life of the product.

Both of the stable copper isotopes are of comparable abundance, and therefore the last two of the above factors are the most important in defining the level of contamination.

Table (8.5) A portion of the Segrè chart showing nuclides involved in Zn production using a proton-induced reaction. Stable isotopes are shown surrounded by a heavy border with the percentage natural abundance at the top and the neutral mass in atomic mass units (a.m.u.) at the bottom. Unstable isotopes are shown with the half-life at the top of the box. When two half-lives are shown, the left-hand figure is the half-life of the isomeric state and the right-hand figure the half-life of the ground state.

31	-	-	2.6 min ^{64}Ga 63.9571	15 min, 8 min ^{65}Ga 64.9532	9.45 hr ^{66}Ga 65.9525	78.0 hr ^{67}Ga 66.9496
30	88 s ^{61}Zn 60.9578	9.33 hr ^{62}Zn 61.9536	38.3 min ^{63}Zn 62.9530	48.89% ^{64}Zn 63.9493	245 d ^{65}Zn 64.9498	27.81% ^{66}Zn 65.9469
29	24 min ^{60}Cu 59.9566	3.33 hr ^{61}Cu 60.9521	9.72 min ^{62}Cu 61.9518	69.1% ^{63}Cu 62.9494	12.82 hr ^{64}Cu 63.9499	30.9% ^{65}Cu 64.9484
28	80 000 yr ^{59}Ni 58.9531	26.2% ^{60}Ni 59.9499	1.25% ^{61}Ni 60.9497	3.66% ^{62}Ni 61.9476	80 yr ^{63}Ni 62.9495	1.16% ^{64}Ni 63.9481
27	9.0 hr, 72 d ^{58}Co 57.9539	100% ^{59}Co 58.9519	11 min, 5.3 yr ^{60}Co 59.9529	1.65 hr ^{61}Co 60.9513	1.6 min, 14 min ^{62}Co 61.9529	-
Z ↑ N →	31	32	33	34	35	36

Table (8.5) shows that the production of ^{62}Zn from ^{63}Cu requires either a (p,2n), (d,3n) or (α,p4n) reaction. As a general rule, a proton-induced reaction will have the

largest yield because of the reduced Coulomb barrier. The same reaction on ^{65}Cu will produce none of the product nucleus ^{64}Zn because it is already stable (*i.e.* it has an infinite half-life). Using 1.00815 amu and 1.00899 amu as the masses of the proton and neutron respectively, and the masses of Zn and Cu from Table (8.5), we obtain the reaction Q-value as -13.07 MeV, and the threshold proton energy from Eq.(8.2) as 13.28 MeV.

A guide to the magnitude of the cross-sections associated with isotopic, as opposed to natural, targets may be obtained from tabulations such as [4]. When 20 MeV protons irradiate a natural copper target, the various contributions to the overall activity are shown in Table (8.6).

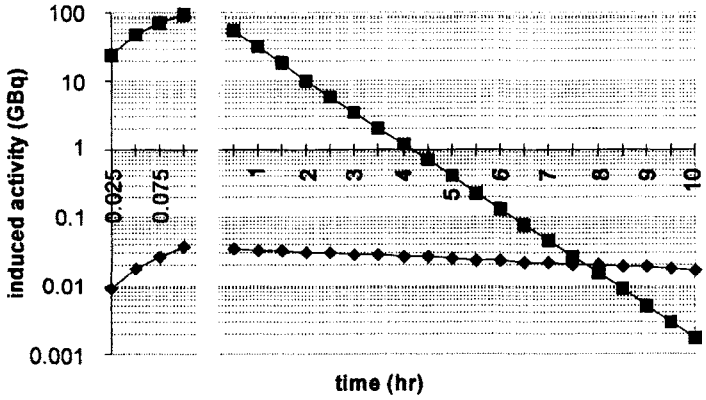

Fig.(8.5) Build-up and decay of activity $B(t_1,t_2)$ of a natural copper target by a 100 μA, 20 MeV proton beam. The irradiation begins at t = 0 to t_1=0.1 hr (end of bombardment) and is followed by a long decay period from t_1 to t_2= 10 hr. Note the difference in the time scales for irradiation and decay in this figure. ◆ ^{62}Zn ; ■ ^{62}Zn.

Many other unstable nuclides will be produced from proton irradiation in addition to the required ^{62}Zn. These "impurities" may or may not be a serious problem depending on how their individual half-lives compare with that of the desired product (in this case, 9.33 hr). If the impurity has a short half-life it may decay to insignificant amounts, even if produced with high probability. During the time period required for chemical separation and extraction of the Zn product, this is indeed the case for ^{63}Zn and ^{61}Zn produced by (p,n) and (p,3n) reactions on ^{63}Cu with half-lives of 38 min and 88 s respectively. On the other hand, an impurity product with a half-life as long as 245 d will not be produced in any large quantities unless it has a very large activation cross-section. Again, over the irradiation time needed to produce optimum quantities of ^{62}Zn, the production of ^{65}Zn from a (p,n) reaction on ^{65}Cu is insignificant.

The most serious contaminant is the production of ^{64}Cu having a yield and half-life similar to that of the desired product ^{62}Zn. However, when chemical extraction

methods can ensure that radioactive Zn atoms can be efficiently separated from the Cu, Table (8.6) shows that only the first two reactions need be considered.

Table (8.6) The Yields and product half-lives of the principal impurity reactions when natural copper is irradiated by 20 MeV protons in order to produce ^{62}Zn.

Reaction	Yield,Y(MBq μA^{-1} hr^{-1})	Product Half-life
^{63}Cu (p, 2n) ^{62}Zn	**48.8**	**9.33 hr**
^{63}Cu (p, n) ^{63}Zn	90.4×10^{2}	38 min
^{65}Cu (p, n) ^{65}Zn	60×10^{-2}	245 d
^{63}Cu (p, d) ^{62}Cu	12.2×10^{3}	9.8 min
^{65}Cu (p, d) ^{64}Cu	58.4	12 hr

In Fig.(8.5), use has been made of Eq.(8.19), since an irradiation time, t_1, of 6 min is not sufficiently small with respect to the shortest half-life of 38 min. The lower curve corresponds to a small value of Yield (4.9 GBq) and a long half-life, e.g. 9.33 hr for ^{62}Zn. The upper curve corresponds to a large value of Yield (904 GBq) but a much shorter half-life, e.g. 38.3 min for ^{63}Zn. Even with such a large difference in yield, the induced activity of ^{62}Zn becomes larger than that of ^{63}Zn at about 8hr after the end of bombardment (EOB).

References

[1] W.H.Sullivan, *Tri-linear chart of nuclides*, (United States Atomic Energy Commission, 1957)

[2] W.Seelmann-Eggebert, G.Pfennig and H.Munzel, *Karlsruher Nuklidkarte*, (Kernforschungszentrum, Karlsruhe 1974).

[3] K.H.Beckurts and K.Wirtz: *Neutron Physics*, (Springer-Verlag, Berlin,1964).

[4] P.P.Dmitriev, *Radionuclide yield in reactions with protons, deuterons,α-particles and ^{3}He ions*, (IAEA Report,1986, INDC(CCP)-263/G+CN+SZ).

CHAPTER 9

RADIOTHERAPY

9.1 Introduction

The primary aim of radiotherapy is the irradiation of a diseased volume of tissue with a lethal dose while at the same time causing minimum damage to the surrounding normal tissue. As a consequence, the treatment is always limited by normal tissue tolerance. The sequence of steps in a treatment is as follows :

- The clinician first identifies the volume to be treated from the examination of the patient, and from images of the treatment volume. These can be images from diagnostic X-rays, Computerized Tomography, Ultrasound or Magnetic Resonance.
- The method of irradiation is then chosen. This normally requires a choice between photons or electrons or a combination of these, together with a decision on beam energy, size of field and number of fields.
- A decision is then made on the number of dose fractions, the dose per fraction and the overall total dose. These decisions are based largely on clinical experience which has been built up over many years.
- The implementation of the prescribed dose regime is the responsibility of the physicist, who must deliver the required dose(s), certainly to a precision of $\pm$ 5% and preferably to $\pm$ 3%.

Although modern radiotherapy is still dominated by external beam facilities which use photons and electrons, a small number of specialist beams of protons and negative pions are also used at centres where high energy particle accelerators are available. Likewise, in the vicinity of a nuclear reactor, a special application of neutron therapy - Boron Neutron Capture Therapy - is still under consideration as an effective modality for certain types of tumour. Continuing developments in all areas have now added further possibilities to an increasing array of therapeutic techniques.

There are two approaches to radiotherapy – teletherapy and brachytherapy.

Teletherapy (*therapy from a distance*) :

- This mostly uses external beams of photons and electrons. Protons, pions and heavy ions are used at a few institutions. Conventional teletherapy with high energy neutrons is no longer used.
- Boron Neutron Capture Therapy (BNCT) uses beams of low energy neutrons.

Brachytherapy (*therapy in close proximity*) :

- This technique uses the insertion into the patient of a physically small, but highly radioactive, source in order to achieve the localized irradiation of diseased tissue. It requires very precise dosimetry and very careful control of source positioning. Low, Medium and High Dose Rates are used (LDR, MDR and HDR). LDR is used as a continuous irradiation up to the total required dose. HDR, on the other hand, must be given in fractions of the order of minutes. This is a time which is short compared with the characteristic time, ~1.5 hr, in which sub-lethally damaged cells can repair.
- Interstitial radiosurgery. Use is made of a non-radioactive source which is sufficiently small to be inserted into a cannula.

9.2 Photons

Codes of Practice which deal with the standardization of dosimeters, (see sections 7.11.1 and 7.11.2), indicate the energy regions which are now routinely used in photon teletherapy.

- Low energies – orthovoltage X-rays have a Half-Value-Layer (HVL) in the range 1.0 to 8.0 mm Al [1]. Superficial X-rays have a HVL in the range 0.1 to 4.0 mm Al [2]. These correspond approximately to anode voltages up to 200 kVp and 100 kVp respectively.
- Medium energies – These are specified by a Half-Value-Layer in the range 0.5 to 4.0 mm Cu and correspond to anode voltages up to ~300 kVp.
- High energies – megavoltage. Photons in this energy range come either from a ^{60}Co radioactive source (γ photons up to 1.33 MeV) or from a linac operated at energies between 4 and 25 MeV. The X-ray photon beams in these cases are referred to as 4 MV and 25 MV.

Low energies are used in superficial and contact therapy (e.g. see also section 9.7.4) for the treatment of skin and superficial tumours. For these purposes a radiation is required which has its dose maximum at the surface, and not below it as is the case for increasingly higher photon energies. There are relatively simple demands on collimation when only a single radiation field is used. Capital and running costs are low as a result.

Two important considerations at these low energies are :

- The dominance of the photoelectric effect at photon energies <150 keV which gives rise to a large differential absorption between bone and soft tissue, Fig.(9.1). This is a positive advantage when dealing with diseased bone, but a disadvantage

when treating underlying tissues since the overlying tissues receive considerable dose.

The importance of scatter at all energies up to ~500 keV demands that full account be taken of the large scatter due to Compton and Rayleigh interactions, Fig.(9.2).

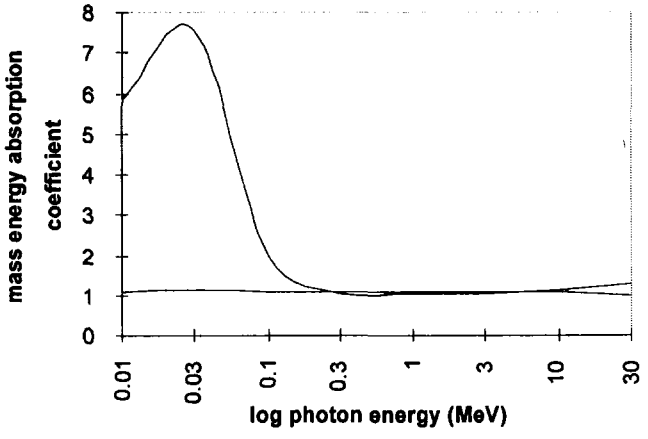

Fig.(9.1) Energy dependence of mass energy absorption coefficient ($\mu_{en}/\rho = \mu_{ab}/\rho$) normalized to that of air at STP. (n_0 = electron density).
Upper curve: Adult skeletal cortical bone, ρ = 1920 kg m^{-3}, $n_0 = 5.95 \times 10^{26}$ kg^{-1}. Lower curve: Adult skeletal muscle, ρ = 1050 kg m^{-3}, $n_0 = 3.006 \times 10^{26}$ kg^{-1}. Data taken from [3].

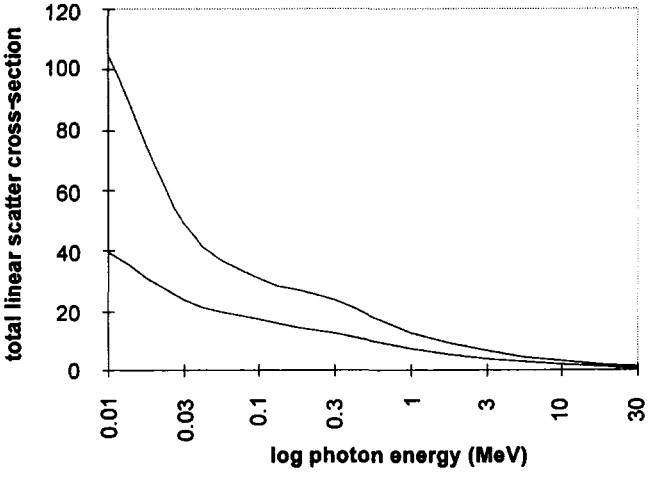

Fig.(9.2) Energy dependence of total scatter cross-section ($\sigma_{coh} + \sigma_{incoh}$)(m^{-1}) in adult skeletal cortical bone (upper curve) and adult skeletal muscle (lower curve). Data taken from [3].

The effects of differential absorption and low energy scatter require careful consideration at kilovolt energies whenever inhomogeneities in density or atomic number are present, Figs.(9.1) and (9.2).

For deeper tumours, photons generated in the megavoltage range have a number of important advantages over those at lower energies. These are :

- The existence of skin sparing because the dose maximum is now slightly below the surface.
- Greater penetration leads to an improved percentage depth dose.
- Less scattered radiation, Fig.(9.2). This results in a narrower penumbra.
- It is possible to use beam-shaping filters and wedges, see section 9.2.5.
- There is less differential absorbed dose in bone, Fig.(9.1).

However, care has to be taken to minimize the large exit dose which can sometimes result from the use of high energy photons on small patient cross- sections.

9.2.1 Geometrical factors

An important consideration with any type of radiation at any energy, is the degree of penumbra at the edges of the intended field. This appears as an annular ring surrounding the projection of the target volume onto a plane perpendicular to the beam central axis. Within this area there is not only a reduced intensity of radiation but also a likely change in beam quality (i.e. in the energy spectrum).

The extent of the penumbra is determined by the :

- size of the source. In the plane of Fig.(9.3) the important dimension is the diameter, *S*.
- the source surface distance, *SSD*.
- the distance between the source and the lower surface of the collimator, *L*.
- the distance between the end of the collimator and the surface of the phantom or patient, $x = SSD - L$.

Although the size of the geometric penumbra is given by :

$$P = S\left(\frac{SSD - L}{L}\right) = S\left(\frac{SSD}{L} - 1\right)$$

the clinical field size is usually defined as the distance between the 50% intensity points, Fig.(9.3).

Good definition of the irradiated area on the phantom surface is therefore

achieved with a small source diameter, *S*, and small distance from the end of the collimator to the surface, *x*. Too large a value of *L* can result in a large secondary electron flux at the patient's skin due to photon interactions with the collimator material. This problem can be severe at large field sizes.

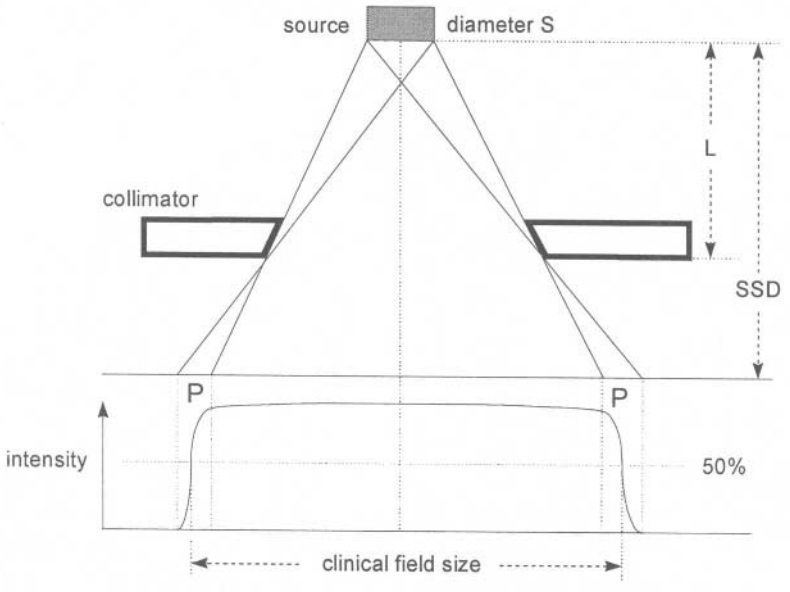

Fig.(9.3) Formation of penumbra, *P*, due to an extended source diameter, *S*, [5]. With permission from Charles C.Thomas Ltd., Springfield, Ill., USA.

In practice, however, this is only important for ^{60}Co gamma rays (1.33 and 1.17 MeV) which generally use an *SSD* of 80 cm. The problem can be partly overcome by the introduction of a low Z electron filter between the end of the collimator and the skin. For linac-generated photons, which normally use an *SSD* of 100 cm, an air gap of 30 – 40 cm is sufficient to stop most of these electrons.

9.2.2 Specification of dose ratios

There are two essential quantities to be determined when preparing the delivery of a prescribed radiotherapy dose :

- The dose in air at a certain distance from the machine exit window, and
- the dose in a phantom at a constant measuring position, when all the machine parameters – energy, fluence, collimator length and area – are kept constant.

Fig.(9.4) shows three arrangements in which the geometrical beam width is the same at a total distance r_0 from the exit window. Measurement of dose at P_0 is the

dose in air D_0. When a phantom is introduced and measurements D_1 and D_2 are made at points P_1 and P_2 then the Tissue Air Ratio (*TAR*) is defined for the two cases as :

$$TAR_1 = \frac{D_1}{D_0} \quad \text{and} \quad TAR_2 = \frac{D_2}{D_0} \tag{9.1}$$

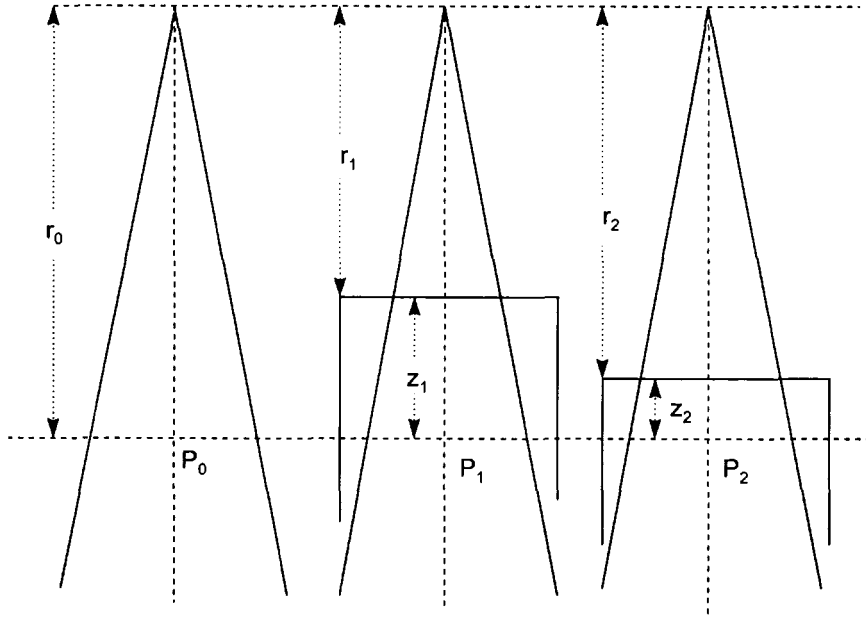

Fig.(9.4) Diagram to illustrate the distinction between tissue-air and tissue-phantom ratios. The energy of the radiation and the size of the radiation field at the measurement points, P_0, P_1 and P_2 must be constant.

When high energy photons are used, however, the measurement of a tissue-air ratio is not appropriate because of the need to establish electronic equilibrium in the dosimeter (generally an ion chamber). This difficulty becomes more acute the higher the energy and the smaller the beam area. The Tissue Phantom Ratio (*TPR*) is therefore introduced by using a reference depth P_2 which is generally chosen to be slightly deeper than the dose maximum. Thus,

$$TPR = \frac{D_1}{D_2} = \frac{TAR_1}{TAR_2} \tag{9.2}$$

It is important to note that :

- The *TAR* depends only on field size and photon energy.

- The field size must be equivalent at all three measurement positions.
- The dose at any given depth must be normalized to the dose maximum to give a Percentage Depth Dose (*PDD*). For high energy radiation the dose maximum does not occur at the surface because of the increasingly forward momentum of the secondary electrons (Figure 7.4). This is called Build-up. At lower energies the combined effects of attenuation and scatter can also produce a dose maximum which does not occur at the surface. This is especially true when large field sizes are used.

9.2.3 The effects of scattered radiation - field size and backscatter

The variation of absorbed dose with depth in a phantom depends primarily on SSD because of the Inverse Square Law decrease with distance. Additionally, it depends on beam area due to the effects of secondary scatter. This is particularly important at low incident photon energies.

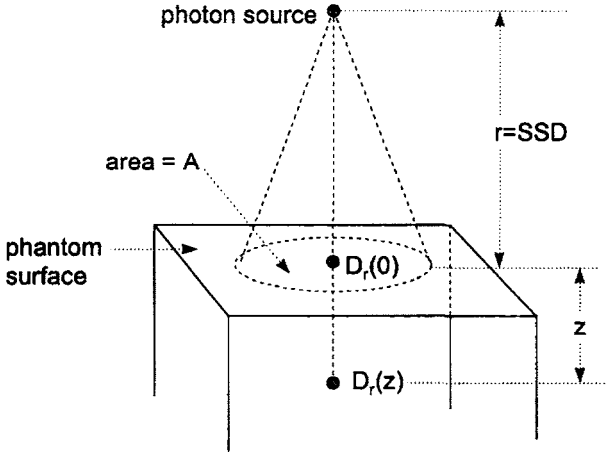

Fig.(9.5) Irradiation of a phantom by a photon beam of area *A* and *SSD* = *r*.

In Fig.(9.5), it is assumed that an isotropic point source emitting *N* photons per second, irradiates an area *A* of a phantom surface at an *SSD* = *r*. The dose at the surface is proportional to the photon fluence, $N\,A/4\pi r^2$, over this area. If the photon energy is sufficiently low that there is no dose build-up, the dose maximum at the surface can be written :

$$D_r(0) = \frac{k\,N\,A}{4\,\pi\,r^2}$$

At a depth z in the phantom the dose is reduced firstly due to the increased distance by the inverse square law and secondly by the exponential attenuation due to the material of the phantom. We can neglect any exponential attenuation in the air above the phantom. Thus at depth z the dose is :

$$D_r(z) = \frac{k\ N\ A}{4\ \pi\ (r+z)^2}\ exp(-\mu z) \tag{9.3}$$

where μ is the total linear attenuation of the phantom material at the mean incident photon energy. Eq.(9.3) does not include any effects of scatter. These are present, however, even when $z = 0$ due to the scatter back to the surface of photons which have interacted initially at greater depths within the phantom.

If the phantom material is uniform in composition and density, the extra dose due to the scattered radiation will be some fraction, f, of the primary intensity. This will depend on depth, z, and field area, A. Thus :

$$f = K\ z\ A$$

The constant K gives the probability per unit volume that an interaction other than absorption has taken place. We then have :

$$D_r(z)_{total} = D_r(z)_{primary} + D_r(z)_{scatter}$$

$$D_r(z)_{total} = D_r(z)_{primary}[1 + K\ z\ A] \tag{9.4}$$

The fractional dose, F, at depth z, to that at the phantom surface is then given as:

$$F = \frac{D_r(z)}{D_r(0)} = [1 + K\ z\ A]\ \frac{r^2}{(r+z)^2}\ exp(-\mu z) \tag{9.5}$$

Note that only in the limits that $r \rightarrow \infty$ and $A \rightarrow 0$ can the value of μ be determined. Constant K contains all the parameters which relate to a given type and energy of radiation, to a particular geometry and to the material of the phantom.

There are several instances in radiotherapy where it is necessary to determine the amount of backscatter from a surface. The general definition of a Back Scatter Factor is:

$$BSF = \frac{\text{"Radiation Effect" at the surface of a phantom in a beam of given area}}{\text{"Radiation Effect" at the same position without scatter}}$$

The "Radiation Effect" could refer to either exposure or absorbed dose with and without the phantom. When using an ionization chamber, the BSF can be conveniently expressed as :

$$BSF = \frac{\left[X\,(\mu_{tr}/\rho)_{air}^{water}\right]_{phantom}}{\left[X\,(\mu_{tr}/\rho)_{air}^{water}\right]_{free-in-air}} \tag{9.6}$$

In Eq.(9.6), X is the measured exposure at the surface of the phantom and at the same point in free air, and $(\mu_{tr}/\rho)_{air}^{water}$ is the mass energy transfer coefficient ratio in water and air.

Strictly speaking, this ratio does not cancel out in Eq.(9.6). This is because the photon energy spectrum responsible for the ion chamber readings is slightly different in the two cases due to the contribution from backscattered photons when the phantom is present. These ratios depend on the incident photon energy and on the depth in, and the material of, the phantom. Theoretical calculations show that these ratios do not vary by more than ~10% for photon energies between 10 keV and 10 MeV. The differences are therefore small enough for the mass transfer coefficients in Eq.(9.6) to be cancelled out.

At a constant photon beam energy, the dose $D_{z,A}$ at a depth z in the phantom at field size A can be related to the dose D_{z,A_0} at the same depth, but different field size A_0, by :

$$D_{z,A} = D_{z,A_0}\,\frac{BSF(A)}{BSF(A_0)}$$

Although most BSF and Depth:Dose data are given for square or circular fields, rectangular or irregular fields can be interpolated by using the integration of equivalent squares or circles [4].

Table (9.1) Backscatter factors for circular fields applicable to photons in the 100kV to 400kV range. Data selected for Al and Cu from a more comprehensive list in [5].

HVL	10 cm²	20 cm²	50 cm²	100 cm²	150 cm²	200 cm²
1.0 mm Al	1.108	1.138	1.179	1.205	1.218	1.229
4.0 mm Al	1.141	1.190	1.265	1.314	1.334	1.350
0.5 mm Cu	1.186	1.235	1.314	1.376	1.406	1.430
4.0 mm Cu	1.076	1.104	1.152	1.197	1.220	1.240

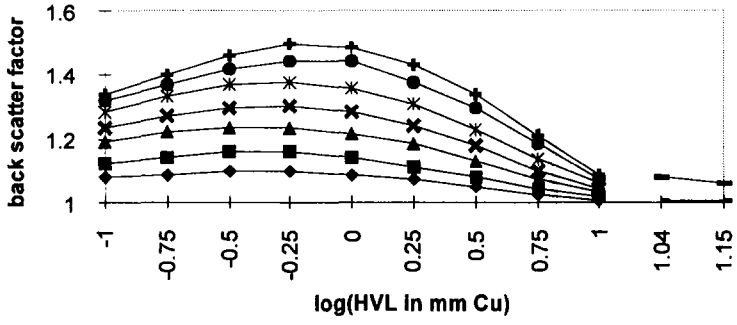

Fig.(9.6) Photon backscatter factors versus the log(Half Value Layer in mm) of added copper filtration. The curves apply to square fields of X-rays up to an HVL of 10 mm. The sides of the square fields are : ◆ 2 cm : ■ 3 cm : ▲ 5 cm : ✖ 7 cm : ✱ 10 cm : ● 15 cm : ✚ 20 cm. Data points are also given at approximate HVL values of 11 mm and 14 mm for ^{137}Cs and ^{60}Co gamma rays respectively at the extreme fields sizes of 2 cm and 20 cm square sides. Data taken from [4].

9.2.4 Dependence of fractional depth dose on TAR, TPR and BSF

The dose ratios expressed in Eqs.[9.1] to [9.6] are easily related. Referring to Fig.[9.4] we call D_{01} and D_{02} the dose measured at the phantom surfaces when the *SSD* values are r_1 and r_2 respectively.

In the first case, D_{01} is expressed in terms of the in-air dose D_0 corrected for the inverse square law increase to an *SSD* of r_1. Thus, the backscatter factor can be expressed :

$$BSF_1 = \frac{D_{01}}{D_0 \, (r_0^2 / r_1^2)}$$

The fractional depth dose at depth x_1 can now be written :

$$F_1 = \frac{D_1}{D_{01}} = \frac{D_0 \, TAR_1}{D_{01}} = \frac{TAR_1}{BSF_1 \, (r_0^2 / r_1^2)}$$

with a similar expression for a depth x_2. The tissue-phantom-ratio now becomes :

$$TPR_{12} = \frac{D_1}{D_2} = \frac{TAR_1}{TAR_2} \, \frac{r_1^2}{r_2^2} \, \frac{BSF_2}{BSF_1}$$

These ratios and factors are given in standard data tables [4] for different photon beam energies (expressed as Half Value Layers), field areas and shapes (circular or square) and depths in the phantom. Although the Tissue Air Ratio and backscatter

factors are independent of the Source Surface Distance, the Tissue Phantom Ratio is quoted for a specific reference depth in the phantom.

9.2.5 Filters, compensators and shields

In radiography the primary function of a filter is to modify the energy spectrum of the incoming radiation (Chapter 10). In a therapy context the intention is to modify the spatial intensity distribution. Even though there is always some degree of energy spectrum change when poly-energetic radiation interacts with matter, this is of minor concern when photons are used for therapy.

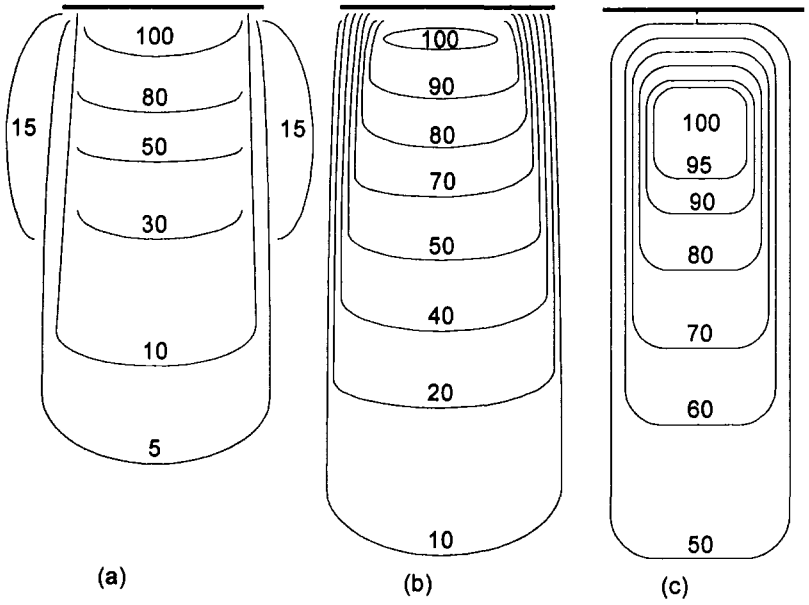

Fig.(9.7) Representations of isodose contours from photon beams at (a) 200 kV, (b) 2MV, (c) 20 MV. The depths of the dose maxima in each case are approximately 0 cm, 0.75 cm and 4 cm respectively, [5]. With permission from Charles C.Thomas Ltd., Springfield, Ill., USA.

Schematic representations of isodose contours from X-ray photon beams at 0.2, 2 and 20 MV operating potentials are shown in Fig.(9.7). These show :

- Increased penetration at the larger energies, and a dose maximum which occurs at the surface (0.2 MV), and at approximate depths of 0.75 cm (2 MV) and 4 cm (20 MV) respectively.
- At the lowest energy, Fig.(9.7a), a sharp discontinuity in dose is observed at the edge of the beam. This is primarily due to the small focal spot size. As the source size increases, the discontinuity becomes less prominent due to the larger penumbra produced by the beam defining collimators. However, the increased probability of sideways scatter at low energies causes the low-dose contours to extend beyond the beam edges.

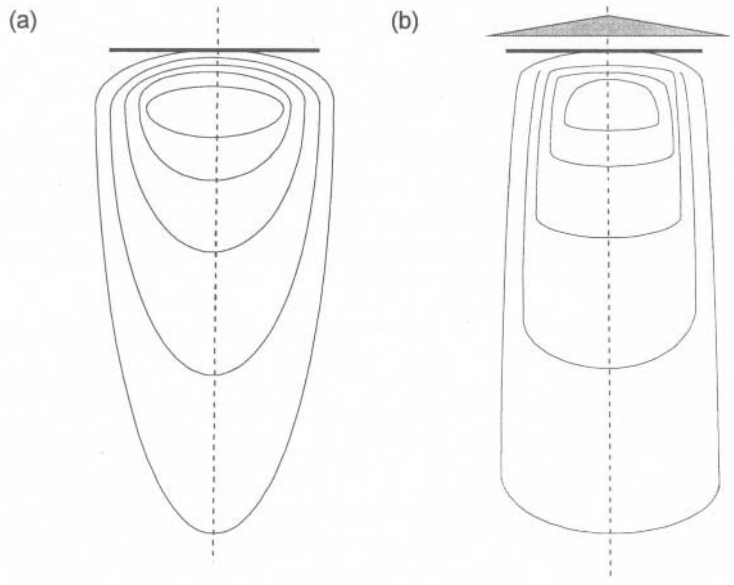

Fig.(9.8) An illustration of the modification of a set of isodose contours in a water phantom being irradiated by a source of MV X-ray photons : (a) without filtering : (b) using a beam flattening filter.

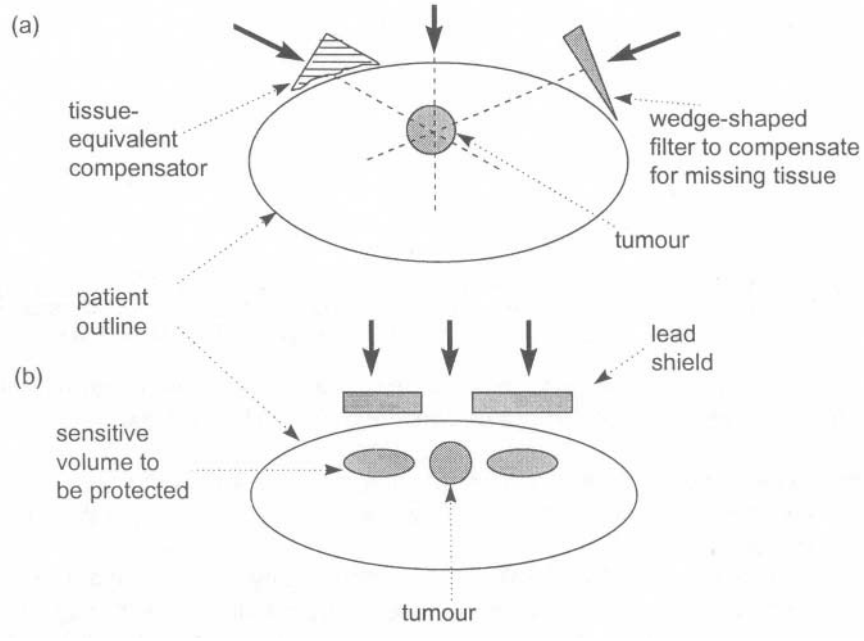

Fig.(9.9) Schematic diagrams to illustrate : (a) the use of multiple fields and methods of dealing with oblique incidence. These include the tissue compensation method (left) and wedge method (right). (b) the use of shadow shields to provide additional protection for sensitive areas.

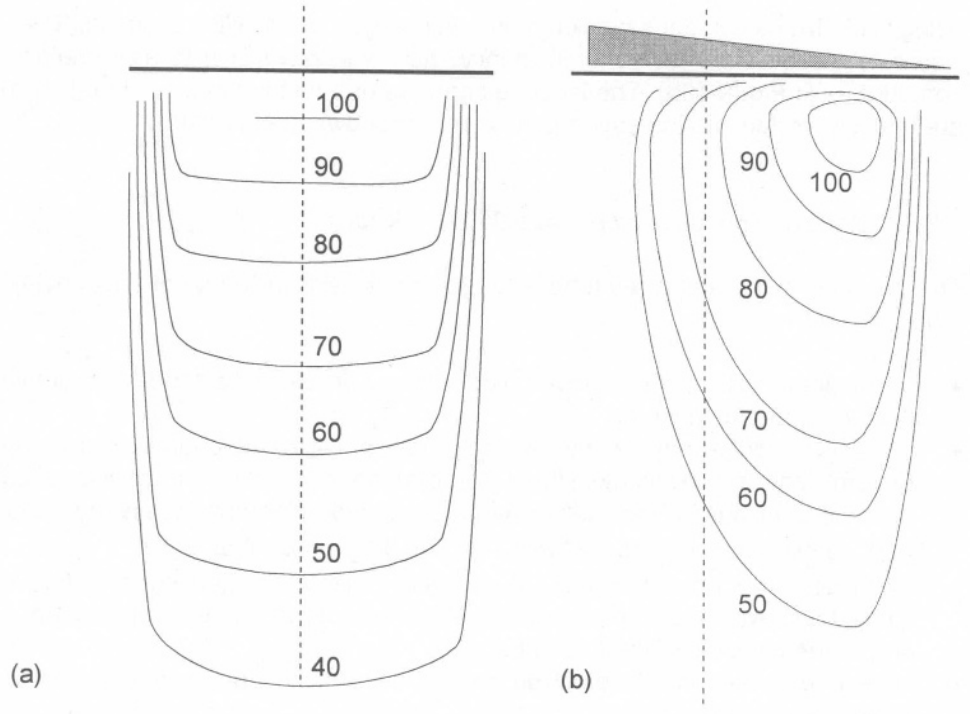

Fig.(9.10) Illustration of the effect of a normal incidence wedge filter on an MV photon beam.

- At 2 MV, Fig.(9.7b), the contours become narrower as the photons become more and more forward directed along the beam axis. In this event the dose distribution across the beam axis ceases to be sufficiently uniform for practical purposes. The situation is recovered by the use of a beam-flattening filter, Fig.(9.8).

Isodose contours are generally determined using a water or tissue-equivalent phantom whose surface is perpendicular to the beam axis. With these data, a number of important factors need to be considered in the implementation of a treatment plan. These are illustrated in Fig.(9.9).

- The position of the tumour target in relation to other sensitive organs within the patient. This leads to the use of multifields.
- The angle the beam central axis is required to make with the surface of the patient. This leads to the use of wedge-shaped filters or tissue-compensation devices to recover a uniform dose distribution at the target.
- Protection of sensitive tissue can be achieved by the use of shadow shields, Fig.(9.9b).

The devices illustrated in Fig.(9.8) are used to achieve a uniform dose in a tumour when there is no need to avoid sensitive tissues nearby. Symmetrical isodose contours can be produced in the patient with a beam entering at oblique incidence

using either tissue compensation or, more frequently, a wedge filter, as in Fig.(9.9a). Use of a wedge filter at normal incidence, however, gives rise to asymmetrical contours as in Fig.(9.10b). The isodose contours of a flattened beam, Fig.(9.10a) are then converted into the asymmetric contours shown in Fig.(9.10b).

9.2.6 Orthovoltage glass tube (up to 300 keV X-rays)

The design of a therapy X-ray tube is fundamentally similar to that of a diagnostic tube, except that :

- There needs to be increased insulation between anode and cathode to maintain the higher anode voltages.
- There is no longer any need for a small focal spot size. Although spot sizes up to 1 cm diameter are common, there is less importance attached to the increased penumbra because of the use of external collimation. Target angles are typically ~30° to the vertical compared with ~17° for diagnostic tubes.
- Because of the higher electron energies and currents, the filament is nested in a focusing cavity and surrounded by a shield in order to constrain the electrons only in the direction of the anode target.
- High energy secondary electron emission from the anode now becomes important because :
- electrons which reach the tube envelope will tend to deposit charge, the field from which can disturb the focusing of the primary beam,
- if the tube envelope is glass, high fluxes of electrons will cause radiation damage,
- electrons stopped by the tube produce *bremsstrahlung*. This can affect the sharpness of the emerging beam.
- The problem of secondary emission is overcome by the use of a "hooded" anode in which a copper tube intercepts the secondary electrons before they reach the tube envelope. The X-rays produced by the copper are then absorbed by an additional sleeve of tungsten.
- The primary X-ray beam emerges through a thin beryllium window inset into the copper and tungsten sleeves surrounding the anode hood. An additional thinning of the glass envelope adjacent to the beryllium window allows even more penetration of the emerging beam. These windows stop the secondary electrons but do not significantly attenuate the photon beam.

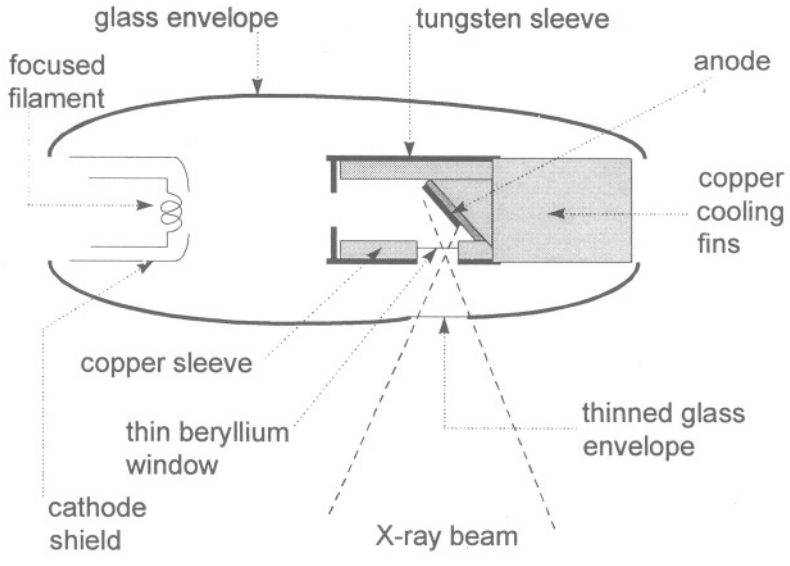

Fig.(9.11) Schematic diagram of a glass envelope ortho-voltage X-ray therapy tube, [5]. With permission from Charles C.Thomas Ltd., Springfield, Ill., USA.

9.2.7 Orthovoltage metal-ceramic tube

A more recent design of orthovoltage X-ray tube uses a metal-ceramic separation between anode and cathode. This confers a number of important advantages :

- The anode is now kept at ground potential, thereby facilitating simple water cooling.
- The negative high voltage is applied to the cathode by means of a single cable which fits into a metal-ceramic connector.
- The overall diameter of the tube can be reduced to 10 cm with a short focus-window distance.
- An exit beryllium window is welded to the outer steel tube to give a typical inherent filtration of only 2.2 mm Be.
- The small tube diameter and inherent filtration lead to a high output which can run down to 50% of the rated tube current and 20% of the rated tube voltage without unduly affecting the beam quality.

9.2.8 The Greinacher constant-potential voltage-doubling circuit

The steady output applied to the anode is almost twice the peak transformer voltage, because of the arrangement of the capacitors and diodes. When point P in Fig.(9.12) is positive, current flows through diode D2 charging capacitor C2. In the next half

cycle, when point P is negative, diode D1 conducts to give charge on capacitor C1 in the same direction as D2. The tube voltage is thus twice the peak.

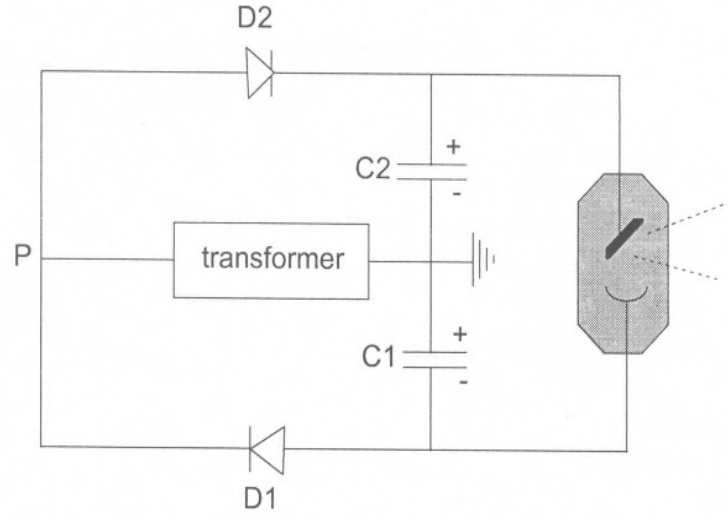

Fig.(9.12) Schematic diagram of a Greinacher constant-potential voltage-doubling circuit

9.2.9 γ-ray photons

A highly radioactive isotope emitting high energy γ-rays can be used as a source of photons for therapy. Two isotopes have been used :

- ^{137}Cs – produced from U fission, $U(n,f)^{137}Cs$ with $T_{1/2}$ = 30.1yr. The reliance on fission for the production of this isotope means that the specific activity is fixed at ~2.6 TBq kg^{-1}. Such a source will also consist of a small amount of ^{134}Cs with $T_{1/2}$ = 2.1 yr. This produces a number of photons with much greater energy, up to 1.4 MeV, and has implications for shielding.
- ^{60}Co – produced by the reaction, $^{59}Co(n,\gamma)^{60}Co$ with $T_{1/2}$ = 5.26 yr. For typical reactor fluxes employed for such irradiations, the resulting specific activity is high (~7.4 TBq kg^{-1}).

Because of the low specific activity of ^{137}Cs, dose rates that are sufficiently high for external beam therapy can only be achieved from physically large sources working at short SSD. The result is a large penumbra and therefore a poor depth dose distribution. The latter is approximately the same as that produced by 250 kV X-rays. Consequently, ^{137}Cs is nowadays only used for brachytherapy (section 9.7).

The higher photon energies from ^{60}Co, Fig.(9.13), together with a higher specific activity and an intrinsically stable output continues to give the ^{60}Co source some

limited value in radiotherapy. Typical source strengths are 2×10^{14} Bq (200 TBq ≡ 5405 Ci).

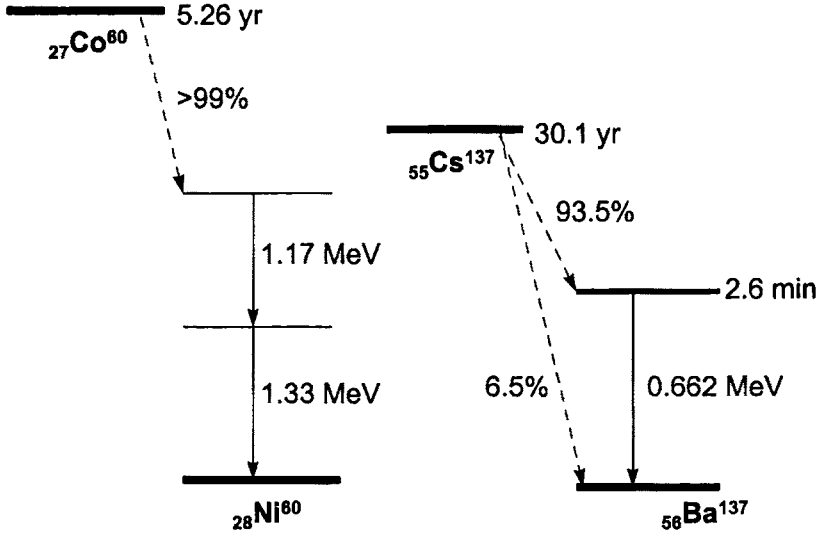

Fig.(9.13) Decay schemes of ^{60}Co and ^{137}Cs.

Two designs are in use, both of which contain the high activity source within a large sphere of shielding material. In the first design the source moves between two positions, one closed the other open. In the second, the source is stationary but a moveable shutter is used.

In the first design, the radioactive material consists of about 8 cobalt discs, 2 mm thick, 17 mm diameter, sealed into a double-walled stainless steel casing of external diameter 25 mm and height 39 mm. This casing is contained within a lead-filled drum which can rotate about a vertical axis within two lead-filled stainless steel spheres. When the casing is in the "safe" position the source resides in the larger diameter (~60 cm) sphere. When in the "open" position, it moves to the centre of the smaller (~30 cm) sphere to permit the photons to emerge through an exit port.

Noteworthy features of this type of source are :

- It is inefficient because of the small fraction of the (isotropic) photon emission that can be used in the therapeutic beam.
- Although the primary photon flux is monoenergetic, (1.17 and 1.33 MeV from ^{60}Co) there is a *bremsstrahlung* component due to the stopping of the energetic β^- particles ($E_{\beta,max}$ = 0.31 MeV) in the stainless steel casing.
- The design of the head should ensure that when the source is in the "safe" position, the leakage radiation at 1 metre distance should not exceed 0.1% of the useful beam at that distance.

- The collimator system is largely composed of a copper-tungsten alloy. Although more expensive than lead, its greater density makes it a superior attenuator at energies greater than ~1 MeV (where Compton interactions dominate). In addition, its physical properties make it easier to engineer and fabricate.
- Compared with therapeutic X-ray sources, the need to achieve high source activity generally means that the source size is large (~17 mm diameter). The geometric penumbra therefore also tends to be large since, for two sources of equivalent volume, a source having long cylindrical geometry would have more self-absorption than one with a flat disc geometry.

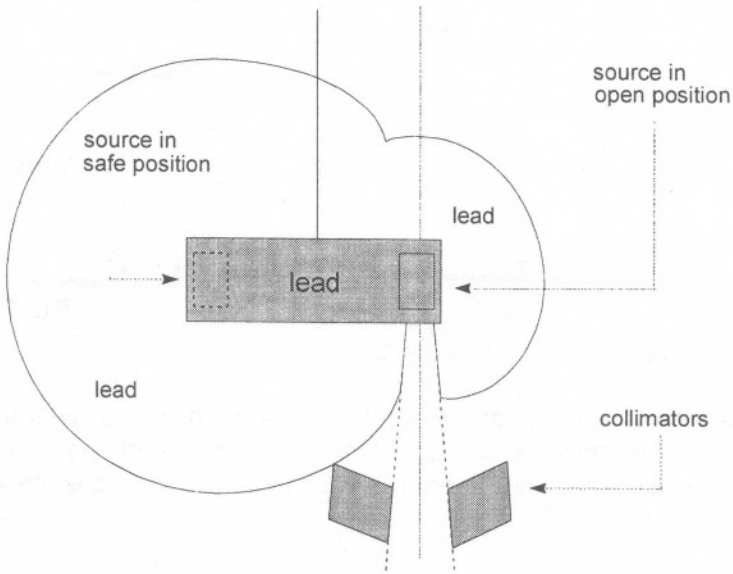

Fig.(9.14) Diagrammatic section through one design of ^{60}Co beam unit

9.2.10 Linac-based MeV X-rays

Linear electron accelerators are used to produce therapy photon beams in the 4 – 25 MeV range. An incident electron energy, say 6 MeV, produces photon energies from 0 up to a maximum of 6 MeV. The precise energy spectrum depends on collimation and filtration, with a mean somewhere in the range 2 – 3 MeV. Such a beam is conventionally referred to as a 6 MV beam.

Acceleration of electrons in a linac is described in Chapter 1 up to the point at which they emerge from the end window of the rf waveguide. In the treatment head of a medical accelerator, the end window is removed in order to allow the electrons to traverse either an array of achromatic bending magnets, Fig.(9.15), a 90° bending magnet, Fig.(9.16) or a 270° achromatic system, Fig.(9.17). The final window (made from titanium, tantalum or stainless steel) which separates the machine high-vacuum from ambient pressures is then mounted at the end of the bending stage.

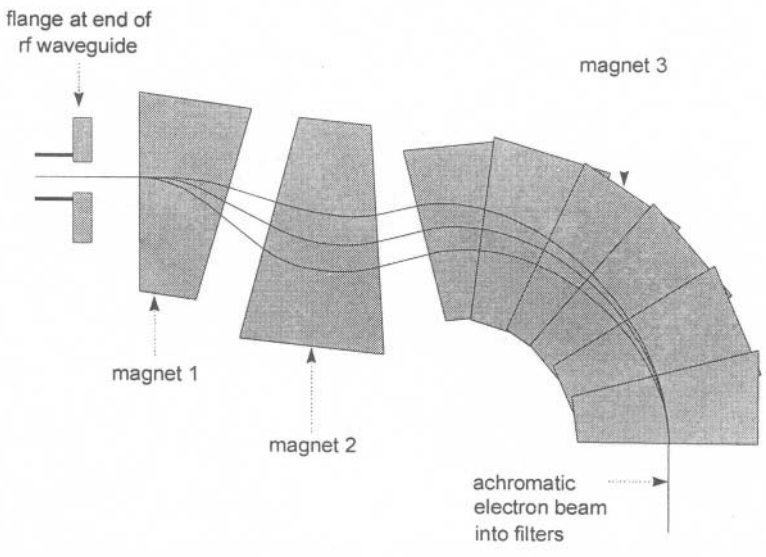

Fig.(9.15) A "slalom" achromatic triplet magnet array. With permission from Elekta Oncology Systems Ltd.

In the conversion of a (nearly) horizontal beam into a vertical one to make it suitable for isocentric operation, an achromatic system is superior to a 90° bending magnet. This is because :

- it reduces the energy dispersion and thereby achieves a final emerging beam at the exit window which is as tightly focused as the incident trajectories will allow. Although it is more compact, a simple 90° bending magnet is less satisfactory because of the dispersion it produces.
- it overcomes the serious problems associated with variation in electron energy due, for example, to temperature changes which affect the resonance conditions in the rf waveguide. If these occur, the dispersion in a 90° magnet may produce a change in exit position which, because of the fixed collimator system, can affect the symmetry of the output beam.

On the other hand, a dispersive 90° bending system, Fig.(9.16), provides a convenient means of finding the beam energy. In addition, it can fulfil the role of an energy selector in those machines capable of accelerating electrons over a wide energy range.

An alternative means of achieving an achromatic beam to the one shown in Fig.(9.15) is a single 270° magnet. An energy dispersed beam entering the system on the axis will also emerge on an axis 90° to the original direction, particles with different energies having traversed different trajectories within the magnet field, Fig.(9.17).

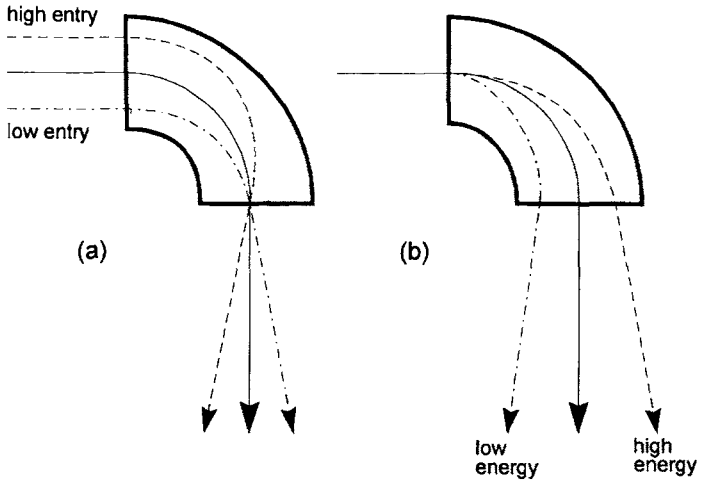

Fig.(9.16) A 90° bending magnet showing the dispersion due to (a) electrons with high and low trajectories with respect to the central ray and (b) electrons with high and low energies with respect to the central ray (see references [8] and [9] Chapter 1).

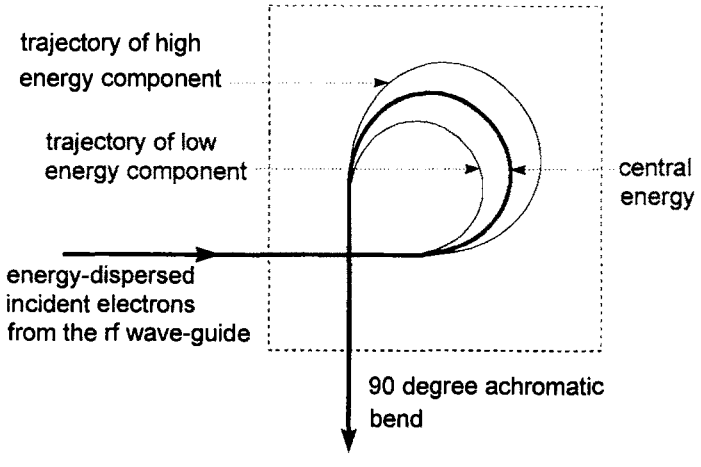

Fig.(9.17) Achromatic 270° bending magnet (pretzel) (see references [8] and [9] Chapter 1).

9.2.11 Depth:dose distributions

In general, a depth:dose distribution depends on the following four parameters. They are illustrated in Fig.(9.18).

- The inverse square law. Eq.(9.3) shows that the SSD, *r*, as well as the depth in the phantom, *z*, must be considered.
- The beam energy. This determines the attenuation of the primary photons with depth.
- The field size. Eq.(9.5) indicates that dose due to scattered photons adds to the contribution of the primary beam.
- The field shape. Both field shape and size are more important at low photon energies.

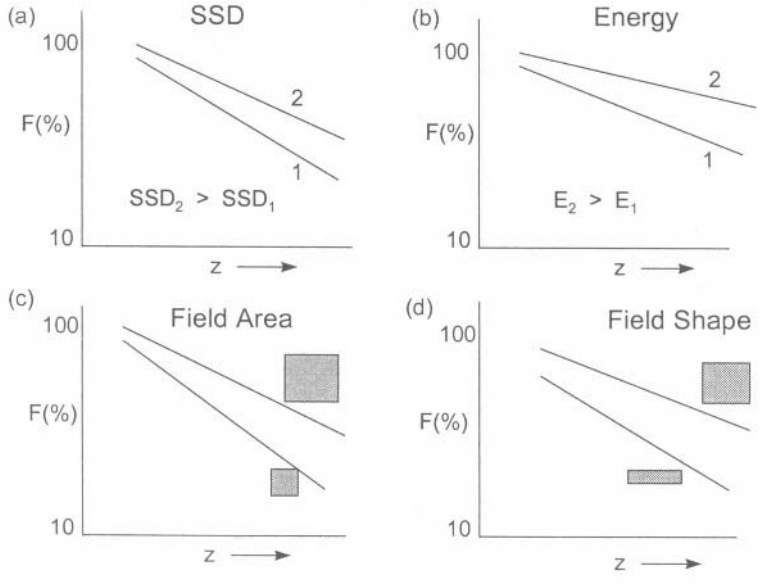

Fig.(9.18) The major parameters which determine the depth:dose distribution

Figs.(9.19) and (9.20) show the percentage depth doses for four photon beams over two different depth regions in a water-equivalent phantom. Note the logarithmic dose axis and the suppressed zero on the depth axis in Fig.(9.20).

With the exception of the ^{60}Co beam, the quoted beam energies refer to the mean energy of the electrons which strike the X-ray target (e.g. 4 MeV). The energy spectrum of the emerging photons is broad, however, because of the nature of the *bremsstrahlung* X-ray production process. In addition, the spectrum is also determined by the extent of beam filtration, collimation, and by the field size and SSD used. In view of the possibility of slight differences arising because of these factors, a therapeutic beam using 4 MeV electrons is therefore designated 4 MV. The mean photon energy is likely to be in the approximate range 1.5 – 2.5 MeV.

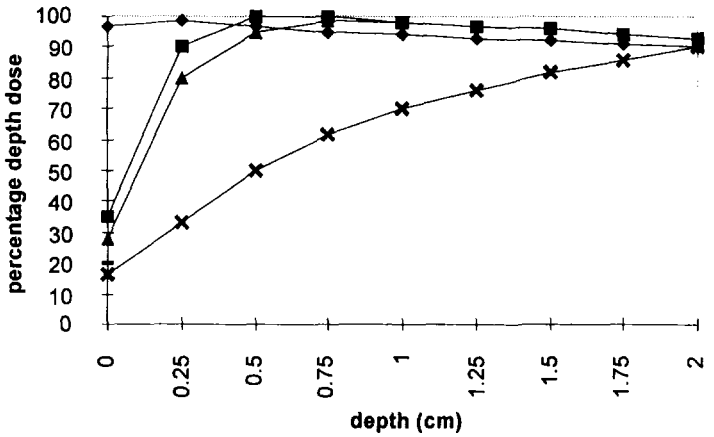

Fig.(9.19) Percentage depth dose in a water-equivalent phantom. Data taken from [5].
◆ 200 kV,10 cm × 10 cm, SSD = 50 cm ; ■ ^{60}Co, 10 cm × 10 cm, SSD = 100 cm ;
▲ 4 MV, 10 cm × 10 cm, SSD = 100 cm ; ✖ 22 MV, 10 cm × 10 cm, SSD = 70 cm.

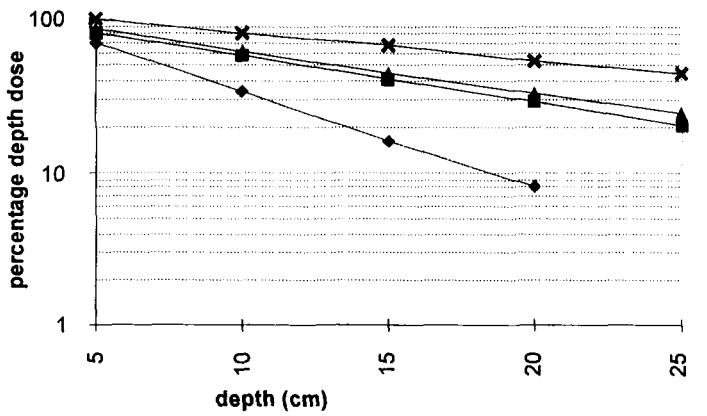

Fig.(9.20) Percentage depth dose in a water-equivalent phantom. Data taken from [5].
◆ 200 kV, 10 cm × 10 cm, SSD = 50 cm ; ■ ^{60}Co, 10 cm × 10 cm, SSD = 100 cm ;
▲ 4 MV, 10 cm × 10 cm, SSD = 100 cm ; ✖ 22 MV, 10 cm × 10 cm, SSD = 70 cm.

The depth of the dose maximum, z_{max}, is a function of mean photon energy. Table (9.2) gives the theoretical value of z_{max} in water. For photon beam energies ≤ 400 kV, the dose maximum is conventionally taken to be at z = 0, since the average thickness of skin epidermis is ~ 0.12 cm. A skin dose is therefore received at these low energies.

Table (9.2) The depth of maximum dose in water for photon beams between 100 kV and 15 MV.

E	100 kV	185 kV	^{137}Cs	^{60}Co	4 MV	8 MV	15 MV
z_{max}	30 μm	50 μm	120 μm	0.5 cm	1.0 cm	2.0 cm	3.0 cm

In practice, however, the depth of the measured dose maximum is generally less than the values of z_{max} in Table (9.2) because of the presence of electron contamination. This arises in the collimators, filters and the intervening air path and is a function of field size. Table (9.3) shows figures for the dose build-up region in water for ^{60}Co, 4 MV and in polystyrene for 10 MV photons using an SSD of 100 cm. A determination of the electron scatter contribution was made at 10 MV [6]. In all these cases, the surface dose is not zero.

Table (9.3) The decrease in the depth of the dose maximum due to electron contamination

	Field size (cm^2)	z_{max} (theory) (cm)	z_{max} (expt) (cm)
^{60}Co	5 × 5	0.5	0.3
	35 × 35		0.2
5 MV	4 × 4	1.3	0.9
	40 × 40		0.7
10 MV	5 × 5	2.15	2.2
[6]	30 × 30	2.1	1.75

9.2.12 Photon energy spectrum

Precise photon therapy requires detailed knowledge of the photon energy spectrum emerging from the machine exit window. The spectrum critically affects the design of :

- the beam flattening and wedge filters,
- multileaf collimators, and
- the factors needed to convert ionization chamber measurements to absorbed dose.

Various experimental and theoretical methods are used to determine these spectra. One of the most convenient, uses the measurement of transmission data and its reconstruction using numerical analysis, Fig.(9.21). For narrow-beam conditions, the transmission through thickness x of material is given by :

$$T(x) = \int_0^{E_{max}} exp\left[-\mu(E)\, x\right] F(E)\, dE \qquad (9.7)$$

In Eq.(9.7), $\mu(E)$ is the linear attenuation coefficient of the material, $F(E)$ is the fraction of photons transmitted with energies between E and $E+dE$, and E_{max} is the maximum energy of the photon spectrum. Francoise et.al. [7] used the spectral vectorial algebra of the matrix A in the direct solution of the matrix system :

$$A * F = T$$

where T is the relative transmission vector having components :

$$T_i = \sum_{j=1}^{n} A_{ij} . F_j$$

A_{ij} is an element of the attenuation matrix A and $F(E_j)$ is the fraction of the transmitted signal corresponding to photons in unit energy interval around E_j. Physical solutions to the above matrix system can be found with acceptable accuracy for clinical practice without the need to use a pre-shaped starting spectrum.

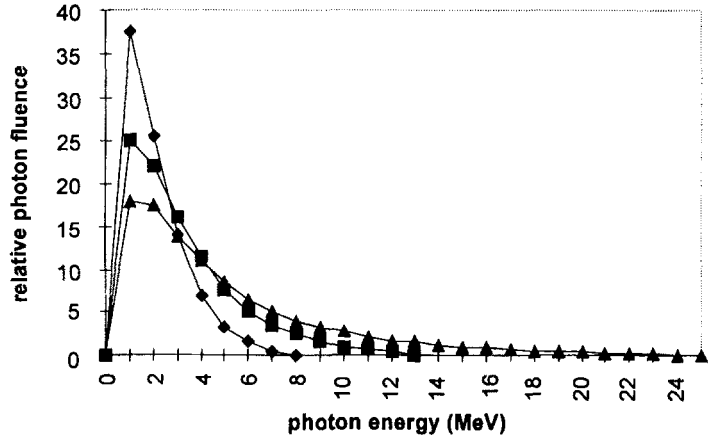

Fig.(9.21) Reconstructed photon spectra from transmission data (adapted from [7]) using nominal electron energies of 6 MeV (◆), 12 MeV (■) and 25 MeV (▲).

9.2.13 Neutron contamination of X-ray beams

In addition to the production of *bremsstrahlung* X-rays by energetic electrons, two other reactions are also possible at sufficiently high energies – electro-neutron production (e,n or e,e'n) and electron-induced fission (e,f). Neither of these becomes significant if the X-ray target material has an atomic number less than that of bismuth (Z = 83). Neutron generation from these reactions is therefore of little concern so long as targets and collimators are not made from materials such as depleted uranium.

Neutrons that are produced by the *bremsstrahlung* photons themselves – photoneutrons – can, however, contribute to the dose received in the phantom. In addition, they add to the general background in the vicinity of the accelerator and actually cause activation in some parts of the treatment head itself.

Photoneutron reactions (γ,n : γ,2n : γ,pn : etc.) can occur in the X-ray target and also in the high density materials which make up the beam hardening and flattening filters and collimators Fig.(9.22). The principal elements of concern are :

- tungsten (x-ray target and collimators)
- stainless steel (iron, carbon, manganese, nickel, tin, chromium, molybdenum - flattening filters)
- lead, antimony (wedge filters and collimators)
- aluminium (ionization chamber)

The spectrum of photoneutrons produced in the head of an electron linac is rather similar to the fission spectrum, with a most probable energy of ~2 MeV. As a general rule, however, neutron production can be ignored for photon energies ≤10MeV.

The total neutron dose, measured 2 m from the isocentre in the plane of the patient, depends on field size and on photon energy. For a 15 MV beam, the equivalent dose is ~ 4 mSv hr^{-1} for the minimum field size and ~ 2 mSv hr^{-1} for a 40 × 40 cm^2 field. Measurements with track etch detectors at the isocentre suggest that a neutron dose of 0.5 mSv per Gray of photon dose is received [8].

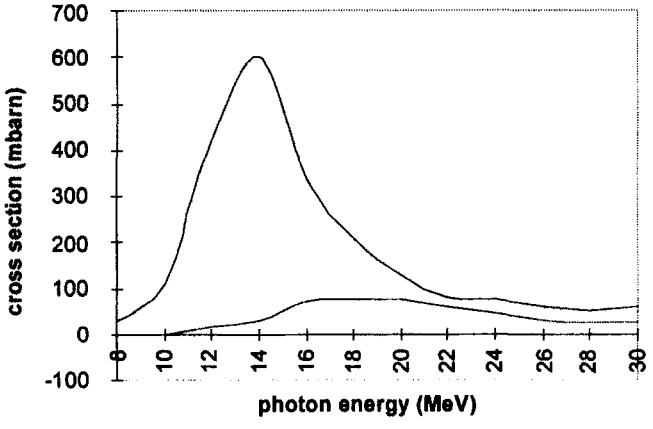

Fig.(9.22) Total photoneutron cross-section (γ,xn where x = 1,2...is the number of neutrons emitted) versus incident photon energy. Top curve, ^{206}Pb : bottom curve, natural Cu. Data taken from [8].

Activation of material in the treatment head of the accelerator is likely to take

place principally by (γ,n) reactions. The most important of these is $^{63}Cu(\gamma,n)^{62}Cu$, the product of which decays via positron emission with a half-life of 9.72 minutes (see section 8.6). In summary therefore :

- Annihilation photons at 511 keV are the result of most of the activation within the treatment head.
- Although other γ-photons, with energies in the range 0.1 – 2.1 MeV, are detectable at the isocentre following activation by many other reactions, these are not significant.
- Although (n,γ) reactions can also occur in principle, it has been shown that their contribution also is negligible [8].

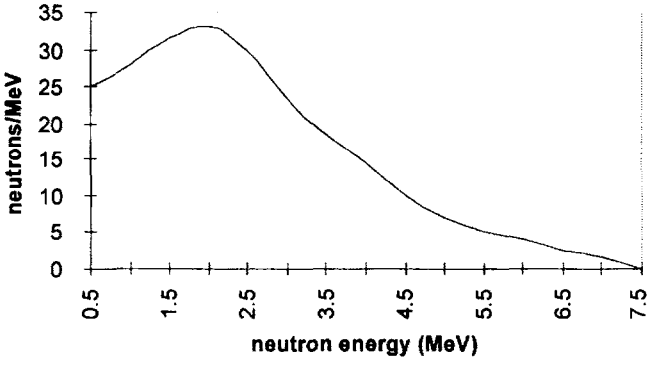

Fig.(9.23) Number of neutrons per unit energy interval produced by a 15 MV *bremsstrahlung* spectrum in lead (data taken from [8]). Note the suppressed zero on the energy scale.

Fig.(9.24) shows the physical arrangement of the major components in a linac head when it is to be used for photon therapy. For low energies, the beam hardening filter and the low-Z flattening filter are moved away from the axis. For high energies, it is the flattening filter for low energy X-rays which is moved.

9.3 Electrons

The most widely used modern method of accelerating electrons for clinical purposes uses a standing-wave linear accelerator operating in the S-band at 2998 MHz. This gives a wavelength of 10 cm in free space. Acceleration of electrons takes place in pulses at a repetition rate in the range 50 - 300 Hz. At a typical energy of 10 MeV, the current in the pulse is in the order of 200 mA. In this case, the power in the pulse is 10×10^6 V $\times$ 200 $\times$ 10^{-3} A = 2 MW. For a pulse length of 5 μS and a repetition rate of 200 Hz (5 ms between pulses), the mark-space ratio is 1000. Therefore, the mean power in the beam is 2 kW.

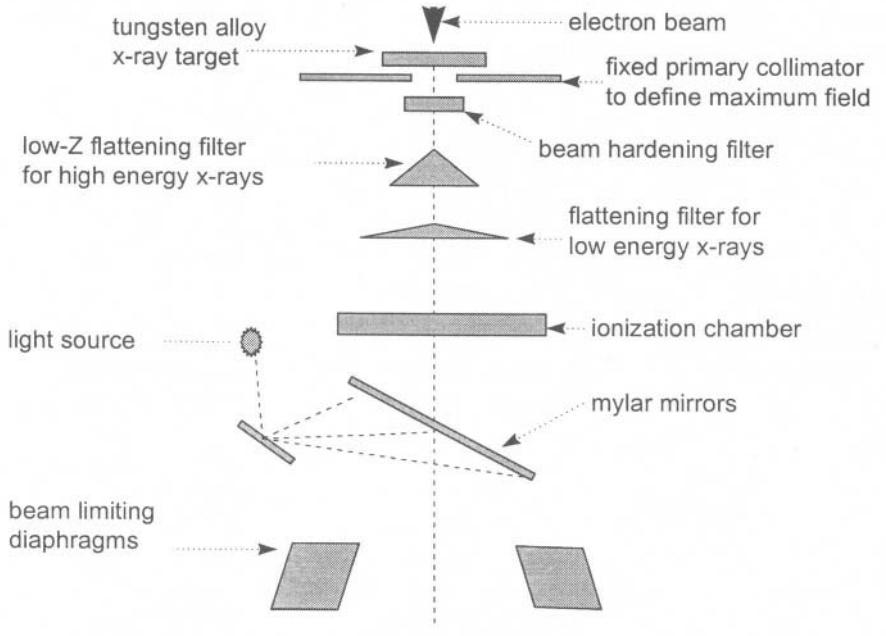

Fig.(9.24) The major components of a linac treatment head showing the arrangement of the filters for use with low-energy and high-energy x-rays.

The electron energy distribution before the beam emerges through the final exit window depends on the type, and design, of the electron accelerator. Typical values for the energy widths – measured as Full-Width-Half-Maximum (FWHM) – are ~ 20 keV (betatron), ~ 40 keV (microtron) and ~ 50 keV (linac) [9]. After transmission through the exit window there is a downward energy shift of ~ 5% in the mean energy, as well as a broadening of approximately the same magnitude. It is this beam, with a diameter in the range 4 - 6 mm, which is transported through the bending magnets to the scattering foils.

Using the above figures for the mean power in the beam, together with a mean projected range of 5 cm for a 10 MeV electron in water, Eq.(2.5), the power density is :

$$\frac{2\times10^{3}W}{\frac{\pi\left(5\times10^{-3}\right)^{2}}{4}5\times10^{-2}m^{3}} = 2040 \text{ MW m}^{-3}$$

Such a large value cannot be sustained by anything other than high melting

point materials. For therapy purposes it is therefore necessary to reduce the density either through scatter in a metallic foil or by scanning the beam over a larger area in a raster fashion. The former method of power density reduction is by far the most widely used in clinical machines.

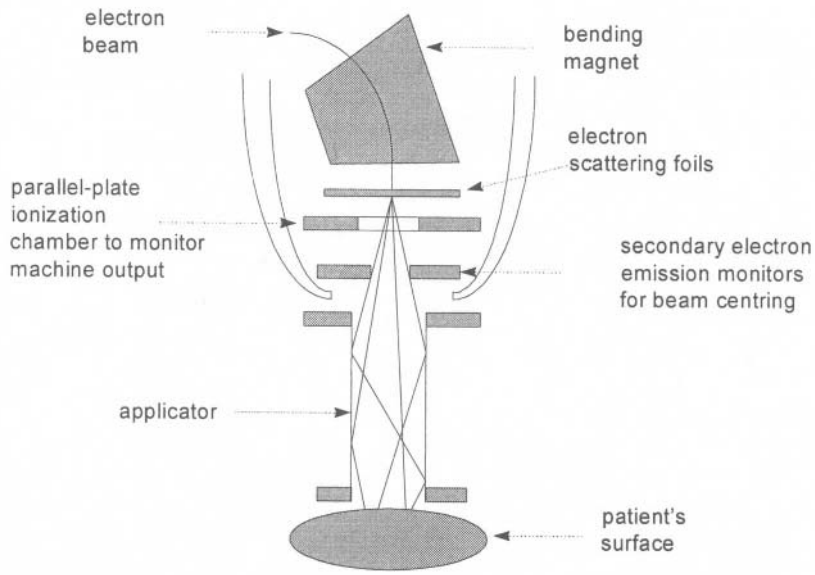

Fig.(9.25) The main features of a linac treatment head for use with electrons

Subsequent progress through the scatter foils, ionization chamber monitor, beam alignment foils and patient set-up mirrors will all introduce further energy degradation. A typical energy distribution at the patient/phantom surface for a nominal 10 MeV beam is shown in Fig.(9.26).

The main features of an electron therapy beam after it has emerged from the applicator and entered the phantom/patient are [10] :

- an appreciable change in energy as the electrons approach the end of their range,
- the small amount of contamination from *bremsstrahlung* and neutrons, due to electron interactions within the collimator system, and
- a much sharper fall-off in dose with depth compared with photons, Fig.(2.7).

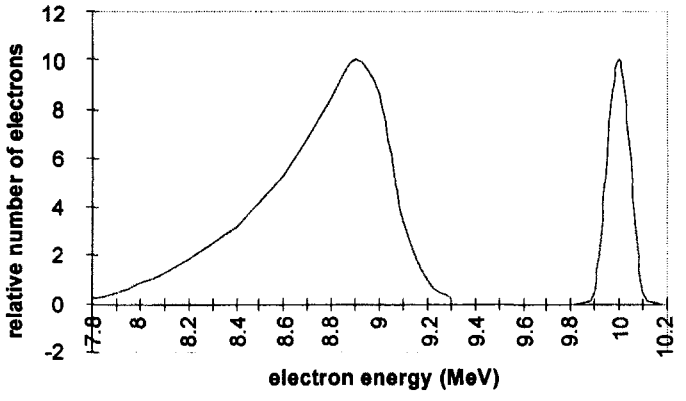

Fig.(9.26) A representation of the typical energy degradation of an electron spectrum - before emerging from the machine exit window (right) and after having passed through the filters, collimators etc. in the machine head (left). The left hand spectrum will approximate to that which irradiates the phantom/patient surface. Both energy shift and broadening vary with different arrangements of filters, applicators, SSD, etc. The most probable energies, E_p (mode), are 10.0 and 8.9 MeV. The mean energy of the degraded spectrum, E_m ~ 8.75 MeV, is lower and the maximum energy, E_{max} = 9.3 MeV, higher. The more the energy spectrum becomes degraded the larger the difference between the mean and mode energies due to the increasing asymmetry of the distribution [10]. For the purpose of illustration, the integrated area of the right hand spectrum has been reduced.

9.3.1 Determination of electron energy at depth in the phantom

In view of the differences between mean, modal and maximum energies of the electron spectrum and their intimate relationship with dosimetry, it is essential to be able to relate the selected machine energy with the energy at a specified depth in the phantom.

Harder [11] has shown that a linear dependence of the most probable energy on depth exists for all but the largest depths :

$$E_{p,z} = E_{p,0}\left(1 - \frac{z}{R_p}\right) \tag{9.8}$$

where the additional subscripts, *z* and *0,* refer to depth and surface respectively. R_p is the practical range of the electron beam, Fig.(2.7). This relation extends also to the mean energies $E_{m,z}$ and $E_{m,0}$ with less, but acceptable, accuracy.

Under the assumption that collision stopping power is relatively constant with energy, and radiative stopping power is directly proportional to mean energy, Andreo and Brahme [12] derived an exponential relation between mean energy and depth :

$$E_{m,z} = E_{m,0} \frac{S_{tot}\ exp\left(-\frac{zS_{rad}}{E_{m,0}}\right) - S_{coll}}{S_{rad}}$$

The stopping powers S_{tot}, S_{coll} and S_{rad} are quoted at the mean energy $E_{m,0}$ in the phantom material. When the exponential term is expanded, we get :

$$E_{m,z} = E_{m,0} - z\ S_{tot}\left[1 - \frac{S_{rad}(E_{m,0})\ z}{2\ E_{m,0}}\right] \tag{9.9}$$

Deviation from the linear expression in Eq.(9.8) is only significant near the end of the electron range.

From the point of view of dosimetry, the specification of beam energy is most sensibly based on the most probable energy at the phantom surface, $E_{p,0}$. This then permits the comparison of one beam with another to be made solely on the basis of the phantom geometry and material, SSD, field size, etc. and not on any of the machine parameters, such as filters or other components of the beam handling system. When this is done, the settings on the accelerator can then be calibrated against this most probable energy.

There are three principal methods that are available for a determination of the primary electron beam energy. They are, however, not generally available in a medical physics department and are also not generally the most appropriate for energies below 20 MeV.

- Magnetic spectrometry: This uses the relation between magnetic field strength B, radius of curvature r and particle momentum p, and hence E, when the B and r are known. If e is the electronic charge and E_0 the electron rest energy, (0.511 MeV) :

$$p = Ber \qquad \text{and} \qquad p = \frac{1}{c}\sqrt{E(E + 2E_0)}$$

- Nuclear reactions: This relies on the production of measurable radioactivity of a foil which is initiated by an incident electron or photon whose energy is above the reaction threshold. The foil activity is measured as the energy is reduced from above the threshold until no activity is measurable. Reactions of the type (e,e'n) and (γ,n) are used (see Chapter 8). Although there are many elements which have thresholds between 10 and 30 MeV, there are very few – e.g ^{109}Ag with a threshold of 9.3 MeV [13] – below this range.
- Cerenkov radiation: This method rests on the emission of optical radiation when

a charged particle passes through a dielectric medium with a velocity greater than the phase velocity of light in that medium. For a medium of refractive index n and a particle of velocity $v = \beta c$, the condition $\beta n > 1$ gives rise to the emission of light within a cone of semi-angle φ such that $\sin\varphi = 1/\beta n$. If n is known, the point at which light ceases to be emitted within the cone gives the value of β and hence the particle energy. This method is largely restricted to energies greater than 30 MeV where the other methods become less convenient.

The most useful practical method of energy determination, however, is to use empirical range-energy relations. These have been developed using the results of Monte-Carlo calculations and an analysis of experimental depth-ionization or depth-absorbed dose data, Figs.(2.6) and (2.7).

Using a calibrated β-spectrometer, Markus [14] determined a relation valid between 3 and 15 MeV in low atomic number materials. The practical range, R_p, is related to the most probable energy, $E_{p,0}$, at the surface of a phantom of density ρ by:

$$\rho R_p \frac{Z}{A} = 0.285 E_{p,0} - 0.137 \tag{9.10}$$

where Z/A is the ratio of the mean atomic number to atomic mass ($Z/A = 0.555$ for water). Eq.(9.10) has been found to agree with experimental data to within 0.43% in the range 3 - 15 MeV and 1.9% for 3 - 30 MeV [15].

At higher energies, where radiative energy losses become increasingly important, the relation becomes non-linear. In the range 1 - 50 MeV the expression :

$$E_{p,0} = 0.22 + 1.98 R_p + 0.0025 R_p^2 \tag{9.11}$$

gives agreement to within ~2%.

An equally important set of relations comes from the results of Monte Carlo calculations. These suggest that the mean beam energy, $E_{m,0}$, is related to the depth at which the absorbed dose falls to 50% of its peak value, R_{50}, Fig.(2.7). The ease with which R_{50} can be measured, and the importance of $E_{m,0}$ in defining the correct stopping power data for dosimetry calculations, prompted the recommendation :

$$E_{m,0} = 2.4 R_{50} \tag{9.12}$$

For Eq.(9.12) to be valid, R_{50} must be measured using a constant source chamber distance rather than a constant SSD which is usually the case for a conventional depth dose determination. A recent review of these relationships has been given by

Fernandez-Varea et.al. [16]. A summary of the values in water is taken from [9].

Table (9.4) Range-Energy parameters calculated for nominal electron energies using Eqs.(9.10), (9.11) and (9.12). The figures quoted in column 6 use a constant value of 2.33 and not 2.40 as in Eq.(9.12).

energy (MeV)	R_{50} (cm)	R_p (cm)	$E_{p,0}$ Eq.(9.10)	$E_{p,0}$ Eq.(9.11)	$E_{m,0}$ Eq.(9.12)
4	1.55	2.1	4.58	4.39	3.61
6	2.4	3.05	6.44	6.28	5.59
8	3.1	4.0	8.30	8.18	7.22
10	3.95	4.85	9.60	9.88	9.20
12	4.85	5.95	12.11	12.09	11.30
15	6.03	7.38	14.90	14.96	14.05
18	7.45	9.05	18.16	18.34	17.36

However, the more recent IPEMB electron dosimetry code of practice [17] specifies a constant SSD of 100 cm and distinguishes between :

- $R_{50,D}$ = the depth at which the dose is 50% of the maximum, and
- $R_{50,I}$ = the depth at which the ionization is 50% of the maximum.

This distinction is necessary in absolute dosimetry because an ionization chamber measures only the number of ionizations per unit mass of chamber gas without any consideration of the resulting secondary electron energy spectrum. However, the absorbed dose depends on the mass collision stopping powers of the secondary electrons averaged over the electron fluence. Account should therefore be taken of the increased secondary electron ranges at high primary electron energies. If this is not done, the dose averaged over a small volume at a given point will underestimate the primary electron energy. Furthermore, expressions such as Eq.(9.12) assume a mono-energetic, mono-directional and uncontaminated primary beam. None of these restrictions apply in practice.

The corrected expressions now recommended [17] are therefore :

$$E_{m,0} = 0.818 + 1.935R_{50,I} + 0.040(R_{50,I})^2$$
$$E_{m,0} = 0.656 + 2.059R_{50,D} + 0.022(R_{50,D})^2 \qquad (9.13)$$

where E is in MeV and R is in cm. A difference between $R_{50,I}$ and $R_{50,D}$ in water at an SSD of 100 cm becomes apparent at an electron energy of ~14 MeV above which $R_{50,D}$ is larger by ~2%. For the same reasons, Eq.(9.8) is no longer recommended for accurate work.

9.3.2 *Bremsstrahlung contamination of electron beams*

There are two sources of photon contamination in an electron beam and each contributes rather differently to the overall depth dose distribution. These are :

- Treatment-head photons. The generation of these photons begins as soon as the energetic electrons leave the UHV conditions of the accelerator tube. This is because of the need for high-strength, high-thermal-conductivity materials to withstand the large energy-density radiation in the head of the accelerator. The exit window of the waveguide, scattering foils, ionization chamber and collimator walls will all tend to have high atomic numbers and high densities and will therefore provide ideal targets for unwanted X-ray production.
- Phantom-generated photons. This smaller contribution can come from anywhere within the phantom. They can be generated at any point between the surface and the depth of the practical electron range, R_p, and with all energies up to the allowed maximum.

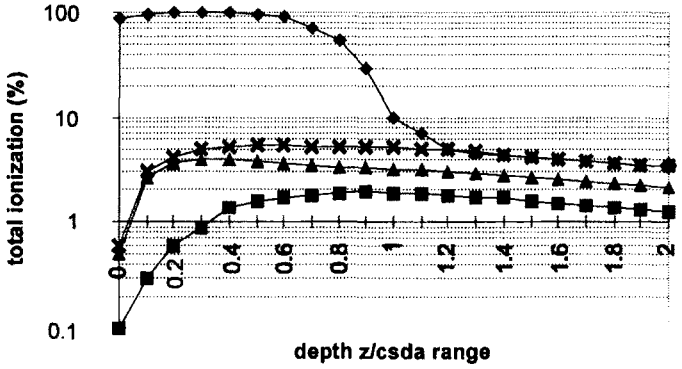

Fig.(9.27) Total percentage ionization versus z/r_0 calculated for 20 MeV electrons in water [20]. z is the real depth in the phantom and r_0 = 9.18 cm is the csda range of a 20 MeV electron in water. ◆ ionization due to primary electrons ; ■ ionization due to phantom-generated bremsstrahlung ; ▲ ionization due to accelerator-generated bremsstrahlung ; ✖ total bremsstrahlung ionization.

Independent experimental determinations of these contributions are difficult. The major component – from the accelerator head – can be found by magnetically deflecting the primary electron beam away from the phantom so that it is only the photons that contribute to the depth dose. The alternative is to extrapolate the depth dose data from beyond the practical range of the primary electrons using a combination of inverse square law and exponential attenuation. The latter method has been used, [18] [19], to produce an algorithm to describe the major contribution from the treatment head. Monte Carlo simulations [20] are, of course, capable of distinguishing between each of the two contributions.

Fig.(9.27) shows the total ionization measured in a water phantom irradiated by 20 MeV electrons [20]. The contributions due to primary electrons, and to photons generated in the treatment head and within the phantom itself, are shown as a function of depth normalized to the csda range of the incident electrons. Note that the maxima in each of these components occurs at $z/r_0 = 0.3$ and 0.9 respectively and show a photon component of ~ 4.5% at the total dose maximum.

At the lower treatment energies, 6 MeV and 8 MeV, *bremsstrahlung* contamination tends to be ~1%.

9.4 Heavy Particles

Radiobiological arguments for using heavy particles for therapy rest on the empirical evidence which shows the dependence of two radiobiology parameters – Relative Biological Effectiveness (RBE) and Oxygen Enhancement Ratio (OER) – on the physical parameter Linear Energy Transfer (LET).

- LET is defined as the loss of energy ΔT by a charged particle as the result of electronic collisions which take place along a track length Δx. It is therefore equal to the collision stopping power, with the proviso that account must be taken of the electron cut-off energies (section 2.5.2). LET_∞ is the total collision stopping power.
- RBE of a certain radiation is defined as the ratio :

  $$\frac{\text{dose of a reference radiation to produce a certain biological end-point}}{\text{dose of the certain radiation to give the same end-point}}$$

  The reference radiation is generally 250 kV X-rays. An irradiation with X-rays therefore has an RBE = 1, by definition.
- OER is defined as the ratio :

  $$\frac{\text{dose required to give a certain effect in the absence of oxygen}}{\text{dose required to give the same effect in the presence of oxygen}}$$

Fig.(9.28) shows that X-rays generally have a high OER (~3) and therefore require 3 times more dose to kill the hypoxic tumour cells than the surrounding well-oxygenated normal cells. As the LET increases towards 100 eV nm^{-1}, the rise in RBE and fall in OER indicate the real advantages in using high LET radiation for therapy.

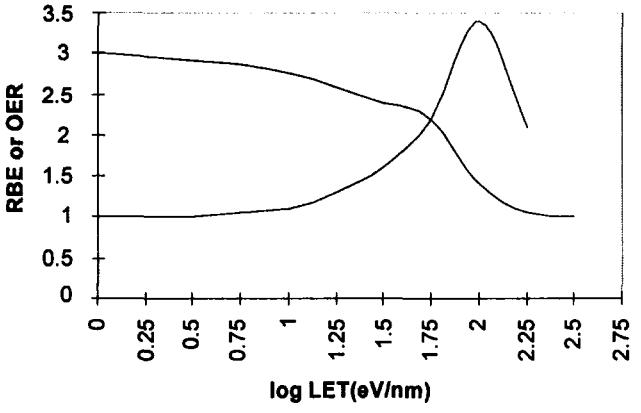

Fig.(9.28) Representative empirical relations showing the fall in OER with LET and the increase in RBE from unity at low LET to a maximum of ~ 3.5 at 100 eV nm^{-1}. These are based on the results of many radiobiological studies of mammalian cells using a number of different biological end-points.

In addition to the radiobiological advantages of using charged heavy particles for therapy, there are also good physical reasons for doing so. These rest on the high stopping powers and short ranges, even in low Z and unit density materials. Stopping power of a heavy charged particle rises to a maximum as the particle approaches the end of its range, Fig.(2.25). A beam of charged particles therefore produces a dose maximum which is referred to as the Bragg Peak. This occurs for protons in water when the mean proton energy has fallen to ~ 100 keV at which point the mean stopping power is ~ 100 keV μm^{-1}. Although the ultimate secondary particle produced from heavy particle interactions is the electron in all cases, intermediate products arise in external beams of neutrons, negative pions and heavy ions to give particular energy deposition characteristics.

Table (9.5) Secondary particles produced from heavy primary particles.

primary particle	intermediate particles	ultimate particle
proton	-	electron
neutron	protons, α-particles, γ-rays	electron
negative pion	protons, deuterons, tritons, He ions, etc	electron
heavy ions	fragmentation products	electron

In any radiation field in which there is more than one component (*e.g.* electrons and X-rays, neutrons and γ-rays, protons and electrons...), the isodose contours

are often different to the iso-effect contours. Iso-effect contours refer to a particular biological end-point such as cell death, chromosome aberration, etc. This is because of the different micro-dosimetry associated with different charged secondary particles, Fig.(2.17). Even the same particle (*e.g.* an electron), will have different energy spectra when produced from different initial particles. This is particularly the case in hadron therapy (heavy charged particles) where heavy secondaries (*e.g.* protons, He ions...) as well as electrons contribute to the overall dose.

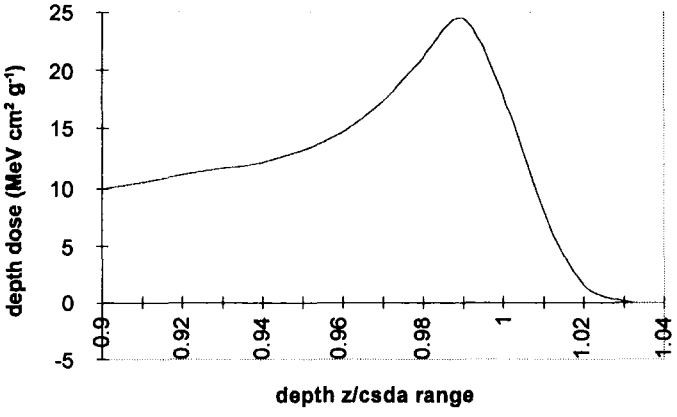

Fig.(9.29) Depth dose (MeV cm^2 g^{-1}) for 200 MeV monoenergetic protons in water [21] versus z/r_0. (Note the suppressed zero on the abscissa axis and the unconventional dose units).
The dose maximum, D_m, occurs at depth z_m. The dose at the csda range (z/r_0 =1) is D_{rg}. The width of the Bragg peak at 50% of D_m is w_{50}, and the distal depth (behind the peak) at which the dose falls to 50% is z_{50}.
For 200 MeV protons in water the above parameters are : r_0 = 27 cm : D_m = 24 MeV cm^2 g^{-1} : D_{rg} = 18 MeV cm^2 g^{-1} : $z_m = 0.99 \times 27 = 26.7$ cm : $w_{50} = (1.006 - 0.927) \times 27 = 1.86$ cm : $z_{50} = 1.006 \times 27 = 27.2$ cm. Data taken from [22].

9.4.1 Protons

Physical characteristics

Depth dose characteristics are illustrated in Fig.(9.29) for 200 MeV protons in water. These show a totally different depth dependence in the comparison with 20 MeV electrons in water, Fig.(9.27).

In the comparison of protons and electrons note :

- the linear, Fig.(9.29), and logarithmic, Fig.(9.27), dose axes respectively,
- the broad fall-off in dose at the end of the electron distribution ($z/r_0 \approx 0.6 - 1.2$ with r_0 = 9.18 cm) in Fig.(9.27)

- the rapid fall-off from D_m ($z/r_0 = 0.99 - 1.02$ with $r_0 = 27$ cm) in Fig.(9.29).
- the difference in the amount of potential skin sparing. This is ~10% for 20 MeV electrons, Fig.(9.27) and a factor of ~2.5 for 200 MeV protons, Fig.(9.29).

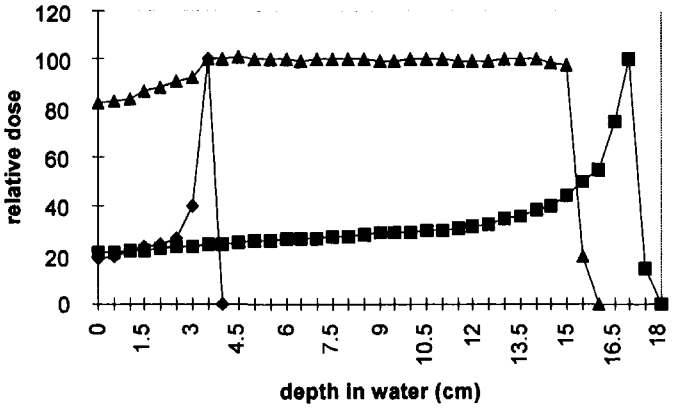

Fig.(9.30) Relative proton dose versus depth in water : ◆ unmodulated 72 MeV [22] : ■ unmodulated 158.6 MeV [23] : ▲ Spread-Out-Bragg-Peak (SOBP) 158.6 MeV [23].

A clinical proton beam is therefore characterized by :

- The ratio of the maximum dose in the Bragg peak to the lowest dose before the peak. In Fig.(9.30) the Peak:Plateau ratio is ~ 5.
- The way in which the Bragg peak is spread out in 3-dimensions in order to achieve suitable isodose contours for a particular target.
- The need to consider the variation in beam quality throughout the target volume.

Beam modulation

As in the case of electron beams -- and for the same reason – there is a need to scan a proton beam over a larger area than the initial width of the emerging beam (lateral spreading). In addition, there is sometimes a need to broaden the depth distribution along the beam axis (range spreading). Either type of spreading can be achieved passively or actively resulting in a Spread-Out-Bragg-Peak (SOBP). An exception, however, is the use of protons in ocular or pituitary treatments, where a small lateral beam spread may be a definite advantage.

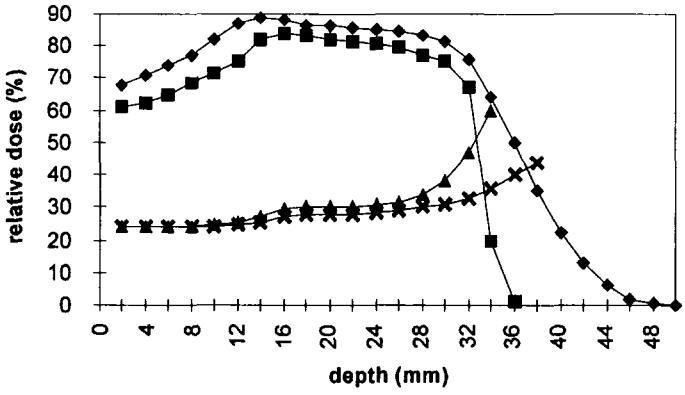

Fig.(9.31) Calculated proton doses required to achieve a flat biological dose distribution of 2 Gy (100% X-ray equivalent) between depths 15 - 32 mm. The calculations were based on a biological model in which the end-point was the aerobic survival of Chinese hamster cells.
◆ 155 MeV protons with passive modulation, ■ protons with active modulation in the range 41 - 61 MeV.
The depth dependence of the overall quality of the beam is represented by the two lower curves which show the Relative Biological Effectiveness (RBE) starting from a value of 1 at depth = 0 mm and rising to 1.9 in the Active Modulated beam at the depth 35 mm (▲), and to a value of 1.4 at the depth 38 mm (✖). The difference in beam quality at the end of the proton range is considerable. Data taken from [24].

Lateral beam spreading is achieved either by scatter foils (passive) or by magnetic scanning (active) :

- Although scatter foils are by far the simpler method, for a given field size and dose rate they require higher beam energies and slightly greater beam currents.
- The magnetic scanning method requires considerably less beam energy and slightly less beam current. It provides much greater control of the 2-dimensional conformation of dose to the target area. In principle, it is able to perform the same function for protons that multileaf collimators fulfil for photons. There is always a sharper distal fall-off compared with passive spreading. However, it has the disadvantage of necessitating much greater complexity in the beam diagnostic equipment, and of putting greater constraints on the beam delivery gantry due to its greater weight.

Range spreading is carried out :

- passively, by degrading the beam energy by sending it through different foil thicknesses on the periphery of a rotating wheel, or
- actively, by using energy modulation in the accelerator.

Beam quality

Fig.(9.28) shows that radiation with an LET in the order of 100 keV μm^{-1} is likely to

correspond to a high RBE. Fig.(2.125) shows that this value is appropriate to a proton energy of 100 keV. It is therefore to be expected that the RBE will rise on the distal side of the Bragg peak as the particles in the beam reach the end of their range.

Clinical proton beams

Fig.(9.31) shows that ocular conditions are best treated with protons in the energy range up to 60 MeV, whereas more deep-seated and/or large volume tumours require energies greater than ~150 MeV. A cyclotron or synchrotron is therefore required in both cases. Typical characteristics are the following :

- The available dose rates vary typically between 30 – 40 Gy min^{-1} for small target volumes (< 50 cm^3) and 2 – 10 Gy min^{-1} for volumes in the range 50 – 2000 cm^3).
- The field size can range from 5 mm diameter for ocular tumours to 15 × 15 cm^2 for head and neck treatments.
- A typical SSD lies in the range 2 - 3 m.
- Since no national standard protocols have been set in place, dosimetry is generally carried out on the basis of particle fluence measured with a Faraday Cup. This is then used to make a local calibration with an ionization chamber [25],[26] or a TLD system [27].

9.4.2 Neutrons

It was not until the technology of fast neutron beams had improved to the point where valid comparisons could be made with megavoltage photon therapy, that it became clear that the early expectations of neutron therapy were not going to be realized. The clinical effectiveness of fast neutron therapy – pioneered in the UK at the Hammersmith Hospital using proton and deuteron reactions on thick targets of Be and D – was thought to rest on the neutron's known interaction with atomic nuclei rather than with electrons. Consequently the neutron beam would generate high LET components during its passage through tissue. These are due to :

- heavy proton recoils by elastic scattering from hydrogen atoms, and
- other heavy charged particles (protons, α-particles and heavier nuclear recoils) from the reactions listed in Table (8.2).

A comprehensive review of the physics and radiobiology of fast neutron beams is provided in [28].

Neutron energy spectra

Two reactions have been used to generate neutrons for therapy.

- The reaction $^{3}He(^{2}H,n)^{4}He$ generates quasi-monoenergetic neutrons at 14.4 MeV (Chapter 1). A major disadvantage of this reaction is the virtually isotropic emission from the target and the consequent need for severe collimation. This inevitably produces a large γ component in the beam.
- The beryllium target reactions $^{9}Be(^{1}H,n)^{9}B$ and $^{9}Be(^{2}H,n)^{10}B$. These can be used with either thick or thin Be targets. For a thin target, the reaction is typically referred to as p(65)Be(25) signifying that 65 MeV protons hit a thin Be target from which they emerge with 25 MeV on average. The total neutron fluence is lower than that from a thick target, all other things being equal, but the mean neutron energy will increase as the target thickness decreases.

The degradation of the initial energy spectrum as the neutrons penetrate into the tissue is due primarily to the moderation of the incident beam by the low Z components. A typical result of this moderation, together with the inverse square fall-off in fluence, is shown in Fig.(9.32).

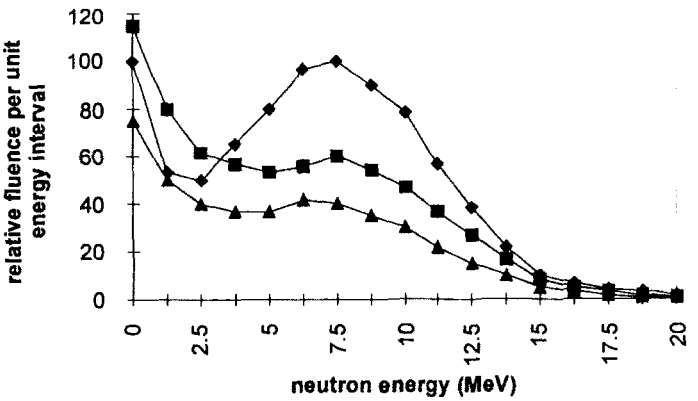

Fig.(9.32) Energy spectra of the neutron fluence at various depths on the central axis of a water phantom irradiated by a 9.5 × 9.5 cm² field of neutrons from 16 MeV deuterons hitting a thick beryllium target. ◆ surface : ■ 5 cm deep : ▲ 10 cm deep. Data taken from [29].

Central axis depth dose

The resulting central axis depth dose distribution for a 14 MeV (d,T) beam is compared with that for ^{60}Co γ-rays in Fig.(9.33). Note that the penetration of the neutron beam is slightly less than that of the ^{60}Co gamma rays – the depth at which 50% maximum

dose is achieved being ~10cm in both cases. Most clinical neutron beams had 50% penetration depths in the range 9 – 15cm.

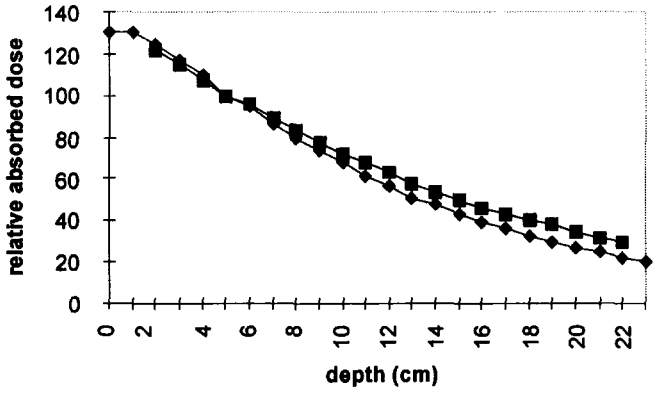

Fig.(9.33) Relative central axis depth doses in a water phantom normalized to 100% at 5 cm depth. ◆ 14 MeV neutrons ■ ^{60}Co γ-rays. Both beams used a 10 × 10 cm^2 field and a 80 cm SSD. Data taken from [28].

Radiation Quality

In spite of the similar depth dose characteristics, significant differences are seen, by both calculation and experiment, in the microdosimetry of neutron beams compared with X-rays or photons. Although LET is widely used as the physical parameter against which to compare different biological effects, a more appropriate measure is that of lineal energy (chapter 6). This is because :

- There is not a unique relation between particle energy and stopping power. Fig.(2.125) shows that the same stopping power can frequently be observed at two energies - one low and one high. In a beam of neutrons, therefore, the energy variation with depth gives rise to a large variation in secondary particle type and energy. Consequently there is a complex dependence of the overall mean stopping power on depth.
- Heavy recoils ^{14}C, ^{13}N,.. from the reactions in Table (8.2) are likely to experience a significant change in stopping power over a volume as small as a DNA molecule. When in addition, secondary electrons can start in, stop in or cross this small volume, the variation in possible event sizes is very large.
- All interactions are stochastic in nature, so it is not appropriate to describe a distribution of dose deposition events by a continuously variable parameter such as LET.

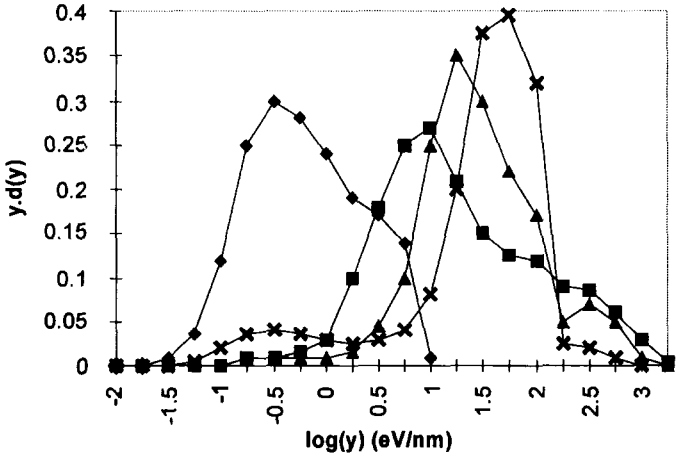

Fig.(9.34) The distribution of lineal dose versus lineal energy, y, for a number of neutron beams. Each distribution is identified by the value of lineal energy at the mode. ◆ ^{60}Co γ-rays : ■ 65 MeV protons on Be : ▲ 20 MeV deuterons on Be : ✖ 4 MeV deuterons on Be. Data taken from [28],[30].

Fig.(9.34) shows that the dose from a ^{60}Co beam is deposited in the approximate range 0.1 – 10 keV μm^{-1}. All neutron beams deposit energy up to ~1000 keV μm^{-1}, and show a sharp discontinuity just above 100 keV μm^{-1}. This corresponds to the maximum stopping power of protons in low-Z, unit density material. The most energetic beams, from 20 MeV deuterons and 65 MeV protons on Be, show considerable dose deposition between 100 and 1000 keV μm^{-1}. This is due largely to heavy recoils.

9.4.3 Negative Pions

Of the three types of π-meson it is the negatively charged version, with a rest mass of ~ 273 m_0, that is used in radiotherapy. Normally referred to as the negative pion, it undergoes a strong interaction with nucleons. This follows the formation of a mesic atom and the subsequent spallation reaction. The sequence is the following :

- The pion slows down to thermal energies, primarily by energy loss collisions with the atomic electrons of the medium (see chapter 2).
- The capture in a hydrogen-like Bohr orbit of a low-Z atom of the medium. This has a much smaller radius than the comparable hydrogen orbits, $(n\hbar)^2/Ze^2m_0$, because of the greater rest mass of the pion.
- The large overlap between the wave functions of the pion and the nuclear volume produce the finite probability of a spallation reaction.

The products of spallation reactions are heavy charged particles. Thus protons, deuterons, tritons, He, Li, and C nuclei are released into the medium from the point at which the pion thermalized and formed a mesic atom. These particles provide an additional contribution – called the spallation or "star" dose – to the Bragg peak of the original pion. Of the rest mass of a pion (273×0.511 MeV $\cong$ 140 MeV), about 40 MeV is used in overcoming the binding energy of the nucleus, about 70 MeV appears as kinetic energy of neutrons, and the remainder is released as charged particle kinetic energy.

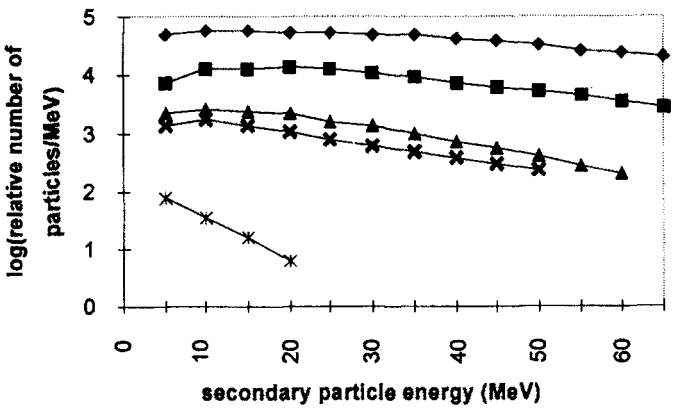

Fig.(9.35) A representation of the thick target spectra of charged particles emitted at the Bragg peak (depth ~14cm) of 160 MeV/c negative pions in water.
◆ protons : ■ deuterons : ▲ tritons : ✖ He nuclei : ✳ Li nuclei. [31].

The wide range of secondary particle energies shown in Fig.(9.35) generates the Star Dose at a slightly greater depth than the Bragg Peak. The latter corresponds to the peak in the stopping power of a charged particle, Figs.(2.25) and (9.29), whereas the Star Dose is centred on the point at which pion thermalization occurs. The heavy secondary particles are emitted isotropically from this point. Contributions to the overall depth dose, shown in Fig.(9.36), include the contamination from :

- electrons. These come mainly from the conversion of neutral pions within the target, $\pi^0 \rightarrow 2\gamma$, $\gamma \rightarrow e^+ + e^-$,
- muons come from the decay of the pion in flight to produce a muon and a neutrino, $\pi^- \rightarrow \mu^- + \nu$,
- neutrons. These can arise external to the target itself and internally from spallation reactions.

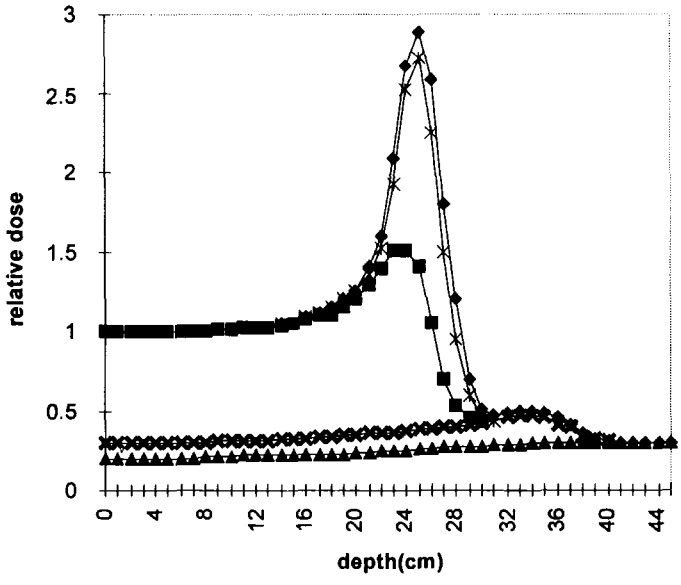

Fig.(9.36) Contributions to the depth dose of 190 MeV/c negative pions in water normalized to the entrance dose. The beam contains approximately 65% pions, 25% electrons and 10% muons at an energy of 100 MeV. Data taken from [32]. The distribution is characterized by the sum of Bragg peak plus Star Dose at depth, and a plateau region roughly mid-way between the surface and the overall peak.
▲ electrons : ✖ muons : ■ pions : ✳ stars : ◆ total dose. The small difference between the star dose and the total dose is due to neutrons.

Data of the type shown in Fig.(9.35) have also been taken from the plateau region of the dose distribution. A reduction is observed in the yield of charged particles generated between 5 and 25 MeV of ~3 for protons, deuterons and tritons and ~9 for heavier ions.

Approximate ranges in water of 20 MeV spallation particles are 5 mm(protons), 2.4 mm(deuterons), 1.5 mm(tritons), 0.35 mm(He nuclei) and 0.03 mm(Li nuclei). Although there is a large spread in secondary particle energies (up to ≥70 MeV for protons) their ranges are comparable to the width of the Bragg peak of the initial pion.

9.4.4 Heavy Ions

Fig.(9.37), shows that there is an increase in maximum stopping power as the charge and mass of the particle increases. If ions heavier than carbon nuclei are to be used for a therapeutic beam, the trend evident in Fig.(9.37) means that :

- The initial ion energies required to achieve a Bragg peak at 20 cm depth are 4, 9 and 25 GeV for carbon, neon and argon ions respectively [33].

- The associated Bragg peak decreases in width. There is no Star Dose.
- The mean lineal energy in the peak increases, Fig.(9.34).

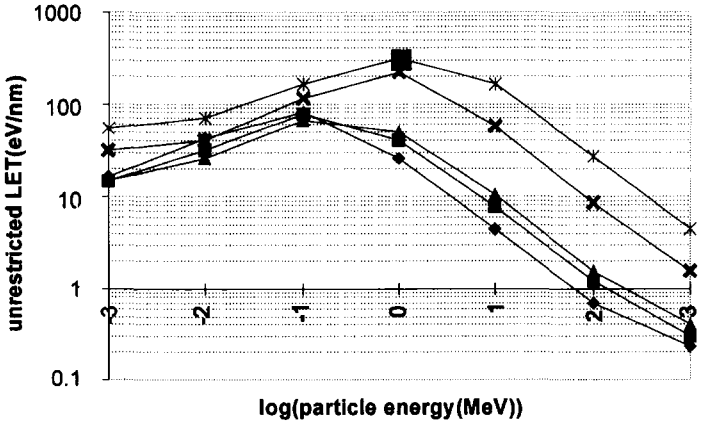

Fig.(9.37) Mass Stopping Powers of spallation products from Fig.(9.35) in water. ◆ protons : ■ deuterons : ▲ tritons : ✖ He nuclei : ✳ Li nuclei. Note that the peak in the stopping power shifts to higher values and occurs at higher energies as the ions become heavier. Data taken from [33].

As in the case of protons beams, a narrow Bragg peak has to be broadened to make it clinically useful. However, the very small penumbra to the depth dose distributions make heavy ions highly suitable for targeting tumours which are close to very sensitive normal tissues.

The issue of radiation quality within the Bragg peak, and in the tissues through which the heavy ion has to pass to reach the tumour, is complex. This is made the more so by the possibility of ion fragmentation which results in radioactive products accompanying the original ion. For these reasons Heavy Ion therapy always makes use of stereotactic techniques (section 9.6.1). A review of heavy ion radiotherapy is given in [34].

9.5 Boron Neutron Capture Therapy (BNCT)

9.5.1 General principles

BNCT uses the combination of :

- low energy neutron irradiation, and
- the targeting of a tumour site with a suitable boron-containing compound.

The intended sequence of operation is as follows :

- The tumour is first implanted with a pharmaceutical containing as high a mole

fraction of boron as possible, consistent with its compatibility with the tissue.

- A beam of epithermal neutrons is used to irradiate the patient. Energy moderation, which results from interactions with the intervening tissue, produces thermal neutrons at the site of the boron-containing tumour.
- High LET particles are produced from within the tumour according to the following reactions :

$$^{10}_{5}B + ^{1}_{0}n \rightarrow ^{7}_{3}Li + \alpha + 2.79(MeV)$$
$$^{10}_{5}B + ^{1}_{0}n \rightarrow ^{7}_{3}Li^{*} + \alpha + 2.31(MeV)$$
$$^{7}_{3}Li^{*} \rightarrow ^{7}_{3}Li + \gamma + 0.478(MeV)$$

- The ranges of the reaction products in tissue are ~ 9 μm (Li) and ~ 5 μm(α).
- Since the mammalian cell is typically 10 - 20 μm in diameter, nearly all the exothermic energy of the above reactions is absorbed within the cell.

BNCT is an attractive possibility for the treatment of gliomas. These are tumours of the glial cells which, when functioning normally, nourish and support the neurons of the brain. Such tumours are resistant to X-ray irradiation and are virtually inoperable. Conventional surgery gives an average survival time of the patient of ~ 6 months.

Very few molecular carriers are suitable for transporting the boron to the tumour. As in other branches of nuclear medicine, the binding strength of the metal ion to the carrier (or pharmaceutical) must be higher than that to other macromolecules that might be encountered in its journey from the injection site to the tumour. Needless to say, it must also have a stronger affinity to cancerous tissue than to normal tissue.

The carrier mostly used is BSH (boro-captate sodium $Na_2B_{12}H_{11}SH$) which does bind well to tumours. However, it can also bind to other non-cancerous tissue, thereby loosing some of its usefulness. The attractive possibility of using monoclonal antibodies to carry the boron to the tumour is diminished by the requirement that they need to carry $10^3 - 10^4$ boron atoms per molecule.

Neutron irradiation of a suitably selective pharmaceutical, which can also be labelled with a sufficiently high loading of boron, is accomplished by irradiation with reactor neutrons at epithermal energies. The choice of energy range of the incident neutrons is determined by the following criteria :

- The above reactions have their highest cross-section (3840 barn) at thermal energies.
- To achieve maximum penetration within the brain, the incident neutron energy should be higher than thermal, in order to reach the tumour site through the skull and intervening brain tissue.
- The higher the incident energy, however, the more likely it is that the neutron will undergo proton recoil reactions with hydrogen atoms within normal tissue

(the probability of proton recoil rises steeply for neutron energies above 10 keV).

The solution is therefore to use an epithermal (keV) reactor beam which is filtered by a combination of Fe, Al and S. This gives a relatively "pure" beam at 24 keV because of a window in the cross-section.

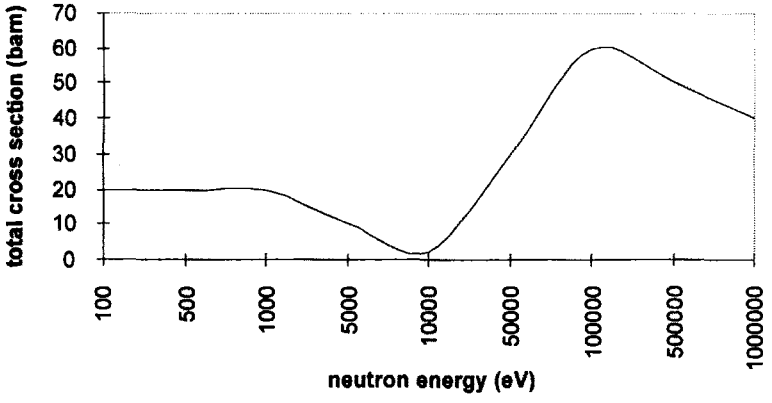

Fig.(9.38) Total neutron cross-section of a Fe:Al:S alloy showing the window in the 8 — 25 keV energy range.

The mean window energy shown in Fig.(9.38) is still rather high. From the penetration point of view, a better filter would be one made from scandium which has a window at 2 keV. This material is very expensive however.

The major problems confronting BNCT are therefore :

- The level of boron that needs to be administered is very high and may possibly be toxic (~80 $\mu g\ ml^{-1}$).
- There is no sure way of getting the boron compound only to the tumour site and nowhere else.
- The additional reactions $^{14}N(n,p)$ and $^{1}H(N,\gamma)$ are unavoidable and produce secondary radiation with considerably larger range. The γ-rays in particular, together with the γ-rays in the primary beam, generate a non-negligible gamma dose in the target volume.
- Epithermal neutrons that are outside the window and/or those that do not thermalize within the target volume, together with the fast neutron component of the beam, will produce recoil protons. The sum of the fast neutron and gamma doses can vary between 20% and 100% of the total, depending on the location and boron content of the target [35].

9.5.2 *Practical implementation*

Although accelerator-based neutrons are useful in principle, the large neutron fluxes that are necessary for BNCT are only available from high flux reactors. The primary purpose is then to convert the neutron and γ-ray spectra within the reactor core (see Chapter 1) into an emerging beam of neutrons in the energy range 2 - 30keV with minimal γ-ray contamination. The clinical epithermal neutron beam (HB11) at Petten in the Netherlands is represented in Fig.(9.39).

- The core fission neutron spectrum is modified in the Cd, Al, Ti and S filters by attenuation and in the water shutter by moderation. A 1.5 m long tank of liquid argon provides efficient attenuation of the γ-component as well as providing further moderation of the neutrons.
- Neutron beam monitoring is achieved by means of two fission chambers mounted either side of the beam in a vertical plane, while Geiger-Muller detectors above and below the beam are used to monitor any possible failure of the liquid argon cryostat.
- Even at constant reactor power, the neutron beam output varies during the course of a fuel cycle by ~5% and between different cycles by ~15%. The need for a reliable beam monitor is necessary in order that treatment times are governed by integrated neutron flux and not by real time.
- The total γ-component in the phantom derives from incident photons in the beam and photons produced within the phantom from thermal neutron induced reactions. The induced component is 60% at 2 cm [36].

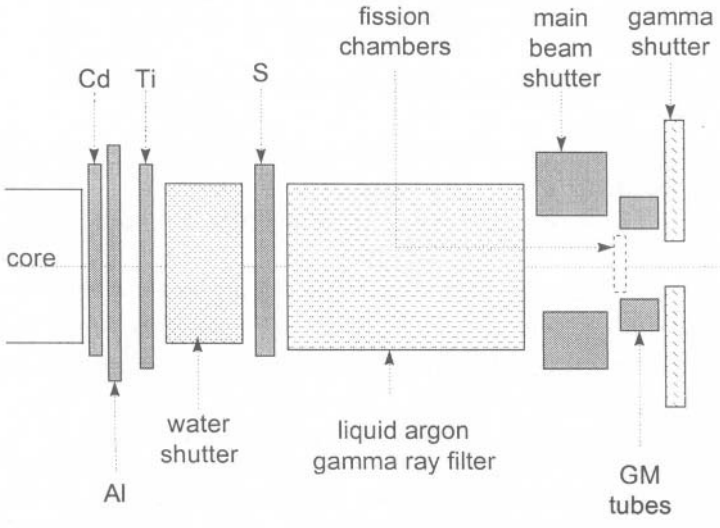

Fig.(9.39) The principal elements of a high-flux reactor beam line (taken from [35]).

9.6 Modern Developments in Teletherapy

9.6.1 Stereotactic methods

Stereotactic techniques were developed because of the demanding requirements of dose localization in treatments of the brain. In its basic form a stereotactic frame is fixed to the patient's head in order to define the precise location of the target before the radiation is administered. The target volume is generally small and the dosimetry therefore challenging because of the need for steep dose gradients at the edges of the treatment volume.

Two forms of stereotactic therapy exist.

- Stereotactic radiosurgery applies to a single treatment. Stereotactic radiotherapy refers to multiple treatments or fractions. These mostly use an external beam of linac-based X-rays which are restricted to ~ 6 MV because larger penetration depths are not required for head and neck treatments. Heavy charged particle facilities (He ions) are also available at a few institutions – mainly in the USA – where the dose fall-off at the distal edge of the target is a great advantage. Within a single treatment, a tightly collimated beam is rotated about the target which has to be located precisely at the isocentre of the moveable beam.
- The Gamma knife uses simultaneous irradiation from 201 ^{60}Co sources contained within a hemispherical structure. A central body within the hemisphere contains 201 beam channels which intersect at the focus with a mechanical precision of 0.3 mm. Final collimation is provided by a helmet containing 201 channels which contain inserts to adjust the final collimation between 4 mm and 18 mm at the focus. Occlusive plugs can also be inserted to protect sensitive structures near the target volume. The sources are arranged in an arc $\pm 48^{\circ}$ along the longitudinal axis of the treatment couch and $\pm 80^{\circ}$ transverse to the couch [37].

Target localization

A primary requirement in stereotactic therapy is the target identification in relation to the frame which is fixed to the patient's skull. A reproducibility of 1 mm in each of the 3 orthogonal directions is required in :

- the positional accuracy of the target volume within the frame, and
- the position of the frame itself in relation to the beam focus or isocentre.

This is best achieved by CT or MRI imaging of the target volume together with a set of fiducial markers. The digitized image can then be transferred directly to the dose-planning software.

Good mechanical accuracy is essential in the alignment of the stereotactic frame, the patient couch, the axis of collimation and the moveable gantry of the linac head

or the gamma knife hemisphere. A true mechanical isocentre cannot be achieved to better than 0.5 - 0.7mm, even if the mean positions of the axes intersect, because of the inevitable sag in the component structures.

Dose distributions

Dosimetry in stereotactic beams needs to be practised with extreme caution :

- In order to minimize the dose to the healthy surrounding tissue, the dose gradients at the edges of the target should be high. A consequence of this is the lack of lateral electronic equilibrium thereby making accurate dosimetry very difficult. Film dosimetry, diodes, small ionization chambers and TLD all have disadvantages to some degree in relation to poor spatial resolution, large energy dependence and poor tissue equivalence. Diamond detectors have now been added to this list [38] (see also Chapter 7).
- The dimensions of the sensitive volume of the dosimeter must always be smaller than the field size being measured.

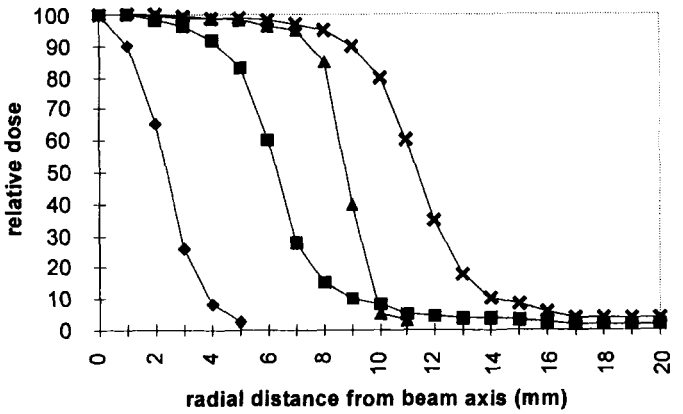

Fig.(9.40) Transverse dose profiles of typical stereotactic beams. ◆ ^{60}Co gamma knife, 4 mm collimator : ■ 6 MV X-rays, 12.5 mm collimator : ▲ ^{60}Co gamma knife, 18 mm collimator : ✖ 6 MV X-rays, 22.5 mm collimator. Note that the smaller field sizes have the larger penumbra.

Fig.(9.40) shows transverse beam profiles for 6 MV X-rays irradiating a water phantom using 12.5 mm and 22.5 mm diameter collimators. The points represent the mean of three dosimeters. These are an ionization chamber with an effective aperture of 0.8 mm, a laser film digitizer with an effective aperture of 0.5 mm and a scanning film densitometer with an aperture of 1 mm [39]. Dose profiles from a single beam of a ^{60}Co gamma knife are also shown in Fig.(9.40). These were determined in an 8 cm diameter polystyrene sphere in order to simulate a human head. In this case the dosimeter was film which had been calibrated for ^{60}Co γ-rays and scanned by a densitometer with a 0.75 mm aperture. The profile shown is that measured at the

focus along the direction of the ± 80° arc of sources. The profile orthogonal to this, along the ± 48° arc, will be sharper [37].

In conjunction with the advances in stereotactic techniques, much effort is being placed in the development of fast 3-dimensional dose computation algorithms. These are required in the treatment planning of small, frequently non-spherical, target volumes [40], [41], [42].

9.6.2 Conformal therapy

In conformal therapy the beam profile is conformed to the cross-section of the target. Formerly, this was done using shadow shields, blocks and wedges (section 9.2.5) placed within the collimator structure. Although these methods are still used in certain cases, there is an increasing trend towards the use of multileaf collimators. These have a much greater intrinsic capability to follow the desired field shape and are used in both conventional and stereotactic therapy. They were also used for external neutron beams [28].

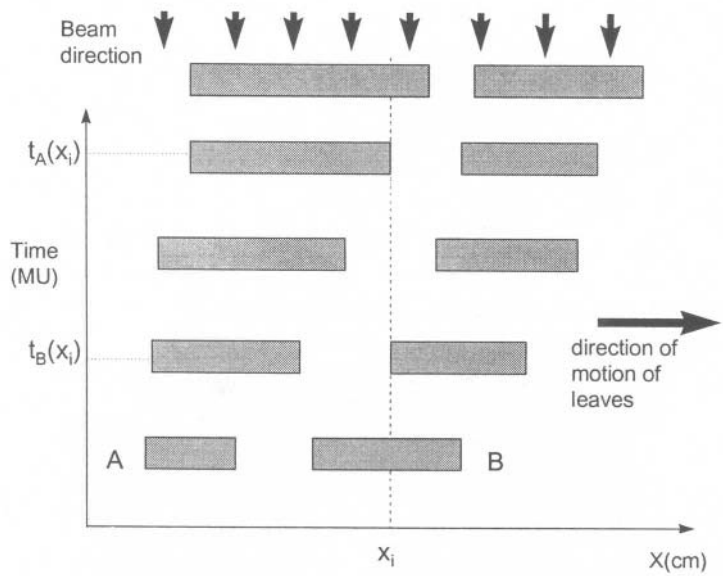

Fig.(9.41) The principle of dynamic conformal therapy. The shaded areas represent the leaves of the multileaf collimator which move along direction X, [43].

Notable features of conformal therapy are the following :

- It facilitates the treatment of large non-spherical volumes which are in close proximity (~5 mm) to critical structures.
- Computer control of the jaws or leaves of the field-shaping collimator enables dynamic conformal therapy to be carried out. This permits the independent

movement of small vanes to trim, say, an existing circular field.

The principle of dynamic conformal therapy is illustrated in Fig.(9.41) by a time:distance plot of a pair of collimator leaves, A and B, orthogonal to a vertical beam direction. The movement along the abscissa axis is related to time (in monitor units, MU) along the ordinate axis [43]. The time-intensity profile at point x_i is given by the time during which it is exposed to the beam :

$$t_A(x_i) - t_B(x_i) = F(x_i)$$

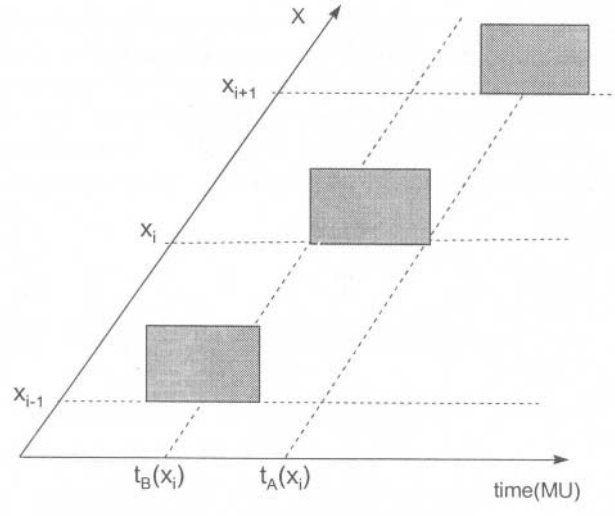

Fig.(9.42) Time-position irradiation profile of Fig.(9.41), [43].

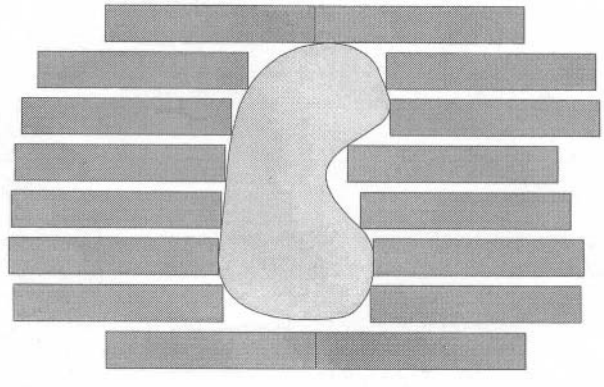

Fig.(9.43) A "beam's eye" view of a kidney-shaped target (hatched) which is "conformed" by a series of leaf collimators. The diagram illustrates the difficulty of following a curved surface with square section collimators. Clearly, the thinner the leaves the better. In principle the collimator leaves could be adjusted to be converging, parallel or diverging.

When the leaves A and B are arranged to move at different speeds, the intensity of the beam irradiating area between $1 \leq x_i \leq N$ can be varied as a function of time. Fig.(9.42) shows the principle of a time-position irradiation using the simple arrangement in Fig.(9.41). In reality, the plane of the flat collimator leaves is usually parallel to the beam direction and not orthogonal to it in as shown in Fig.(9.41).

9.6.3 Portal imaging

A portal image is one produced by exposing a detector on the distal side of the patient to the beam which emerges from the port of a therapy unit. The purpose is to eliminate set-up errors before actual treatment begins by ensuring that the co-ordinates of the target (both on and within the patient) are aligned with the co-ordinates of the beam itself. Since a method of reliable image registration is vital in stereotactic treatments, developments in stereotactic, conformal and portal imaging techniques have tended to go hand-in-hand.

Although real-time digital (or electronic) portal imaging based on silicon diodes [44] and liquid-filled ionization chambers [45], is now becoming more widely used, the traditional detector for portal imaging has been radiographic film. This uses a film cassette placed in contact with the patient during the exposure and which is later developed using normal radiographic procedures.

Those features of diagnostic radiology which make for good image quality, such as low photon energy and small source size, are entirely absent in portal imaging. This is characterized by the following.

- There is poor contrast due to the dominance of Compton scatter at megavoltage energies. The images therefore show the spatial variation of density, and not atomic number.
- The high energies of secondary electrons and scattered photons cause intrinsic image degradation.
- A large source size gives rise to significant penumbra in the image due to effects in both collimator and patient (or phantom).
- Long exposure times (relative to diagnostic imaging) increase the probability of patient and organ movement during exposure.
- Attempts to use a diagnostic quality X-ray simulator in place of the therapeutic beam must replicate precisely the geometry and movements of the therapy unit.

When film is used as the portal imaging detector, three different types of image can be generated :

- A localization radiograph: The film is exposed for a time much shorter than the daily treatment time. This permits the adjustment of the patient's position and

checks on machine parameters before the main part of the treatment begins.
- A verification radiograph: Here, the film is exposed during the whole of the (daily) treatment. It requires a very insensitive (slow) film.
- A double exposure radiograph: an image is taken of both the shaped treatment field and the whole of the patient outline on the same film. This confirms the location of the treatment volume in relation to the patient's anatomy.

Digital portal imaging

The alternatives to conventional film radiography are the digital methods of recording portal images [44]. These involve :

- Digitizing the film image using low-light video camera or laser scanning techniques. Conventional film as well as Reusable Imaging Medium (RIM) can be used. The latter can be loaded in daylight and laser scanned in less than one minute to produce a 2048 × 2048 matrix with 4096 shades of grey.
- Liquid-filled ionization chamber capable of a producing 256 × 256 matrix.
- Video-based fluoroscopy.
- Scanning ionization chamber.

9.7 Brachytherapy

Interstitial, Intracavity and Surface Applicator brachytherapy have a history almost as long as teletherapy, although Surface Applicator techniques have now largely been replaced by increasingly available low energy electron beams. In addition to advances in Interstitial and Intracavity radioisotope methods, however, there have also been developments in Interstitial Radiosurgery.

Brachytherapy is the name given to the treatment of diseased tissue by one or more radiation source in close proximity to the target volume. The surgical insertion of a sealed photon-emitting radioactive source (e.g. ^{60}Co, ^{103}Pd ^{137}Cs, ^{125}I, ^{192}Ir or ^{198}Au) is called interstitial brachytherapy. When placed in a natural body cavity (oesophagus, uterus...) the technique is intracavity brachytherapy. The source, encapsulated in a thin sheath of stainless steel, platinum or titanium ($\leq$0.1mm), can be delivered to the tissue by the following means :

- a catheter which generally delivers a single high-activity source, ~ 10 TBq.
- by surgical insertion of several moderately-active needles, wires or pins, ~ 10 MBq.
- using surface application of a mould which contains a number of sources.

Whichever means of delivery is used, a consistent procedure must be adopted in order to achieve both the absolute value and the uniformity of the prescribed dose

to better than 10%. The Manchester system [46], the Quimby system [47] and the more recent Paris system [48] address each of the three methods above. They provide a set of tables which relate source activity, number, size and geometry to the absorbed dose in a certain prescribed volume.

These tables, originally devised per mg of radium (^{226}Ra), can be used for other nuclides so long as proper account is taken of the differences in emission energies, filtration and geometry. The initial decay of ^{226}Ra takes place via α-particle emission with a principal energy of 4.777 MeV. Subsequent decay of the daughter products gives rise to a number of α-particles, the maximum energy of which is 7.68 MeV and a number of β-particles, the most energetic having a maximum energy of 3.26 MeV. Precise photon dosimetry surrounding a brachytherapy source therefore demands the removal of such high stopping power radiation. In the case of radium the necessary filtration was normally achieved with 0.5 mm platinum.

Any slight differences in the filtration and/or geometry of radium-substitute sources have now led to the present convention of expressing source strength in terms of air kerma rate at 1m.

A radium-substitute source of activity A, Table (9.6), is converted to an equivalent activity of radium, Ra_{eq}, by :

$$Ra_{eq} = A\frac{\Gamma}{\Gamma_{Ra}} \tag{9.14}$$

where Γ is the exposure (or air kerma) rate of the substitute source and Γ_{Ra} is the exposure (or air kerma) rate of the equivalent radium source. These exposure rates should be specified for the energy spectra, geometries and filtrations of the two sources.

Table (9.6) Physical characteristics of photon sources used in brachy-therapy. The mean photon energies are those before any filtration by the source encapsulation material. The third column gives the maximum energy of β-particle emission. The mean value is approximately 1/3 of the maximum. The presence of other (lower) emission energies reduces the mean β energy even further.

Radionuclide	half-life (days)	$E_{\beta,max}$ (keV) or EC	maximum photon energy (keV)	mean photon energy (keV)
^{60}Co	1926	1480	1330	1250
^{103}Pd	16.97	EC	23.0	20.6
^{137}Cs	11020	1170	662	662
^{125}I	59.4	EC	35.5	28.4
^{192}Ir	74.02	670	612	397
^{198}Au	2.69	1370	676	420

A broad distinction is made between low- medium- and high-dose-rate treatment These are referred to as LDR, MDR and HDR, depending on the source activity

Although photon emission from a radioactive source is isotropic, different isotop and encapsulation assemblies introduce a certain amount of anisotropy. This depenc on :

- The photon emission spectrum. This comes from decay γ-rays plu *bremsstrahlung* X-rays from preceding β-particles.
- The material and thickness of the encapsulation. This will absorb and scatt the emitted γ-rays and also cause the production of characteristic X-rays followir photoelectric interactions.

The specification of a brachytherapy source solely in terms of its activity therefore inadequate. Since dosimetry is determined by the photon spectrum, eac of the above isotopes give a different dose per unit of activity. The preser universally-adopted, procedure is therefore to determine the dose-rate in the mediu at a point close to the source without any specific reference to the source activit This is carried out in three stages :

- Measurement is made of the air kerma rate at a reference point (1m) in air.
- This is converted to air kerma rate in the medium at given point close to th source.
- Conversion is then made to dose-rate at the point close to the source.

9.7.1 Interstitial and intracavity brachytherapy

Source specification

In each of the above activity regimes, the reference air kerma rate is specified μGy hr^{-1}, μGy min^{-1} or μGy s^{-1} at a point along the transverse bisector of the sourc in free space. Since the distances over which the dose must be determined are n large compared to the source size, it cannot be regarded as a point source.

Recommendations for the specification of brachytherapy source dosimetry hav been made by the BIR/IPSM [49] and the AAPM [50]. The specification of sourc strength is slightly different in the two cases since the AAPM protocol specifies a Air Kerma Strength, S_k, as the air kerma rate at a certain calibration distance, multiplied by that distance squared.

$$S_k = \dot{K}(d) \times d^2$$

A source is then typically specified in units of cGy cm^2 hr^{-1}.

A dose-rate constant, Λ, is defined as the dose-rate to water at a distance of 1cm on the transverse axis from a source of unit Air Kerma Strength. Thus :

$$\Lambda = \frac{\dot{D}(r_0,\theta_0)}{S_k}$$

The dose-rate at any other position (r,θ) is then given by :

$$\dot{D}(r,\theta) = S_k \ \Lambda \ \frac{G(r,\theta)}{G(r_0,\theta_0)} \ g(r) \ F(r,\theta) \qquad (9.15)$$

where $G(r,\theta)$, $g(r)$ and $F(r,\theta)$ are factors defined as follows :

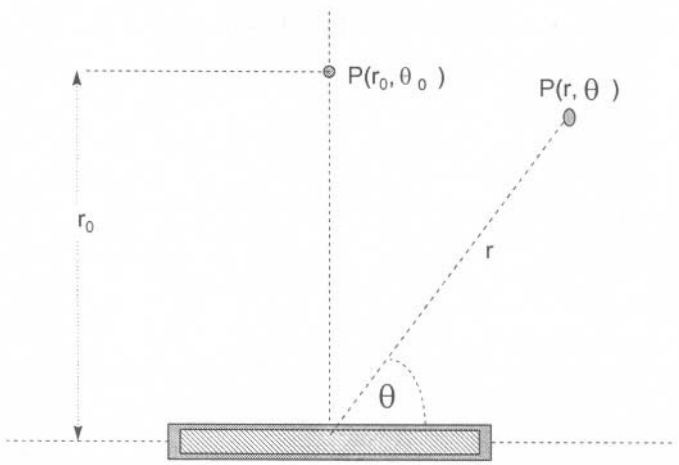

Fig.(9.44) Geometry of a line source surrounded by encapsulation. A point $P(r_0,\theta_0)$ specifies the dose reference position. The dose at any other position $P(r,\theta)$ can then be defined in terms of functions which consider (i) the distribution of activity within the source, (ii) the attenuation and scatter in the direction of the reference point and (iii) the anisotropy in dose in the plane of the figure (cylindrical geometry ensures that only this plane needs to be considered), [50].

- the geometry factor, $G(r,\theta)$, arises because of the spatial distribution of activity within the source. It reduces to $1/r^2$ for a point source, and approximates to $\beta/(L\ r \sin\theta)$ for a line source of length L when β is the angle subtended by the source at the point at distance r.
- the radial dose function, $g(r)$, describes the fall-off in dose-rate only along the transverse axis due to absorption and scatter in the medium.

$$g(r) = \frac{\dot{D}(r,\theta_0)}{G(r,\theta_0)} \frac{G(r_0,\theta_0)}{\dot{D}(r_0,\theta_0)}$$

- the anisotropy function, $F(r,\theta)$, accounts for the change in dose-rate at a constant distance r as θ is varied. It is affected by energy spectrum changes of the emitted photons due to absorption and scatter within the source material itself and in the encapsulation material.

$$F(r,\theta) = \frac{\dot{D}(r,\theta)}{\dot{D}(r,\theta_0)} \frac{G(r,\theta_0)}{G(r,\theta)}$$

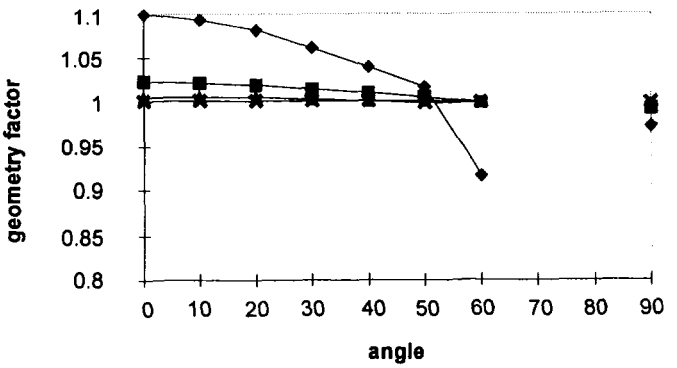

Fig.(9.45) Geometry factor, $G(r,\theta) \times r^2$, for a 3 mm long source calculated for different distances. ◆ 5 mm : ■ 10 mm : ▲ 20 mm : ✖ 50 mm, [50].

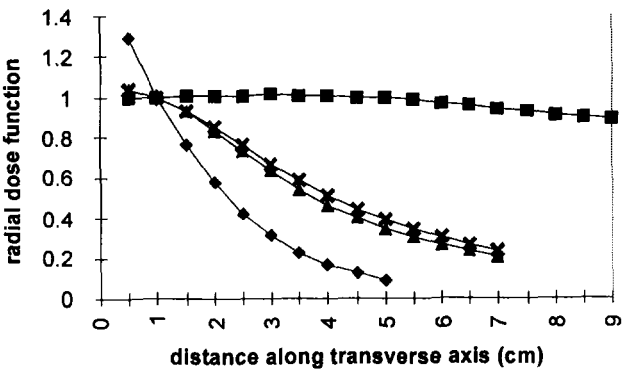

Fig.(9.46) Radial dose function g(r) ◆ ^{103}Pd : ■ ^{192}Ir : ▲ ^{125}I : ✖ ^{125}I : Different coefficients were used in the polynomial expressions for the two ^{125}I curves, [50].

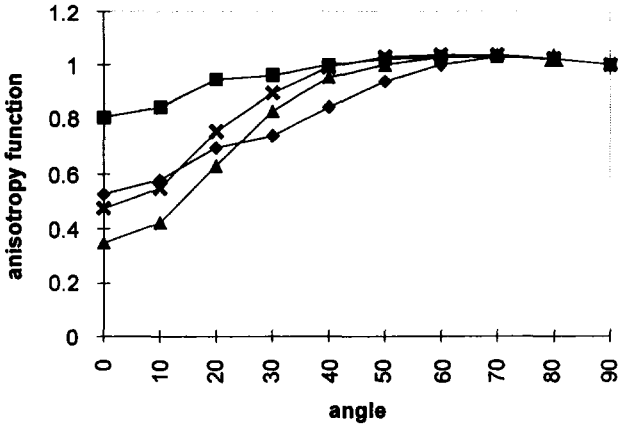

Fig.(9.47) Anisotropy functions F(r,θ) in solid water at a distance of 1 cm from the source. ◆ ^{103}Pd : ■ ^{192}Ir : ▲ ^{125}I : ✖ ^{125}I : At such a small distance large dose gradients make it difficult to both measure and calculate the dose anisotropy, [50].

Dose rate calculations from Reference Air Kerma Rate (RAKR)

Specification of the air kerma rate in free space, *i.e. in vacuo*, 1 m from the source centre is required. This is point $P(r_0,\theta_0)$ in Fig.(9.44).

It is important to recall that the convention of stating an air kerma rate in an another medium, such as vacuum or tissue, is an acknowledgement that the effects of attenuation and scatter in the intervening medium must be considered. RAKR *in vacuo* implies that these effects can be neglected in the initial specification. In the later determination of dose-rate in tissue they therefore have to be addressed separately.

Interstitial sources that cannot be treated as being effectively point sources are specified in terms of RAKR per unit length. e.g. μGy hr^{-1} mm^{-1}. The steps in the procedure for determining the dose rate in tissue at small distances from a brachytherapy source are the following :

- The RAKR is measured in air (free space) 1m from the source using an ionization chamber calibrated against a national standard. For a normal sized chamber and sources of low activity this is not an easy measurement to make. It does, however, define the Air Kerma Strength and it should agree with the source strength specified by the source supplier.
- The dose-rate is then determined at 1 cm along the transverse axis using the dose-rate constant, Λ. This constant includes the effects of source geometry, the spatial distribution of radioactivity within the source volume, the effects of

self-absorption and self-filtering within the source itself and in the encapsulation material.

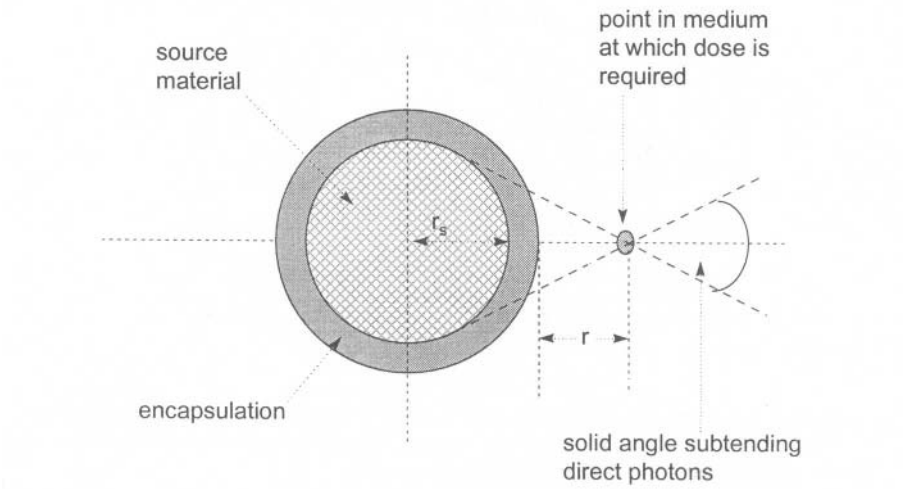

Fig.(9.48). A magnified representation of the geometry in the transverse plane of Fig.(9.44), when point $P(r,\theta_0)$ is at $\theta_0 = 90°$ and $r \leq r_s$, where r_s is the radius of the source material.

Normalization of the radial dose function g(r)

Reference to Figs.(9.44) and (9.48) shows that the kerma rate in air at any point P distance r from the source in the transverse plane can be obtained from the Air Kerma Rate, K_{RAKR}, specified at 1m as :

$$\dot{K}_{r,air} = r^2 \; K_{RAKR}$$

when *r* is measured in metres. If a small volume of water is placed around point P, the dose-rate in water is :

$$\dot{D}_{r,water} = \dot{K}_{r,air} \; \frac{(\mu / \rho)_{water}}{(\mu / \rho)_{air}}$$

When water occupies the intervening space between the source and point P, the dose-rate becomes corrected for attenuation and scatter in the medium. Thus ;

$$\dot{D}_{r,water,as} = \dot{D}_{r,water} \; g(r)$$

where *g(r)* is the radial dose function (sometimes called the attenuation-scatter function) at distance *r*.

Each source encapsulation combination should have its own *g(r)*, with a shape determined by :

- the source geometry,
- the emitted energy spectrum, and
- the encapsulation.

In addition, the attenuation properties of the medium give rise to different contributions from direct and scattered photons which further affect the dose at any given point. Therefore :

- At large distances from a source, the change of dose-rate with distance is mainly determined by attenuation in the intervening medium.
- At the smaller distances which are of most interest, up to 2 – 3 cm, scatter in all directions from the surrounding medium plays an increasingly important role.
- Immediately adjacent to the source attenuation is zero. A point will inevitably exist at which the contributions to total dose from direct and scattered photons are equal.

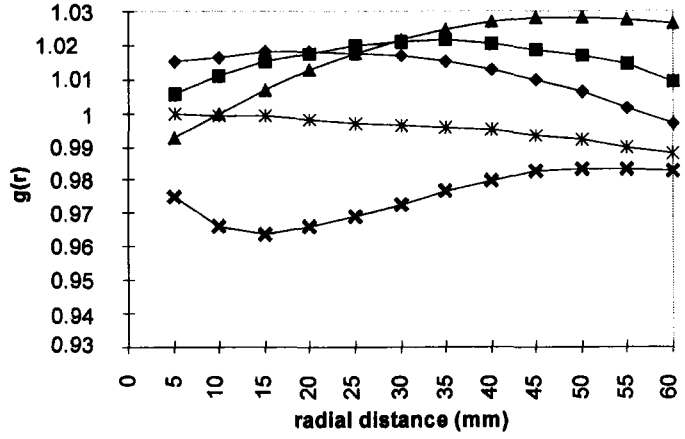

Fig.(9.49) Determinations of radial dose function g(r) for ^{192}Ir. ◆ [51] ; ■ [52] ; ▲ [53] ; ✖ [54] ; ✳ [55].

In the determination of *g(r)* for a given source encapsulation combination, great importance is attached to the distance at which *g(r)* becomes unity. Fig.(9.46) shows different *g(r)* functions for the same source combination, ^{125}I, using different polynomial fits to the calculated dose.

The difficulty in determining $g(r)$ as $r \rightarrow 0$, whether by calculation or by experiment, compounds the uncertainty in agreeing on a normalization procedure. Values are not available for $r \leq 0.5$ cm. At distances up to 5 cm uncertainties of ~5% give rise to dosimetry errors which are particularly significant for HDR brachytherapy. Fig.(9.49) shows the extent of the uncertainties for ^{192}Ir.

A presently unanswered question is the way in which g(r) should be normalized. The choices are :

- At r = 0. This would appear to be physically unreasonable because of the large and poorly determined contribution from both back-scattered and forward-scattered photons.
- At r = 1cm. An arbitrary position has little theoretical significance other than being a typical distance over which a large therapeutic dose is required.
- The distance at which g(r) = 1. Here, attenuation and scatter contributions to the dose are equal.

9.7.2 The principles of the Paris system

The Paris system [56] is based on the following requirements for the disposition of a number of sources, whether they are straight, curved or looped.

- The sources should be parallel and arranged so that their centres are in the same (central) plane.
- The sources should be equidistant, with a minimum separation of 5 mm for small target volumes and a maximum of 20 mm for large volumes.
- The central plane should be at right angles to the axis of each source.
- The linear activity (and therefore the linear reference kerma rate) of each source should be uniform along its length and be identical for all the sources.
- For volume implants, the distribution produced in the central plane should be either an equilateral triangle or a square.

The initial requirements in the planning of a brachytherapy procedure are :

- The dose prescription to the 85% Basal Dose Rate – e.g. 50Gy to 85% BDR.
- The radioactive source test report from the supplier – e.g. a nominal activity of 2.59 GBq (70 mCi) giving an Air Kerma Rate of 573.10 nGy hr^{-1} (65.65 μR hr^{-1}) at 1 m per mm of wire at 12.00 GMT on day zero. The wire would be specified for length (500 mm), diameter (0.3 mm), form (coil) and content (^{192}Ir – platinum clad).

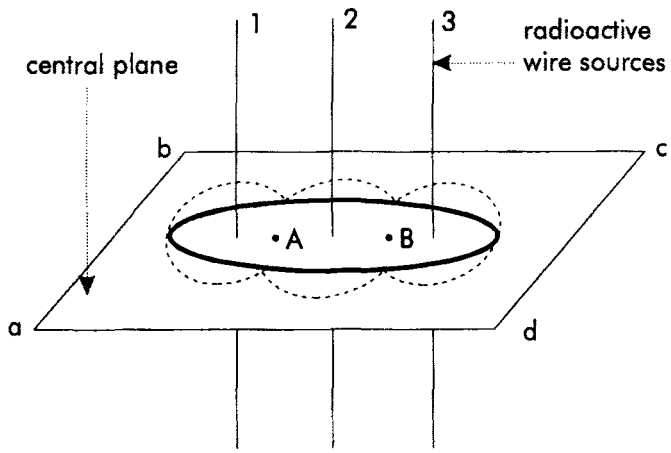

Fig.(9.50) A system of 3 wire sources intersecting the central plane (a b c d) of the (elliptical) target volume. The Reference Dose Rate (shown dotted) is 85% of the Basal Dose Rate and encloses the target volume. The Basal Dose Rate is defined as the minimum dose rate between a pair or group of sources in the central plane, i.e. at points A and B, [56].

In the relation between old and new radiological units we have :

1 Roentgen (R) (exposure) = 2.58 10^{-4} C kg^{-1}.
W/e = 33.92 J C^{-1} (amount of energy required to produce a Coulomb of charge).
1R = 0.00873 J kg^{-1} = 0.00873 Gy in air.
1R = 0.00957 Gy in soft tissue.

The old unit of specific gamma ray constant for ^{192}Ir is Γ = 0.469 R $Ci^{-1} hr^{-1}$ at 1m.

Since 1Ci = 3.7× 10^{10} Bq, the equivalent new unit for air kerma is

$$0.469\frac{R}{Ci\ hr} \rightarrow \frac{0.469\times 2.58\times 10^{-4}\times 33.92}{3.7\times 10^{10}\times 3600}\frac{J}{kg\ Bq\ s} = 3.081\times 10^{-17}\,Gy\ Bq^{-1}\ s^{-1}$$

For the above source, therefore, the activity per mm of wire is :

$$\frac{66.65}{0.469}\frac{\mu R\ h^{-1}}{R\ Ci^{-1}\ h^{-1}} = \frac{573.10\times 10^{-9}}{3.081\times 10^{-17}}\frac{Gy\ h^{-1}}{Gy\ Bq^{-1}\ s^{-1}} = 139.65\mu Ci$$

The clinical specification of total dose to a certain volume of tissue will determine the size, activity and disposition of the sources.

A prescription of 50 Gy to 85% BDR over a volume of approximately 3×2.5×1 cm^3, Fig.(9.50), could be achieved with wire lengths of 2.3 cm, 2.6 cm and 2.3 cm separated

by 0.89 cm (wires 1 and 2) and 1.17 (wires 2 and 3).

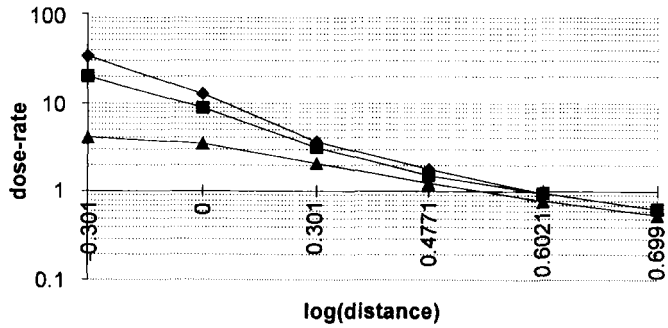

Fig.(9.51) The Oxford cross line curves for a 2 cm long ^{192}Ir wire source, giving dose rate in cGy hr^{-1} for 1 mg radium equivalent per cm of wire.
◆ central plane (0 cm) : ■ 1 cm above and below : ▲ 2 cm above and below central plane.

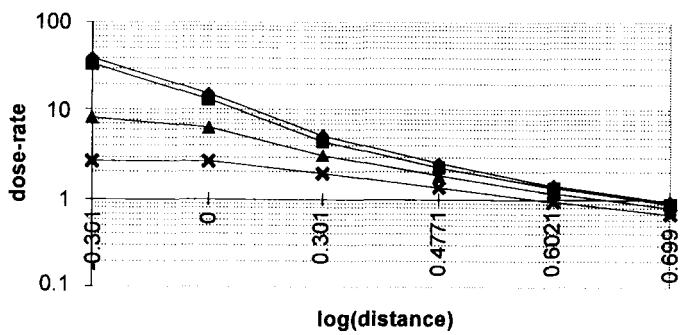

Fig.(9.52) Cross line curves for a 3 cm long ^{192}Ir source. Symbols as in Fig.(9.51) with ✖ 3 cm.

Table (9.7) Total dose-rates in cGy hr^{-1}(mg radium equivalent)$^{-1}$ cm^{-1} computed for points A and B in Fig.(9.50).

Wire	1	2	3	total dose-rate (cGy hr^{-1}(mg Ra$_{eq}$)$^{-1}$cm^{-1})
distance to A	0.45	0.45	1.62	
dose-rate @A	41.7	42.9	6.2	90.8
distance to B	1.48	0.59	0.59	
dose-rate @B	7.06	30.4	29.2	66.67

The mean BDR is then given by:

$$BDR = \frac{(90.8 + 66.67)}{2} \times \frac{0.957}{0.97} = 77.68 \text{ cGy hr}^{-1} (\text{mgRa}_{eq})^{-1} (\text{cm})^{-1}$$

in which 0.957 converts dose in air to dose in soft tissue and 0.97 accounts for the mean attenuation between source wires and points A and B.

The Reference Dose Rate is thus 66.03 cGy.hr^{-1} (mg radium equivalent)$^{-1}$ cm^{-1}.

If treatment is due to start at 12.00 GMT on day two, the source activity becomes :

$$139.65 \times exp\left(-0.693 \frac{2}{74.02}\right) = 137.06 \text{ mCi mm}^{-1}$$

This is converted to mg radium equivalents using equation (9.14) :

$$1.3706 \times \frac{0.469}{0.825} = 0.7792 \text{ mgRa}_{eq} \text{ cm}^{-1}$$

giving the final dose rate at the start of treatment as :

$$0.7792 \times 66.03 = 51.45 \text{ cGy hr}^{-1}$$

The approximate time to deliver 50 Gy is therefore 4.05 days. However, since this period is not insignificant with the source half life, the activity needed to determine the treatment time is taken from the dose-rate mid way through the treatment.

$$\frac{50}{0.7792 \times exp\left(-0.692 \frac{2.025}{74.02}\right) \times 66.03 \times 10^{-2} \times 24} = 4.127 \text{ day}$$

The overall treatment time is thus 4 days 3 hours and 3 minutes.

9.7.3 Experimental HDR brachytherapy dose distribution measurements

Precision measurement of high dose rates at mm distances from an intense radioactive source are exceedingly difficult. The need to achieve a high spatial resolution points to the use of small volume ionization chambers or TLD or diamond dosimeters. Since water is the most useful medium in which to make comparative

and standardization measurements, an arrangement shown in Fig.(9.53) can be used.

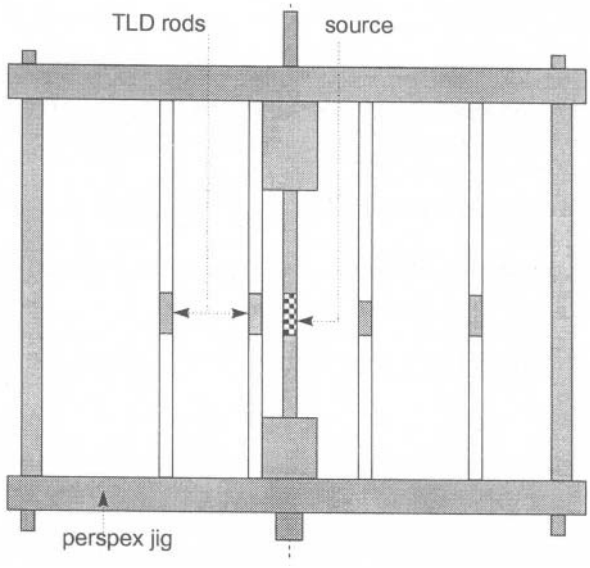

Fig.(9.53) An elevation view of a circular perspex jig which is immersed in a water tank. The brachytherapy source is positioned within the central catheter. TLD rods are held in a series of catheters at increasing radii from the source holder. Rods are positioned in the central transverse plane of the cylindrical source (shown) as well as above and below this plane (not shown). 2-3 mm is the minimum separation between source and the nearest TLD rod.

In order to establish the radial dose functions to the required accuracy of 2 – 3%, a very large number of careful measurements with a consistent batch of calibrated rods is required in order to overcome the intrinsic reproducibility problems of TLD.

9.7.4 Interstitial radiosurgery

This is a novel development in brachytherapy which does not require the insertion of a radioactive source into the patient. It can be used either to irradiate the tumour bed immediately following surgery or as a source of radiation which can be inserted directly into a tumour along the same track as a biopsy cannula. It makes use of a miniature X-ray source, having a mean energy ~20 keV, at the end of a 3 mm diameter probe.

Tube current is produced by radiofrequency ohmic heating of a barium oxide thermionic cathode maintained at a negative accelerating potential. This ensures that the thin gold target at the end of the 100 mm probe is grounded. Electrons are transported a total length of 210 mm between gun and target using an extraction electrode, a focusing element and an acceleration lens to focus the beam down to a final diameter of 0.35 mm. Deflection coils along the electron path ensure a symmetric

and fairly isotropic output.

Power is supplied by a NiCd rechargeable battery which, in conjunction with a Cockcroft-Walton voltage multiplier circuit, is capable of producing 40 kV. A fully-charged battery is able to produce 20 μA for 2 hours at 40 kV [57].

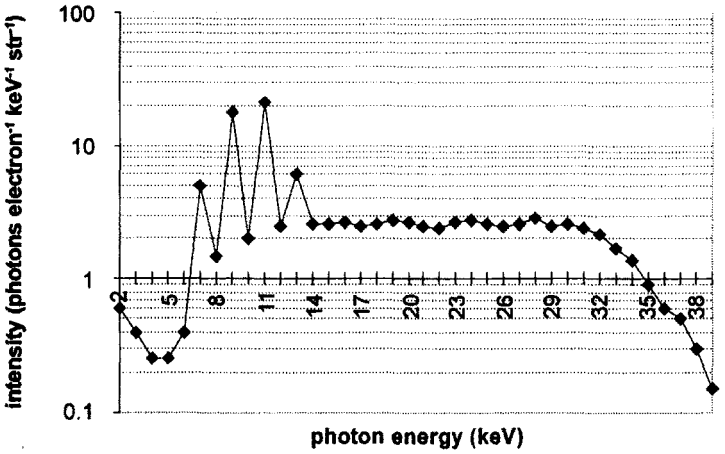

Fig.(9.54) Intensity of X-rays measured through a 1 mm diameter aperture with a Si(Li) detector in air, 1 m from the probe tip. Operating conditions were 40 kV, and 1.25 μA current. The intensity scale should be multiplied by 10^{-6}.

The main features of the output are [58] :

- The total energy comprises 85% *bremsstrahlung* and 15% characteristic photons. The former shows a constant intensity between 14 and 30 keV while the latter shows peaks due to transitions in the gold target and the nickel of the target tube, Fig.(9.54).
- The mean energy is 19 keV. Without any effect due to attenuation in air, as in the spectrum in Fig.(9.54), the mean energy is 16 keV.
- The intensity is isotropic to within 10%.
- The dose fall-off in water goes approximately as distance^{-3}.
- Dose-rates of up to 500 Gy min^{-1} are achievable at the centre of a tumour and 0.6 Gy min^{-1} at the periphery of a lesion 30 mm in diameter. These dose-rates are roughly equivalent to those produced with a 3×10^{11} Bq ^{125}I source.

References

[1] The IPEMB Code of Practice for the determination of absorbed dose for X-rays below 300 kV generating potential, *Phys.Med.Biol*, **41**(1996) 2605.

[2] IAEA Report, *Absorbed dose determination in photon and electron beams : an International Code of Practice*, 2nd Ed, **TRS 277** (1997).
[3] ICRU Report 46, *Photon, Electron, Proton and Neutron Interaction Data for Body Tissue*, (International Commission on Radiation Units and Measurements, Maryland USA, 1992).
[4] Central axis depth dose data for use in radiotherapy, *Brit.J.Radiol.* Supplement **17** (1983) 130.
[5] H.E.Johns and J.R.Cunningham, *The Physics of Radiology* (4th Edition, Charles.C.Thomas, Springfield, Illinois.USA, 1983).
[6] K.E.Sixel and E.B.Podgorsak, *Med.Phys.* **21**(3) (1994) 411.
[7] P.Francois, F.Coste, J,Bonnet and O.Caselles, *Med.Phys.* **24**(5)(1997) 769.
[8] NCRP Report 79 (National Council on Radiation Protection and Measurements, 1984).
[9] S.C.Klevenhagen, *AMPI Medical Physics Bulletin*, **17**(4) (1992) 34.
[10] S.C.Klevenhagen, *Physics and Dosimetry of Therapy Electron Beams*, (Medical Physics Publishing, Madison, Wisconsin, USA,1993)
[11] D.Harder, *Symposium on High-Energy electrons (1994)*, (eds. A. Zuppinger and G.Poretti, Springer, Berlin, 1965) p.291.
[12] P.Andreo and A.Brahme, *Med.Phys.* **8** (1981) 682.
[13] P.R.Almond, *Phys.Med.Biol.* **12** (1967) 13.
[14] B.Markus, *Phys.Med.Biol.* **31** (1986) 657.
[15] ICRU Report 35, *Radiation Dosimetry, Electron beams with energies between 1 and 50 MeV*, (International Commission on Radiation Units and Measurements, Maryland USA, 1984).
[16] J.M.Fernandez-Varea, P.Andreo and T.Tabata, *Phys.Med.Biol.* **41** (1996) 1119.
[17] D.I.Thwaites, D.T.Burns, S.C.Klevenhagen, A.E.Nahum and W.G.Pitchford, *Phys.Med.Biol.* **41** (1996) 2557.
[18] N.S.Rustgi and J.E.Rogers, *Med.Phys.* **14** (1987) 884.
[19] S.C.Klevenhagen, *Phys.Med.Biol.* **39** (1994) 1103.
[20] B.B.Sorcini, S.Hyodynmaa and A.Brahme, *Phys.Med.Biol.* **41** (1996) 2657.
[21] M.J.Berger, Report NISTIR 5226 (National Institute for Standards and Technology 1993).
[22] H.Palmans and F.Verhaegen, *Phys.Med.Biol.* **42** (1997) 1175.
[23] G.Arduini, R.Cambria, C.Canzi, F.Gerardi, B.Gottschalk, R.Leone, L.Sangaletti and M.Silan, *Med.Phys.* **23**(6) (1996) 939.
[24] H.Paganetti and Th.Schmitz, *Phys.Med.Biol.* **41** (1996) 1649.
[25] C.S.Mayo, M.Wagner, B.Gottschalk, J.M.Sisterson, and A. Koehler, *Med.Phys.* **18** (1991) 625.
[26] R.Cambria, J.Herault, N.Brassart, M.Silari and P.Chauvel, *Phys.Med.Biol.* **42** (1997) 1185.
[27] Th.Loncol, M.Hamal, J.M.Denis, S.Vynckier, A.Wambersie and P.Scalliet, *Phys.Med.Biol.* **41** (1996) 1665.

[28] D.K.Bewley, *The Physics and Radiobiology of Fast Neutron Beams* (Adam Hilger, Bristol, 1989).
[29] D.E.Bonnett and C.J.Parnell, *Br.J.Radiol.* **55** (1982) 48.
[30] ICRU Report 36, *Microdosimetry*, (International Commission on Radiation Units and Measurements, Maryland USA, 1983).
[31] A.G.Perris, F.A.Smith and D.R.Perry, *Phys.Med.Biol.* **23** (1978) 111.
[32] M.R.Raju and C.Rickman, *Current topics in Radiat.Res.* **8** (1972) 159.
[33] D.E.Watt, Report Biophys/2/94 (University of St Andrews, 1994).
[34] TECDOC-799, *Atomic and molecular data for radiotherapy and radiation research*, (International Atomic Energy Agency, Vienna, 1995).
[35] C.P.J.Raaijmakers, E.L.Nottelman, M.W.Konijnenberg and B.J.Mijnheer, *Phys.Med.Biol.* **41** (1996) 2789.
[36] C.P.J.Raaijmakers, P.R.D.Watkins, E.L.Nottelman, H.W.Verhagen, T.J.M.Jansen, J.Zoetelief and B.J.Mijnheer, *Med.Phys.* **23** (1996) 1581.
[37] A.Wu, A.H.Maintz, A.M.Keland, et.al, *Int.J.Radiat.Oncol.Biol.Phys.* **18** (1990) 941.
[38] M.Heydarian, P.W.Hoban and A.H.Beddoe, *Phys.Med.Biol.* **41** (1996) 93.
[39] M.C.Schell, V.Smith, D.A.Larson et.al., *Int.J.Radiat.Oncol.Biol.Phys.* **20** (1991) 1325.
[40] T.S.Suh, F.J.Bova, S.C.Yoon, B.Y.Choe, M.C.Kim, K.S.Shinn, Y.W.Bahk, S.W.Ha and C.I.Park, *Phys.Med.Biol.* **41** (1996) 675.
[41] K-U.Gardey, T.Bortfeld, W.Schlegel and B.Rhein, *Phys.Med.Biol.* **42** (1997) 717.
[42] A.Ertl, R.F.E.Hartl, M.Zehetmayer, K.Kitz and W.Griffitt, *Phys.Med.Biol.* **41** (1996) 2679.
[43] S.V.Spirou and Chen-Shou Chui, *Med.Phys.* **23**(1) (1996) 1.
[44] S.S.Young, *Phys.Med.Biol.* **41** (1996) 1621.
[45] R.Boellaard, M.van Herk and B.J.Mijnheer, *Med.Phys.* **23**(9) (1996) 1601.
[46] R.Paterson and H.M.Parker, *Br.J.Radiol.***11** (1938) 252.
[47] E.H.Quimby, *Radiology*, **43** (1944) 572.
[48] B.Pierquin, A.Dutreix, C.H.Paine, D.Chassagne, G.Marinello and D.Ash, *Acta Radiologica Oncology* **17** (1978) 33.
[49] BIR/IPSM, Report *Recommendations for brachytherapy dosimetry,* (1992).
[50] R.Nath, L.L.Anderson, G.Luxton, K.A.Weaver, J.F.Williamson and A.S.Meigooni, *Med.Phys.* **22**(2) (1995) 209.
[51] L.L.Meisberger, K.J.Keller and R.J.Shalek, *Radiology* **90** (1968) 953.
[52] L.Sakelliou, K.Sakellariou, K.Sarigiannis, A.Angelopoulos, A.Perris and G.Zarris, *Phys.Med.Biol.* **37** (1992) 1859.
[53] R.G.Dale, *Br.J.Radiol.* **55** (1982) 748.
[54] R.O.Kornelson and M.J.Young, *Br.J.Radiol.* **54** (1981) 136.
[55] H.J.van Kleffens and W.M.Star, *Int.J.Radiat.Oncol.Biol.and Phys.* **5** (1979) 557.
[56] B.Pierquin, A.Dutreix, C.H.Paine, D.Chassagne, G.Marinello and D.Ash, *Acta Radiologica Oncology* **17** (1978) 33.

[57] M.Dinsmore, K.J.Harte, A.P.Sliski, D.O.Smith, P.M.Nomikos, M.J.Dalterio, A.J.Boom, W.F.Leonard, P.E.Oettinger and J.C.Yanch, *Med.Phys.* **23**(1) (1996) 45.

[58] J.Beatty, P.J.Biggs, K.Gall, P.Okunieff, F.S.Pardo, K.J.Harte, M.J.Dalterio and A.P.Sliski, *Med.Phys.* **23**(1) (1996) 53.

CHAPTER 10

IMAGING

10.1 Introduction

The principle features that characterize an imaging modality are :

- its contrast resolution,
- its spatial resolution,
- its sensitivity,
- the radiation dose or other potentially harmful consequences to the object,
- the nature of the interactions which underlie the imaging process.

Conventional X-ray imaging – now referred to as diagnostic radiology – formed the mainstay of all medical and industrial uses from the beginning to the middle of the 20th century. Radioisotope techniques then found increasing use, mainly in medical applications. The development of computerized tomography with X-rays in the 1960's began the explosion of interest which led to the sophisticated technology of the present-day. Computerized tomography now also forms the basis of nuclear medicine and, since the early 1970's, magnetic resonance imaging.

In addition to diagnostic radiology therefore, which has also undergone considerable development, many medical radiology departments now have access to :

- X-ray computerized tomography (CT),
- single photon emission computerized tomography (SPECT),
- positron emission tomography (PET),
- magnetic resonance imaging (MRI).

Each of these modalities is based on different physical interactions between the radiation and the tissue being imaged. The information contained within each type of image is therefore unique to that method.

10.2 Image Quality

10.2.1 Spatial frequency and spatial resolution

The spatial resolution of an imaging system is quantified by measuring its response to an infinitely small, high contrast, input function which ideally contains all possible spatial frequencies. The response of the system to this ideal input is described by

the following response functions :

- Point Spread Function (PSF) – This is the response of the system to a point object. The input point object is convolved with the PSF to give an output point which will be blurred.
- Edge Response Function (ERF) - This determines the response to an infinitely sharp edge object. The sharp edge is convolved with the ERF to give a more blurred image of the sharp edge.
- Line Spread Function (LSF) - The response to an infinitely narrow line object. An infinitely narrow line input is broadened as the result of its convolution with the LSF.

To proceed further, it is necessary to consider the meaning of spatial frequency, and the way in which the response function modifies an observed image. The response function can be described as the summation of a number of components having different spatial frequencies.

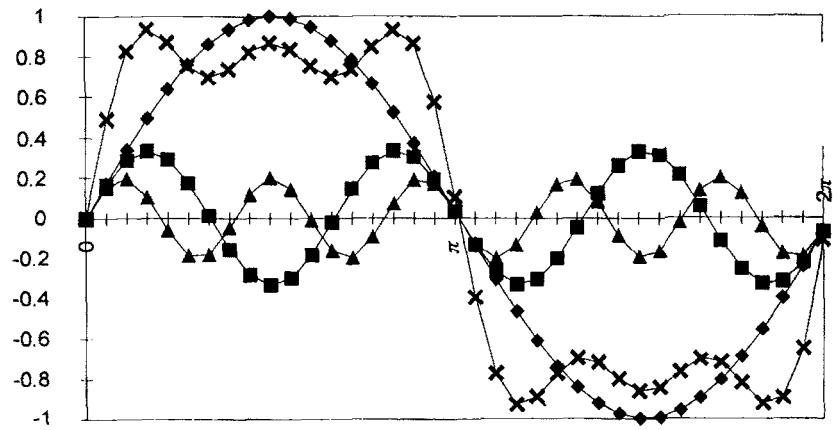

Fig.(10.1) Approximation to a continuous square wave using Eq.(10.1). ● n = 1 : ■ n = 3 : ▲ n = 5 : ✖ summation of n = 1,3,5. The abscissa axis is n f x, where f is the fundamental spatial frequency. Terms with even values of n introduce asymmetry and cannot be used to describe a regular and continuous square wave.

A continuous square wave can be described in terms of a fundamental spatial frequency, *f*, and its harmonics, *nf*, using Eq.(10.1). The larger the number of components, *n*, (i.e. the higher the harmonic frequencies used) the better the approximation, Fig.(10.1).

$$y = \sum_{odd-n-only} \frac{1}{n} sin(nfx) \qquad (10.1)$$

However, a point, edge or line, is not describable in terms of discrete frequencies

as in the case of a wave train. A single feature requires that the frequency distribution is continuous. Again, the higher the frequencies the better the representation of the input function. Fig.(10.2) considers a single, square input pulse of radiation exposure onto an imaging device. This might be a film, a scintillation crystal backed by position-sensitive photomultiplier tubes or a CCD camera.

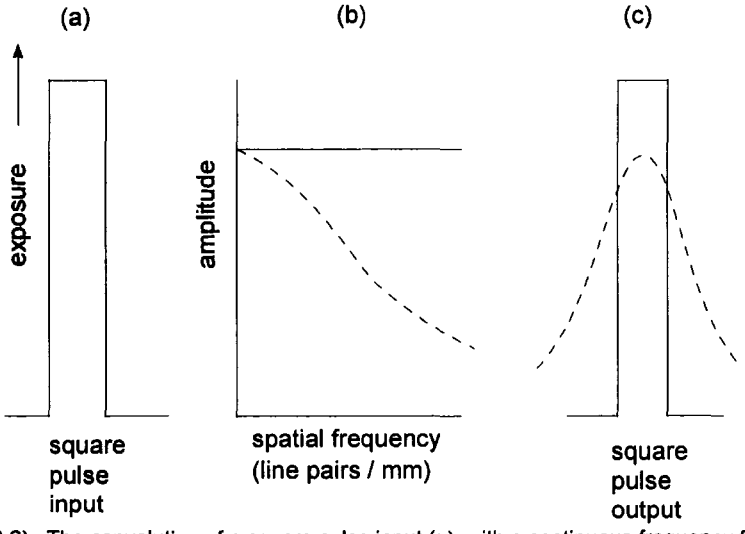

Fig.(10.2) The convolution of a square pulse input (a), with a continuous frequency function (b). This gives a square pulse output (c) in a ideal imaging system. A real imager is described by a frequency function whose amplitude decreases at higher frequencies (dotted line in b). The consequence is that the convolution produces a broadened output function (dotted line in c).

10.2.2 Modulation Transfer Function

The modulation transfer function is a mathematical description of the capability of a system to produce in the image the whole range of spatial frequencies in the object. It is defined as :

$$\text{MTF} = \frac{\text{amplitude:frequency spectrum which produces the given image}}{\text{amplitude:frequency spectrum to produce an image identical to the input}}$$

Since the denominator in this definition is unity at all frequencies in the ideal system, see (b) in Fig.(10.2), the MTF of a real imaging system is the Fourier transform of the imager output when the input is an infinitely sharp point, edge or line.

The relation between the amplitude and the spatial frequency in such a transform can be demonstrated by measuring the MTF of an X-ray film which is used with, and without, an intensifying screen. In a diagnostic X-ray examination, the purpose of an intensifying screen is to reduce the exposure needed for a given optical density on the film (see section 10.4.3). Although dose to the patient is thereby reduced, this

reduction is achieved at the expense of a loss in spatial resolution. A demonstration requires the following items of equipment, Fig.(10.3) :

- A diagnostic X-ray source,
- A strip (width ~ 8 – 10 cm) of diagnostic X-ray film together with a strip of intensifying screen (width ~ 4 – 5 cm) to cover half the film area,
- Facilities for developing and fixing the exposed film, and
- A scanning densitometer.

In order to achieve the ideal conditions of a square input pulse, Fig.(10.2a) :

- The distance between X-ray source and film should be large enough (≥ 2 m) to ensure a uniform photon fluence over the total film area, and
- The thickness of the infinitely absorbing material, A in Fig.(10.3), should be as small as possible, but sufficient to achieve an infinitely sharp edge function.

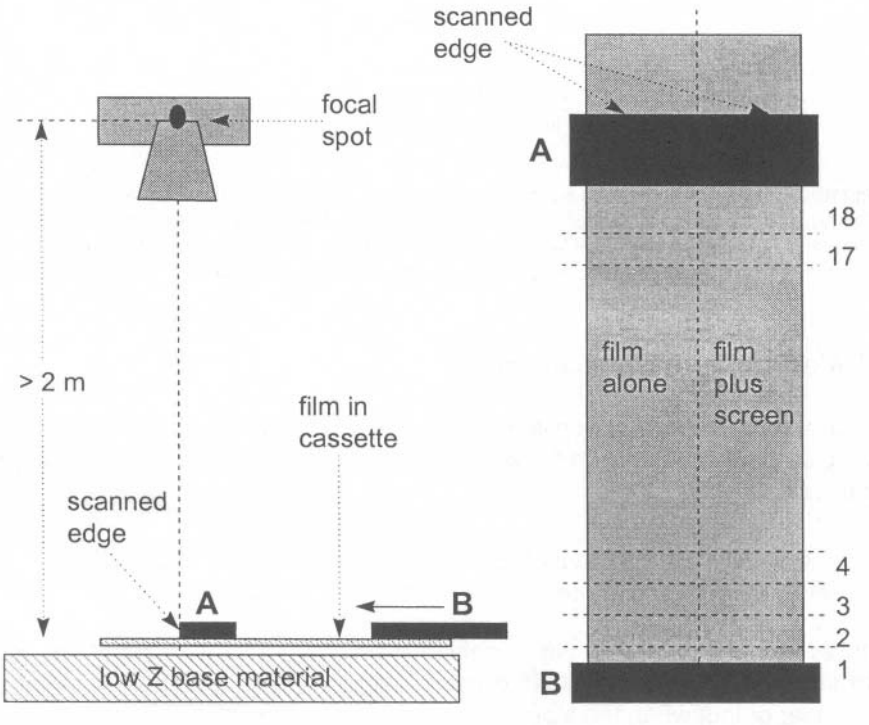

Fig.(10.3) An experimental determination of the Modulation Transfer Function of a film alone and a film+screen combination. Acceptable experimental parameters are : a source-film distance of > 2 m, a stationary lead absorber (A) of thickness 4 mm, a 58 kVp anode potential, a moveable lead plate (B) of thickness 4 mm.

The focal spot of the X-ray tube in Fig.(10.3) is placed at a large distance directly in line with a fixed, infinitely-absorbing edge at A. One half of the film width is backed

by the intensifying screen, the other by cardboard of equivalent thickness. The film cassette is placed on a low-Z base material in order to minimize backscatter. Lead plate B, of equivalent thickness to A, progressively covers 18, 1cm wide, strips marked on the cassette. Exposures are made at constant tube output for increasing times as B is moved from strip 1 to strip 18. Data shown in Fig.(10.4) are determined for a tube output of 58 kVp and 3 mA.

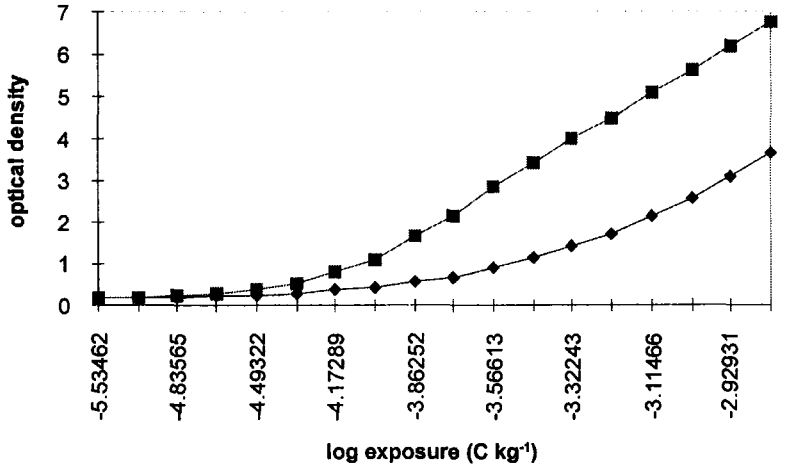

Fig.(10.4) Characteristic curves of film alone (◆), and film with intensifying screen (■). The exposure is adequately determined with a 180 cm^3 air ionization chamber placed at the same position relative to the x-ray head as the film cassette. Exposure rate = 0.584×10^{-5} C kg^{-1} s^{-1}.

Measured optical densities of the 18 strips of film are plotted against the known exposures in Fig.(10.4) to yield characteristic curves for the film with and without the intensifying screen. A scanning densitometer is used to measure the optical density profile across the sharp edge of absorber A.

The definition of a Modulation Transfer Function in Fig.(10.2), however, is given in terms of the amplitude of an incoming wave front. The ability of the imaging system to respond faithfully to all the frequencies in this wave front is contained within the MTF. Output is therefore still expressed in terms of wave amplitudes. As a consequence, the measured output response of the imaging system – the film optical density – must first be converted to X-ray intensity incident upon the film. This is proportional to exposure, so long as the tube output is constant.

A densitometer scan across the edge of absorber A, Fig.(10.5), is therefore converted to a scan of intensity, Fig.(10.6), using the characteristic curve in Fig.(10.4). The two edge profiles in Fig.(10.6) are sampled at intervals along the abscissa and Fourier transformed. For N sampling points taken at interval Δx, each transform point is separated by $2\Delta x/(N+2)$.

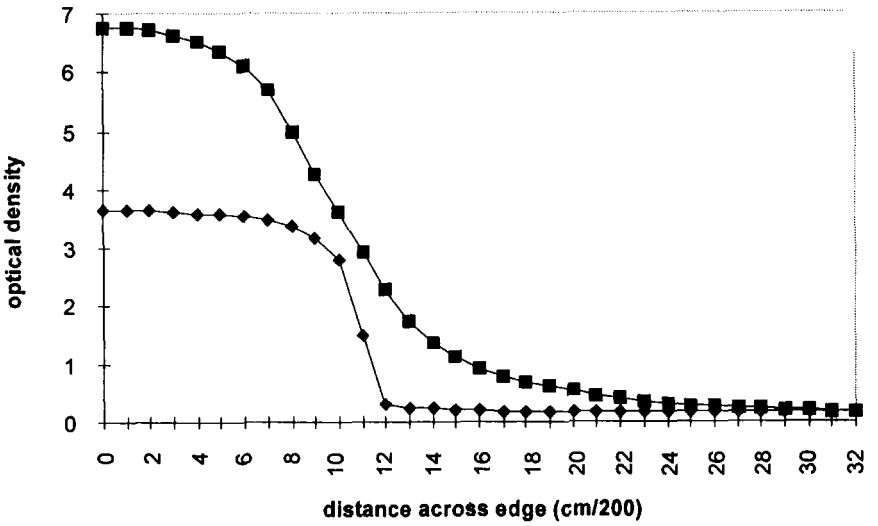

Fig.(10.5) Scanning densitometer scan across a sharp, infinitely absorbing edge. Film alone (◆), Film plus intensifying screen (■). The optical densities at the left- and right-hand sides of the scan correspond to the maximum and minimum densities respectively given in Fig.(10.4).

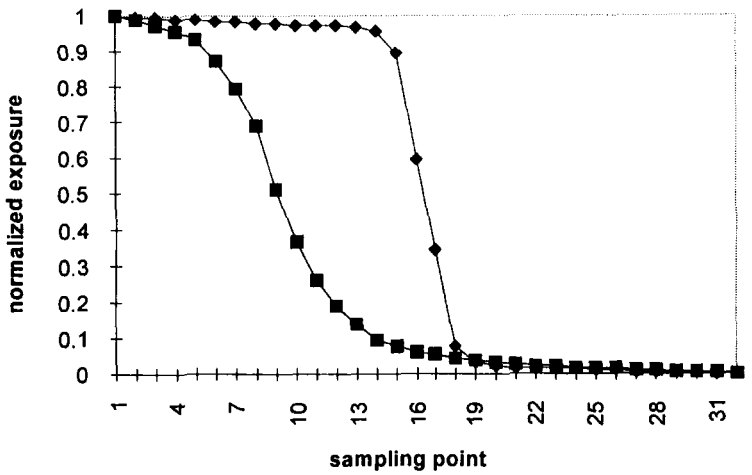

Fig.(10.6) Data from Fig.(10.5) are converted to exposure using the characteristic curve in Fig.(10.4) and normalized to maximum exposure. The abscissa scale is identical to Fig.(10.5). (◆) film alone : (■) film plus screen. Note that the fall-off is sharper and more symmetrical about the mid-point than in Fig.(10.5) due to the logarithmic dependence of optical density on exposure.

To compare the loss of spatial resolution when an intensifying screen is used, a spatial frequency is quoted for which a given difference in intensity between two features is needed before they can be distinguished.

A factor of 2 difference in intensity ($\sqrt{2}$ in amplitude) gives the MTF value of 0.707. Fig.(10.7) shows that the film alone will yield this contrast at spatial frequencies up to 6.7 line pairs per mm. At this same level, when used with a screen, the film cannot reproduce details closer than 1.2 line pairs per mm.

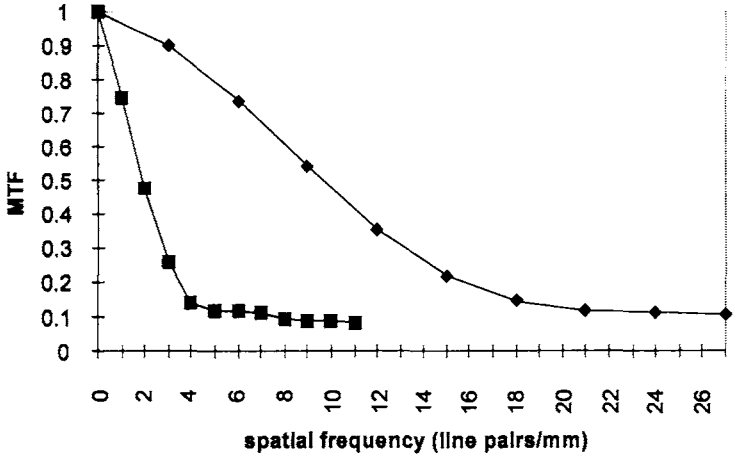

Fig.(10.7) MTF functions for film alone (◆) and film+screen (■). For the film alone, the spatial frequency is 6.7 line pairs mm^{-1} when the MTF has fallen to 0.707. When a screen is added the imaging system can only resolve 1.2 line pairs mm^{-1} for an equivalent fall of 0.707 in the MTF.

10.2.3 Contrast

This is the parameter which quantifies the ability to distinguish two neighbouring features of an image. The quantity being distinguished does, of course, depend on the way the image has been produced. Thus :

- In diagnostic radiology, contrast is due to the differences in optical density on the developed film.
- In X-ray computerized tomography, it is caused by differences in linear attenuation coefficient in the object. These alter the intensity of transmitted X-rays arriving at the detectors.
- In nuclear medicine, contrast is due to the spatial variation in uptake of the radiopharmaceutical. This gives rise to differences in the count-rates at the scintillators which detect the emitted photons.
- In MRI, differences in proton density, or in spin-lattice or spin-spin relaxation times give rise to differences in the absorption of radiofrequency energy at a certain frequency.

Contrast therefore has to be considered in the context of each imaging modality. The effects of noise are clearly important in the measurement of low contrast objects, the contributions to which also depend on the nature of the imaging system.

10.3 X-ray Techniques

10.3.1 X-ray beam modification for imaging

Production of X-rays for both diagnostic and therapeutic purposes is achieved by the acceleration and rapid stopping of an energetic charged particle. Details of the methods of production were given in Chapter 1 and the relevant theory in Chapter 2.

The primary X-ray energy spectrum, however, frequently needs to be modified to adapt it for a particular purpose. A number of techniques are used either to increase or to decrease the mean energy. These are known as *filtration* and they give a filtered spectrum of X-rays which depends upon :

- the energy of the electrons striking the target i.e. the kV applied to the tube,
- the atomic number Z of the target, and
- the thickness, density and atomic number of any material between the target and the detector or patient.

The first of these – electron energy and the target atomic number Z – determine the relative importance of the two X-ray production mechanisms. Although both the continuous *bremsstrahlung* component and the discrete characteristic component are always present, their relative intensities in the primary beam are determined by the electron energy. Clearly, no characteristic K X-rays can be produced by electron energies (E_e) which are less than the K-shell binding energies $(BE)_K$ of the target material.

In cases where $E_e > (BE)_K$ the intensity of characteristic radiation is approximately 30% of the total at low (diagnostic) energies, falling to about 2% at energies about 500 kV.

10.3.2 The filtration of X-ray beams

The design and use of a filter rests on the atomic level schemes of the target and filter materials. Four of the most commonly used materials are tungsten (Z = 74) and molybdenum (Z = 42) as targets and molybdenum, copper (Z = 29) and aluminium (Z = 13) as filters.

Decreasing the mean energy

Mammography demands the ability to image structures with low inherent contrast when microcalcification features as small as 100μm need to be visualized. Low energies are the most suitable, in order to capitalize on the strong Z dependence of the photoelectric absorption and, thereby, to increase the contrast.

Table (10.1) Electron sub-shell binding energies in keV

level	tungsten W	molybdenum Mo	copper Cu	tin Sn
K_I	69.525	20.000	8.979	29.200
L_I	12.099	2.866	1.096	4.465
L_{II}	11.542	2.625	0.951	4.156
L_{III}	10.205	2.520	0.931	3.929
M_I	2.820	0.505	0.120	0.884
M_{II}	2.575	0.410	0.074	0.757
M_{III}	2.281	0.393		0.71
M_{IV}	1.872	0.230	0.002	0.494
M_V	1.810	0.227		0.485
N_I	0.595	0.062		0.137
N_{II}	0.492	0.035		0.089
N_{III}	0.426			
N_{IV}	0.259	0.002		0.024
N_V	0.246			
N_{VI}	0.037			
N_{VII}	0.034			
O_I	0.077			0.001
O_{II}	0.047			0.001
O_{III}	0.037			
O_{IV-V}	0.006			

Table (10.1) shows that the characteristic K lines are determined from the binding energies of the initial and final states. Thus, for a molybdenum target the K X-rays have energies :

$$K_{\alpha_1} = (BE)_{K_I} - (BE)_{L_{III}} = 20.00 - 2.52 = 17.48 \text{ keV}$$

$$K_{\alpha_2} = (BE)_{K_I} - (BE)_{L_{II}} = 20.00 - 2.625 = 17.375 \text{ keV}$$

When these pass through a molybdenum filter, Fig.(10.8) shows that the attenuation coefficient is some 7 – 8 times lower just below the absorption edge than for energies either side. A molybdenum filter therefore acts as a band pass filter to the characteristic X-ray emission from the same target material. This results in a transmission spectrum which is quasi-monoenergetic, Fig.(10.9).

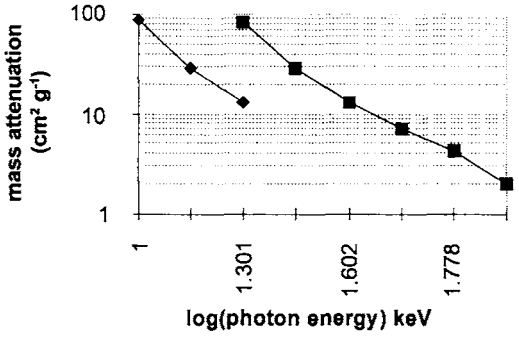

Fig.(10.8) Total mass attenuation coefficient ($cm^2\ g^{-1}$) in molybdenum showing the K-absorption edge at 20 keV (Table 10.1). The first L-absorption edge occurs at 2.866 keV and is therefore not visible on the figure.

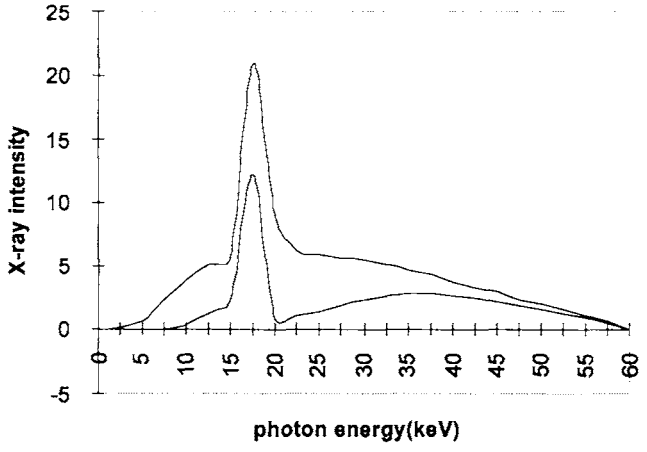

Fig.(10.9) The effect of filtering an X-ray spectrum generated by 60 keV electrons impinging on a molybdenum target, with a molybdenum filter of thickness 0.03 g cm^{-2} (0.029 mm). The incident X-ray spectrum has a characteristic component at ~ 17.4 keV which is ~ 30% of the total (K_α and K_β lines are not resolved in this figure). The (lower) spectrum which emerges from the filter is more monochromatic than the (upper) incident spectrum and also has a slightly lower mean energy.

Increasing the mean energy

In normal diagnostic radiography, and also in orthovoltage radiotherapy, it is often necessary to increase the mean energy in order to :

- reduce the absorbed dose in the surface layers, and
- increase the beam penetration.

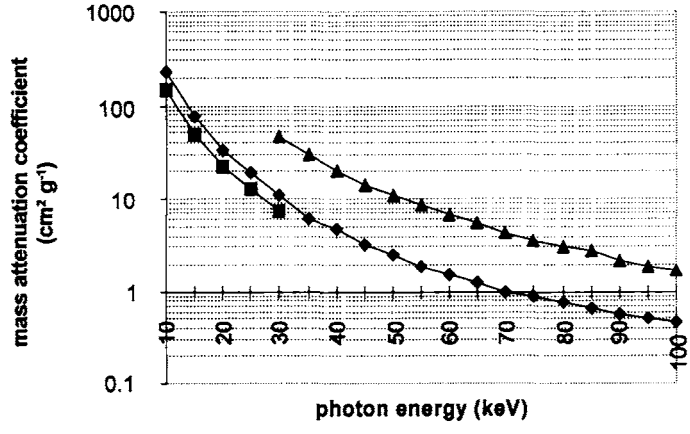

Fig.(10.10) Mass attenuation coefficient ($cm^2\ g^{-1}$) for copper and tin showing the K-absorption edge in tin at 29.2 keV. ◆ copper, the K - edge at 8.979 keV is not visible on the figure : ■ tin below the K-edge at 29.2 keV : ▲ tin above the K - edge.

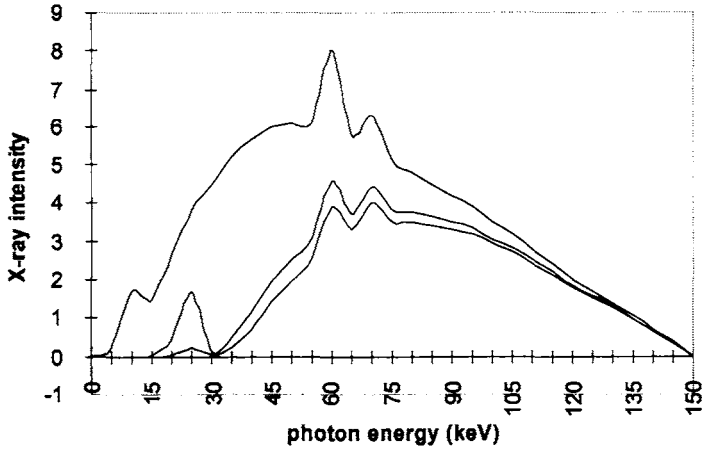

Fig.(10.11) The filtration of X-rays from a tungsten target. The effects of filtering with a layer of tin greatly reduces the relative number of low energy photons. Further filtration with a layer of copper partially removes the peak at the K-edge of tin.

The upper curve in Fig.(10.11) shows the spectrum emerging from a tube operated at 150 kV. Characteristic X-rays account for ~4% of the total intensity giving K_α and K_β lines at 59 keV and 68 keV respectively. These K-lines are not resolved in this figure. A small contribution from L X-rays is also seen near 10 keV, Table(10.1). When the primary spectrum is passed through 0.08 g cm^{-2} (0.11 mm) of tin, the mean photon energy increases but shows a significant peak at the tin K-edge. Further filtration with an additional 0.10 g cm^{-2} (0.11 mm) of copper greatly reduces this feature, as shown by the bottom curve in Fig.(10.11).

When a combination of different filters is used, it is most important that the emerging photons exit from the lowest atomic number material in order that any K-edge component is shifted to the lowest possible energy.

10.4 Diagnostic Radiology (DR)

This is the name given to conventional X-ray imaging in which the photon energies are sufficiently low to make photoelectric effect the dominant interaction. Anode potentials are generally 100 kVp or less. The image is then formed as a result of differential absorption in tissue volumes having different mean atomic numbers (Z).

Fig.(10.12) shows a typical arrangement for reflection geometry.

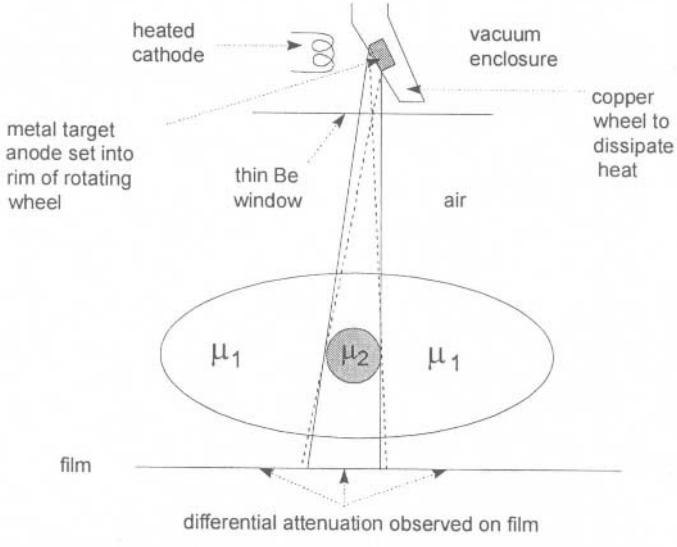

Fig.(10.12) A schematic diagram of image production on a film detector due to differential attenuation of a polyenergetic X-ray beam by a body containing regions of different attenuation coefficients μ_1 and μ_2.

The spectrum of X-rays that emerges from an X-ray tube is polyenergetic because :

- X-ray production takes place at all energies between the anode potential and zero as the electron de-accelerates in the target,
- X-rays produced at different depths within the target receive different amounts of attenuation within the target material itself. This is called self-absorption.
- X-rays emerge into ambient air either through a thinned portion of the glass envelope or through a thin beryllium window. These produce a certain amount of inherent filtration. Additional filtration can then be added according to the

requirements of the object being radiographed.

Transmitted X-rays can be detected either by film or in real-time.

10.4.1 Film

X-ray film is similar to optical film in which microcrystals of silver bromide are dispersed in a gelatin matrix. The main differences are that in a nuclear emulsion the grains sizes are smaller (~ 0.1 – 0.6 μm compared with ~ 1 – 3.5 μm in an optical emulsion) and their concentration by weight higher (~ 80% compared with ~ 50%) [1]. The speed of the film is determined by the distribution of grain sizes – the larger the range of sizes the faster the film [2].

On exposure to radiation, the silver in the AgBr grains is converted to elemental silver to form a latent image. Although the concentration of silver at this stage is too small to be visible, these Ag seeds enhance the production of much greater quantities of silver when the film is developed.

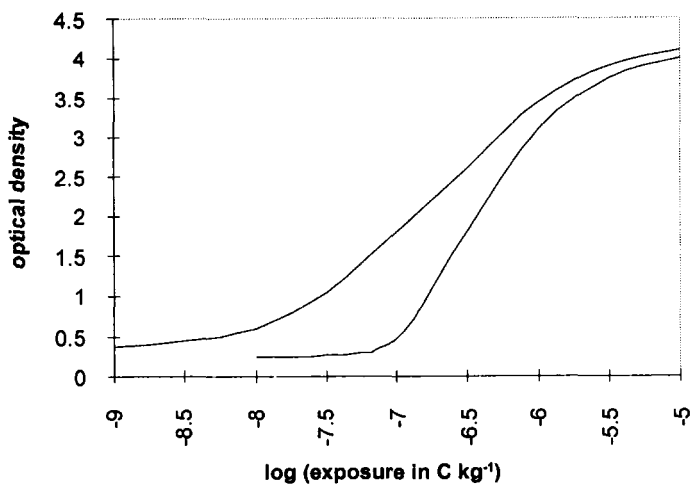

Fig.(10.13) Characteristic curves of typical radiographic films. The left hand curve corresponds to the faster film because it produces an optical density of unity at the lower exposure. It has a wider distribution of grain diameters which accompanies a larger mean grain diameter. This produces a smaller film Γ. The relative speed of the two films at OD = 1 is approximately 7.
The values of the film Γ are 1.8 (left hand) and 3.4 (right hand). The latitudes are approximately 3 × 10^{-8} to 10^{-6} C kg^{-1} (left hand) and 2 × 10^{-7} to 10^{-6} C kg^{-1} (right hand).

The larger the amount of radiation received by the film, the larger the number of seeds in the latent image and the larger will be the final amount of silver when the film is developed. Areas of the film having the higher concentration of silver will appear more opaque i.e. they will have a higher optical density (O.D).

It must be remembered that the AgBr grains in a film will be converted to elemental silver even without the initial presence of a latent image. The process of conversion is faster, however, when the latent image is present. Hence the importance of the developing time to achieve the optimum contrast between regions of different optical density.

Each nuclear emulsion has its own characteristic curve of optical density versus logarithm of exposure as shown in Figs.(10.4) and (10.13). A given film is distinguished by :

- the maximum slope, called the film Γ,
- the range of exposures over which the curve is quasi-linear, called the latitude,
- the range of optical density between the fogging level and the saturation density,
- the speed (or sensitivity). This is the reciprocal of the exposure necessary to produce a given optical density (usually O.D. = 1).

The Optical Density of a film is defined as :

$$O.D = log_{10}\left(\frac{I_0}{I}\right)$$

where I is the intensity of white light transmitted through the film when I_0 is the incident intensity. The Film Γ gives the maximum Contrast and is defined as :

$$\Gamma = \frac{OD_1 - OD_2}{log(E_1) - log(E_2)} \qquad (10.2)$$

where E_1 and E_2 are X-ray exposures.

10.4.2 Reduction of contrast due to scatter

Although the photoelectric effect is the interaction of importance in diagnostic radiology, scatter cannot be ignored since it reduces contrast on a radiographic film (Fig.10.14).

The contribution of scattered photons will tend to be uniformly distributed across the detector face. Two neighbouring regions on the detected image which are due to differences in photoelectric absorption will therefore both have the same scatter background. Table (10.2) uses Fig.(10.13) to illustrate the effect of adding a constant scatter background of 2.46×10^{-8} C kg^{-1} to two features on an image having optical densities 1.1 and 2.25 in the absence of any scatter. The presence of scatter reduces the contrast from 1.15 to 0.95 – a reduction of 17%.

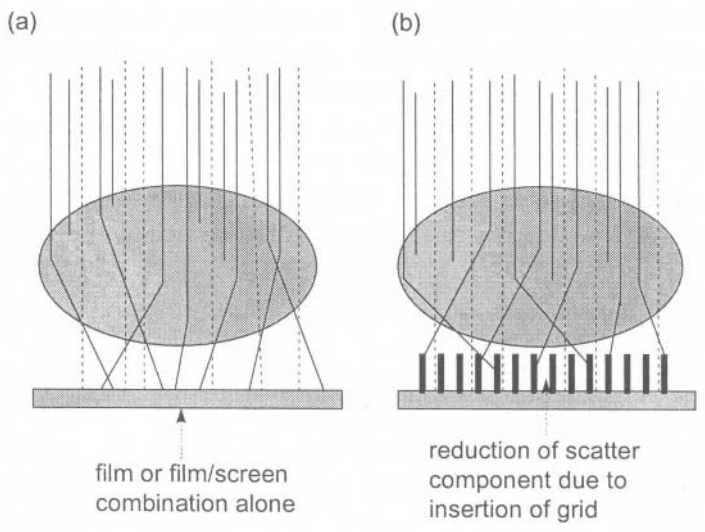

Fig.(10.14) The reduction of scattered photons received on a radiographic detector can be achieved by, (a) minimizing the distance between the detector and the object, and (b) by interposing a grid between the object and the detector. In each diagram, 4 photons have interacted by the photoelectric effect and have stopped in the object, 7 photons have scattered and 6 photons have not interacted in the object at all, and have reached the film without any deviation.

Table (10.2) Reduction in contrast between two features when an additional scatter component of 2.46×10^{-8} C kg^{-1} reaches the radiographic film in Fig.(10.13).

⌈——————no scatter ——————⌉			⌈——————with added scatter——————⌉		
OD	log E	E (C kg^{-1})	E (C kg^{-1})	log E	OD
1.1	-7.5	$3.16\ 10^{-8}$	$5.62\ 10^{-8}$	-7.25	1.4
2.25	-6.75	$1.78\ 10^{-7}$	$2.03\ 10^{-7}$	-6.69	2.35

10.4.3 Intensifying screens

The sensitivity of a film can be increased by converting some of the incident X-ray photons into optical photons to which the film is more sensitive. This is achieved by means of a fluorescent material, in close contact with the emulsion layer, with the following properties :

- It must have a high Z in order to maximize its absorption in the low energy region where the photoelectric effect is dominant.
- It must possess a high quantum efficiency to emit a large number of optical photons at a wavelength which matches the optical absorption spectrum of the emulsion.
- The fluorescence should have a short lifetime so that there is no significant afterglow.

Screens can be intensifying (for normal radiography employing cassettes) or fluorescence (for real-time observation). The emission characteristics of the two types are slightly different since emulsion sensitivity generally peaks near 400 nm while the sensitivity of the human eye is greatest in the green – yellow region of the optical spectrum (~ 550 nm).

Thus, calcium tungstate and zinc sulphide (which peak ~ 430 nm) are used in intensifying screens while zinc cadmium sulphide (peaking near 550 nm) is a typical material used for fluorescence screens. The conversion is determined by the quantum efficiency :

$$QE = \frac{N_o h\nu_o}{N_x h\nu_x} \tag{10.3}$$

where N_o and N_x are the numbers of optical and x-ray photons at frequencies of ν_o and ν_x respectively.

Since fluorescence emission is isotropic, it produces a smearing about the sharpest edge, the consequences of which are illustrated in Figs.(10.5) and (10.6). The effect of a screen on the overall resolution is therefore to reduce the MTF considerably.

10.4.4 Real-time detectors for X-ray imaging

Fluoroscopy replaces the film+intensifying screen combination with a fluorescence screen. Until the advent of television monitors and image intensifiers, this had to be viewed directly by the radiologist in a darkened room. This is no longer necessary, however, now that electronic amplification of the image is possible. The principle of the image intensifier makes use of two fluorescence screens and an electron acceleration section, Fig.(10.15) :

- X-rays emerging from the patient, as in Fig.(10.15), strike the input fluorescence screen.
- The input screen emits optical photons over its characteristic emission spectrum. This must match as closely as possible the spectral sensitivity of a photocathode screen with which it is placed in immediate contact. (A scintillation crystal is matched to its photocathode in the same way, see Chapter 5).
- Electrons emitted from the photocathode are accelerated through electron lenses while retaining the relative spatial positions of the input optical photons. These electrons strike the output fluorescence screen where they produce optical photons more efficiently due their higher energy. A brighter image is the result.
- The isotropic nature of fluorescence emission requires that a thin layer of

aluminium be placed on the photocathode side of the output screen to prevent photons from interacting again with the photocathode. If this were to happen, further electron generation would take place and create a uniform background at the output. Contrast would thereby be reduced.

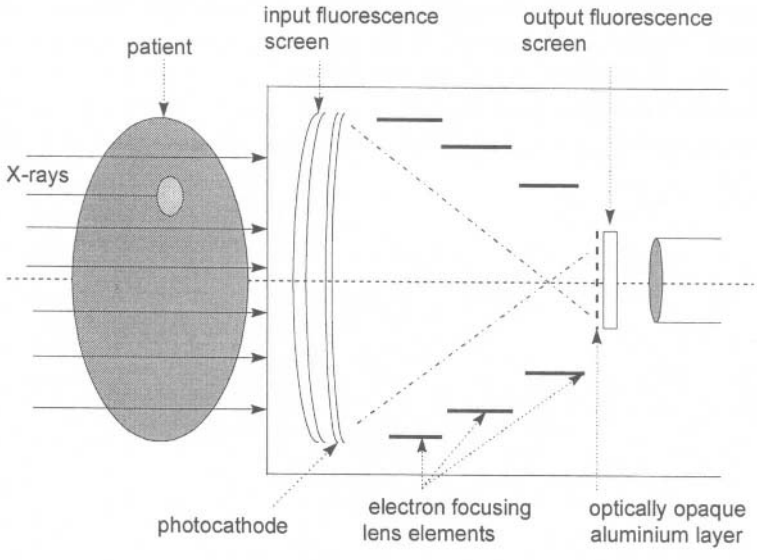

Fig.(10.15) A schematic diagram of an image intensifier.

The development of solid-state detector technology has opened up new possibilities in the use of digital image formation. Two main approaches are being followed. The first converts the X-ray image into optical photons and then into charge. The second converts the X-rays directly into charge. Charge images are produced in both cases and these can then be read out electronically. Examples of work in this area are :

The conversion of X-rays first into optical photons and then into charge. For low energy X-rays, as in mammography, a phosphor-coated charge-coupled detector (CCD) has been used [3]. The CCD device is coated with a 100 μm thick layer of Gd_2O_2S:Eu scintillator screen (GadOx) directly onto the surface of the electrodes, Fig.(5.29a). This scintillator has a peak optical emission (630 nm) which matches the spectral response of the CCD. At molybdenum K_α energies, (17.4 keV, see Table (10.1)), the scintillator has ~ 92% attenuation of X-rays giving a peak signal of ~ 4×10^5 electrons per pixel. The resolution is slightly better than a conventional film+screen mammography combination. For an MTF of 0.7 the CCD system can resolve ~ 2.8 line pairs/mm compared with 2.2 line pairs/mm for the film+screen combination [3]. Amorphous silicon together with a metal plate/scintillation screen combination has also been developed for use

in portal imaging [4].

- the direct conversion of an X-ray image into charge using amorphous selenium [5],[6],[7],[8]. For the direct conversion of X-rays into charge, a photoconductive layer of amorphous selenium is deposited onto an active matrix array of thin-film transistors. The latter comprises an array of CdSe transistors with a 160 μm pixel pitch onto which is evaporated a 300 μm layer of amorphous selenium. A thin indium layer is evaporated on the top of the selenium to provide the high voltage bias. In this case, however, the X-ray image is converted directly into a charge image which is then read out in real-time using the active matrix. A resolving capability of ~ 3.3 line pairs/mm was measured at an MTF of 0.7 [6].

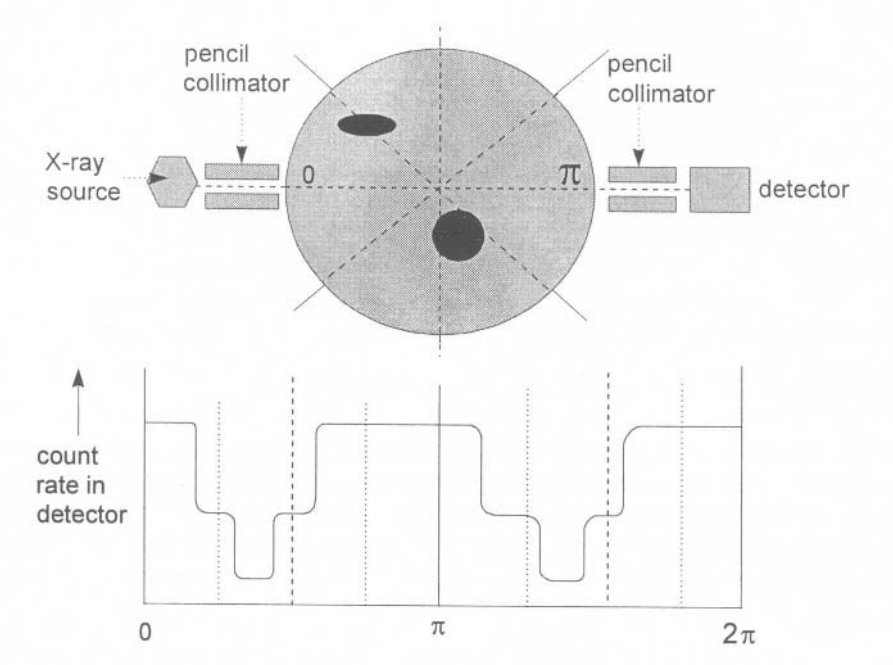

Fig.(10.16) Arrangement of X-ray Computed Tomography system. Regions of high attenuation are indicated in black. The X-ray source/detector combination in this example gives approximate count rates versus angle as shown.

10.5 Computerized Tomography (CT)

The principle of CT is shown in Fig.(10.16). A narrow beam of X-rays is rotated about the long axis of the patient and transmitted photons are recorded at each angular position. Count rate information of the type illustrated in Fig.(10.16) is then reconstructed to give a 2-dimensional map of attenuation coefficient over the whole transaxial slice.

The object of a CT scan is to determine a difference in attenuation coefficient between neighbouring regions of tissue. Reference is made to water since this is the major component in human body tissue. Thus, a CT number is defined for each pixel of the scan :

$$\text{CT number} = \frac{\mu_{tissue} - \mu_{water}}{\mu_{water}} \qquad (10.4)$$

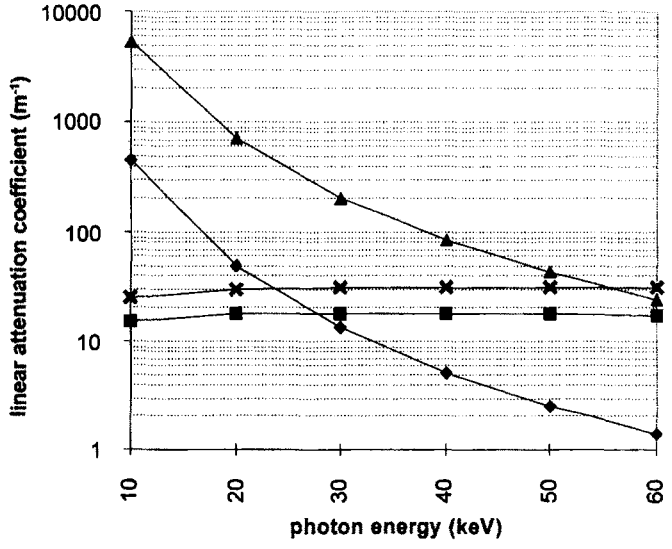

Fig.(10.17) Linear attenuation coefficients versus photon energy for typical body tissues [9]. Average Adult Soft Tissue (ICRU 33): ◆ photoelectric absorption, ■ Compton. Adult Cortical Bone: ▲ photoelectric absorption, ✖ Compton.

Detectors in a CT scanner are real-time solid state devices with a much higher detection efficiency than radiographic film. It is necessary to increase the mean photon energy in order to :

- maximize transmission through the patient. Counting statistics are mainly responsible for limiting the precision with which the CT number can be determined.
- reduce patient dose. The price paid for the great improvements in image quality is the large number of exposures required. A higher photon energy corresponds to lower attenuation coefficients in order to give less dose per exposure.

Fig.(10.17) gives the linear attenuation coefficients for average soft tissue and adult cortical bone [9]. Depending upon the examination, conventional diagnostic radiology uses tube voltages in the approximate range 30 – 80 kVp. The mean

photon energies therefore lie in the approximate range 15 – 30 kV over which the photoelectric effect is dominant. Tube voltages in CT, however, vary in the range 120 – 140 kVp. Fig.(10.17) shows that at a mean energy near 40 kV, it is Compton interactions that are now the most probable. As a consequence, CT images represent tissue density, and not atomic number, since all tissues contain the same number of electrons per kg to within ~ 5%.

10.5.1 Spatial resolution

A determination of the resolving capability of a CT scanner is made from an initial measurement of a point spread function (PSF) or a line spread function (LSF). As in any other branch of medical physics, quality assurance demands that protocols are followed in the setting-up of equipment for use on patients. For this purpose, test objects containing a number of features of differing size and contrast are used. The measurement of a line spread function, for example, would use a test object as shown in Fig.(10.18).

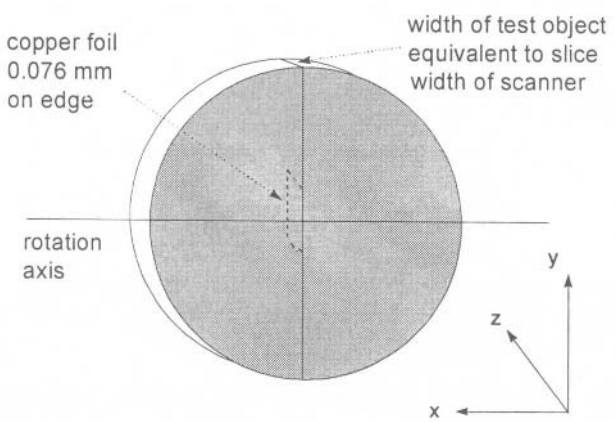

Fig.(10.18) A Line Spread Function test object [10]. A thin copper foil (0.076 mm) is placed at the centre of a disc of Perspex (PMMA) of diameter 20 cm and thickness 1.5 – 2.5 cm.

A disc of Perspex, with thickness equivalent to the slice width of the scanner, (~10 mm) is mounted in the plane of the detectors. The 0.076 mm thick copper foil, with a width equal to that of the Perspex disc, is orientated vertically across the central rotation axis. So long as the orientation of the copper foil is orthogonal to the pixel rows along the x-axis, interpolation between the measured points gives the point spread function. The Fourier transform of the PSF, as carried out in section 10.2.2, gives the MTF.

A very much simpler method of finding the MTF can be followed under the assumption that the PSF is Gaussian [11]. It was established that this is indeed the case for five widely-used scanners. Earlier work [12] had shown that when a

generalized PSF, *f(x,y)*, is simplified for radial symmetry, *f(r)*, the MTF at spatial frequency ν can be written :

$$MTF(\nu) = \frac{\left| \int_0^\infty f(r) j(2\pi\nu r) r dr \right|}{\int_0^\infty f(r) r dr} \tag{10.5}$$

where $j = \sqrt{-1}$. With the assumption of a Gaussian PSF we have :

$$PSF(r) = f(r) = e^{-\alpha^2 (r-\varepsilon)^2} \tag{10.6}$$

In Eq.(10.6) ε is the displacement of the centre of the PSF with respect to the origin of the co-ordinate system of the CT pixels, and α is related to the FWHM of the PSF by $\alpha = 1.665/\text{FWHM}$. Substituting Eq.(10.6) into Eq.(10.5) and integrating [13] gives :

$$MTF(\nu) = e^{-(\pi\nu/10\alpha)^2} \tag{10.7}$$

In Eq.(10.7) the factor 10 appears when the FWHM is measured in mm so that α has units of mm^{-1}. Spatial frequency ν is given in line pairs cm^{-1}.

10.5.2 Contrast

Discrimination between low contrast objects is limited largely by the amplitude and frequency characteristics of noise in the detector system. Again, it is determined for a given system by scanning a test object, as in Fig.(10.18), in which the copper foil is replaced by thin foils of plastic having graded sizes and densities.

Subject contrast, *SC*, between two neighbouring regions of an image is related to the differences in attenuation coefficients, as in Eq.(10.4). Thus :

$$SC = \frac{k}{\mu_W(E)} \left[\mu_1(E) - \mu_2(E) \right] \tag{10.8}$$

where k is the CT scaling constant (k = 1000) and the subscripts on the linear attenuation coefficients refer to water and regions 1 and 2 of the image. Assuming that the attenuation coefficients 1 and 2 differ from that of water by a constant which is energy independent, and that regions 1 and 2 are identical in composition but differ only in density, the subject contrast can be written [10] :

$$SC = \frac{k}{\mu_W(E)} \frac{\mu_1(E)}{\rho_1} [\rho_1 - \rho_2] \qquad (10.9)$$

10.5.3 Radiation dose

Radiation dose must be considered from the point of view of both the patient and the operating personnel. Scanner manufacturers should supply data on normalized scatter air kerma rates, measured along the central axis of the machine, at 1m distance from the centre of the detector plane. Together with this data, iso-exposure curves should also be given in plan view and in vertical elevation [10]. Typical values for normalized scatter air kerma rates at 1m for machines in current use lie in the range 0.7×10^{-3} to 3.8×10^{-3} mGy mA^{-1} min^{-1}.

Fourth generation scanners have a stationary ring of detectors within which the X-ray tube rotates in a concentric path. With anode voltages in the range 120 – 140 kVp, each scan is further specified by :

- The product of tube current (mA) and the time of the scan (s) in mAs.
- The slice width. This is generally 10 mm but it can be as small as 5 mm for brain scans.
- The pitch. This is the separation of the contiguous slices. The pitch is unity when the separation between slices is equal to the slice width.

In the UK, the NRPB publish guidelines on the determinations of total effective dose and organ dose for different scans [14]. Together with the lower figures for the latest technique in helical scanning, these are shown in Table (10.3) for representative scanners, and compared with figures for conventional diagnostic radiology (DR) for similar examinations.

Table (10.3) A comparison of representative doses for four types of X-ray examinations. All doses are given in mSv. Figures in columns 2 and 4 come from [14]. Figures in columns 5,6 and 7 come from the comparison between a typical 4th Generation CT scanner and a helical CT scanner.

Exam	DR	Organ with max dose	CT Effective Dose	CT Organ Dose	Helical Effective Dose	Helical Organ Dose
Brain	0.2	Brain	3.5	45.9	0.7	20.0
Chest	0.05	Thymus	9.1	39.1	2.2	9.8
Abdomen	1.4	Kidney	8.8	38.7	2.1	9.1
Pelvis	1.2	Bladder	9.4	39.9	2.4	9.5

Considerably lower patient doses are achieved by the use of helical scanning

(HCT). Here there is a continuous movement of the patient at a constant speed through the detector plane. This reduces the time during which no data is taken to practically zero, and is a significant improvement on the step-wise scan-movement-scan-movement sequence of the 4th generation scanners. Doses given in columns 5, 6 and 7 in Table (10.3) show a large reduction in both overall effective dose as well in organ doses when a pitch of 1.3 is used in HCT. In this case the movement of the patient through the detector plane is 30% faster than in non-helical scanning. Just some of the many additional complexities of image reconstruction which arise in HCT are treated in [15],[16] and [17].

10.6 Nuclear Medicine

This title refers to the imaging of any radioactive material within a human body. Different applications include:

- Whole body imaging: The body can be either viewed when stationary by wide-angle detectors or moved slowly across the field of view of detectors which subtend a small solid-angle of a particular region. Two principal types of investigation exist - (a) the determination of small amounts of radioactive contamination *e.g.* the study of actinide ingestion of radiation workers for which detectors with high efficiency are required. (b) bone scans following the administration of bone-seeking radiopharmaceuticals. Isotopes employed are mostly ^{99m}Tc, but ^{67}Ga and ^{111}In are also used in particular cases. This technique is also known as γ-ray autoradiography.
- Single Photon Emission Computerized Tomography (SPECT): This uses the Anger Gamma Camera, or another dedicated system, and is the most widely-used technique. It can give two types of image – static or dynamic. The former gives a 2-dimensional histogram of total activity within the field of view of the camera face. The latter gives time-dependent information from a selected Region-of-Interest (ROI) of that view. Tomographic information is obtained by the rotation of the camera head about the body being imaged.
- Positron Emission Tomography (PET): Here, there is coincidence counting of annihilation photons at 511 keV by detectors placed either side of the body along a line through the region of interest. Each detector views this region of interest. Since the two photons are correlated, the spatial resolution is somewhat higher that in SPECT. The resolution in image space is limited by the smoothing necessary to reduce the noise due to poor counting statistics. Typical Full-Width-Half-Maximum image resolutions are 1 – 2 cm in SPECT and 7 – 9 mm in PET.

10.6.1 Compartmental analysis with radioisotope tracers

Compartmental Analysis is used to quantify the time-dependence of the uptake of a radiopharmaceutical. A model is constructed of the various organs (compartments)

involved in the transport within the body of an injected radiopharmaceutical. The complexity of the model increases with the number of compartments and on their nature. It matters, for example, whether the system is considered to be open or closed.

An appropriate model is used in conjunction with the clinical measurements to give information on the pathology of the organ systems. This information can be :

- rate constants which give information on the flow *between* organs,
- the distribution of transit times of blood flow *through* an organ,
- the total rate of blood flow *through* an organ.

As a rule, the half-life of the isotope is chosen to be roughly equal to the length of the scan in order to minimize dose to the patient. A correction for isotope decay is therefore required in the determination of time-dependent processes.

Consider a closed 3-compartment model.

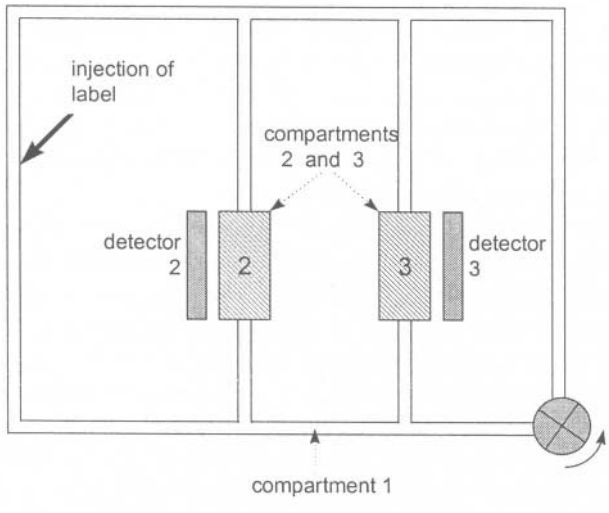

Fig.(10.19) Illustration of a 3-compartment closed system. At t = 0, radioactivity is injected into compartment 1. Compartments 2 and 3 can take up radioactivity from 1 with rate constants K_{12} and K_{13}. The radioactivity can be returned to 1 from the respective compartments with rate constants K_{21} and K_{31}. Uptake is monitored in each compartment by detectors d2 and d3.

10.6.2 Rate constants

The flow of activity between the compartments, Fig.(10.19), following the injection of amount q_0 into compartment 1 at time t = 0 is described by the following differential equations :

$$\frac{dq_1}{dt} = K_{21}q_2 + K_{31}q_3 - K_{12}q_1 - K_{13}q_1$$

$$\frac{dq_2}{dt} = K_{12}q_1 - K_{21}q_2$$

$$\frac{dq_3}{dt} = K_{13}q_1 - K_{31}q_3$$

The rate constant K_{xy} expresses the transfer from compartment x to compartment y. The limiting conditions at time t = 0 are $q_1 = q_0$, $q_2 = q_3 = 0$. For an isotope with decay constant λ in a closed system, we also have the amount of circulating activity given by, $q_{0t} = q_0 \exp(-\lambda t)$.

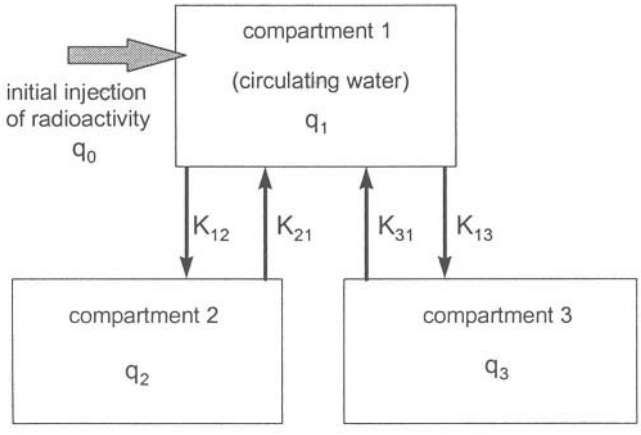

Fig.(10.20) The model of a closed three-compartment system as represented in Fig.(10.19). An initial injection of radioactive material, q_0, is made at time t = 0. At a later time the quantities in each of the three compartments are q_1, q_2 and q_3.

When there is no reversible transfer of activity from compartments 2 and 3 back to 1 (i.e. $K_{21} = K_{31} = 0$) the general solutions of the above equations are :

$$q_2 = \frac{-K_{12}}{K_{12} + K_{13}} q_0 e^{-Kt} + C_2 \qquad (10.10)$$

$$q_3 = \frac{-K_{13}}{K_{12} + K_{13}} q_0 e^{-Kt} + C_3 \qquad (10.11)$$

where $K = K_{12} + K_{13}$. The constants of integration, C, represent the amounts of

activity in each of the two compartments as t approaches infinity, and are obtained from the limiting conditions at t = 0. Under the restrictions imposed by the need to minimize dose, however, the isotope lifetime should never be significantly greater than the time required for the clinical investigation. Except in cases where the decay constant of the isotope, λ, approaches zero, therefore, the values of :

$$C_2 = \frac{K_{12}}{K_{12}+K_{13}} q_{0t} \quad \text{and} \quad C_3 = \frac{K_{13}}{K_{12}+K_{13}} q_{0t} \tag{10.12}$$

are not constant but have a time-dependence due to the radioactive decay of the isotope. Substituting Eqs.(10.12) into Eqs.(10.11) and (10.10), we get :

$$q_2 = q_0 e^{-\lambda t} \frac{K_{12}}{K}\left[1 - e^{-Kt}\right] \quad \text{and} \quad q_3 = q_0 e^{-\lambda t} \frac{K_{13}}{K}\left[1 - e^{-\lambda t}\right] \tag{10.13}$$

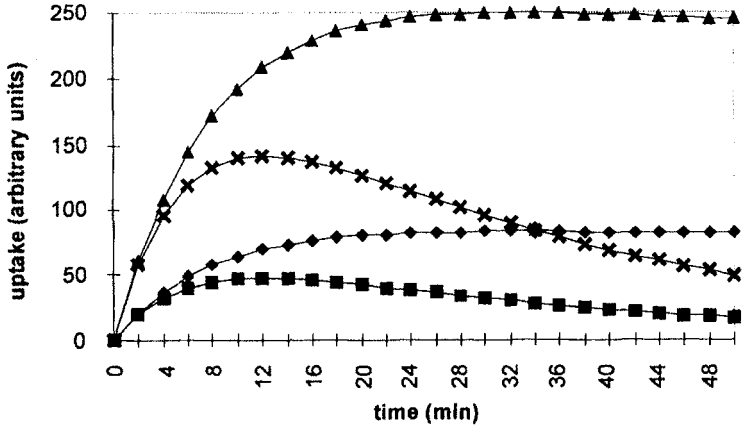

Fig.(10.21) The uptake in compartments 2 and 3 using Eqs.(10.13) for ^{99m}Tc and ^{11}C. Values assumed for the rate constants are : K_{12} = 0.0325 min^{-1}, K_{13} = 0.0975 min^{-1}, K = 0.13 min^{-1}. Decay constants are : ^{99m}Tc, λ = 0.00192 min^{-1} : ^{11}C, λ = 0.034 min^{-1} : q_0 = 360 arbitrary units. ◆ q_2 ^{99m}Tc : ▲ q_3 ^{99m}Tc : ■ q_2 ^{11}C : ✖ q_3 ^{11}C.

10.6.3 Transit times

Another important aspect of dynamic tracer studies is the study of the distribution of transit times of blood through an organ or through the vascular bed of a tissue. Mathematical modelling of such studies generally assumes :

- that the input into the system of a radioactive label occurs instantaneously (i.e. it is a delta function),Fig.(10.22),

- the output from the system (organ, tissue...) will be the summation of flow of the label through all the pathways available.

Under these circumstances, a distribution of transit times will be observed at the output. The Mean Transit Time is the mean value of the transit time distribution of the outflow curve h(t). Thus :

$$\bar{T} = \frac{\int_0^\infty t\ h(t)\ dt}{\int_0^\infty h(t)\ dt} \qquad (10.14)$$

The denominator of Eq.(10.14) is unity if there is no loss of label in the system (*i.e.* it is a conservative system) when the mean transit time becomes :

$$\bar{T} = \int_0^\infty t\ h(t)dt \qquad (10.15)$$

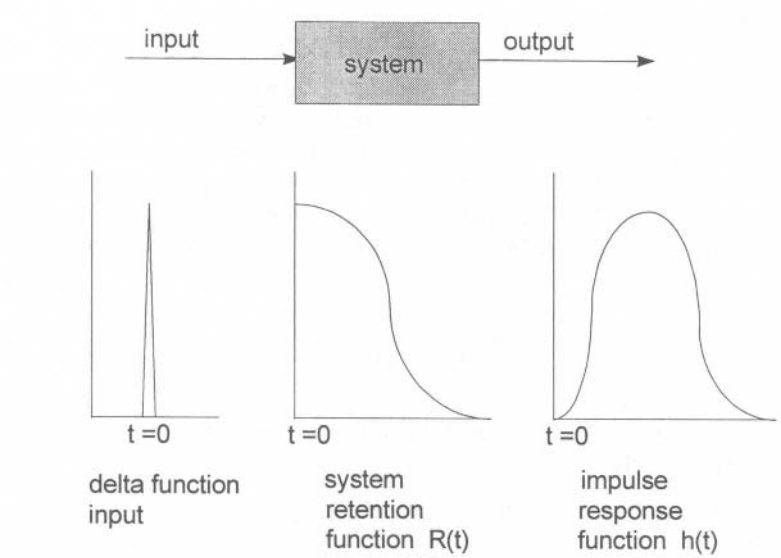

Fig.(10.22) Time-dependent functions that describe the passage of radioactive tracer through a system.

The amount of activity retained by the system at any time t is the system retention function *R(t)* :

$$R(t) = 1 - \int_0^t h(t)\ dt$$

giving $h(t) = -dR/dt$. Integrating Eq.(10.15) by parts, with $u = t$, $dv/dt = h(t)$ and $v = (1-R(t))$, we have :

$$\bar{T} = uv - \int v\, du / dt$$

$$\bar{T} = \int_0^\infty R(t)dt \qquad (10.16)$$

The mean transit time is therefore the total area under the system retention function.

In general, the input is not a delta function but will have a distribution $I(t)$. The output is then described by a function $O(t)$ which is the convolution of $I(t)$ with the impulse response function $h(t)$.

$$O(t) = I(t) \ast h(t)$$

10.6.4 Flow rates through a single channel

Blood flow through vessels and its perfusion of organs and tissues is a widely used investigation in nuclear medicine. In a simple analogue system such as Fig.(10.19) a known amount of tracer, Q, is injected into compartment 1 as a bolus with a time distribution assumed to be a delta function. A sample volume dV withdrawn downstream from the injection point at a time t following the injection, has a tracer concentration, $C(t) = dQ/dV$. If the sample is collected over a time dt, the flow rate is:

$$F = \frac{dV}{dt} = \frac{dQ}{C(t)dt}$$

Under the assumption that the mixing is uniform, the sample is representative of the whole system such that :

$$\frac{dQ}{Q} = \frac{C(t)dt}{\int_0^\infty C(t)dt}$$

The flow-rate then becomes :

$$F = \frac{Q}{\int_0^\infty C(t)dt} \qquad (10.17)$$

Eq.(10.17) embodies the Stewart-Hamilton principle of indicator-dilution. Its application in an investigation of cardiac output, for example, entails the measurement

of an activity:time curve, proportional to $C(t)$, over the heart following an intravenous injection. In this case, blood recirculation ensures that $C(t)$ reaches an equilibrium value over a measurement time period which is much shorter that the isotope half-life.

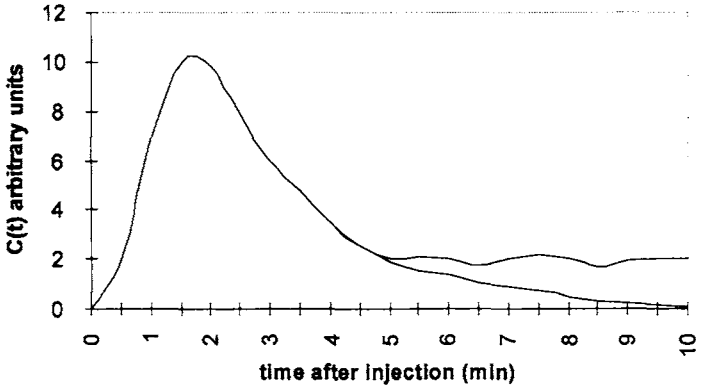

Fig.(10.23) A typical activity:time curve, proportional to $C(t)$, measured over the heart. The lower curve would be observed without any recirculation of the injected activity, for example, when the blood volume is infinitely large and there is only one pass of the activity through the heart. The upper curve shows the equilibrium value, C_{eq}, achieved when the injected activity becomes uniformly distributed.

The flow-rate generated by the heart, F, can then be determined by measuring the equilibrium value of the output curve, C_{eq}, and equating it to Q/V' where V' is a blood sample volume taken at equilibrium. Thus Eq.(10.17) is modified to :

$$F = \frac{C_{eq}}{\int_0^\infty C(t)dt} V' \qquad (10.18)$$

The numerator of Eq.(10.18) must be the integrated area of the lower curve in Fig.(10.23) – that is, C(t) corrected for recirculation.

10.6.5 Flow through an organ having multiple channels

The complex micro-circulation within an organ can be modelled as a system of parallel elements which start at the input and end at the output. At the boundary of the organ at A, Fig.(10.24), the tracer input, Q, divides in proportion to the flow in each channel. Thus :

$$\frac{dQ}{Q} = \frac{dF}{F}$$

From the Stewart-Hamilton principle, Eq.(10.17) :

$$dF = \frac{F}{Q} dQ = \frac{dQ}{\int_0^\infty C(t)dt} \tag{10.19}$$

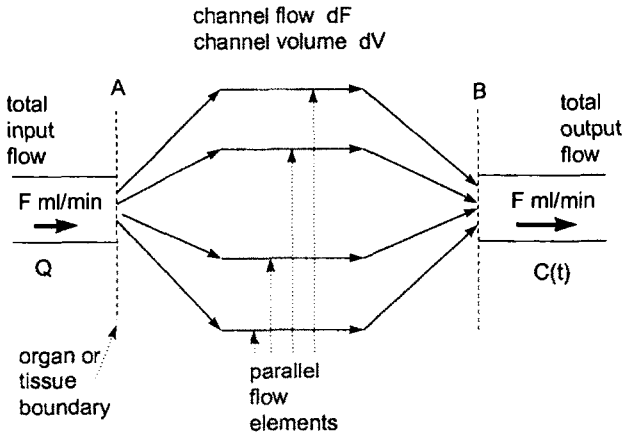

Fig.(10.24) Model of parallel flow through an organ or tissue.

The fluid volume which arrives at the output B from each channel in time t is $dV = t\,dF$. Substituting Eq.(10.19) we have :

$$dV = \frac{t dQ}{\int_0^\infty C(t)dt}$$

Since dQ is the quantity of tracer delivered at the output between times t and $t + dt$ in each channel, $dQ = C(t)\,F\,dt$ so that :

$$dV = \frac{C(t)Ftdt}{\int_0^\infty C(t)dt} \tag{10.20}$$

The total volume, V, is the sum of all individual channel volumes :

$$V = \frac{F\int_0^\infty tC(t)dt}{\int_0^\infty C(t)dt}$$

When the tracer input is delivered as a delta function, $C(t)$ can be replaced by the impulse response function $h(t)$,

$$V = \frac{F\int_0^\infty th(t)dt}{\int_0^\infty h(t)dt} = F\bar{T} \tag{10.21}$$

The mean transit time in Fig.(10.25) is defined as :

$$\bar{T} = \frac{\sum_i t_i N_i \Delta t}{\sum_i N_i \Delta t} \tag{10.22}$$

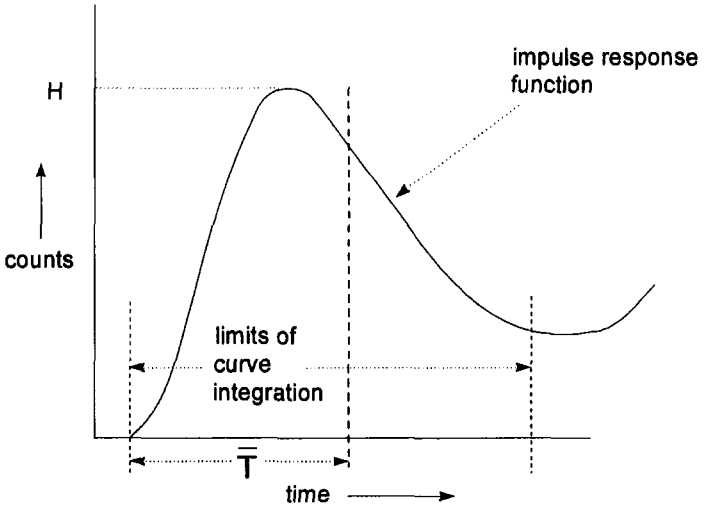

Fig.(10.25) An impulse response function $h(t)$. Counts N_i are recorded at time t_i in the time interval Δt – that is, between t_i and $t_i + \Delta t$.

10.7 Positron Emission Tomography (PET)

10.7.1 Basic principles

PET is usually carried out with one of the short-lived isotopes shown in Table (10.4). All except ^{18}F must be produced by a cyclotron which is close to the site of the scanner.

The main clinical application of ^{18}F is in oncology, when it is used in the form 2-[^{18}F]fluoro-2-deoxy-D-glucose. It is referred to simply as FDG. Other uses of PET are found in neurology, cardiology and for amino-acid synthesis using ^{11}C-methionine. The isotope having the shortest half-life, ^{15}O, can be used for injection as $H_2{}^{15}O$ or inhalation as $C^{15}O_2$. Additionally, $^{11}CO_2$ can also be used. The latter examples result in rapid perfusion of the whole body and raise important dosimetry considerations [18].

Table (10.4) Characteristics of the most widely used positron emitters for PET.

Isotope	$E_{\beta+,max}$ (keV)	half-life	reaction	target
^{18}F	635	1.87 hr	$^{20}Ne(d,He)^{18}F$ $^{18}O(p,n)^{18}F$	$H_2{}^{18}O$
^{11}C	961	20.4 min	$^{11}B(p,n)^{11}C$ $^{12}C(p,d)^{11}C$	CO_2
^{15}O	1723	2.05 min	$^{16}O(p,pn)^{15}O$ $^{15}N(p,n)^{15}O$	H_2O $^{15}N_2$
^{13}N	1190	10.1 min	$^{14}N(\gamma,n)^{13}N$ $^{14}N(p,pn)^{13}N$ $^{16}O(p,He)^{13}N$	

A nuclear medicine investigation that is made with a positron-emitting isotope has the following characteristics :

- The annihilation event between the positron and an electron yields two co-incident and anti-co-linear γ-rays at 0.511 MeV.
- Positron emitters in Table (10.4) are compatible with biological systems. Many more radiopharmaceuticals can therefore be produced for a specific study.
- The half-lives are short, – under two hours.
- Section 1.3.1 shows that positron emission may also be accompanied by electron capture. Although ^{11}C, ^{13}N and ^{15}O have no competing electron capture decay route, ^{18}F has decay probabilities of 97% positron emission and 3% electron capture. This means that 3% of all ^{18}F decays produce the 520 keV oxygen K X-ray.
- Coincidence counting is able to reduce scatter background and, thereby, the need for extensive collimation.

Although the above characteristics are largely advantageous, there are a number of disadvantages in PET:

- There is a large capital investment needed in the installation of a cyclotron, the PET scanner itself and the hot-labs needed for rapid radiopharmaceutical preparation.

- There is an irreducible, intrinsic spatial resolution because of the finite range of the positron. Since annihilation only takes place when the positron has thermalized, the mean projected range of the positron – emitted with energies between 0 and $E_{\beta+,max}$ – produces a spherical volume around the location of the emitter within which annihilation can take place.

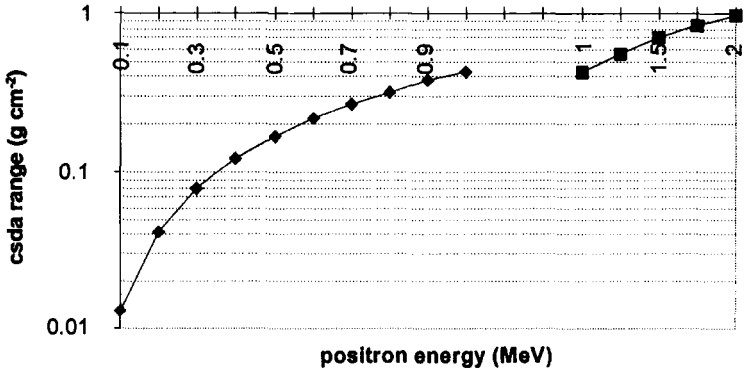

Fig.(10.26) The csda range (g cm^{-2}) in adipose tissue versus positron energy. Note the change in the abscissa scale at 1 MeV. Assuming that the mean positron energy is $E_{\beta+,max}$ /3, and the mean range is csda range/2 then, with a tissue density of 0.92 g cm^{-3}, the approximate mean ranges of positrons from the sources in Table (10.4) are :
0.24 mm (^{18}F), 0.49 mm (^{11}C), 0.65 mm (^{13}N), 1.1 mm (^{15}O)

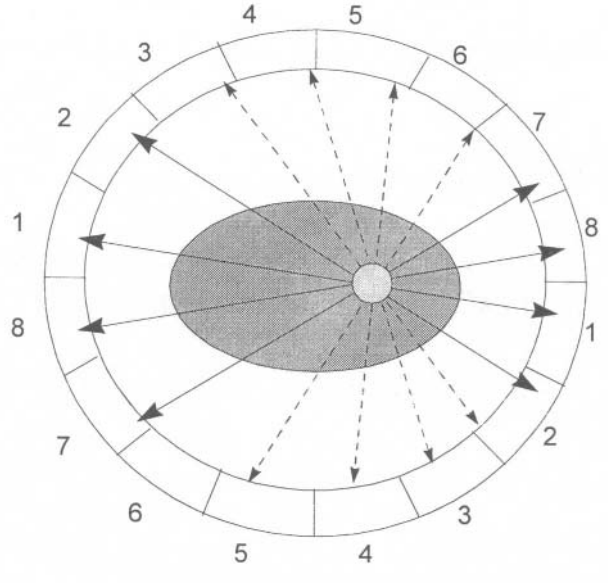

Fig.(10.27) The principle of coincidence detection in PET. The arrows represent the annihilation photons emitted from a volume of tissue containing a positron emitting isotope.

In Fig.(10.27) a small region of high activity (hatched) within a body (shaded) is viewed by eight pairs of detector. Coincidence signals can only be obtained in pairs 1,2,7 and 8 (heavy solid lines) from annihilation gamma rays which originate in the hatched area. Signals at 511 keV which are received in the upper arc of detectors 3,4,5 and 6 will not receive the corresponding coincidence signal in their opposite number in the lower arc. No signal will therefore be registered. The intersection of the heavy lines defines the location of the high activity region. An increase in the angular resolution of detectors (smaller than the 0.39 radians subtended by the 16 detectors at the centre of Fig.(10.27) results in an improved spatial resolution.

10.7.2 A 2-compartment model with reversible flow

The use of a two-compartment model having reversible flow would be appropriate in a PET study of blood flow across the blood:brain barrier.

Using Fig.(10.20) and making k_{13} and k_{31} both zero, q_1 and q_2 now represent the quantities of activity in the blood and brain compartments respectively. If there is no loss of activity, for example by excretion, then the rate equations become :

$$\frac{dq_1}{dt} = -k_{12}q_1 + k_{21}q_2$$

$$\frac{dq_2}{dt} = k_{12}q_1 - k_{21}q_2$$

With the limiting conditions $q_1 + q_2 = q_0$, $q_1 = q_0$ at $t = 0$ and $q_2 = 0$ when $t = 0$, we have :

$$\frac{dq_2}{dt} = k_{12}q_0 - q_2(k_{12} + k_{21}) = k_{12}q_0 - q_2K \qquad (10.23)$$

Here, $K = k_{12} + k_{21}$ and not as previously as in Eqs.(10.10) and (10.11). Eq.(10.23) can be solved for q_2 by multiplying by $exp(\int Kdt) = exp(Kt)$ to give :

$$e^{Kt}\frac{dq_2}{dt} + Kq_2e^{Kt} = k_{12}q_0e^{Kt} = \frac{d}{dt}\{q_2e^{Kt}\}$$

$$q_2e^{Kt} = q_0\left[\frac{k_{12}}{K}e^{Kt} + C\right]$$

Since the limiting conditions make $C = -k_{12}/K$ we have :

$$q_2 = q_0 \frac{k_{12}}{k_{12} + k_{21}} \left\{1 - exp\left[-\left(k_{12} + k_{21}\right)t\right]\right\} \qquad (10.24)$$

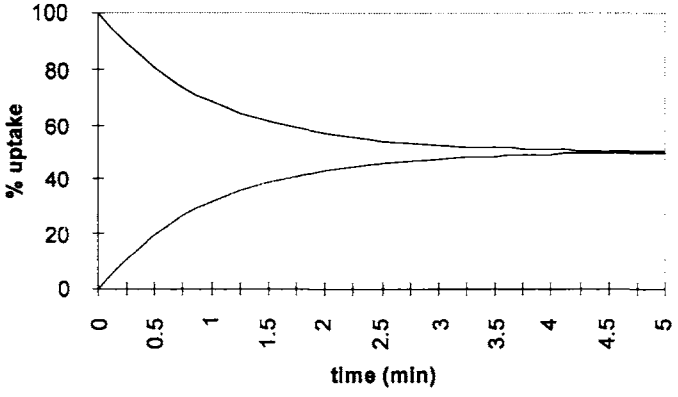

Fig.(10.28) Uptake of activity in the "brain" compartment (lower curve) using a two-compartment reversible transfer model. Eq.(10.24) is used with $k_{12} = k_{21} = 0.5$ min^{-1}. The model assumes no decay and no loss of activity.

10.7.3 Clinical aspects in PET

Uptake efficiency of the injected radiopharmaceutical in a target organ or tumour is described in terms of the Standard Uptake Value (SUV).

$$SUV = \frac{r}{W / D} \times RC \times g \qquad (10.25)$$

In Eq.(10.25) r is the number of counts in MBq/ml, W is the lean body weight of the patient in kg, D is the injected dose (MBq), and RC is the recovery, or partial volume, coefficient. This accounts for the possibility that some of the pixels at the edge of the reconstructed image only partially cover the edges of the volume of interest. The native glucose concentration, g, is used only in FDG scans. Although SUV values can range from 4 to 12, and can sometimes be as high as 20, in practice a range for benign/malignant uptake is quoted. This range clearly depends on all of the factors in Eq.(10.25).

Practical aspects of PET using FDG are :

- The use of fluoro-deoxy-glucose (FDG) usually results in a large uptake in the brain whatever the primary target organ. However, abnormal brains may have a lower uptake.
- A typical injected activity of FDG is in the range ~ 200 – 370 MBq in order to

achieve a target concentration of ~ 25 - 35 kBq ml^{-1}.

- Patients are required to drink plenty of fluid before the procedure. These must not be glucose-containing drinks which would otherwise prevent FDG uptake from the blood pool. Diabetic patients have to be especially well controlled.
- Intravenous injection of the radiopharmaceutical is made ~ 30 – 75 minutes before the start of the scan in order to clear the bulk of the activity from the blood pool. Normal physiological uptake may be seen in the liver, urinary system and the heart as well as in the brain.
- A typical voxel size is a 3.375 mm cube.
- A typical scanner consists of 3 rings of detectors, each ring comprising many scintillator crystal/photo-multiplier units, Fig.(10.29).
- Each unit consists of a block of 8 × 8 bismuth germanate (BGO) crystals which are viewed by 4 square-section photo-multiplier tubes. Each crystal is approximately 6 mm square with a 1 mm gap between the adjacent crystal in the array. Because of its high density (7.13 g cm^{-3}) the thickness can be as small as 4 mm. Tungsten or lead septa may be inserted between the detector rings in order to prevent out-of-plane scatter (*i.e.* scatter from material in the plane of one detector ring into the plane of an adjacent ring), Fig.(10.29).
- the total width along the couch of the detector rings is 15 – 20 cm and the transaxial field is ~ 40 cm diameter.
- It is not possible to define a SUV for objects less than twice the FWHM of the spatial resolution.

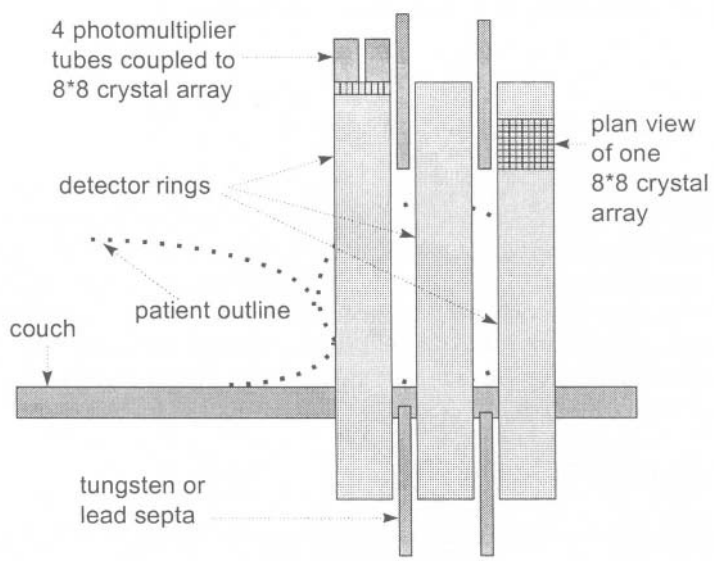

Fig.(10.29) Schematic view of a typical arrangement of BGO detector rings.

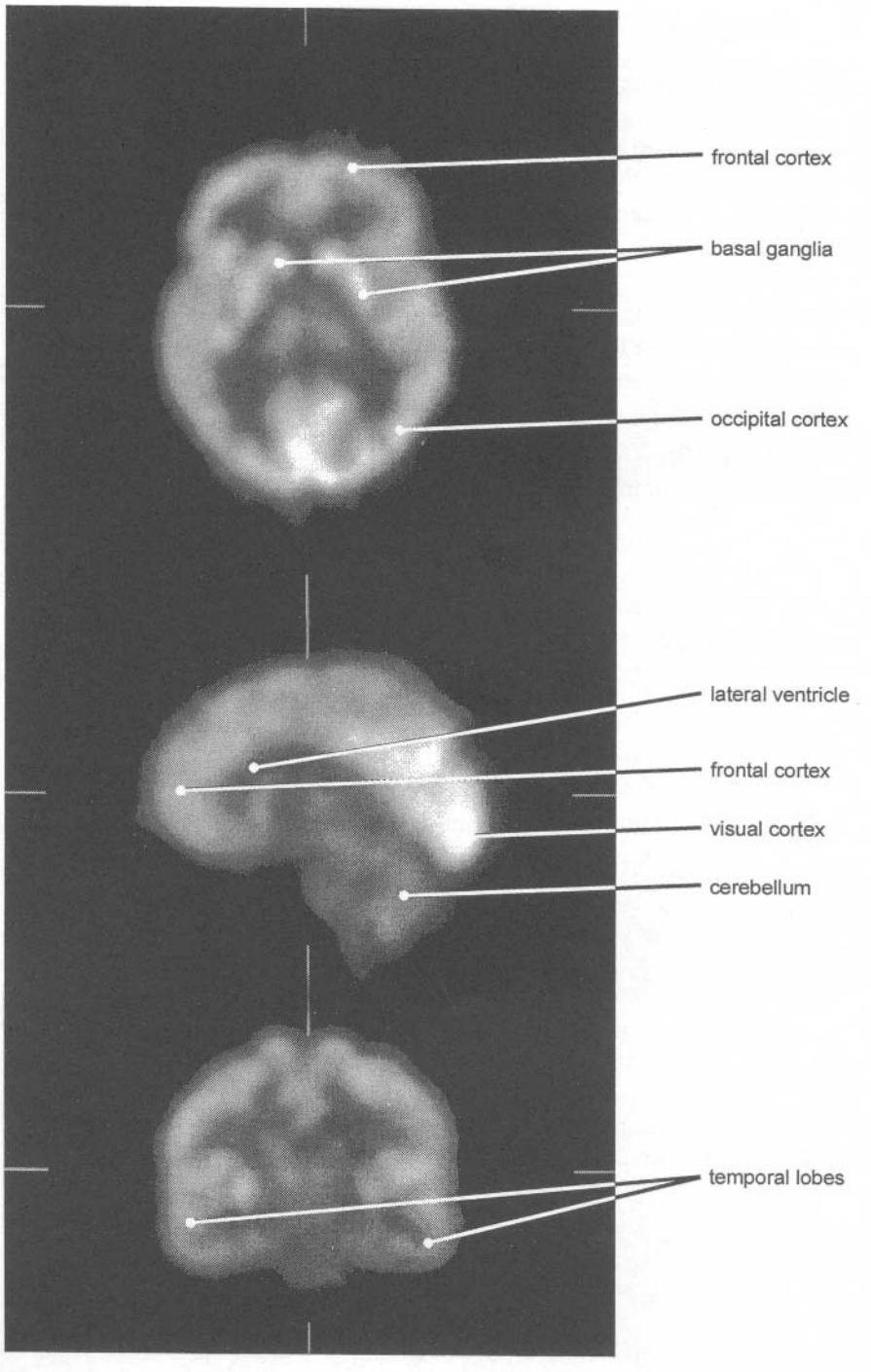

Fig.(10.30) Transaxial (top), Sagittal (centre) and Coronal PET images of a human brain using ^{18}FDG. The side markers indicate the positions through which each orthogonal sections are taken.

10.8 Magnetic Resonance Imaging

10.8.1 Basic quantities

The spectroscopy used in MRI is inherently insensitive because of the small difference in the distribution of spins that is attainable at normal temperatures. It depends on the alignment of paramagnetic nuclear spins using a strong (1 – 3 Tesla) axial magnetic field.

- The ground state nuclear spin quantum number I is determined by the way the nucleons combine their intrinsic spin and orbital quantum numbers.
- The nuclear spin angular momentum quantum number = $I\hbar$ (where $\hbar = h/2\pi$ = 1.054×10^{-34} J s) For a proton, I = ½ ; for a deuteron, I = 1 ; for a helium-4 nucleus, I = 0.
- The nuclear magnetic dipole moment is given by :

$$\mu = \gamma \frac{h}{2\pi} \sqrt{I(I+1)} \tag{10.26}$$

where γ is the gyromagnetic ratio. The units are MHz T^{-1} (s^{-1} T^{-1}). For the above examples :

$$\mu_{1_H} = 1.41 \times 10^{-26} JT^{-1}$$

$$\mu_{2_H} = 0.43 \times 10^{-26} JT^{-1}$$

- In a static magnetic field, B_0, the dipole moment will precess with an angular frequency (the Larmor precession frequency, ω) given by $\omega = \gamma B_0$. Writing $\mu = \gamma \hbar I$ from Eq.(10.26), we get

$$\nu = \frac{\mu}{h} \frac{B_0}{I} \quad \text{and therefore} \quad \Delta E = \frac{\mu B_0}{I} \tag{10.27}$$

- A nuclear spin I has 2I+1 orientations in a static magnetic field. In a system containing protons (I = ½), the two allowed orientations of the magnetic moment are shown in Fig.(10.31).

The distribution of spins between the two energy states is determined by the Boltzmann distribution :

$$\frac{n^-}{n^+} = exp\left(\frac{-\Delta E}{kT}\right) = exp\left(\frac{-\gamma \hbar B_0}{kT}\right) \tag{10.28}$$

Substituting the proton gyromagnetic ratio, γ = 42.6 MHz T^{-1}, the rationalized Planck constant, $\hbar$ = 1.054×10^{-34} J s together with the Boltzmann constant k = 1.38

$\times 10^{-23}$ J K^{-1} in Eq.(10.28), gives the difference in the populations at 300 K and 1 Tesla as ~ 1 in 10^6.

The total magnetization, M_0, produced in the sample is equal to the difference in number of spins, times the magnetic moment of each one. Since the difference in the spin population $\left(n^+ - n^-\right) > 0$, M_0 is aligned in the direction of B_0. Thus :

$$M_0 = \left(n^+ - n^-\right)\mu_{1H} \tag{10.29}$$

A larger static field therefore gives a greater sensitivity. Different nuclei have different sensitivities because of their different gyromagnetic ratios.

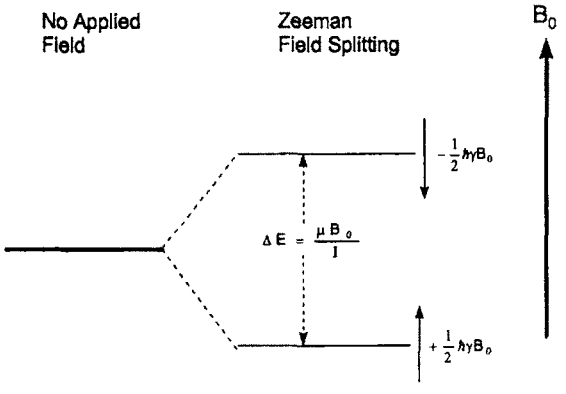

Fig.(10.31) The splitting of energy levels of a spin ½ nucleus in a magnetic field B_0.

10.8.2 A nuclear magnetic resonance experiment

- The equilibrium distribution given in Eq.(10.28) is disturbed by the absorption of energy at the frequency given by Eq.(10.27).
- Referring to Fig.(10.32), the application of a radiofrequency field, B_1, at the resonant frequency converts, say, 10 spins in the lower state to 9, and increases the number in the upper state from 9 to 10. The "small" difference in the number of spins between the states before the application of B_1 represents the almost equal numbers, n^+ and n^- given by the Boltzmann distribution, Eq.(10.28).
- In Fig.(10.33), the net magnetization of the sample, M_0, in the direction of the static field B_0, is reduced by the application of the radiofrequency field B_1 orthogonal to B_0.

Table (10.5) NMR parameters for nuclei that could be used in MRI.

Nucleus	gyromagnetic ratio (MHz T^{-1})	relative sensitivity
^{1}H	42.58	1.0
^{19}F	40.06	0.83
^{23}Na	11.26	0.0925
^{31}P	17.24	0.066
^{13}C	10.71	0.016

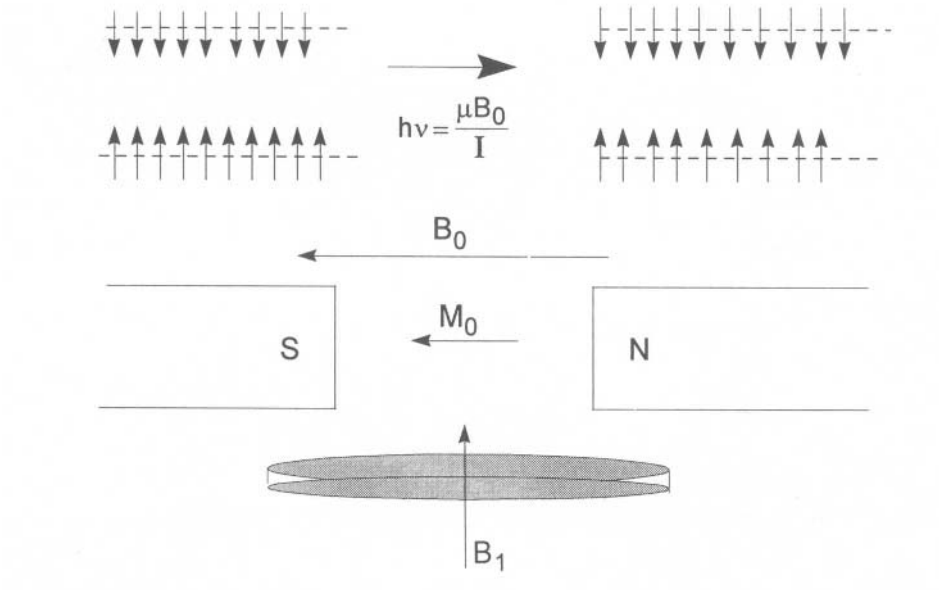

Fig.(10.32) The absorption of energy at the Larmor Resonance Frequency

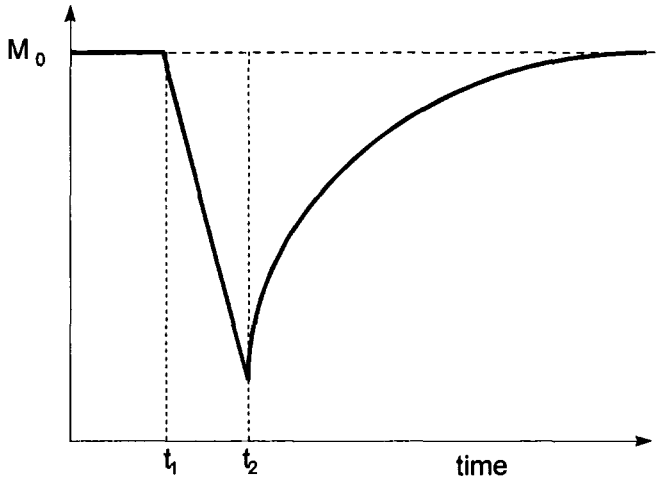

Fig.(10.33) The time course of magnetization along the B_0 direction. Before the rf pulse is applied, the equilibrium magnetization is given by Eq.(10.29). The B_1 field, applied between times t_1 and t_2 reduces this magnetization by increasing n^- at the expense of n^+. When the rf field is turned off at t_2, the z magnetization returns to the original value, M_0, with a characteristic time T_1. This is the Spin-Lattice relaxation time.

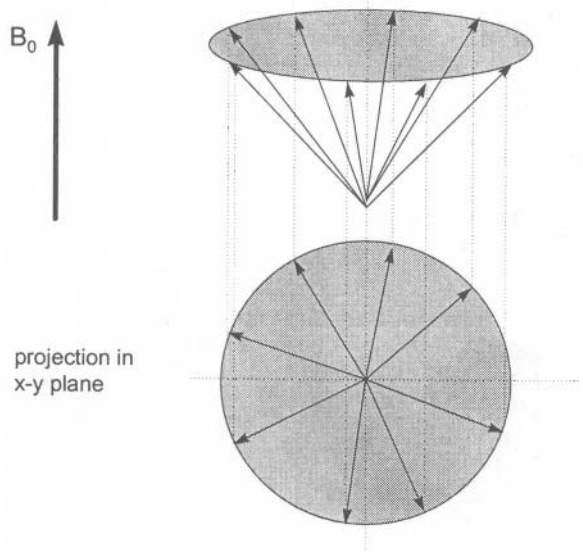

Fig.(10.34) The isotropic projection of spins in the x-y plane when only the static B_0 field is applied

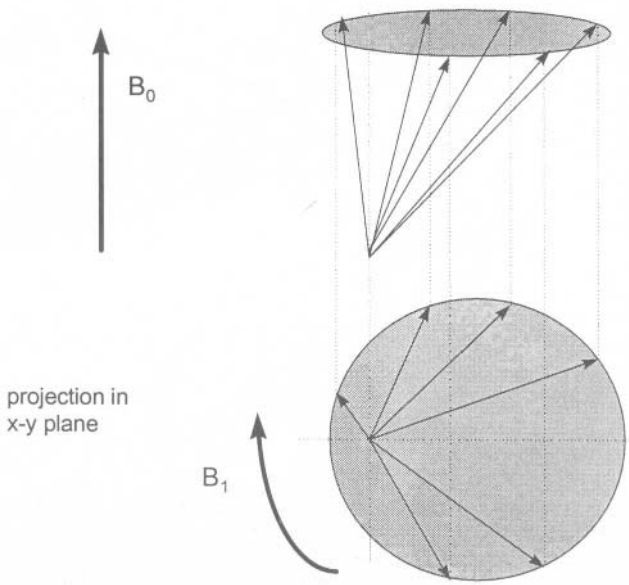

Fig.(10.35) The anisotropic projection of spins in the x-y plane after the time-dependent B_1 field is applied.

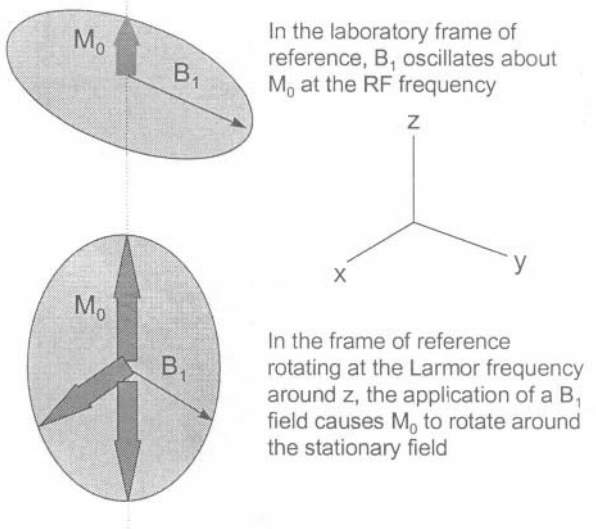

Fig.(10.36) The precession of the net magnetization M_0 about the rf field B_1 in the rotating frame of reference. A relation similar to Eq.(10.27) gives the period of rotation of each spin as $h/\mu B_1$. The application of B_1 for ¼ and ½ of this time gives 90° and 180° pulses respectively.

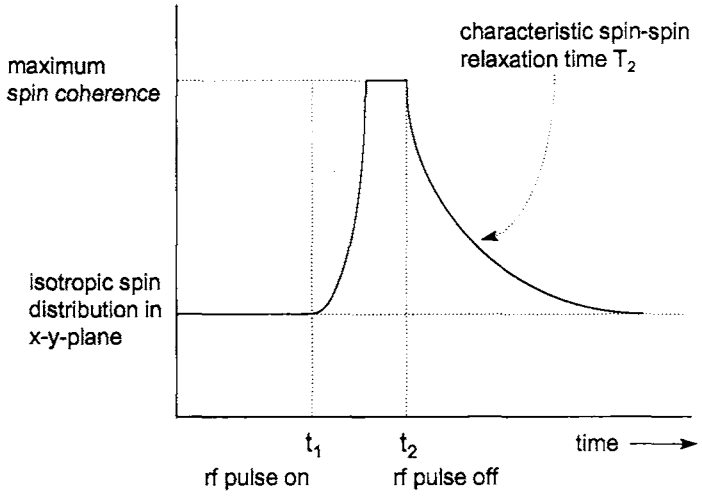

Fig.(10.37) Time dependence of the coherence of spins in the x-y plane which rotate about the *z* axis at the rf frequency of the B_1 field. When this is removed at the end of the RF pulse, the spins lose their coherence and return to an isotropic distribution with a characteristic spin-spin relaxation time T_2.

Relaxation of the magnetization in the *x-y* plane described in Fig.(10.37) applies to the ideal case of a uniform B_0 and a uniform magnetic susceptibility of the object. In practice, however, there is :

- a slight non-uniformity in the susceptibility over the slice width and,
- a small non-uniformity in the applied field. Although modern systems produce fields which are uniform to parts per million in the central region, rather less uniformity is often produced around the edges of the field of view.

These two effects introduce a term T_2^+. The measured relaxation time, T_2^*, is then related to the true value, T_2, through :

$$\frac{1}{T_2^*} = \frac{1}{T_2^+} + \frac{1}{T_2}$$

10.8.3 Magnetic field gradients for projection reconstruction imaging

The unique relation between resonance frequency and applied magnetic field in Eq.(10.27) permits the encoding of the spatial position of a spin when a known field gradient is applied.

Thus, a gradient $\partial B_z/\partial z$ imposed along the *z*-direction creates resonance

conditions at frequency ν_z for all spins in an *xy* plane at a distance Δz from some reference point on the central *z* - axis :

$$\nu_z = \frac{\mu}{hI}\left(B_0 \pm \frac{\partial B_z}{\partial z}\Delta z\right) \qquad (10.30)$$

Slice selection is not restricted to a single frequency, however. To avoid the excitation of spins in only a very small volume, a band of frequencies, centred about a certain value, is selected. This bandwidth determines the slice width. The two are related by :

$$\text{Slice width (in mm)} = \frac{\delta\nu}{\gamma G_z} \qquad (10.31)$$

where $\delta\nu$ is the rf bandwidth and G_z is the magnetic field gradient along the *z* axis.

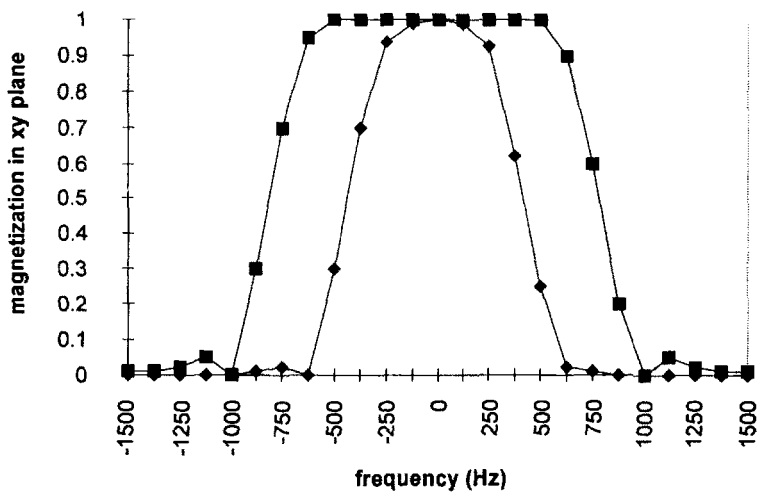

Fig.(10.38) Simulations of rf bandwidths associated with a 6 mm slice width. ◆ G_z = 1 mT m^{-1} : ■ G_z = 6 mT m^{-1}. Bandwidths calculated from Eq.(10.30) are 255 and 1533 Hz respectively using the proton gyromagnetic ratio, γ = 42.58 MHz T^{-1}.

The magnetic field gradient strength is hardware dependent and is usually chosen to be the maximum that the machine is capable of producing. Larger gradients can select sharper slices with less of a Gaussian frequency profile along the *z* axis, Fig.(10.38). Modern machines have gradients up to 20 mT m^{-1}.

Gradients imposed also along the *x* and *y* directions then select only certain spins within the *xy* plane. These are applied simultaneously and in such a way that their resultant direction is given by :

$$\sqrt{\left(\frac{\partial B_y}{\partial y}\right)^2 + \left(\frac{\partial B_x}{\partial x}\right)^2}$$

This is rotated about the z - axis in increments of about 1°. These encoding field gradients, G_{xy}, determine the bandwidth per pixel in an adaptation of Eq.(10.31). Thus :

$$\text{bandwidth per pixel} = \frac{\gamma G_{xy}\ FOV}{N_{pixels}} \qquad (10.32)$$

where *FOV* is the field-of-view and N_{pixels} is the number of pixels in the slice. For a 256 × 256 matrix (N_{pixels} = 256), a *FOV* of 0.35 m and an encoding field gradient G_{xy} of 10 mT m^{-1}, a bandwidth of 582 Hz is obtained for a pixel of size 1.37 mm. The resonance frequency for protons in water and in fat differs by ~220 Hz, so there would be little chemical shift under these conditions. If the pixel size were to be halved however, the bandwidth would reduce to 291 Hz making possible a small discrimination between protons associated with water and with fat.

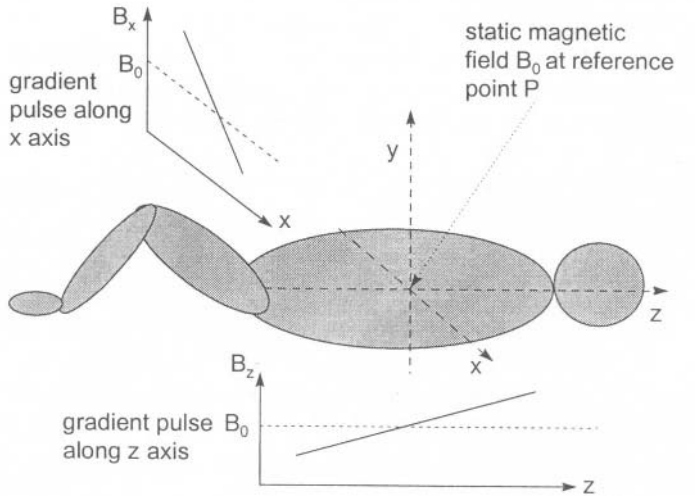

Fig.(10.39) The application of a gradient field in the z direction (B_z) defines the static field B_0 at point P in the *xy*-plane. A further gradient field in the *x*-direction (B_x) defines P along the *x*-axis. The *y* co-ordinate of point P is then specified by another gradient field along the *y*-direction.

Field gradient selection along the *z* axis gives a transaxial image, along the *x*-axis a sagittal image and along the *y*-axis a coronal image. Since all the gradient fields are time-dependent, they are capable of being sequenced in order to select

spins in a certain volume. The signal emitted by the decay of magnetization, along the *z*-axis and in the *x-y* plane, is Fourier analysed to extract the frequencies at which absorption has occurred. It is from this amplitude : frequency spectrum that the final MRI image is produced.

10.8.4 Pulse sequencing

The time correlation between the pulses of radiofrequency and gradient magnetic fields is fundamental to the operation of a MRI scanner.

The Free-Induction-Decay sequence

This is the simplest sequence and although no longer used for medical imaging, serves to introduce the basic ideas [19].

- In period 1, Fig.(10.40), the rf field is applied for a time $h\mathrm{I}/4\mu B_1$ in order to turn the net magetization vector through 90°.
- During periods 1 and 2, the *z*-gradient coils are pulsed. Only those spins in a slice determined by the bandwidth and which is orthogonal to the *z*-axis, for which Eq.(10.30) applies, will resonate and absorb energy.
- Period 3 sees the application of a gradient field in successive 1° intervals to spatially encode in the *xy*-plane. The MRI signal – the decay in the magnetization – is observed in the rf pick-up coils during this period.
- Period 4 must be long enough for the spins to return to their equilibrium state, in order that the next pulse of rf can repeat the process. The total time between rf pulses in period 1 is the called the recovery time, TR .

The magetization M in a given small volume element (voxel) is given by :

$$M = K\,\rho\left[1 - exp\left(-\frac{TR}{T_1}\right)\right] \tag{10.33}$$

In Eq.(10.33) ρ is the density of spins in the voxel, K is a constant and T_1 is the spin-lattice relaxation time. When $TR >> T_1$ there has been sufficient time for all the spins to relax back along the B_0 direction, in which case $M \propto \rho$.

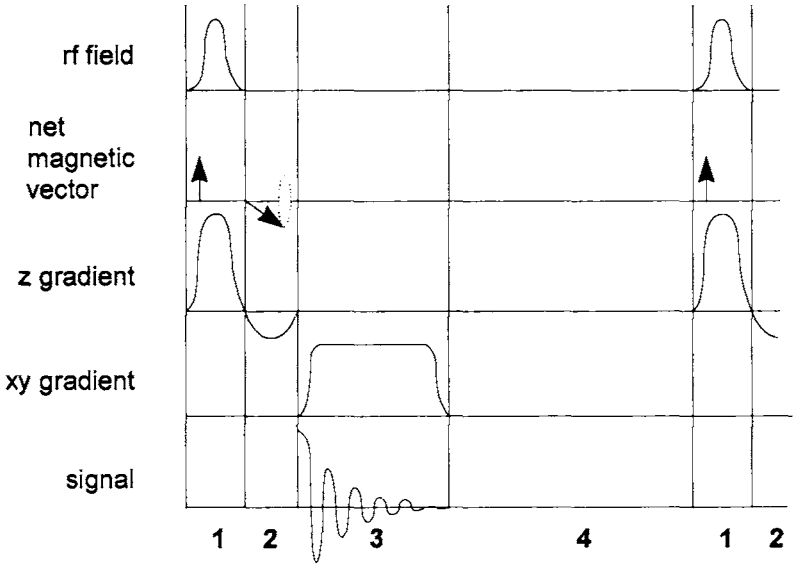

Fig.(10.40) The Free-Induction-Decay sequence. The total time between the 90° rf pulses in each interval 1 is *TR*.

The basic Inversion-Recovery sequence

- In this sequence the rf field is first applied for a time $hI/2\mu B_1$ (a 180° pulse) to orientate the spins anti-parallel to the static field B_0.
- The *z*-axis magnetization relaxes back during period 2 with a time constant T_1 (the spin-lattice relaxation time).
- A second (90°) rf pulse is then applied in period 3. This can only affect those spins which have had time to relax back to the +z direction. If the time between the 180° and 90° rf pulses (τ) is short compared with T_1 then only a small fraction of the original magnetization will have recovered to be turned back into the *xy*-plane.
- During periods 3 and 4 the *z*-axis slice is selected by the *z*-gradient coils and the Free Induction Decay sequence followed from this point.

The size of the signal is now determined by the relative magnitudes of τ and T_1 in addition to the spin density. If $T_1 << \tau$ a large signal is obtained and if $T_1 >> \tau$ there is a small signal. Magnetization in a given voxel is now given by :

$$M = K\,\rho\left[1 - 2exp\left(\frac{-\tau}{T_1}\right) + exp\left(\frac{\tau - TR}{T_1}\right)\right] \qquad (10.34)$$

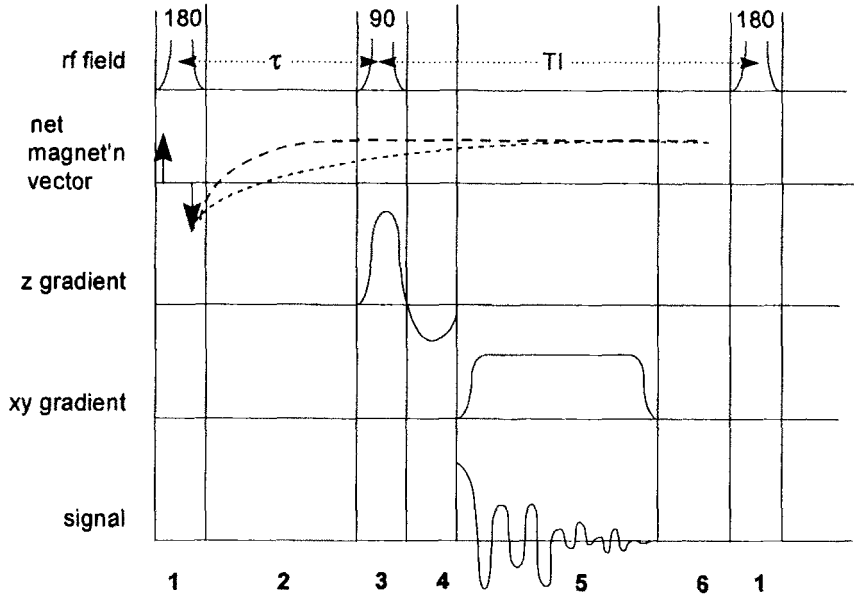

Fig.(10.41) The Inversion-Recovery sequence. The time delay between the 180° pulse in interval 1 and the 90° pulse in interval 3 is τ. The recovery time *TR* is the time between the 180° pulses in intervals 1. The Inversion Recovery time $TI = TR - \tau$.

The Spin-Echo sequence

- A 90° pulse is applied in period 1 and the z-slice selected in periods 1 and 2.
- In period 3 the spins are allowed to relax back along the B_0 direction (as in Free Induction Decay) for a time τ. The characteristic time for this relaxation is T_1 during which the spins begin to de-phase in the *xy*-plane.
- A 180° pulse (period 4) flips all the spins that have relaxed to the +*z* direction during period 3 back into the -*z* direction. Spins that were de-phasing in the *xy*-plane before the 180 pulse are now brought back into phase in the -*z* direction after the elapse of a further period τ (period 5).
- When the *xy*-gradient is applied and the nmr signal gathered in period 6, the magnetization now relaxes back to zero from a negative value.

In addition to the dependence on spin density, the spin-echo signal is now also dependent on T_1, T_2, the echo time $TE = 2\tau$, and the repetition time *TR*.

$$M = K\,\rho\left[1 - 2\exp\left(\frac{-TR}{T_1}\right)\exp\left(\frac{TE}{2T_1}\right) + \exp\left(\frac{-TR}{T_1}\right)\right]\exp\left(\frac{-TE}{T_2}\right) \qquad (10.35)$$

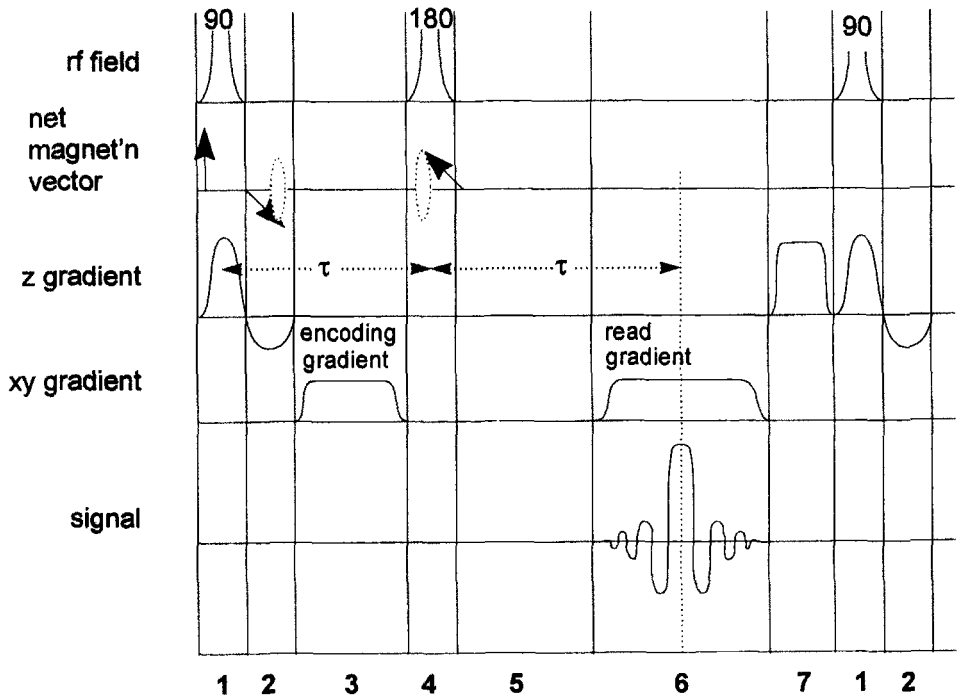

Fig.(10.42) The Spin-Echo sequence. The echo time, $TE = 2\tau$, extends from the centre of the 90° pulse of period 1 to the centre of the echo which occurs mid-way through the *xy*-gradient of period 6. The *spoiler* in period 7 destroys any remaining transverse magnetization and thereby prevents image artefacts.

Under usual imaging conditions, TE is in the order of 5 ms and T_1 lies in the range ~ 6 – 800 ms in a static field of 1.5 T. In this case, Eq.(10.35) reduces to :

$$M = K\,\rho\left[1 - exp\left(\frac{-TR}{T_1}\right)\right] exp\left(\frac{-TE}{T_2}\right) \qquad (10.36)$$

A comparison of images presented in Figs.(10.43) and (10.30) illustrates some important features of PET and MRI techniques. Anatomical structures of tissue can be characterized by either proton density, spin-lattice or spin-spin relaxation times in MRI with good contrast and good spatial resolution. The inferior spatial resolution of PET, on the other hand, is compensated by its ability to provide functional images. Thus, the normal brain in Fig.(10.30) would reveal a different distribution of uptake if there was present a tumour or other lesion which had an abnormal pathology.

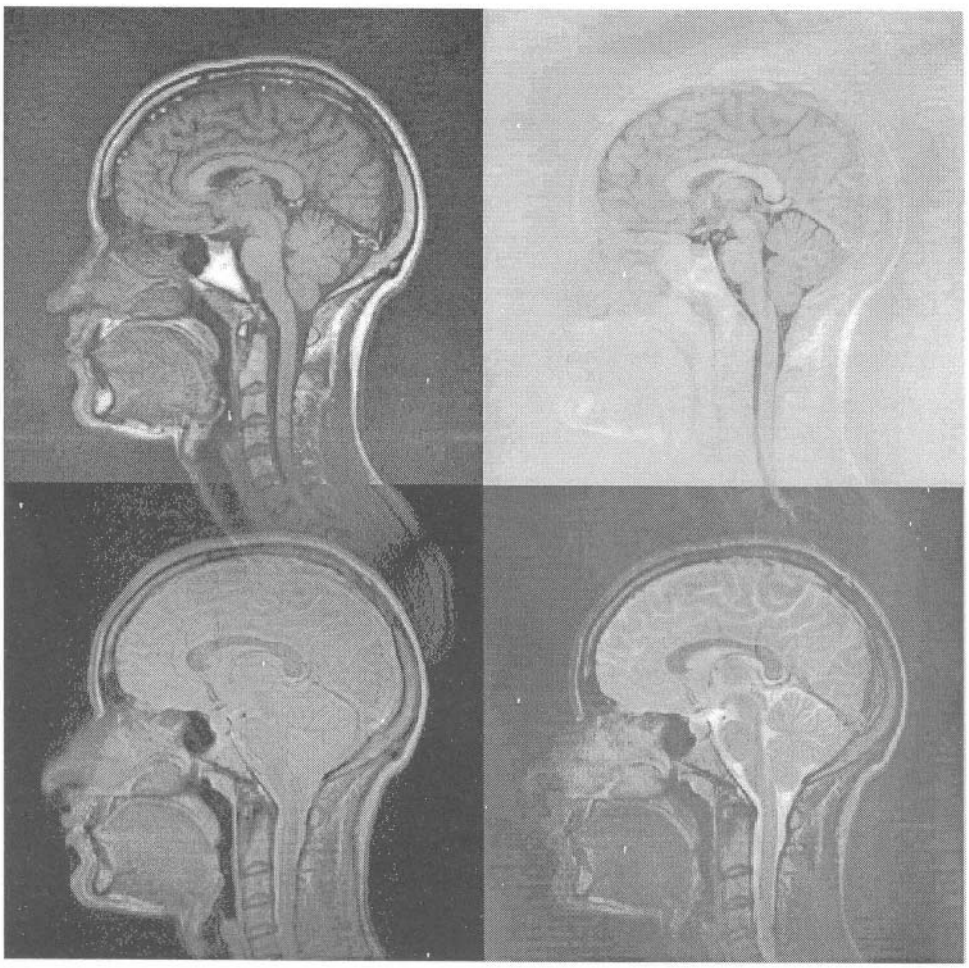

Fig.(10.43) Sagittal MRI images taken at B_0 = 1.5 T. Clockwise from the top-left: T_1 weighted : Inversion recovery : T_2 weighted : Proton density.

References

[1] E.Fenyves and O.Haiman, *The Physical Principles of Nuclear Radiation Measurements*, (Academic Press, New York, 1969).

[2] W.J.Meredith and J.B.Massey, *Fundamental Physics of Radiology*, 3rd Edition (John Wright and Sons,Ltd, Bristol 1977).

[3] M.Gambacini, A.Taibi, A Del Guerra, M.Marziani and A.Tuffanelli, *Phys.Med.Biol.* **41**(12) (1996) 2799.

[4] J.R.D.Earnhart and E.L.Chaney, *Phys.Med.Biol.* **42**(12) (1997) 2531.

[5] W.Zhao and J.A.Rowlands, *Med.Phys.* **24**(12) (1997) 1819.
[6] W.Zhao, I.Blevis, S.Germann, J.A.Rowlands, D.Waechter and Z.Huang, *Med.Phys.* **24**(12) (1997) 1834.
[7] W.Zhao, D.Waechter and J.A.Rowlands, *Med.Phys.* **25**(4) (1998) 527.
[8] W.Zhao, J.Law, D.Waechter, Z.Huang and J.A.Rowlands, *Med.Phys.* **25**(4) (1998) 539.
[9] ICRU Report 46, *Photon, Electron, Proton and Neutron interaction data for Body Tissues,* (International Commission on Radiation Units and Measurements, Bethesda, Maryland, 1992).
[10] AAPM Report 39, *Specification and Acceptance Testing of Computed Tomography Scanners*, (American Institute of Physics, New York, 1993).
[11] E.L.Nickoloff and R.Riley, *Med.Phys.* **12**(4) (1985) 437.
[12] C.E.Metz and K.Doi, *Phys.Med.Biol.* **24**(6) (1979) 1079.
[13] *CRC Handbook of Chemistry and Physics*, Ed.R.C.Weast, (CRC, Boca Raton, USA,1983) p. A–99.
[14] Documents of the NRPB, *Protection of the Patient in X-ray Computer Tomography*, **3** (4) (1992).
[15] J.Hsieh, *Med.Phys.* **24**(9) (1997) 1375.
[16] G.Wang and M.W.Vannier, *Med.Phys.* **24**(10) (1997) 1635.
[17] D.J.Heuscher and M.Vembar, *Med.Phys.* **26**(2) (1999) 277.
[18] S.Narayana, R.D.Hichwa, L.L.Boles Ponto, J.A.Ponto and G.L.Watkins, *Med.Phys.* **23**(1) (1996) 159.
[19] Med Phys ref on blood;brain
[20] A.Kumar, D.Welti and R.R.Ernst, *J.Mag.Res.* **18** (1975) 69.
[21] W.A.Edelstein, J.M.S.Hutchison, G.Johnson and T.Redpath, *Phys.Med.Biol.* **25** (1980) 751.

CHAPTER 11

RADIATION PROTECTION

11.1 Introduction

The International Commission on Radiation Protection (ICRP) aims to provide a general system of radiological protection that can be applied to any situation in which humans are, or are likely to be, exposed to radiation [1]. It publishes recommendations, the latest being ICRP 60 [1], which draw on scientific evidence as well as using value judgements to assess the relative risks of radiation exposure.

At low dose levels, which are the main concern for protection of the general population, it is most important to establish whether or not there exists a dose threshold below which no effect is present. If there is not, then a finite risk must always be accepted however low the dose. Conversely, if there is a threshold, it no longer becomes possible to apply the following proportional relationships that are the basis of practical radiation protection [2]. These are that :

- the dose received by an organ or tissue can be averaged over the organ or tissue,
- doses received at different times can be added, and
- the dose from one source can be considered independently of the dose from any other source.

11.2 Units and Special Parameters

In section 9.4 reference was made to the concept of Relative Biological Effectiveness (RBE). This was used to relate the biological response of tissue to absorbed dose from radio-therapeutic beams of different qualities. Publication 60 of the ICRP [1] redefined this relation by making use of two parameters :

- the Equivalent Dose in an organ, and
- the Effective Dose.

For the sole purpose of expressing dose limits, Equivalent Dose and Effective Dose have been recommended by ICRP as being the best way to correlate radiation exposure with the risk of developing cancer.

In this chapter, the use of the term "dose", in units of Sievert (Sv), is applied to Effective Dose unless otherwise stated. It applies to all exposure conditions, whether

caused internally or externally, and represents an absorbed dose weighted for different radiations and for the carcinogenic biological sensitivity of different organs.

11.2.1 Equivalent dose

The Equivalent Dose $H_{T,R}$ (in Sv) received by tissue T which has been exposed to a dose $D_{T,R}$ (in Gy) of radiation R is then specified using :

$$H_{T,R} = w_R \; D_{T,R}$$

Table (11.1) Radiation Weighting Factors from [1], [3]. Both Reports give the identical weighting factors apart from the value for protons. Note how the radiation weighting factor reflects the distribution of radiation quality, see Fig.(9.34).

Radiation and energy range	w_R (NCRP-116)	w_R (ICRP-60)
X-and γ-rays, electrons, positrons, muons	1	1
Neutrons, $E_n < 10$ keV	5	5
$10 < E_n < 100$ keV	10	10
$0.1 < E_n < 2$ MeV	20	20
$2 < E_n < 20$ MeV	10	10
$E_n > 20$ MeV	5	5
Protons, $E_p > 2$ MeV (not recoil protons)	2	5
α - particles, fission fragments, etc	20	20

Table (11.2) Tissue Weighting Factors from references [1] and [3]

Tissue	w_T
Gonads	0.20
Red bone marrow	0.12
Colon	0.12
Lung	0.12
Stomach	0.12
Bladder	0.05
Breast	0.05
Liver	0.05
Oesophagus	0.05
Thyroid	0.05
Skin	0.01
Structural bone	0.01

Since many radiation fields consist of more than one component – for example, photons and neutrons with a range of energies – the overall equivalent dose is given by :

$$H_T = \sum_R w_R \, D_{T,R} \tag{11.1}$$

11.2.2 Effective dose

To account for the different radio-sensitivity of different body tissues, a tissue weighting factor w_T is also used, Table (11.2). This then defines the Effective Dose, E.

$$E = \sum_T w_T H_T \tag{11.2}$$

In the compilation of a table of tissue weighting factors it is implicitly assumed that w_T does not depend on radiation quality. It is therefore assumed to be independent of w_R [4].

11.3 Background Levels

Figures given in Table (1.1) for contributions to the average radiation background in the UK hide important variations for certain sub-groups of the population. The National Radiological Protection Board (NRPB) provides estimates for some of these regional and occupational distributions [5]. Changes in the estimates for the years prior to 1986 and those up to 1994 are due largely to :

- the improvements in the monitoring of local radon concentrations,
- the more widespread use of computerized tomography in diagnostic radiology, and
- reduced discharges and radioactive fallout to the environment.

Variations in geographical region and occupational grouping within the UK can result in significant changes from the mean annual background dose burden.

The following figures and table show variations due to :

- a reduced radioactive fallout with time, Fig.(11.1)
- the increased cosmic ray contribution with altitude above mean sea level, Fig.(11.2)
- the geographical variation of radon contribution to the total burden, Table (11.3)
- the reduced radioactive discharge to the environment in a particular region, Fig.(11.3)

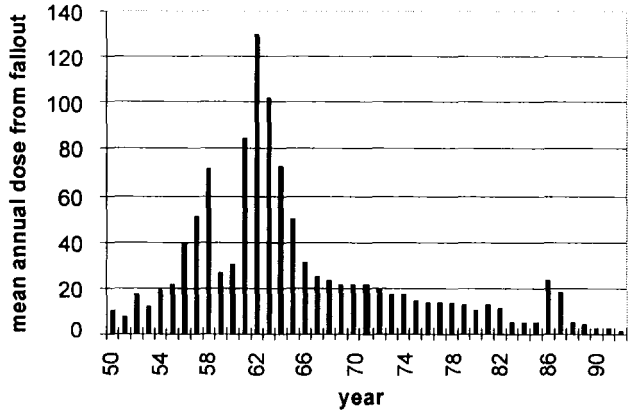

Fig. (11.1) The annual mean dose to the UK public (μSv) from radioactive fallout. The large peaks in the late 1950's and early 1960's are due to weapons testing. The smaller peak in 1986 is due to the Chernobyl accident. Although the current mean is ~ 5 μSv, areas with heavy average rainfalls receive doses up to 15 μSv [5]. With permission from NRPB.

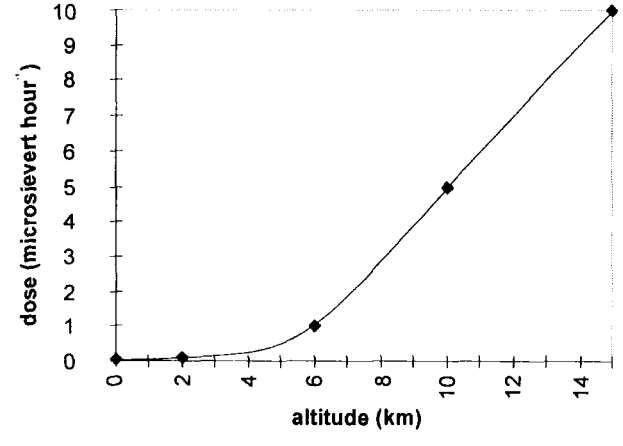

Fig.(11.2) Increase in dose due to cosmic rays (μSv hr^{-1}) with altitude. The annual dose at mean sea level varies with latitude in the range 200 - 300 μSv. Points correspond to the altitudes above mean sea level, a high altitude city such as Mexico, a Himalayan Peak, and subsonic and supersonic airliner travel. Frequent air travellers can raise their mean annual dose from cosmic rays from 260 μSv to ~700 μSv [5]. With permission from NRPB.

It is apparent from Fig.(11.2) that radiation levels for astronauts in earth orbit (~300 km) are well in excess of sea level values. Special limits are therefore likely on the Maximum Permissible Dose for annual and career-accumulated exposures [6], [7]. Doses of ~150 mSv have been measured for a six month mission in orbit.

Table (11.3) The variation of average radon dose with region in the UK. High levels in South West and Central England and North East Scotland are due to the relatively large (but still small in absolute terms) deposits of uranium in the geological strata. The country-wide mean dose from radon is 1.3 mSv. Levels out of doors and in buildings with under-floor ventilation are considerably less than the quoted figures [5]. In any one area, radon dose can vary by several orders of magnitude.

Region	Radon Dose (mSv)	Total Dose (mSv)	%
Cornwall	6.4	7.8	82
Devon	4.0	5.3	75
Somerset	3.3	4.5	73
Northants	2.6	4.0	65
Derbyshire	2.4	3.7	65
London	0.9	2.1	43

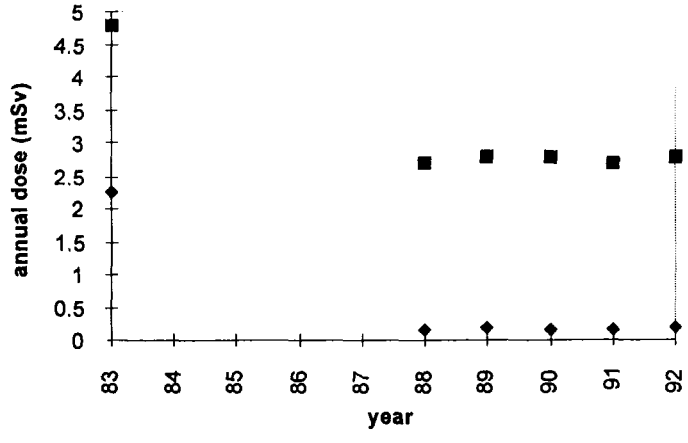

Fig. (11.3) Annual dose received by heavy consumers of seafood in Cumbria. ■ total dose: ◆ dose due to radioactive discharges from nuclear industry: The current dose burden for this group due to discharges continues to be in the range 150 - 200 μSv. The current national average due to discharges from all sources (nuclear industry and medical) is 0.4 μSv [5]. With permission from NRPB.

11.4 Stochastic and Deterministic Effects of Radiation

Exposure of living organisms to radiation gives rise to two types of effect :

- The possibility, however small, that increased exposure to radiation will result in an increased probability of genetic mutations or cancer induction. These are the stochastic (random) effects of radiation and they may not become evident for some considerable time after the exposure.

- Where the severity of the response to radiation increases with dose. This is a deterministic (formerly non-stochastic) effect. In the case of a radiation accident, for example, where the doses may well have been appreciable, deterministic effects such as skin erythema (reddening and breakdown) or cataract formation become evident quite soon after the exposure. It is likely that a non-stochastic effect will also be accompanied by stochastic effects.

The delayed reaction to a stochastic effect is expressed by a risk factor (also known as a probability coefficient). These factors can be individually assigned to different conditions (leukaemia) or grouped together to include an overall category (solid cancers of all types).

If the risk factor for leukaemia induction is 3×10^{-6} mSv^{-1}, for example, then a population of 10^6 irradiated with 1 mSv would be expected to yield 3 extra cases, on average, over and above the normal incidence. Alternatively, the risk factor for the excess number of solid cancers over a lifetime in the population at large is expressed as 50×10^{-6} mSv^{-1}. The interpretation is that 50 extra patients with solid cancers would be expected in a one million population irradiated with 1 mSv. Risk Estimates agreed by both ICRP and NCRP [1],[3] are summarized in [4],[8].

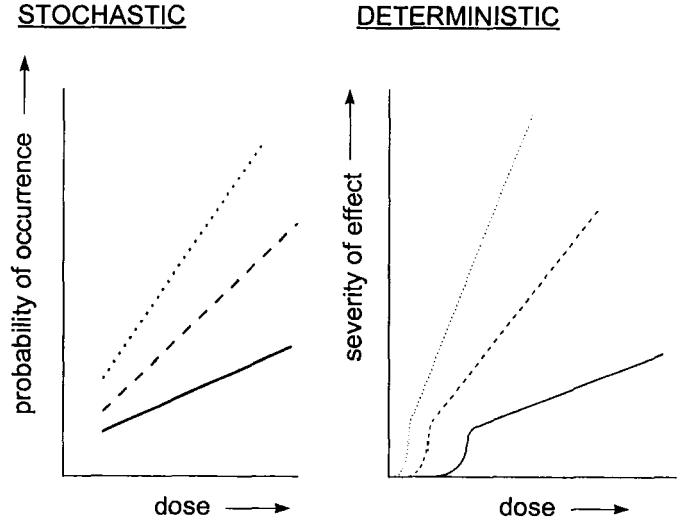

Fig.(11.4) The different lines on the stochastic graph refer to different conditions, e.g. leukaemia, chromosome aberrations, etc. Different lines on the deterministic graph refer to the response of different groups of people, e.g. to skin damage, cataract formation, etc. Note the presence of a threshold in the deterministic effects.

An example of the progression from severe deterministic to stochastic effects of radiation was provided by a case of industrial exposure of a worker's hand. The dose to the hand was probably ~100 Gy and to the whole body ~10 Gy over a time

span of about a decade. Outward evidence of exposure was first provided by redness and swelling of the right index finger. This was followed by dermatitis and heavy infection which eventually required amputation of the finger. Several years later acute myeloid leukaemia eventually culminated in the death of the person [9].

Table (11.4) Risk Estimates for Stochastic Effects. The figures refer to the lifetime risk of contracting one of the outcomes for all ages (Whole Population) and for the working population (Adult Worker).

Outcome	Whole Population	Adult Workers
Fatal Cancer	50×10^{-6} mSv^{-1}	40×10^{-6} mSv^{-1}
Non-fatal Cancer	10×10^{-6} mSv^{-1}	8×10^{-6} mSv^{-1}
Genetic Effects	13×10^{-6} mSv^{-1}	8×10^{-6} mSv^{-1}

11.5 Radiation Carcinogenesis

The data sets which are used as the bases of radiation protection come from a variety of sources [8],[10]. Some of these are :

- the study of disease and mortality rates of the Hiroshima and Nagasaki atomic bomb survivors,
- the survival rates of patients who had suffered from ankylosing spondylitis,
- tuberculosis patients given chest fluoroscopies,
- irradiation of children for ringworm of the scalp,
- the national registers of radiation workers.

In many of these cases, the greatest difficulty in associating the pathological condition with the radiation exposure lies in the precision of the dosimetry. The data therefore have to be complemented by controlled radiation biology experiments on both cellular and mammalian systems.

11.5.1 Dose : response relationships

The mechanisms of radiation action are a continuing area of study. Many factors are responsible for the large uncertainty between the exposure to radiation and the ensuing biological response. This is especially true at the low doses experienced under radiation protection conditions. These factors are :

- the stochastic nature of energy deposition resulting from both primary and secondary charged particles,
- the complexity of the target (ultimately the DNA) and the manner in which the energy deposited manifests itself in a pathological condition,
- the dynamic nature of the target system,

- the large number of end-points (chromosome aberrations, cell death, *etc.*).

Radio-biology experiments have established certain dose:response functions to describe the incidence of different end-points in a number of cellular as well as mammalian systems irradiated by different types of radiation. These functions are formulated on the basis of models which consider the spatial correlation between single- or multihit events within the target. These models are applied in the following circumstances :

- In radiotherapy the target is a collection of tumour cells, sometimes at a specific location and sometimes distributed throughout the body. The cell death end-point is clearly of relevance to the high doses delivered here. Analysis of cell survival is described adequately using a linear-quadratic function :

$$N = N_0 \exp\left(-\alpha D - \beta D^2\right) \tag{11.3}$$

  This gives the number, N, of surviving cells after irradiation to dose D. The coefficients α and β are generally regarded as being associated with non-repairable and repairable damage respectively, with values in the range 1—0.1 Gy^{-1} and 0.1— 0.01 Gy^{-2}.
- End-points such as point mutations and chromosome aberrations in cells might be more relevant to initiation events which eventually lead to cancer. Experiment shows that these mutational events in cells are induced with a linear-quadratic, $(\alpha_1 D + \alpha_2 D^2)$, dependence on dose. Thus, cancer induction data might be modelled using an induction term for mutational events in cells and a cell killing term as in Eq.(11.3). This results in Eq.(11.4) [8].

$$P = \left(\alpha_0 + \alpha_1 D + \alpha_2 D^2\right) exp\left(-\beta_1 D - \beta_2 D^2\right) \tag{11.4}$$

  Here, the α terms describe defect induction resulting from spontaneous, (α_0), 1-hit and 2-hit components, while the β terms describe 1-and 2-hit components for cell death.

11.5.2 Effects of dose, dose-rate and LET in cancer induction

Experimental verification of radiation action has only been obtained for doses large enough to have produced a measurable and statistically significant response. For most biological systems, however, these doses are greater than those of concern in radiation protection. Since the ultimate purpose of radiation protection is to assess the probability of cancer induction from the known dose received by an individual, it is first necessary to extrapolate the effects at high dose down to the low doses of interest. The task is then to relate all factors which influence the pathway between energy deposition in the prime target - DNA in the cell nucleus - and its subsequent

expression as a cancer. This is done with a model such as Eq.(11.4).

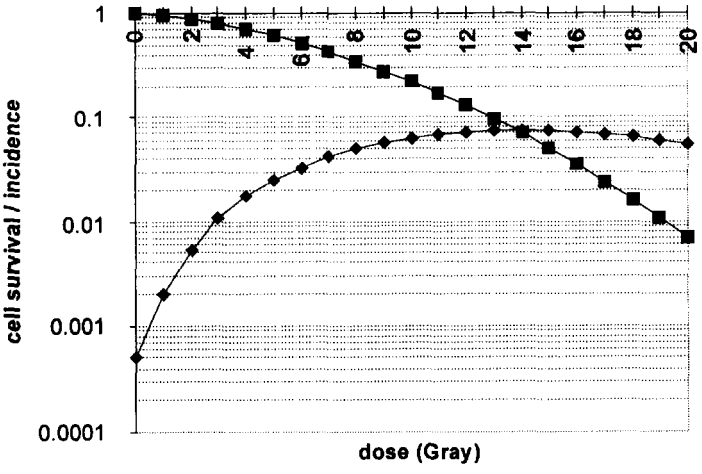

Fig. (11.5) Typical survival and incidence curves against dose (Gy) in the range 0 - 20 Gy.
(■) Cell survival using Eq.(11.3) and $\alpha = 0.05$ and $\beta = 0.005$:
(◆) Incidence of a defect and eventual cell death using Eq. (11.4) together with $\alpha_0 = 0.0005$, $\alpha_1 = 0.0005$, $\alpha_2 = 0.001$, $\beta_1 = 0.001$ and $\beta_2 = 0.005$.

The relevant factors to be considered are :

- Whether the action is direct. In this case the energy is deposited directly into the DNA by the primary or secondary radiation.
- Whether energy is deposited initially into a neighbouring molecule - producing an $OH^{\bullet}$ radical in water, for example - which then interacts with the DNA target. This is called indirect action.
- The efficiency of damage repair processes.
- Whether one or more hits are produced by the same primary particle in the same target molecule.

The physical parameters that govern the above factors are total dose, dose-rate and LET (section 9.4). Fig. (11.6) illustrates the link between cancer incidence and the α and β coefficients in Eq. (11.4).

Most experimental evidence of cancer induction comes from high doses of low LET radiation at high dose-rate. In this case, the small probability of a multihit event comes either from low energy electron tracks which traverse a DNA strand or from a high spatial concentration of individual radiation spurs (section 6.6). The probabilities of induced effect (α terms) and cell death (β terms) are therefore both small except at large doses, as shown in curve C, Fig.(11.6). At very low doses, the induction is determined solely by the α_1 term (= 0.0002) which is generally assumed to be dose-rate independent.

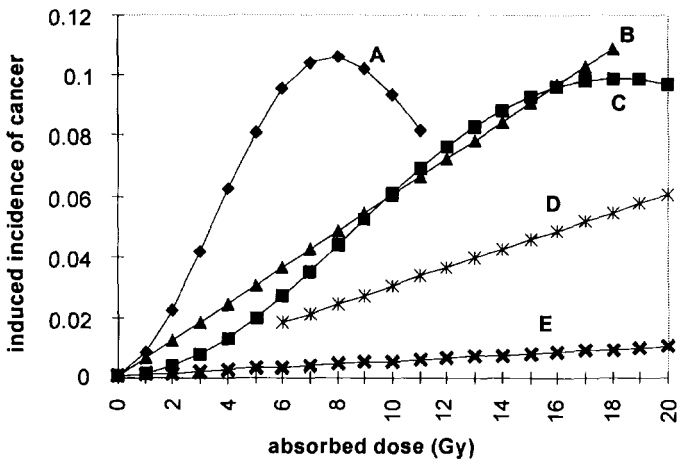

Fig. (11.6) Dose-response relationships for cancer induction using Eq. (11.4) and spontaneous incidence coefficient $\alpha_0 = 0.0005$: Data taken from [8] with permission.
◆ high LET: $\alpha_1 = 0.004$, $\alpha_2 = 0.004$, $\beta_1 = 0.005$, $\beta_2 = 0.015$. Curve A.
▲ low LET: linear, no threshold: $\alpha_1 = 0.006$. Line B.
■ low LET: high dose-rate: $\alpha_1 = 0.0002$, $\alpha_2 = 0.0008$, $\beta_1 = 0.0004$, $\beta_2 = 0.003$. Curve C.
✱ low LET: low dose rate: $\alpha_1 = 0.003$. Line D.
✖ low LET: limiting slope for low dose-rate. $\alpha_1 = 0.0002$. Line E.

However, if a linear relation were to be used to fit the high dose experimental data, as in line B, the induction at low doses would be very much higher than if only the linear term of curve C were used (line E). Thus, a dose of 2 Gy would have an induction coefficient of ~ 0.01 for line B and 0.0004 for line E. This has considerable importance in the definition of what might constitute a "safe" dose of radiation. The ratio of these slopes (line B/line E) is sometimes used as an estimate of the reduction factor to be applied to data obtained at higher doses and high dose-rates in setting risk estimates for radiation protection.

Information on this critical dose:response relation at low doses can be obtained from experimental low LET studies at different dose-rates. These point to the effectiveness of the repair mechanisms which tend to reduce the biological effect following a given dose delivered at a low dose-rate, Fig.(11.7). Ultimately the dose-rate becomes so high that the damage is irreparable and this puts an upper limit on the initial slope of the dose:response relation, Fig.(11.6). Many of the experimental data which underpin present knowledge of low dose effects may have been performed at dose-rates which were not sufficiently high to reach this limit. It is therefore present practice to allocate a response function – such as line D – which has a slope (=0.003) approximately between the two extremes (0.0002 and 0.006). This factor of ~ 2 reduction for the effects of dose-rate in the extrapolation of high to low doses is referred to as the Dose-Rate-Effectiveness Factor (DREF) [8].

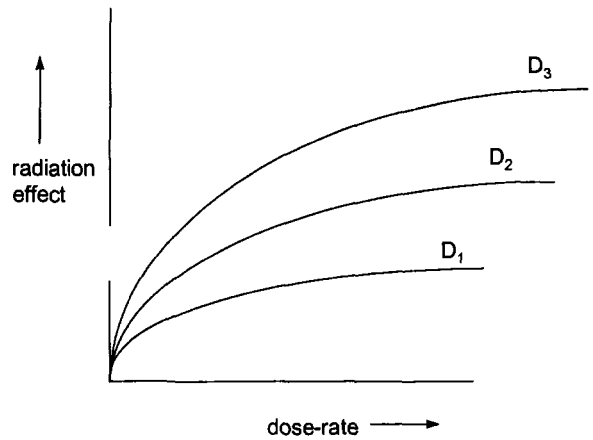

Fig. (11.7) The effect of dose-rate on the radiation response for total doses $D_3 > D_2 > D_1$. For a given total dose at low dose-rates, repair mechanisms are able to reduce the biological response. Eventually the dose-rate becomes so high that the biological damage becomes irreparable.

There is a higher probability that a densely ionizing particle traverses a DNA target molecule in high LET radiation. This then produces a greater fraction of multihit events and gives rise to much larger α_1 and β_1 coefficients in Eq.(11.4). Curve A in Fig.(11.6) indicates the likely dose:response relation. In general, a larger probability of cancer induction is accompanied by a larger probability of cell death. Cell death is the more likely consequence at high doses however. Exposure to low doses of high LET radiation (α-particles, neutrons..) are therefore more likely to induce cancer than the same absorbed dose at low LET.

The existence of protective, as distinct from repair, mechanisms has been studied by a small number of workers. If such processes are initiated by radiation exposure there is the possibility that low doses of radiation may be life enhancing. This effect is known as Radiation Hormesis. There is no general acceptance that available data can be interpreted in these terms.

11.6 Maximum Permissible Levels of Exposure

The principles of radiation protection are enshrined in the following :

- Any practice using ionizing radiation must be justified. The advantages must outweigh the disadvantages and there must be no other way of achieving the stated objective.
- Doses both to workers and to the public must be optimized. This means that doses must be reduced until it is no longer economic to reduce them further.
- Doses must be below the prescribed limits which are judged to be at the boundary between acceptability and intolerability. If the dose limits cannot be met the

practice cannot be justified.

Recommended dose limits are set at a judged level of risk. The two categories for which exposure limits are set are :

- the public at large, and
- those who receive exposure through their occupation.

Evidence of detrimental effects of radiation exposure are gathered from many sources before assessment by a number of national (NRPB in the UK, NCRP in the US) and international (ICRP) bodies. Reports are issued periodically to suggest the adoption of limits of exposure for the two categories above [1],[3]. These are summarized in Table (11.5) [4].

The recommended dose limits are set at a judged level of risk. These are that a worker should not be expected to accept a lifetime risk of cancer greater than 3 - 4 % while a member of the public should not have to accept a risk greater than 0.3 - 0.4%. Using risk estimates for fatal cancer from Table (11.4) and the lower of these numbers in each case, we have :

- Workers with a working life of 40 years: $0.03 = (40 \text{ years}) \times (40 \times 10^{-6} \text{ mSv}^{-1}) \times$ (dose limit), giving a dose limit of $\sim 20 \text{ mSv yr}^{-1}$.
- Member of the public with a life-span of 70 years: $0.003 = (70 \text{ years}) \times (50 \times 10^{-6} \text{ mSv}^{-1}) \times$ (dose limit), giving a dose limit of $\sim 1 \text{ mSv yr}^{-1}$.

11.7 Practical Methods of Reducing Dose

The three main principles of protection from an external (to the body) source of radiation are :

- to minimize the time spent by the person in the vicinity of the source,
- to maximize the distance between the person and the source,
- to use sufficient and appropriate shielding material between the source and the person.

While the precepts of dose reduction are self-evident in many ways, judgement is always necessary in selecting the most appropriate line of defence from exposure. For example, in seeking to keep the total exposure within permissible levels :

- long handled tongs may be used to increase the distance between a worker and a task which needs to be performed on or near an intense source. If the task is so delicate or precise and the tongs insufficiently manipulative that the worker spends a considerable length of time making unsuccessful attempts, it may be less detrimental to forego the use of tongs and decrease the distance

for the shorter time it takes to carry out the task by hand.

- the appropriate selection of shielding, if employed, is paramount. Secondary radiation can be produced in the shield material itself and reduce its effectiveness in contributing to overall protection.

Points to remember when selecting the most suitable shielding material for the following different types of radiation are :

- β-particles and electrons. The higher the energy the more likely it is that bremsstrahlung photons will be produced. The most appropriate initial shielding is therefore low Z material (e.g. perspex) to degrade the electron energy by collision loss. Secondary shielding of lead can then be used if necessary to provide further protection against photons.
- Positrons. Positrons of whatever energy will always be a source of annihilation photons at 511 keV. Lead shielding is most effective.
- Neutrons. These should first be moderated to thermal energies using material with a high concentration of H or C atoms. A layer of B, Cd or Gd, all of which have high absorption cross-sections for thermal neutrons, then absorbs the neutron flux. Both of these functions are sometimes combined by the use of borated polyethylene or similar. Secondary γ-rays, both prompt and decay, are then generated. These are attenuated using a further layer of lead or concrete shielding.
- Photons. Shielding against MeV photons is most easily (and less expensively) achieved using high density concrete rather than lead. This is because MeV photons interact primarily by Compton scatter and not photoelectric absorption. A large electron density is therefore more appropriate than a high Z nucleus.
- Photon scatter is most easily reduced by minimizing the amount of high Z material visible to the source and by the avoidance of a direct line of sight. This technique is employed in the construction of interlocking maze entrances to linac rooms.

Table (11.5) Summary of Maximum Permissible Levels of Exposure for the public at large and occupationally exposed radiation workers from [1] and [3].
All limits apply. The limits to specific organs are necessary to prevent deterministic effects to some organs even when effective dose is not exceeded.

Parameter	ICRP 60 [1]	NCRP 116 [3]
Public		
Effective Dose:		
Annual	1mSv: 5y average $\leq$ 1 mSv	1 mSv: if continuous 5 mSv: if infrequent
Equivalent Dose:		
Annual	15 mSv: eye lens 50 mSv: skin, hands, feet	15 mSv: eye lens 50 mSv: skin, hands, feet
Occupational		
Effective Dose:		
Annual	50 mSv	50 mSv
Cumulative	$\leq$100 mSv in 5 yr	10 mSv $\times$ age (yr)
Equivalent Dose:	150 mSv: eye lens	150 mSv: eye lens
Annual	500 mSv: skin, hands, feet	500 mSv: skin, hands, feet

References

[1] ICRP Publication 60, *Annals of the ICRP,* **21**(1-3) (Pergamon Press, New York 1991).

[2] R.H.Clarke, *J.Radiol.Prot.* **18**(3), (1998) 18.

[3] NCRP Report 116, *National Council on Radiation Protection and Measurements*, (Bethesda, Maryland 1993).

[4] J.E.Turner, *Atoms, Radiation and Radiation Protection*, (J.Wiley, New York, 2nd edition 1995)

[5] NRPB, *Radiation Doses - Maps and Magnitudes*, (National Radiological Protection Board, 2nd edition 1994).

[6] W.K.Sinclair, *Advances in Space Research*, **6** (1986) 335.

[7] F.A.Cucinotta et.al. *NASA Technical Paper 3098*, (NASA Office of Management, 1991, Washington).

[8] R.Cox, C.R.Muirhead, J.W.Stather, A.A.Edwards and M.P.Little, Doc.NRPB, **6**(1) (1995).

[9] D.C.Lloyd, A.A.Edwards, E.J.Fitzsimons, C.D.Evans, R.Railton, P.Jeffrey, T.G.Williams, A.D.White, M.Ikeya and H.Sumitomo, *Occup.Environ.Med.* **51** (1994) 713.

[10] United Nations Scientific Committee on the Effects of Atomic Radiation, (UNSCEAR Reports 1988,1993,1994 United Nations, New York).

Index

Symbols

A

B

C

D

E

F

G

H

I

J

K

L

M

N

O

P

Q

R

S

T

U

V

W

X

Y

Z